Magnetic strain contributions in laser-excited metals studied by time-resolved X-ray diffraction

ALEXANDER VON REPPERT

PUBLIKATIONSBASIERTE DISSERTATION

zur Erlangung des akademischen Grades
doctor rerum naturalium (Dr. rer. nat.)
in der Wissenschaftsdisziplin: Experimentalphysik

Universität Potsdam
Mathematisch-Naturwissenschaftliche Fakultät
Institut für Physik & Astronomie
Ultraschnelle Dynamik in kondensierter Materie
Disputation: 03. November 2021

Betreuer: Prof. Matias Bargheer
Weitere Gutachter: Prof. Steve Johnson (ETH Zurich), Prof. Pascal Ruello (Le Mans Universite)

Published online on the
Publication Server of the University of Potsdam:
https://doi.org/10.25932/publishup-53558
https://nbn-resolving.org/urn:nbn:de:kobv:517-opus4-535582

Abstract

In this work I explore the impact of magnetic order on the laser-induced ultrafast strain response of metals. Few experiments with femto- or picosecond time-resolution have so far investigated magnetic stresses. This is contrasted by the industrial usage of magnetic invar materials or magnetostrictive transducers for ultrasound generation, which already utilize magnetostrictive stresses in the low frequency regime.

In the reported experiments I investigate how the energy deposition by the absorption of femtosecond laser pulses in thin metal films leads to an ultrafast stress generation. I utilize that this stress drives an expansion that emits nanoscopic strain pulses, so called hypersound, into adjacent layers. Both the expansion and the strain pulses change the average inter-atomic distance in the sample, which can be tracked with sub-picosecond time resolution using an X-ray diffraction setup at a laser-driven Plasma X-ray source. Ultrafast X-ray diffraction can also be applied to buried layers within heterostructures that cannot be accessed by optical methods, which exhibit a limited penetration into metals. The reconstruction of the initial energy transfer processes from the shape of the strain pulse in buried detection layers represents a contribution of this work to the field of picosecond ultrasonics.

A central point for the analysis of the experiments is the direct link between the deposited energy density in the nano-structures and the resulting stress on the crystal lattice. The underlying thermodynamical concept of a Grüneisen parameter provides the theoretical framework for my work. I demonstrate how the Grüneisen principle can be used for the interpretation of the strain response on ultrafast timescales in various materials and that it can be extended to describe magnetic stresses. The class of heavy rare-earth elements exhibits especially large magnetostriction effects, which can even lead to an unconventional contraction of the laser-excited transducer material. Such a dominant contribution of the magnetic stress to the motion of atoms has not been demonstrated previously. The observed rise time of the magnetic stress contribution in Dysprosium is identical to the decrease in the helical spin-order, that has been found previously using time-resolved resonant X-ray diffraction. This indicates that the strength of the magnetic stress can be used as a proxy of the underlying magnetic order. Such magnetostriction measurements are applicable even in case of antiparallel or non-collinear alignment of the magnetic moments and a vanishing magnetization.

The strain response of metal films is usually determined by the pressure of electrons and lattice vibrations. I have developed a versatile two-pulse excitation routine that can be used to extract the magnetic contribution to the strain response even if systematic measurements above and below the magnetic ordering temperature are not feasible. A first laser pulse leads to a partial ultrafast demagnetization so that the amplitude and shape of the strain response triggered by the second pulse depends on the remaining magnetic order. With this method I could identify a strongly anisotropic magnetic stress contribution in the magnetic data storage material iron-platinum and identify the recovery of the magnetic order by the variation of the pulse-to-pulse delay. The stark contrast of the expansion of iron-platinum nanograins and thin films shows that the different constraints for the in-plane expansion have a strong influence on the out-of-plane expansion, due to the Poisson effect. I show how such transverse strain contributions need to be accounted for when interpreting the ultrafast out-of-plane strain response using thermal expansion coefficients obtained in near equilibrium conditions.

This work contributes an investigation of magnetostriction on ultrafast timescales to the literature of magnetic effects in materials. It develops a method to extract spatial and temporal varying stress contributions based on a model for the amplitude and shape of the emitted strain pulses. Energy transfer processes result in a change of the stress profile with respect to the initial absorption of the laser pulses. One interesting example occurs in nanoscopic gold-nickel heterostructures, where excited electrons rapidly transport energy into a distant nickel layer, that takes up much more energy and expands faster and stronger than the laser-excited gold capping layer. Magnetic excitations in rare earth materials represent a large energy reservoir that delays the energy transfer into adjacent layers. Such magneto-caloric effects are known in thermodynamics but not extensively covered on ultrafast timescales. The combination of ultrafast X-ray diffraction and time-resolved techniques with direct access to the magnetization has a large potential to uncover and quantify such energy transfer processes.

Kurzdarstellung

In dieser Arbeit untersuche ich den Einfluss magnetischer Ordnung auf die laser-induzierte, ultraschnelle Ausdehnung von Metallen. In Experimenten mit Femto- oder Pikosekunden Zeitauflösung sind magnetische Drücke bisher kaum erforscht. Dies steht im Kontrast zur industriellen Verwendung von magnetischen Invar Materialien oder magnetostriktiven Ultraschallgebern, in denen magnetische Drücke bereits in niedrigeren Frequenzbereichen Anwendung finden.

In meinen Experimenten untersuche ich, wie der Energieeintrag durch die Absorption von Femtosekunden-Laserpulsen in dünnen Metallschichten zu einem ultraschnellen Druckanstieg führt. Dabei nutze ich, dass der Druckanstieg zu einer Ausdehnung führt, welche Deformationswellen auf der Nanometerskala, sogenannte Hyperschallpulse, in angrenzende Schichten aussendet. Sowohl die Ausdehnung als auch die Deformationspulse ändern den mittleren Abstand zwischen den Atomen in der Probe, welcher mittels Röntgenbeugung an einer Laser-getriebenen Plasma-Röntgenquelle mit einer Subpikosekunden-Zeitauflösung detektiert wird. Das Verfahren der ultraschnellen Röntgenbeugung gelingt auch in Heterostrukturen mit vergrabenen Detektionsschichten, zu denen optische Methoden aufgrund ihrer limitierter Eindringtiefe in Metallen keinen Zugang haben. Ein Beitrag dieser Arbeit zum Feld der Pikosekunden-Akustik ist es, aus der Ausdehnung einer solchen Detektionsschicht Rückschlüsse auf die initialen Energietransferprozesse zu ziehen.

Der direkte Zusammenhang zwischen der eingebrachten Energiedichte in die Nanostrukturen und dem resultierenden Druck auf das Atomgitter ist ein zentraler Punkt in meiner Analyse der Experimente. Das zu Grunde liegende thermodynamische Konzept des Grüneisen-Parameters bildet den theoretischen Kontext meiner Publikationen. Anhand verschiedener Materialien demonstriere ich, wie dieses Prinzip auch zur Analyse der Ausdehnung auf ultraschnellen Zeitskalen verwendet werden kann und sich auch auf magnetische Drücke übertragen lässt. Insbesondere in der Materialklasse der schweren, seltenen Erdelemente sind Magnetostriktionseffekte sehr groß und führen dort sogar zu einem ungewöhnlichen Zusammenziehen des Materials nach der Laseranregung. Solch ein bestimmender Einfluss des magnetischen Drucks auf die Atombewegung ist bisher nicht gezeigt worden. Die Zeitskala des magnetischen Druckanstiegs entspricht dabei der beobachteten Abnahme der helikalen Spin-Ordnung, welche zuvor mittels zeitaufgelöster, resonanter Röntgenbeugung ermittelt wurde. Dies zeigt, dass die Stärke des magnetischen Drucks als Maß für magnetische Ordnung dienen kann, insbesondere auch im Fall von antiparalleler oder nicht-kollinearer Ordnung der magnetischen Momente in Proben mit verschwindender Magnetisierung.

In Metallfilmen ist die Dehnung des Atomgitters in der Regel durch Druck von Elektronen und Gitterschwingungen geprägt. Um den magnetischen Druckbeitrag auch in solchen Fällen zu extrahieren, in denen systematische Experimente oberhalb und unterhalb der magnetischen Ordnungstemperatur nicht praktikabel sind, habe ich ein neuartiges Doppelpuls-Anregungsverfahren entwickelt, welches allgemein für die Untersuchung von Phasenübergängen nützlich ist. Der Energieeintrag durch den ersten Laserpuls führt dabei zu einer partiellen, ultraschnellen Demagnetisierung, sodass die Amplitude und Form der Gitterausdehnung nach dem zweiten Puls von der Stärke des verbliebenen magnetischen Drucks und somit von der verbliebenen magnetischen Ordnung abhängt. Mit dieser Methode ist es möglich

geworden, einen stark richtungsabhängigen, magnetischen Druckbeitrag im Speichermedium Eisen-Platin zu identifizieren und mittels Variation des Puls-zu-Puls Abstands auch die Rückkehr der magnetischen Ordnung zu zeigen. Die unterschiedliche Ausdehnung von Eisen-Platin Nanopartikeln und dünnen Filmen zeigt dabei, dass die verschiedenen Zwangsbedingungen für die Ausdehnung entlang der Probenoberfläche aufgrund des Poisson-Effekts einen entscheidenden Einfluss auf die ultraschnelle Ausdehnung senkrecht zur Probenoberfläche hat. Ich analysiere, wie die zugrunde liegende Querkontraktion bei der Interpretation der ultraschnellen Ausdehnung auf der Basis von thermischen Ausdehnungskoeffizienten im Quasi-Gleichgewicht berücksichtigt werden kann.

Meine Arbeit erweitert die Literatur um einen Beitrag zur ultraschnellen Magnetostriktion und entwickelt eine Methodik mittels derer räumlich und zeitlich variierende Druckbeiträge anhand einer Modellierung der Form der Deformationswellen extrahiert werden können. Energietransferprozesse spiegeln sich dabei durch eine Änderung des Druckprofils gegenüber dem Absorptionsprofil der Laserpulse wider. Experimente in nanoskopischen Gold-Nickel Heterostrukturen zeigen ein faszinierendes Beispiel, in dem laser-angeregte Elektronen Energie ultraschnell in die entferntere Nickelschicht transportieren, die somit deutlich mehr Energie aufnimmt und sich schneller und stärker ausdehnt als die zuvorderst liegende Goldschicht. Insbesondere in den seltenen Erden stellen magnetische Anregungen ein großes Energiereservoir dar, das den Wärmeübertrag in angrenzende Schichten verlangsamt. Magnetokalorische Effekte sind in der Thermodynamik bekannt, aber auf ultraschnellen Zeitskalen bisher kaum diskutiert. An dieser Stelle zeigt die Kombination aus ultraschneller Röntgenbeugung und zeitaufgelösten Messungen der Magnetisierung großes Potential zur Bestimmung der Energietransferprozesse.

Table of Contents

Abbrevations

AFM	antiferromagnetic
BST	Barium-Strontium-Titanate ($BaSrTiO_3$)
FEM	finite element method
FM	ferromagnetic
FEL	free electron laser
HAMR	heat-assisted magnetic recording
LLG equation	Landau-Lifshitz-Gilbert equation
LSMO	lanthanum-strontium manganate ($La_{0.7}Sr_{0.3})MnO_3$)
MgO	magnesium oxide
MOKE	magneto-optic Kerr effect
PM	paramagnetic
PXS	plasma X-ray source
RSM	reciprocal space map
RSS	reciprocal space slice
SEM	scanning electron microscopy
STO	strontium titanate ($SrTiO_3$)
SRO	strontium ruthenate ($SrRuO_3$)
TEM	transmission electron microscopy
UXRD	ultrafast X-ray diffraction
XMCD	X-ray circular magnetic dichroism

List of Figures

List of Tables

CHAPTER ONE

Introduction

This chapter outlines the motivation for the presented research and the scientific background for the experiments that probe the strain response in magnetic materials on ultrafast timescales. It contains the general context of this work by providing the references to previous results on the related fields of ultrafast demagnetization, time-dependent magneto-elastic couplings and ultrafast strain generation.

1.1 Motivation

All matter is made of atoms, that experience attractive and repulsive forces. These forces determine the mechanical, electrical, chemical, magnetic and optical properties of macroscopic objects due to their effect on the atomic arrangement and spacing. This atomistic idea dates back to the pre-socratic philosophers Leucippus and his student Democritus approximately 450 BCE in Abdera.[1] Pondering over the erratic motion of dust particles in the sunlight and the slow abrasive wearing of cart wheels they arrived at the conclusion that matter must be granular, made out of small indivisible units called atoms.[1] Their claim is that in reality there is "only atoms and void", and that all perceptible properties result from the different combination of atoms.[1, 2] This atomic hypothesis was debated until the beginning of the 20th century. Evidence in support of the granular nature of matter is now abundant. Among others it is given by the analysis of Brownian motion[3], large angle alpha particle scattering on thin gold foils[4, 5], the interpretation of sharp lines in atomic absorption spectra[6], and even imaging of atomic steps with the use of scanning tunneling microscopy[7]. Contemporary solid-state research now strives to increase the understanding of the fundamental forces between atoms since these forces determine the properties of matter, which we exploit in our daily life.

One way to study such fundamental forces in solids is to investigate their effect on the inter-atomic spacing d whose relative change from the equilibrium or reference distance d_0 is called strain η ($\eta = \frac{d-d_0}{d_0}$). The following order of magnitude analysis outlines the requirements on the spatial and temporal sensitivity for experimental techniques that probe atomic motions on their intrinsic length- and timescale. Starting with the required spatial sensitivity: It has been observed that many solid materials melt when the root mean square of the atomic displacement is on the order of $10\,\%$ of the interatomic distance.[8, 9] This rough empirical finding, called the Lindemann criterion, illustrates that small changes in atomic-positions can lead to large changes in material properties. Experiments in solids are often required to detect strains with a precision better than 1% of the atomic separation, that itself is on the order of $1\,\text{Å}$ ($10^{-10}\,\mathrm{m}$). As for the temporal resolution it is known that typical vibration periods of atoms within solids exhibit a frequency on the order of THz ($10^{12}\,\mathrm{s}^{-1}$). To study experimental processes at these time- and length scales thus requires sub-picometer ($< 10^{-12}\mathrm{m}$) spatial- and sub-picosecond ($< 10^{-12}\,\mathrm{s}$) temporal-resolution. This challenges conventional electronics, which is too slow to record data at THz rates as well as experimental

schemes that employ visible light, that exhibits a wavelength ($400 - 800\,\mathrm{nm}$) which is too large to resolve inter-atomic spacings.

Time-resolved X-ray diffraction with sub-picosecond X-ray pulses used in a pump-probe detection scheme is one experimental technique, that is now routinely applied to observe reversible processes in crystalline materials.[10–12] Hard X-ray radiation has a wavelength on the order of one picometer so that the interference pattern of the light that is scattered from regularly spaced atoms provides a sensitive measure of the inter-atomic distance. Ultrafast pump-probe experiments employ a femtosecond laser stimulus that triggers reversible processes, which are subsequently observed by a sub-picosecond probe-pulse with variable, often mechanical, delay that can be set with (sub-)femtosecond precision. This combination of techniques called ultrafast X-ray diffraction (UXRD) yields both the subpicosecond time- and the subpicometer-spatial resolution to study laser-induced non-equilibrium dynamics of the crystal lattice.

This thesis reports laser-induced strain observed via UXRD with a focus on metals that host magnetic order. The observation of structural dynamics in laser-excited magnetic materials is motivated by the search for signatures of coupling mechanisms between atomic motions and magnetic order on ultrafast timescales. It is known that atomic vibrations, whose elementary excitations are called phonons, often provide the largest bath for the energy transfer processes in laser-excited materials. The general sequence of events in the reported experiments can thus be sketched roughly as follows: A femtosecond laser-pulse is first absorbed in a metal thin film. The deposited energy density creates a stress within the material, to which the atomic lattice reacts with a strain. UXRD probes the time-dependent strain, that contains the length- and timescales of the physical processes subsequent to the light-matter interaction. This comprises light-absorption-, electron-propagation- and electron-phonon interaction processes and their potential modifications due to the magnetic degrees of freedom. In principle UXRD can also detect the relative motions of atoms within a crystal unit-cell (optical phonons)[13], shear motions (transverse phonons)[14–16], non-equilibrium phonon populations via thermal diffuse scattering [17, 18], and surface acoustic waves[19, 20], but these processes are not discussed in this thesis.

Magnetic materials are not only fascinating for fundamental research that explores the various features of the collective order of magnetic moments but also for applications that use magnetic domains to store data. The coupling between magnetism and lattice degrees of freedom is inevitable since the atoms provide the framework and set the geometrical arrangement of the magnetic moments that often determines their interaction strength. Hence all magnetically ordered materials exhibit some degree of magnetostriction, i.e. they show a lattice strain of variable size in response to a change of magnetization[21]. UXRD now allows studing magneto-elastic couplings within thin films in the time domain. The goal of this work is to explore magnetic contributions to the strain response across different metallic materials with magnetic order. The observed strain response then provides information that is complementary to the experiments that report the evolution of the magnetic order in ultrafast demagnetization[22], all-optical magnetization switching[23, 24], ultrafast spintronic[25] and magnonic[26] experiments. The reported experiments aim to provide a step towards the understanding of the coupling between the electron, spin and phonon degrees of freedom within matter that is subjected to an ultrashort optical-stimulus.

1.2 Scientific context, general definitions and common models

It is important to acknowledge the large amount of previous work in picosecond ultrasonics[27, 28], ultrafast magnetism[29, 30] and time-resolved diffraction[10, 31] that provides the basis and background of this work. The following overview is restricted to a brief compilation of existing research in time-

resolved investigations of spin-lattice couplings up to the current state at the time of writing. It begins with the required definitions of the strain response and two frequently used models in the field of ultrafast magnetism and lattice dynamics. The following list of the relevant literature is inherently subjective but it provides a digest of the ideas that have influenced the presented experiments.

1.2.1 Definition of stress and strain

Because the strain η and stress σ are central to this work, it is necessary to first introduce the employed definitions and nomenclature before explicitly discussing their contributions.[1] In daily life, strain is often referred to a relative change in length $\eta = \frac{l-l_0}{l_0} = \frac{\Delta l}{l_0}$ of a rod of length l_0 in response to a force. The strain response to a uniaxial force of a beam with fixed in-plane dimensions is illustrated in figure 1.1(a). In reality, a free beam of finite size also reacts with an additional transverse contraction Δd along the two directions perpendicular to the uniaxial force (see Fig. 1.1(b)). This so-called Poisson effect originates from the coupling of the elastic response along different crystallographic directions. It can be quantified by the Poisson ratio $\nu = -\frac{\Delta d}{\Delta l}$, which is approximately 0.3 in common metals. It ranges between $\nu = 0.5$ for incompressible substances such as water and $\nu = 0$ for materials without transverse strain such as cork. If the same uniaxial force is applied in figure 1.1(a) and (b) Δl_{free} will be larger than $\Delta l_{\text{clamped}}$. The relevance of this Poisson effect for the picosecond strain response is discussed explicitly for laser-excited FePt-nanograins in comparison to a laser-excited FePt continuous film in chapter 5.

In case the force is applied isotropically and the elastic properties of the sample are also independent of the direction, the elastic body responds with a change in volume $\frac{\Delta V}{V_0} = 3\frac{\Delta l}{l_0}$ and a homogeneous strain η along all directions (see Fig 1.1(c)). This is the case for the thermal expansion of amorphous bulk materials, polycrystalline materials or materials with cubic lattice symmetry. The general elastic response in anisotropic crystals is given in dedicated textbooks[32].

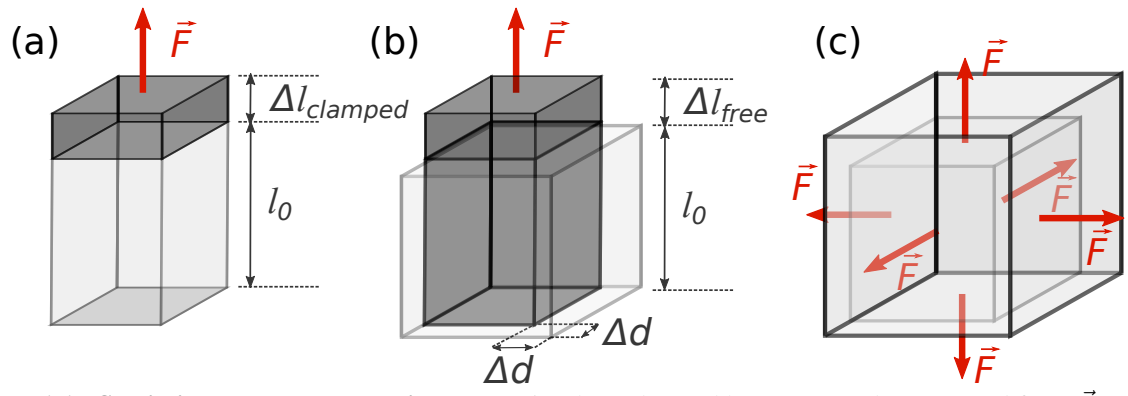

Figure 1.1: Strain in common geometries: (a) An in-plane clamped beam exposed to a normal force $\vec{F}$ reacts with a change in length Δl (here denoted as $\Delta l_{\text{clamped}}$) in the direction of the force. The resulting strain is referred to as $\left(\eta = \frac{\Delta l_{\text{clamped}}}{l_0}\right)$. (b) A real beam of finite size reacts in addition with a transverse contraction Δd along the in-plane directions due to the so-called Poisson effect and with a Δl_{free} that is larger than $\Delta l_{\text{clamped}}$. (c) If the force is applied isotropically the strain response is also isotropic and results in a volume change $\frac{\Delta V}{V} \approx 3\eta$. Figure adapted from Groß - Marx[33, chapter 4].

More complex deformations such as bending, shearing and torsion occur when the force is either applied inhomogeneously across the surface or tangentially to it. The discussions in this thesis are

[1] In some of the later discussed publications we used ε as a variable for strain as it is common in the context of engineering and previous works of the group. In this thesis and future studies I intend to use η because it avoids the ambiguity with the dielectric constant ε that occurs in the context of ferroelectric materials and plasmonics that are also relevant fields of research for our group.

limited to the normal strains since they are directly observable in the reported UXRD experiments. The generation of laser-induced shear strains requires an in-plane symmetry breaking that can be provided by the crystallographic sample cut[34], anisotropic in-plane thermal expansion[14], a nanostructured opto-acoustic transducer geometry[35] or an in-plane magnetization component[15, 36]. The detection of shear strain furthermore requires dedicated probing geometries both for all-optical[35] as well as for X-ray diffraction experiments[15, 16]. The experiments in this work are carried out in the coplanar, symmetric, diffraction geometry (depicted in chapter 3) that is insensitive to shear strains.

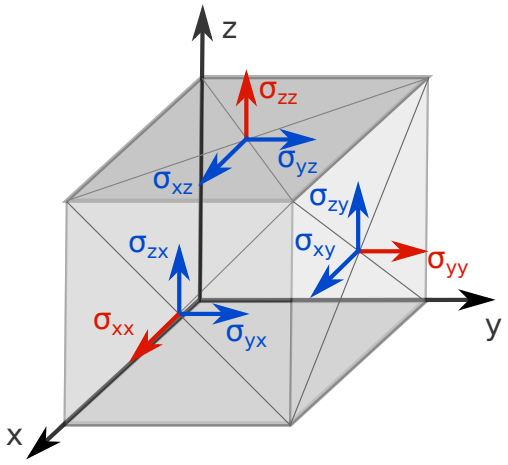

Figure 1.2: Nomenclature of stress components: The cube shows stress components σ_{ij} with $i,j \in (x,y,z)$. Components with $i = j$ correspond to normal stresses whereas $i \neq j$ are referred to as shear stresses, because unbalanced tangential forces would lead to a shearing motion. The used definition follows chapter 4 of the solid state physics book by Groß and Marx[33], from which this figure is adapted.

A common, more general definition for strain, that goes beyond changes in length is given in the field of continuum elasticity theory. This theory does not account for effects that result from the discreteness of matter and considers processes that occur on length scales that are larger than the inter atomic spacing. The material response is described by a continuous displacement field $\vec{u} = \vec{r} - \vec{r}_0 = u_x\vec{e}_x + u_y\vec{e}_y + u_z\vec{e}_z$ relative to an arbitrarily defined equilibrium position. The general definition for strain that includes both longitudinal and shear displacements is then given by:

$$\eta_{ij} = \frac{1}{2}\left(\frac{\partial u_i}{\partial j} + \frac{\partial u_j}{\partial i}\right) \text{ where } i,j \in x,y,z \tag{1.1}$$

The experimentally observed strain of this work is exclusively longitudinal, so that equation (1.1) can be simplified using $i = j$, to yield $\eta_{ii} = \left(\frac{\partial u_i}{\partial i}\right)$. The index is sometimes replaced using the Voigt notation that defines the following mapping:

$$xx \to 1,\ yy \to 2,\ zz \to 3,\ yz \to 4,\ xz \to 5,\ xy \to 6. \tag{1.2}$$

In the context of this thesis, only strains η_β with the Voigt indices $\beta = 1,2$ and 3 appear. The generalized version of Hooke's law linearly relates stress and strain for small strains according to:

$$\sigma_{ij} = \sum_{k,l=1}^{3} c_{ijkl}\eta_{kl} \tag{1.3}$$

Symmetry arguments reduce the number of $3^4 = 81$ possible independent elastic constants c_{ijkl} significantly to at maximum 21 independent values.[32] By introducing the Voigt notation, relation 1.3 can then be written as $\sigma_\alpha = \sum_{\beta=1}^{6} c_{\alpha\beta}\eta_\beta$. Further simplifications for the entries of $c_{\alpha\beta}$ depend on the crystal

symmetry, which are elaborated in dedicated textbooks.[32, 37]

1.2.2 Phenomenological model for magneto-elastic coupling

The following paragraph outlines the main ingredients for a macroscopic, phenomenological magneto-elastic coupling model that has been used to rationalize various experimental results. This includes microwave excitation close to the ferromagnetic resonance (FMR)[38], coupling of surface acoustic waves (SAWs) to the magnetization[39], as well as the magnetization response to longitudinal acoustic and transverse acoustic picosecond strain pulses[40, 41]. Its core idea is that the strain and the magnetization of a sample assume the values that minimize the total free energy F. A frequently cited list of the different energy contributions to F and their connection to magnetostriction has been provided by Charles Kittel in 1949[42] although different variations exist in previous literature. This model yields the equilibrium position of the magnetization $\vec{M} = M(m_\mathrm{x}\vec{e}_\mathrm{x} + m_\mathrm{y}\vec{e}_\mathrm{y} + m_\mathrm{z}\vec{e}_\mathrm{z})$ and the strain η $\left(\eta_\mathrm{ij} = \frac{1}{2}\left(\frac{\partial u_\mathrm{i}}{\partial j} + \frac{\partial u_\mathrm{j}}{\partial i}\right)\right)$. The strain consists of longitudinal contributions along the crystallographic directions $(\eta_\mathrm{xx}, \eta_\mathrm{yy}, \eta_\mathrm{zz})$ and shear contributions $(\eta_\mathrm{xy}, \eta_\mathrm{yz}, \eta_\mathrm{xz})$. The equilibrium values of $\vec{M}$ and η minimize the total free energy F, which has both magnetic and elastic contributions and mixed terms:

$$F = \underbrace{F_\mathrm{Zeeman} + F_\mathrm{anisotropy} + F_\mathrm{shape}}_{\text{magnetic contributions}} + \underbrace{F_\mathrm{elastic}}_{\text{elastic contribution}} + \underbrace{F_\mathrm{me}}_{\text{mixed terms}} \tag{1.4}$$

The type of terms that are considered are often adapted to the specific experimental situation. One of the simplest forms of the free energy F that only contains terms to the lowest order in $\vec{\mathrm{M}}$ and η in a cubic symmetry (see for example[43, chapter 1]) reads as:

$$\begin{aligned}
F_\mathrm{Zeeman} &= -\mu_0 \vec{M}\cdot\vec{H}_\mathrm{ext} = -\mu_0 M H_\mathrm{ext}\cos\theta \\
F_\mathrm{anisotropy} &= \begin{cases} -K_\mathrm{u}\cos^2(\theta) = -K_\mathrm{u} m_\mathrm{z}^2, & \text{uniaxial anisotropy} \\ K_1(m_\mathrm{x}^2 m_\mathrm{y}^2 + m_\mathrm{y}^2 m_\mathrm{z}^2 + m_\mathrm{x}^2 m_\mathrm{z}^2), & \text{cubic anisotropy} \end{cases} \\
F_\mathrm{shape} &= \frac{\mu_0 M_s}{2} m_\mathrm{z}^2, \text{ thin film geometry} \\
F_\mathrm{elastic} &= \frac{1}{2}c_{1111}(\eta_\mathrm{xx}^2 + \eta_\mathrm{yy}^2 + \eta_\mathrm{zz}^2) + c_{1122}(\eta_\mathrm{xx}\eta_\mathrm{yy} + \eta_\mathrm{yy}\eta_\mathrm{zz} + \eta_\mathrm{xx}\eta_\mathrm{zz}) + \frac{1}{2}c_{2323}(\eta_\mathrm{xy}^2 + \eta_\mathrm{yz}^2 + \eta_\mathrm{xz}^2) \\
F_\mathrm{me} &= b_1(\eta_\mathrm{xx} m_\mathrm{x}^2 + \eta_\mathrm{yy} m_\mathrm{y}^2 + \eta_\mathrm{zz} m_\mathrm{z}^2) + b_2(\eta_\mathrm{xy} m_\mathrm{x} m_\mathrm{y} + \eta_\mathrm{yz} m_\mathrm{y} m_\mathrm{z} + \eta_\mathrm{xz} m_\mathrm{x} m_\mathrm{z})
\end{aligned} \tag{1.5}$$

The angle-dependence of the contributions to the free energy F that depend on the direction of the magnetization $\vec{M}$ are depicted in figure 1.3.

The stated equations so far consider a homogeneous material the where strain η and the magnetization $\vec{M}$, as well as the introduced effective material parameters K_u (uniaxial anisotropy constant) ,K_1 (cubic anisotropy constant), c_{ijkl} (elastic tensor components), b_1 and b_2 (magneto-elastic coupling parameters) are homogeneous or sufficiently well approximated by their average value. A more thorough discussion of the contributions to the free energy in this phenomenological model is provided textbooks dedicated to magnetostriction.[43, 44]

All quantities that appear in 1.5 vary in general as a function of the sample position, local temperature and thus also relative time in a pump-probe experiment. This becomes especially relevant in non-equilibrium situations that are often realized in laser-excited metal films that host magnetic order, which are considered in this work. Spatio-temporal models for the strain, temperature and magnetization are thus necessary to predict the coupling between strain and magnetization from this simplified phenomenological

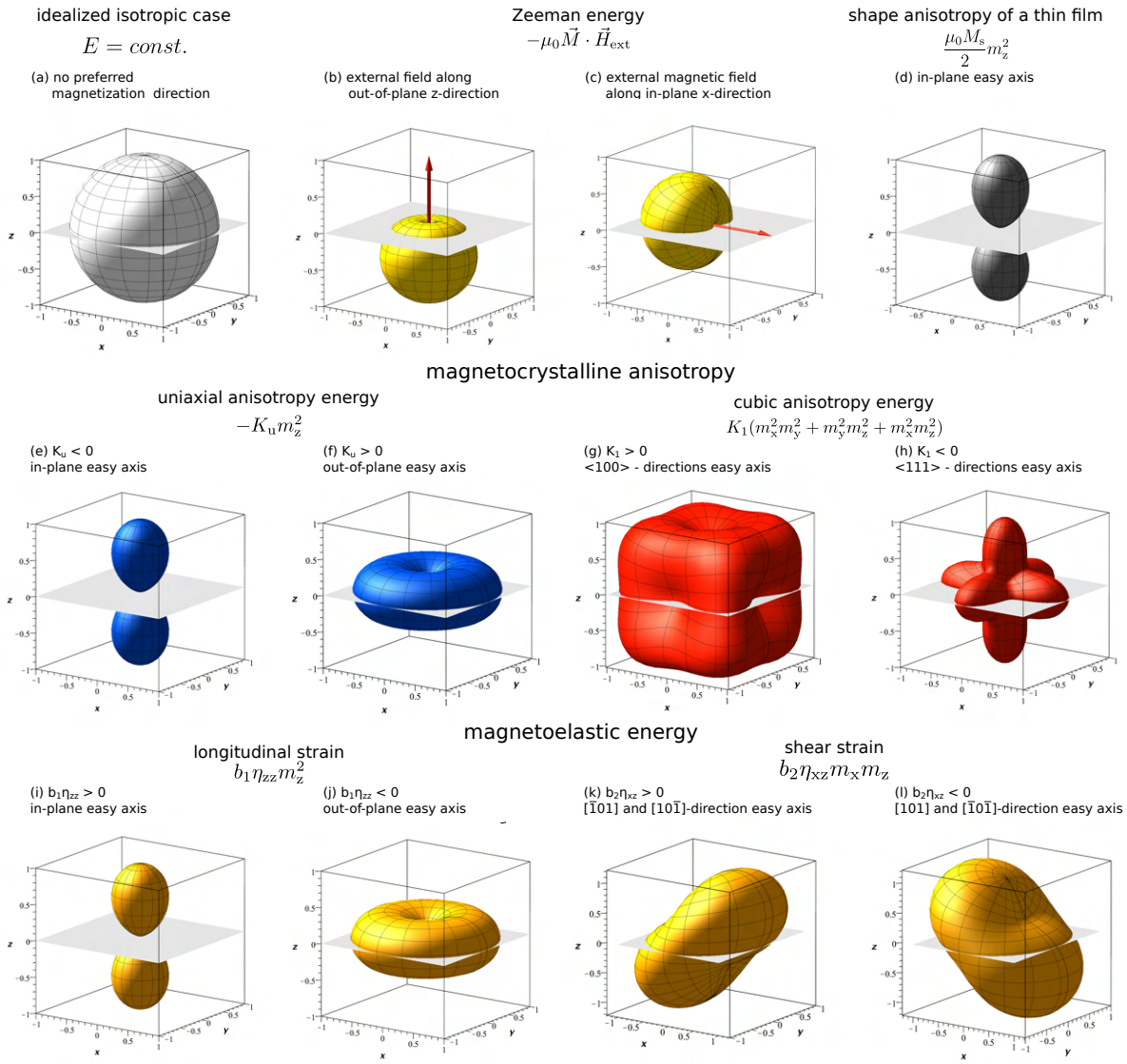

Figure 1.3: Shapes of the anisotropic, magnetic contributions to the free energy: The distance between the displayed surface and the origin of the coordinate system is proportional to the energy cost when the magnetization points along that direction. A thin film sample is indicated as grey, flat surface in each plot and chosen to lie in the x-y-plane so that the z-axis corresponds to its out-of-plane direction. Panel (a) shows the hypothetical case of an isolated spin where no anisotropies exist. In panel (b) and (c) an external magnetic field is introduced that breaks the symmetry and yields a direction of preferential order. The shape anisotropy of a thin film sample that originates from the minimization of the stray fields is shown in (d). The uniaxial and cubic anisotropy energies of lowest order in the magnetization are depicted in (e)-(f) and (g)-(h) for the different signs of the anisotropy constants respectively. Panels (i)-(j) and (k)-(l) show the angular dependence of the strain induced magnetocrystalline anisotropy for the case of a longitudinal and a shear strain respectively. The amplitudes of the displayed energy contributions strongly depend on the investigated material and are chosen arbitrarily in this overview. As indicated in 1.4, the different contributions are additive and the magnetization of the sample is aligned to minimize the total free energy F in equilibrium conditions.

model. In order to capture antiferromagnetic, ferrimagnetic or even more complex types of magnetic order, one also needs to relax the assumption of a homogeneous magnetization and also include so-called magnetic exchange contributions to the free energy. The most common model for this contribution is the symmetric exchange energy, often called Heisenberg exchange interaction energy, which reads:

$$F_{\mathrm{Heisenberg}} = -\frac{1}{2}\sum_{i,j} J_{ij}\langle \vec{s}_i \cdot \vec{s}_{\mathrm{j}} \rangle \approx -J_{\mathrm{ex}} s^2 \cos\phi \tag{1.6}$$

In the simplification of equation 1.6 I consider only nearest neighbor interaction of the exchange energy and assume that all magnetic moments $\vec{s}$ have the same magnitude and distance, so that the only free parameter is the average angle ϕ between them. Despite its many simplifications this contribution can be used to motivate the temperature dependent exchange-striction contribution that couples strain and magnetization due to the strain dependence of the effective exchange constant $J_{\mathrm{ex}} = J_{\mathrm{ex}}(\eta)$ and the temperature dependence of the magnetic order parameter $M^2(T)$ as detailed in section 4.4.3. Textbook examples for the exchange coupling between magnetic moments range from a direct overlap of the wave-function of electrons (direct exchange-interaction), exchange interaction mediated by diamagnetic oxygen atoms (super-exchange-interaction) or by a free electron gas (RKKY-interaction)[45, 46]. More complex exchange interactions such as the antisymmetric exchange, also known as Dzyaloshinskii-Moriya interaction ($F_{\mathrm{DMI}} = D_{ij}\langle s_i \times s_{\mathrm{j}} \rangle$) exist. The antisymmetric exchange interaction is in general weak but can lead to spin-textures with a non-trivial topology, such as magnetic skyrmions, which are not discussed in this work although their response to picosecond strain pulses is certainly interesting as they are subject to current research.[47, 48]

In the remainder of this section I neglect the exchange energy contributions and utilize the simple free energy model given by the equations (1.5) to derive the effective field $\vec{B}_{\mathrm{eff}} = -\nabla_{\mathrm{m}} F$ that drives the sample magnetization dynamics and the stress $\sigma = -\nabla_{\eta} F$ that drives the strain response. Two commonly used equations of motion for the magnetization and the atomic displacement are the Landau-Lifshitz-Gilbert equation (LLG equation) and the elastic wave equation where the effective field and the stress serve as an input. Solutions to both equations under idealized conditions are discussed briefly for illustration purposes. The mixed terms that contain both strain contributions η_{ij} and magnetization contributions m_{k} introduce a coupling of the lattice and magnetization response via the terms b_1 and b_2. A discussion of some of the microscopic origins for this coupling is deferred to chapter 4.

The LLG equation describes the equation of motion for the net-magnetization that is subjected to an effective field that results from the gradient of the total free energy as introduced before. If the resulting effective field is non-collinear with the magnetization it exerts a torque that drives a time-resolved magnetization change according to the LLG equation. Similar to the different contributions to F, there exist different variants of the LLG equation depending on the physical problem.[49] The following relation is a common, basic version that includes a precession and a damping term:

$$\frac{\partial \vec{M}}{\partial t} = \underbrace{-\gamma \vec{M} \times \vec{B}_{\mathrm{eff}}}_{\text{precession term}} + \underbrace{\alpha \vec{M} \times \left(\vec{M} \times \vec{B}_{\mathrm{eff}} \right)}_{\text{damping term}} \quad \text{where} \quad \vec{B}_{\mathrm{eff}} = -\vec{\nabla}_{\mathrm{m}} F = -\begin{pmatrix} \frac{\partial F}{\partial m_{\mathrm{x}}} \\ \frac{\partial F}{\partial m_{\mathrm{y}}} \\ \frac{\partial F}{\partial m_{\mathrm{z}}} \end{pmatrix}, \tag{1.7}$$

wherein γ represents the gyromagnetic ratio and α a phenomenological damping coefficient that is often referred to as Gilbert damping. The existence of a damping also originates from energy dissipation between magnetic excitations and other degrees of freedom. In magnetic insulators the damping term originates mainly from the energy transfer to phonons[38], which is another indirect evidence of the coupling between spin excitations and phonons.

To illustrate the contributions to the effective field one can explicitly consider the following example:

Assuming an external in-plane magnetic field $\vec{B}_{\mathrm{ext}} = B_0\vec{e}_{\mathrm{x}}$ and a thin film sample with strong uniaxial out-of-plane anisotropy in the absence of any transverse strains the effective field is:

$$\vec{B}_{\mathrm{eff}} = -\vec{\nabla}_{\mathrm{m}}F = -\begin{pmatrix} \frac{\partial F}{\partial m_{\mathrm{x}}} \\ \frac{\partial F}{\partial m_{\mathrm{y}}} \\ \frac{\partial F}{\partial m_{\mathrm{z}}} \end{pmatrix} = \begin{pmatrix} -B_0 - 2b_1 m_{\mathrm{x}}\eta_{\mathrm{xx}} \\ -2b_1 m_{\mathrm{y}}\eta_{\mathrm{yy}} \\ 2K_{\mathrm{u}}m_{\mathrm{z}} - \mu_0 M_{\mathrm{s}} m_{\mathrm{z}} - 2b_1 m_{\mathrm{z}}\eta_{\mathrm{zz}} \end{pmatrix}. \tag{1.8}$$

Equation (1.8) shows the contributions to the effective field that defines the equilibrium position of the magnetization. If now the absorption of a femtosecond laser-pulse heats the magnetic layer one generally observes a decrease in the anisotropy $K_{\mathrm{u}}(T)$, so that the magnetization is displaced from the position that minimizes F. The LLG equation describes the damped precessional motion of $\vec{M}$ towards the new equilibrium[50, 51]. This is schematically depicted in figure 1.4. The occurrence of η in these equations shows that strain provides another way to change the effective field. Both the strain and the anisotropy can change very fast upon femtosecond laser excitation in comparison to the changes of an external field. For more detailed discussions of the magnetization dynamics described by variants of the LLG equation see reviews by Atxitia et al. [49] and Azzawi et al. [38] and references therein.

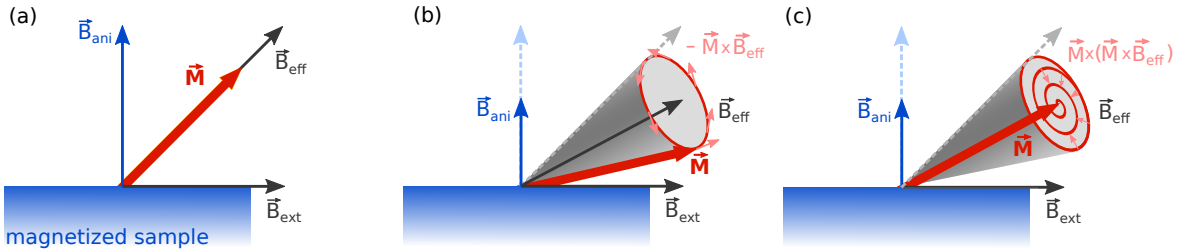

Figure 1.4: Schematic magnetization response according to the LLG equation: (a) Equilibrium situation where the magnetization vector $\vec{M}$ is aligned along the effective field $\vec{B}_{\mathrm{eff}}$ that results from the superposition of an externally applied field $\vec{B}_{\mathrm{ext}}$ along the in-plane direction and an out-of-plane anisotropy field $\vec{B}_{\mathrm{ani}}$. When an external stimulus changes $\vec{B}_{\mathrm{ani}}$, $\vec{M}$ starts to precess around the new equilibrium as shown in (b). The second term in the LLG equation corresponds to the damping of the precession that leads to a spiral trajectory of M towards the new equilibrium orientation. Small red arrows indicate the precessional torque in (b) and the damping torque in (c).

The same contributions to the free energy from relation (1.4) can also be used to calculate the stress for a given magnetization orientation. The stress acts as a forcing that drives a displacement $\vec{u}(\vec{r},t)$. Given the same situation of a polycrystalline, thin film sample with cubic symmetry, the resulting stress $\sigma = -\nabla_\eta F$ from the different contributions to the free energy (relations 1.5)) is:

$$\begin{pmatrix} \sigma_{\mathrm{xx}}^{\mathrm{tot}} \\ \sigma_{\mathrm{yy}}^{\mathrm{tot}} \\ \sigma_{\mathrm{zz}}^{\mathrm{tot}} \\ \sigma_{\mathrm{yz}}^{\mathrm{tot}} \\ \sigma_{\mathrm{xz}}^{\mathrm{tot}} \\ \sigma_{\mathrm{xy}}^{\mathrm{tot}} \end{pmatrix} = \begin{pmatrix} \frac{\partial F}{\partial \eta_{\mathrm{xx}}} \\ \frac{\partial F}{\partial \eta_{\mathrm{yy}}} \\ \frac{\partial F}{\partial \eta_{\mathrm{zz}}} \\ \frac{\partial F}{\partial \eta_{\mathrm{yz}}} \\ \frac{\partial F}{\partial \eta_{\mathrm{xz}}} \\ \frac{\partial F}{\partial \eta_{\mathrm{xy}}} \end{pmatrix} = \underbrace{\begin{pmatrix} c_{1111}\eta_{\mathrm{xx}} + c_{1122}(\eta_{\mathrm{yy}} + \eta_{\mathrm{zz}}) \\ c_{1111}\eta_{\mathrm{yy}} + c_{1122}(\eta_{\mathrm{xx}} + \eta_{\mathrm{zz}}) \\ c_{1111}\eta_{\mathrm{zz}} + c_{1122}(\eta_{\mathrm{xx}} + \eta_{\mathrm{yy}}) \\ c_{2323}\eta_{\mathrm{yz}} \\ c_{2323}\eta_{\mathrm{xz}} \\ c_{2323}\eta_{\mathrm{xy}} \end{pmatrix}}_{=\sigma^{\mathrm{elastic}}} + \underbrace{\begin{pmatrix} 2b_1 m_{\mathrm{x}} \\ 2b_1 m_{\mathrm{y}} \\ 2b_1 m_{\mathrm{z}} \\ b_2(m_{\mathrm{y}}m_{\mathrm{z}}) \\ b_2(m_{\mathrm{x}}m_{\mathrm{z}}) \\ b_2(m_{\mathrm{x}}m_{\mathrm{y}}) \end{pmatrix}}_{=-\sigma^{\mathrm{ext}}}. \tag{1.9}$$

The inhomogeneous elastic wave equation is the equation of motion for the sample displacement field. The total stress σ^{tot} in relation (1.9) is separated into an elastic part $\sigma^{\mathrm{elastic}}$ that also occurs in the homogeneous elastic wave equation and an external part σ^{ext} that acts as a forcing. The general form

where external stresses are added explicitly reads as:

$$\rho \frac{\partial^2 u_i}{\partial t^2} = \sum_{j=1}^{3} \frac{\partial \sigma_{ij}^{\mathrm{tot}}}{\partial x_j} = \sum_{j=1}^{3} \frac{\partial}{\partial x_j} \left(\sum_{k,l=1}^{3} \left(c_{ijkl} \eta_{kl} - \sigma_{ij}^{\mathrm{ext}} \right) \right). \tag{1.10}$$

Therein ρ represents the local mass density, c_{ijkl} are the direction dependent elastic constants and σ^{tot} the total stress that consists of the elastic stress due to local strain and the stress due to an external forcing. The minus in front of the external stress $\sigma_{ij}^{\mathrm{ext}}$ is chosen such that a positive, normal stress $\sigma_{\mathrm{ii}}^{\mathrm{ext}}$ leads to an expansion response ($\eta > 0$) and a negative stress to a contraction in the steady state where $\frac{\partial u}{\partial t} = 0$. A common geometry in picosecond ultrasonics experiments is that a spatially large, femtosecond laser pulse excites a continuous metallic transducer. The in-plane symmetry of this situation simplifies equation (1.10) significantly. Due to the absence of any in-plane symmetry breaking, only longitudinal strain along the out-of-plane direction of the thin film can occur. The wave equation then simplifies to a one-dimensional problem:

$$\rho \frac{\partial^2 u_3}{\partial t^2} = c_{3333} \frac{\partial \eta_{33}}{\partial z} - \frac{\partial \sigma_{33}^{\mathrm{ext}}}{\partial z} \underbrace{=}_{\eta_{33} = \frac{\partial u_3}{\partial z}} c_{3333} \frac{\partial^2 u_3}{\partial z^2} - \frac{\partial \sigma_{33}^{\mathrm{ext}}}{\partial z}. \tag{1.11}$$

This simplification shows that spatial gradients in the elastic strain or the driving stress are required to drive an atomic displacement. Inserting the stress from (1.9), the right hand side of (1.11) thus becomes $\frac{\partial}{\partial z}\left(c_{1111}\eta_{\mathrm{zz}} + 2b_1 m_{\mathrm{z}}\right)$ so that an explicit stress can be calculated when η_{zz} and m_{z} are known. For illustration purposes it is instructive to consider the strain response to an instantaneous stress that decays exponentially within a homogeneous material. This idealized situation can be described analytically[27, 52]. The time-dependent strain profile then consists of a localized expansion in the laser-excited region and a bipolar strain pulse that propagates away from the sample surface at the speed of sound. The observation of the localized strain in the near surface region and the propagating picosecond strain pulses is a recurring theme in all experiments that are discussed in this thesis. Figure 1.5 provides the strain profile for this simplified case as an illustration. Therein an exponential stress-profile with a decay length $\xi = 20\,\mathrm{nm}$ and a speed of sound of $5\,\frac{\mathrm{nm}}{\mathrm{ps}}$ is assumed. From the phenomenological model of the free energy one observes that the magnetization and the elastic response are coupled by a magnetostrictive contribution. This magnetostriction is, to lowest order in η, parametrized by the mixed terms with the pre-factors b_1 and b_2. Strain and magnetization are in addition linked indirectly via the temperature effects that act on the absolute value of the magnetization $|vecM|$, the magnetic anisotropy energy, and the thermal expansion response. Both presented equations of motion can be extended and adapted to account for multiple effects that occur under different experimental circumstances. As for the LLG equation one can include thermal fluctuations in the magnetization due to finite temperatures using a noise term[54, 55], quantum statistic effects[56, 57], demagnetization effects via the introduction of a transverse relaxation term that leads to the Landau-Lifshitz-Bloch equation[49, 58, 59] and even spin waves by the introduction of an exchange interaction in atomistic LLG simulations[60, 61]. For the case of the elastic wave equation, the displacement response and strain are mainly dictated by the driving spatio-temporal stress $\sigma_{\mathrm{z}}(\vec{r},t)$ that is inserted as inhomogeneity. A review of the different physical mechanisms for the laser induced stress generation is provided by Ruello et al. [28]. The granularity of matter gains importance as the central wavelength of the excited phonon-wavepackets becomes comparable to the inter-atomic distance. Then one can replace the elastic wave equation by a one-dimensional linear chain of masses and springs for thin films[62, 63] or three dimensional molecular dynamics models in nanoparticles[64]. While the continuum approach is found to work well for the description of the low frequency acoustic mode of very small nanoparticles that contain less than 100 atoms[65, 66] it does not capture the excitation of optical phonons. Additional terms need to be added to account for non-linear phonon-phonon interactions[67, 68].

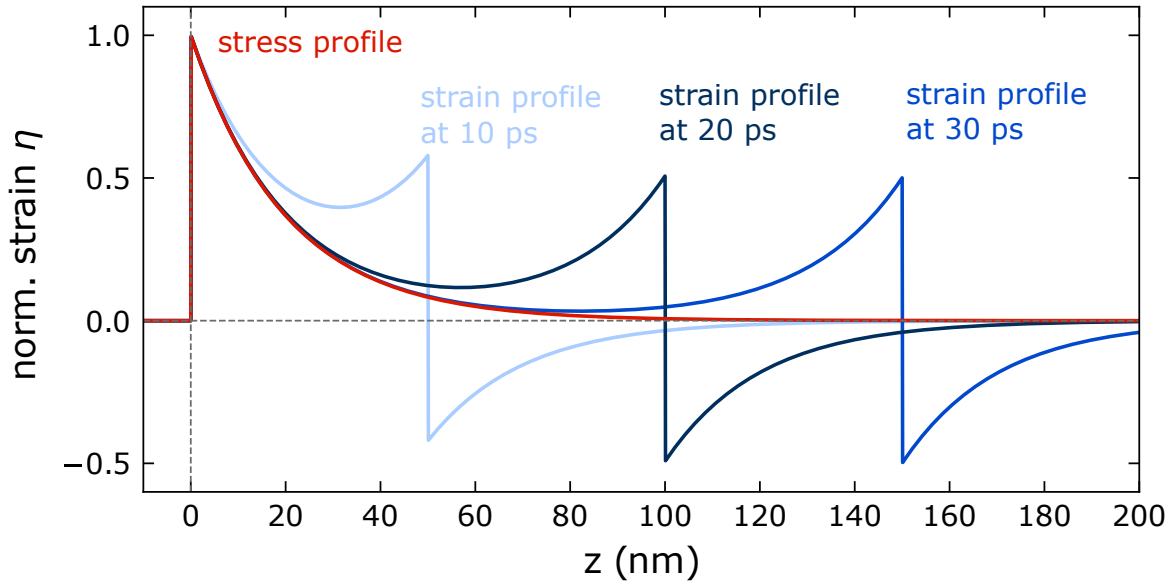

Figure 1.5: Strain response according to the elastic wave equation: This figure displays the idealized strain response of a laser excited bulk-material with an exponentially decaying stress profile of 20 nm, a speed of sound of 5 $\frac{\text{nm}}{\text{ps}}$ in absence of damping, thermal diffusion, interfaces and non-linear effects assuming an instantaneous stress generation. It consists of a localized strain close to the laser-excited sample surface and a propagating bipolar strain pulse. For details on the modeling, see the seminal paper by Thomsen et al. [52], a more recent review by Matsuda et al[27] or a publication dedicated to X-ray detection by Schick et al. [53].

Both the LLG equation and the elastic wave equation operate at a phenomenological level and parametrize the sample response using the macroscopic quantities free energy (F), magnetization (M), temperature (T), effective field B_{eff}, stress σ and strain η. A motivation for this macroscopic coupling of the magnetization to the strain via the parameters $b_1, b_2, K_{\text{U}}, K_1$ and the adjustable external field is given in chapter 4 which discusses the mechanisms for stress generation upon femtosecond laser excitation that are relevant to this work.

1.2.3 N-temperature models for the subsystem equilibration

While the above-mentioned phenomenological model for the magnetoelastic coupling provides an intuition for the coupling between strain and magnetization, it does not address the flow of energy within laser-excited materials. It is evident that the femtosecond laser excitation of matter creates a non-equilibrium situation within the materials because the laser pulse deposits energy into electronic degrees of freedom.

In laser-excited, para- or dia-magnetic metals electron excitations and phonons usually constitute the main energy reservoirs. Energy transfer between these subsystems occurs typically on a timescale that is on the order of 1 ps. A conceptually simple and frequently employed model for the time-dependent electron-phonon equilibration is given by the two-temperature model that was introduced to the English literature by Anisimov et al. [69] and later derived analytically by Philip Allen[70]. In its most simple form, that neglects any spatial variations, the two-temperature model is a rate equation for the energy transfer between the electrons (e) and phonons (pho), which reads as:

$$C_{\text{el}} \frac{\partial T_{\text{el}}}{\partial t} = G_{\text{el-pho}}(T_{\text{pho}} - T_{\text{el}}) + S(t) \tag{1.12}$$

$$C_{\mathrm{pho}}\frac{\partial T_{\mathrm{pho}}}{\partial t} = G_{\mathrm{el-pho}}(T_{\mathrm{el}} - T_{\mathrm{pho}}). \tag{1.13}$$

The energy deposition into the electronic system by the laser pulse is given by $S(t)$ and C_{el}, C_{pho}, $G_{\mathrm{el-pho}}$, are material parameters that represent the heat capacity of electronic excitations, the heat capacity of phonons, and the electron-phonon coupling constant, respectively. This system of coupled differential equations can be solved analytically, assuming an instantaneous temperature increase $\Delta T_{\mathrm{el},0}$ at $t = 0$ in the electron system with respect to T_{start} and temperature independent material parameters. Using that $C_{\mathrm{el}} \ll C_{\mathrm{pho}}$ this solution for $T_{\mathrm{el}}(t)$ and $T_{\mathrm{pho}}(t)$ can be simplified for $t \geq 0$ to:

$$T_{\mathrm{el}}(t) - T_{\mathrm{start}} = \frac{C_{\mathrm{el}}}{C_{\mathrm{pho}}}\Delta T_{\mathrm{e},0} + \Delta T_{\mathrm{el},0} e^{-\frac{G_{\mathrm{el-pho}}}{C_{\mathrm{el}}}t} \tag{1.14}$$

$$T_{\mathrm{pho}}(t) - T_{\mathrm{start}} = \frac{C_{\mathrm{el}}}{C_{\mathrm{pho}}}\Delta T_{\mathrm{e},0}\left(1 - e^{-\frac{G_{\mathrm{el-pho}}}{C_{\mathrm{el}}}t}\right). \tag{1.15}$$

Although the negligence of the temperature dependence of C_{el} and spatial variations in T_{el} and T_{pho} are a strong oversimplification, the solution still shows the important ingredients for the electron-phonon coupling time $\tau_{\mathrm{el-pho}} = \frac{C_{\mathrm{el}}}{G_{\mathrm{el-pho}}}$. Thus it is plausible that the temperature dependence of the electronic heat capacity within the Sommerfeld model for the free electron gas $C_{\mathrm{el}}(T) = \gamma_{\mathrm{S}} T_{\mathrm{el}}$ will in general increase $\tau_{\mathrm{el-pho}}$ with increasing laser-excitation fluence.

Magnetic degrees of freedom represent an additional energy reservoir in materials that host magnetic order, which needs to be taken into account for the subsystem equilibration process. It is in this context natural to extend the two-temperature model to a three-temperature model, which was already applied to rationalize the first subpicosecond demagnetization of nickel in the seminal paper of Beaurepaire et al. [22]. In its simple form it reads:

$$C_{\mathrm{el}}\frac{\partial T_{\mathrm{el}}}{\partial t} = G_{\mathrm{el-pho}}(T_{\mathrm{pho}} - T_{\mathrm{el}}) + G_{\mathrm{el-mag}}(T_{\mathrm{el}} - T_{\mathrm{mag}}) + S(t) \tag{1.16}$$

$$C_{\mathrm{pho}}\frac{\partial T_{\mathrm{pho}}}{\partial t} = G_{\mathrm{el-pho}}(T_{\mathrm{el}} - T_{\mathrm{pho}}) + G_{\mathrm{pho-mag}}(T_{\mathrm{mag}} - T_{\mathrm{pho}}) \tag{1.17}$$

$$C_{\mathrm{mag}}\frac{\partial T_{\mathrm{mag}}}{\partial t} = G_{\mathrm{el-mag}}(T_{\mathrm{el}} - T_{\mathrm{mag}}) + G_{\mathrm{pho-mag}}(T_{\mathrm{pho}} - T_{\mathrm{mag}}), \tag{1.18}$$

wherein T_{mag} represents the introduced temperature that is used to describe magnetic excitations and $G_{\mathrm{el-mag}}$ and $G_{\mathrm{pho-mag}}$ represent their coupling to the electronic excitations and phonons. While the 2-temperature model can be derived analytically[70] so that $G_{\mathrm{el-pho}}$ can be calculated for a number of elemental metals[71], currently no derivation exists for this 3-temperature model so that $G_{\mathrm{el-mag}}$ and $G_{\mathrm{pho-mag}}$ remain phenomenological fit parameters. One approach to address this problem is the microscopic 3-temperature model.[72] It uses a 2-temperature model ((1.12) and (1.13)) for the electron and phonon temperature and models the magnetization change by the relation:

$$\frac{\partial m}{\partial t} = Rm\frac{T_{\mathrm{pho}}}{T_{\mathrm{C}}}\left(1 - m\coth\left(\frac{mT_{\mathrm{el}}}{T_{\mathrm{C}}}\right)\right), \tag{1.19}$$

wherein the prefactor R contains the material-dependent properties[72]. This model assumes spin-flip scattering upon electron-phonon collisions to be the main channel for ultrafast demagnetization and categorizes the laser-induced demagnetization into one- and two-step behavior based on different regimes of electron and phonon temperatures with respect to the Curie Temperature T_{C}. An additional non-local channel for the demagnetization is given by ultrafast spin-transport in metallic heterostructures[73, 74] which is utilized in experiments in the field of ultrafast spintronics[75, 76].

For illustration, figure 1.6(a) and (b) show the results of a 2- and 3-temperature model for a 10 nm

thin laser-excited FePt layer on an insulating substrate. A laser pulse length of 100 fs is assumed in these simulations and $t = 0$ defined as the time of the maximum energy transfer. The temperatures within the thin film are assumed to be homogeneous and the excitation laser fluence is 6 $\frac{\mathrm{mJ}}{\mathrm{cm}^2}$. Figure 1.6(a) compares the assumption of a fixed C_{el} to the Sommerfeld model $C_{\mathrm{el}} = \gamma_S T_{\mathrm{el}}$ in a 2-temperature model. The incorporation of the magnetic subsystem using a 3-temperature model with a fixed magnetic heat capacity is shown in panel (b).

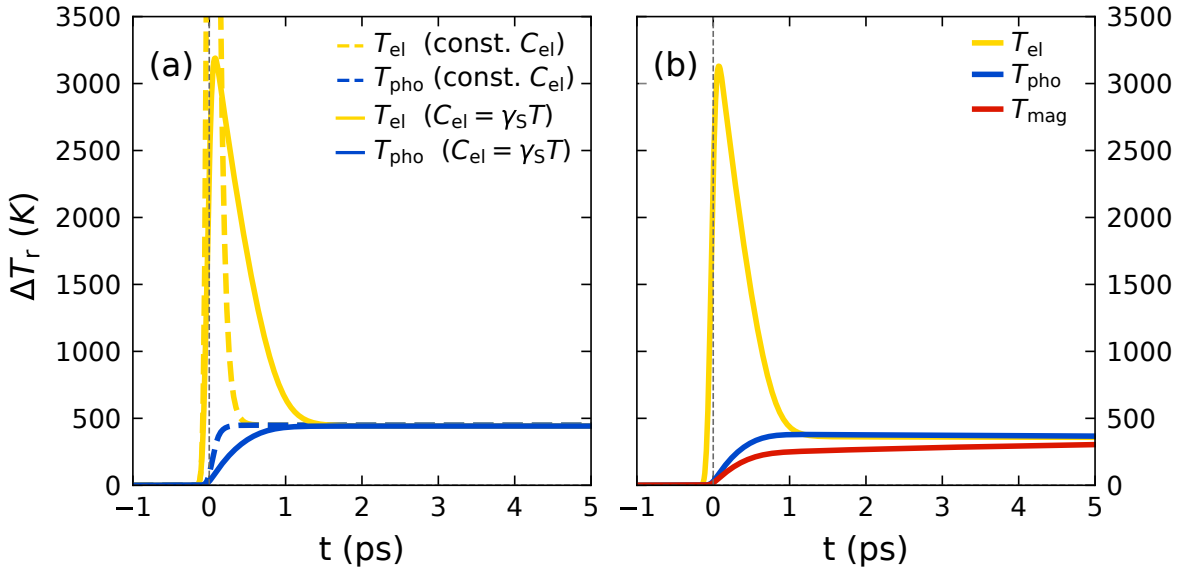

Figure 1.6: Two- and three-temperature model for the subsystem equilibration: (a) In case of a para- or diamagnetic metal, the sub-system equilibration is often modeled using a two temperature model with electrons and phonons as the main energy reservoirs. (b) In magnetic samples the magnetic excitations represent an additional degree of freedom that is incorporated into a three temperature model. The graphs show the subsystem temperature evolution of 10 nm thin laser-excited FePt as illustration based on values provided by Kimling et al. [77]. The simulations are carried out using the UDKM1DSIM-toolbox Matlab library[63] for illustrating the importance of the temperature dependent heat capacity of the electron system and the effect of energy transfer to magnetic excitations. This leads to a smaller equilibrium temperature at 5 ps.

In general, N-temperature models can be used to describe the time-dependence of the energy transfer via the equilibration of the temperatures for a number of N virtual subsystems[78, 79]. These more complex models can be used to capture the potential non-equilibrium among electron excitations and within the phonon modes. The scientific interest in non-thermal populations increases as the selectivity, time-resolution and sensitivity of experimental approaches improve.[78–83]

Given the wide-spread use of 2- and 3-temperature models, it is important to be aware of their implicit assumptions that are discussed, for example, by Kimling et al. [77], by Maldonado et al. [79] and by Wilson and Coh[84]. First of all, such N-temperature models assume that the considered subsystems are internally thermalized so that their excitation spectrum can be described using a temperature. This has been critically investigated for phonons[79, 81], magnetic excitations[85] and also electrons[84, 86]. For large temperature excursions one has to account for the temperature dependence of the heat capacities $C(T)$ and coupling factors $G(T)$. In that regard, it is especially important to take into account that the magnetic heat capacity peaks at the phase transition.[77, 87] Using the simplified Sommerfeld model of a free electron gas, the electronic heat capacity is approximated to increase linearly with temperature $C_{\mathrm{el}} = \gamma_S T_{\mathrm{el}}$ but ab-initio density functional theory investigations yield that for electron temperatures on the order of few thousands of kelvin, non-linear effects due to the material specific band-structure may become relevant[71, 88]. When the experiment is carried out at low temperatures $T < T_{\mathrm{Debye}}$ where not

all phonons are thermally excited, one has to also account for the temperature dependent changes of the phonon heat capacity. In many cases, a simplified Debye model for phonons captures the increase of C_{pho} towards higher temperatures up to the point that all phonon excitations are thermally populated. When the sample thickness is so large, that the laser excitation is not uniform across the probed sample depth or the modeled time-scale is large, one has to account for heat transport by adding a spatial dependence ($T_{\mathrm{r}} = T_{\mathrm{r}}(z)$) and a heat diffusion term $\left(\frac{\partial}{\partial z}\left(\kappa_{\mathrm{r}}\frac{\partial T_{\mathrm{r}}}{\partial z}\right)\right)$ to the right side of each equation, wherein κ_{r} denotes the subsystem-specific contribution to the heat conductivity. Heat transport in heterostructures requires models for the thermal resistance at the interfaces for each transport channel. The resulting parameter-space thus becomes very large, which limits the predictive power of such N-temperature models when independently determined literature values or analytical expressions for these parameters are lacking.

It requires more advanced models to rationalize the flow of angular momentum upon ultrafast laser-induced demagnetization. The question about the underlying mechanisms dates back to 1915 when Einstein and de-Haas reported on the rotation of a suspended magnetic cylinder upon magnetization change[89], which was previously conjectured by Richardson[90] in 1908. This angular momentum transfer, now often referred to as the Einstein-de Haas effect, shows that the crystal lattice acts as sink for the angular momentum. However, the underlying processes that account for the angular momentum transfer during ultrafast demagnetization experiments are an active field of research[15, 72, 73, 91] ever since the first demonstration of sub-picosecond demagnetization in 1996[22]. Microscopic, quantum-mechanical approaches that aim to model the ultrafast demagnetization processes are required to capture the occupation changes of the majority and minority spin states within the electronic band-structure including spin-flip scattering[72], spin-transport effects[73], and optical intersite spin transfer[92–95]. While the existence of these mechanisms is experimentally supported by a multitude of experiments, their specific contribution depends on the material and the sample geometry that ranges from a homogeneously magnetized bulk, an alloy with magnetic order, a magnetically ordered thin film in an insulating surrounding to a metallic environment. The references within the most recent works on ultrafast demagnetization dynamics[91, 93–95] point to information on the current experimental and theoretical state of the art in the field of femtomagnetism.

1.3 Research question

This thesis aims to identify experimental signatures of mechanisms by which the ultrafast demagnetization influences the lattice dynamics. More specifically, this project quantifies signatures of the demagnetization process in the picosecond to nanosecond strain response in nanoscopic thin films using ultrafast X-ray diffraction. Such observations provide a test for theoretical models that can be used to refine the current understanding and may ultimately lead to a control of the lattice motion by magnetic degrees of freedom. The schematic depiction in figure 1.7 illustrates effects of the strain-induced magnetization dynamics that could be labeled as ultrafast inverse magnetostriction. Such effects contain magnetization precession[34, 96, 97] and even switching on picosecond to nanosecond timescales[98, 99]. In addition to the coherently excited phonons, experiments in insulators have shown that incoherently excited phonons also serve as a thermal bath that can provide energy to the spin-system and contribute a demagnetization process by spin-lattice couplings[72, 100].

While ultrafast demagnetization is widely explored, its contribution to the ultrafast lattice response appears to have received less attention. In particular, the modification of the picosecond strain in the presence of a demagnetization process (i. e. ultrafast magnetostriction) may be expected, but systematic experimental investigations with regard to the amplitude and timescale of such effects are scarce. The

role of the spin system as a reservoir for thermal energy and its influence on the nanoscale heat transport across magnetic layers is another effect, that has not been subjected to exhaustive research. These effects, that are investigated in this work are schematically depicted in the lower part of figure 1.7.

On the one hand, one observes that the established use of magnetic domains as bits in data storage applications increases the research focus to the ultrafast magnetization dynamics. The desire for faster data recording at higher data densities is driven by a large industry that develops future information technology. From a fundamental physics perspective, ultrafast demagnetization[22], all-optical magnetization switching[23, 24] and ultrafast spintronics[25, 75, 76, 106] represent fruitful fields of research. The aim for improved magnetization manipulation with regard to speed and energy efficiency creates a desire to develop microscopic models for the required angular momentum and energy transfer processes in different classes of magnetic materials.

One additional reason for the experimental focus on the magnetization dynamics might be that laser-based, all-optical setups have achieved a very high sensitivity for (de-)magnetization induced changes of the polarization from the time-resolved Kerr- and Faraday effect. Commercially available lasers provide a relatively stable, high photon flux. Lock-in amplifiers and balanced detection schemes deliver a high signal-to-noise ratio. It is however key that difference schemes between different magnetization orientations can eliminate most non-magnetic contributions to the magneto-optical signals. Smart doping and the use of spectral resonances can be used to enhance the magneto-optical contrast even further. This results in the fact that precession angles of less than 1° for example in doped Yttrium-Iron-Garnet are well above the detection threshold.

On the other hand, there exist experiments dedicated to ultrafast strain detection by all-optical means, which are referred to as picosecond-ultrasonics. While this field of research also profits from the advances in femtosecond laser setups and lock-in techniques, it generally requires more effort to discriminate magnetic from non-magnetic contributions in these experiments. Difference schemes often fail to work because the magnetostriction effect is proportional to the square of the magnetic order parameter and thus invariant under the inversion of the magnetization vectors by an external field. One experimental way to identify magnetic effects on the laser-induced lattice dynamics are temperature dependent measurements that exhibit effects, which are proportional to $|M|^2(T)$ where $|M|(T)$ is the temperature dependent magnetization. Saturation effects that lead to a non-linear fluence dependence in the sample response are often a fingerprint of a (magnetic-) phase transition. A conclusive interpretation however requires further theoretical support to exclude non-linear, non-magnetic contributions. These complications may explain, at least partially, why the field of ultrafast lattice dynamics in magnetic materials has been emerging more recently in comparison to ultrafast magnetization dynamics.

The main questions that arise and motivate this report are:

- What are the signatures of magnetic excitations on the strain response and how can they be observed experimentally?
- How fast and how large is the energy transfer between spin and lattice degrees of freedom?
- Are there speed limits for magnetostrictive effects that occur on ultrafast timescales?
- Does the magnetic invar-effect, i.e. the absence of a thermal expansion over a large temperature range due to the compensation of contractive magnetic stresses and expansive phonon pressure, also occur on ultrafast timescales?
- What concepts can be used to describe the ultrafast strain response in magnetic materials?

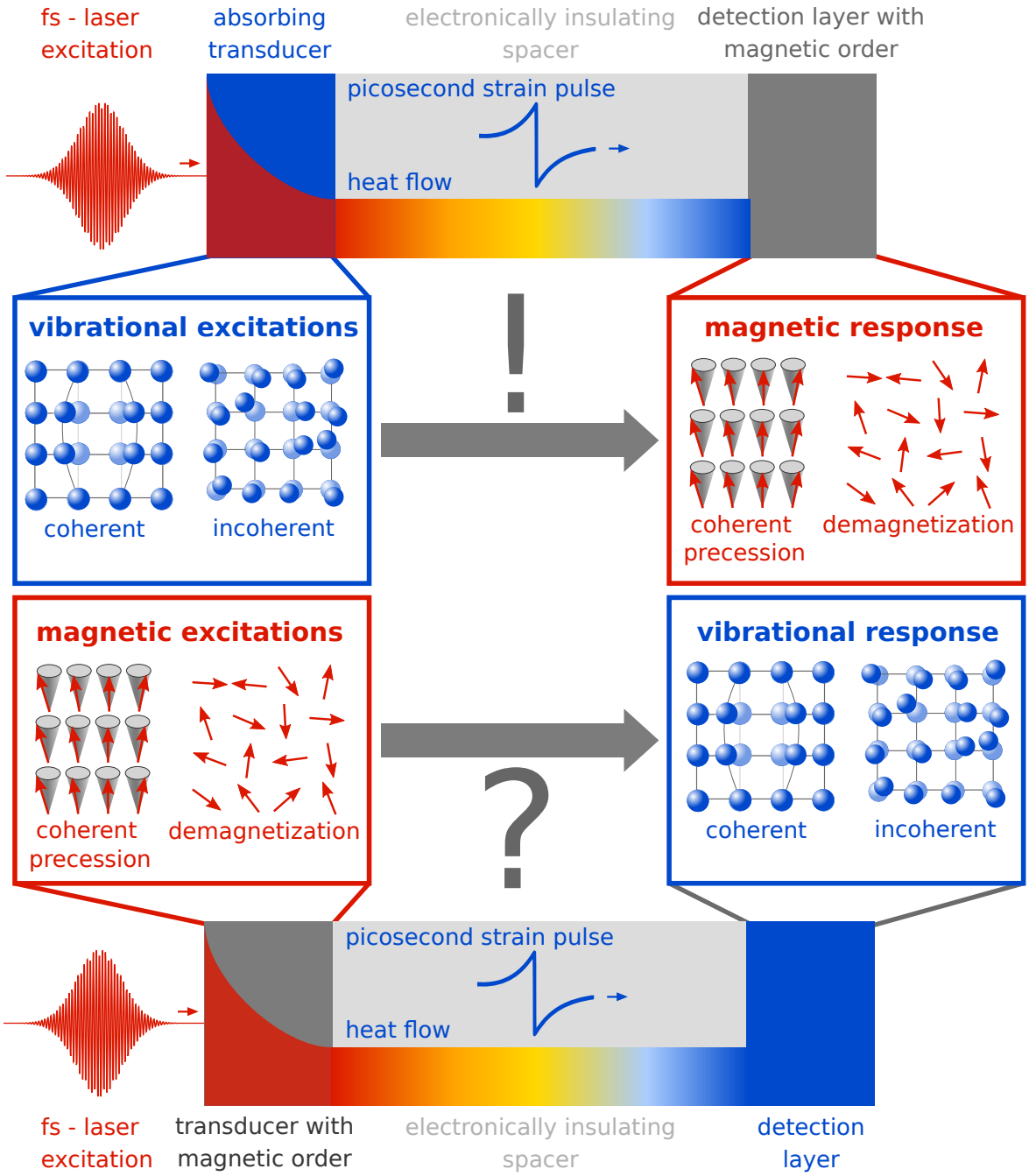

Figure 1.7: Sketch of the research question: Previous reports have demonstrated and studied magnetization manipulation by coherent and incoherently excited lattice vibrations (phonons)[34, 96, 101–105]. The involved processes are schematically depicted in the top half. This work is dedicated to the investigation of the inverse process, especially the strain that results in response to magnetic excitations. It is interesting to investigate to which extent the picosecond strain response in laser-excited films is influenced by magnetic excitations that can possibly be tuned by external fields. For conceptual clarity, this depiction separates the generation region of vibrational and magnetic excitations from the detection area. In real experiments they may be identical and electronic excitations can then contribute an additional coupling between these subsystems, especially in metals.

1.4 Related work on ultrafast magnetostriction

In addition to the so far mentioned models there exists a number of related works on time-domain investigations of the coupled spin-lattice dynamics that have inspired this work. They are only enumerated briefly along with the key concept in order to outline the context of the scientific debate at the time of writing this thesis. In general, the publications can be grouped into either magnetic effects, triggered by strain, and lattice dynamics triggered by magnetization changes.

A comprehensive overview over the entire literature on magnetostriction and ultrafast magnetization effects is beyond the scope of this thesis. Selected experimental milestones for this field are provided in the timeline shown in figure 1.8. The bottom panel of this figure also provides the number of scientific publications that are listed in the "Web of Science" by Clarivate Analytics[107] for the different topics. Although certainly not all relevant publications are covered in these graphs, they nevertheless provide a rough trend on the emergence and development of research related to the topics "ultrafast", "magnetism" and "magnetostriction". It shows that the time-resolved investigations of magnetization dynamics and their coupling is a development that starts in the middle of the 1990s, whereas the field of research in ultrafast effects started approximately 20 years earlier. The overview shows that the field of magnetism has experienced research interest throughout the years, whereas magnetostriction research strongly increased since the mid 1960s when giant magnetostriction effects where discovered. Among the considered keywords, the combination of ultrafast and magnetostriction measurements is a most recent development.

Multiple experiments have demonstrated that the inverse magnetostriction can be used to trigger magnetization dynamics on ultrafast timescales. A combined ultrafast, all-optical recording scheme in nanoscopically stable bits is one of the scenarios that motivates many research projects in time-resolved spin-lattice interactions. A selection of the related research is provided in the following list:

- Experiments by Scherbakov et al. [101] and Thevenard et al. [102] show that picosecond strain pulses can induce a magnetization precession in the Mn-doped semiconducting GaAs, which is analyzed theoretically by Linnik et al. [40].
- Kim et al. [105, 108] demonstrate the magnetization precession triggered by strain pulses in metallic nickel films.
- Experiments on Galfenol FeGa by Jäger et al. [34, 96] demonstrate the effective magnetization manipulation by transverse and longitudinal picosecond strain pulses in a thin film with large magnetostriction. Linnik et al. [41] provides an in-depth analysis of the underlying change of the magneto-crystalline anisotropy due to the picosecond transverse- and longitudinal strain pulses as well as the laser-induced heating.
- Deb et al. reported the excitation of a long-lived magnetization precession[103] and higher order standing spin-waves[104, 109] in insulating Bismuth doped yttrium iron-garnet $(\mathrm{Bi_xY_{1-x}Fe_5O_{12}})$ by coherently and incoherently excited phonon modes.
- Maehrlein et al. [100] report the magnetization dynamics in doped Yttrium Iron Garnet upon a selective excitation of the transverse optical Fe-O phonon mode using THz radiation. They report a fast $\tau = 1.4\,\mathrm{ps}$ coupling directly after the resonant excitation and a slow $\tau = 90\,\mathrm{ns}$ timescale attributed to the coupling of incoherent phonons to the spin system. The observed magnetization response could be rationalized as a modulation of the super-exchange coupling constant by the excited optical phonon.
- The works of Thevenard et al. [39] and Camara et al. [110] demonstrate strain assisted magnetization switching using surface acoustic waves.
- Reviews by Hono et al. [111] and Weller et al. [112] outline heat-assisted magnetic recording (HAMR)-schemes that promise to substantially increase the magnetic data density by reducing the

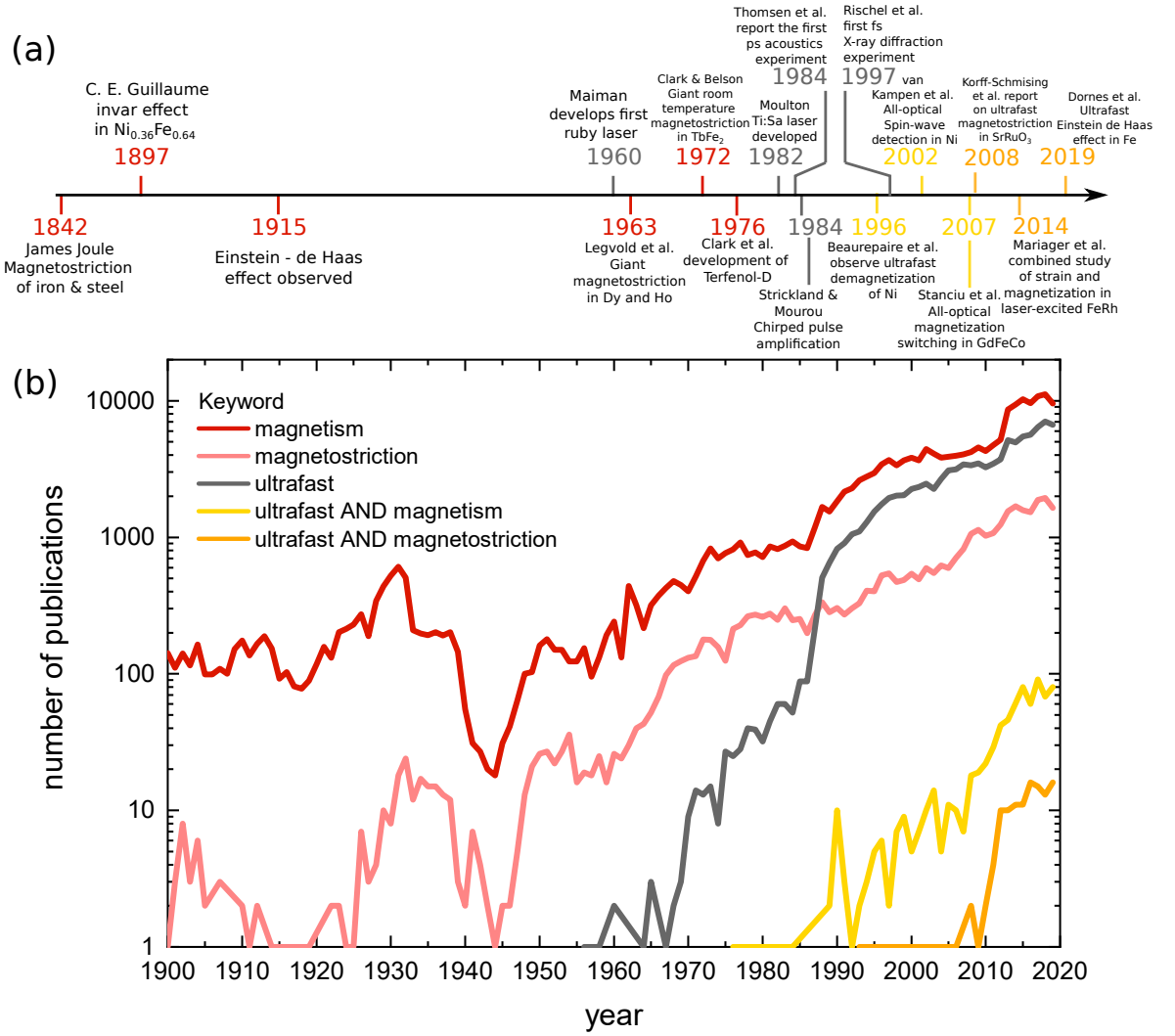

Figure 1.8: Timeline in the field of ultrafast magnetostriction: The top panel depicts a selection of experimental events that are important for the development in the field of ultrafast magnetostriction. The bottom panel depicts the number of publications related to different key words as listed in the databases linked to the "Web of Science" by Clarivate analytics.[107] Although this depiction is far from complete, it provides a rough historical survey of the development of the related research fields over time.

size of stable- but writable magnetic bits by transiently lowering the anisotropy using a heat pulse. A very recent review by Kimel et al. [24] on photo-ferroic recording provides the basic concepts for all-optical switching of magnetic order and ferroelectric polarization states.

Studies on time-resolved effects of the lattice dynamics in magnetic materials are less numerous. The following list presents the papers in their approximate chronological order alongside their main idea:

- Korff-Schmising et al. [113] show that the magnetostrictive stress in a superlattice that contains magnetic perovskite material $SrRuO_3$ rises within the first picosecond. This indicates the potential for ultrafast stress generation by changes in the magnetic order.
- Mariager et al. [114] and Quirin et al. [115] report the lattice dynamics in FeRh that shows an expansive magnetic stress, which rises on the same picosecond timescale as the metamagnetic phase-transition from the antiferromagnetic to the ferromagnetic phase of FeRh.
- Janušonis et al. [116, 117] demonstrate the selective excitation of coupled magneto-elastic waves using a transient grating excitation scheme when the external field is chosen such that the magnon

and phonon modes are in resonance.

- Henighan et al. [81] study coherently excited phonon modes of high-frequency in a laser-excited thin Fe film. They report a non-equilibrium distribution of the energy within the phonon modes that lasts up to 20 ps but observe no effect of the lattice response from the orientation of the magnetization.
- Parpiev et al. [36, 118] and Pezeril[119] discuss the generation of transverse strain pulses by a laser induced demagnetization. The presence of these transverse phonon modes is seen by their different speed of sound that induces a beating in the observed time-resolved reflectivity.
- Jal et al. [120] demonstrate the combination of lattice and magnetic dynamics by time-resolved resonant and non-resonant soft-X-ray reflectometry from a thin film heterostructure that contains a nickel layer. The presented experimental approach can be used to observe both the demagnetization and strain response using the same pump-pulses, which facilitates the direct comparison.
- Krasniqi et al. [121] show an increased damping especially for long-wavelength acoustic phonon modes by magnetic impurities in the magnetic semiconductor $\mathrm{GaMn_{0.09}As_{0.91}}$. It is found that these magnetic impurities decrease the heat transport by the localization of phonon modes.
- A combination of ab-initio modeling, resonant X-ray scattering and ultrafast electron diffraction on free standing FePt grains is presented by Reid et al. [122]. They observe a large in-plane expansion and a transient out-of-plane contraction that is explained to be driven both by magnetic stresses and anisotropic phonon-phonon interactions.
- Hashimoto et al. [123] and Hioki et al. [124] measure magnetoelastic waves and their dispersion relation in Yttrium Iron Garnet, which is a ferrimagnetic insulator that is frequently studied in magnonics.
- Dornes et al. [15] show signatures of transverse phonon generation in X-ray diffraction experiments upon ultrafast demagnetization in a laser-excited Fe film. The results indicate that the angular momentum transfer to the phonon system occurs already within the first few picoseconds.

1.5 Structure of the thesis

This work is structured as follows:

- Chapter 1 contains the motivation, central definitions and scientific context for this work. It is designed to outline the research question of the strain generation in magnetic materials.
- Chapter 2 presents a list of published articles that are the core of this publication based thesis and briefly discusses their content and relation to the topic of this thesis. The full articles are attached at the end of this work.
- Chapter 3 presents the used experimental setup based on three examples that demonstrate the capabilities of the laser-based plasma X-ray source. It contains the vibration and cooling of metallic nano-particles, unconventional energy transport in nanoscale gold-nickel heterostructures and the tracking of picosecond strain pulses in a buried detection layer.
- Chapter 4 summarizes the strain generation mechanisms and introduces the concepts behind the usage of a Grüneisen parameter to describe the observed strain in magnetic thin films.
- Chapter 5 discusses the ultrafast strain in laser-excited granular and continuous FePt and presents a two-pulse excitation scheme that can be used to extract the magnetic stress contribution.
- Chapter 6 is dedicated to the time-resolved strain in laser-excited dysprosium that serves as a representative for the class of heavy rare earth materials where contractive magnetic stresses have a dominant influence on the laser-induced strain response.
- Chapter 7 summarizes the experimental findings and provides a perspective on possible future work.

Chapter Two

List of Articles

The main part of this dissertation is based on the following articles that I (co-)authored in the course of my PhD work from 2016 - 2020 in the ultrafast dynamics in condensed matter group headed by Prof. Matias Bargheer at the University of Potsdam. The articles and manuscripts are sorted with respect to their appearance in the discussion. The content of each article, its contribution to the scientific field and my personal contribution are summarized briefly below each item.

The first three publications demonstrate the capabilities of the laser-based UXRD setup to observe lattice strain in nanoscopic (hetero-)structures using a plasma-X-ray source. Ultrafast diffraction with subpicosecond time and sub-ångström spatial resolution in addition to the large penetration depths of hard X-rays is otherwise limited to high-cost, large-scale facilities such as free electron lasers or dedicated slicing beamlines at synchrotrons. These articles provide the introduction into the measurement principle, based on examples where magnetic contributions to the strain response are not of primary importance.

I **Watching the vibration and cooling of ultrathin gold nanotriangles by ultrafast x-ray diffraction** **139**

Alexander von Reppert, Radwan Mohamed Sarhan, Felix Stete, Jan-Etienne Pudell, Natalia Del Fatti, Aurélien Crut, Joachim Koetz, Ferenz Liebig, Claudia Prietzel, and Matias Bargheer, *The Journal of Physical Chemistry C* 120, 28894-28899 (2016)

This publication demonstrates that UXRD using a plasma-X-ray source can observe the laser-induced lattice strain of approximately 6 nm thin triangular gold-nano-platelets. The scientific novelty originates from the laboratory based scattering experiments on nanoscopic objects that consist of less than 30 atomic layers. We observed the 2 ps oscillation period of the breathing motion that is consistent with the sound-velocity in the (111) direction of gold. We quantify the transient laser-induced electron and lattice-temperature rises in plasmonic nanoparticles whose role in light-driven catalysis processes is a current topic of research.

I conducted the UXRD experiments together with Jan-Etienne Pudell, carried out the data evaluation, discussed the strain modeling with Matias Bargheer and commented on the manuscript.

II **Layer specific observation of slow thermal equilibration in ultrathin metallic nanostructures by femtosecond x-ray diffraction** **147**

Jan-Etienne Pudell, Alexei A. Maznev, Marc Herzog, Matthias Kronseder, Christian H. Back, Gregory Malinowski, Alexander von Reppert, and Matias Bargheer, *Nature Communications* 9, 3335 (2018)

This article demonstrates the capability of UXRD to investigate energy transport processes in nanoscale heterostructures that are thinner than the optical penetration depth and thus are hard to disentangle by all-optical spectroscopy. The counter-intuitive observation is that the lattice vibrations of the thin gold film in such heterostructures are heated significantly slower compared to the prediction by the heat diffusion equation. The utilized material specificity of the UXRD response can be applied in future investigations of nanoscale-heat transport properties in many different sample geometries if a sufficient degree of crystallinity is provided in at least one of the layers within the sample.

I conducted the UXRD experiments and data evaluation together with Jan-Etienne Pudell. I interpreted the results together with Alexei Maznev, Marc Herzog, Jan-Etienne Pudell and Matias Bargheer. I contributed significantly to the modeling and preparation of the manuscript for which I am corresponding author.

III **Tracking picosecond strain pulses in heterostructures that exhibit giant magnetostriction** **157**

Steffen Peer Zeuschner, Tymur Parpiiev, Thomas Pezeril, Arnaud Hillion, Karine Dumesnil, Abdelmadjid Anane, Jan-Etienne Pudell, Lisa Willig, Matthias Rössle, Marc Herzog, Alexander von Reppert, and Matias Bargheer, *Structural Dynamics* 6, 024302 (2019)

This publication illustrates the possibility to carry out picosecond-acoustics experiments where laser-generated strain pulses are detected via X-ray diffraction. This allows for a direct detection of the average strain amplitude that can only be inferred indirectly by modeling the acousto-optical response in all-optical picosecond acoustic experiments. The large penetration depth of X-ray pulses allows for probing laser-generated strain pulses in a spatially separated detection layer that is buried below an optically opaque transducer. The different propagation speeds of coherent and incoherent phonon excitations (i.e. hypersound and heat) separate the strain pulses from the strain response due to thermal expansion in the time-domain. We show that multiple echoes of the strain pulses occur as signals in the magneto-optical Kerr effect of the giant magnetostriction material $TbFe_2$. The access to strain pulses with an amplitude calibrated by X-ray diffraction will be useful in future magneto-acoustics experiments, where the amplitude and shape of the strain-induced magnetization precession or even switching is of central interest.

I conducted the UXRD experiments, data evaluation, interpretation and modeling together with Steffen Peer Zeuschner and Jan-Etienne Pudell. I wrote the manuscript with comments from the co-authors and I am corresponding author of this article.

The following articles investigate the strain response of laser-excited magnetic materials due to magnetic stresses. The first group of publications is dedicated to the strain and magnetization response of approximately 10 nm thin FePt in two different morphologies i.e. as continuous FePt film and as nanograins embedded in an amorphous carbon matrix. Especially the magnetization dynamics in FePt

have received large interest due to the application of this material in heat-assisted magnetic recording schemes. Article IV and article V show that both the strain response and the evolution of the magnetization depend on the elastic and thermal boundary conditions defined by the morphology. In article VI we combine insights from the strain- and magnetization-dynamics and provide an experimental method to identify the magnetic stress contribution to the strain response of FePt that competes with the strain response driven by strongly anisotropic phonon stresses of this material.

IV **Ultrafast laser generated strain in granular and continuous FePt thin films** **175**

Alexander von Reppert, Lisa Willig, Jan-Etienne Pudell, Matthias Rössle, Wolfram Leitenberger, Marc Herzog, Fabian Ganss, Olav Hellwig, and Matias Bargheer, *Applied Physics Letters* 113, 123101 (2018)

This article compares the strain response of approximately 10 nm thin FePt specimen. We find that a continuous FePt film and FePt nanoparticles attached to a MgO substrate exhibit an expansion or only a short-lived transient contraction compared to the laser induced-contraction that is reported for free-standing FePt grains by Reid et al. [122]. Using a one-dimensional modeling approach we report the temporal shape of the total stress perpendicular to the sample surface, that is necessary to rationalize the observed strain response. This publication highlights the effects of the film morphology - granular vs. continuous for the ultrafast strain response on otherwise identical materials.

I conducted the UXRD experiments and the data evaluation together with Jan-Etienne Pudell. I performed the modeling of the strain response and wrote the manuscript with comments from all co-authors.

V **Finite-size effects in ultrafast remagnetization dynamics of FePt** **185**

Lisa Willig, Alexander von Reppert, Marwan Deb, Fabian Ganss, Olav Hellwig, and Matias Bargheer, *Physical Review B* 100, 224408 (2019)

This publication shows the morphology-dependent remagnetization of FePt. While the small FePt nano-grains inherently form single domain states, multiple domain states that minimize the stray field exist in continuous FePt thin films under equilibrium conditions. This leads to domain wall-motion effects that influence the field-dependent remagnetization for thin FePt films, which we do not observe for the nano-granular FePt. The fastest possible remagnetization is observed under a high-magnetic field that enforces a single-domain state whose magnetization recovery is limited by heat dissipation processes to the substrate. This article adds to the substantial amount of literature that is dedicated to the ultrafast demagnetization process, by providing an experimental study of the remagnetization process. This is of equal importance for maximizing data storage rates in all-optical magnetization manipulation schemes. It quantifies the relevant timescale for the remagnetization process in FePt nanograins to be 100 ps for high-fluence excitation conditions that are present in our setups. This result is used in the analysis of the recovery of the spin-stress contribution.

I assisted Lisa Willig in the MOKE measurements as well as in the analysis and interpretation of the results. I contributed to the writing of the manuscript.

VI **Spin stress contribution to the lattice dynamics of FePt** **193**

Alexander von Reppert, Lisa Willig, Jan-Etienne Pudell, Steffen Peer Zeuschner, Gabriel Sellge, Fabian Ganss, Olav Hellwig, Jon Ander Arregi, Vojteč Uhlíř, Aurélien Crut, and Matias Bargheer, *Science Advances* 6, eaba1142 (2020)

This manuscript demonstrates a versatile experimental method that directly shows the presence of a spin-stress contribution in FePt by using a two-pulse excitation scheme. The first laser pulse induces a demagnetization, while the second pulse triggers a strongly magnetization-dependent lattice response in the FePt nanograins. This work combines the insights gained by the previous two articles on the morphology-dependent strain and magnetization evolution. Using finite element methods we can qualitatively model the strain response of cylindrical FePt particles that are subjected to different in-plane boundary conditions and anisotropic stresses. The applied continuum elasticity theory accounts for the coupled in-plane and and out-of-plane motion and confirms the hypothesis of article IV that the observed out-of-plane strain response is significantly influenced by the varying extent of in-plane motion for the investigated FePt specimen. The experimental approach of a two-pulse excitation can be used in future investigations to disentangle saturable stress contributions that occur at phase-transitions from electron-phonon contributions.

I conducted the UXRD experiments together with Jan-Etienne Pudell, carried out the data evaluation and interpretation and wrote the manuscript together with Matias Bargheer using comments from the co-authors.

The following group of articles reports the strain response of Dysprosium, Gadolinium and Holmium upon femtosecond laser excitation. These materials belong to the class of heavy rare earth elements, which are interesting subjects for picosecond acoustic experiments since they exhibit giant magnetostriction i.e. relative lattice strains in excess of 0.1% upon changes in the magnetization. The following articles show that such effects are also present in the picosecond strain response that is observed by time-resolved experiments in rare earth containing heterostructures. Both the picosecond strain pulses and the slowly varying transient strain that occurs due to heat diffusion encode information on the energy transfer processes to phonons and magnetic excitations within the samples.

VII **Unconventional picosecond strain pulses resulting from the saturation of magnetic stress within a photoexcited rare-earth layer** **215**

Alexander von Reppert, Maximilian Mattern, Jan-Etienne Pudell, Steffen Peer Zeuschner, Karine Dumesnil, and Matias Bargheer, *Structural Dynamics* 7, 024303 (2020)

This article provides a comprehensive overview of the picosecond strain response of a Dy thin film studied by UXRD. The investigated metallic heterostructure also contains a Niobium film that serves as a buried detection layer for the picosecond strain response, which shows strong deviations from the conventional bipolar shape due to the presence of contractive magnetic stresses within the Dysprosium film. This work combines many different aspects of the investigations that are listed in the following and discusses the signatures of the saturable energy transfer to magnetic excitations to the picosecond strain pulse and the observed thermal transport. The modeling approach in this article provides a space- and

time-dependent magnetic stress profile that adds to the electron-phonon stresses that can be calibrated from strain response of the sample in its paramagnetic state. The required rise times of the magnetic stress that reproduce the strain response in the antiferromagnetic phase of Dysprosium are in close agreement with the recently reported demagnetization timescales. This indicates that the strain response can serve as a proxy for the time-dependent magnetic ordering within an antiferromagnet.

I conducted the UXRD experiments with the help of Jan-Etienne Pudell and Steffen Peer Zeuschner. Maximilian Mattern and I carried out the modeling of the stress with the advice from Jan-Etienne Pudell on the implementation in the UDKM1DSIM toolbox. I wrote the manuscript with the input of the co-authors.

This article represents the first study of the picosecond strain response of an antiferromagnetic Dysprosium thin film upon femtosecond laser-excitation. Our analysis employs the thermodynamic principle of a Grüneisen constant that relates the stress on the lattice to the energy density. Although this concept has mostly been applied to electronic and phononic energy density, we extend the model to magnetic excitations. We find that energy deposited into the magnetic subsystem generates stress with opposite sign and three times more effectively than energy in electron and phonon excitations. The total stress is modeled as the sum of magnetic and phonon stresses, which allows us to track the energy-density in each of the subsystems separately. The resulting, time-dependent energy density distribution suggests a long-lasting non-equilibrium between the phonon and the magnetic system that becomes especially pronounced in experiments close to the Néel temperature. In this publication we advocate the use of thermal energy distributions within the subsystems instead of subsystem-temperatures for the modeling of the strain response. This concept of an energy density that creates a stress is applicable also in non-equilibrium situations, where a temperature may not be a well-defined quantity.

I conducted the measurements and raw data evaluation with the help of Jan-Etienne Pudell and Flavio Zamponi. I carried out the modeling and worked significantly on the manuscript.

This work extends the analysis of the energy distribution within the Dysprosium layer to track the energy transport through the entire metallic heterostructure by observations of the

strain response of all layers within the metallic heterostructure. The high stability, sensitivity and large accessible delay range at the X-ray pump-probe beamline (KMC-3 XPP) at the synchrotron radiation facility BESSY II allowed us to track the energy flow up to hundreds of nanoseconds. This publication shows that magnetic excitations of the antiferromagnetic Dysprosium layer can store energy, which reduces the energy flow within the heterostructure. It demonstrates the utility of synchrotron based, timeresolved X-ray diffraction, which can monitor the energy transport through nanoscale heterostructures on large timescales that are inaccessible at our plasma-X-ray source.

I assisted in the interpretation of the results, advised Azize Koç on the modeling and commented on the manuscript.

X **Grueneisen-approach for the experimental determination of transient spin and phonon energies from ultrafast x-ray diffraction data: gadolinium** **269**

Azize Koç, Matthias Reinhardt, Alexander von Reppert, Matthias Rössle, Wolfram Leitenberger, Markus Gleich, Martin Weinelt, Flavio Zamponi, and Matias Bargheer, *Journal of Physics: Condensed matter* 29, 264001 (2017)

In this publication we demonstrate the applicability of the Grüneisen concept to the strain response of a laser-excited, ferromagnetic Gadolinium layer. Among the heavy rare earth elements Gadolinium represents the special case of a half filled 4f-electronic shell with a vanishing orbital-angular momentum. In the resulting absence of the spin-orbit coupling we observe a strain response that can be analyzed using the previously established language of a Grüneisen model, which documents the utility of the concept. This hints at the importance of the distance-dependent exchange interaction in the magnetostriction of Gd.

I assisted in the interpretation of the results and commented on the manuscript.

XI **Ultrafast negative thermal expansion driven by spin disorder** **279**

Jan Pudell, Alexander von Reppert, Daniel Schick, Flavio Zamponi, Matthias Rössle, Marc Herzog, Hartmut Zabel, and Matias Bargheer, *Physical Review B* 99, 094304 (2019)

This study finds an agreement between the reported demagnetization timescales for the heavy rare earth holmium and our time-dependent energy transfer model between phonons and magnetic excitations. It provides the first example how the picosecond strain pulse, launched from the laser-excited rare-earth layer, changes between the high temperature paramagnetic and the low-temperature antiferromagnetic phase. It furthermore connects the thermodynamic concepts that have been applied to describe negative thermal expansion under near equilibrium conditions to the laser-induced processes on ultrafast timescales. It highlights the importance of the volume dependence of the spin-entropy for the strain response, which is particularly pronounced in the heavy rare earth materials that host the largest magnetic moments per atom of all elements.

I conducted the UXRD experiments and the data evaluation together with Jan-Etienne Pudell and Flavio Zamponi. I commented on the interpretation and the manuscript.

Chapter Three

Capabilities of the plasma-based X-ray diffraction setup

This chapter briefly presents the laser-driven, plasma-based X-ray diffraction setup that I primarily used to study the strain-dynamics in magnetic materials. Based on three examples, I discuss the capabilities of the technique. In addition to relating the discussed publications to the general context of this thesis, I present so far unpublished data to further support and supplement the conclusions of the introduced papers.

3.1 Description of the experimental setups

In the majority of the discussed experiments I employ the laser-based plasma X-ray source (PXS) that was constructed in the course of the PhD thesis of Daniel Schick at the University Potsdam[125]. The setup is described in a dedicated publication[126] and the data analysis for the ultrafast reciprocal space mapping with a convergent beam is also discussed by Schick et al. [127] and my MSc thesis[128]. Figure 3.5 serves as a schematic sketch of the experiment. It schematically introduces the static and time-resolved diffraction techniques that are used in this thesis alongside the corresponding X-ray generation mechanism.

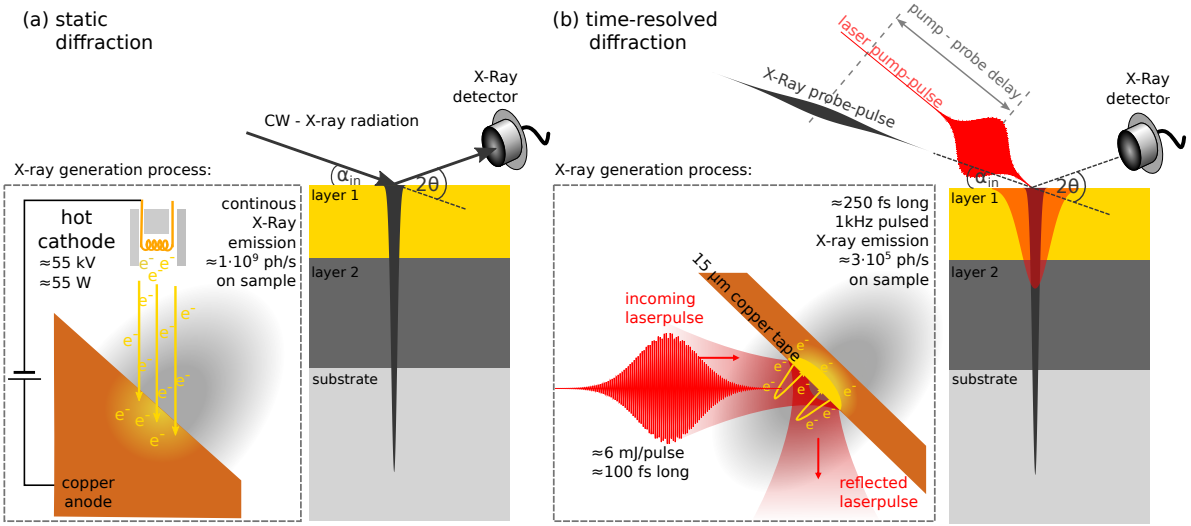

Figure 3.1: Schematic diagram of an (U)XRD experiment: (a) static diffraction experiment where a microfocus X-ray tube is used as source. (b) time-resolved diffraction experiment with a laser-pump - X-ray probe pulse setup, where the femtosecond laser generates a non-equilibrium state that is probed by X-ray pulse at variable delay. The inset in (b) is adapted from the original work by Weißhaupt et al. [129].

Although the two operation modes contrasted in figure 3.1 employ different target designs and sources for high-energy electrons, the X-ray generation process for the K-α emission is similar. It is based on inelastic electron-electron scattering events that create holes in the Cu-1s states, which are predominantly refilled by electrons that occupy the higher energetic Cu-$2p_{3/2}$ and $2p_{1/2}$ states. The excess energy between the Cu-1s and Cu-2p states can be released by the emission of photons or by Auger electrons. The PXS utilize the X-ray fluorescence process, which yields an incoherent source of unpolarized photons that are initially emitted isotropically. Both the X-ray tube and the plasma-generation process exhibit the maximum X-ray yield at the energies of the Cu-$K_{\alpha,1}(2p_{3/2} \rightarrow 1s)$ and Cu-$K_{\alpha,2}$ $(2p_{1/2} \rightarrow 1s)$ electronic transitions, which have an energy of 8047.8 eV and 8027.8 eV respectively. We employ a Montel-multilayer optic that is optimized for reflecting light with these energies onto the sample, so that the continuous Bremsstrahlung-background as well as other characteristic lines are suppressed. Details about the multilayer optic in comparison to other X-ray optics were published by Bargheer et al. [130]. Specific details on the optics, the transmitted X-ray spectrum and further references about the development and functional principle of the plasma X-ray generation process are provided in my MSc thesis[128].

Experiments without time-resolution are carried out using a commercial micro-focus X-ray tube (Oxford instruments X-ray Microfocus, UltraBright, 60kV, Cu) that continuously emits X-rays using externally generated electrons that are accelerated onto the solid copper anode by an applied electric field. This setup is employed to observe temperature dependent changes of the lattice constant d that occur upon slow heating and cooling where all internal degrees of freedom are given minutes to thermalize with the cryostat. The advantage of the static source is its high stability, its autonomous operation in combination with an approximately 100 times higher X-ray flux per second compared to the PXS. Thus, it is useful for sample pre-characterizations without laser-excitation. The main observable in the temperature dependent experiments is the strain $\eta(T)$ with respect to a reference temperature T_0. It is obtained from the temperature dependent Bragg-peak shift that yields the average lattice constant $d(T)$ and thus $\eta(T)$ according to:

$$\eta(T) = \frac{d(T) - d(T_0)}{d(T_0)}. \tag{3.1}$$

The main part of this thesis is based on time-resolved experiments that employ the pump-probe scheme. In these experiments a short laser-pulse deposits energy in the sample, which triggers a strain response that is subsequently probed by an X-ray pulse at a variable delay. By scanning the delay between the pump laser- and the probe X-ray -pulse we can observe the time-dependent diffraction peak shift that results from the transient change of d of the materials within the excited sample. The main observable in these experiments is the time-dependent lattice strain $\eta(t)$ relative to the lattice constant before excitation:

$$\eta(T) = \frac{d(t) - d(t < 0)}{d(t < 0)}. \tag{3.2}$$

The pump-probe delay time $t < 0$ corresponds to a setting, where the X-ray diffraction pulse arrives before the laser pump-pulse. The usage of $d(t < 0)$ as a reference for the strain determination implies that the sample has returned to its equilibrium lattice spacing before the next laser pulse hits. In our setup the time between subsequent laser pulses is 1 ms and the experiments are thus limited to reversible processes that recover on that time-scale. Non-reversible effects, such as melting or other irreversible phase transitions can be identified by comparing the diffraction signal with- and without laser illumination when the X-ray pulse is chosen to arrive few picoseconds before the laser excitation. Time-resolved experiments of irreversible effects in a pump-probe scheme require dedicated setups that either provide a fresh sample for each pump-pulse or record the full time trace after a single excitation pulse.

3.1.1 Diffraction geometry and data analysis

This section introduces the diffraction geometry, briefly presents the data analysis routine and frequently observed broadening effects of the X-ray peaks that occur in both the static and the time-resolved experiments. The experiments have in common that X-rays with a wavevector $\vec{k}_{\mathrm{in}}$ are incident on the sample at an angle α_{in} relative to the sample surface and are reflected at an angle α_{out} relative to the sample surface. In our research group we often refer to the angle of incidence relative to the lattice planes from which the diffraction occurs by ω and denote the diffraction angle relative to the X-ray beam by 2θ. This is sketched in figure 3.2. In the setup one can scan α_{in} by turning the sample relative to the X-ray beam and choose the detector position to detect the X-rays at a suitable value of 2θ using a two circle goniometer. Diffraction maxima in the detected X-ray intensity occur when the Laue condition

$$\vec{k}_{\mathrm{out}} - \vec{k}_{\mathrm{in}} = \vec{G} \tag{3.3}$$

is fulfilled. Therein $\vec{k}_{\mathrm{in}}$ and $\vec{k}_{\mathrm{out}}$ are the wave-vectors of the elastically scattered X-rays ($|\vec{k}_{\mathrm{in}}| = |\vec{k}_{\mathrm{out}}| = k = \frac{2\pi}{\lambda_{\mathrm{X-ray}}}$) and $\vec{G}$ is the reciprocal lattice vector for a set of lattice planes from which the diffraction occurs. $\vec{G}$ fulfills the relation $|\vec{G}| = \frac{n2\pi}{d}$ where d is the average spacing between the lattice planes and n the order of the reflection. This already implies that the application of the diffraction technique requires samples with a sufficient degree of crystallinity so that a reciprocal space-vector $\vec{G}$ is defined. All presented experiments are carried out in the coplanar geometry so that $\vec{k}_{\mathrm{out}}$ lies in the scattering plane defined by $\vec{k}_{\mathrm{in}}$ and the sample surface normal. More specifically, the here reported experiments are carried out close to the symmetric diffraction condition where α_{in} is approximately equal to α_{out}. Experiments in the symmetric diffraction geometry are sensitive to the out-of-plane lattice constant and thus the strain along this direction. Figure 3.2 schematically compares the symmetric and asymmetric X-ray diffraction geometries.

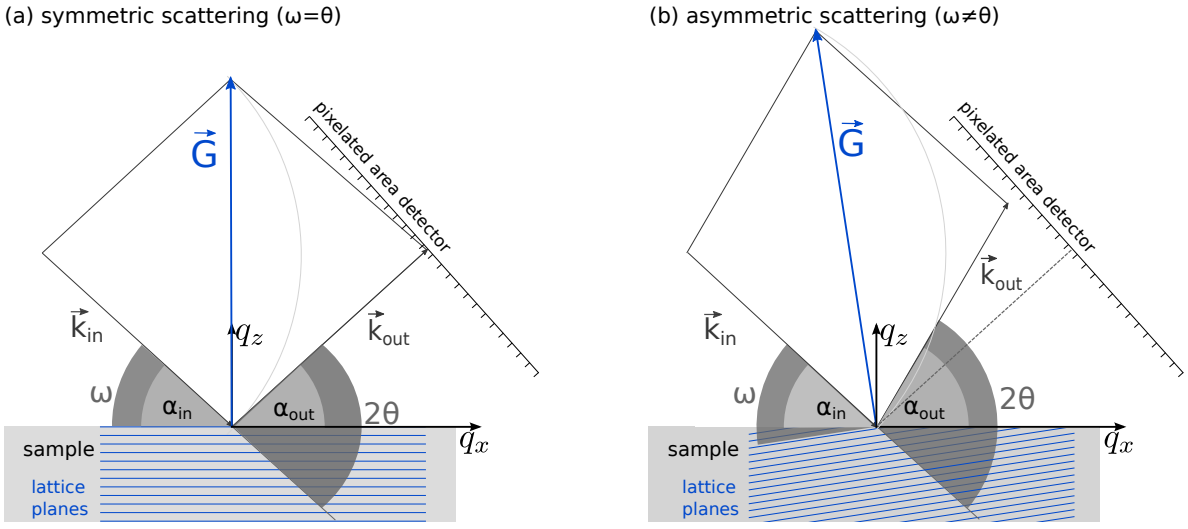

Figure 3.2: Sketch of the diffraction geometry: (a) symmetric diffraction geometry where the angle of incidence relative to the sample (α_{in}) is equal to the reflection angle (α_{out}). In this case the reciprocal scattering vector is aligned along the out-of plane reciprocal space direction $\vec{q}_{\mathrm{z}}$. (b) Sketch of an asymmetric scattering event where reflection occurs from a reciprocal space vector that has a component along the in-plane reciprocal space coordinate $\vec{q}_{\mathrm{x}}$. Both diffraction processes are elastic so that $|\vec{k}_{\mathrm{in}}| = |\vec{k}_{\mathrm{out}}|$, but the scattered photons are detected on different pixels of the area detector. Only case (a) is described sufficiently by equation (3.4), whereas the relation (3.5) also accounts for case (b) which frequently occurs in thin films that exhibit a mosaic spread of the crystal orientation so that not all lattice planes are parallel to the sample surface. Sketch adapted from the book of Holý et al. [131].

One important property of X-rays is their relatively large penetration depth into materials. The grey

shading in figure 3.1 is chosen to indicate the relatively large extinction length of X-rays compared to the extinction length for visible light that is typically on the order of 5-50 nm in metals. The X-ray extinction length for Cu-K$_\alpha$ photons is also material-dependent but ranges typically between 1-50 µm for the materials used in the subsequently presented experiments. This allows both XRD-setups to probe the material-specific average strain response within nanoscopic heterostructures. This is used in multiple experiments presented in this thesis. The selectivity is thereby achieved due to the material-specific lattice spacings d, which lead to different diffraction angles 2θ. This can be seen most easily from the Bragg diffraction condition:

$$n\lambda = 2d\sin\theta \tag{3.4}$$

where λ corresponds to the wavelength of the X-rays (in our case $\lambda \approx 0.154\,\mathrm{nm}$, for Cu-K$_{\alpha 1}$), n to the order of the reflection and θ to half of the angle between the incident and diffracted X-ray beam. A detailed discussion of the theory of X-ray diffraction can be found in dedicated books[132–134], and treatises that specialize on diffraction from thin films[131] or time-resolved X-ray diffraction[127, 130, 135], which I do not repeat here. Bragg's law given in (3.4) describes the symmetric, coplanar diffraction from an infinite set of spatially coherent lattice planes using a parallel, monochromatic beam of X-rays that are scattered elastically. These assumptions are approximations, which are to some degree violated in real samples and experimental setups. This leads to broadening effects on the diffraction peaks that are observed in real experiments. A general discussion of these effects is given in the book of Holy et al. [131], which Schick et al. [127] applies specifically to the plasma X-ray diffraction setup with a convergent X-ray beam. Although Bragg's law is often used in introductory explanations because of its conceptual simplicity, the actual analysis of our X-ray diffraction experiments uses the reciprocal space relations for diffraction from thin films in the co-planar geometry that read[127, 131]:

$$\vec{q} = \begin{pmatrix} q_x \\ q_z \end{pmatrix} = |\vec{k}| \begin{pmatrix} \cos(\alpha_{\mathrm{out}}) - \cos(\alpha_{\mathrm{in}}) \\ \sin(\alpha_{\mathrm{in}}) + \sin(\alpha_{\mathrm{out}}) \end{pmatrix}. \tag{3.5}$$

These relations can be rationalized using the reciprocal space coordinate system attached to the sample as defined in figure 3.2. They also account for asymmetric X-ray reflection processes that occur from crystallites with lattice planes that are tilted with respect to the sample surface. Due to the restriction to co-planar diffraction, only the q_{x} coordinate appears as in-plane direction. The q_{y} direction that is perpendicular to the scattering plane is omitted in the analysis. For thin films without any in-plane symmetry breaking, q_x and q_y are equivalent. Large differences in these in-plane dynamics are not expected because the in-plane forces for homogeneously excited thin films balance each other. An analysis of asymmetric in-plane dynamics would require a three-dimensional reciprocal space mapping approach that can be implemented for example using the *xrayutilities* package[136]. This is used at the XPP-KMC3 BESSYII beamline[137, 138] that is operated by our group, where a four circle goniometer provides the flexibility to scan the reciprocal space along arbitrary directions. For details on the complementary capabilities of the UXRD setup of our group at BESSYII see the recent overview article by Rössle et al. [138].

All data analysis for the presented experiments is carried out based on the relations (3.5) using the Python programming language without dedicated X-ray analysis libraries. A condensed depiction of the data analysis steps from raw detector images to the reciprocal space projection is provided in figure 3.3. It shows a symmetric, reciprocal space scan along the q_{z} direction using the static X-ray tube setup of (111)-oriented triangular gold nanoparticles on a (111)-oriented silicon substrate. This example is chosen because the observed diffraction from the silicon substrate and the thin gold nano-particles represent the limiting cases of a highly ordered bulk crystal and a very mosaic thin film. The time-resolved lattice dynamics of these nano-particles are discussed in section 3.2. Details of the data analysis are covered in

[128] and only a brief overview is provided here.

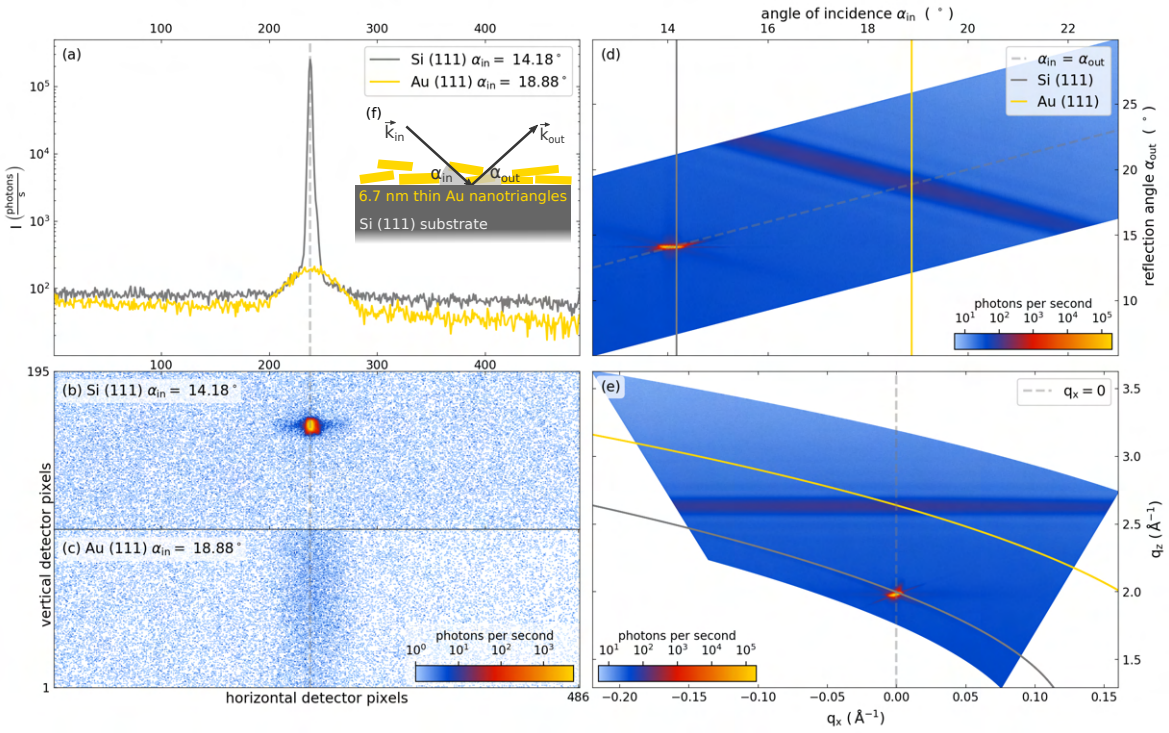

Figure 3.3: Steps from raw data images to the reciprocal spacemap: The depicted data correspond to a symmetric diffraction measurement using the static X-ray tube from gold-nano triangles on silicon substrate that is schematically depicted in inset (f). The raw X-ray area detector images shown in (b) and (c) are summed along the vertical direction to yield the reciprocal space slices shown in (a). The complete intensity recording from a symmetric variation of α_{in} and α_{out} is provided in (d). The resulting reciprocal space projection after the transformation given by equation (3.5) is shown in (e). Slices at the gold and silicon Bragg angle are indicated by the yellow and grey solid line, respectively. The dashed line indicates the symmetric diffraction condition that occurs at the central detector pixel where $\alpha_{\mathrm{in}} = \alpha_{\mathrm{out}}$.

The raw detector images for the case that α_{in} of the X-rays is set to the Bragg angle of the silicon and gold (111)-reflections are shown in figure 3.3(b) and (c). The "Pilatus 100k" area detector from Dectris allows for single photon counting as long as the number of photons is below 10^6 per second and pixel due to the dead time of the pixels of approximately 1 µs.[139] This dead time does not present a limitation to the measurements because of the relatively low X-ray flux so that the proportionality can be ensured by monitoring that less than 1000 photons per pixel and second are detected. The center pixel of the X-ray detector (indicated by the dashed line) corresponds to the symmetric diffraction condition $\alpha_{\mathrm{in}} = \alpha_{\mathrm{out}}$, whereas the other pixels correspond to slightly asymmetric scattering events with a different α_{out}. It is evident that the Si substrate peak exhibits a very intense diffraction maximum at the position of the center pixel, whereas the gold peak is much weaker but broader along q_{x} in comparison. In the first step of the data reduction routine, the X-ray intensity is summed along the vertical detector dimension to yield the reciprocal space slice depicted in panel 3.3(a). This integration reduces the diffraction data to a two-dimensional slice of the reciprocal space and eliminates the coordinate q_{y} that is expected to yield identical results as q_{x}. Many of such reciprocal space slices are recorded by varying $\alpha_{\mathrm{in}} = \alpha_{\mathrm{out}}$ via a rotation of the sample and the detector using the two-circle goniometer. The accumulated diffraction slices are combined in the 2D-representation of the diffraction intensity in angle-space ($I(\alpha_{\mathrm{in}}, \alpha_{\mathrm{out}})$) shown in panel 3.3(d). Using relation 3.5, this intensity is mapped to the reciprocal-space to yield $I(q_{\mathrm{x}}, q_{\mathrm{z}})$, depicted in graph 3.3(d). The solid, colored lines in (d) and (e) indicate the position of the reciprocal space slices

from (a). The grey dashed line at $q_x = 0$ corresponds to the intensity detected at the center pixel position. The comparison of panel 3.3(d) and (e) shows that the mapping 3.5 from the real space angles to the reciprocal space coordinates is non-linear especially for small angles. The depicted diffraction intensity in the reciprocal space projection ($I(q_x, q_z)$) can then be integrated along the q_x-direction or sliced at $q_x = 0$. The average out-of-plane lattice constant d of the material can then be inferred by $d = n2\pi/q_{z,max}$, wherein $q_{z,max}$ refers to the q_z value at which the maximum intensity is observed. As discussed by Schick et al. [127], the slice of the reciprocal space map at $q_x = 0$ yields the highest resolution in reciprocal space, while the integral along the q_x direction yields a rocking curve with significantly higher intensity for peaks that are broadened along the q_x-direction. This advantage of the reciprocal space mapping becomes evident for materials with a large mosaicity and small in-plane coherence length. Both effects are frequently observed broadening mechanisms that are discussed in the remainder of this section.

The actual shape of the diffraction peak in reciprocal space is determined by different broadening mechanisms that originate either from sample imperfections or instrumental properties. A qualitative overview of the different contributions in angle space and reciprocal space based on experience with the diffraction setup is given in figure 3.4. The top row (a)-(d) corresponds to the main sample-dependent broadenings and the bottom row (e)-(h) lists instrumental effects. For the ideal case of a perfectly crystalline infinitely large bulk substrate that is measured using a perfectly parallel, monochromatic beam of X-rays the diffraction peak will be very close to a point in reciprocal space. Its remaining Darwin width needs to be calculated using dynamical diffraction theory that takes multiple X-ray scattering events and the finite extinction length of the X-rays into account.[132]

The subsequently discussed diffraction results are all obtained in thin film samples that are supported by a crystalline substrate. This thin film geometry leads to a broadening of the X-ray diffraction peak due to the finite amount of lattice planes that contribute to the scattering as shown in case (a) of figure 3.4. Due to a lattice constant mismatch between the substrate and the thin film, the film can be epitaxially clamped, which leads to a strain that often relaxes further away from the interface. Thus, the thin film might exhibit a distribution of lattice constants along the out-of-plane direction, which leads to the broadening discussed in case (b). Similar to case (a), a finite coherence length along the in-plane direction adds an additional in-plane component to the reciprocal space vector. If the coherence length varies randomly, the peak becomes broad along the q_x direction. However, if the sample exhibits a well defined coherence length for example by nano-structured in-plane patterns, then discrete peaks along the q_x direction occur. Another effect is expected when the different nano-crystalline domains are tilted with respect to each other. This mosaicity effect also leads to a broadening of the thin film diffraction peaks along the in-plane direction as depicted in case (d), but results in a curvature of the diffraction peak in reciprocal space. For very large angular distributions of the crystallites, the diffraction pattern becomes a ring. This corresponds to the diffraction from polycrystalline specimen with random orientation of the lattice planes that is often referred to as powder diffraction or Debye-Scherrer diffraction.[132]

With regard to the instrument function, the most pronounced features in our case arise from the combination of an X-ray focusing optic that provides a divergence of $\Delta\alpha_{in} \approx 0.3^\circ$ and a polychromaticity due to the presence of both Cu-Kα lines in the X-ray emission spectrum. These effects are captured by case (e) and (f) of the broadening mechanisms and their combination leads to the characteristic tilted double ellipse in the instrument function of the setup shown by Schick et al. [140]. The finite source size effect (case (g)) is not a dominant broadening mechanism, because a proper alignment of the X-ray optics leads to an X-ray spot size on the order of 300 µm on the sample, which is comparable to the X-ray detector pixel size of 172 µm. However, it leads to a diffraction response that often averages over multiple crystalline domains within the film. The specular X-ray reflectivity effect (case (h)) decays rapidly for larger scattering angles so that it leads to a background in the diffraction peaks that can be eliminated

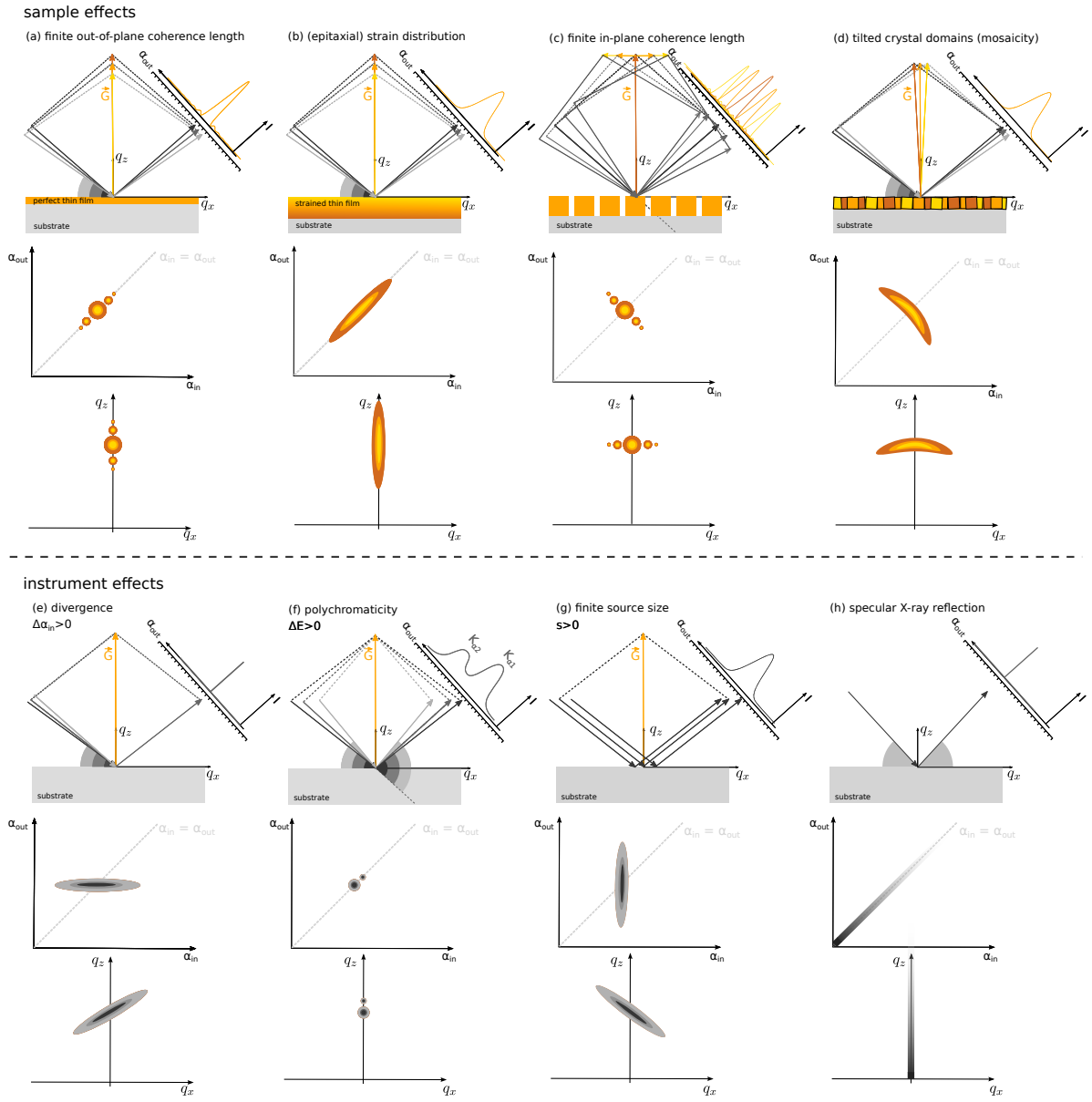

Figure 3.4: Schematic diagram of diffraction peak broadening mechanisms relevant to the PXS-setup: (a)-(d) peak broadening mechanisms due to sample effects that occur in the reflection from a thin film with different crystalline imperfections. (e)-(h) peak broadening due to various instrument effects that occur upon reflection on a perfect crystalline substrate. In reality, multiple broadening effects occur simultaneously, but this figure considers them individually. The top graph of each plot provides a schematic sketch of the considered broadening effect in the diffraction diagram, the middle row an idealized diffraction intensity in angle space $(I(\alpha_{\mathrm{in}}, \alpha_{\mathrm{out}}))$ and the bottom row the transformed intensity in reciprocal space $(I(q_{\mathrm{x}}, q_{\mathrm{z}}))$.

by subtraction. Scattering of the X-rays from air molecules and X-ray fluorescence effects that are not depicted add to the background of the diffraction curves. For thin film samples with a high degree of crystalline order, one observes a combination of instrumental broadening and sample broadening effects. The diffraction shape of other thin films is dominated by finite in-plane coherence length effects and the mosaicity, so that the instrument function remains masked. Regardless of the broadening mechanism, the maximum diffraction intensity occurs at the reciprocal space coordinates that correspond to the average out-of-plane distance irrespective of the broadening.

3.1.2 Description of the UXRD setup

Only a brief account of the main features of the PXS setup is given here since a detailed description of the setup is presented in previous works [126, 128, 141]. A schematic sketch of the subsequently discussed PXS setup is shown in figure 3.5.

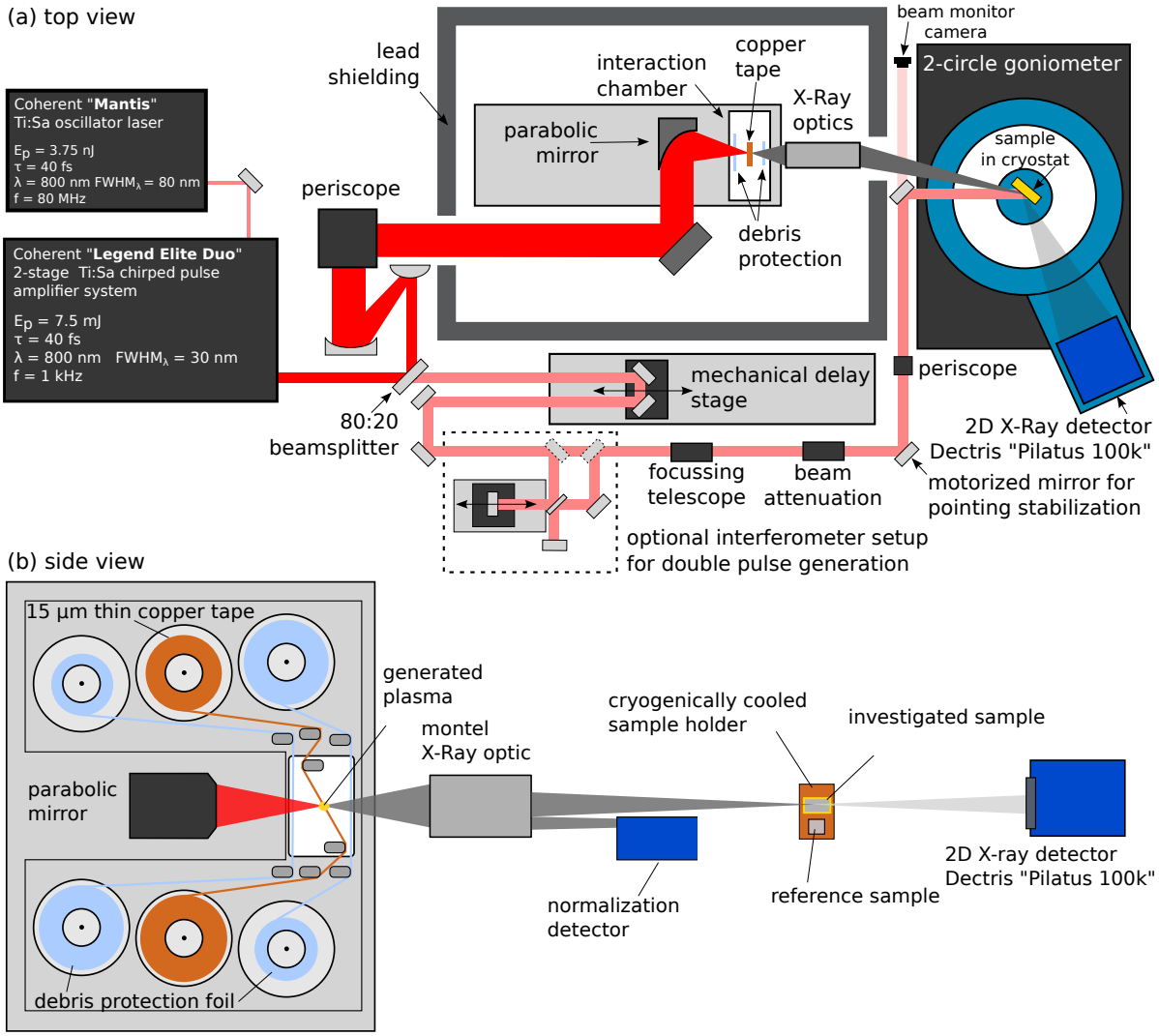

Figure 3.5: Schematic sketch of the PXS setup: (a) top view projection of the main components of the employed laser driven plasma X-ray source setup. (b) Side view of the plasma-X-ray source. A brief description is given in the text. This sketch is updated to include the optional double-pulse generation setup and adapted from the work by Schick et al. [126]. Technical details and available extensions of the PXS setup are discussed in the MSc- and PhD thesis of my colleague Jan-Etienne Pudell [141, 142].

The pump-laser-pulses from a commercial high-power femtosecond laser are split into two parts to generate the required, short X-ray probe pulses for the UXRD experiments and the laser pump-pulses that trigger the sample response. The majority of the pump power is focused onto a continuously exchanged, $\approx 15\,\mu m$ thin copper tape by a parabolic mirror with a focal length of approximately 10 cm. The resulting high light energy density of the laser pulses releases the copper-valence electrons, which then form a plasma at the focal spot of the laser. The high amplitude, oscillating electric field of the driving laser pulses accelerates the free electrons to large kinetic energies so that the same emission processes of X-rays occurs upon collision with the Cu-core electrons as in an X-ray tube. The main difference is that the driving field for the emission process is only present during the laser pulse, making the X-ray pulses comparably short as the driving femtosecond lasers. These X-rays bursts are monochromatized and focused onto the sample using a multilayer Montel optic[130] with a divergence of $\Delta\alpha_{\mathrm{in}} = 0.3^{\circ}$. The focal spot size of the X-rays on the sample is approximately 200-300 µm.[126] The diffracted X-rays are detected using an area X-ray detector that samples different diffraction angles α_{out} at once. This combination allows the user to avoid time-consuming $\alpha_{\mathrm{in}} - \alpha_{\mathrm{out}}$ mesh scans if the peak shifts are sufficiently small for the peak to stay well within the divergence of the source. The remainder of the initially split-off laser serves as pump-laser pulses that initiate dynamics in the sample. They are sent across a mechanical stage that is used to set the length of the optical path for the pump-beam, which determines the delay t between the pump- and probe-pulses. For experiments with a double pulse excitation a Michelson interferometer setup is inserted as sketched in the dashed box in figure 3.5. The optical path for the pump pulses contains a wave-plate and polarizer combination that is used to set the desired pulse energy E and a Galilei lens-telescope that is used to adjust the pump-laser spot-size at the sample position. The pump-laser spot-sizes d_{x} and d_{y} as well as the beam position are monitored using the weak transmission of a backside-polished mirror using a camera that is located at the same distance from the mirror as the sample. A motorized mirror automatically stabilizes the beam position on the sample with a correction frequency of approximately 4 Hz to compensate long-term drifts of the laser system. The pulse energy E and the spot-sizes d_{x} and d_{y} determine the incident pump laser fluence F that is calculated according to:

$$F = \frac{E}{A} = \frac{4 \cdot E \sin(\alpha_{\mathrm{in,laser}})}{\pi d_{\mathrm{x}} d_{\mathrm{y}}} = \frac{4 \cdot E \sin(\alpha_{\mathrm{in,X-ray}} + 20^{\circ})}{\pi d_{\mathrm{x}} d_{\mathrm{y}}} = \frac{4 \cdot E \sin(\alpha_{\mathrm{in,X-ray}} + 20^{\circ})}{\ln(2) \pi d_{\mathrm{x,FWHM}} d_{\mathrm{y,FWHM}}}. \tag{3.6}$$

The used definition of the laser fluence employs the top-hat approximation that distributes the entire pump-pulse energy homogeneously across an area that is represented by an ellipse which has the widths at the $1/e$ value of the intensity from the fitted 2D Gaussians as major axis. Using the laser fluence as a measure of the excitation energy density is useful because it is comparable across laser-setups with different repetition rates. A comparison between the excitation fluence values from different research groups is sometimes complicated by the different definitions that are used for the area A to which the pulse energy is normalized and the distinction between incident and absorbed laser fluence values. To convert between the two, one has to determine the reflection and transmission of the sample, which depends on the polarization of the laser light. For all experiments reported here, p-polarized laser light is used, because it generally exhibits a lower reflection especially close to the Brewster angle of the material at the sample surface.

3.1.3 Determination of the temporal overlap

The presented UXRD measurements require the determination of the best temporal overlap between the laser-pump- and X-ray probe-pulses. We use the periodic, fast response of a laser-excited Barium-Strontium-Titanate ($BaSrTiO_3$) (BST) - lanthanum-strontium manganate ($La_{0.7}Sr_{0.3})MnO_3$) (LSMO)

superlattice that is shown schematically in figure 3.6(d). The details of the experiment have been described by Schick et al. in the reference publication for the PXS setup[126]. The observed oscillation of the diffraction intensity is extrapolated to determine t_0 using:

$$t_0 = t_1 - \frac{1}{2}(t_2 - t_1). \tag{3.7}$$

The times t_1 and t_2 in (3.7) are determined via Gaussian fits to the first two oscillation maxima as indicated in 3.6(a). This superlattice oscillation serves as a reference experiment to determine the temporal and spatial overlap on a daily basis. Because some of the reported experiments employ two excitation laser pulses that are generated using a Michelson interferometer, it is necessary to calibrate and control their relative timing Δt separately. Panel (b) and (c) of figure 3.6 demonstrate the control of the superlattice oscillation amplitude by two excitation pulses. The relative timing and excitation energy density of the second pump-pulse can be set using a separate mechanical delay stage and beam attenuation to either enhance or suppress the superlattice oscillation.

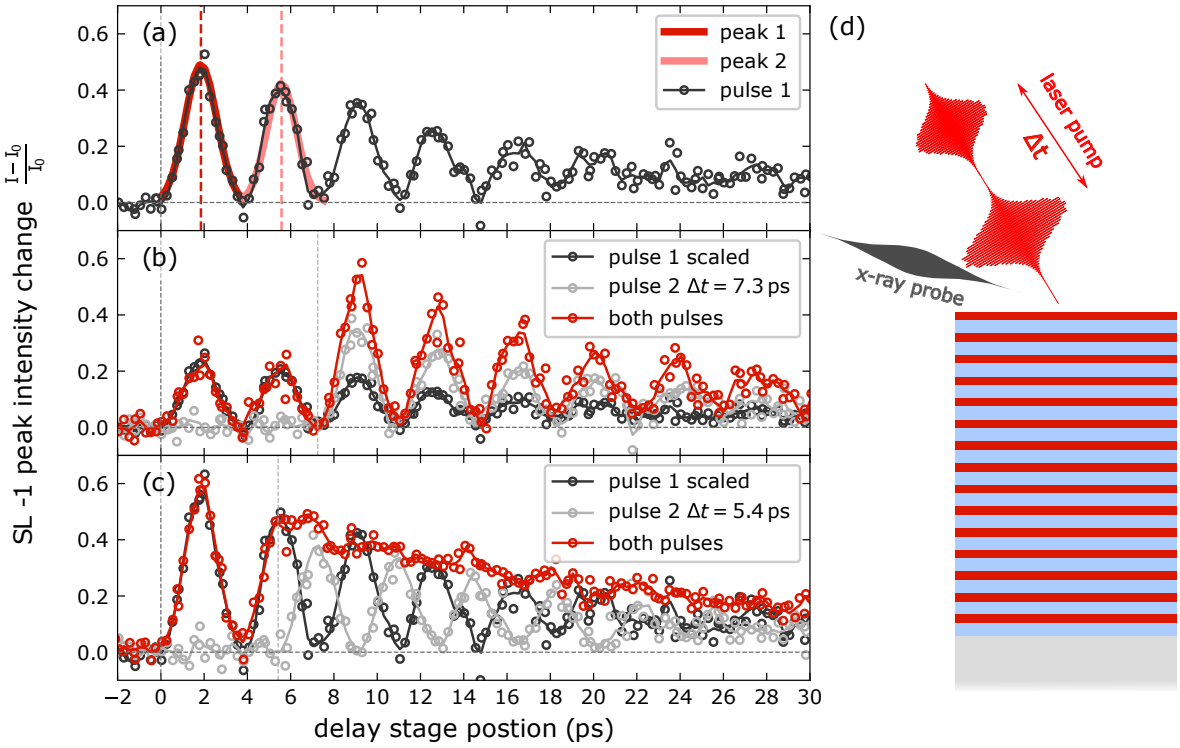

Figure 3.6: Time zero determination using the intensity oscillations of the SL-1 peak in a laser-excited superlattice structure: Panel (a) shows the intensity change upon single pulse excitation where two Gaussian functions are used to obtain the timing of the first and second oscillation maximum. Half the oscillation period is used to estimate the time $t = 0$ that corresponds to the temporal overlap between the pump and probe pulses according to equation (3.7). Panel (b) shows the double pulse excitation where the pulse-to-pulse separation Δt is chosen such that an amplification of the superlattice oscillation is achieved when both pulses are combined. Panel (c) shows the double pulse excitation with Δt chosen such that the oscillation is suppressed. Schematic sketch of the experiment on the BST-LSMO superlattice sample shown in (d).

The reference sample in the experiments reported in figure 3.6 consists of 15 double-layers of the absorbing LSMO metal and the transparent, dielectric BST on-top of a (strontium titanate ($SrTiO_3$) (STO)) substrate. The layout of the sample both in real space and the estimated diffraction intensity in the reciprocal space are schematically depicted side by side in figure 3.7. All materials crystallize in the perovskite structure with the unit cell ABO_3, with similar lattice constants, which leads to the epitaxial growth of the layers.

The intensity oscillation of the SL-1 peak (as defined in Fig. 3.7(f)) can be rationalized by the shift of the envelope functions (shown in Fig. 3.7(d)) that are determined from the transient thickness change of the thin BST and LSMO layers.[143] Initially, the metallic LSMO expands by compressing the adjacent dielectric BST layers. This shifts the intensity maximum of the BST-envelope to larger q_z and the LSMO amplitude to lower q_z, while leaving the period of the superlattice essentially intact. Thus, the diffraction intensity of the SL-1 peak is transiently enhanced and oscillates with the period that is defined by the layer thicknesses and sound velocities by $d_{\mathrm{LSMO}}/v_{\mathrm{LSMO}} + d_{\mathrm{BST}}/v_{\mathrm{BST}} \approx 3.8\,\mathrm{ps}$, which corresponds to a frequency of approximately 260 GHz. For more details on superlattice oscillations detected by UXRD see the work of Herzog et al. [143] and references therein.

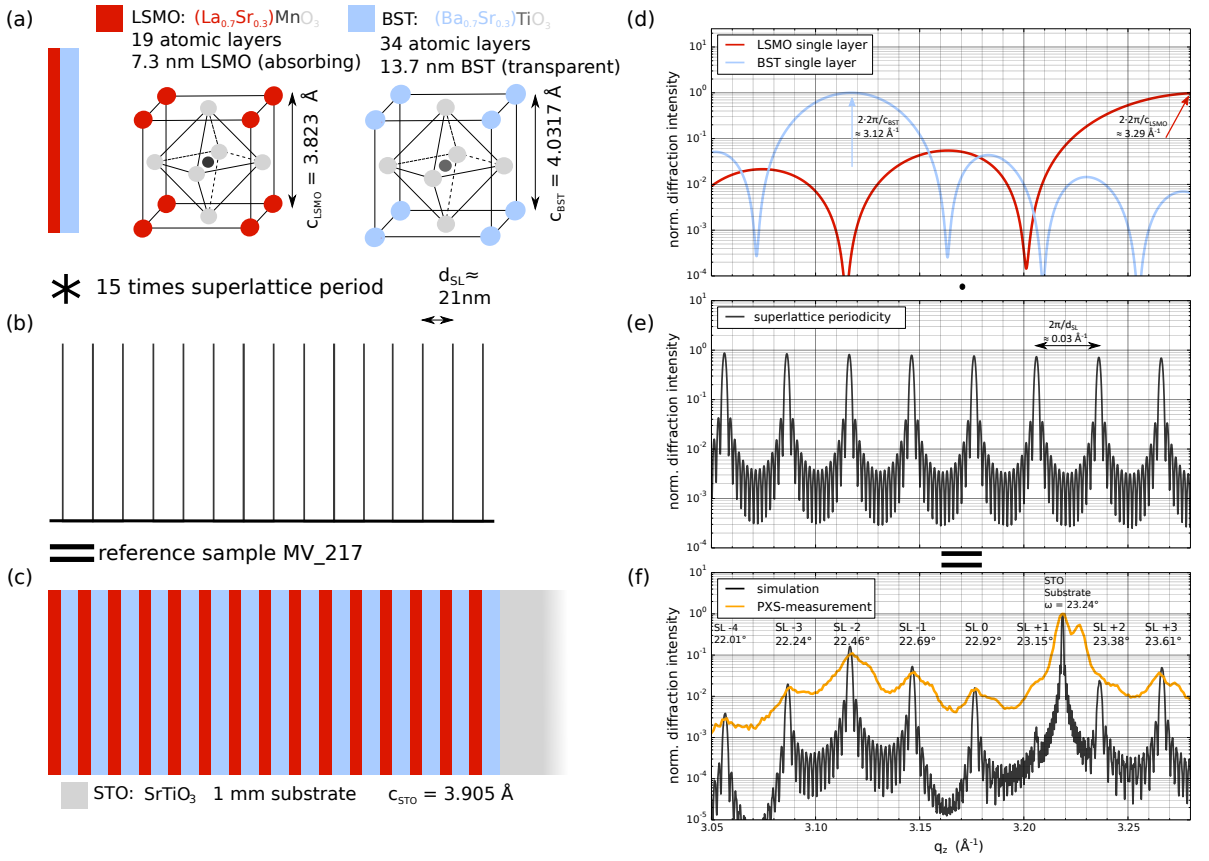

Figure 3.7: Structure of the superlattice reference-sample in real- and reciprocal space: Panels (a)-(c) on the left side show the real space features of the reference sample which consists of a convolution of a BST-LSMO bilayer with a periodic structure of 15 layers. Panels (d)-(f) show the corresponding reciprocal space depiction of the sample, which consists of a multiplication of the broad envelope functions of the thin-bilayer structures (d) with the superlattice-period given by the stacking periodicity (f). This figure is adapted from earlier works[128, 144].

The presented peak intensity oscillation period is furthermore used to optimize the spatial overlap between the laser-pump and X-ray probe pulses. Setting the timing between the pulses to the first maximum t_1, one can scan the pump-laser position relative to the fixed X-ray probe spot to attain the maximum diffraction intensity from the SL-1 superlattice peak, which then marks the point of the best spatial overlap.

3.1.4 Time resolution of the PXS setup

The time-resolution in the presented experiments using the PXS setup can be estimated to be approximately 500 fs or better, based on the modulation amplitude of the observed superlattice oscillation shown in the previous section.[128] The time-resolution is determined by multiple effects that are discussed in this section. It originates from the convolution of the pulse-lengths of the pump laser and probe X-ray pulses, in combination with their relative timing jitter and the time-smearing effect due to the non-collinear pump- and probe paths.

While the pump-laser pulse length can be determined via a commercial single-shot autocorrelator to be approximately 100 fs or better, the pulse length of our X-ray source is not exactly determined. Auto-correlation approaches are not feasible due to the low intensity of the X-ray pulses that prohibits the usage of non-linear effects for the pulse-length determination. Based on reports of similar plasma source setups, the pulse length is estimated to be on the order of 150-200 fs.[145, 146] The timing jitter of the laser-based setup is only due to mechanical fluctuations in the optics because the X-ray pulses and the pump-pulses are derived from the same laser system and thus inherently synchronized. This is one advantage in comparison to synchrotron based approaches that require a dedicated synchronization scheme between the pump- and probe pulses. Fluctuations in the optical path length of 30 µm are necessary to generate a timing jitter of 100 fs. Although such fluctuations cannot be excluded, they are minimized by a dedicated housing of the laser and the usage of a vibration damped laser-table. An important contribution to the time resolution of our setup is the non-collinearity of the pump and probe laser pulses. It introduces a time smearing effect with an upper limit on the order of 500 fs for the common range of $15° \leq \alpha_{\text{in}} \leq 30°$. It can be estimated from the fixed 20° offset between the pump-laser pulses and the X-ray probe pulses and the X-ray spot-size of approximately $d_{\text{X-ray}} = 300\,\mu\text{m}$ using the relation:

$$\Delta t = \Delta t_{\text{X-ray}} - \Delta t_{\text{laser}} = \frac{\Delta l_{\text{X-ray}}}{c_0} - \frac{\Delta l_{\text{laser}}}{c_0} \tag{3.8}$$

$$= \frac{d_{\text{X-ray}}}{c_0 \sin \alpha_{\text{X-ray}}} (\cos \alpha_{\text{X-ray}} - \cos \alpha_{\text{laser}}). \tag{3.9}$$

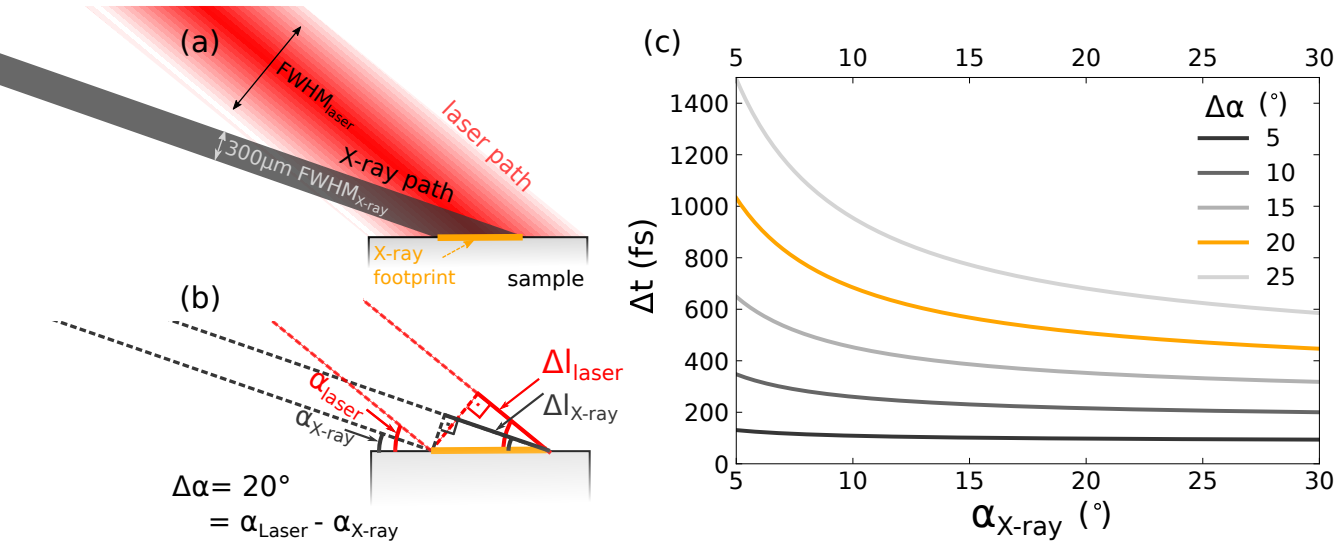

Figure 3.8: Estimation of the time smearing due to the non-collinear pump-probe geometry: (a) depiction of the laser and X-ray path that is reduced to the relevant lines to explicitly show the path length differences Δl_{laser} and $\Delta l_{\text{X-ray}}$ in (b). The resulting time smearing estimate according to equation (3.8) is plotted in (c) for different offset angles $\Delta\alpha$. The case $\Delta\alpha = 20°$, highlighted orange corresponds to the angular offset in the used PXS-setup.

This estimation calculates the time difference of the light propagation time between the left and the right side of the X-ray footprint, as illustrated in figure 3.8. Relation (3.8) represents an upper limit of the time-smearing effect on the experimental time-resolution because the absolute time-difference from the center of the X-ray footprint is then only half of the reported value. The finite offset between the laser and the X-ray pulses in the PXS-setup is chosen to spatially separate both beams after their reflection from the sample so that the X-ray detector is not exposed to the intense pump laser light. The offset furthermore ensures that the laser and X-ray pulses can enter the vacuum chamber through different windows of the cryostat, which are individually optimized to withstand the laser radiation and transmit as much of the X-ray radiation as possible.

3.2 Strain response in laser-excited gold-nanotriangles

The time-resolved X-ray diffraction on gold nano-triangles is the first example that outlines the main principle of the experimental technique and its capabilities. The findings have been presented in **article I: Watching the vibration and cooling of ultrathin gold nanotriangles by ultrafast x-ray diffraction**.

In article I, we describe a measurement of the expansion, vibration and cooling of triangular, approximately 6.4 nm thin, laser-excited gold-nano prisms on a Si substrate that is functionalized by organic linker molecules. This experiment shows the main ingredients of an ultrafast diffraction study of a laser-excited metal, where both electrons and phonons contribute a time-dependent expansive stress on the lattice. The analysis applies the model for the time-dependent stress σ_{ext} to the strain response of gold-nano particles as it was used for a continuous $\approx 100\,\mathrm{nm}$ thick Au films by Nicoul et al. [147]. To aid the discussion, figure 3.9 reproduces the UXRD data and the simulation for the strain rise of the gold-nanoparticles from the article. In addition to the modeled strain response, I explicitly display the time-dependence of the driving stress $\sigma_{\mathrm{ext}}(t)$ that is described by:

$$\sigma_{\mathrm{ext}}(t) = \sigma_{\mathrm{el}} + \sigma_{\mathrm{pho}} = \sigma_{\infty} H(t) \left(1 + \left(\frac{\Gamma_{\mathrm{el}}}{\Gamma_{\mathrm{pho}}} - 1\right) e^{-\frac{t}{\tau_{\mathrm{el-pho}}}}\right). \tag{3.10}$$

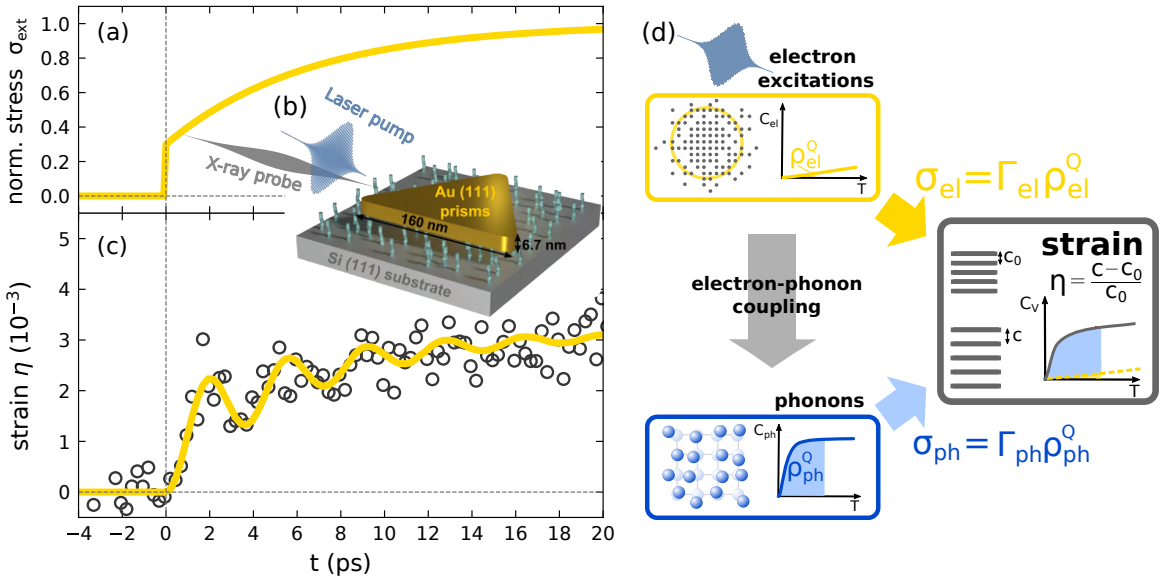

Figure 3.9: UXRD on triangular gold nano-prisms: (a) Time-dependent stress with an instantaneous electron- and a delayed phonon-contribution. (b) Schematic sketch of the experiment. (c) Observed strain response (open circles) and modeled strain. (d) Schematic sketch of the contributing subsystems that affect the strain response.

In this work, we employ a simplified approach for the strain response using a harmonic oscillator to describe the thickness oscillations that are driven by the time-dependent, displacive stress $\sigma_{\mathrm{ext}}(t)$ from relation (3.10). The stress has two contributions: one instantaneous rise that represents the nearly instantaneous excitation of electrons and a delayed rise that occurs upon the subsequent energy transfer from electronic excitations to phonons. The rise in the stress originates from the higher Grüneisen coefficient of the phonons in gold in comparison to the electrons. The Grüneisen parameter Γ relates the stress to the energy density, so that our reported ratio $r = \frac{\Gamma_{\mathrm{el}}}{\Gamma_{\mathrm{pho}}} \approx \frac{1}{3}$ implies that the phonons in gold are approximately three times more efficient in the strain generation as compared to electronic excitations under the given high fluence excitation conditions. The concept of a Grüneisen parameter is discussed to more detail in chapter 4. The here-presented harmonic oscillator model covers only the fundamental breathing mode of the thickness oscillations for the laser-excited nano-particles and does not reflect the full spatio-temporal strain. Owing to the lateral size dispersion of the probed gold-nano-triangles, this is the only relevant feature in the data and thus this level of detail suffices for the description. The resulting phenomenological equation of motion for the strain is:

$$\frac{\mathrm{d}^2\eta}{\mathrm{d}t^2} + 2\gamma\frac{\mathrm{d}\eta}{\mathrm{d}t} + {\omega_0}^2\eta = P\sigma_{\mathrm{ext}}(t). \tag{3.11}$$

The constant pre-factor P is introduced for dimensional reasons. The electronic contribution to $\sigma(t)$ is assumed to occur instantaneously upon laser excitation and the phonon-pressure rises with a time-scale $\tau_{\mathrm{el-pho}} \approx 6.5\,\mathrm{ps}$ as energy is transferred from electrons to phonons. The oscillating strain response to the time-dependent stress is damped by an empirical damping constant $\gamma = 0.15\,\mathrm{ps}^{-1}$. The energy transfer could also be modeled using a two temperature model without spatial dependence because hot electrons are expected to equally distribute the energy within the thin gold particles. The fact that both sub-systems contribute a time-dependent stress that results in the strain response of the lattice is captured schematically by figure 3.9(d).

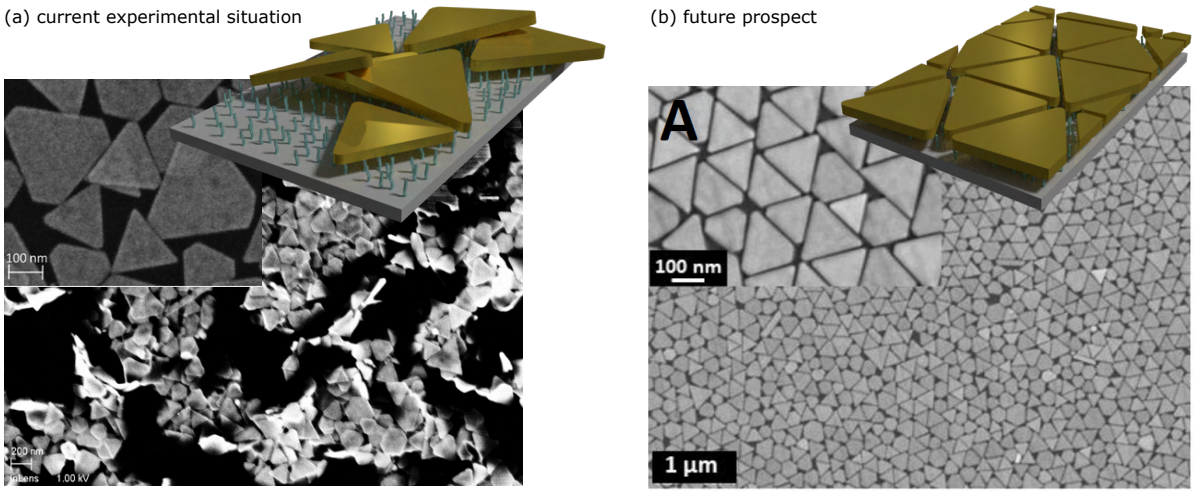

Figure 3.10: Outlook: UXRD on ordered nano-prisms: (a) SEM images of the state of the investigated sample, where particles with a significant size distribution and stacking have been studied in the UXRD experiment. Monolayers of ordered Au-nanoprisms with a smaller size distribution as shown in (b) have been realized in our group in the course of the PhD thesis of Radwan M. Sarhan [148]. Future experiments on these specimen could significantly increase the experimentally accessible level of detail on the vibration and cooling of the nano-prism. The overlaid schematic visualizations are by courtesy of Felix Stete.

What is remarkable in this experiment is that the flatness of the thin gold-nano triangles allows UXRD measurements in the symmetric diffraction geometry, which requires a preferential orientation

of the lattice planes. The favorable aspect ratio of the nano-particles that exhibit an edge-length on the order of 150 nm, while being only 6.4 nm thin leads to the orientation of the particles on the substrate. While the laser-excited vibration of metal-nanoparticles are well studied on a qualitative level using all optical tools[149–151], UXRD experiments provide direct quantitative access to the strain. This work demonstrates that UXRD experiments on metal nano-particles with as little as 24 atomic layers are possible even in this laboratory-based setup. Similar experiments using a free electron laser (FEL) demonstrate the capability of the UXRD method to image the three-dimensional vibration of individual laser-excited metal nano-particles.[64]

scanning electron microscopy (SEM) images show that the size dispersion and stacking behavior of the investigated gold-nano-prism specimen is far from ideal. Figure 3.10 provides SEM images of the gold-nano-particles used in the UXRD-study in comparison to the recently prepared mono-layers of gold nano-prisms that have been realized in the PhD work of Radwan M. Sarhan[148] in our group. Future experiments on these specimen could provide insights into the amplitude of additional breathing modes, that were hitherto obscured due to the large size distribution. Contributions of the stacking behavior to the nano-scale heat-transport between the gold-particles and the substrate across the polymer chains could thus be excluded in further experiments.

3.3 Nanoscale energy transport in metal heterostructures

This section outlines that the strain response observed by X-ray diffraction provides access to signatures of energy transport within nano-scale heterostructures. The discussed examples represent an extension to the results of **article II: Layer specific observation of slow thermal equilibration in ultrathin metallic nanostructures by femtosecond x-ray diffraction**, where we apply UXRD to a gold-nickel bilayer that is thinner than the optical penetration depth of the laser-pulses.

The reported experiments exploit the selectivity of the X-ray diffraction to the different inter-atomic spacings in the constituent materials. From the shift of the well-separated Bragg peaks of the gold and nickel layer shown in article II, we detect the strain response of the approximately 5.6 nm thin gold layer and the 12.4 nm thin nickel layer. In the metallic bilayer sample, we find that the nickel layer expands first and compresses the adjacent gold. This effect occurs regardless of the absorption profile that depends on the used wavelength of the pump laser pulses, which in our case was changed between 800 nm and 400 nm excitation pulses. The strain response indicates that the energy is rapidly equilibrated within the electronic systems of the metal stack and as a result transferred to the nickel layer due to its larger electronic heat capacity and larger electron-phonon coupling constant. The gold layer expands on a much slower 100 ps timescale as the energy flows to the phonons in gold. The electronic excitations in both metals are coupled strongly and are assumed to be equilibrated with the phonons in the nickel layer. The strain in both layers decreases on a nanosecond timescale due to the energy transfer to the insulating magnesium oxide (MgO) substrate.

The following discussion presents UXRD data on additional samples that support and enhance the findings of article II. All samples are grown by molecular beam epitaxy by Matthias Kronseder in the group of Prof. Back. Due to the relatively low number of electrons in nickel-atoms ($Z = 28$), the X-ray scattering cross-section is smaller and thus the resulting Bragg peak weaker compared to gold ($Z = 79$). For samples with a nickel-layer thickness close to or below 10 nm the Bragg peak is, in some cases, too weak to be observed in our setup, while the gold peak can be detected in all samples. An overview of the reciprocal space projection and the time-resolved diffraction peak shift that is observed in the UXRD experiments is provided in figure 3.11. This figure compares a gold-nickel bilayer sample very similar

to the structure of article II and a trilayer where an insulating MgO interlayer is introduced to suppress the electron transport between the metal layers. The trilayer structure exhibits an additional peak at $q_z \approx 3.08\,\text{Å}^{-1}$ that corresponds to the Au-(200) reflection that is not observed in the bilayer. Both textures are known to occur for thin Au layers on MgO[152, 153] but in both cases we probe the fraction of the film with the (111)-orientation. The time-resolved evolution of the diffraction peaks upon laser excitation is contrasted for bi- and trilayer samples. While the response of the nickel layer is qualitatively similar for both samples, the gold peak shifts initially to larger q_z in the bilayer, whereas it shifts to smaller q_z in the trilayer. The diffraction peak position is obtained by a Gaussian fit to the time-dependent diffraction peak intensity and the peak center position is indicated by solid black lines in panels (c),(d),(h) and (j) of figure 3.11. The resulting out-of-plane strain $\eta_\perp$ is then calculated from the time-dependent q_z position of the diffraction peak according to :

$$\eta_\perp(t) = \frac{d(t) - \overline{d(t<0)}}{\overline{d(t<0)}} = \frac{\overline{q_z(t<0)}}{q_z(t)} - 1. \tag{3.12}$$

The overline indicates the temporal averaging of the data points for $t < 0$ that is carried out to reduce the influence of fluctuations on the reference value $d(t < 0)$. Relation (3.12) makes use of the relation $d_\perp = \frac{2\pi}{q_z}$ between the reciprocal space coordinate q_z and the real space out-of-plane inter-atomic spacing $d_\perp$. The subscript $\perp$ that is used here for clarification is dropped in the following because the symmetric diffraction geometry probes the out-of-plane direction in all subsequently reported experiments. The resulting strain for these samples is displayed in panel (e) and (f) of figure 3.12 that compares the response of multiple bi-and trilayer structures of different thicknesses.

Panels (a)-(e) in figure 3.12 show that the time-dependent strain effects reported upon excitation with 800 nm pump laser pulses are reproduced for different film thicknesses of the metallic bilayer samples. The samples exhibit an expansion of the buried nickel layer while the gold layer is initially compressed and the maximum of the thermal expansion in gold is reached on a time-scale of 100 ps. This is much later compared to the electron-phonon coupling time of single gold films but in agreement with the discussion in article II. Panel (f) and (g) show the strain response in a trilayer heterostructure where an insulating MgO interlayer is introduced between the metal films. In this case, the electron transport between the metallic layers is suppressed and the gold film expands. The gold film reaches its maximal thermal expansion on the 10 ps timescale that is expected from the intrinsic electron-phonon coupling of strongly laser-excited single gold layers and very similar to the response of the isolated gold-nanotriangles discussed in the previous section. The oscillations in the initial strain response originate from the fast-rising stress that launches picosecond strain pulses that propagate within the heterostructure. These oscillations cease due to the partial transmission of the strain pulses towards the substrate and dephasing effects upon reflections at inhomogeneous interfaces. Rationalizing the oscillations requires a spatially resolved simulation of the elastic response that is discussed in the publication but not introduced in this qualitative analysis.

A key result of article II is that the shape of the strain response in the metallic bilayer sample does not depend on the excitation wavelength of the laser pulses. This comparison is reproduced in figure 3.13(a) alongside the estimated light absorption profile that results from a transfer matrix model in panel (c) and (d). While the light absorption differs between 800 nm and 400 nm excitation, the observed strain response is qualitatively the same due to the fast electron equilibration within the heterostructure. This is not the case for the trilayer sample, where an MgO layer suppresses the electronic transport. In this case the strain within the gold layer increases for laser excitation at 400 nm due to the higher absorption coefficient and because the energy density remains within the gold film. The cooling of the gold layer is furthermore delayed with respect to the cooling of the nickel layer due to the thermally insulating MgO interlayer. The reported absorption of the gold capping layer is estimated from literature values of the

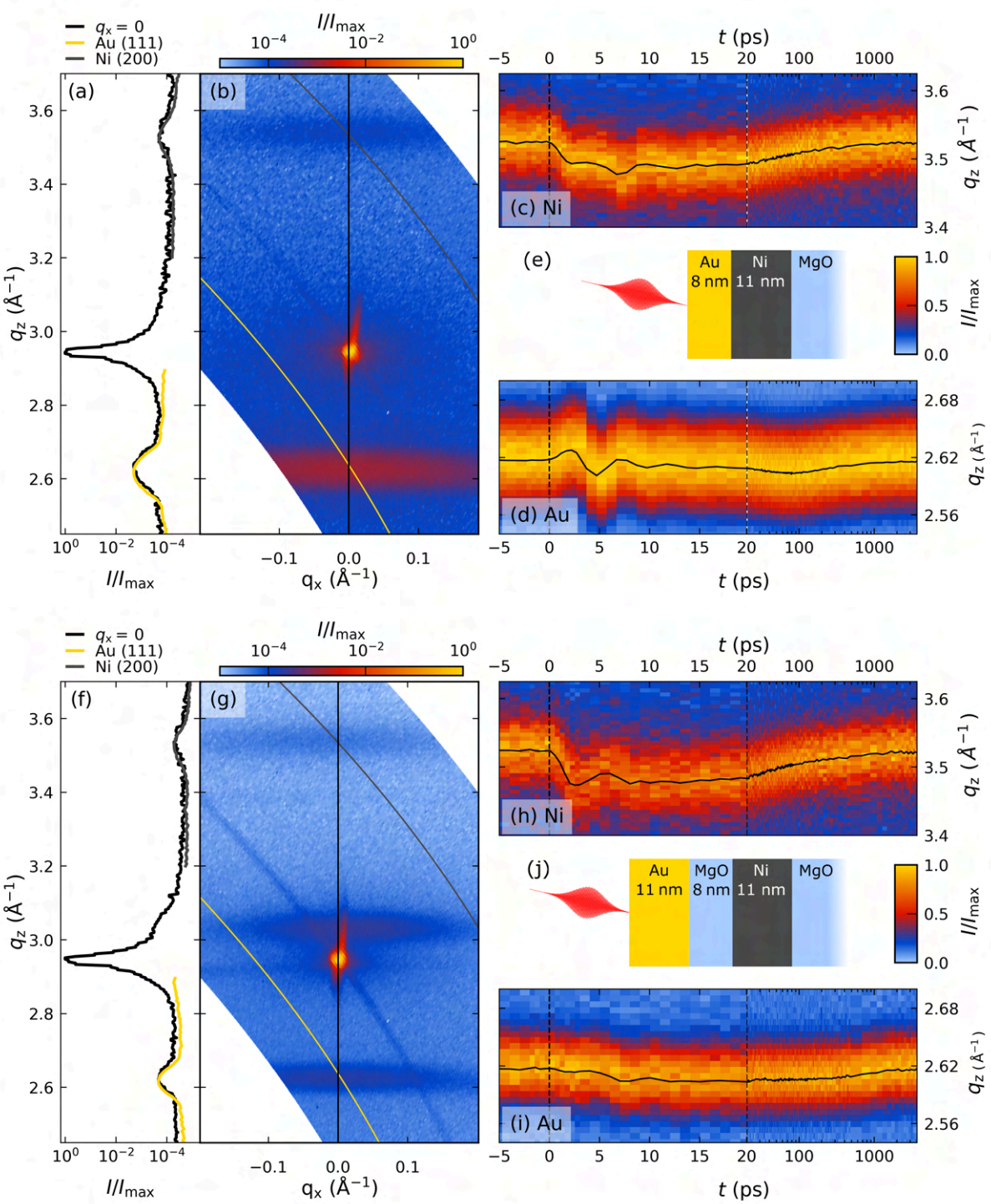

Figure 3.11: Au-Ni diffraction peaks and their time-resolved shift in bi- and trilayer samples: Panels (a) and (b) depict the reciprocal space-map and the diffraction curves for the Au-Ni bilayer sample depicted in inset (e). The solid yellow and grey line denote the reciprocal space slice of the Ni (200) and Au (111) reflection that are probed in the time-resolved diffraction experiment for a fixed α_{in}. The results of the corresponding UXRD experiment are depicted in (c) and (d) where the solid black line indicates the shift of the diffraction peak center obtained by a Gaussian fit to the measured intensity on the detector. Panels (f)-(j) show the equivalent data for a trilayer structure where a thin MgO interlayer insulates the Au and Ni films. Both samples where subjected to the same incident laser pulses that have 3 mJ pulse energy and a laser spot profile of 1.3×1.4 mm FWHM. The variation of the beam footprints leads to a 12 % difference in the incident fluence that is 10.5 $\frac{\mathrm{mJ}}{\mathrm{cm}^2}$ for the measurement of the Ni(200)-peak ($\alpha_{\mathrm{in,laser}} \approx 46°$) and 9.2 $\frac{\mathrm{mJ}}{\mathrm{cm}^2}$ for the Au (111)-peak ($\alpha_{\mathrm{in,laser}} \approx 39°$). The important difference between the samples is the response of the Au layer peak that is initially shifting to larger q_z in the bilayer, whereas it directly shifts to smaller q_z in the trilayer.

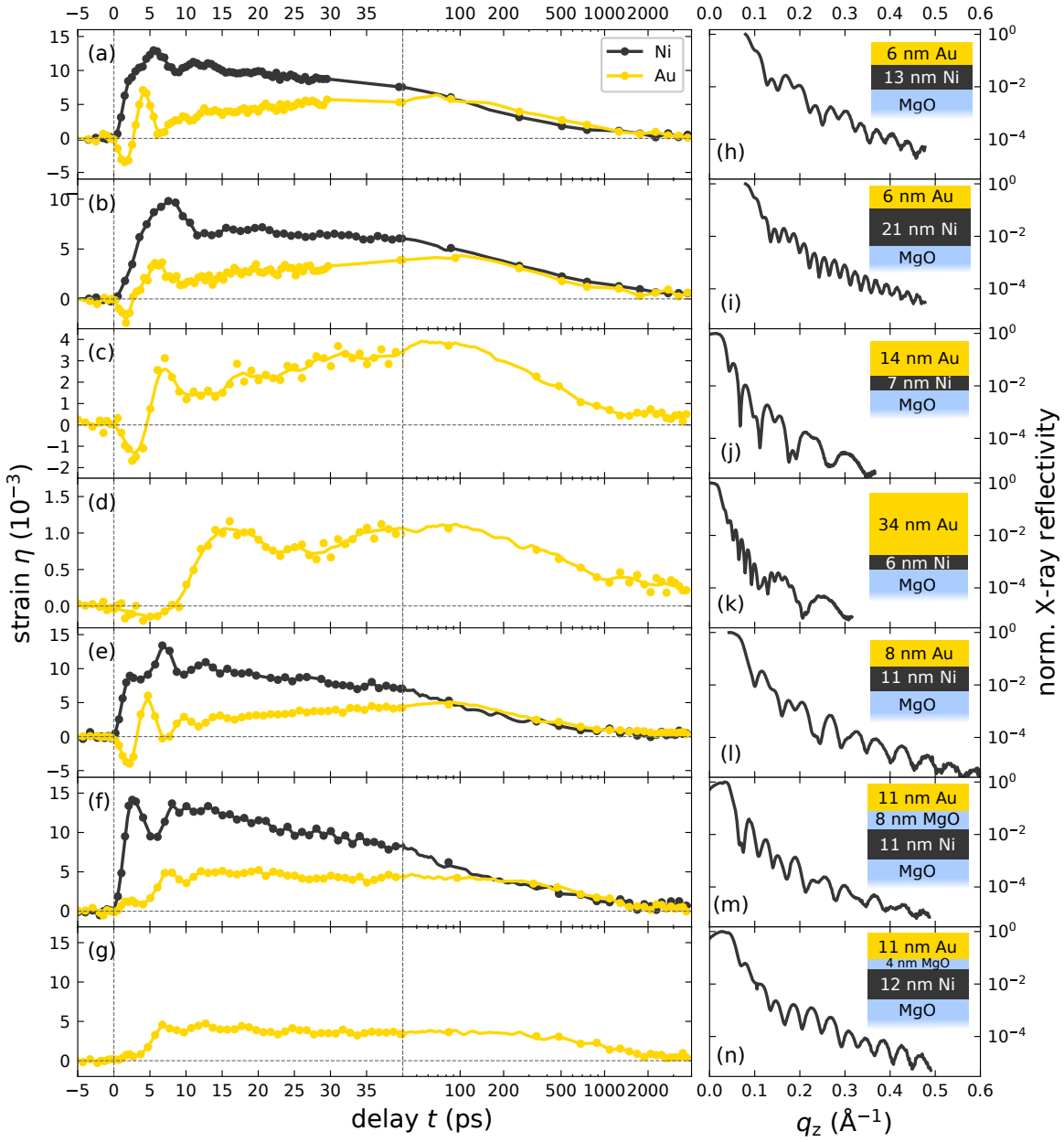

Figure 3.12: Strain response of laser-excited Au-Ni bi- and trilayer structures: The strain of multiple laser-excited nanoscopic Au-Ni bilayers (a)-(e) upon 800 nm laser excitation shows a slow expansion of the gold layer that reaches its maximum only after 80 ps, whereas the Ni thin film expands significantly faster. The incorporation of an insulating MgO layer (f) and (g) leads to a fast expansion of the Au layer that reaches its maximum already on the timescale of 10 ps. Solid lines are spline interpolations that serve as a guide to the eye. Plots to the right in each row (h)-(n) show the X-ray reflectivity measurements of these samples from which we extract the layer thicknesses by modeling the observed oscillations using the reflectometry analysis software package "reflpak"[154].

complex refractive index of similarly thin gold layers on MoS_2.[155] The reported refractive index values serve as an input to a transfer matrix model[156] from which the absorption can be estimated. A variety of complex refractive indices are reported for gold specimen of different thickness and degrees of crystallinity [155, 157, 158] but the results share that the absorption at 400 nm excitation is significantly higher than for 800 nm excitation.[159]. This is in qualitative agreement with the observed larger strain response upon 400 nm excitation of the insulated gold layer in the trilayer structure. A quantitative comparison would require the exact knowledge of the optical properties of the constituent materials that is currently not available. The reported strain responses in figure 3.13(a) and (b) are normalized to the maximum strain in the nickel film, which serves as a measure of the absorbed total energy density in the layer.

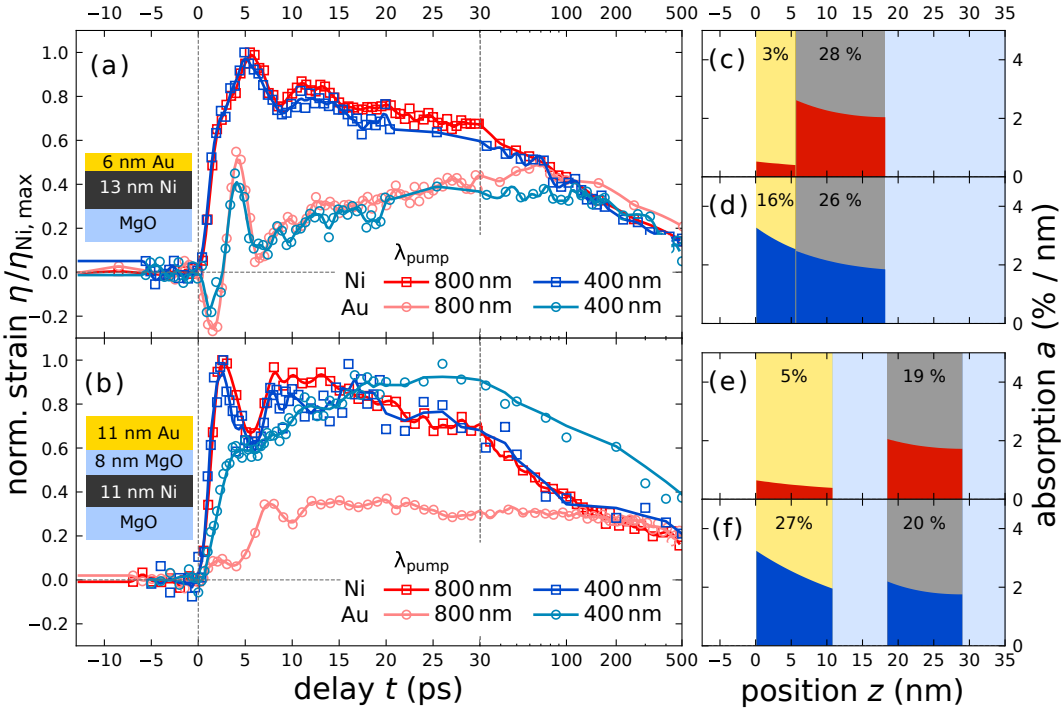

Figure 3.13: Strain response to wavelength-dependent absorption profiles in bi- and trilayer Au-Ni samples: Comparison between the strain response of a sample without insulating barrier (a) and with insulating MgO barrier (b) subjected to a laser pulses with 800 nm and 400 nm central wavelength. For the sample without barrier, it does not matter how the energy is deposited initially; the strain response is nearly identical, because hot electron transport distributes the energy rapidly within the electron system. This process is suppressed in (b) by the MgO layer. This results in a change of the relative amplitude of the expansion of the gold film with respect to the nickel expansion. Solid lines are spline interpolations to the data that serve as guide to the eye. Graphs (c)-(f) represent the modeled energy deposition in the bi- and trilayer structure from a transfer matrix model that uses the refractive indices for similarly thin gold films[155].

These experiments demonstrate that the strain response in heterostructures can be probed with (sub-) picosecond time-resolution and material specificity using the laser-driven PXS-setup. This technique can thus be refined and extended to yield a thermometer that can measure the flow of energy in few nanometer thin films, on the timescale of picoseconds as discussed in article II. It uses the effect of thermal expansion that was one of the first measures for temperature in bulk materials under equilibrium conditions, but also appears in laser-excited nano-structures. The calibration of such an ultrafast, nano-scale thermometer requires an understanding of additional interactions and effects that affect the strain response i.e. magnetic,

ferroelectric or geometric stresses as well as coherent strain pulses.

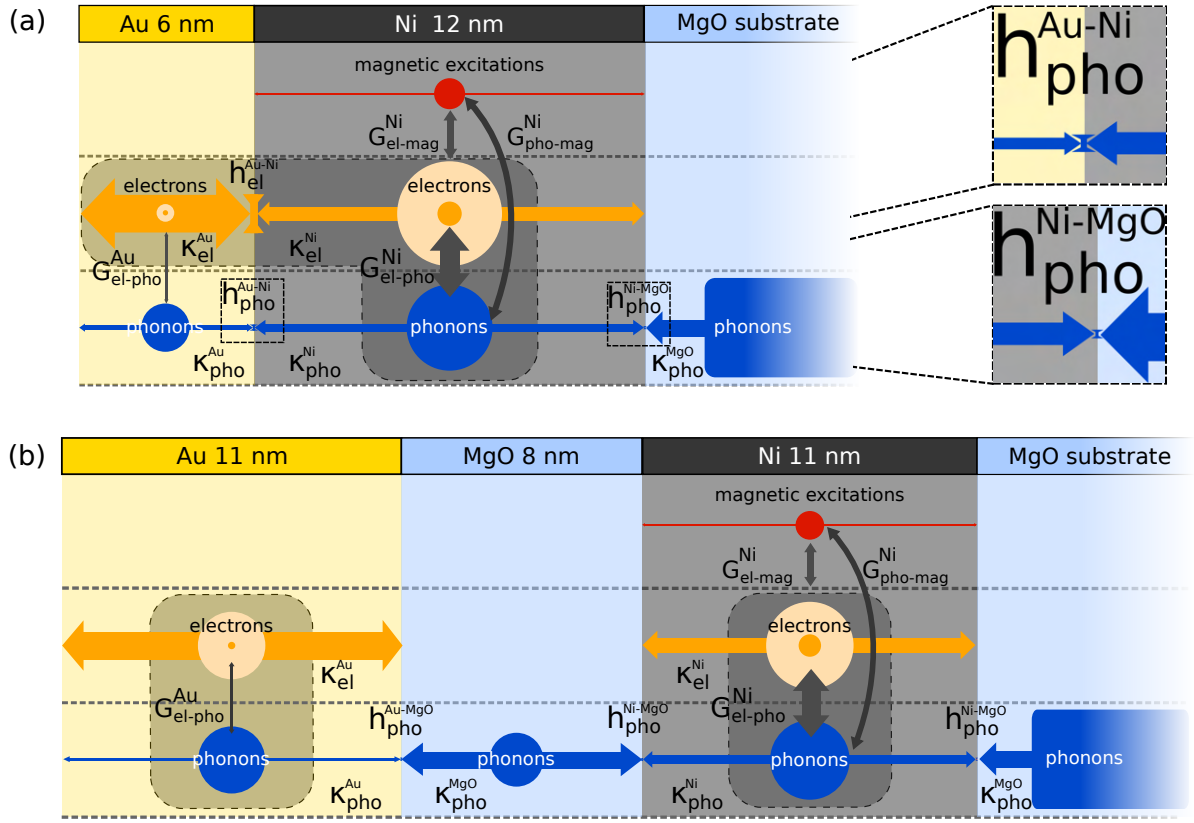

Figure 3.14: Schematic sub-system-couplings in Ni-Au bi- and trilayer structures: Energy transfer channels between phonons, magnetic and electronic excitations are schematically depicted for the Au/Ni-bilayer shown in (a) and the trilayer structure shown in (b). Areas of the circles indicate the amount of energy that is stored in each subsystem for a temperature change of $\Delta T = 300\,\mathrm{K}$ based on the material-specific, temperature-dependent bulk heat capacities that are compiled in figure 3.16. The light orange circles in the electron system correspond to the energy that would be stored transiently in electronic excitations for the idealized situation that the electronic degrees of freedom are in thermal equilibrium but no energy has been transferred to other subsystems. Energy transfer channels are depicted by arrows that indicate the estimated thermal conductance, based on the coupling constants reported in a recent work by Kang and Choi[160]. This graphic combines the conductances from subsystem couplings G, conductivities κ and interface resistances h in units of $\frac{W}{K}$. Due to the large spread of the relative size of the thermal conductance, the width of the arrows is scaled by the square root of the value to limit the size of the electronic conductance. The addition of an MgO interlayer in (b) suppresses the electronic energy transfer channel that is dominant in the metallic bilayer sample in (a). The smallest conductance in these subsystems is given by the phonon interface resistance between the metals and MgO.

In the current discussion and article II, we neglect the energy flow into magnetic excitations that comprise both orbital and spin degrees of freedom. The stress and strain due to the energy transfer into the magnetic subsystem in nickel is so far not taken into account. A recent study by Zahn et al. [161] and a report by Tengdin et al. [87] find signatures of the diverging heat capacity of nickel in vibrational and spectroscopic measurements respectively. Literature values of the thermal expansion in nickel however suggest that the magnetic stress represents only a relatively small correction to the expansion[162] and only a small fraction to the total heat capacity is contributed by magnetic excitations[163]. A compilation of the near-equilibrium thermal properties from the literature is provided in 3.16. A schematic sketch of the different possible sub-system couplings and energy reservoirs in gold-nickel bi- and trilayer heterostructures is shown in figure 3.14 as an overview. Light grey shadings with a dashed contour in this

sketch indicate strongly coupled subsystems that equilibrate faster in comparison to the energy transfer to other sub-systems. The corresponding literature values of the thermophysical properties for this overview graph have been compiled in a recent work by Kang and Choi[160] for the low fluence limit where their temperature dependence can be neglected. The laser-induced temperature excursions in our experiment are often on the order of 200 K or more. The temperature-dependence of the relevant parameters is surveyed in figures 3.15 and 3.16.

From the equilibrium literature values of the thermal expansion in bulk nickel[162], one expects that the magnetic stress upon demagnetization in nickel is expansive and thus has the same sign as the thermoelastic expansion that results from energy deposition into the phonon subsystem. The two-pulse excitation scheme discussed in chapter 5 provides a tool to discern the magnetic contribution to the strain response in future experiments.

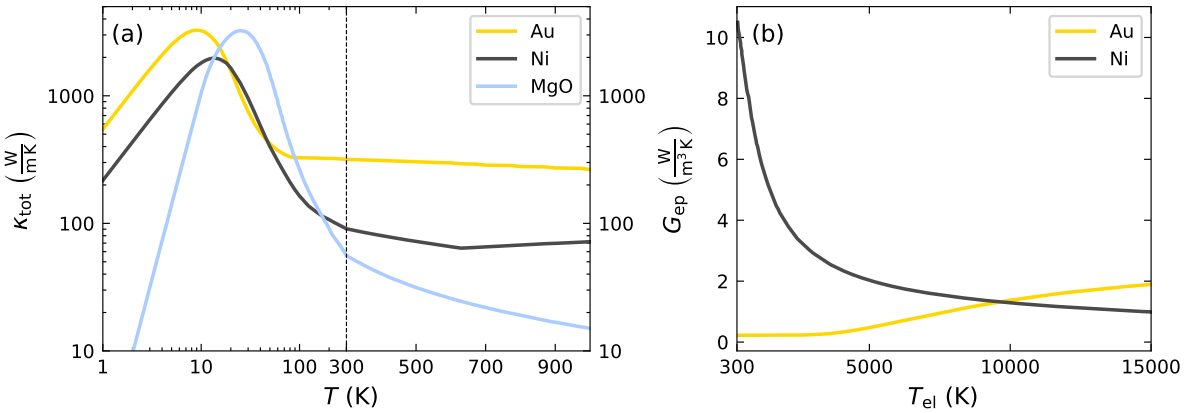

Figure 3.15: Coupling constants and thermal conductivity of bulk of Au, Ni and MgO: In addition to the heat capacities and thermal expansion coefficients one requires literature values for the temperature-dependent thermal conductivities and electron-phonon coupling to set up a spatially resolved two-temperature model. (a) summarizes the literature values for the total thermal conductivity[164] and (b) the electron-phonon coupling parameters derived by Lin et al. [71]. These values represent the inter-material and intra-material energy transfer properties, respectively.

Ultrafast energy transport by electrons in metallic heterostructures has also been reported and utilized in all-optical experiments.[165–167] The material specificity of UXRD can quantify the strain response in metallic structures that are difficult to analyze by optical probes due to the mixture of responses of different layers within the probing depth. UXRD can be a useful tool to complement the established all-optical approaches of time-domain thermoreflectance and picosecond ultrasonics in single-digit nanometer films. A recent, related publication from our group discusses the ultrafast energy transport of hot electrons through approximately 100 nm copper into a buried nickel layer.[168]

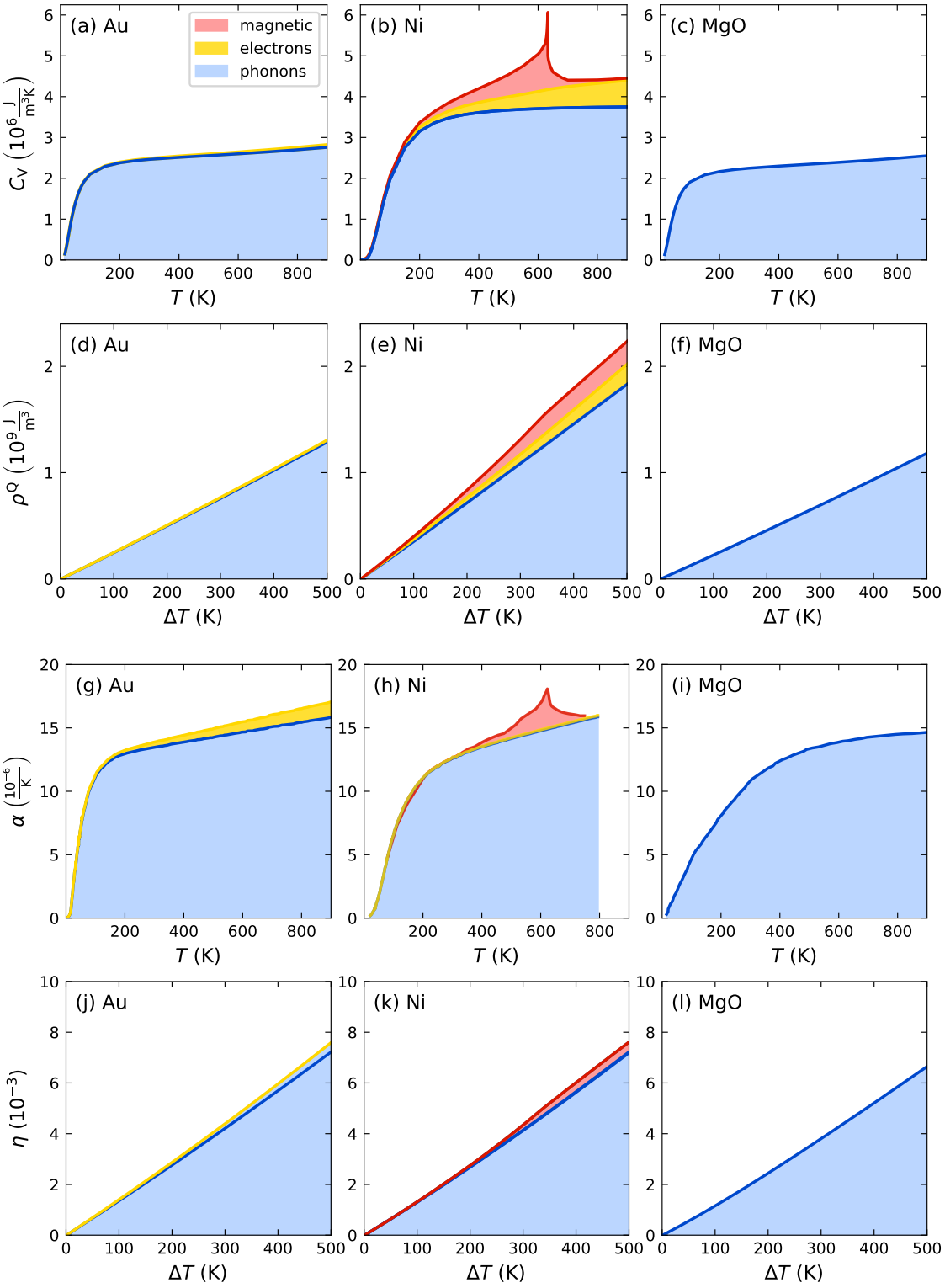

Figure 3.16: T-dependence of the energy reservoirs, strain contributions and conductivities for Ni, Au and MgO: The heat capacities (a)-(c) that are taken from the literature for Au[169, 170], Ni[163] and MgO[171, 172]. Panels (d)-(f) show the integrated heat capacities to show the relative size of the energy distributions depending on the energy deposition. The bulk thermal expansion coefficients[162, 173, 174] shown in (g)-(i) and the resulting strain (j)-(l) exhibit a qualitatively similar temperature dependence as the heat capacities, which is used in the concept of a Grüneisen parameter that is introduced in chapter 4. These parameters are shown to illustrate that the expected magnetic contribution to the thermal expansion and energy distribution in Nickel for a $\Delta T \approx 300\,\mathrm{K}$ is on the order of or less than 10%.

3.4 Detection of picosecond strain pulses in a buried layer

In the hitherto discussed examples, the strain response is observed in metal films that are thinner than the optical penetration depth of the laser-excitation. The strain generation and detection thus occur in the same laser-excited region. The signal is then a superposition of the localized thermoelastic strain and picosecond strain pulses that propagate back and forth within the heterostructure due to reflections at the interfaces. This complicates the analysis of the time-dependent strain and thus simulations of the strain propagation are required to rationalize and interpret the results.

In **article III: Tracking picosecond strain pulses in heterostructures that exhibit giant magnetostriction**, we demonstrate in a UXRD experiment on a thick transducer that one can separate the propagating, acoustic strain response from the localized thermal expansion by observing the strain in a thin, buried detection layer. There we observe picosecond strain pulses that are generated within the 30 nm laser penetration depth in a 350 and 450 nm thick $TbFe_2$ layer. Strain waves propagate at the speed of sound into a 50 nm thin Nb detection layer, where they arrive before thermal diffusion transports a signifcant amount of energy into this sample region. This leads to a background-free observation of the amplitude and shape of the strain pulses. This probing technique has multiple advantages compared to the observation of the strain pulses within the thick transducer layer. The thinner detection layer is more sensitive to the spatial shape of the strain pulses, and thus also the stress profile, because the peak shift in an UXRD-experiment only probes the average strain within the material. The strain detection in a crystalline, buried layer also works for non-crystalline transducers and thus extends the applicability of the X-ray diffraction technique to a larger class of materials. Modeling of the amplitude and shape of the strain response yields access to the spatio-temporal shape of the stress generation, which contains the physics of light-matter interaction. The buried detection-layer scheme is used extensively in the analysis of the strain response of the heavy rare earth-containing heterostructures that are discussed in chapter 6.

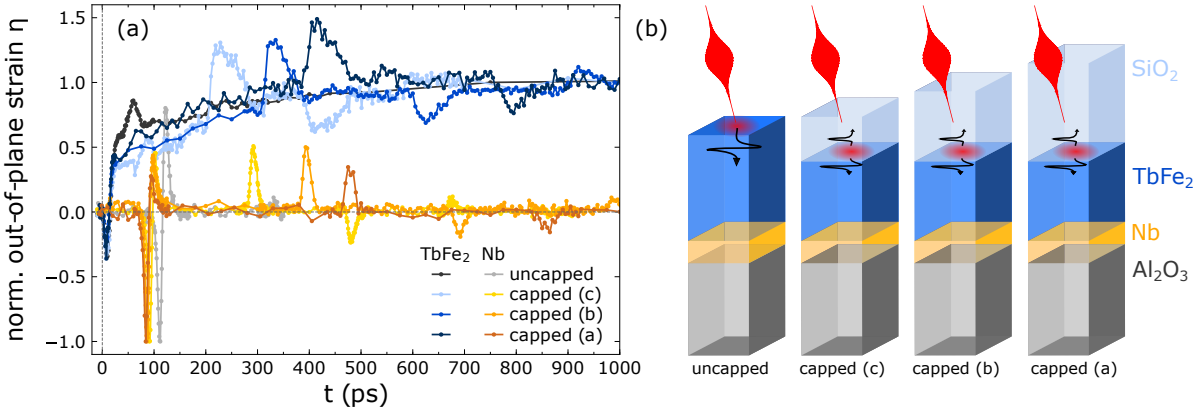

Figure 3.17: Picosecond strain pulses in $TbFe_2$-containing heterostructures with different SiO_2-cappings: (a) Strain-response of the $TbFe_2$ transducer layer (in grey and blue) and corresponding strain in the buried Nb detection layer (in light grey and orange). (b) Schematic sketch of the samples with an increasing thickness of optically transparent SiO_2 capping. The measured strain responses have been normalized to allow for a direct comparison of the relative timings in order to suppress effects from the different laser-excitation densities used in the experiments.

To support the findings reported in article III, figure 3.17 displays the strain response of a sample series of similarly prepared sample structures with different, amorphous SiO_2 capping layers. The different layer thicknesses in the investigated samples are summarized in table 3.1. They are extracted from simulations of the observed strain response as discussed in article III. There we only discuss the results from the uncapped and one capped sample, since the other heterostructures show a similar qualitative behavior. The main difference is the delay between the unipolar strain pulses that travel back and forth within

the amorphous, transparent SiO_2 capping that acts as an acoustic delay line. As the thickness of the amorphous silica capping gets thicker, the picosecond strain pulses are broadened and damped, as shown in article III, where we observe multiple acoustic echoes that undergo a different number of round-trips within the SiO_2 capping layer. In principle, this allows for investigations of non-linear phonon-phonon interactions that lead to the damping and broadening of the picosecond strain pulses using an UXRD experiment, but this is not the focus of the current investigation.

Table 3.1: Layer thicknesses of the $TbFe_2$ samples with and without SiO_2 capping layer: This table summarizes the layer thicknesses of the four different $TbFe_2$-containing metallic heterostructures. These values were extracted from simulations of the strain response, especially the timing and shape of the picosecond strain pulses, using the thermophysical material properties as detailed in paper article III and its supplementary. Thickness values are provided here as reference for further investigations.

	uncapped	capped (c)	capped (b)	capped (a)
SiO_2 thickness (nm)	0	565	882	1135
$TbFe_2$ thickness (nm)	436	356	346	326
Nb thickness (nm)	50	50	50	50

This example outlines the method of picosecond ultrasonic experiments with X-ray probing at a PXS setup. To obtain the strain response of one of the layers with the presented signal-to-noise level requires approximately 2-3 hours measurement time so that multiple picosecond ultrasonics experiments can be carried out per day. This series of measurements is presented to showcase the usefulness of a laboratory based UXRD setup because it allows for systematic studies of the strain response without strict beamtime-limitations that are common at synchrotron and FEL facilities. The direct sensitivity of the UXRD technique to the sign and amplitude of the generated picosecond strain pulses and its depth-sensitivity and material specificity facilitate the interpretation. This is especially useful when multiple time- and space-dependent strain generation mechanisms superimpose as will be shown in chapter 6.

Chapter Four

Models and mechanisms of strain generation

This thesis discusses experiments in which a femtosecond laser-pulse transfers energy into a sample, where it triggers a strain response. This type of experiment is often referred to as picosecond ultrasonics. It is schematically depicted in figure 4.1. The right hand side of this sketch separates the series of events into four conceptual steps in accordance to the review article on picosecond laser ultrasonics by Matsuda and coworkers[27]. The observed strain response in this type of experiments contains information on all four conceptual steps i. e. the energy deposition profile (1), the strain generation from the stress (2), the strain pulse propagation and reflection (3) and the thermal transport (4) that occur in response to the light-matter interaction between the femtosecond laser pulse and the sample. The remainder of the chapter is dedicated mainly to a discussion of the stress that initiates the picosecond strain response.

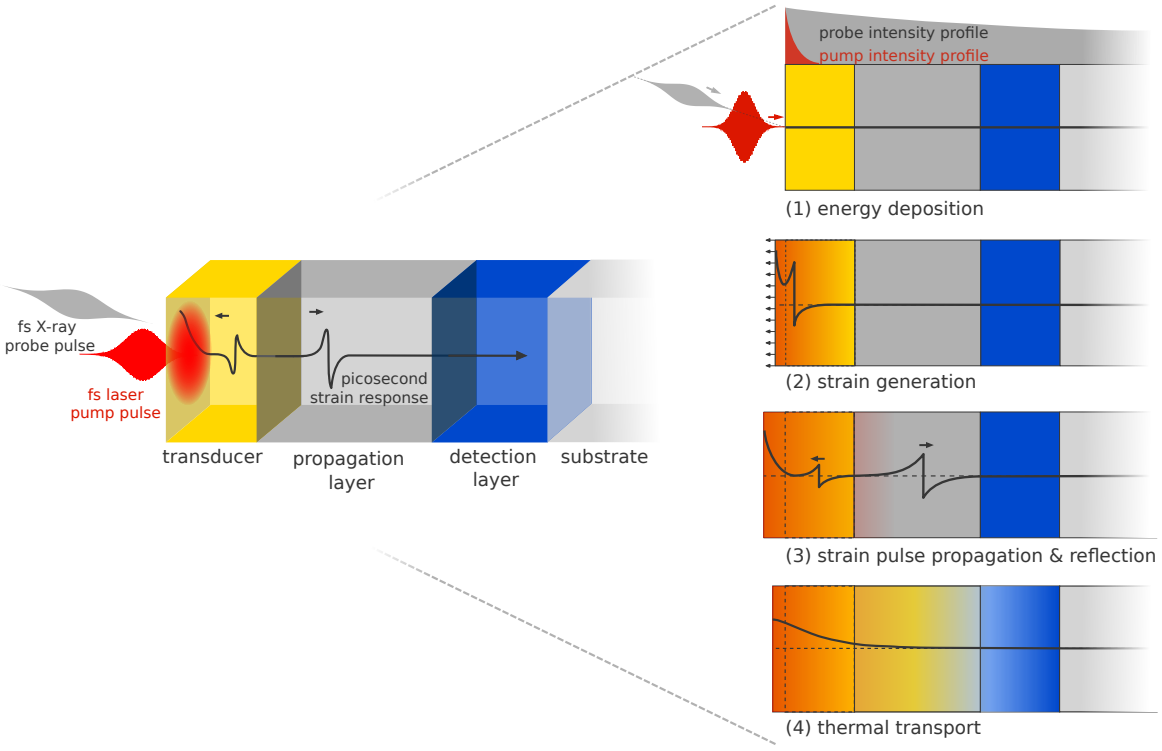

Figure 4.1: Schematic sketch of a picosecond ultrasonics experiment: A femtosecond laser pulse excites a metallic heterostructure that consists of multiple, often nanoscopically thin layers i. e. a transducer (orange), a propagation layer (dark grey) and a detection layer (blue) grown on top of a substrate. The right hand side of this figure displays a schematic order of events that is common to all picosecond ultrasonics experiments regardless of the probing as indicated in the review by Matsuda et al. [27]. The schematic figures on the right hand side are limited to effects in metallic heterostructures that are homogeneously excited along the in-plane dimensions so that the probed strain response is, to a good approximation, one-dimensional.

This field of research was pioneered by Christian Thomsen and Holger Grahn in the group of Prof. Humphrey Maris in 1984 at Brown University in Rhode Island.[52, 175] Many picosecond ultrasonics experiments have since then been conducted to study different aspects of the strain response, mainly by all-optical probing techniques. As exemplified in chapter 3, we track the Bragg peak shift in reciprocal space seen by UXRD as the detection mechanism for the strain response. This approach provides a material-specific probe that has a depth-sensitivity. The extinction length of the 8 keV X-rays is typically on the order of few micrometers. The penetration depth of the hard X-rays is roughly two orders of magnitude larger than the penetration depth of optical pulses that usually penetrate few tens of nanometers into metallic layers.

The first section of this chapter lists multiple effects that occur in fs-laser-excited materials to provide a context for my experiments and related fields of research. This overview is designed to outline potential contributions to the observed picosecond strain response in magnetically ordered samples and to identify relevant effects for the experiment. The second section presents mechanisms for the stress generation on the crystal lattice, first from a general thermodynamic perspective and second by a brief overview of the underlying microscopic mechanisms. The discussion is restricted to the stress by energy transfer to electrons, phonons and magnetic excitations. Additional mechanisms that apply for semiconductors and ferroelectrics are discussed in the review of Ruello and Gusev.[28]

The main part of this chapter is focused on the Grüneisen parameter that I use to transfer the general thermodynamic approach to the time-resolved experiments. The Grüneisen parameter relates the energy density stored in different types of quantum excitations i.e. electrons, phonons and magnetic excitations to their stress on the atomic lattice. This concept provides a useful first approximation and approach for the discussion of the stresses that originate from different degrees of freedom within a solid. The strain response that results from the space- and time-dependent stress can be modeled using a linear masses, sticks and springs model that yields a visual approach. This masses and springs model is modified to include ultrafast negative thermal expansion given by the release of magnetostriction. A general and complete discussion of the applicability and validity of thermodynamic arguments on ultrafast timescales is beyond the scope of this thesis. Limitations and possible modifications of the Grüneisen parameter concept are mentioned at the end of the chapter.

4.1 Contributing effects in picosecond ultrasonics

In order to analyze the light matter interaction using a picosecond ultrasonics experiment, it is instructive to consider the related experimental steps. A coarse and certainly subjective overview of the experimental procedure and the related physical effects is given in figure 4.2. This schematic lists ten general steps that are required for a picosecond ultrasonics experiment that employs the pump-probe technique. Steps (2)-(8) contain physical effects that occur in the response to the sample-specific light-matter interaction. Their contributions motivate the observation of the picosecond strain response as a way to access physical effects in nanoscale layers on ultrafast timescales.

Figure 4.2 indicates that the picosecond strain response may contain effects from a multitude of nanoscale energy transfer processes that occur between the light-absorption (2) and the strain detection (8). This is interesting because nanoscale energy transfer determines a multitude of functional processes in our daily life, such as data storage, heat transport and optical properties, but it can only be observed by tracing transient excited states of matter. Energy is a concept that is used to describe the state of matter with a scalar quantity and the conservation of energy helps to rationalize the time series of events. However, energy cannot be observed directly. Its presence can only be inferred by its effects on physical observables

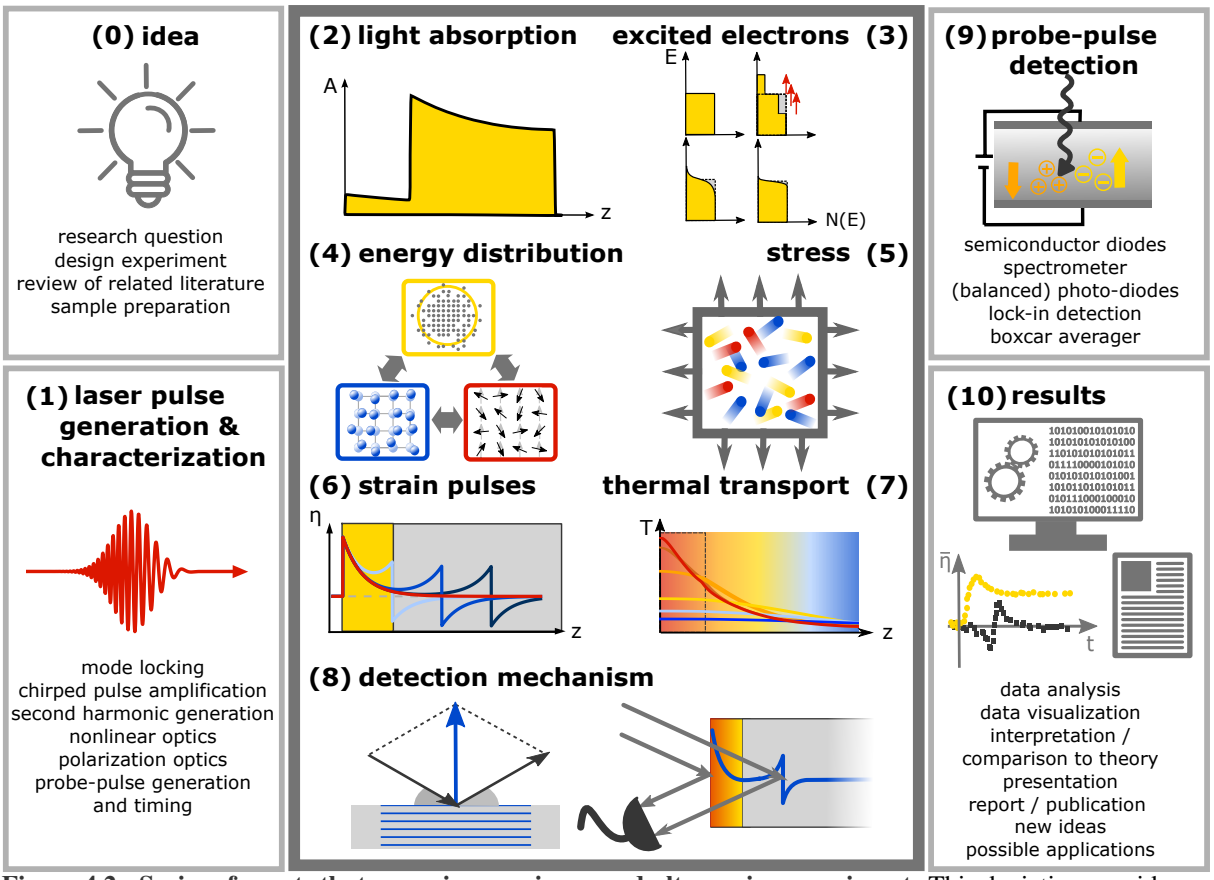

Figure 4.2: Series of events that occur in any picosecond ultrasonics experiment: This depiction provides an overview of the steps and physical effects that are relevant for the experiments discussed in this thesis. The grey boxes contain steps that are common to all ultrafast experiments that employ the pump-probe scheme. Steps (2)-(8) represent sample-specific effects that are related to physical processes that occur as a result of the light-matter interaction in the material. The graphics serve as iconographic representation for each process. A more detailed representation of the sample-specific processes and related key words is provided in figure 4.3.

that are accessible in experiments.

Current experimental approaches to track ultrafast, nanoscale energy transfer processes in solids detect, for example, the transient population of excited electronic states[87, 176] or selected phonon modes[78, 82, 83, 177], the increase in vibration amplitudes of atomic nuclei[178–181], the change of optical properties by time-domain thermoreflectance[160, 165, 182, 183] or local magnetization changes[184]. Picosecond ultrasonics experiments that track the local displacement of atoms from their equilibrium position are another way of detecting timescales of energy transfer. This can be done via the photoelastic effect in the visible range [52, 185, 186] or by diffraction studies such as presented in article II and article IX of this thesis.

Frequently occuring sample-specific effects and processes in the presented picosecond ultrasonics experiments are summarized in figure 4.3 in more detail. The approximate line of events is given by the enumerated boxes (2)-(8), which contain potential effects that are common to laser-excited metallic transducers with the corresponding keywords listed in black. The red insets and keywords list effects that modify the response of the transducer if a magnetic order is present within the sample. Red boxes on the right column list processes that occur in parallel when the picosecond ultrasonics experiment is carried out in a sample that exhibits some form of magnetic order. Magnetic effects may either influence the nanoscale energy transfer or be influenced by the picosecond strain response. They are listed to indicate the potential connection of the presented experiments to other fields of research.

The provided overview is not exhaustive but rather designed to acknowledge the complex interplay of effects that results in the picosecond strain response or is affected by it. Each of the listed boxes can be considered as a separate area of research with dedicated literature. In the remainder of this chapter I focus on the stress generation mechanisms that are schematically depicted in box (5) of figure 4.3. Especially the effect of magnetostriction and the occurrence of stress on the lattice exerted by the spin system is explored in this experimental work.

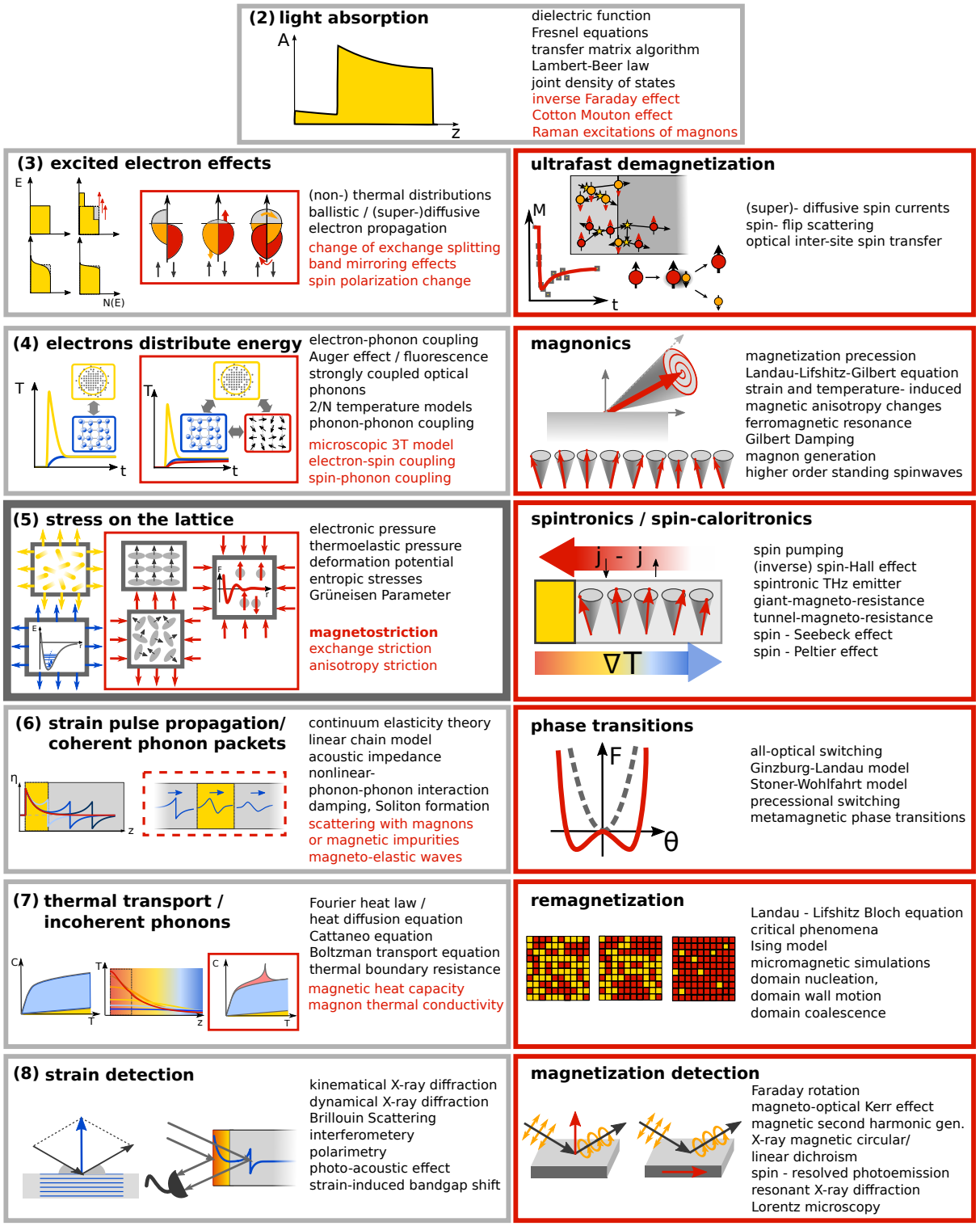

Figure 4.3: Sample-specific effects that occur in a picosecond ultrasonics experiment: The left column provides details for the steps (2)-(8) mentioned in figure 4.2. Related key words for effects and concepts that contribute to each step are provided as a guide for further reading. Terms added in red represent modifications that may arise in samples that exhibit a form of magnetic order. Boxes in the right column list additional effects that only arise in magnetically ordered samples. These processes can either influence the coherent and incoherent phonon response or are influenced by it. This graph provides an overview for further studies. Icons are adapted from various works: band-mirroring [187], ultrafast demagnetization[22], spin-flip scattering[188], super-diffusive spin-currents[73]

4.2 Thermodynamics of near-equilibrium thermal expansion

Femtosecond laser excitation experiments represent the limiting case of an approximately instantaneous energy deposition in a material. The other limit i.e. the strain response to slow heating processes, is referred to as (equilibrium) thermal expansion. In these experiments, the material is given sufficient time to equilibrate the energy distribution among all its degrees of freedom before the measurement takes place. The underlying concepts of thermal expansion can be developed from thermodynamic principles. A brief introduction to the concepts of thermal expansion is presented, because these general concepts are applicable to all materials, regardless of their microscopic differences.

Thermal expansion is an effect that connects the microscopic inter-atomic interactions with the macroscopic properties of the materials. Extensive previous scientific work has established a formalism to discuss the strain response of many different materials upon slowly heating materials under conditions close to thermal equilibrium. This section compiles the basic thermodynamic principles that to some extent also form the background for the analysis and discussion of the time-resolved UXRD experiments. This section contains a condensed form of the arguments presented within the reviews on thermal expansion behavior by Barrera et al. [189], White [190] and Barron et al. [191].

Thermodynamic analysis has established that any closed system at a constant pressure p and temperature T in thermal equilibrium will minimize the thermodynamic potential G (also called Gibbs energy).[190] G can be obtained by successive Legendre transformations of the internal energy U that is minimized under the conditions of constant volume V and entropy S:

$$G = U - TS + pV. \tag{4.1}$$

Given the full differential of U: $\mathrm{d}U = T\mathrm{d}S - p\mathrm{d}V + \mu\mathrm{d}N$ that results from the first law of thermodynamics, the differential of G follows to be:

$$\mathrm{d}G = \mu\mathrm{d}N - S\mathrm{d}T + V\mathrm{d}p. \tag{4.2}$$

where μ is the chemical potential and N denotes the number of particles in the system. The quantities in subscript next to the vertical line are fixed in the differentiation process. The remaining partial derivatives of G yield the relations:

$$V = \left.\frac{\partial G}{\partial p}\right|_{T,N} \qquad S = -\left.\frac{\partial G}{\partial T}\right|_{p,N} \qquad \mu = \left.\frac{\partial G}{\partial N}\right|_{T,p}. \tag{4.3}$$

The term $\mu\mathrm{d}N$ is neglected in the subsequent discussion because I only consider systems where the number of electrons and atoms is conserved or where the chemical potential μ is zero, which is the case for phonons and magnons. Using the symmetry of the remaining second derivatives of G, one finds the following expression for the volume thermal expansion coefficient β:

$$\beta = \left.\frac{1}{V}\frac{\partial V}{\partial T}\right|_p = \frac{1}{V}\frac{\partial^2 G}{\partial T \partial p} = \frac{1}{V}\frac{\partial^2 G}{\partial p \partial T} = -\left.\frac{1}{V}\frac{\partial S}{\partial p}\right|_T \tag{4.4}$$

In addition, one finds that the equality $\frac{\partial^2 G}{\partial T \partial p} = \frac{\partial^2 G}{\partial p \partial T}$ leads to one of the so-called Maxwell-relations $\left.\frac{\partial V}{\partial T}\right|_p = -\left.\frac{\partial S}{\partial p}\right|_T$. An overview of all Maxwell relations that involve only the quantities S, T, p and V is provided in table 4.1.

As shown by Barrera et al. [189], the derivation for the thermal expansion coefficient β can be manipulated further to demonstrate that the sign of the thermal expansion depends on the change of entropy S with the volume V:

$$\beta = \left.\frac{1}{V}\frac{\partial V}{\partial T}\right|_p = -\left.\frac{1}{V}\frac{\partial S}{\partial p}\right|_T = -\left.\frac{1}{V}\frac{\partial V}{\partial p}\right|_T \left.\frac{\partial S}{\partial V}\right|_T = \kappa_T \left.\frac{\partial S}{\partial V}\right|_T \tag{4.5}$$

Table 4.1: Thermodynamic potentials, their differentials and the corresponding Maxwell relations: Summary of the thermodynamic potentials, that are minimized under different boundary conditions. The resulting Maxwell relations are used in the analysis of the thermal expansion behavior.

name	symbol	defining relation	differential	Maxwell relation
Internal energy	$U(S,V)$		$\mathrm{d}U = \quad T\mathrm{d}S - p\mathrm{d}V$	$\left.\frac{\partial T}{\partial V}\right\|_S = -\left.\frac{\partial p}{\partial S}\right\|_V$
Enthalpy	$H(S,P)$	$H = U + pV$	$\mathrm{d}H = \quad T\mathrm{d}S + V\mathrm{d}p$	$\left.\frac{\partial T}{\partial p}\right\|_S = \quad \left.\frac{\partial V}{\partial S}\right\|_p$
Helmholtz free energy	$F(T,V)$	$F = U - TS$	$\mathrm{d}F = -S\mathrm{d}T - p\mathrm{d}V$	$\left.\frac{\partial S}{\partial V}\right\|_T = \quad \left.\frac{\partial p}{\partial T}\right\|_V$
Gibbs free energy	$G(T,p)$	$G = U - TS + pV$	$\mathrm{d}G = -S\mathrm{d}T + V\mathrm{d}p$	$\left.\frac{\partial S}{\partial p}\right\|_T = -\left.\frac{\partial V}{\partial T}\right\|_p$

This relation holds because the isothermal compressibility $\kappa_T = -\frac{1}{V}\left.\frac{\partial V}{\partial p}\right|_T$ is always positive. Daily experience with thermal expansion in common materials shows that, more often than not it is the case that $\beta > 0$, which corresponds to an entropy increase with increasing volume $\left(\left.\frac{\partial S}{\partial V}\right|_T > 0\right)$. Within the model of an ideal gas that represents the most basic model for a material that consist of non-interacting particles it can be shown that the thermal expansion coefficient β is always positive. The existence of negative thermal expansion of polymer chains, water and some magnetic materials however illustrates that interactions between particles can change that.

More explicitly, one finds that the thermal expansion response can be thought to consist of two different processes that appear upon reformulation of relation 4.5, which leads to:

$$\beta = \kappa_\mathrm{T}\left.\frac{\partial S}{\partial V}\right|_T = -\frac{1}{V}\left.\frac{\partial V}{\partial p}\right|_T \left.\frac{\partial S}{\partial V}\right|_T = \underbrace{-\frac{1}{V}\left.\frac{\partial V}{\partial p}\right|_T}_{\substack{\text{step 2:} \\ p \text{ relase at constant } T}} \quad \underbrace{\left.\frac{\partial p}{\partial T}\right|_V}_{\substack{\text{step 1:} \\ p \text{ increase at fixed } V}} \tag{4.6}$$

The resulting volume change from the increased pressure occurs in the direction that minimizes the Gibbs free energy $G = U - (T + \Delta T)S + p(V + \Delta V)$ by maximizing the entropy S. This is a consequence of $\mathrm{d}G = -S\mathrm{d}T$ at constant pressure. A visualization of this two-step thought-process for the thermal expansion is shown in figure 4.4. This figure represents an adaptation of a schematic sketch of two isothermal surfaces in a $G-V$ diagram from the review of Barrera [189]. For positive expansion the new minimum of G lies at a larger V whereas for negative thermal expansion the state that minimizes the Gibbs energy occurs for a smaller V.

4.3 Grüneisen parameter model for subsystem-specific stresses

The so far presented relations for the thermal expansion do not explicitly distinguish between different degrees of freedom that exist within solids. In the following discussion, I differentiate between excitations of electrons, lattice vibrations (phonons) and magnetic degrees of freedom that each represent an energy reservoir within metals that host magnetic order. This section introduces the concept of a sub-system specific Grüneisen parameter Γ_r . The Grüneisen parameter relates the energy density ρ_r^Q in different types of quantum excitations to their stress on the atomic lattice. This parameter provides a first approximation for the discussion of time-dependent stresses that originate from the energy flow between different degrees of freedom within solids.

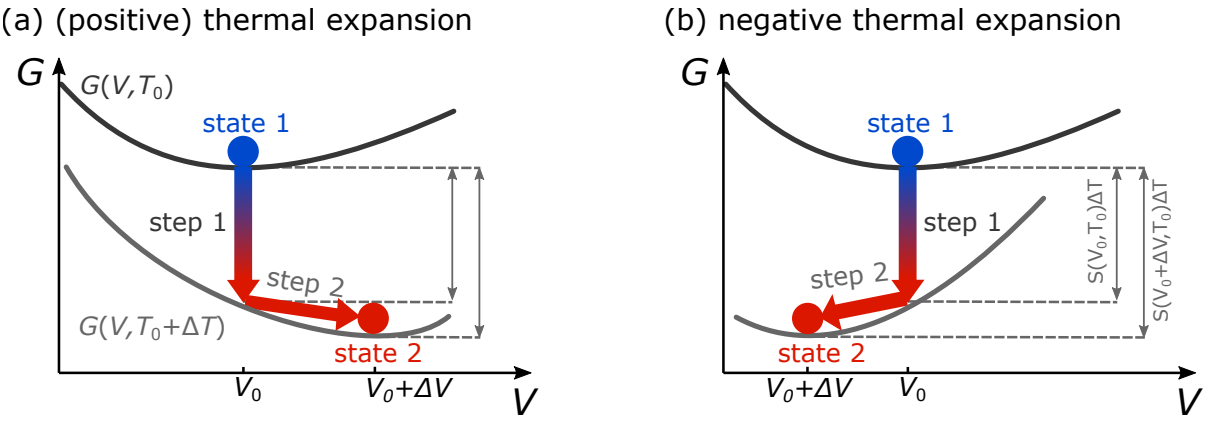

Figure 4.4: Two-step picture for the thermal expansion process: Case (a) represents the potential landscape that leads to an increase in volume upon heating, whereas case (b) minimizes G by a decrease in volume. Both cases consist of a pressure increase due to increasing temperature at a fixed volume (step 1) and a subsequent release of pressure at the increased temperature towards the minimum in the potential (step 2) that are reflected by the separate coefficients in relation (4.5). This figure is adapted from a review on negative thermal expansion effects by Barrera et al. [189].

After a brief, general introduction of the concept of a Grüneisen parameter, I derive the subsystem-specific Grüneisen coefficients based on simple textbook models for the different quantum excitations. Very simplified models are chosen to convey the essence of the Grüneisen parameter model. The simple models do not consider the manifold complexities that arise real in thin film samples, that are often anisotropic in their elastic properties and electronic bandstructure as well as subject to boundary conditions due to epitaxial strains. The application of thermodynamic principles is subsequently supplemented by a discussion of the microscopic ideas that govern the stress generation for each type of quantum excitation. I include a brief discussion of anisotropic Grüneisen parameters that occur in real solids and provide a list of limitations and approximations that need to be considered when applying the concept of a Grüneisen parameter in time-resolved experiments. I conclude this section with a compilation of typical time-scales for physical effects that occur in picosecond ultrasonics experiments in laser excited metals, because they determine the evolution of the combined total stress $\sigma_{\mathrm{tot}}(t,z)$. The numerical approach to extract the resulting strain response $\eta(t,z)$ is presented in the the final section of this chapter.

4.3.1 General concept of a Grüneisen parameter

The so far presented relations for the thermal expansion do not explicitly distinguish between different degrees of freedom that exist within solids. In the following I differentiate between excitations of electrons, lattice vibrations (phonons) and magnetic degrees of freedom that each represent an energy reservoir within metals that host magnetic order. This section introduces the concept of a sub-system specific Grüneisen parameter Γ_r. The Grüneisen parameter relates the energy density ρ_r^Q in different types of quantum excitations to their stress on the atomic lattice. It provides a first order approximation for the discussion of time-dependent stresses that originate from the energy flow between different degrees of freedom within solids. The theoretical background of this is discussed here because it is used in the analysis of the time-dependent stresses in almost all articles of this thesis.

The Grüneisen parameter is named after Eduard Grüneisen who investigated the effect of the volume change on the vibrational frequencies in solids for the first time in 1912. [192] Many different representations of the Grüneisen parameter have since then been derived and here I present relations that may be useful in the context of picosecond ultrasonics experiments. The discussion starts with a general

introduction and definition. The bulk Grüneisen parameter is defined as [189]:

$$\Gamma = \frac{KV\beta}{C_{\mathrm{V}}} = \frac{V\beta}{\kappa C_{\mathrm{V}}}, \tag{4.7}$$

where K represents the bulk modulus, β the volume expansion coefficient, V the sample volume and C_{V} the heat capacity at constant volume. The alternative form uses the compressibility $\kappa = 1/K$. An extensive derivation of relation 4.7 is not repeated here since it is provided in standard textbooks of solid state physics (see for example in chapter 25 of the book of Ashcroft and Mermin [193] or in chapter 11.3 in the book by Dove[194]). Instead, I make use of this definition to derive the Grüneisen parameter from different free energy contributions to the sub-system.

Based on the previous definitions and Maxwell relations, one can rewrite the thermal expansion coefficient β as:

$$\beta = \frac{1}{V}\frac{\partial V}{\partial T}\bigg|_p = -\frac{1}{V}\frac{\partial S}{\partial p}\bigg|_T = -\frac{1}{V}\frac{\partial V}{\partial p}\bigg|_T \frac{\partial S}{\partial V}\bigg|_T = \kappa_{\mathrm{T}}\frac{\partial p}{\partial T}\bigg|_V \tag{4.8}$$

At this point one should note that the temperature dependence of the thermal expansion coefficient β originates mainly from the temperature dependence of the term $\frac{\partial p}{\partial T}\Big|_V$, since the isothermal compressibility κ_T is nearly independent of T. Inserting relation (4.8) into the definition (4.7) for Γ one arrives at:

$$\Gamma = \frac{V}{C_{\mathrm{V}}}\frac{\partial p}{\partial T}\bigg|_V \tag{4.9}$$

Here, it is instructive to identify the change in energy density of a system as $\Delta\rho^Q = C_V \partial T/V$ so that one arrives at:

$$\Delta p = \Gamma \Delta \rho^Q. \tag{4.10}$$

This illustrates that the Grüneisen parameter represents the proportionality constant between the pressure increase Δp and the increase in energy density ρ^Q. This correspondence is sometimes referred to as the Mie-Grüneisen equation of state.[195] This equation describes a relation between the pressure p and the energy density E/V. In its most simple form, it reads:

$$p(E,V) = p_0 + \Gamma\frac{E - E_0}{V} \tag{4.11}$$

In general, one finds that the Grüneisen parameter is volume dependent ($\Gamma = \Gamma(V)$), but this correction is not considered in the following analysis because volume changes in solids are relatively small in comparison to gases that are easily compressible. Furthermore, one can use the thermodynamical potentials that provide a relation for the pressure p as:

$$p = -\frac{\partial U}{\partial V}\bigg|_S \quad \text{or} \quad p = -\frac{\partial F}{\partial V}\bigg|_T \tag{4.12}$$

and the known relations for the heat capacity

$$C_{\mathrm{V}} = \frac{\partial \langle E\rangle}{\partial T}\bigg|_V = \frac{\partial U}{\partial T}\bigg|_V = T\,\frac{\partial S}{\partial T}\bigg|_V = -T\,\frac{\partial^2 F}{\partial T^2}\bigg|_V \tag{4.13}$$

Combining this and inserting the result into (4.7) we find the following recipes for calculating the Grüneisen parameter Γ for different conditions:

$$\Gamma = \frac{V}{C_{\mathrm{V}}}\frac{\partial p}{\partial T}\bigg|_V \tag{4.14}$$

$$= -\frac{V}{\frac{\partial U}{\partial T}\Big|_V}\,\frac{\partial}{\partial T}\bigg|_V \frac{\partial U}{\partial V}\bigg|_S \quad \text{(isentropic definition)} \tag{4.15}$$

$$= \frac{V}{T \left.\frac{\partial^2 F}{\partial T^2}\right|_V} \left.\frac{\partial}{\partial T}\right|_V \left.\frac{\partial F}{\partial V}\right|_T \text{(isothermal definition)} \tag{4.16}$$

These definitions can now be used to derive the Grüneisen parameter for a given internal energy U or free energy F. Analytical derivations for Γ are thus provided in the framework of different theoretical models for the degrees of freedom within solids. More generally, one can define the Grüneisen parameter using the partition function Z that can be derived within the framework of statistical physics. Depending on the considered situation, the appropriate definition of Z varies. For illustrative purposes, I provide only the most simple cases for one particle in one dimension. Using the shorthand $\beta^* = \frac{1}{k_B T}$, one obtains the relations:

$$Z = \begin{cases} \sum_i e^{-\beta^* E_i} & \text{classical, discrete } E_i \\ \frac{1}{h} \int e^{-\beta^* H(q,p)} \mathrm{d}q \mathrm{d}p & \text{classical, continuous } E \end{cases} \tag{4.17}$$

The partition function can be used to derive multiple useful expressions such as

$$\langle E \rangle = -\frac{\partial \log Z}{\partial \beta^*} \tag{4.18}$$

$$\text{so that } C_V = \left.\frac{\partial \langle E \rangle}{\partial T}\right|_V = -\left.\frac{\partial}{\partial T}\right|_V \left(\frac{\partial \log Z}{\partial \beta^*}\right) \tag{4.19}$$

$$\text{and } F = -k_B T \log Z = -\frac{1}{\beta^*} \log Z \tag{4.20}$$

$$\text{so that } p = -\left.\frac{\partial F}{\partial V}\right|_T = \frac{1}{\beta^*} \left.\frac{\partial \log Z}{\partial V}\right|_T \tag{4.21}$$

This leads to the general expression of the Grüneisen parameter in terms of the partition function [196] that reads:

$$\Gamma = \frac{V}{C_V} \left.\frac{\partial p}{\partial T}\right|_V = V \frac{\left.\frac{\partial}{\partial T}\right|_V \left(-\left.\frac{\partial F}{\partial V}\right|_T\right)}{\left.\frac{\partial U}{\partial T}\right|_V} = -V \frac{\left.\frac{\partial}{\partial T}\right|_V \left(\frac{1}{\beta*} \left.\frac{\partial \log Z}{\partial V}\right|_T\right)}{\left.\frac{\partial}{\partial T}\right|_V \left(\frac{\partial \log Z}{\partial \beta^*}\right)} \tag{4.22}$$

If a partition function Z for a system is known, one can thus derive the Grüneisen parameter. Examples based on the partition function for an ideal gas or a Van-der-Waals gas are provided in the article by Souza et al. [196]. In the following, I will discuss the Grüneisen parameter for common simple models that are used to describe phonons, electrons and magnetic order in solids as illustration for the general concept.

4.3.2 Phonon Grüneisen parameters

In his original publication, Eduard Grüneisen considered the thermal expansion by lattice vibrations of elements for isotropic solids with one atom per unit cell.[192, 197] He already found an interesting correlation between the heat capacity $C_V(T)$ and the thermal expansion $\beta(T)$ and reported a Grüneisen parameter γ that is nearly independent of temperature T and pressure p.

The original considerations however neglect the temperature-dependent population of phonon modes, that are captured by the Bose-Einstein distribution function. The Einstein model[198] where the lattice vibrations are captured by a single phonon with frequency ω_E, populated in accordance to quantum statistics, shall be the first test case for the derivation of the Grüneisen parameter. In this framework we have no entropy S so that the inner energy U is equal to the free energy $F = U - TS$ because there exists only one single microscopic realization for a macroscopic state with a given energy $\langle E \rangle$ in the harmonic

oscillator. Thus one can directly derive the Grüneisen parameter as follows:

$$U = F = \langle E \rangle = \hbar\omega_{\mathrm{E}} \left(\frac{1}{e^{\frac{\hbar\omega_{\mathrm{E}}}{k_{\mathrm{B}}T}} - 1} + \frac{1}{2} \right) \tag{4.23}$$

$$\Rightarrow C_{\mathrm{V}} = \left. \frac{\partial U}{\partial T} \right|_V = k_{\mathrm{B}} \left(\frac{\hbar\omega_E}{k_{\mathrm{B}}T} \right)^2 \frac{e^{\frac{\hbar\omega_{\mathrm{E}}}{k_{\mathrm{B}}T}}}{\left(e^{\frac{\hbar\omega_{\mathrm{E}}}{k_{\mathrm{B}}T}} - 1 \right)^2} \tag{4.24}$$

$$p = -\left. \frac{\partial F}{\partial V} \right|_T \approx -\hbar \left. \frac{\partial \omega_{\mathrm{E}}}{\partial V} \right|_T \left(\frac{1}{e^{\frac{\hbar\omega_{\mathrm{E}}}{k_{\mathrm{B}}T}} - 1} + \frac{1}{2} \right) \tag{4.25}$$

$$\left. \frac{\partial p}{\partial T} \right|_V = -\left. \frac{\partial \omega_{\mathrm{E}}}{\partial V} \right|_T \frac{1}{\omega_{\mathrm{E}}} \left(\frac{\hbar\omega_E}{k_{\mathrm{B}}T} \right)^2 \frac{e^{\frac{\hbar\omega_{\mathrm{E}}}{k_{\mathrm{B}}T}}}{\left(e^{\frac{\hbar\omega_{\mathrm{E}}}{k_{\mathrm{B}}T}} - 1 \right)^2} \tag{4.26}$$

$$\Rightarrow \Gamma_{\mathrm{Einstein}} = \frac{V}{C_{\mathrm{V}}} \left. \frac{\partial p}{\partial T} \right|_V = -\frac{V}{\omega_{\mathrm{E}}} \left. \frac{\partial \omega_{\mathrm{E}}}{\partial V} \right|_T = -\left. \frac{\partial \log \omega_{\mathrm{E}}}{\partial \log V} \right|_T \tag{4.27}$$

This illustrates that C_{V} and $\beta = \kappa_T \left. \frac{\partial p}{\partial T} \right|_V$ share the same complex temperature dependence, but that their ratio becomes independent of temperature. In this derivation, I used the so called quasi-harmonic approximation, which assumes that the harmonic expansion around the potential minimum holds, but the frequency of the phonon mode ω_{E} depends on the volume. The derivative of ω_{E} with respect to the volume in the exponential is neglected as it would lead to a correction that is second order in $\frac{\partial \omega_{\mathrm{E}}}{\partial V}$. For most phonon modes, we observe that the frequency increases as the volume decreases so that the corresponding Grüneisen parameter is positive.

The presented result corresponds to the mode-specific definition of the phonon Grüneisen parameter. A mode averaged definition of the phonon Grüneisen parameter is given by:

$$\Gamma_{\mathrm{pho}} = \frac{\sum_{i,q} C_{i,r} \gamma_{i,r}}{\sum_{i,q} C_{i,r}}, \tag{4.28}$$

where the index i, enumerates all phonon modes with their different polarizations r. This corresponds to a average of the mode specific phonon Grüneisen parameters ($\gamma_{i,r}$) weighted by their mode-specific contribution to the heat capacity of the solid ($C_{i,r}$). Solid state textbooks[33, ch.6][193, ch.25] derive the Grüneisen parameter for the frequently used Debye-approximation as

$$\Gamma_{\mathrm{Debye}} = -\left. \frac{\partial \log \omega_{\mathrm{D}}}{\partial \log V} \right|_T, \tag{4.29}$$

where the volume-dependence of the Debye frequency $\omega_{\mathrm{D}} = v_{\mathrm{sound}} (6\pi^2 \frac{N}{V})^{\frac{1}{3}}$ serves to approximate the phonon Grüneisen parameter of the solid.

4.3.3 Electron Grüneisen parameters

The Sommerfeld model of a free electron gas is the simplest possible description of a free electron gas, which takes into account that the electronic states are populated according to the quantum mechanical Fermi-Dirac statistics ($f(E,T)$) and the Pauli-principle. Using the density of states $D(E)$, the inner energy of this model can be written as:

$$U = \langle E \rangle = \int_0^\infty E' D(E') f(E',T) \mathrm{d}E' \tag{4.30}$$

$$\text{with } D(E) = \frac{V}{2\pi^2}\left(\frac{2m}{\hbar^2}\right)^{\frac{3}{2}}\sqrt{E} \tag{4.31}$$

$$\text{and } f(E,T) = \frac{1}{e^{\frac{E-\mu}{k_\mathrm{B}T}}+1} \tag{4.32}$$

$$\Rightarrow U = \frac{V}{2\pi^2}\left(\frac{2m}{\hbar^2}\right)^{\frac{3}{2}}\int_0^\infty \frac{\left(\sqrt{E'}\right)^3}{e^{\frac{E'-\mu}{k_\mathrm{B}T}}+1}\mathrm{d}E' \tag{4.33}$$

This integral cannot be solved analytically. An approximate solution is provided by the so-called Sommerfeld expansion, which reads:

$$U(T) = U_0 + \frac{\pi^2}{6}D(E_\mathrm{F})(k_\mathrm{B}T)^2 \tag{4.34}$$

$$= U_0 + \frac{\pi^2}{2}\frac{m}{\hbar^2}\left(3\pi^2\right)^{-\frac{2}{3}}V^{\frac{2}{3}}N^{\frac{1}{3}}(k_\mathrm{B}T)^2 \tag{4.35}$$

where the Fermi energy $E_\mathrm{F} = \frac{(\hbar k_\mathrm{F})^2}{2m} = \frac{\hbar^2}{2m}\left(3\pi^2\frac{N}{V}\right)^{\frac{2}{3}}$ and $D(E_\mathrm{F}) = \frac{3}{2}\frac{N}{E_\mathrm{F}}$ and the shorthand $U_0 = U(T = 0) = \int_0^{E_\mathrm{F}} E'D(E')f(E',T)\mathrm{d}E'$ are used. Because multiple states contribute to the inner energy we have a non-vanishing entropy S contribution that needs to be taken into account in order to obtain the free energy $F = U - TS$.

$$S = \int \frac{C_\mathrm{V}}{T}\mathrm{d}T = \frac{k_\mathrm{B}^2 m}{\hbar^2}\left(\frac{\pi}{3}\right)^{\frac{2}{3}}V^{\frac{2}{3}}N^{\frac{1}{3}} = \frac{\pi^2}{3}D(E_\mathrm{F})k_\mathrm{B}^2T \tag{4.36}$$

$$F = U - TS = U_0 - \frac{\pi^2}{6}D(E_\mathrm{F})(k_\mathrm{B}T)^2 \tag{4.37}$$

$$= U_0 - \frac{\pi^2}{2}\frac{m}{\hbar^2}(k_\mathrm{B}T)^2 \tag{4.38}$$

From the inner energy U stated in (4.35) one obtains the heat capacity C_V and from relation (4.38) for the free energy F one derives the pressure p in order to calculate the Grüneisen parameter in the Sommerfeld model as follows:

$$C_\mathrm{V} = \left.\frac{\partial U}{\partial T}\right|_V = 2\frac{\pi^2}{2}\frac{m}{\hbar^2}\left(3\pi^2\right)^{-\frac{2}{3}}V^{\frac{2}{3}}N^{\frac{1}{3}}k_\mathrm{B}^2T \tag{4.39}$$

$$= \frac{\pi^2}{3}D(E_\mathrm{F})k_\mathrm{B}^2T = \gamma_\mathrm{S}T \tag{4.40}$$

$$\left.\frac{\partial p}{\partial T}\right|_V = \left.\frac{\partial}{\partial T}\right|_V\left(-\left.\frac{\partial F}{\partial V}\right|_T\right) = \frac{2}{3}2\frac{\pi^2}{2}\frac{m}{\hbar^2}\left(3\pi^2\right)^{-\frac{2}{3}}V^{-\frac{1}{3}}N^{\frac{1}{3}}k_\mathrm{B}^2T \tag{4.41}$$

$$= \frac{2}{3V}\frac{\pi^2}{3}D(E_\mathrm{F})k_\mathrm{B}T = \frac{2}{3V}\gamma_\mathrm{S}T \tag{4.42}$$

$$\Rightarrow \Gamma_\mathrm{Sommerfeld} = \frac{V}{C_\mathrm{V}}\left.\frac{\partial p}{\partial T}\right|_V = \frac{2}{3} \tag{4.43}$$

The positive value for the Grüneisen parameter indicates that an increase in energy the free electron gas leads to an expansive stress on the lattice. This model does not consider the electron band-structure of the solid and the experimentally determined Grüneisen parameters for electrons in metals turn out to be slightly larger and lie the range of approximately 1-2. [199, p.70ff] It interesting to note that a negligence of the entropy contribution S to the free energy would lead to a Grüneisen parameter of $-\frac{2}{3}$, which underlines the large effect that entropy can have on the thermal expansion.

The presence of electronic stress contributions in addition to the contribution of phonons and their description via electron Grüneisen coefficients is established in the literature for equilibrium thermal expansion of metals at low temperature.[200–202] The concept of electron and phonon Grüneisen paramters is also established for the analysis of the strain response in metals that are subjected to femtosecond laser pulses, which trigger a strong transient non-equilibrium between electron excitations and phonons[28, 147, 203–205].

4.3.4 Magnetic Grüneisen parameters

Magnetic order results from interaction between different magnetic moments. The following arguments show that this order also contributes to the free energy and thus results in magnetostrictive strain, that can be described using a magnetic Grüneisen parameter.

One model for the energy contribution to the magnetic order is provided by the Heisenberg Hamiltonian $H = -\sum_{i,j} J_{ij}\vec{s}_i \cdot \vec{s}_j$ where J_{ij} represents the exchange constant and the sum runs over all pairs of magnetic moments $\vec{s}_i$ and $\vec{s}_j$, where $i \neq j$. Various simplifications of this model exist, which make the potentially infinite sum of spin-spin interactions mathematically manageable. In the most simple case one only considers an interaction between nearest neighbors of spins and assumes that all spins behave in the same way. Thereby one arrives at a mean field model approach that yields the following a free energy contribution:

$$U = F = \langle E \rangle = -\sum_{i,j} J_{ij}\vec{s}_i \cdot \vec{s}_j \tag{4.44}$$

$$\approx J\langle \vec{s}_i \cdot \vec{s}_j \rangle = JM^2 \cos(\phi). \tag{4.45}$$

In this model, I note that J is the exchange constant between neighboring magnetic moments and $\langle \vec{s}_i \cdot \vec{s}_j \rangle$ is the average alignment of the neighboring magnetic moments, which relates to the (sublattice) magnetization M and the angle ϕ between neighboring magnetic moments. This relation can be used to derive the magnetostriction from the distance dependence of the exchange interaction $J = J(r)$ as shown by Kittel [206]:

$$F = F_{\text{elastic}} + F_{\text{mag}} \tag{4.46}$$

$$= \frac{1}{2} YV \left(\frac{r - r_{\text{T}}}{r_{\text{T}}} \right)^2 - J(r) V \langle \vec{s}_i \cdot \vec{s}_j \rangle \tag{4.47}$$

$$\approx \frac{1}{2} YV \left(\frac{r - r_{\text{T}}}{r_{\text{T}}} \right)^2 - \underbrace{\left(J(r = r_T) + \frac{\partial J}{\partial r}(r - r_T) \right)}_{\text{Taylor expansion}} V \langle \vec{s}_i \cdot \vec{s}_j \rangle \tag{4.48}$$

The additional term in the free energy shifts the minimum in the free energy to a new equilibrium distance that is different from r_{T} that minimizes F_{elastic}, where Y, represents the appropriate elastic constant. This can be seen by evaluating $\partial F / \partial r = 0$, which yields:

$$0 = Y \frac{r - r_{\text{T}}}{r_{\text{T}}^2} - \frac{\partial J}{\partial r} \langle \vec{s}_i \cdot \vec{s}_j \rangle \tag{4.49}$$

$$\Leftrightarrow \eta_{\text{mag}} = \frac{r - r_{\text{T}}}{r_{\text{T}}} = \frac{r_{\text{T}}}{Y} \frac{\partial J}{\partial r} \langle \vec{s}_i \cdot \vec{s}_j \rangle = \frac{r_{\text{T}}}{Y} \frac{\partial J}{\partial r} M^2 \cos(\phi) \tag{4.50}$$

This general line of arguments motivates the occurrence of a magnetostrictive strain η_{mag} based on the distance-dependence of the exchange constant J. This contribution is proportional to the sublattice magnetization M^2 regardless of the angle ϕ between neighboring spins. Furthermore, one can use this

energy contribution to derive a magnetic Grüneisen parameter for this interaction similar to the previous work by Pytte[207]:

$$U = F = \langle E \rangle = J(r) M^2 \cos(\phi) \tag{4.51}$$

$$C_\mathrm{V} = \left.\frac{\partial U}{\partial T}\right|_V = 2J\, M \left.\frac{\partial M}{\partial T}\right|_V \tag{4.52}$$

$$\left.\frac{\partial p}{\partial T}\right|_V = \left.\frac{\partial}{\partial T}\right|_V \left(-\left.\frac{\partial F}{\partial V}\right|_T \right) = -\left.\frac{\partial J}{\partial V}\right|_T 2\, M \left.\frac{\partial M}{\partial T}\right|_V \tag{4.53}$$

$$\Rightarrow \Gamma_\mathrm{exchange} = \frac{V}{C_\mathrm{V}} \left.\frac{\partial p}{\partial T}\right|_V = -\frac{V}{J} \left.\frac{\partial J}{\partial V}\right|_T = -\left.\frac{\partial \log J}{\partial \log V}\right|_T \tag{4.54}$$

This shows that the sign of the magnetic Grüneisen parameter is determined by the sign of $-\frac{1}{J}\frac{\partial J}{\partial V}$, so that both the value J and its volume derivative contribute. This derivation considers the mechanism of exchange-striction and yields that the absolute value of the corresponding magnetic stress increases with increasing magnetization and with increasing gradient $\frac{\partial J}{\partial V}$.

A derivation of the Grüneisen parameter from the magneto-crystalline anisotropy energy contribution to the free energy ($F = U = \langle E \rangle - K_\mathrm{u} \cos^2(\theta)$) does not yield a simple term. The corresponding result would be $\Gamma_\mathrm{anisotropy} = -V \left(\frac{\partial^2 K_\mathrm{u}}{\partial T \partial V}\right) \left(\frac{\partial K_\mathrm{u}}{\partial T}\right)^{-1}$ since the anisotropy constant K_u depends both on the volume and the temperature. This term can only be evaluated if further details about the magneto-crystalline anisotropy are known. If, for example, the volume dependence and the temperature dependence in the anisotropy contribution occur as separate factors one would obtain $\Gamma_\mathrm{exchange} = -\left.\frac{\partial \log K_\mathrm{u}}{\partial \log V}\right|_T$, similar to the previous results.

In general, one can conclude that that any contribution to the free energy that depends on the volume of the crystal manifests as a contribution to the thermal expansion (see also review by Doerr and Rotter [208]). The corresponding Grüneisen parameter can be evaluated via:

$$\Gamma = \frac{V}{C_\mathrm{V}} \left.\frac{\partial p}{\partial T}\right|_V = \frac{V}{\left.\frac{\partial U}{\partial T}\right|_V} \left.\frac{\partial}{\partial T}\right|_V \left(-\left.\frac{\partial F}{\partial V}\right|_T \right) \tag{4.55}$$

The previous calculations derive the corresponding Grüneisen parameter for three conceptually simple theoretical models. In the publications article VII, article X and article XI we extract the Grüneisen parameters for the combined electron-phonon system and magnetic excitations from experimental data of the temperature-dependent thermal expansion in order to avoid the (over-)simplifications that allow for the presented analytical treatment of the Grüneisen parameter.

The concept of magnetic Grüneisen parameters and their derivation from the analysis of the near-equilibrium thermal expansion behavior in materials with magnetic order has been established by previous works [209] on various materials such as Europium-Oxide (EuO)[210], $RbMnF_3$ [211] and Holmium[210]. The application of magnetic Grüneisen parameters for the analysis of the corresponding magnetic stress contribution in time-resolved experiments appears to be less established even though the demonstration of ultrafast demagnetization in various materials motivates the occurence of magnetic stresses on (sub-)picosecond timescales.

4.4 Microscopic models and timescales for stress generation

At this point, it is instructive to consider mechanisms that lead to the thermal expansion from different energy reservoirs within the solid in more detail. Thermodynamic considerations are general but do not

yield microscopic insights into the physical processes that cause the strain response. Microscopic models help to intuitively interpret the results of UXRD experiments, because the underlying mechanisms exhibit characteristic time- and length scales that can be distinguished in the spatio-temporal strain response using picosecond-ultrasonics experiments. In this section, I summarize the main microscopic mechanisms for the stress generation in metallic materials and add effects that may arise in the presence of magnetic order. This section is a summary and adaptation of insights from existing literature. A more general overview of the physical mechanisms for strain generation in picosecond ultrasonics experiments is provided by a review of Ruello and Gusev[28]. Stresses that lead to (negative-) thermal expansion in near equilibrium scenarios are discussed in reviews by Barron[191], Barrera et al. [189] and Dove and Fang[212]. The article by Doerr et al. [208] treats magnetostrictive stresses in rare-earth materials. I conclude this section with an overview of the approximate timescales for selected physical processes that occur in laser-excited metals that adapt arguments from a review by Sundaram and Mazur[213] in combination with the timescales for magnetic effects reported in the book on magnetism of Stöhr and Siegmann[214].

4.4.1 Thermoelastic stress from incoherent phonons

One major contribution to the thermal expansion of solid materials in near equilibrium conditions is given by excitation of atomic vibrations. The stress contribution of phonons is sometimes also referred to as thermoelastic stress.[28] However, it is important to acknowledge that the (thermal) population of phonon modes itself does not directly exert a pressure on the lattice if the interatomic potential is completely symmetric around the equilibrium position. An increased vibration amplitude of the atoms contributes to the thermal expansion only if the underlying inter-atomic potential $U(r)$ is asymmetric around the equilibrium position. Asymmetries only occur when contributions of higher order than r^2 are considered in the Taylor expansion of the inter-atomic potential around the potential minimum. These anharmonic contributions are necessary in order to rationalize the finite thermal conductivity of insulators and their thermal expansion as described in text-books on solid state physics.[45, 194]

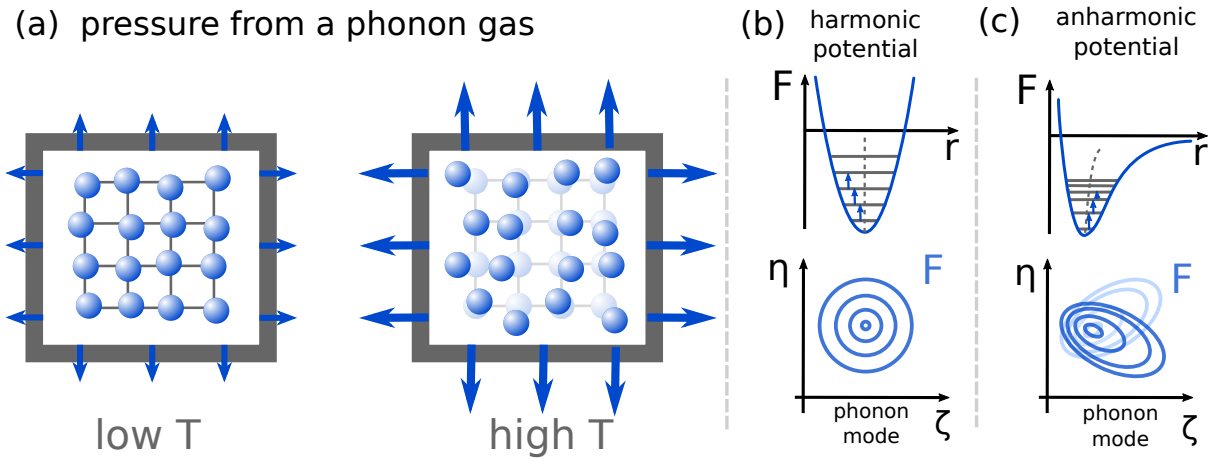

Figure 4.5: Stress generation by incoherent phonons: Panel (a) schematically depicts the motion of atoms around their equilibrium position, that results from a population of different phonon modes. Arrows indicate an expansive stress that results from the anharmonic potential effects. Panel (b) shows the simplified pair-potential of di-atomic molecules to illustrate that an asymmetric potential shape leads to a shift of the equilibrium position (grey dashed line) upon increasing the vibration amplitude. Real solids contain many phonon modes. Panel (c) displays that the strain η changes upon population of an arbitrarily selected phonon mode ξ with different signs of the mode-specific Grüneisen parameter γ_ξ.

Figure 4.5 schematically visualizes the pressure that results from the population of phonon modes. Depending on their k-vector and the dispersion relation, it requires energies on the order of meV to excite phonons in a solid. The vibration amplitudes of the atoms around their equilibrium position are thus smaller at low temperatures where ($T \ll T_{\mathrm{Debye}}$), and larger at high temperatures ($T \geq T_{\mathrm{Debye}}$) as depicted in panel (a). Quantum excitations in a purely harmonic potential do not shift the equilibrium position as opposed to excitations in asymmetric potential shapes as indicated by the grey dashed line in panel (b). The depicted pair potential that describes the vibration of di-atomic molecules is, however, an oversimplified representation for a solid because it only has one degree of freedom. Real solids contain on the order of 10^{23} atoms and phonon modes, where the population of any phonon mode ξ can induce a relative shift of the equilibrium position η. This is acknowledged in panel (c) that shows the projection of the multidimensional free energy F onto the $\eta - \xi$ plane for the different signs that the mode-specific Grüneisen parameters γ_ξ may potentially have.

The thermoelastic expansion mechanism is also relevant on ultrafast timescales, because one important channel for the relaxation of laser-excited electrons to their low temperature ground-state is the transfer of energy and momentum to phonons. The generated phonons originate from stochastic collision processes with electrons, so that an incoherent background of phonons is excited. The pressure on the crystal lattice by the excitation of phonons results from the same anharmonicity that is present for equilibrium thermal expansion experiments.

At this point, it is instructive to consider why longitudinal phonons often have a positive Grüneisen parameter $\gamma_{i,\mathrm{LA}} > 0$ whereas transverse phonons often exhibit a negative Grüneisen parameter $\gamma_{i,\mathrm{TA}} < 0$. This can be rationalized with a classical mechanical picture shown in figure 4.6, which adapts two sketches from the review of Barrera et al. [189]. The so-called bond stretching effect for longitudinal vibrations shown in panel (a) results from the anharmonic shape of the potential that often has a stronger repulsion for $r < r_{\mathrm{eq}}$ in comparison to the attraction that occurs if $r > r_{\mathrm{eq}}$. In this case. one finds that the increase of the vibration amplitude along the bond axis tends to elongate the bond because the net force averaged over one vibration period is repulsive. The excitation of transverse vibrations leads to an elongated distance between neighboring atoms as shown in figure 4.6(b). The distance-dependent potential leads to a net attractive force that shortens the projection along the initial bond axis. An excitation of vibrations transverse to the interatomic bond thus tends to decrease the inter-atomic distance along the direction of the equilibrium bond.

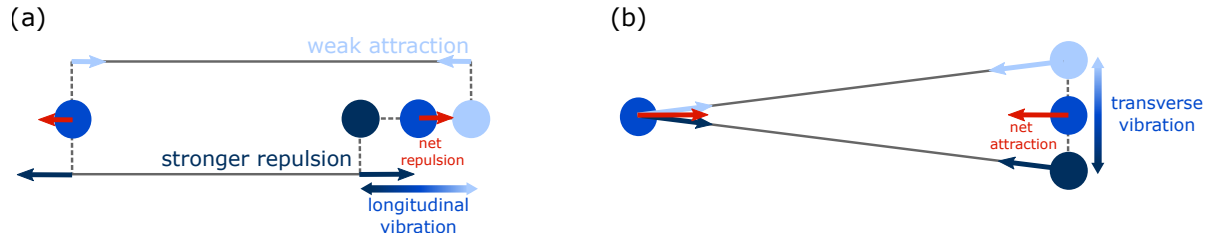

Figure 4.6: Vibration effects: (a) Bond stretching effect of longitudinal acoustic vibrations along the bond. (b) Bond tension effect for vibrations transverse to the bond. Figure adapted from Barrera et al. [189] For description see text.

LA-phonons exhibit a higher energy compared to TA-phonons at the same k-vector, which is reflected in the steeper dispersion relation $\omega(k)$ near the Brillouin zone center where $k \approx 0$. The temperature-dependent change in the relative occupation of these different types of phonon modes thus leads to a temperature dependence in the average Grüneisen parameter of the phonon system:

$$\Gamma_{\mathrm{pho}} = \frac{\Sigma_i C_i \gamma_{i,\mathrm{TA/LA}}}{\Sigma_i C_i} \tag{4.56}$$

The predominant excitation of TA-phonons at low temperatures results in a reduced, sometimes even negative, thermal expansion of many semiconductors such as Si, ZnS, HgTe, CdTe at low temperatures.[191] The related diamond and zincblende structures of these materials facilitate transverse vibrations due to the relatively open structure.[191] For temperatures above half the Debye temperature, Γ_{pho} often becomes positive and nearly temperature independent, since all phonon-modes become populated and thus contribute to the thermal expansion.[190, 215]

It is relevant for the modeling of picosecond ultrasonics experiments to realize that femtosecond laser-excitation in general leads to a non-equilibrium phonon distribution. Recent experiments demonstrate that laser-excited metals may exhibit an athermal phonon distribution over many picoseconds.[79–81] In theory, it is possible to account for the mode-specific contribution of each phonon mode to the thermal expansion[79] but in practice the computational complexity for modeling the time-dependent - mode-specific energy distribution and the resulting stress is very high. Although the transient phonon distribution in the metals may be athermal, it is seldom pathological in the sense that a single mode with an atypically large or small Grüneisen parameter is excited preferentially. This is why the average phonon Grüneisen parameter Γ_{pho} represents a useful approximation also for non-equilibrium situations. In such situations, the total energy density represents a well defined quantity, whereas a phonon temperature cannot be defined due to the lack of a non-thermal phonon population.

4.4.2 Electron stresses

A pressure due to electrons that are delocalized within the solid is an effect that represents a specific feature of metals. The expansion of metals at low temperature shows that a free electron gas contributes an expansive stress that is proportional to the temperature T.[191] This term adds to the ever-present contribution of phonons that usually scales with T^3 in accordance to an increase of phonon mode occupation captured in the Debye model for lattice vibrations at low temperatures. For near-equilibrium thermal expansion processes that are driven by quasi-static heating at temperatures larger than 10 K, one can usually neglect the electronic pressure because its contribution is small in comparison to the contribution by phonons. In non-equilibrium scenarios that occur upon femtosecond laser excitation, the electronic pressure is however not negligible. For example, if one employs fluences on the order of $1\,\mathrm{mJ/cm^2}$ it is, however, common that the electron distribution is driven to a state which corresponds to a temperature of multiple thousands of Kelvin. It is established that the thermalization process from the non-equilibrium laser-excited state to the high temperature Fermi-Dirac distribution generally occurs via electron-electron scattering and electron-phonon scattering processes, but details of the process are subject to ongoing theoretical and experimental research. [80, 82, 84]

Multiple experiments have shown that the hot electron gas in laser-excited metals leads to a significant stress on the lattice.[147, 203, 204, 216] Their contribution is often dominant prior to the energy distribution to phonon excitations that occur via electron-phonon coupling within the first picosecond. In a purely classical picture, one would consider the electrons as gas particles that exert pressure due to collisions with their confinement. This classical picture of non-interacting gas particles in a box is schematically sketched in figure 4.7(a). It is refined, when the electrons are considered to be quantum mechanical particles with a spin of $1/2\,\hbar$, which occupy quantized states in momentum space in accordance to Fermi-Dirac statistics and the boundary conditions of the solid. The resulting Sommerfeld model acknowledges that only the fraction of electrons that occupy states with an energy in the vicinity of $\approx k_{\mathrm{B}}T$ near the Fermi level can undergo changes in momentum due to thermal excitations. However, their absolute momentum is much higher than expected from classical Boltzmann statistics because all lower momentum states are filled due to the Pauli exclusion principle. The thermal excitations of the quantum-mechanical free electron gas is

schematically sketched in figure 4.7 (b), that shows the occupation of states for different temperatures. More details on the Sommerfeld model of a free electron gas are discussed in solid state textbooks [45, chapter 6] and [217, chapters 4 and 15].

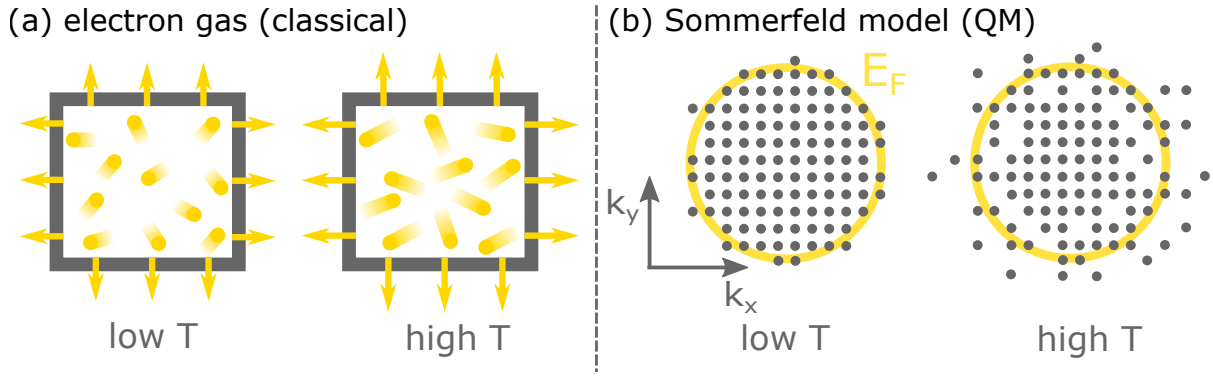

Figure 4.7: Electron pressure: (a) Schematic representation of the pressure that results from an ideal gas of free electrons in a solid. (b) Quantum mechanical representation of a 2D-free electron gas in a Sommerfeld model, where the orange line indicates the Fermi energy and the grey dots indicate occupied electronic states in reciprocal space.

As previously discussed, the corresponding Grüneisen parameter $\Gamma = \frac{\partial p}{\partial U}$ is 2/3 for a free electron gas. Measurements in real solids extract values for the electronic Grüneisen coefficient that range between 1-3.[191, 199] This deviation from the quantum mechanical result for a free electron gas can be attributed in parts to the neglect of the interaction of the electrons with the positive charge of the nuclei. The resulting periodic potential of ions in a crystal leads to the band-structure of electrons, which modifies the density of states near the Fermi level and the effective mass of electrons. Regardless of the level of detail for the electron gas in the solid, one expects an electronic pressure that becomes experimentally accessible in the high non-equilibrium situations between the electron and phonon subsystem upon fs-laser excitation. This electronic pressure is often negligible in near-equilibrium thermal expansion experiments due to the relatively small electronic heat capacity. However, it may dominate the subpicosecond stress generation. It would be interesting to investigate whether metal alloys such as $Fe_{0.64}Ni_{0.36}$ (or tailored alloys of FePt and FePd) that exhibit volume invar behavior upon equilibrium heating[218] would exhibit a strain response upon fs-laser excitation. A short expansive stress could be expected if the electronic pressure is not completely balanced by a contractive magnetic pressure within the first picosecond.

4.4.3 Magnetic stresses

Magnetostriction i.e. the change of the crystal dimensions upon magnetization is one of the most direct interactions between magnetism and the crystal lattice. The hitherto presented thermodynamic arguments motivate the general presence of magnetic stresses but do not provide microscopic insights for the relation between magnetization and lattice strains. Inverse magnetostriction effects that change the magnetization state via changes in the lattice configuration originate from the same mechanism. The following paragraphs discuss exchange striction and anisotropy striction as two major mechanisms that lead to magnetostriction. I provide schematic visuals that may help to develop an intuition of the relevant microscopic effects. It needs to be acknowledged that magnetism i. e. the collective order of the magnetic moments in atoms, is an inherently quantum-mechanical effect according to the Bohr-Van Leeuwen theorem. Purely classical pictures for magnetic effects are thus inherently flawed but may still be useful for more detailed discussions. A theoretical discussion of many aspects of magnetostriction is provided in the book by de Lacheisserie[44], whereas the book by Engdahl[43] provides a phenomenological approach to giant magnetostrictive materials.

Exchange striction

The exchange-striction mechanism originates from the distance-dependence of the magnetic exchange interaction.[206] It is sometimes referred to as two-ion contribution to magnetostriction.[219] Two-ion contributions may result from a distance-dependence of the dipolar interaction, pseudo-dipolar and exchange interaction.[219] Among them, the exchange interaction usually contributes the largest effect. It is captured by a distance-dependent exchange coupling parameter $J_{ij}(r)$ in a Heisenberg Hamiltonian of the form: $H_{\mathrm{ex}} = -\sum_{\mathrm{i,j}} J_{ij}\vec{s}_i \cdot \vec{s}_j$. The resulting energy modifies the total free energy of the system and shifts the equilibrium distance upon magnetic order in any magnetic material.

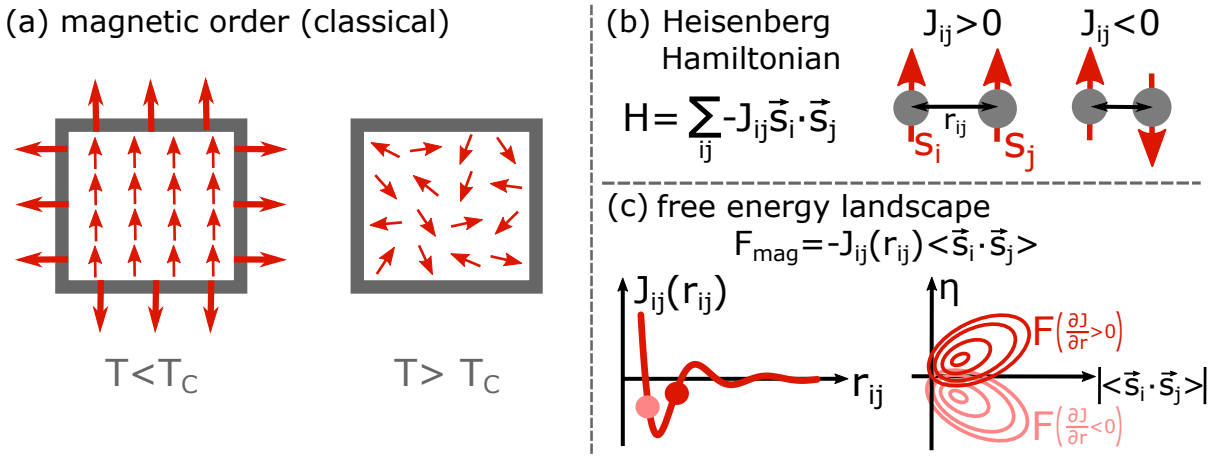

Figure 4.8: Schematic sketch of exchange striction: (a) classical representation of aligned magnetic moments at low temperatures that correspond to a magnetization that vanishes at high temperatures where $T > T_{\mathrm{C}}$. The appearance of the magnetic order can be rationalized using a Heisenberg model in the Hamiltonian, where the sign of the exchange constant J_{ij} determines the preferential alignment of the spin moments as depicted in (b). Panel (c) schematically shows the distance dependence of the indirect RKKY-interaction mechanism that is dominant for rare-earth materials. The sign of the derivative $\partial J/\partial r$ determines the sign of the magnetic strain that results from change in the total free energy upon the appearance of magnetic order ($<\vec{s}_i \cdot \vec{s}_j> \propto M^2 \cos\phi \neq 0$).

Figure 4.8 is an attempt to schematically visualize the exchange striction effect. Panel (a) depicts a magnetic stress that occurs only when the temperature is below the magnetic ordering temperature $T < T_{\mathrm{C}}$. Quantum mechanical models often rationalize the occurrence of magnetic order by introducing a Heisenberg Hamiltonian that captures the interaction between individual magnetic moments $\vec{s}_i$. The exchange constant determines the relative orientation of the magnetic moments in the solid as indicated in panel (b). The distance-dependence of $J_{\mathrm{ij}}(r)$ leads to a shift of the minimum of the total free energy upon the occurrence of magnetic order $<\vec{s}_i \cdot \vec{s}_j> = M^2 \cos\phi$, where M corresponds to the (sublattice) magnetization and ϕ to the angle between neighboring spins. The sign of the magnetostrictive strain thus depends on the derivative $\frac{\partial J}{\partial r}$ if the relative orientation ϕ remains fixed. The resulting contribution to the free energy is sketched in panel (c).

It is relevant to note that the exchange striction effect is present regardless of the type of magnetic order, also in absence of a net angular momentum $L = 0$ or for non-collinear spin orientations. The mathematical shape of the distance dependence in $J(r)$ depends on the type of magnetic interaction and varies between direct and indirect exchange interaction mechanisms. An introduction of the different types exchange interaction is provided for example in the book of Blundell [chapter 4][46] and Coey [chapter 5.2][220] The current visualization depicts the oscillatory distance dependence of the indirect RKKY-interaction of localized magnetic moments via the spin-polarization of conduction band electrons. It is the dominant mechanism in the heavy rare-earth metals that are discussed in chapter 6. The temperature-dependent magnetostriction is very similar for all heavy rare earth elements including Gadolinium that exhibits no net

angular momentum. This indicates that exchange-striction is the dominant magnetostriction mechanism for this class of materials as opposed to the anisotropy striction that requires anisotropic electronic orbitals with $L \neq 0$.

Anisotropy striction

The magnetostriction effects that result from spin-orbit interaction is often called anisotropy-striction, Joule-striction, crystal field striction[208] or referred to as single-ion mechanism[219, 221]. It arises when an anisotropic charge distribution couples to the spin orientation as schematically depicted in figure 4.9. This figure shows that the orientation of the magnetization determines the relative orientation of the anisotropic electronic orbitals, which in turn changes the interatomic distances.

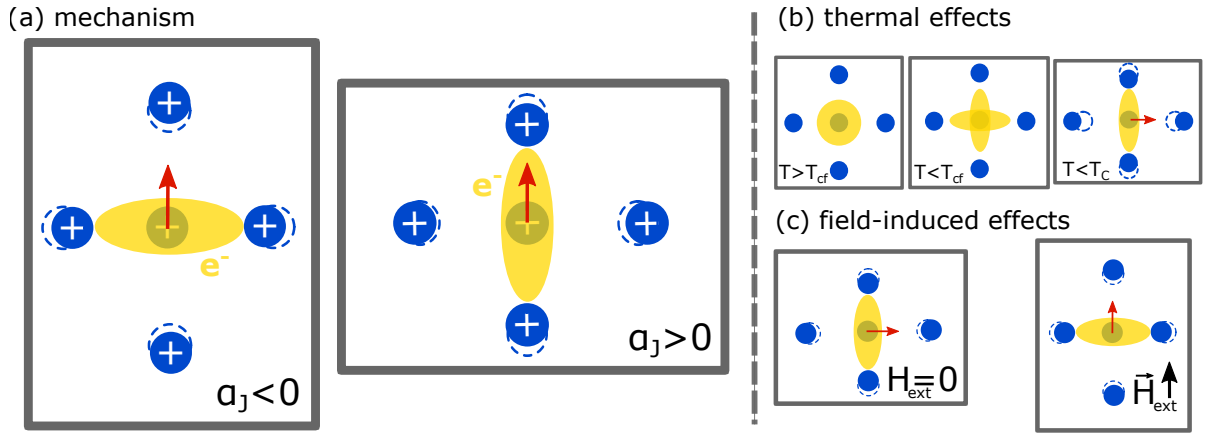

Figure 4.9: Schematic sketch of anisotropy striction: This mechanism is based on anisotropic electron orbitals that exhibit a preferential orientation with respect to the magnetic moment of the atom due to spin-orbit coupling. Different alignments of spin moments lead to different orientations of the orbital with respect to the crystal field. The crystal field is a model that subsumes the interactions of the valence electrons with other charges within the solid, which determines the binding distances between the atoms. This figure is adapted from similar representations in [208] and [43, chapter 1]

.

One important ingredient for the interaction between the magnetic order and the crystal lattice via anisotropy striction is the spin-orbit coupling. In an abstract way, the spin-orbit interaction is an additional term in the Hamiltonian that is proportional to the scalar product of the orbital angular momentum L and the spin s.

$$H_{\mathrm{SO}} = \lambda_{\mathrm{SO}} \vec{L} \cdot \vec{S} \tag{4.57}$$

Depending on the proportionality constant λ_{SO} that describes the material-specific strength of the spin-orbit interaction, it is energetically favorable for the spin and angular magnetic moments either to align or anti-align.

Figuratively speaking, the spin-orbit coupling arises because the electronic magnetic moments experience a magnetic field in its rest-frame that originates from the motion of the nucleus around it. This leads to a preferential orientation of spin magnetic moment with respect to the electronic distribution (electronic orbit). As such, spin-orbit coupling is responsible for the existence of the crystal anisotropy that leads to the preferential alignment of the magnetization along certain high-symmetry directions of magnetic materials.[208] The spin-orbit interaction strength is in general larger for heavy elements and is expected to induce an energy splitting between different orbital momentum states proportional to Z^4 in hydrogen-like atoms.[46, Appendix c].

By rotating the magnetization (spin-orientation), the anisotropic electron distribution (electron orbit)

rotates with it due to the spin-orbit interaction. This leads to a repulsion of the adjacent, positively charged ions along the direction where the electronic charge density decreases and an attraction of the ions along the directions where the electronic charge density increases. This effect is in general volume conserving.[222]

As briefly discussed at the end of section 4.3.4, it is not a priory clear that the contribution to the free energy of this mechanism can be formulated such that a magnetic Grüneisen parameter can be associated with it. I nevertheless discuss it because it provides the main mechanism for the giant room temperature magnetostriction in rare-earth intermetallic alloys such as $TbFe_2$ [43, 223] that was studied in article III.

4.4.4 Relevant timescales for microscopic processes

One motivation for time-resolved investigations is their ability to provide access to signatures of transient states within matter that arise when the latter is subjected to a time-dependent external stimulus. The transient non-equilibrium states that occur between the initial and final state of the investigated sample often provide insights into the mechanism that may help to manipulate the outcome in laser-based experiments by tailoring the employed excitation (wavelength, pulse duration, pulse energy, chirp), external parameters (temperature, applied fields, pressure, strain) or investigated material (composition, thickness, growth method, substrate).

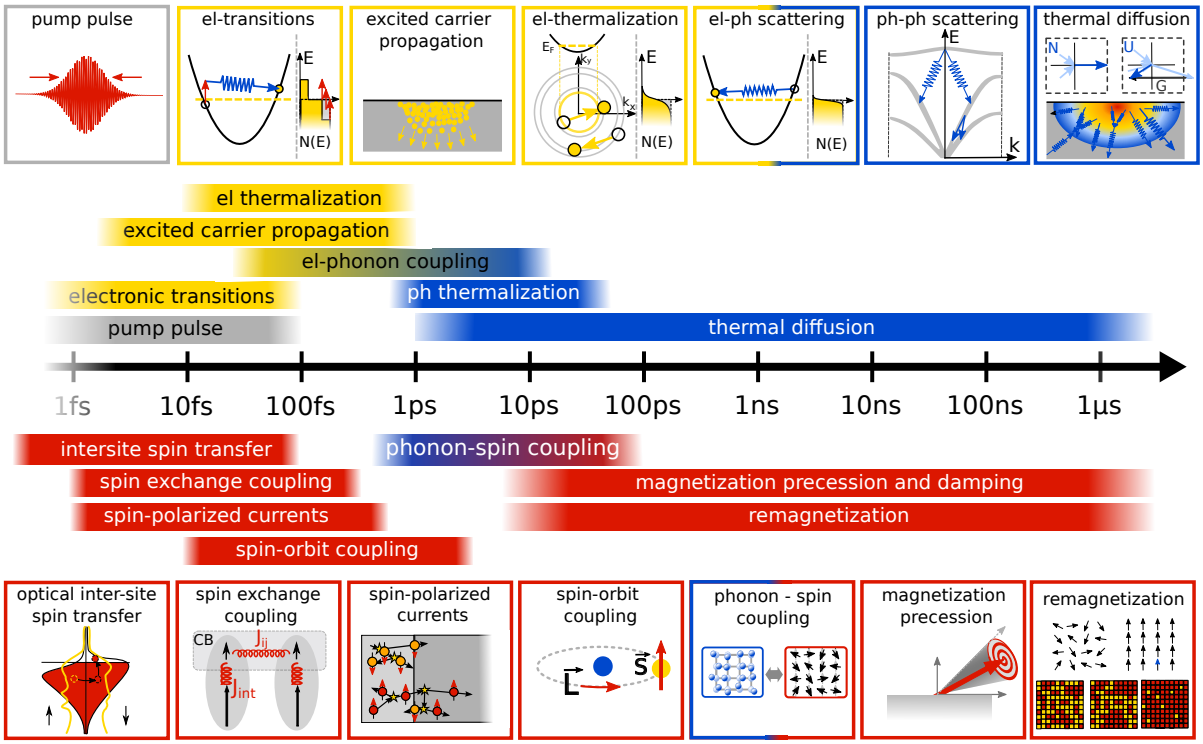

Figure 4.10: Approximate timeline in a picosecond ultrasonics experiment This schematic presents the approximate timescales of selected processes in laser-excited metals. It adapts ideas from a review article on laser-excited semiconductors by Sundaram and Mazur[213] and the timescales presented in a review on ultrafast magnetization dynamics by Bigot and Vomir[30] and the book of Stöhr and Siegmann[214] supplemented by the recently reported optical intersite spin transfer in magnetic heterostructures[93]. The top part represents general effects in laser-excited metals, whereas the bottom part requires the presence of magnetic order. The provided timescales represent an order of magnitude estimation that may be refined depending on the specific materials. This depiction is designed to illustrate that time-resolved experiments can separate and identify physical effects based on their timescales, which span multiple orders of magnitude.

Figure 4.10 provides a schematic timeline of a selection of important processes that occur in laser-excited metals. While the top part of the time-line shows processes that occur in all metals, the bottom part exhibits processes and timescales that occur in samples with magnetic order. Electron excitations couple to phonons and magnetic excitations already within the first picosecond after laser-excitation. The shown selection of physical effects spans multiple orders of magnitude in time and a thorough discussion of this schematic remains beyond the scope of this work. The figure however illustrates the need for experiments with sub-picosecond time-resolution. Models that attempt to rationalize the picosecond strain response in metals with magnetic order thus need to account for the sub-system specific stress contributions that may vary on the indicated timescales in response to the listed effects.

4.4.5 Combined stress contributions to the laser-driven strain response

It is by now clear that the strain response results from the combination of stresses that act on the crystal lattice and subsystem-specific Grüneisen parameters have been introduced to model individual contributions. A graphical visualization of the approach is provided in figure 4.11, which schematically combines the sub-system specific stresses from electronic excitations, phonons and magnetic excitations. This depiction contains the main idea that is used for the modeling of the strain response in all articles that are related to the stress generation in rare-earth metals.

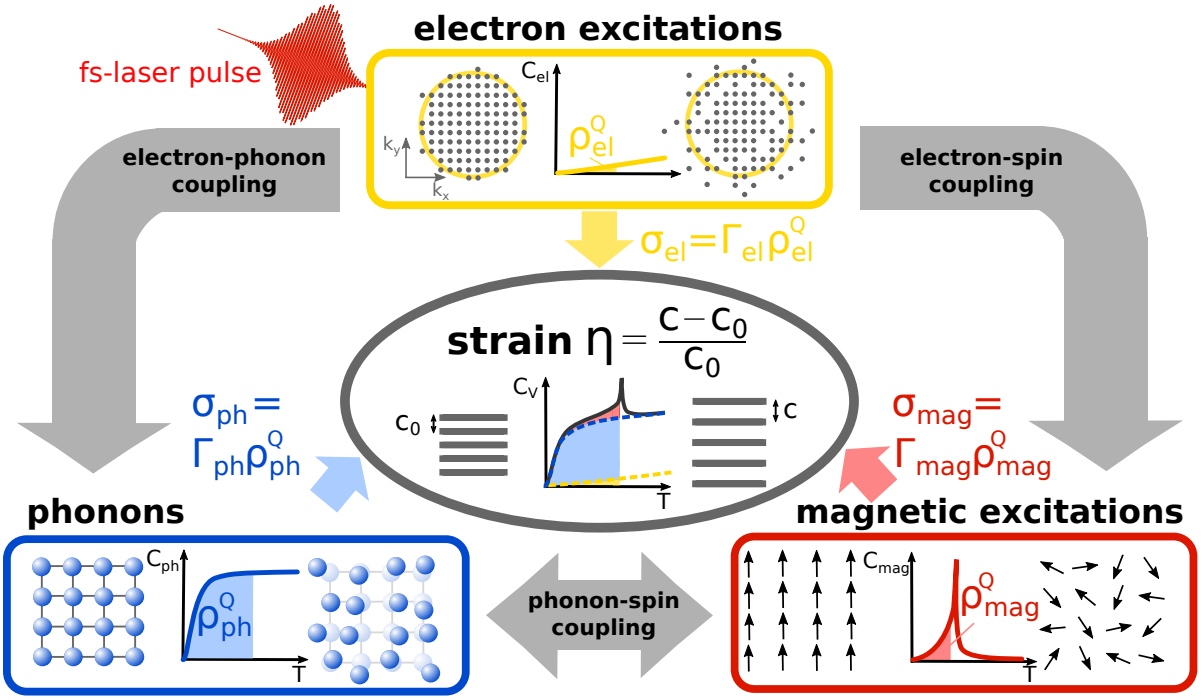

Figure 4.11: Subsystem-specific stress contributions to the lattice strain: The femtosecond laser pulse creates excited electron states and thus deposits energy density in the metal. The subsequent energy flow between the coupled excitations leads to a time-dependent stress $\sigma(t,z)$ that results from the different Grüneisen parameters of each subsystem. The crystal lattice responds to the stress with a spatio-temporal strain $\eta(t,z)$ that leads to the shift and change of shape in the diffraction peaks observed in the UXRD experiment. The observed strain response thus contains signatures of the energy transfer in time and space within the subsystems of the sample structure. Each colored box represents the microscopic excitations and their equilibrium energy density that are present within the solid as previously discussed.

The figure motivates that the total stress σ_{tot} becomes time-dependent as the coupled subsystems within the solid starts exchanging energy to regain their initial equilibrium state. The total stress varies not only

due to (thermal) diffusion processes within the sample but also in response to energy transfer processes between subsystems with different Grüneisen parameters. One important aspect is that it conceptually separates the relative change of the lattice constant (η) from the energy density stored in phonons that describe the excitation of vibration modes around the equilibrium position. The concept of a lattice temperature and a phonon temperature should be distinguished with care because the strain response of the lattice and the occupation of the phonon modes is only one contribution to the strain response.

Figure 4.11 encodes that the laser-induced external stress in a generic picosecond experiment may exhibit the following contributions:

$$\sigma_{\mathrm{ext}}(t,z) = \sigma_{\mathrm{el}}(t,z) + \sigma_{\mathrm{ph}}(t,z) + \sigma_{\mathrm{mag}}(t,z) \tag{4.58}$$

$$= \Gamma_{\mathrm{el}}\rho^{\mathrm{Q}}_{\mathrm{el}}(t,z) + \Gamma_{\mathrm{pho}}\rho^{\mathrm{Q}}_{\mathrm{pho}}(t,z) + \Gamma_{\mathrm{mag}}\rho^{\mathrm{Q}}_{\mathrm{mag}}(t,z). \tag{4.59}$$

The number of required subsystems in this modeling approach varies depending on the peculiarities of the studied materials. Each subsystem r yields a stress contribution σ_r given by $\sigma_{\mathrm{r}} = \Gamma_{\mathrm{r}}\rho^{\mathrm{Q}}_{\mathrm{r}}$, where Γ_{r} is the subsystem-specific Grüneisen parameter and $\rho^{\mathrm{Q}}_{\mathrm{r}}$ is the energy density in that system. The second relation that is required to be fulfilled is given by the energy conservation. Locally this leads to the relation:

$$\rho^{\mathrm{Q}}_{\mathrm{tot}}(t,z) = \rho^{\mathrm{Q}}_{\mathrm{el}}(t,z) + \rho^{\mathrm{Q}}_{\mathrm{pho}}(t,z) + \rho^{\mathrm{Q}}_{\mathrm{mag}}(t,z) \tag{4.60}$$

The deposited laser energy density $\rho^{\mathrm{Q}}_{\mathrm{tot}}$ can sometimes be calibrated in the high temperature paramagnetic phase of the transducer, where the strain response is driven exclusively via electron and phonon stresses.

The implementation of a time-dependent stress based on subsystem-specific Grüneisen parameters still requires a model for the flow of energy between the subsystems. Depending on the electronic bandstructure, phonon dispersion relation and magnetic excitations and the required level of details, this remains a challenge for theoretical approaches. For a given Grüneisen parameter, one can however often develop a self-consistent analysis using a model that yields a strain response in agreement with the observed data. The time-constants and amplitudes of the energy transfer can be taken as fitting parameters. This rather phenomenological approach is frequently employed to identify signatures of different contributions in time-resolved experiments.[224–226] One advantage of the application of Grüneisen parameters to model the stress contributions is that it does not require the thermalization of the sub-systems, that is implicitly assumed by the application of two, three or N-temperature models that are common for modeling stresses in laser-excited materials. Approaches using the Grüneisen parameter to approximate the stress on the lattice can thus work in situations where the energy density represents a well-defined quantity, although the energy distribution may be non-thermal among the subsystems or even within the subsystems.

4.4.6 Grüneisen concept in real solids: Refinements and limitations

It was already indicated at the beginning of this section that the concept of the Grüneisen parameter needs to be modified, when the anisotropic thermal expansion response of thin films on a substrate is considered. For further reference and possible improvements I list the limitations of the presented Grüneisen analysis, that remains work in progress.

Grüneisen concept in anisotropic materials

It is important to acknowledge that real solids are in general anisotropic, so that the volume thermal expansion coefficient β needs to be replaced by direction-dependent linear thermal expansion coefficients $\alpha_{\mathrm{i}} = \frac{1}{x_{\mathrm{i}}}\partial x_i/\partial T$.

If the in-plane thermal expansions $\alpha_\parallel$ and the out-of-plane thermal expansion $\alpha_\perp$ are known one can obtain the thermal expansion at any angle ψ relative to the out-of-plane direction. This is captured by the so called Voigt-relation for the thermal expansion of crystals[199]:

$$\alpha_\psi = \alpha_\perp \cos^2\psi + \alpha_\parallel \sin^2\psi \tag{4.61}$$

where $\alpha_\perp = \alpha_3$ for $\psi = 0°$ and $\alpha_\parallel = \alpha_1$ for $\psi = 90°$. Equation 4.61 illustrates that the thermal expansion in cubic crystals where $\alpha_\parallel = \alpha_\perp$ is isotropic. For such isotropic materials we have $\beta = 3\alpha$ and the macroscopic Grüneisen coefficient is defined as:

$$\Gamma = \frac{1}{\kappa_\mathrm{T}}\frac{3\alpha}{C_\mathrm{V}} = \frac{1}{\kappa_\mathrm{s}}\frac{3\alpha}{C_\mathrm{p}}. \tag{4.62}$$

wherein $\kappa_\mathrm{T} = -\frac{1}{V}\left.\frac{\partial V}{\partial p}\right|_T$ and $\kappa_\mathrm{s} = -\frac{1}{V}\left.\frac{\partial V}{\partial p}\right|_S$ are the isothermal and adiabatic compressibilities, α is the linear thermal expansion coefficient and $C_\mathrm{p} = \frac{1}{V}\left.\frac{\partial U}{\partial T}\right|_p$ is the heat capacity per volume at constant pressure.

Since both the thermal stresses as well as the elasticity are anisotropic in non-cubic materials[189] also the Grüneisen parameters will be anisotropic. This requires an extension of the previous discussion so that it can be applied to the tetragonal and hexagonal materials FePt and Dy, that are investigated in this thesis. Directional Grüneisen constants can be introduced, by replacing the bulk-modulus $K = \frac{1}{\kappa} = \frac{c_{1111}+2c_{1122}}{3}$ with the appropriate directional elastic constants[1] c_{iijj}:

$$\Gamma_\parallel = \frac{(c_{1111}+c_{1122})\alpha_\parallel + (c_{1133}\alpha_\perp)}{C_\mathrm{p}} \tag{4.63}$$

$$\Gamma_\perp = \frac{c_{3333}\alpha_\perp + (2c_{1133}\alpha_\parallel)}{C_\mathrm{p}} \tag{4.64}$$

These formulas are taken from the work of Barron [191, 228], White[227] and coworkers. A more detailed discussion of Grüneisen parameters in anisotropic materials is provided in the Master thesis of my colleague Maximilian Mattern[229] and not repeated here.

One additional result of article VI, which is also described in[229] is that one needs to take care to account for the Poisson effect when using the quasi-static thermal expansion response in order to extract the Grüneisen parameter. For the example of the near equilibrium thermal expansion of a thin film with tetragonal or hexagonal symmetry, one finds that the out-of-plane stress is modified by a Poisson contribution that arises from the in-plane expansion according to:

$$\sigma_{33} = \underbrace{c_{3333}\alpha_\perp \Delta T}_{=\sigma_\mathrm{ext}} - \underbrace{c_{1133}(2\alpha_\parallel \Delta T)}_{=\sigma_\mathrm{Poisson}} \tag{4.65}$$

The quasi-static situation is therefore different from the ultrafast expansion because it permits an in-plane expansion of the thin films. The contribution by the in-plane expansion needs to be accounted for when extracting Grüneisen parameters that are applied on ultrafast timescales. Our recent study on a metallic perovskite thin film exemplifies the extraction of anisotropic Grüneisen parameters from the equilibrium thermal expansion in more detail.[230]

Limitations of the Grüneisen concept

The following list compiles the limitations and approximations that indicate directions for further improvement and research on the application of the Grüneisen concept on ultrafast timescales.

[1] In discussed measurements on hexagonally closed packed Dy and the tetragonal $L1_0$ phase of FePt, the c-axis points out-of-plane. The notation for the out-of-plane ($\perp$) and in-plane ($\parallel$) direction is therefore reversed in comparison to the publications by Barron[191] and White[227] in order to be consistent with the nomenclature that is common in thin film research

- The Grüneisen coefficient is only truly independent of temperature when all modes of a subsystem have the same Grüneisen coefficient so that their temperature dependent relative occupation does not matter. In general, one needs to consider mode-specific populations especially at temperatures significantly below the Debye temperature of phonons. The effective macroscopic constant Grüneisen parameter thus represents an approximation.
- The current model does not provide microscopic details on the electronic pressure in any detail that goes beyond distinguishing energy densities in each subsystem. As the electron system thermalizes subsequently to the laser-excitation by electron-electron scattering processes its state changes from few highly excited electrons directly after excitation to many electrons with lower excitation energy. The negligence of the non-thermal state of the electron subsystem is a common shortfall also for the frequently used two-temperature model. It is impossible to address it without a microscopic model. The mode specific pressure of excited electrons is especially important in semiconductors and insulators where above-bandgap excitations exist for an extended time-period before recombination. The resulting electronic pressure from interband-excitations is referred to as deformation potential mechanism[28], which is not included in the previous discussion.
- Mechanisms for the stress generation in solids that are based on the generation of external (electric-) fields or mechanisms that create internal fields are not captured by a Grüneisen parameter. Such situations may occur for the excitation of ionic crystals using THz pulses, or by the occurrence of inverse piezoelectricity effects in general. Changes of internal fields may be created by the Photo-Dember effect in semiconductors or depolarization field screening in ferroelectrics. Such effects have been described in the general article by Ruello and Gusev[28] but they are not considered in this work, since metals do not sustain a long-lasting charge separation.
- In general, it is an open question to what extend thermodynamic arguments need to be modified to describe the (sub)-picosecond evolution of the subsystem evolution. At this point, the Grüneisen model is put forward because it provides a first order approach that allows discussing the strain response upon energy transfer to multiple reservoirs, which circumvents the explicit usage of temperatures.

4.5 Modeling the picosecond strain response

The previous analysis provides equations and a microscopic intuition for the stress generation upon femtosecond laser-excitation. In this section, I briefly explain and illustrate how the stress translates into a strain response using a linear chain model of masses and springs. Variations of the here discussed approach have been used to model the strain response in almost all publications that are part of this thesis.

The importance for the modeling of the strain response from a given stress profile arises from the possibility of a comparison between the simulated average strain of a layer and the experimentally observed Bragg peak shift. The result may either yield sufficient agreement, or, in case of deviations, stimulate more advanced modeling and/or refined measurement approaches. This empirical approach is also used to yield insights into the energy transfer processes between electrons and phonons or even magnetic excitations in laser-excited transducers. Validated models can also be used as a tool to predict the result for situations where systematic experimental studies would be too time consuming or even impossible due to constraints such as a limited photon flux or the lack of crystalline order. Systematic parameter variations on the stress generation profile such as conducted in the supplementary of article VII help to develop an intuition for the analysis of experimental strain response.

4.5.1 General modeling approach based on the elastic wave equation

As introduced in chapter 1, one can approximate the strain response in a solid using the inhomogeneous elastic wave-equation. In the following analysis, I drop all directional indexes because the strain response is taken to be one-dimensional. For this case, the elastic wave equation simplifies to:

$$\rho\frac{\partial^2 u}{\partial t^2} - c\frac{\partial^2 u}{\partial z^2} = -\frac{\partial \sigma_{\mathrm{ext}}}{\partial z} \quad \Big| \, \eta = \frac{\partial u}{\partial z} \tag{4.66}$$

$$\Leftrightarrow \quad \rho\frac{\partial^2 u}{\partial t^2} = -\frac{\partial \sigma_{\mathrm{ext}}}{\partial z} + c\frac{\partial \eta}{\partial z} \tag{4.67}$$

$$\Rightarrow \rho\frac{\partial^2 u}{\partial t^2} = -\frac{\partial \sigma_{\mathrm{tot}}(t,z)}{\partial z} \tag{4.68}$$

$$\text{where} \;\; \sigma_{\mathrm{tot}}(t,z) = \sigma_{\mathrm{ext}}(t,z) + \sigma_{\mathrm{elastic}}(t,z) \tag{4.69}$$

$$\text{i.e.} \; \sigma_{\mathrm{tot}}(t,z) = \left(\Gamma_{\mathrm{el}}\rho^{\mathrm{Q}}_{\mathrm{el}}(t,z) + \Gamma_{\mathrm{pho}}\rho^{\mathrm{Q}}_{\mathrm{pho}}(t,z) + \Gamma_{\mathrm{mag}}\rho^{\mathrm{Q}}_{\mathrm{mag}}(t,z)\right) - c\eta(t,z) \tag{4.70}$$

Equation 4.68 shows that gradients in the total stress accelerate the displacement of atoms $u(t,z)$. The total stress $\sigma_{\mathrm{tot}}(t,z)$ has two contributions that are labeled external stress $\sigma_{\mathrm{ext}}(t,z)$ and elastic stress $\sigma_{\mathrm{elastic}}(t,z)$. The sign of $\sigma_{\mathrm{ext}}(t,z)$ is chosen such that a positive external stress leads to an expansion ($\eta > 0$). The external stress arises from the laser-induced increase of energy densities within the quantum excitations and the elastic stress from the local strain response. Both contributions balance each other in equilibrium. Different approaches for the solution of the inhomogeneous elastic wave equation for a given $\sigma_{\mathrm{ext}}(t,z)$ exist. Analytical solutions for the strain field can be constructed for time-independent stress profiles as shown in [27, 52, 67]. Numerical approaches[63] may be easier to implement, when the time-dependence of the stress by sub-system couplings, thermal diffusion and interface effects need to be accounted for.

4.5.2 Numerical solutions using a linear masses and springs model

Numerical approaches for the solution of (partial-) differential equations require a discretization of the problem. A natural spatial grid in the simulation of the strain response of thin films is provided by the layers of atoms. Atomically resolved simulations represent the smallest physically meaningful discretization of the strain response. Linear chain models of masses and springs provide one approach for the numerical calculation of the strain field ($\eta(t,z)$) with unit-cell precision.[62]

In the presented articles, I frequently employ the implementation of a linear chain model of masses and springs that is provided by the modular UDKM1DSIM MATLAB library, which is documented in a publication by Schick et al. [63]. In this section, I briefly mention the underlying simulation steps that are listed in figure 4.12.

The UDKM1DSIM code inherently uses N-temperature models to calculate the spatio-temporal energy flow and employs thermal expansion coefficients to calculate the resulting stresses. In the simulation of the magnetic stresses, we often introduce user-defined procedures that implement magnetic and electronic stresses based on the previously presented Grüneisen approach using phenomenological time-scales or previously determined coupling constants. A detailed description of such a procedure is given in the supplementary material of article VII. The supplementary also includes the mathematical formulas that are used in the modeling, which are not repeated here.

While the first three steps are mandatory to obtain a strain response, the last step is necessary for a direct

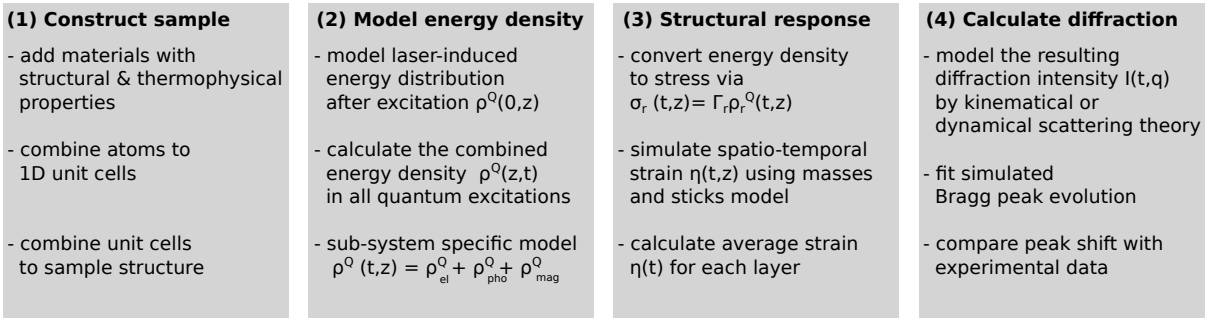

Figure 4.12: Steps in the simulation of a strain response: This schematic lists selected conceptual steps that are necessary for the modeling of diffraction signals, based on the time-dependent strain response. The numbered grey boxes indicate the subsequent usage of different classes provided by the UDKM1DSIM library.[63]

comparison to the diffraction peak shift that is accessible by the UXRD-experiments. I have observed that the center of mass evolution extracted from the diffraction peak shift and the underlying, layer-averaged strain are often very similar. This impression is based on multiple simulation scenarios that were carried out for the different samples studied in this thesis. The layer-averaged strain that is obtained at the end of simulation step three may thus be sufficient when features of the strain response in laser excited thin films are discussed on a qualitative level. Scenarios where picosecond strain pulses occur that are much shorter than the thickness of the detection layer need to be treated with care. Previous work has shown that fitting the peak position by a Gaussian function does not yield the average strain but rather the strain that occurs within the majority of the thin film.[53] The center of mass analysis is a much more robust proxy for the average strain, because it also takes into account that shoulders on the Bragg peak occur in the presence of coherent strain pulses within the layer[11, 53]. Systematic investigations of the strain from the center of mass evolution and the simulated average strain within a layer may provide further insight into the sensitivity function of the X-ray diffraction technique. This would extend previous work carried out at synchrotron facilities on nanosecond thermal transport[231] and extend it to the observation of hypersound waves containing frequencies on the order of hundreds of GHz. In that context, it would be interesting to observe (sub)-picosecond strain pulses generated by transducers that are thinner than $\approx 5\,\text{nm}$. For such cases, I find that simulations predict a difference of the average strain in a 100 nm thick detection layer from the center of mass evolution of the peak shift. For the experiments presented in this thesis, I find that a center of mass evolution of the modeled Bragg peak reflects the average strain in the layer sufficiently.

4.5.3 Strain response visualization for common stress scenarios

I finish this section with a visualization that contains a mechanical representation of the simulation approach, the contributing terms in the elastic response can be identified. In addition, I discuss typical results of the strain modeling for a generic laser-excited transducer scenario.

Linear masses and springs models represent an approach that is frequently employed for the simulation of crystal lattice dynamics in solid state physics. In this framework, crystals are modeled as equally spaced masses, which are connected via springs that represent the inter-atomic potential. Simple forms of this model are used in basic solid state physics lectures to derive the dispersion relation of phonons.[45, chapter 4] If one introduces non-linear force constants (i. e. anharmonic potentials) between the atoms, one arrives at variations of the so called Fermi-Pasta-Ulam-Tsingou model[2].[233] The nonlinearity in

[2]Research on the scientific history of this model indicates that the contribution of Mary Tsingou, who implemented the model in 1955 on one of the first existing computers, should be acknowledged.[232].

the interatomic potential allows for energy transfer between different phonon modes and, under special circumstances, also for the appearance of solitary phonon waves (solitons).[67, 234] Nonlinear phononics and research on chaotic systems in computer experiments use this model to great extent[67, 235], but such effects are neither discussed nor taken into account here.

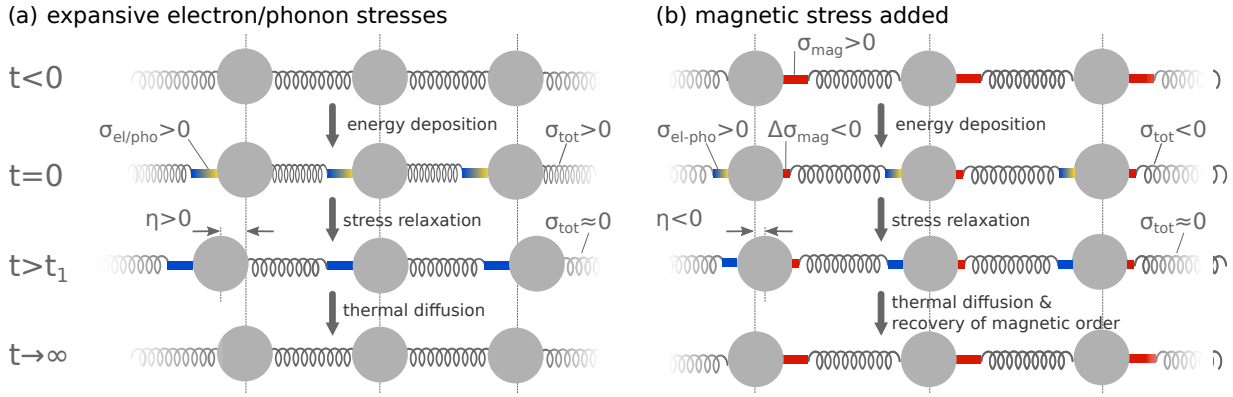

Figure 4.13: Schematic lattice response in a linear masses and springs model: Panel (a) depicts the lattice response to expansive laser-induced stresses at selected times similar to the previous work in our group.[62] The insertion of yellow/blue sticks represents the laser-induced pressure increase by electron excitations and phonons. The inserted sticks represent the external stress (σ_{ext}), the elastic stress ($\sigma_{\mathrm{elastic}} = -c\eta$) can be seen implicitly by the displacement of the atoms. The resulting total stress ($\sigma_{\mathrm{tot}} = \sigma_{\mathrm{ext}} + \sigma_{\mathrm{elastic}}$) is indicated qualitatively by the elongation and compression of the spring relative to its initial state. This model can be extended to capture contractive magnetostrictive stresses via the partial removal of red sticks as shown in (b). The laser excitation in this scenario can lead to positive or negative strain depending on the balance of laser-induced magnetic and electron/phonon stresses.

In the framework of such a linear chain of masses and springs model one can picture the effect of the laser-induced sub-system-specific stresses $\sigma_{\mathrm{r}}(t,z)$ by rigid spacer sticks that are inserted into the bindings between atoms upon excitation. This approach has been established for the stress generation of electron and phonon excitations with positive Grüneisen constants.[62, 63] A natural extension of this concept for energy reservoirs with a negative Grüneisen constant is the removal of existing repulsive spacer sticks upon laser excitation. This results in a balance of contractive and expansive stresses within the solid. Panels (a) and (b) in figure 4.13 display these two scenarios using the established schematic representation of a linear chain model. This mechanical representation of the masses and sticks model has been established by previous works of our group[62, 63]. Chapter 2 in the PhD thesis of Marc Herzog contains a discussion of its main features and plots the resulting strain $\eta(t,z)$ and its layer average for different, generic transducer scenarios.[236] In the following overview, I add the occurring spatio-temporal stresses ($\sigma_{\mathrm{ext}}, \sigma_{\mathrm{elastic}}, \sigma_{\mathrm{tot}}$) and the displacement field $u(t,z)$, to make a direct connection to the continuum model approach stated in equation 4.68, which is useful for analytic discussions.

Figure 4.13(a) shows that the atoms exhibit an equilibrium lattice constant c_0 that originates from the inter-atomic potential, which is represented by springs at $t < 0$. The laser-deposition of additional energy-density into the metallic transducer at $t = 0$ leads to additional "external" stresses that can be described via Grüneisen parameters. In this figure, I assume for simplicity that electrons and phonons share the same, positive Grüneisen parameter ($\Gamma_{\mathrm{el}} = \Gamma_{\mathrm{pho}} > 0$). The length of each spacer stick then corresponds to:

$$l_{\mathrm{stick}} = c_0\eta(t > T_1) = c_0\frac{\sigma_{\mathrm{ext}}}{c_{3333}} = c_0\frac{\Gamma_{\mathrm{el}}\rho^Q_{\mathrm{el}} + \Gamma_{\mathrm{pho}}\rho^Q_{\mathrm{pho}}}{c_{3333}} \tag{4.71}$$

wherein c_{3333} represents the out-of-plane elastic constant, σ_{ext} the external stress and $\eta(t > t_1)$ the strain that is attained after coherent strain pulses have left the sample. The length of the inserted sticks and the

resulting displacement are largely exaggerated for visualization purposes since the resulting laser-induced strains in solids (η) correspond to variations of the lattice constant on the order of only 1% or less. The depiction however shows that the insertion of the sticks compresses the springs, which signifies the total stress (σ_{tot}) on the atoms. The stress is released by atomic displacements that start at stress gradients and propagate as coherent strain pulses through the layers. It takes the time $t_1 = v_{\mathrm{sound}}/d_1$ for the strain wave to propagate through the transducer layer. The strain wave propagation between $t = 0$ and $t > t_1$ will be discussed in more detail at the end of this section. After the strain pulses have left the layer at $t > t_1$ one finds that the atoms are displaced by the length of the inserted stick and the spring is in its relaxed state, as the atoms have now been shifted to the new, transient equilibrium position. This is somewhat simplified because the figure represents only a fraction of a laser-excited solid and the total displacement of each atom represents the cumulative strain response as shown in figure 4.14 and 4.15. Thermal diffusion processes subsequently transport energy density out of the material, which leads to the removal of the external stress and the atoms recover their initial distance for large times that are indicated as $t \to \infty$. In this depiction, we find that the inserted sticks represent the external stress (σ_{ext}) and the compression or expansion of the springs signifies the total stress (σ_{tot}). The elastic stress is shown implicitly by the local strain $\sigma_{\mathrm{elastic}} = -c\eta$. When the springs have regained their initial length, one finds that $\sigma_{\mathrm{tot}} = 0$ because $\sigma_{\mathrm{ext}} = -\sigma_{\mathrm{elastic}}$.

Modifications that occur due to additional contractive stress contributions in response to a laser-induced demagnetization process are schematically included in figure 4.13(b). In this representation, I have chosen a material that exhibits a large but negative Grüneisen parameter ($\Gamma_{\mathrm{mag}} < 0$) for magnetic excitations as it is the case for the rare earth Dysprosium. In this case, one finds that expansive stresses from electron excitations and phonons and contractive stresses by magnetic excitations appear simultaneously and superimpose their effects on the lattice response. To model the contractive magnetic stress, I introduce spacer-sticks that exist prior to the laser-excitation, which signify a repulsive magnetostrictive interaction. The effect of the laser-excitation is now twofold. It introduces yellow/blue spacer-sticks that represent expansive electron-phonon stresses and removes red spacer sticks due to the laser-induced disorder in the spin-system. This representation shows that the contractive magnetic stress saturates at the point when the red sticks are removed entirely. This marks the state of complete disorder in the spin system that goes along with complete demagnetization. The time-dependent balance of both laser-induced stresses can lead to contractive or expansive strains and the peculiar shapes of the resulting strain pulses as demonstrated in article VII.

The hitherto established representation of the linear chain model of masses and springs provides a useful intuition that helps to picture the strain response. Figure 4.13 is a small scale representation of the underlying processes for only a few times in absence of surface effects. The last two figures of this chapter represent an extensive visualization of the simulated response for an expanding transducer on a transparent substrate. Figure 4.14 and 4.15 represent a generic situation for a picosecond ultrasonics experiment using metallic transducers for different stress profiles. Differences in the simulation results shown in figure 4.14 and 4.15 are only due to the different stress profiles, since all other parameters are kept constant.

First I discuss the exemplary simulation results for an inhomogeneously excited metallic transducer depicted in figure 4.14. The discussed simulated response represents an extension of the example provided in the UDKM1DSIM toolbox [63]. Adaptations that use the magnetic stress of a Dysprosium transducer are deferred to chapter 6. The simulation represents the strain response of a laser-excited metallic $SrRuO_3$ (SRO) transducer on a transparent $SrTiO_3$ (STO) substrate. The layer thickness is chosen such that the picosecond strain pulse traverses the transducer within $t_1 = 10\,\mathrm{ps}$. The SRO layer has very good impedance matching to the STO substrate and exhibits very fast electron-phonon coupling especially for

high excitation fluences[237], so that it is assumed to be instantaneous for this depiction. Teh graphs in panel (a) show the average strain amplitude of the SRO layer and the substrate, which we frequently use as comparison to the experimental response seen by UXRD measurements. Panel (b) depicts the absorption profile that is identical with the stress profile if instantaneous electron-phonon coupling is assumed. Panel (c) depicts the corresponding linear chain model response, where each mass represents an average over approximately 1/10 of the transducer thickness (i.e. 6.3 nm). Each horizontal line corresponds to a snapshot of the linear chain model for times that are 1 ps apart. The blue spacer sticks that appear at $t = 0$ represent the phonon stress that leads to an expansion that travels towards the substrate as a bipolar strain wave at the speed of sound. This figure shows that the displacement of each mass accumulates over the film thickness and leads to the largest displacement to occur at the air-sample interface. Panel (d) displays the contributions to the elastic wave equation as lineouts at selected, characteristic times from the full spatio-temporal results that are color-coded in panel (e). The signals are normalized to their maximum value because the strain response in this simple model scales linearly with respect to the external stress, which is in turn defined by the absorbed energy density. Small, time-dependent changes in the external stress σ_{ext} occur due to heat diffusion that is included in the simulation.

The first striking feature in the simulation is the observation of a bipolar strain pulse that starts for $t = 0$ at the sample-air interface and propagates at the speed of sound $v_{\mathrm{s}} = \sqrt{\frac{c_{3333}}{\rho}}$ into the layer. It separates the expanded transducer from the compressed fraction of the material. Its characteristic signatures in an UXRD experiment have been discussed in an overview article by Schick et al. [53].

An additional observation from the spatially resolved simulation the oscillation in the elastic stress and strain, that trails the bipolar strain pulse feature. This high-frequency oscillation does not occur in simple analytic solutions of the continuum elastic wave equation that uses plane-wave functions.[52, 67] Linear chain model simulations however always predict the occurrence of this high frequency oscillation that starts at the air-transducer interface[236]. This oscillation is related to the excitation of the surface phonon modes of the semi-infinite crystal. Surface phonon modes occur when complex k-vectors are allowed in the plane wave ansatz, which lead to localized phonon states in addition to the known dispersion relation of linear chain models taught in introductory solid state courses.[238, chapter 5] The observation of phonon effects in the strain signal via UXRD is very challenging because the observed peak shift is proportional to the mean strain within the layer. The predicted oscillations do not appear in the average strain response because they dephase within 3 unit cells for the given simulation. Surface-sensitive techniques such as electron energy loss or helium atom scattering spectroscopy are however able to resolve surface phonon effects[239] and advances in femtosecond laser spectroscopy allow for the time-domain observation.[240–242] They are however not further discussed in this thesis.

A net expansion remains within the transducer when the bipolar strain pulse has traversed the absorbing layer. The semi-infinite substrate exhibits a relatively small, negative strain response as the leading, compressive edge of the bipolar strain that enters the substrate until $t_1 = v_{\mathrm{sound}}/d_1$. At this time, the trailing expansive part has traversed the transducer and entered the substrate, which leads to a decrease of the transducer strain and an increase in the average strain of the substrate. The simulated bipolar strain pulse is symmetric and thus leads to no net strain within the substrate.

To demonstrate the effects that arise form different spatial shapes of the stress profile, I repeat the simulation with the exact same sample parameters but assume a nearly homogeneous laser penetration profile. The result is shown in figure 4.15 for comparison. The timing of the maximum in the strain signal t_1 can be used to calibrate the film thickness from $d_1 = v_{\mathrm{sound}} t_1$, and the shape of the rising edge in the strain pulse indicates the spatial shape of the stress profile. More complex situations that include the effect of a time-dependent contractive magnetic stress are presented in chapter 6.

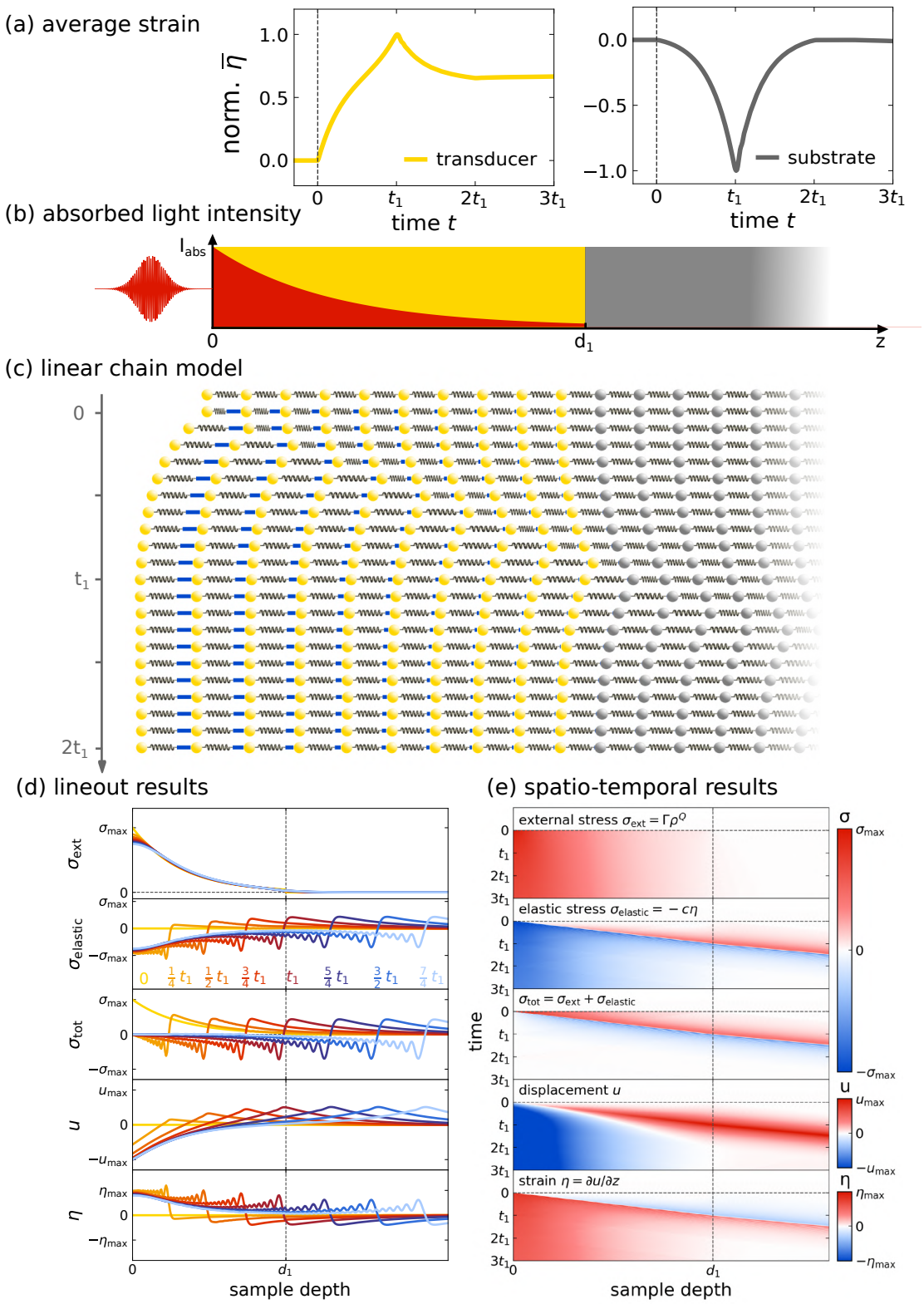

Figure 4.14: Masses and springs model response to an inhomogeneous expansive stress within the transducer: (a) layer averaged strain response. (b) absorbed light intensity that corresponds to the external stress profile. (c) mechanical representation in a linear-masses and springs model where each mass represents approximately 1/10 of the transducer thickness d_1 and each line corresponds to snapshots with a temporal spacing of 1 ps. The position of the masses indicates the displacement field u, the length of the spacer sticks represents the laser induced external stress of phonons and the change in length of the spring represents the total stress. The stress contributions and the resulting displacement and strain are depicted at representative times in (d) and as spatio-temporal map in (e). It takes approximately $t_1 = 10\,ps$ for the strain pulse to traverse the transducer.

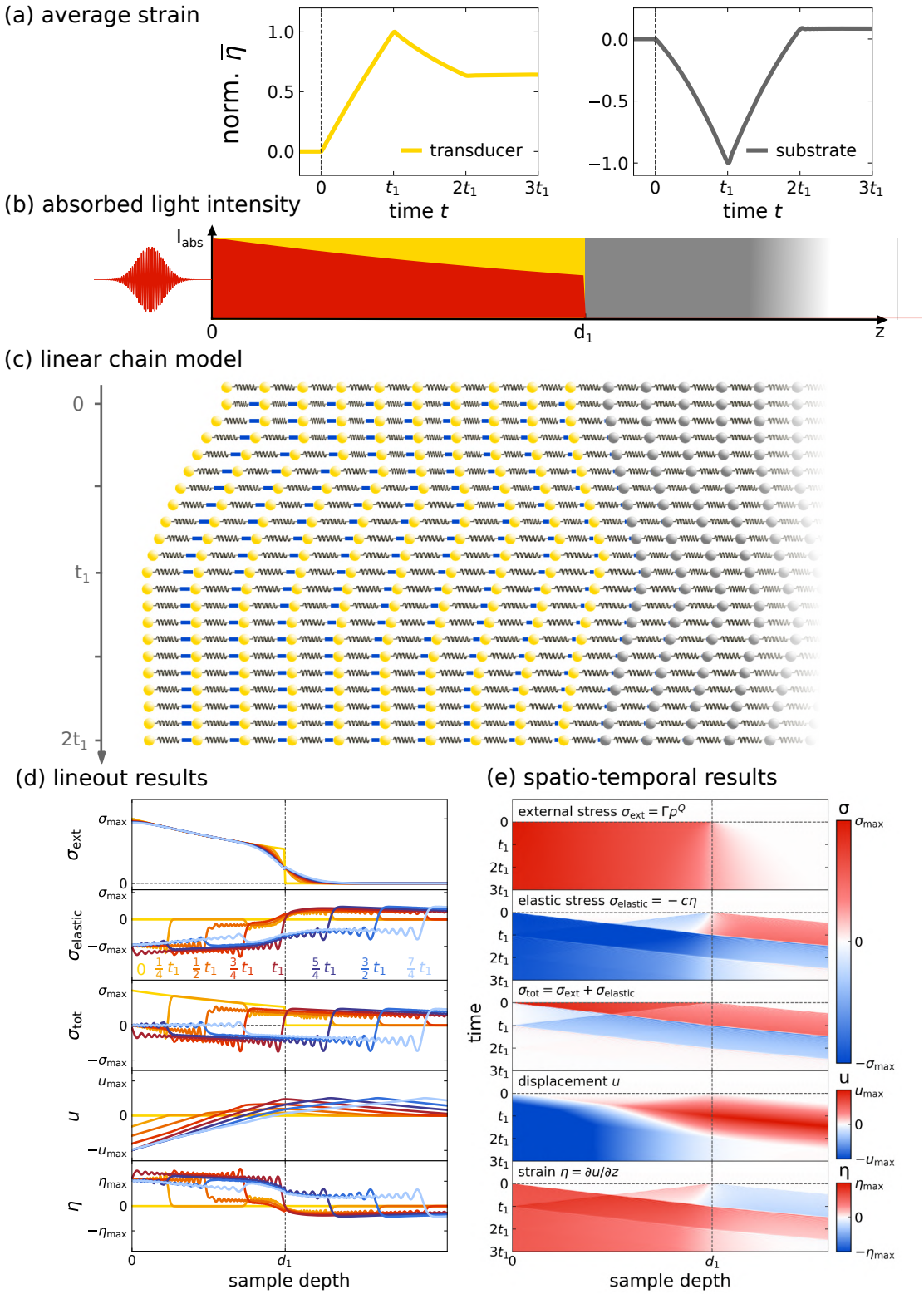

Figure 4.15: Masses and springs model response for a nearly homogeneous expansive stress. Same simulation and plot layout as in figure 4.14 for the a homogeneous stress profile. In this example, one has a step in the laser-induced external stress at the interface to the substrate and the resulting spatial derivative in $\partial\sigma_{tot}/\partial z$ drives two counter-propagating bipolar strain pulses starting at both transducer interfaces. The homogeneous excitation leads to a nearly linear rise in the average strain response. Comparison with panel (a) of figure 4.14 illustrates that an analysis of the strain response may yield the spatial shape of the underlying stress profile.

CHAPTER FIVE

Identification of magnetic stress in FePt

Magnetic stresses are central to this investigation of the ultrafast strain response in laser-excited metals with magnetic order. Pump-probe experiments are suited to investigate the time-dependence of magnetic stresses in relation to the laser-induced demagnetization. It is also interesting to see whether a material that exhibits an invar-like behavior upon equilibrium heating also responds invar-like upon femtosecond laser-excitation. Ultrafast magnetic stresses could potentially allow for the manipulation of the picosecond strain response by macroscopic parameters such as temperature, laser fluence or applied external fields. To identify magnetic stresses however requires a separation of the total stress into contributions from different energy reservoirs i. e. phonons and electron excitations, which are often dominant in the strain response of laser-excited metals. Additional elastic contributions to the strain that need to be considered originate from propagating picosecond strain pulses, epitaxial growth and the Poisson effect that couples the in- and out-of-plane motion in nano-particles.

This chapter is dedicated to the material FePt that is a frequently used material in heat-assisted magnetic recording schemes that allow for writing smaller magnetic bits thanks to its very high magneto-crystalline anisotropy. This chapter supplements the three publications on the strain and magnetization response of laser-excited FePt (article IV, article V and article VI). In the first section, I discuss the relevant magnetic and structural properties of FePt that render it an interesting material both for research and application. The second section reports the findings on the morphology-dependent, ultrafast strain and magnetization response of granular and continuous FePt grown on a substrate in direct comparison to the response of free-standing FePt grains on a transmission electron microscopy (TEM) grid that is reported by Reid et al. [122]. This discussion combines the insights from **article IV: Ultrafast laser generated strain in granular and continuous FePt thin films** and **article V: Finite-size effects in ultrafast remagnetization dynamics of FePt**. The final section supplements **article VI: Spin stress contribution to the lattice dynamics of FePt** where we extract the magnetic stress in granular FePt using a two-pulse excitation scheme. The section provides the modeled in- and out-of-plane strain response to a time-dependent in- and out-of-plane stress that enters as a parameter in the continuum elastic model. The strain response simulation was implemented by Aurélien Crut from the Institut Lumière Matière in Lyon according to our discussions and suggestions. He uses Finite element methods to solve the coupled elastic wave equation for different boundary conditions that represent the investigated sample morphologies. Snapshots of the two-dimensional strain are discussed to highlight the importance of the morphology for the time-resolved strain response.

5.1 Structural and magnetic properties of FePt

FePt is a ferromagnetic material that combines several properties that render it suitable for time-resolved diffraction techniques and high density magnetic recording. It can be grown in a crystalline phase and has a large out-of-plane uniaxial anisotropy, which allows for the growth of isolated nanograins with a high coercive field and a moderate Curie temperature. The following subsection summarizes important thermo-physical properties of the investigated FePt specimen and the basic principle of HAMR.

5.1.1 Thermo-physical properties of the investigated FePt specimen

The intermetallic alloy of Fe and Pt exhibits multiple structural phases with different lattice constants and different degrees of chemical order.[243] Their nomenclature is derived from the binary noble-metal alloy Cu-Au that serves as paradigm for intermetallics.[244]

FePt can be obtained by high throughput sputtering techniques, which is beneficial for the mass-production of magnetic storage media. In general, co-sputtering of Fe and Pt with equiatomic content at room temperature leads to the formation of a disordered, so-called $A1$-phase where the Fe and Pt atoms randomly occupy the atomic positions of a face-centered cubic (fcc) structure.[243, 245] Thermal treatment or sputter deposition at elevated temperatures leads to the formation of FePt in the ordered tetragonal $L1_0$-phase[243, 246], where layers of the $3d$-element Fe and the $5d$-element Pt alternate along the tetragonal c-axis as shown in the conventional unit cell in figure 5.1(c). The growth of $L1_0$-ordered FePt with a shorter c-axis aligned along the out-of-plane direction is facilitated by the use of seed layers and substrates with a larger in-plane lattice constant (negative lattice mismatch).[247]

In this chapter, I analyze the structural and magnetic response upon laser-excitation of two approximately 10 nm thin FePt $L1_0$ samples that differ in their morphology as sketched in figure 5.1 (a) and (b). Sample (a) consists of a continuous FePt film capped by a 1-2 nm thin aluminum layer and sample (b) consists of FePt nanograins that are approximately 10 nm in diameter. The FePt grains are segregated by amorphous carbon and form isolated magnetic domains. The aluminum capping of the film is most likely oxidized to Al_2O_3 because the samples were kept at ambient conditions during and after the measurements. The structural characterization of the two specimen have been discussed in article IV and article VI and the magnetic properties in article V. Figure 5.1 provides an overview and comparison of the relevant properties. The samples have been grown in the group of Olav Hellwig by magnetron sputtering from two Fe and Pt targets and a single FePtC target onto pre-heated MgO substrates. The crystallinity is underlined by the X-ray diffraction measurement shown in 5.1(d). It displays the X-ray intensity detected in a symmetric θ-2θ scan of a point detector, which samples the reciprocal space along the q_z direction in the close proximity of $q_x = 0$ as sketched in figure 3.2(a). The characterization measurements have been carried out by Jon-Ander Arregi in the group of Vojtěch Uhlíř at the CEITEC facility in Brno which provides the possibility of high-temperature diffraction measurements. Besides the sharp, intense MgO substrate peak, one observes only different orders of the (001)-FePt peak, which shows the high degree of crystalline orientation of the desired $L1_0$-phase. In the following time-resolved investigations, we study the behavior of the FePt (002) diffraction peak close to $q_z \approx 3.39\,\text{Å}^{-1}$ of both specimen. It is chosen because it provides sufficient diffraction intensity and larger shifts in comparison to the (001)-peak. The difference of the diffraction peak position of FePt between the two samples hints at a tensile in-plane strain of the FePt film that is clamped onto a MgO substrate, which has an approximately 9.4 % larger in-plane lattice constant ($a_{\text{FePt}} = 3.85\,\text{Å}$ and $a_{\text{MgO}} = 4.212\,\text{Å}$). The FePt grains may be less strongly attached to the MgO due to their carbon surrounding. Epitaxial strains of FePt grown on common substrates and in particular on MgO have been discussed in the literature[247–249], because they affect the formation

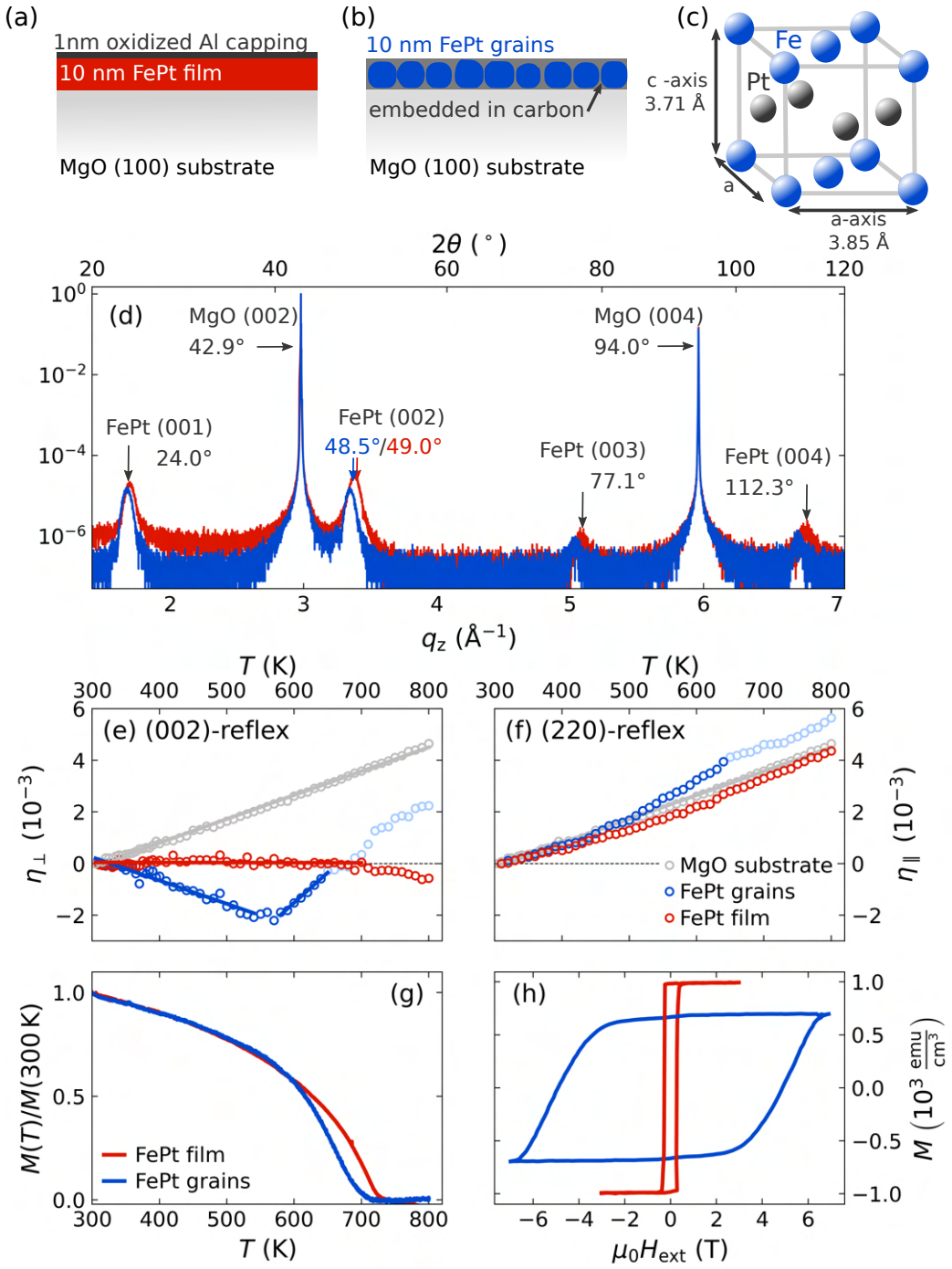

Figure 5.1: Structural and magnetic properties of the continuous film and nano-granular FePt samples: Sketches of the sample geometries (a),(b) and the conventional unit cell of the $L1_0$-FePt. Diffraction intensity $I(q_z)$ for $q_x \approx 0$, which shows multiple orders of the (001)-FePt diffraction peak besides the sharp, intense MgO substrate peak. The evaluation of the temperature dependent peak position of the (002)-peaks and the (220)-peaks (not shown) yield the out-of-plane c-axis and the in-plane a-axis strain shown in (e) and (f) respectively. While the FePt in-plane dimensions exhibit a thermal expansion that matches approximately the behavior the MgO-substrate, the out-of-plane strain yields an invar-behavior for the FePt film and even negative thermal expansion below 580 K for granular FePt. Temperature dependent magnetization and the room-temperature $M(H)$-hysteresis curve of both specimen are reported in (g) and (h) respectively. The structural characterization was carried out at the high temperature diffraction setup of the CEITEC facility of Brno University of Technology by the nanomagnetism and sprintronics group of Vojtěch Uhlíř. Magnetic characterization was conducted by the joined magnetic, functional materials research group of Olav Hellwig at the TU Chemnitz and the Helmholtz Center Dresden-Rossendorf.

of the ordered $L1_0$ phases and thereby the desired strong magneto-crystalline anisotropy. Hard X-ray diffraction as a non-local probe of the average lattice constant within the probe spot does not yield further direct insights on the strain state at the interface. However, it allows for temperature-dependent and time-resolved investigations that are discussed below.

The thermal expansion along the out-of-plane and the in-plane direction is reported in figure 5.1 (e) and (f). It can be extracted from the T-dependent shift of the (002)- and (220)-diffraction peaks of the constituent materials. The in-plane lattice strain ($\eta_{\parallel}$) was measured in a near-grazing diffraction geometry and the shift of the (220)-diffraction peaks (not shown) yields an in-plane thermal expansion that is close to $10^{-5}\,\mathrm{K}^{-1}$ for the granular and continuous FePt. It coincides with the thermal expansion of the MgO substrate, that expands isotropically due to the cubic symmetry of its unit cell. The observed in-plane expansion is in agreement with an epitaxial connection of FePt with the substrate, but also the reported, nearly-matched in-plane thermal expansion coefficient of $L1_0$-FePt and MgO[249]. The thermal out-of-plane strain response ($\eta_{\perp}$) is close to zero for the continuous FePt sample, whereas it shows a negative thermal expansion between 300-580 K for the granular FePt. The data points above 580 K are plotted in a lighter shade because the FePt Bragg peak intensity started to irreversibly decrease to 85% of its room-temperature value, which could indicate the beginning of carbon-interdiffusion into the chemically ordered phase so that the reported strain may not be as reliable as the strain below 580 K.

Reports on the thermal expansion data on single-crystalline, thin FePt in the $L1_0$-phase are scarce but our observation of an anisotropic thermal expansion of FePt and the resulting out-of-plane invar-behavior are in agreement with a neutron diffraction report by Tsunoda et al. [250] on a large specimen of polycrystalline FePt. The FePt-alloy with the more iron rich stochiometry Fe_3Pt is known to exhibit volume-invar-behavior below its Curie temperature[251, 252]. Understanding and modeling the underlying electronic states and magnetic excitations in the electronic band structure of Fe and its compounds is a prominent challenge in solid-state physics theory[253–256] since the first observation of invar behavior in FeNi 1897 by Charles Édouard Guillaume[257]. At this point, I report the experimentally observed strain response of both FePt specimen, which shows a large, in-plane expansion and a vanishing or even negative out-of-plane expansion upon slow, near-equilibrium heating. As a result, the tetragonality of the FePt unit cell increases with increasing temperature. Such a behavior has been rationalized using spin-dependent density functional theory in the publication of Reid et al. [122] by a combination of magnetic contributions and anisotropic phonon stresses. Based on ab-initio calculations of the energetic ground state, they report a smaller c/a-ratio of the tetragonal axis for the paramagnetic state in comparison to the ferromagnetic state of $L1_0$-FePt. From their calculation of mode-specific Grüneisen coefficients they furthermore find a much larger in-plane thermal stress than out-of-plane stress upon increasing the thermal population of the phonon modes. Thus, it can be expected that both phonon- and magnetic stresses will contribute an anisotropic strain response upon femtosecond laser-excitation.

The magnetic characterization of our two samples was carried out in the joined research group of Olav Hellwig at the TU-Chemnitz and the Helmholtz-Zentrum Dresden-Rossendorf by Fabian Ganss and Gabriel Sellge. They measured the magnetic hysteresis loop and the temperature-dependent magnetization that are displayed in panels (g) and (h) of figure 5.1 using a superconducting quantum interference device-vibrating sample magnetometer (SQUID-VSM by Quantum Design). From these measurements, we can extract a Curie Temperature that is close to, but below the literature value of $T_C \approx 750\,\mathrm{K}$ [258] and a coercive field of $\mu_0 H_{\mathrm{ext}} \approx 0.4\,\mathrm{T}$ for the continuous film and $\mu_0 H_{\mathrm{ext}} \approx 5\,\mathrm{T}$ for the FePt-grains. This large difference in the coercive field originates from the different switching mechanisms. While the continuous film can reverse its magnetization by the growth and coalescence of magnetic domains, which nucleate at defects within the film, the FePt grains are inherently single domain because the energetic cost of a domain wall within such a small particle can be estimated to be larger than the gain due to the minimization of the

stray field. For a given temperature, the magnetization of the FePt grains can thus only be reversed by a coherent rotation of the magnetization within the entire grain. This requires a field that is large enough to overcome the energy-barrier given by the magneto-crystalline anisotropy energy. Energetic considerations on domain-wall formation in magnetically ordered nanoparticles are provided for example in the book by Stöhr and Siegmann [214, chapter 11.3] and derived in the book of Hubert and Schäfer [259, chapter 3]. Table 5.1 provides a selection of magnetic properties and resulting characteristics of magnetic domains in $L1_0$-FePt. The overview is based on the work of Klemmer et al. [260], that has been extended and updated by the works of Weller et al. [261, 262].

Table 5.1: Room temperature magnetic properties of FePt in the $L1_0$-phase and derived quantities for magnetic domains. The data is reproduced from Weller et al. [261, 262] and translated from cgs to SI-units as a reference. The exchange stiffness A quantifies the energetic cost of the misalignment of neighboring spins, which can be calculated for simple, cubic geometries. It contains the exchange energy J, the cubic lattice spacing a and the expectation value of the spin alignment $< S^2 >$ and is only estimated based on previous work.[263] The dimension d_c is the estimated maximal particle diameter of a spherical particle for which the single domain state is energetically favorable and the d_s is the minimal particle diameter for which the magnetic state is estimated to be stable against thermal fluctuations for approximately 10 years. Both values depend on the chosen particle geometry (spheres, cylinders, cubes).[262]

property	**symbol/formula**	**value for** $L1_0 - FePt$
Curie temperature	T_C	750 K
saturation magnetization	M_s	$1.14 \cdot 10^3 \frac{emu}{cm^3} = 1.14 \cdot 10^6 \frac{A}{m}$
uniaxial anisotropy energy	K_u	$7 \cdot 10^6 \frac{J}{m^3}$
anisotropy field	$H_{ani} = \frac{2K_u}{M_s}$	$1.16 \cdot 10^5 Oe \approx 9.11 \frac{A}{m}$
exchange stiffness	$A = \frac{J<S^2>}{a}$	$\approx 10^{-6} \frac{erg}{cm} = 10^{-11} \frac{J}{m}$
domain wall energy	$E_W = 4\sqrt{AK_u}$	$32 \frac{erg}{cm^2} = 3.2 \cdot 10^{-2} \frac{J}{m^2}$
intrinsic domain wall width	$d_W = \pi\sqrt{\frac{A}{K_u}}$	3.9 nm
single domain particle diameter	$d_c \approx 1.4 \frac{E_W}{M_s^2}$	340 nm
minimal stable grain diameter	$d_s = \left(60 \frac{k_B T}{K_u V}\right)^{\frac{1}{3}}$	$2.3 - 4$ nm

5.1.2 Magnetocrystalline anisotropy and heat-assisted magnetic recording

There exists a high demand for information storage technologies because the amount of generated digital information is projected to grow with an increasing rate per year.[264] Projections of the contributions of hard disks to the total amount of stored data vary between approximately $60\% - 80\%$ regardless of the projected shift from consumer based to cloud based storage.[264] Innovations that increase the data storage densities are therefore required to sustain the growth of the datasphere at manageable costs in energy and resources. Increasing the data densities of conventional hard disk drives requires reading and writing smaller magnetic bits. Currently realizable data densities are on the order of 1 Terrabit per squared inch (Tbpsi), which translates to a diameter of a cylindrical bit to be approximately 30 nm. Future scenarios with 2 Tbpsi and 4 Tbpsi then result in diameters of approximately 20 nm and 15 nm per bit respectively. For a sufficient signal to noise ratio (SNR) in the readout process, each bit contains approximately 10 isolated magnetic particles so that stable magnetic nanoparticles with a diameter of less than 10 nm are required. For such magnetic particles to be stable against thermal fluctuations, it is

required that the constituent materials exhibit a large, uniaxial magnetic anisotropy K_u. This results from the Néel-Arrhenius relaxation theory[265, pp. 405-427][266] that provides an estimate of the switching time of a nanoscopic magnetic volume (τ) due to thermal excitations. The estimated timescale that it takes to thermally overcome the energy barrier given by the anisotropy energy $\Delta E = K_u V$ is given by:

$$\tau = \tau_0 e^{\frac{K_u V}{k_B T}}, \tag{5.1}$$

where K_u represents the uniaxial anisotropy energy per volume, V the volume of the single-domain nano-particle, T the temperature, k_B the Boltzmann constant and τ_0 a material-specific attempt time that is on the order of 10^{-10} s for FePt[267, 268]. Relation (5.1) directly shows that the timescale for thermal switching in this model depends strongly on the particle volume. Nanoscopic bits are thus prone to the so-called superparamagnetic behavior, where the ferromagnetic order is lost due to thermal excitations. While thermal fluctuations cannot be completely excluded, the desired data retention time in hard disk drives is realized by choosing materials with a high K_u such that $\frac{K_u V}{k_B T} \geq 60$. This value is chosen to guarantee stability of the data for more than 10 years even for a larger grain size distribution.[269]

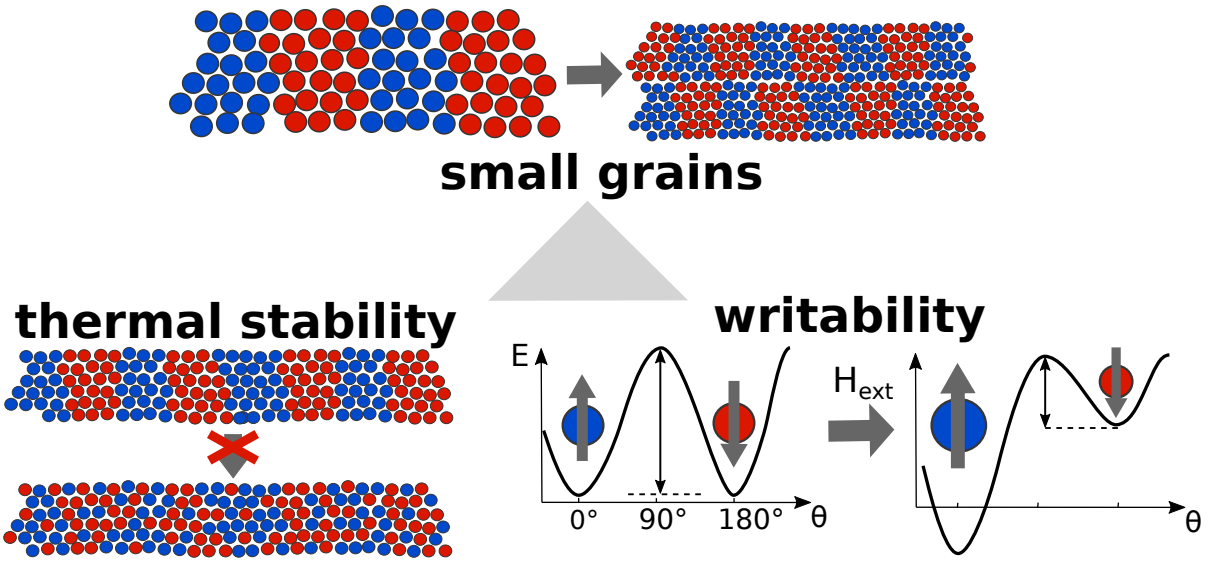

Figure 5.2: Magnetic recording trilemma: Physical constraints for decreasing magnetic bits in order to obtain higher data densities are sketched in the so-called "magnetic recording trilemma"[269] shown here. It is a conflict between small magnetic bits that require high uniaxial anisotropy energies for long-time thermal stability, which then increases the required write field beyond the available head field.

FePt in the $L1_0$-phase has a very high out-of-plane uniaxial anisotropy with $K_u \approx 7 \cdot 10^6 \frac{J}{m^3} > 0$, so that the magnetic easy axis is along the out-of-plane direction. The fact that the magnetization is always aligned along the surface-normal makes this material suitable for perpendicular magnetic recording and leads to thermally stable magnetic nanoparticles. The thermal stability however comes at the cost of very large magnetic fields that are required to write information by switching individual bits as can be seen from the coercive field of $\mu_0 H > 5\,T$ in the granular FePt sample. This leads to the so called "magnetic recording trilemma" between the desired small magnetic bits, sufficient thermal stability and the limited write fields as illustrated in figure 5.2. The magnetic recording trilemma poses a physical limit to further downscaling of the perpendicular magnetic recording approach beyond 1.5 Tbpsi because the write fields are too small to overcome the anisotropy energy barrier that is required for thermal stability. Figure 5.3(a) displays the perpendicular magnetic recording technique for reading and writing magnetic bits in current conventional hard drives that use write fields on the order of $\mu_0 H \leq 2.4\,T$ and sensors based on the tunnel-magnetoresistance effect for reading the data. The heat-assisted magnetic recording approach depicted

in panel (b) solves this trilemma by introducing a light-induced heating of the magnetic medium that transiently lowers the anisotropy energy during the writing process. The magnetic information becomes thermally stable as the anisotropy energy barrier reestablishes itself upon cooling. Although this method keeps the readout process and most of the hard-drive design similar to the conventional perpendicular magnetic recording technique, it is projected to allow for data densities beyond 2 Tbpsi. Reviews by

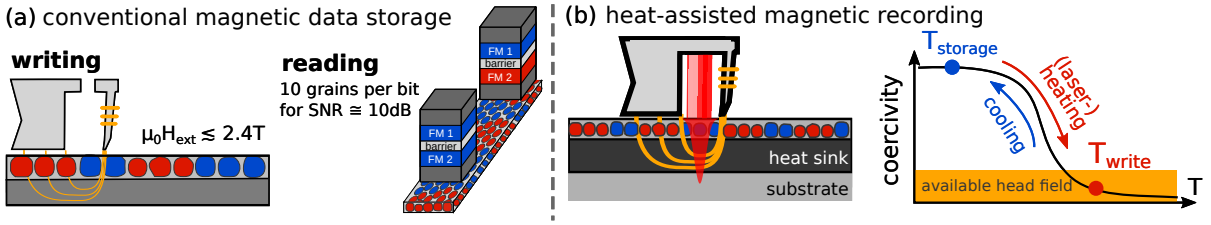

Figure 5.3: Heat-assisted magnetic recording: (a) Schematic of the magnetic write- and read process in the perpendicular magnetic recording geometry that is used in many current hard drives. The heat-assisted magnetic recording approach that transiently lowers the anisotropy energy by laser-heating the writing area is schematically depicted in (b). Parts of the figure are adapted from a review by Weller et al. [112].

Weller et al. [112, 262] and articles in a focus issue of the Materials Research Bulletin[111, 270–274] provide further details of the technological advantages and challenges of this heat-assisted magnetic recording approach. In addition to the choice of the magnetic recording medium[272], they comprise nanoscale thermal transport within the recording layer stack[270], design and material choice of the plasmonic antenna that confines the light to the writing area[271], a stable head-disk interface[271] and downsizing the read sensor technology[274]. While HAMR is not the focus of the following fundamental research experiments, it provides a relevant and fascinating technological context for the investigated material system. In the following, I make use of the fact that $L1_0$-FePt can be grown not only as a thin film, but also as nanoscopically small magnetic grains which are extensively used and developed by the magnetic recording industry.

5.2 Finite size effects on the ultrafast strain response

The following section discusses the strain and magnetization evolution of FePt in the $L1_0$-phase in response to pulsed laser excitation. The (sub-)picosecond strain response of granular FePt upon femtosecond laser excitation has been first explored using a femtosecond electron diffraction experiment on free-standing grains on a TEM grid by Reid et al. [122] They find that the out-of-plane lattice contracts upon laser excitation while the in-plane dimension expands. This finding is seemingly at odds with the laser-induced thermal expansion of a continuous $L1_0$-FePt film reported by Xu et al. [275] who used an X-ray diffraction experiment at the Advanced Photon Source synchrotron storage ring with a time-resolution of 33 ps.

The following section compares the strain response of FePt in the granular and continuous phase on an MgO substrate under identical laser excitation conditions and supplements article IV. A comparison of static X-ray diffraction and the UXRD-data for an excitation fluence of approximately 6 $\frac{\mathrm{mJ}}{\mathrm{cm}^2}$ of the (002) - reflection at the PXS-setup for both FePt specimen is displayed in figure 5.4. The excitation conditions for the UXRD are identical to the report in article IV (p-polarized, ≈ 100 fs, long laser pulses at a central wavelength of 800 nm with an incident fluence of approx 6 $\frac{\mathrm{mJ}}{\mathrm{cm}^2}$. Panel (a) shows the q_x-integrated X-ray diffraction intensity $I(q_z)$ that contains the intense (002)-MgO substrate peak and the broad FePt (002)-layer peaks. Panels (b) and (c) show the extended reciprocal space projection $I(q_x, q_z)$, where the

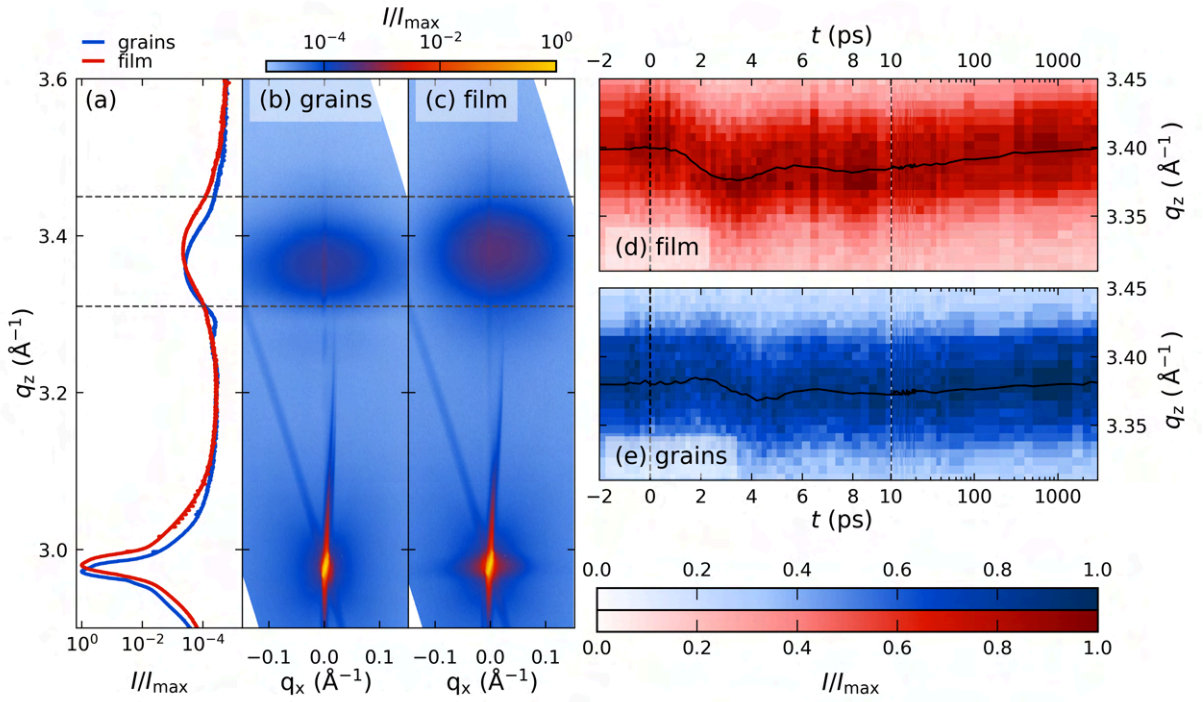

Figure 5.4: Characterization and UXRD response of the FePt-specimen at the PXS-setup: The reciprocal space projection that results from a symmetric $\theta - 2\theta$ scan in the region of the MgO and FePt (002) reflections using the cw-X-ray tube are shown in (b) and (c). The q_x- integrated X-ray diffraction intensity $I(q_z)$ (a) shows that the instrument function of the convergent, slightly polychromatic Montel-optic amplifies the diffraction intensity from the broad FePt-layer peaks in comparison to the sharp substrate peak. The time-dependent peak-shift of the thin film and the granular specimen under identical incident excitation conditions of $\approx 100\,fs$, p-polarized, 800 nm laser pulses at a laser fluence of 6 $\frac{\mathrm{mJ}}{\mathrm{cm}^2}$ in the indicated q_z region are shown in (d) and (e) respectively. For both FePt-morphologies the diffraction peak shifts to lower q_z for $t > 5\,ps$ although the underlying expansion is less pronounced for the granular FePt. Whereas the thin film directly expands, the granular film exhibits a shift to higher q_z within the first 3 ps that can be seen from the overlaid black line that indicates the peak center in (d) and (e).

dashed lines indicate the q_z-section that is enlarged for the time-resolved evolution of the diffraction curves shown in (d) and (e). The shift of the diffraction peak for the laser-excited FePt is extracted by Gaussian fits to the peak profile and the time-dependent peak center is indicated by a black line overlaid on top of the color-coded diffraction intensity. It shows that the continuous film diffraction peak directly shifts to smaller q_z whereas the grains exhibit an initial shift to larger q_z that after 3 ps switches into a shift to lower q_z that is smaller in comparison to the q_z-shift observed in the continuous film under identical excitation conditions.

The observed peak shift of the FePt translates into a strain response that is depicted in figure 5.5. To highlight the qualitative difference of the picosecond strain response for different $L1_0$-FePt morphologies I reproduced out-of-plane strain data for the free-standing FePt grains by Reid et al. [122] on the same time-axis, since they used comparable laser excitation conditions and a fluence of 5 $\frac{\mathrm{mJ}}{\mathrm{cm}^2}$. We observe that the continuous film starts to expand directly, whereas the free-standing FePt grains initially contract before their strain reaches a level of approximately zero out-of-plane expansion. The strain response of FePt grains, which are attached to a MgO substrate, exhibits an intermediate behavior with a short contraction that is replaced by a similar, albeit smaller thermal expansion compared to the continuous FePt-film.

Schematic depictions shown next to the data illustrate the hypothesis for the data interpretation that we put forward to qualitatively rationalize the observed discrepancy. It sketches the original film dimension as a dashed black rectangle and the change in dimension upon laser-excitation in color. Arrows indicate the

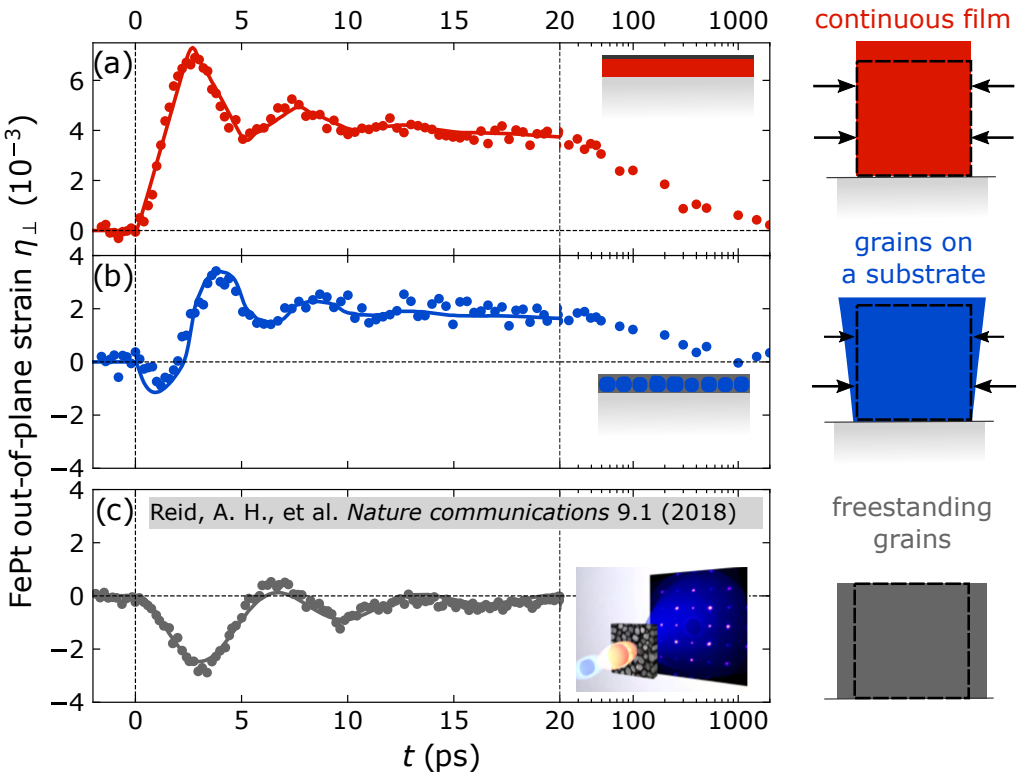

Figure 5.5: Finite size effects on the strain response: Comparison of the out-of-plane strain-response of FePt in three different boundary conditions. (a) continuous thin film (b) FePt nanograins on a substrate (c) free-standing FePt grains on a TEM grid. The data in panel (a) and (b) correspond to the results from article IV that have been acquired at an incident laser fluence of approximately 6 $\frac{\mathrm{mJ}}{\mathrm{cm}^2}$. The data in panel (c) are reproduced from the publication by Reid et al. [122] who used time-resolved electron diffraction in transmission from multiple FePt reflexes with different out-of-plane contributions to infer the FePt out-of-plane strain response. The data shown here originate from a comparable laser fluence of 5 $\frac{\mathrm{mJ}}{\mathrm{cm}^2}$ and are reproduced to highlight the qualitative differences in the observed morphology-dependent strain response.

action of constraining forces that result from the expansion of adjacent unit-cells, the epitaxial growth on a substrate and potentially also the carbon interlayer. It is important to recall that our static, temperature-dependent diffraction has shown a strongly anisotropic thermal expansion, where the in-plane dimension expands as opposed to the out-of-plane dimension, which exhibits invar behavior for the thin film or even negative thermal expansion for the grain. Thus, it may seem counter-intuitive that both the thin FePt film and the grains respond on average by an out-of-plane expansion upon laser-excitation. The response of the free-standing grains however is in qualitative agreement with our observed thermal expansion, because Reid et al. also report a sizable ultrafast expansion of FePt along the in-plane dimension (not shown here) in addition to the out-of-plane invar-behavior that is observed after 20 ps. As outlined in chapter 1, the coupling between the in-plane and out-of-plane motion due to the Poisson effect is expected and quantified by the off-diagonal elements of the stiffness tensor. Reid et al. [122] account for it by using a model of two damped harmonic oscillators with amplitudes that represent the in- and out-of-plane displacement of the FePt grains. The coupling of the oscillations is described by a phenomenological coupling constant. The oscillators are subjected to highly anisotropic stresses that mimic the contributions from electrons, phonons, spins and the carbon matrix. Such free oscillations along the in- and out-of-plane dimension are however only reasonable for free-standing grains. The epitaxial growth on a substrate and the restrictions of the in-plane expansion due to adjacent unit cells in a homogeneously excited thin film suppress the

in-plane expansion partially or completely, so that the resulting contractive out-of-plane stress is absent. This hypothesis stated in article IV is further analyzed in article VI. Therein we report the simplified equation of motion for the out-of-plane displacement $u_\perp(z,t)$ of a needle-like FePt grain to be:

$$\rho \frac{\partial^2 u_\perp}{\partial t^2} = \frac{\partial}{\partial z}\left(c_{3333}\frac{\partial u_\perp}{\partial z} + 2c_{3311}\frac{\partial \eta_\parallel}{\partial z} - \sigma_\perp^{\mathrm{ext}} \right). \tag{5.2}$$

The right hand side of relation 5.2 contains the stresses that cause the time-dependent displacement changes. The term $c_{3333}\frac{\partial u_\perp}{\partial z}$ corresponds to the normal restoring force that is present for the case of a homogeneous elastic wave equation, $2c_{3311}\frac{\partial \eta_\parallel}{\partial z}$ originates from the cross-coupling of the in-plane strain $\eta_\parallel$ to the out-of-plane motion and σ^{ext} is the laser-induced stress where the sign is chosen such that positive stresses lead to an expansion ($\eta_\perp > 0$). This relation provides an analytical insight into the importance of the in-plane strain on the out-of-plane motion. Except for the special case of auxetic materials, which exhibit a negative Poisson number c_{3311} can be assumed to be positive so that an in-plane strain exerts a contractive stress along the out-of-plane dimension.

5.2.1 Strain response with different in-plane boundary conditions

The following analytical considerations start from the general, coupled 3D-elastic wave equation (5.3) known from continuum elasticity theory. This section is inserted in order to provide insights into the assumptions that are necessary for the analytic solution of the equation of motion.

The general equation of motion from elastic continuum theory is given by the following wave equation:

$$\rho \frac{\partial^2 u_i}{\partial t^2} = \sum_{j=1}^{3} \frac{\partial \sigma_{ij}}{\partial x_j} \tag{5.3}$$

Where $u(\vec{x},t)$ is the displacement field for a given time t, ρ is the mass density of the material and $\sigma(\vec{x},t)$ is the time-dependent stress field. The stress field can be separated into elastic stresses in response to an existing strain and external stresses that are, for example, due to deposited energy densities:

$$\sigma_{ij} = \sum_{kl} c_{ijkl}\eta_{kl} - \sigma_{ij}^{ext} \tag{5.4}$$

Shear forces are usually smaller than the longitudinal stresses and they require a symmetry breaking, which is not present in out-of-plane magnetized FePt, where the tetragonal c-axis of the unit cell is aligned with the out-of-plane direction. By neglecting potential shear forces, equation (5.3) can be simplified to read:

$$\rho \frac{\partial^2 u_i}{\partial t^2} = \sum_{j=1}^{3} \frac{\partial \sigma_{ii}}{\partial x_j} = \sum_{j=1}^{3} \frac{\partial}{\partial x_j}\left(\sum_{k=1}^{3} c_{iikk}\eta_{kk} - \sigma_{ii}^{ext} \right) \tag{5.5}$$

In the following, the discussion is focused mainly on the observable $\eta_{33} = \frac{\partial u_3}{\partial x_3}$ that is observed in the UXRD experiment:

$$\rho \frac{\partial^2 u_3}{\partial t^2} = \sum_{j=1}^{3} \frac{\partial \sigma_{33}}{\partial x_j} = -\sum_{j=1}^{3} \frac{\partial \sigma_{33}^{ext}}{\partial x_j} + \sum_{j=1}^{3}\left(\sum_{k=1}^{3} c_{33kk}\frac{\partial \eta_{kk}}{\partial x_j} \right) \tag{5.6}$$

To simplify this general equation of motion, we consider a cubic grain with tetragonal symmetry so that we can assume that the in-plane directions are equivalent, which leads to $c_{3311} = c_{3322}$, $c_{1111} = c_{2222}$, $\eta_{11} = \eta_{22}$, $\frac{\partial \eta_{11}}{\partial x_1} = \frac{\partial \eta_{22}}{\partial x_2}$ and $\frac{\partial \eta_{11}}{\partial x_2} = \frac{\partial \eta_{22}}{\partial x_1}$. These simplifications reduce the relations given in (5.6) to two coupled equations of motion for the out-of-plane and in-plane direction respectively:

$$\rho \frac{\partial^2 u_3}{\partial t^2} = 2c_{3311}\left(\frac{\partial \eta_{11}}{\partial x_1} + \frac{\partial \eta_{11}}{\partial x_2} + \frac{\partial \eta_{11}}{\partial x_3} \right) + c_{3333}\left(\frac{\partial \eta_{33}}{\partial x_1} + \frac{\partial \eta_{33}}{\partial x_2} + \frac{\partial \eta_{33}}{\partial x_3} \right) - \left(\frac{\partial \sigma_{33}^{ext}}{\partial x_1} + \frac{\partial \sigma_{33}^{ext}}{\partial x_2} + \frac{\partial \sigma_{33}^{ext}}{\partial x_3} \right) \tag{5.7}$$

$$\rho\frac{\partial^2 u_1}{\partial t^2} = c_{1122}\left(\frac{\partial\eta_{11}}{\partial x_1}+\frac{\partial\eta_{11}}{\partial x_2}+\frac{\partial\eta_{11}}{\partial x_3}\right)+c_{1133}\left(\frac{\partial\eta_{33}}{\partial x_1}+\frac{\partial\eta_{33}}{\partial x_2}+\frac{\partial\eta_{33}}{\partial x_3}\right)+c_{1111}\left(\frac{\partial\eta_{11}}{\partial x_1}+\frac{\partial\eta_{11}}{\partial x_2}+\frac{\partial\eta_{11}}{\partial x_3}\right)-\left(\frac{\partial\sigma_{11}^{ext}}{\partial x_1}+\frac{\partial\sigma_{11}^{ext}}{\partial x_2}+\frac{\partial\sigma_{11}^{ext}}{\partial x_3}\right) \tag{5.8}$$

If the cube is a fraction of a thin film that is subjected to an approximately homogeneous laser excitation along the in-plane dimensions $\left(\Rightarrow \frac{\partial\sigma_{33}^{ext}}{\partial x_1}=\frac{\partial\sigma_{33}^{ext}}{\partial x_2}=0\right)$, then we can also assume $\left(\eta_1=\frac{\partial u_1}{\partial x_1}=0\right)$ everywhere and $\left(\frac{\partial\eta_{33}}{\partial x_1}=\frac{\partial\eta_{33}}{\partial x_2}=0\right)$ due to symmetry. This reduces relation (5.7) to:

$$\rho\frac{\partial^2 u_3}{\partial t^2} = \frac{\partial\sigma_{33}^{ext}}{\partial x_3} - c_{3333}\frac{\partial\eta_{33}}{\partial x_3} \tag{5.9}$$

Relations (5.7) and (5.8) are applicable to a free-standing nanogranular FePt particle, whereas (5.9) represents the equation of motion for the case of a homogeneously excited thin film. The granular FePt on a substrate with the carbon matrix in between is an intermediate case between free-standing grains that are assumed to have free in-plane movement and the continuous thin film where in-plane strains are suppressed due to the highly symmetric excitation. To arrive at the conceptually simple relation (5.2) presented in the article VI, we furthermore made the assumption of needle-like grains, that are arbitrarily thin so that the in-plane variations do not occur i.e. $\left(\frac{\partial\eta_{11}}{\partial x_1}=\frac{\partial\eta_{11}}{\partial x_2}=\frac{\partial\eta_{33}}{\partial x_1}=\frac{\partial\eta_{33}}{\partial x_2}=0\right)$. Another scenario that justifies this assumption occurs when potential in-plane strain pulses have already damped out.

Further time-dependent evaluations of the equation of motion can be carried out by numerical solution of the coupled differential equations. However, it is instructive to compare the steady-state strains where $\frac{\partial u_i}{\partial t}=\frac{\partial^2 u_i}{\partial t^2}=0$ for both boundary conditions. This corresponds to the situation when picosecond strain pulses have left the probed thin layers towards the substrate and the external stresses prevail because thermal energy transport is sufficiently slow. For the thin film case, (5.9) simplifies to:

$$\frac{\partial\eta_{33}}{\partial x_3} = \frac{1}{c_{3333}}\frac{\partial\sigma_{33}^{ext}}{\partial x_3} \tag{5.10}$$

For the free grains, one obtains two relations for the out-of-plane strain and for the in-plane strain from (5.7) and (5.8) respectively:

$$\left(\frac{\partial\eta_{33}}{\partial x_1}+\frac{\partial\eta_{33}}{\partial x_2}+\frac{\partial\eta_{33}}{\partial x_3}\right) = -2\frac{c_{3311}}{c_{3333}}\left(\frac{\partial\eta_{11}}{\partial x_1}+\frac{\partial\eta_{11}}{\partial x_2}+\frac{\partial\eta_{11}}{\partial x_3}\right)+\frac{1}{c_{3333}}\left(\frac{\partial\sigma_{33}^{ext}}{\partial x_1}+\frac{\partial\sigma_{33}^{ext}}{\partial x_2}+\frac{\partial\sigma_{33}^{ext}}{\partial x_3}\right) \tag{5.11}$$

$$\left(\frac{\partial\eta_{11}}{\partial x_1}+\frac{\partial\eta_{11}}{\partial x_2}+\frac{\partial\eta_{11}}{\partial x_3}\right) = -\frac{c_{1122}}{c_{1111}}\left(\frac{\partial\eta_{11}}{\partial x_1}+\frac{\partial\eta_{11}}{\partial x_2}+\frac{\partial\eta_{11}}{\partial x_3}\right)-\frac{c_{1133}}{c_{1111}}\left(\frac{\partial\eta_{33}}{\partial x_1}+\frac{\partial\eta_{33}}{\partial x_2}+\frac{\partial\eta_{33}}{\partial x_3}\right)+\frac{1}{c_{1111}}\left(\frac{\partial\sigma_{11}^{ext}}{\partial x_1}+\frac{\partial\sigma_{11}^{ext}}{\partial x_2}+\frac{\partial\sigma_{11}^{ext}}{\partial x_3}\right) \tag{5.12}$$

To further proceed in the simplest possible way, I simplify relations (5.11) and (5.12) by assuming cubic symmetry in addition to cubic nanoparticles so that all directions and dimensions are equivalent i.e.: $(\eta_{33}=\eta_{22}=\eta_{11})$ and $\frac{\partial\eta_{33}}{\partial x_1}=\frac{\partial\eta_{33}}{\partial x_2}=\frac{\partial\eta_{33}}{\partial x_3}$. This then yields:

$$\frac{\partial\eta_{33}}{\partial x_3} = -2\frac{c_{3311}}{c_{3333}}\left(\frac{\partial\eta_{33}}{\partial x_3}\right)+\frac{1}{c_{3333}}\left(\frac{\partial\sigma_{33}^{ext}}{\partial x_3}\right) \tag{5.13}$$

$$\Rightarrow \frac{\partial\eta_{33}}{\partial x_3} = -\frac{\frac{1}{c_{3333}}}{1+2\frac{c_{3311}}{c_{3333}}}\left(\frac{\partial\sigma_{33}^{ext}}{\partial x_3}\right) = +\frac{1}{c_{3333}+2c_{3311}}\left(\frac{\partial\sigma_{33}^{ext}}{\partial x_3}\right) \tag{5.14}$$

The next step is to integrate relations (5.10) and (5.14). The integration constants are dropped because a strain offset is irrelevant for our experiment. Thereby, one recovers the general form of Hooke's law for

the case of a granular and a continuous thin film:

$$\eta_{33}^{\mathrm{film}}(z) = \frac{1}{c_{3333}}\sigma_{33}^{ext}(z) \tag{5.15}$$

$$\eta_{33}^{\mathrm{grain}}(z) = \frac{1}{c_{3333}+2c_{3311}}\sigma_{33}^{ext}(z) \tag{5.16}$$

$$\frac{\eta_{33}^{\mathrm{film}}}{\eta_{33}^{\mathrm{grain}}} = 1+2\frac{c_{3311}}{c_{3333}} \tag{5.17}$$

By using the cubic symmetry that implies $c_{3333} = c_{1111}$, $\sigma_{11} = \sigma_{33}$ and the symmetry of the elastic tensor $c_{3311} = c_{1133}$, relation (5.17) can be simplified to:

$$\frac{\eta_{3}^{\mathrm{film}}}{\eta_{3}^{\mathrm{grain}}} = 1+2\frac{c_{1122}}{c_{1111}}. \tag{5.18}$$

The steady state expansion of the thin film along the z direction will therefore be larger by a factor of $1+2\frac{c_{1122}}{c_{1111}}$ in comparison to a nanograin of the same isotropic or cubic material.

This outcome is identical to the results of the gedankenexperiment discussed in the supplementary material of article VII. Therein, we show that a continuous thin film will exhibit an apparently modified thermal expansion coefficient due to the absence of the in-plane expansion on ultrafast timescales:

$$\alpha_{\mathrm{uf},\perp}^{\mathrm{film}} = \alpha_{\mathrm{eq},\perp}^{\mathrm{film}} + 2\frac{c_{1133}}{c_{3333}}\alpha_{\mathrm{eq},\parallel}^{\mathrm{film}} \tag{5.19}$$

Considerations of the Poisson effect are occasionally included in the analysis of time-dependent strain responses[147, 276, 277], but I am currently not aware of a dedicated experimental investigation of its effect on the morphology-dependent strain response. The prefactor $2\frac{c_{1122}}{c_{1111}}$ that occurs in relations (5.18) is related to the Poisson ratio ν of isotropic or cubic materials via $\frac{\nu}{1-\nu} = \frac{c_{1122}}{c_{1111}}$. For most metals $\nu \approx \frac{1}{3}$, so that $2\frac{\nu}{1-\nu} = 1$. More specifically for cubic or isotropic materials where $\alpha_{\mathrm{eq},\perp} = \alpha_{\mathrm{eq},\parallel}$, one obtains that:

$$\alpha_{\mathrm{uf},\perp}^{\mathrm{film}} = \alpha_{\mathrm{eq},\perp}^{\mathrm{film}} + \alpha_{\mathrm{eq},\parallel}^{\mathrm{film}} = 2\alpha_{\mathrm{eq},\perp}^{\mathrm{film}}. \tag{5.20}$$

The presented considerations help to rationalize the trend in the steady state behavior at approximately 20 ps, where the thin FePt film exhibits an expansion, the free nanograins exhibit invar-behavior and the nanograins on a substrate exhibit a reduced expansion due to a partially constrained in-plane expansion. This is an interesting finding because it predicts that the expansion of homogeneously laser-excited continuous films will in general be different from their near equilibrium expansion, due to the clamped in-plane motion. This "Poisson correction" needs to be taken into account when the transient strain is used as a measure of the transient, laser-induced temperature change. One can furthermore conclude that invar-behavior upon equilibrium heating does not correlate with invar-behavior on ultrafast timescales when the in-plane dimensions exhibit nonzero thermal expansion behavior. Only if the corresponding Grüneisen coefficient vanishes can we expect invar behavior both in equilibrium and ultrafast experiments.

The presented qualitative argument raises the question whether it is possible to distinguish a contractive magnetic contribution in the out-of-plane stress $\sigma_{\perp}^{\mathrm{ext,mag}} < 0$ from an expansive electron or phonon pressure along the in-plane direction ($\sigma_{\parallel}^{\mathrm{ext,pho}} > 0$). More specifically, it is interesting to consider whether the transient contraction of the substrate-supported nanogranular FePt can be explained purely by an in-plane expansion driven by the anisotropic phonon stress. From an analytical point of view, in the equilibrium limit it is so that both contributions have the same effect since they result in an out-of-plane

expansion. The time-domain experiments discussed in article VI utilize the saturability of the magnetic stress and the timescale of the recovery of the magnetic order to distinguish both effects. A condensed presentation of the utilized double excitation approach is presented in section 5.3. Before that, I briefly discuss the effects that arise due to the partial transparency of the investigated FePt films, which are thinner than the optical penetration depth, in the next subsection.

5.2.2 Experimental effects in thin films

For the quantitative analysis of the pump-probe experiments it is relevant to know the reflection, absorption and transmission of the optical pump-pulse in the investigated thin films. To that end, we employ a numerical transfer matrix algorithm[156], that uses the complex refractive indices ($N = n + i\kappa$), which have been determined by Cen et al. [278] for similar granular and continuous FePt specimens via ellipsometry measurements. The results are summarized in figure 5.6, which also considers an estimate for the laser-induced temperature change:

$$\Delta T \approx \frac{F_\mathrm{a}}{dC}, \tag{5.21}$$

where d corresponds to the thickness of the FePt layer or particles, C to the heat capacity per volume and F_a to the absorbed laser fluence. F_a is reduced in comparison to the incident laser fluence F_in due to the partial reflection at the sample surface and partial transmission through the nanoscopic layer. Both effects are accounted for by the transfer matrix model that provides the fraction of the reflection R, the transmission T and the estimated absorption A as indicated in panels (a)-(c) in figure 5.6.

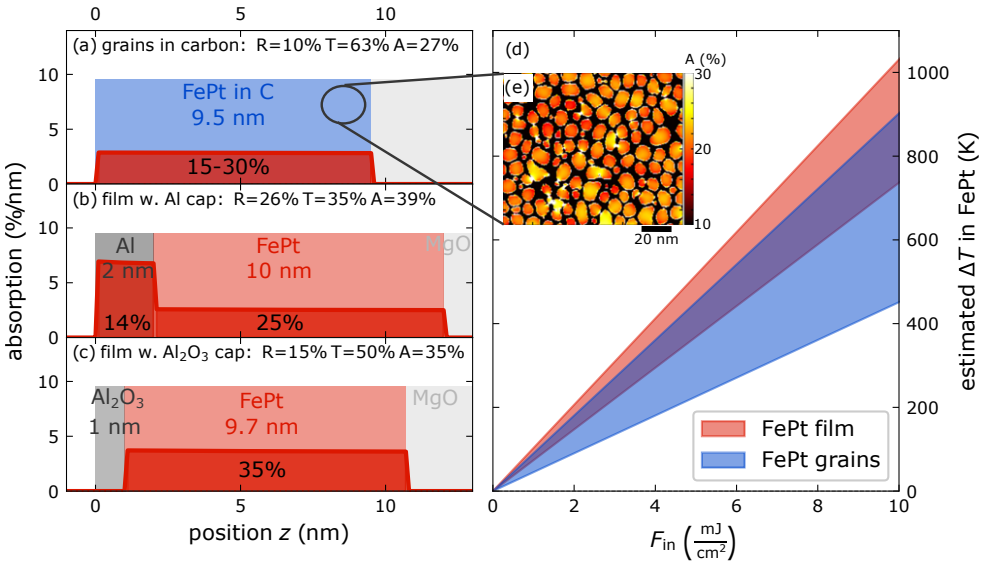

Figure 5.6: Scenarios for the absorption and laser-induced temperature change in FePt: The reflection transmission and absorption of two FePt specimen modeled by a transfer matrix model. (a) Granular FePt absorbs between 15 % - 30 % of the incoming light, depending on the grain size and proximity to other particles as discussed by Granitzka et al. [279] from which inset (e) is adapted. The continuous sample absorbs 25-35% of the incoming energy in FePt. The uncertainty results from the aluminum cap layer which was introduced in the sample growth process and would absorb approximately 14% of the incident energy as depicted in (b). Most likely, the metallic Al oxidizes to a thin non-absorbing Al_2O_3 layer as sketched in scenario (c) because we kept the sample at ambient conditions. The resulting estimate for the temperature change as a function of the incident fluence is depicted in (d). For a fluence of 8.5 $\frac{\mathrm{mJ}}{\mathrm{cm}^2}$, the transient temperature increase ΔT ranges from 930 - 1180 K in the FePt film and from 680 - 1060 K in the grains. Despite the large spread in temperatures, this laser fluence is so large that the FePt is close to or above the Curie temperature (≈ 750 K) in all scenarios so that a full demagnetization is expected.

The FePt grains exhibit an inhomogenous absorption that originates from their inhomogeneous growth and near field enhancement effects that occur when the nano-particles are closer together, as pointed out for example by Granitzka et al. [279] This results in the relatively large spread in the estimated absorption that ranges from 15% - 30%, which then translates to the uncertainty in the laser-induced temperature change. A systematic uncertainty in this estimation arises from the neglected temperature dependence of the heat capacity C that is used as a constant in relation 5.21. The temperature dependence of $C(T)$ is most pronounced close to the Curie temperature where the magnetic contribution increases.[280] However, the phonon contribution represents the largest fraction of the heat capacity and can be estimated to be nearly constant $\left(\approx 3.46\,\frac{\mathrm{J}}{\mathrm{m^3\,K}}\right)$ because the experiments are carried out above the Debye temperature $\Theta_{\mathrm{Debye}} \approx 230\,\mathrm{K}$.[280] The spin-specific heat capacity peaks at a value of approximately $\left(\approx 1.8\,\frac{\mathrm{J}}{\mathrm{m^3\,K}}\right)$ in a very narrow temperature region of approximately 20 K[77], so that the fraction of the energy, which is stored in the spin system is relatively small compared to the energy in the phonons.

The uncertainty in the absorption of the FePt film originates from the nominally $2\,\mathrm{nm}$ thick aluminum capping that is added during the growth process of the thin film sample. The absorption in FePt then varies between 25 % -35 % depending on the oxidation state of the Al-layer. The experiments that are discussed in the following are mostly carried out with a relatively high incident laser-fluence of $8.5\,\frac{\mathrm{mJ}}{\mathrm{cm^2}}$. The resulting ΔT ranges from 930-1180 K in the FePt film and from 680 - 1060 K in the grains, so that one can estimate a near complete demagnetization in both FePt specimen. A simple miscalculation led to a wrong value for the laser-induced temperature change of the thin film given in article IV, which we corrected by an erratum that is appended to the publication. For the given incident fluence of $6\,\frac{\mathrm{mJ}}{\mathrm{cm^2}}$ and an assumed absorption of 25 %, we attain a temperature change of approximately $\Delta T = 440\,\mathrm{K}$. The observed strain in the laser-excited FePt is approximately $4\cdot10^{-3}$, so that one observes an ultrafast expansion with an effective thermal expansion coefficient of approximately $\alpha_{\mathrm{uf}} = \frac{4\cdot10^{-3}}{440\,\mathrm{K}} \approx 9\cdot10^{-6}\,\frac{1}{\mathrm{K}}$. By inserting $\alpha_{\mathrm{eq},\perp} \approx 0$ and $\alpha_{\mathrm{eq},\parallel} \approx 10\cdot10^{-6}$ into relation (5.19) as the temperature-dependent characterizations suggest, and using that $\nu \approx \frac{1}{3}$, we attain $\alpha_{\mathrm{uf}} = \alpha_{\mathrm{eq},\parallel} \approx 10\cdot10^{-6}$, which is in reasonable agreement to the experimental value.

The partial transmission of the pump-pulses through the FePt layer results in a second, delayed excitation upon reflection of the light at the substrate-sample holder interface as illustrated in figure 5.7 (c) and (d). This figure also contains the refractive indices for each of the layers that are used in the modeling of the absorption process and the experimental strain signatures of the back-reflection. The arrival-timing of the back-reflection depends mainly on the thickness of the sample substrate. For the standard 0.5 mm thick MgO substrate, the back-reflection occurs approximately after 5 ps. To mitigate the effect of this back-reflection on the coherent strain oscillations, we added another 2 mm substrate with a non-polished backside during the experiments, which delays the reflection to approximately 25 ps after the initial pump and reduces its amplitude due the diffuse scattering of the laser light. A comparison of the two signals with and without the additional MgO layer is shown in figure 5.7 (a) and (b) for both specimen. This back-reflection is inherent to metallic films that are thinner than the optical penetration depth when they are grown on transparent substrates. Although it is often not stated explicitly, this back-reflection may be one of the reasons that studies of the ultrafast demagnetization in thin metallic films are frequently limited to the first 5 ps.[72, 281, 282] One has to be aware of its presence when planning and analyzing further experiments that aim to investigate the complete time trace of the de- and remagnetization process of laser-excited thin films.

Studies of the recovery process of the magnetization are also of importance when considering applications that aim to employ laser-based or laser-aided switching scenarios. The observed timescale will provide insights into physical limits of the achievable writing rate by all-optical switching, which may be limited by heat flow out of the laser-excited region if the writing process includes energy absorption.

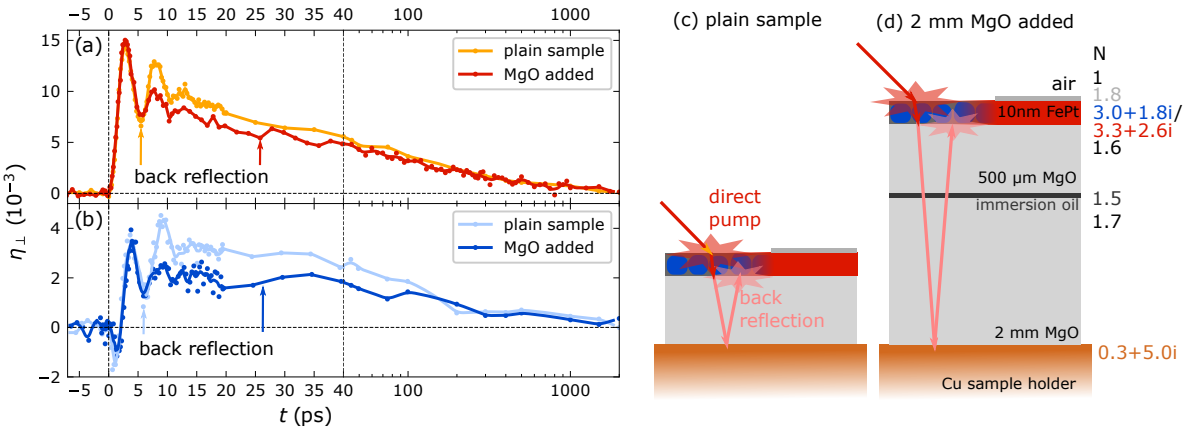

Figure 5.7: Signature and suppression of the back-reflection effect in thin FePt: The reflection of a pump-pulse from the backside of the sample occurs for (semi)-transparent films grown on a transparent substrate and leads to a second excitation. This effect is observed in our samples however, it can be modified by adding a second thicker substrate layer to induce a further optical delay. Arrows in (a) and (b) indicate the timing of the back-reflection for the two geometries with and without an additional MgO substrate that are depicted in (c) and (d) respectively.

Previous works that discuss the remagnetization have conducted qualitative and quantitative studies of the attained level of demagnetization and the remagnetization timescale depending on the temperature and fluence of the employed laser pulses.[85, 224, 283]. With article V, we add a comparison of the remagnetization process between the thin film and granular morphology of FePt to the literature discussion. Therein, we also observe the back-reflection and employ the additional MgO substrate with a rough backside to delay the second excitation to 25 ps and decrease its amplitude. This article V provides insights into the timescale of the remagnetization for both specimen that is important for the recovery of the magnetic stress on the lattice as discussed in article VI.

5.3 Identification of magnetic stress in a double-pulse experiment

This section presents the arguments for the identification of the spin stress contribution in FePt put forward in article V and article VI in a condensed form. While article V is dedicated exclusively to the remagnetization dynamics, article VI has a strong focus on the picosecond strain response of the granular FePt and touches only briefly on the transient magnetization. Furthermore, this section provides two additional graphic depictions from the finite element method (FEM)-modeling results presented in the paper I prepared after the publication of article VI to visualize and compare the simulation results directly.

In order to provide a survey of the time-dependent magnetization change that occurs during the UXRD-measurements, figure 5.8 shows the results of time-resolved magneto-optic Kerr effect (MOKE) experiments in the polar geometry for both FePt specimen. The experiments have been carried out in our group by Lisa Willig in close coordination with me and technical support by Jan-Etienne Pudell. A detailed description and analysis of the FePt results is available in chapter 5 of Lisa Willig's PhD thesis[284] from which parts of the data are published in article V. The excitation conditions of the reported experiments are chosen to reproduce the conditions of the subsequently discussed UXRD experiments. The data shown in figure 5.8 have been acquired using p-polarized 130 fs short pump laser pulses at a central wavelength of 800 nm with a repetition rate of 1 kHz and an incident fluence of 8.5 $\frac{\mathrm{mJ}}{\mathrm{cm}^2}$. The pump-diameter of 1 mm and the probe diameter of 0.3 mm are relatively large in comparison to experiments that employ microscope objectives for focusing the beams on the sample, but they closely resemble the probing conditions at the

PXS-setup. The field-dependent polarization rotation of the frequency-doubled 400 nm probe-pulses is detected on a shot to shot basis using a balanced photo diode and a mechanical chopper that allows for the signal subtraction between the excited and unexcited sample.

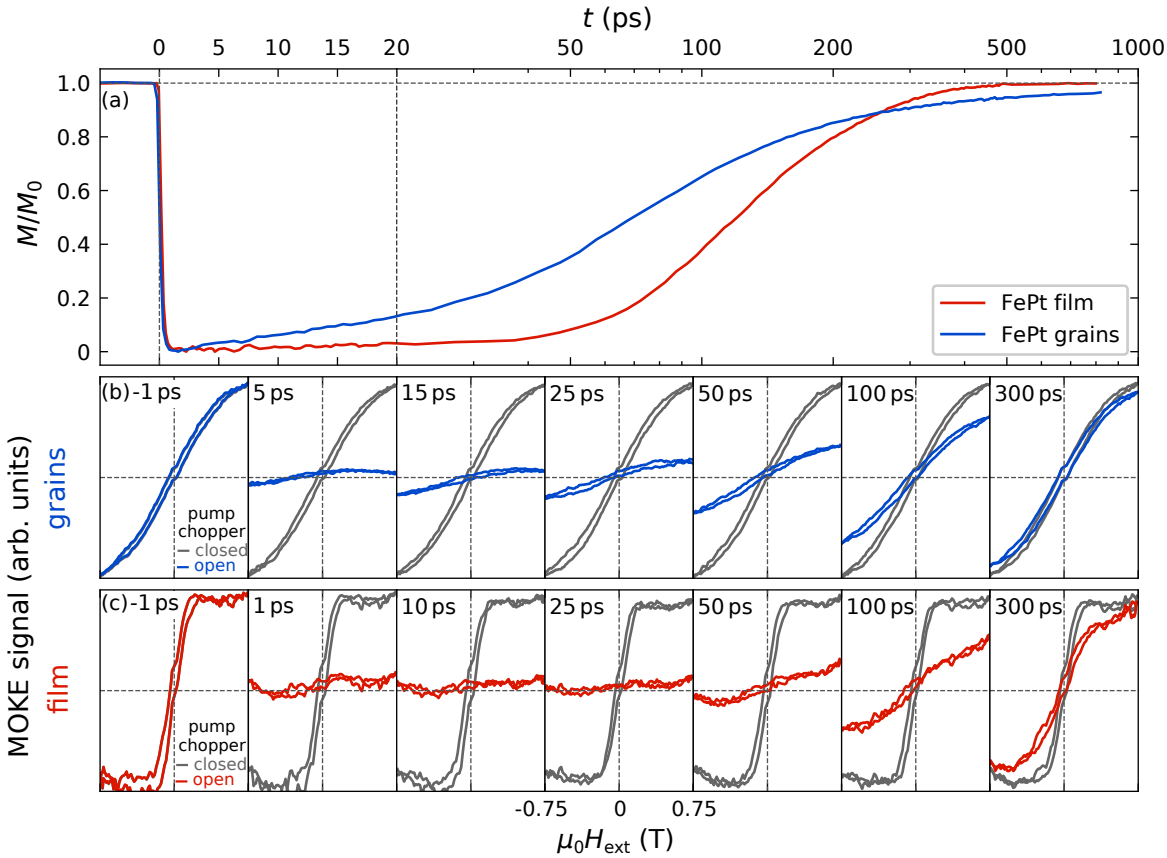

Figure 5.8: Timeresolved MOKE signal of granular and continuous FePt specimen: Panel (a) compares the extracted laser-induced magnetization change from time-resolved polar MOKE measurements using an excitation fluence of 8.5 $\frac{\text{mJ}}{\text{cm}^2}$ with an applied external field of $\mu_0 H_{\text{ext}} = 0.75\,\text{T}$. This depiction allows for a qualitative comparison of the morphology-dependent remagnetization, which is initially faster for the FePt grains, whereas the thin film takes longer to start the remagnetization processes. For t>100 ps, we observe a faster recovery of the thin film magnetization as compared to the grains. For the granular FePt, one observes that 30 % of its magnetization has recovered at 50 ps and approximately 80 % after 200 ps. The corresponding MOKE hysteresis loops that are acquired at different delays of the 400 nm probe pulse are depicted in row (b) and (c) for the granular and continuous FePt specimen respectively. They outline the possibility of laser-assisted switching of the FePt nano-grains and the transient, laser-induced change of the hysteresis that is also used in the HAMR-process.

The presented data in figure 5.8 provide insights into the remagnetization process of FePt. The reported laser-induced demagnetization in FePt occurs with a timescale of approximately 150 fs [122, 279, 282], but the spatial distribution of the demagnetization within the grains and the transient state as well as the underlying demagnetization mechanisms remain current research topics.[285–288] In the here reported tr-MOKE experiments, the demagnetization appears almost as a step-like magnetization drop for both specimen. We focus on the subsequent remagnetization behavior that is initially faster for the granular FePt, whereas the thin film FePt remains in the demagnetized state for approximately 35 ps before the remagnetization sets in. The magnetization recovery can not be captured by a single exponential function but the majority of the magnetization ($\approx 80\,\%$) recovers within the first 200 ps for both specimen. The remaining 20 % of the magnetization are observed to recover faster for the continuous FePt as compared to the granular FePt.

These observations are rationalized in article V by considering the underlying thermal transport. For the granular FePt specimen, the initial remagnetization is thought to occur faster because heat can be quickly dissipated to the adjacent, less absorbing carbon matrix and a larger proportion of the surrounding substrate. The cooling of FePt in the homogeneously excited thin FePt film will however be purely one-dimensional towards the depth of the substrate. The energy that is initially transferred to the carbon matrix will however slow down the cooling process of the FePt grains as the energy flow out of the carbon matrix towards the substrate requires more time. This scenario would explain the observations; however, it would require selective probes of the temperature of the carbon matrix and the surface of the MgO interface to experimentally confirm it. For the analysis of the time-dependent spin-stress contribution, it is sufficient to know that the magnetization of the investigated specimen recovers within the first 200 ps.

Given the time-dependent magnetization change upon femtosecond laser-excitation, one can turn to a detailed experimental analysis of spin-stress contribution to the strain response of FePt. The experimental novelty of the work presented in article VI lies in the two-pulse excitation experiment, which is employed to extract the presence of a spin-stress contribution to the lattice dynamics in the FePt grains. Its principle and the main results are depicted in figure 5.9. In the two-pulse scenario, a first pulse (p_1) is used to transiently demagnetize the sample, whereas the second pulse (p_2) launches the strain response of a partially or fully demagnetized state at a delay Δt, (see inset (d)). The difference between the strain response when both pulses are present ($\eta_1 \& \eta_2$) and the strain response of only the first pulse (η_1) can be compared to the strain response of the action of only the isolated second pulse (η_2). If the fluence of p_1 is set to 8.5 $\frac{\mathrm{mJ}}{\mathrm{cm}^2}$, one observes that the initial contraction that p_2 induces changes to an expansion because p_1 has close to completely demagnetized the sample at $\Delta t = 13$ ps earlier. The experiment is carried out using a Michelson interferometer so both pump-pulses and the X-ray probe pulses are derived from the same laser and thus inherently synchronized and the time-overlap is determined as described in chapter 3. By varying Δt, one observes a recovery of the initial contraction within the first 3 ps of η_2. The observed behavior indicates the presence of a contractive spin stress, which is saturated by the first pulse p_1 and recovers on a 100 ps timescale. Panel (c) in figure 5.9 compares the effective strain signatures of p_2 in the presence of p_1 i.e., $(\eta_1 \& \eta_2 - \eta_1)$ with the strain signature η_2 of p_2 only for different Δt between the two pump-pulses. A gradual recovery of the initial contraction with increasing Δt is observed.

As a cross-check, I conducted the same experiment where p_1 has a reduced fluence of 4.2 $\frac{\mathrm{mJ}}{\mathrm{cm}^2}$, which is not sufficient to completely demagnetize the grains (see article V). In this scenario, one observes that the second pulse induces a very similar initial contraction that is only slightly reduced by the presence of p_1 as shown in figure 5.9(b). The observed behavior can be rationalized by a negative, anisotropic Grüneisen parameter of the spin system in FePt in combination with the finite amount of energy that is available to spin-excitations. In the high fluence scenario, the pump pulse saturates the energy reservoir provided by spin-excitations, so that the second pulse excites almost exclusively electron and phonon degrees of freedom which do not exhibit a saturation as long as the film does not melt. As the FePt grains cool by transferring energy to the substrate and the adjacent carbon atoms, the spin-order recovers so that the second pulse transfers again a fraction of its energy into the magnetic excitations, which then contribute a contractive out-of-plane stress. The experiments have been carried out in remanence of the FePt grains without an applied magnetic field. However the "up" or "down" orientation of the magnetization of the grains does not influence the spin stress contribution since the relevant magneto-elastic contribution to the free energy density is only proportional to the square of the out-of-plane magnetization ($F \propto b_1 \eta_{zz} m_z^2$). An analysis of the Grüneisen parameter of the spin-excitation is provided in article VI.

It is interesting to note that even for the nearly completely demagnetized state, the FePt grains react differently compared to the thin film, which expands almost instantaneously. They exhibit a reduced and delayed expansion as seen in figure 5.9. This is an indication of the concurrent in-plane expansion that

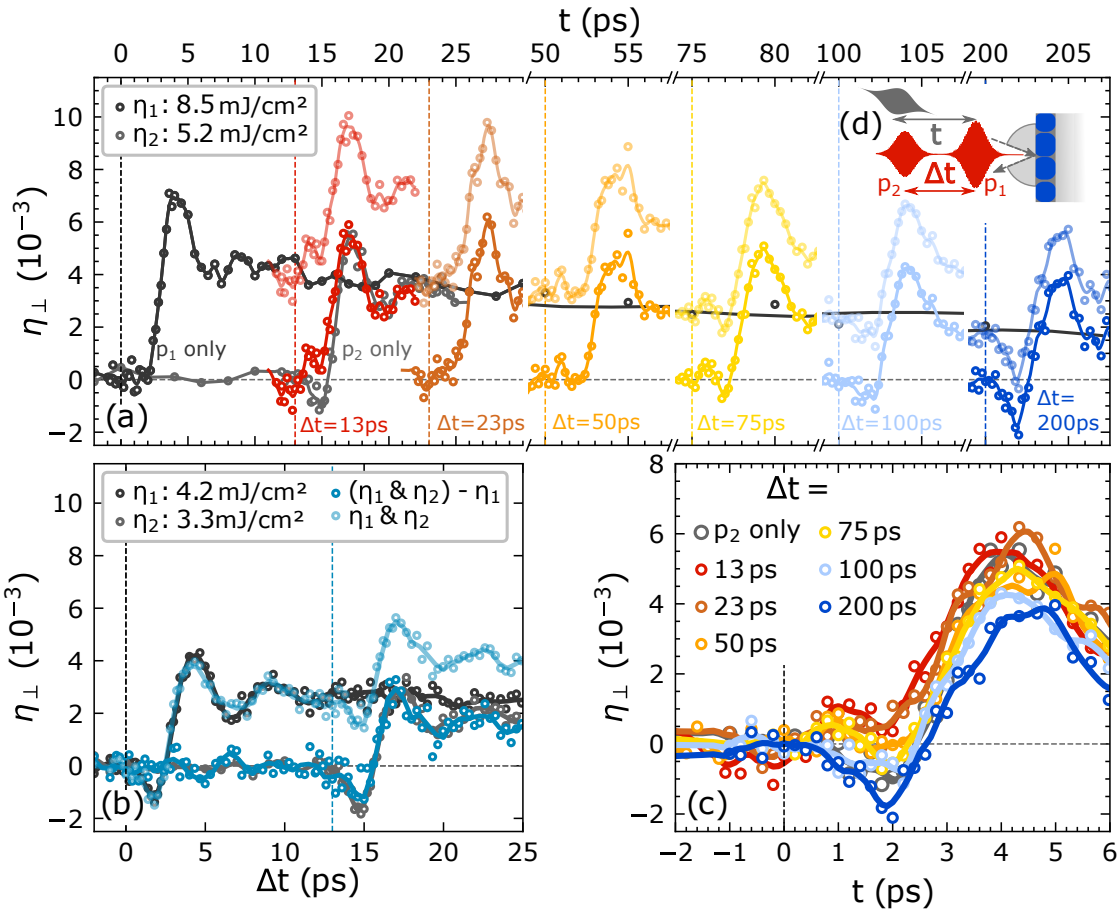

Figure 5.9: Time series of the two pulse excitation in FePt grains: Panel (a) shows the average out-of-plane strain response for the granular FePt sample subjected to two excitation pulses (p_1 and p_2) with a fixed fluence of 8.5 $\frac{\text{mJ}}{\text{cm}^2}$ and 5.2 $\frac{\text{mJ}}{\text{cm}^2}$ respectively and their combined strain response ($\eta_1 \& \eta_2$) in light colors. A schematic sketch of the double-pulse experiment with two pump-pulses at a delay Δt and the X-ray probe-pulse with delay t is shown in inset (d). Vertical dashed lines indicate the arrival-time of the second pump pulse at the sample. The fluence of p_1 is chosen to achieve a transient, nearly completely demagnetized state of the FePt grains as calibrated by MOKE experiments under comparable excitation conditions (see article V). The extracted effective contribution of the second pulse for different Δt ($(\eta_1 \& \eta_2) - \eta_1$) is shown by the bold colored data and lines in (a), which are shifted in time by Δt for direct comparison in panel (c). This shows the gradual recovery of the initial contraction. Panel (b) displays the results of the same type of experiment as panel (a) except for a lower fluence where p_1 does not completely demagnetize the FePt grains and p_2 consequently induces a contraction. Solid lines are spline interpolations to the depicted data points that serve as guide to the eye.

leads to an out-of-plane contraction as discussed in section 5.2.1.

A model for the time- and space-dependent coupled in-plane and out-of-plane motion in response to a given stress provides further insights beyond the average observables that are accessible in UXRD experiments. To that end, we discussed the modeling with Aurélien Crut from the Institut Lumière Matière in Lyon, who set up an FEM model that solves the general equation of motion (5.5) in a cylindrical FePt grain with different boundary conditions. Although some technical details of the modeling are presented in article VI and its supplementary, I would like to outline the time-dependent stress contributions to σ^{ext} that drive the time-dependent displacement and strain response in FePt. The numerical solution of the elastic wave equation for the different boundary conditions provides the potentially complex, but deterministic response to the driving stress, which contains the physical insights into the light-matter interaction and subsequent energy flow.

The total stress (σ_{tot}) consists of contributions from excited electrons (σ_{e}), phonons (σ_{ph}) and spin excitations (σ_{sp}) that may have different amplitudes, time- and directional dependencies. Building on the insights by Reid et al. [122], we know that the phonon stress is anisotropic, with a larger in-plane stress than out-of-plane contribution. The magnetic stress of the FM-PM phase transition has been found to decrease the c/a axis ratio in FePt, so that we approximate it as uniaxial contractive stress along the out-of-plane direction. The electronic stress and the magnetic stress are modeled to rise instantaneously because the laser-excitation and subpicosecond demagnetization are short in comparison to the picosecond strain response. We could attain a qualitative agreement of the resulting strain response by a three times larger in-plane phonon stress in comparison to the out-of-plane phonon stress. For simplicity, we use the same anisotropy in the electronic stress contribution and combine both expansive contributions as electron-phonon stress ($\sigma_{\mathrm{e-ph}}$). As the electronic excitations relax, they transfer their energy to the phonon system. For the electron-phonon energy transfer, we assumed a coupling time of 1 ps, which is a typical time-scale for this relaxation process in metals. To obtain a qualitative agreement with the data we need to assume a three times larger Grüneisen parameter for the phonon system as compared to the electron system so that the combined $\sigma_{\mathrm{e-ph}}$ rises within the first three picoseconds, whereas the contractive spin-stress is captured by a step function of variable amplitude A^{sp}. A^{sp} serves as a parameter for modeling the different levels of spin-stress contribution. We used the same model for the laser-induced stresses $\sigma_{\mathrm{e-ph}}$ and σ_{sp}. The total out-of-plane stress σ_{tot} varies between the morphologies due to the different in-plane constraints that result in the varying transverse Poisson stresses although we use the same parameters for $\sigma_{\mathrm{el-ph}}$ and σ_{sp}.

Figure 5.10 depicts the time-dependent stresses and the resulting strain response for different amplitudes of the spin stress. Panels (a)-(c) present the FEM-modeling results, which are compared to the experimental signatures shown in panels (d)-(f). For the thin-film morphology, we observe that the total expansion normalized to the incident-laser fluence exhibits a slightly delayed rise in the low fluence case when compared to high excitation fluences. This behavior is captured by the FEM-simulations when the relative contribution of the spin stress to σ_{tot} is decreased. The free grain exhibits a strong, direct contraction due to the dominant role of the in-plane expansion that is observed in the experiments on the FePt grains on the TEM grid[122]. The intermediate case of the grains on a substrate exhibits an initial expansion when the magnetic stress contribution is absent and a transient contraction when it is present. The subsequent total expansion is systematically underestimated due to the lacking energy transfer to the carbon matrix that would add an in-plane compression. The simulated strain oscillations continue because the size and shape distribution of the different FePt grains is so far not included.

One advantage of the FEM-model solution to the coupled elastic wave equations is that the coupling between the in-plane and out-of-plane motion is not a free, phenomenological parameter but determined by known elastic properties of FePt. It furthermore provides information on the local displacement

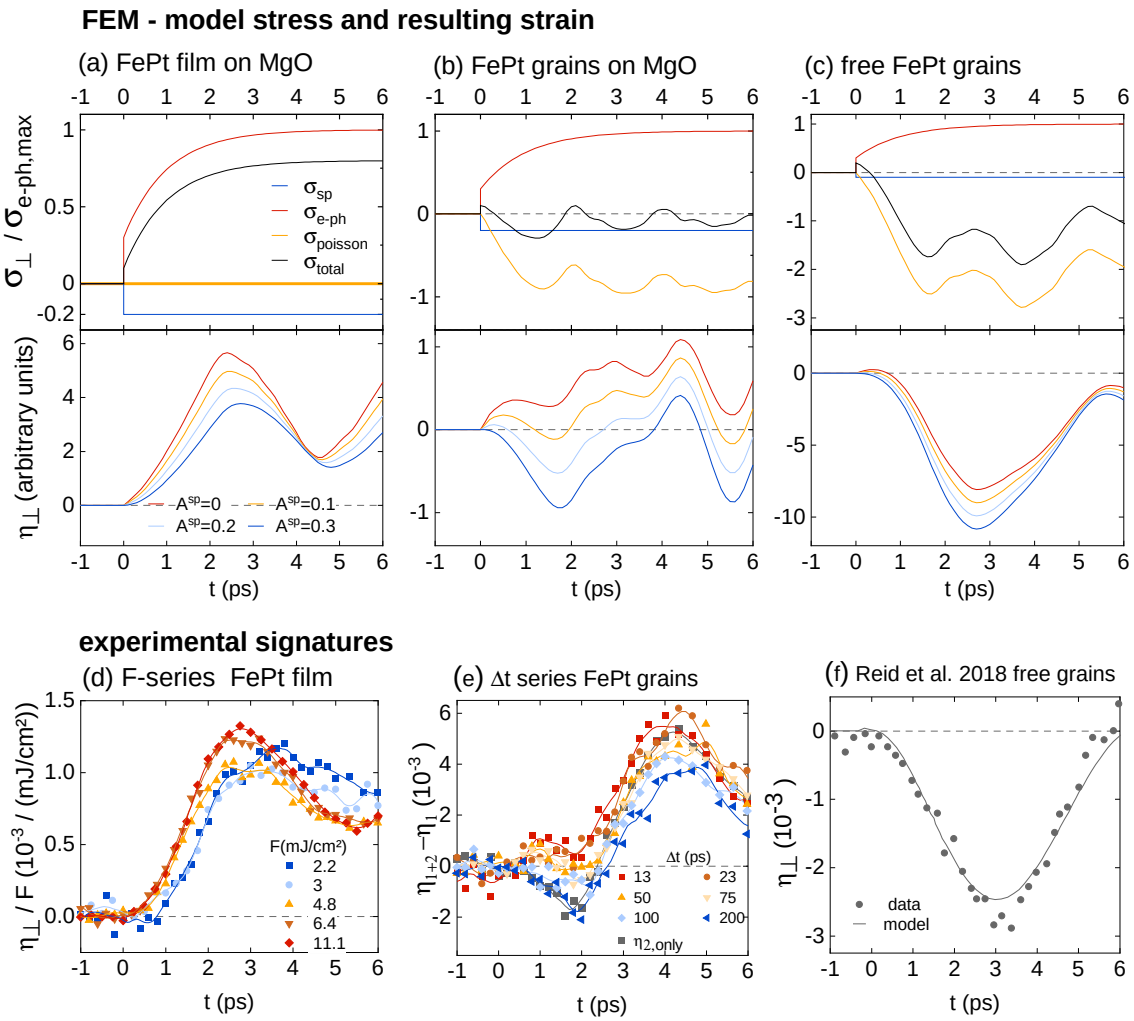

Figure 5.10: FEM-simulation results compared to experimental signatures: Panels (a)-(c) show the stress contributions in FePt for different boundary conditions (top-panels) and the simulated strain response for different amplitudes of the magnetic stress. In the simulation the FePt is subjected to the same time-dependent, anisotropic expansive electron-phonon stress and contractive spin-stress but reacts differently depending on the different boundary conditions. The in-plane motion adds an additional transverse Poisson stress to the total stress that drives the out-of-plane motion of the FePt particles. The strain response is modeled for different amplitudes A^{sp} of the spin stress in relation to the electron-phonon stress amplitude. An increase of the relative contribution of the magnetic stress to the total stress leads to a decreased strain amplitude and a shift of the maximum strain level as it is experimentally observed in a thin-film fluence series shown in (d). When the in-plane motion is not constrained the simulation predicts a direct contraction along the out-of-plane direction as experimentally observed by Reid et al. [122] as shown in (f). The initial contraction with a delayed expansion observed in the Δt-series of the two-pulse experiments shown in (e) is also approximately obtained in the simulation. The level of expansion is systematically underestimated because the increasing stress upon energy transfer into the carbon matrix is not contained in the simulation. An overall qualitative agreement with the experimental signatures is obtained for the same time-dependent electron-phonon and spin stress contribution that is only altered by the different in-plane constraints.

field within the modeled nano-particle for each instant and can accommodate different elastic boundary conditions. Figure 5.11 provides the snapshots of the vibrating FePt nanoparticles and the local out-of-plane strain field for the case of $A^{\mathrm{sp}} = 0.2$. To interpret this depiction correctly, it is important to be aware of the cylindrical symmetry and the used elastic constraints that are indicated schematically in the first column for each morphology.

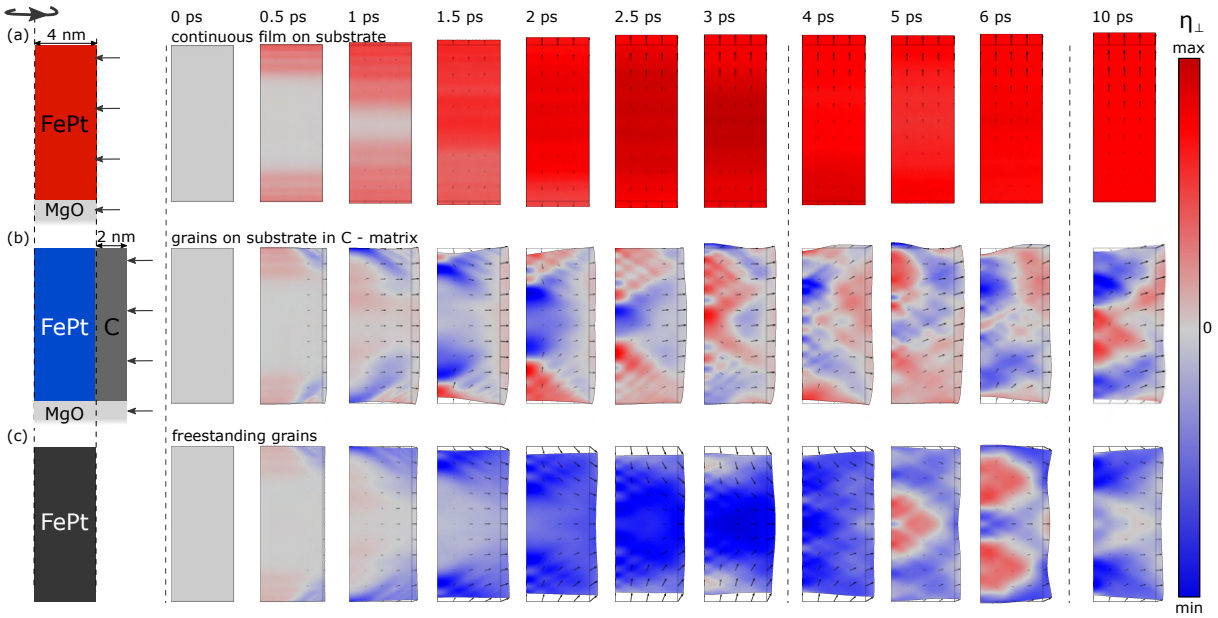

Figure 5.11: Spatio-temporal depiction of the modeled out-of-plane strain according to the FEM-simulation: Temporal snapshots of the strain distribution within cylindrical FePt sections for the three different boundary conditions where the corresponding in-plane constraints are indicated by arrows in the sketches shown in the first column. The cylindrical symmetry is used to reduce the computational costs and the color code depicts the out-of-plane strain $\eta_\perp$: (a) for a continuous thin film where the in-plane motion is constrained (b) for FePt nanograins embedded in a compressible carbon-matrix on a substrate and (c) for free-standing FePt grains. The small, overlaid arrows indicate the local displacement field ($\vec{u}$). While the continuous film expands along the out-of-plane direction, the free-standing grains expand mainly in-plane, which leads to an out-of-plane contraction by transverse strains. It can be seen that the response of the free grains in (c) is highly symmetric, but this symmetry is partially broken in the intermediate case (b) by the attachment of the grains to the MgO substrate.

The reported experiments in this chapter and the corresponding articles demonstrate a morphology-dependent strain response in magnetic nano-particles where the spin stress contribution is one effect among other stress contributions. Its presence can be identified by its saturability and the timescale of the magnetization recovery. To that end, I have applied a two-pulse excitation scheme that may be versatile for identifying stress contributions in various kinds of phase transitions with a finite heat capacity. For example, we have recently identified a magnetic stress contribution in the strain response of the ferromagnetic perovskite material strontium ruthenate ($SrRuO_3$) (SRO).[230]

CHAPTER SIX

Giant magnetic strains in dysprosium

In this chapter, I discuss the lattice dynamics of dysprosium (Dy) which exhibits giant magnetostriction, i.e. strains upon magnetization that are in excess of 10^{-3}. In the class of heavy rare-earth materials, I observe that the magnetic stress contribution can dominate the strain response of laser-excited materials. This chapter treats laser-induced strains in heterostructures that contain a heavy rare-earth layer as an opto-acoustic transducer. It discusses unpublished data on the effect that external magnetic fields have on the strain response of a Dy thin film, which go beyond the ideas presented in article VIII, article IX and article VII. The influence of an external magnetic field on the lattice response is pronounced at the metamagnetic ferromagnetic (FM) to antiferromagnetic (AFM) phase transition of dysprosium, which has not been discussed in the publications and may lead to the possibility of manipulating picosecond strain pulses. The last section shows results of the two-pulse excitation scheme that I used to investigate the spin stress in FePt in the previous chapter. It demonstrates that the magnetostriction could be used as a proxy for the recovery of magnetic order. Given a sufficient sensitivity for the strain, the detection of magnetostrictive effects is expected to be applicable regardless of the type of magnetic order. Thus, it can be used in antiferromagnets that exhibit no net magnetization and consequently no MOKE or X-ray circular magnetic dichroism (XMCD) contrast. Although this chapter explicitly discusses results on Dy, it is important to understand that other heavy rare-earths such as gadolinium (Gd) and holmium (Ho) exhibit a very similar ultrafast strain response that can be analyzed using the same concepts as we have shown in article X and article XI.

6.1 Static properties of heavy rare-earth elements

The laser-induced lattice dynamics of a thin Dy film, that are presented in the following, serve as a representative for the class of magnetic heavy rare-earth materials ${}_{64}\mathrm{Gd}$ - ${}_{69}\mathrm{Tm}$. A recent, very brief introduction to the properties and applications of rare-earth materials is given by Zhou and Fiete.[289] The trends in the properties of rare-earth materials are closely related to their electronic structure that is given by the subsequent filling of the $4f$-orbitals across the lanthanide series. The electronic structure of rare-earth elements is of the type $[\mathrm{Xe}]4\mathrm{f}^{\mathrm{n}}5\mathrm{d}^{1}6\mathrm{s}^{2}$ or $[\mathrm{Xe}]4\mathrm{f}^{\mathrm{n+1}}6\mathrm{s}^{2}$, where the number n of electrons in the $4f$-orbitals increases from $n = 0$ to $n = 14$ from Lanthanum (${}^{57}\mathrm{La}$) to Lutetium (${}^{71}\mathrm{Lu}$). The $4f$-electrons are localized close to the nucleus so that the crystal field of the surrounding atoms is shielded by the 5*d*6*s* valence states that the rare-earth atoms have in common. Due to the comparable valence electron structure, the rare-earth materials exhibit similar chemical properties, so that these elements can often be used interchangeably in compounds and alloys. The magnetic moment per atom and the type of magnetic order varies considerably across the lanthanide series. The combination of various magnetic properties with similar chemical properties makes this material class an interesting testbed for theories in magnetism

and the influence of magnetic order on other material characteristics.

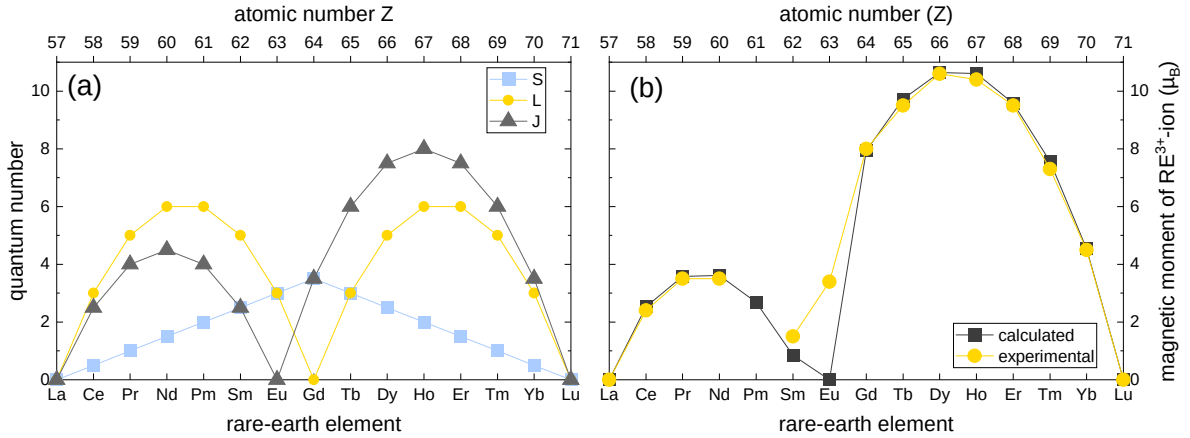

Figure 6.1: Magnetic moments in rare-earth materials (a) Spin- (S), Angular- (L), and combined (J)- quantum numbers according to Hund's rules for the increasingly occupied $4f$-orbitals in the lanthanide series. Panel (b) shows a comparison between the predicted total magnetic moment μ_J for the corresponding rare-earth ions (RE^{3+}) with the experimental observation. Experimental values are reproduced from the book by Groß and Marx [33, chapter 12] and the depiction is adapted from [289].

Due to the electronic screening effect of the valence electrons, the behavior of the $4f$-shell electrons in the lanthanids is well described by Hund's rules that are originally derived for isolated atoms. The resulting angular momentum quantum numbers of the spin-contribution (S), orbital moment contribution (L) and the combined angular moment (J) are depicted in figure 6.1(a). Graph 6.1(b) provides an overview of the resulting magnetic moment per atom for the rare-earth elements. The predicted total magnetic moment μ_J of the ground state is related to S, L and J via the Landé g-factor g_J. It is approximated by:

$$\mu_J = -g_J \mu_B \sqrt{J(J+1)} \tag{6.1}$$

$$\text{with}: \; g_J = 1 + \frac{J(J+1) + S(S+1) - 2L(L+1)}{2J(J+1)}. \tag{6.2}$$

Details and derivations of Hund's rules and definitions of the gyromagnetic ratio are given in solid state[33, 45] and magnetism textbooks[214, 220]. Considering figure 6.1, it is interesting to note that the elements Ho and Dy exhibit the largest magnetic moment per atom of all existing elements and that the magnetic moment in gadolinium originates purely from spin-contributions ($J = S$) with no orbital contribution due to the half filled $4f$-shell ($L = 0$). The good agreement between the experimentally observed magnetic moments and the prediction by Hund's rules is an interesting feature that distinguishes magnetically ordered lanthanides from the ferromagnetic $3d$-elements Nickel (Ni), Iron (Fe) and Cobalt (Co). While the magnetic moment of the $4f$-orbitals is large and localized close to the nucleus, the magnetic moments in the $3d$-elements are carried by the valence-band electrons, which are strongly influenced by crystal field effects of the neighboring atoms. These crystal field contributions are dominant for the alignment of the spin-moments of the light $3d$-elements, whereas spin-orbit interactions are strong for the relatively heavy ($Z > 56$) rare-earth elements.[33, 289] The energy contribution due to the spin-orbit coupling is in general proportional to Z^4, where Z is the atomic number.[220] A relevant consequence of the strong spin-orbit interaction in the heavy rare-earth elements is the large magneto-crystalline anisotropy energy. A large-magneto-crystalline anisotropy has also been observed in FePt, where the heavy element Pt ($Z = 78$) provides the strong spin-orbit coupling and Fe the magnetic moment of approximately $2.15\,\mu_B$ per atom. The strong-spin orbit coupling provides a link between the structural

degrees of freedom and the spin degrees of freedom. The orientation of the electronic orbits shape the crystal field that is responsible for bond-angles and interatomic distances, that are therefore coupled to the orientation of the magnetic moments.

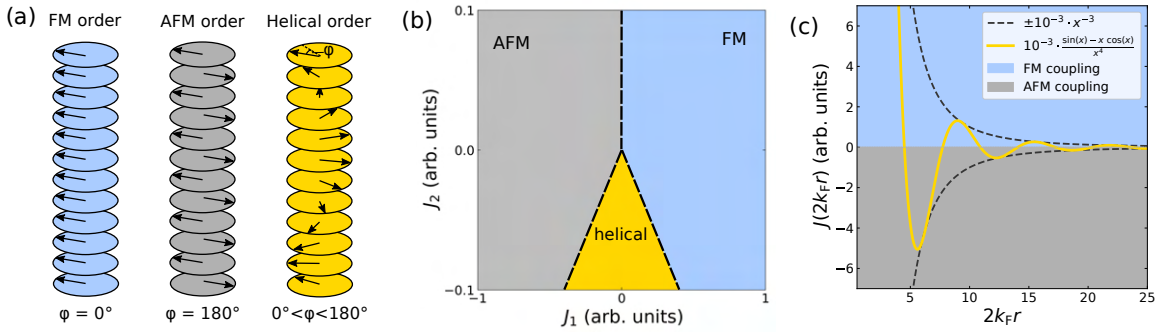

Figure 6.2: Conditions for helical magnetic order: (a) Sketch of different types of magnetic order in a magnet with an in-plane easy axis. (b) Phase diagram of the types of magnetic order in the simplified picture of two different exchange energies J_1 and J_2 for the nearest and next-nearest neighbor interaction. Panel (c) depicts the distance-dependent exchange coupling of an RKKY-interaction between a localized, point-like magnetic moment embedded in a free electron gas with the Fermi wave vector k_F. This depiction is adapted from chapter 5.4 of the book of Blundell[46].

It is not only the magnetic moment per atom that varies within the lanthanide series but also the type of magnetic order. Figure 6.3 provides a schematic overview over the magnetic phases and temperature-dependent lattice constants reported in the literature for the heavy rare-earth elements. The different magnetic orders result from an interplay of both magnetic and structural properties. The heavy rare-earth elements exhibit FM order as well as different types of helical antiferromagntic order. The large and localized magnetic moments of the rare-earth atoms add to a finite magnetization in the FM phase, whereas the net-magnetization in the helical AFM phase is zero. To rationalize the type of collective magnetic ordering, one has to consider the interaction between neighboring magnetic moments. The following simplified discussion of the exchange energy corresponds to the arguments given in the book of Blundell [46, chapter 5.4]. It starts from the commonly used Heisenberg exchange Hamiltonian that describes the interaction energy between neighboring magnetic moments $\vec{S}_i$ and $\vec{S}_j$ that are located at a distance r_{ij}. In the absence of an external field, it can be written as:

$$H = -\sum_{ij} J_{ij}(r_{ij}) \vec{S}_i \cdot \vec{S}_j, \tag{6.3}$$

wherein $J_{ij}(r_{ij})$ is the distance-dependent magnetic exchange energy. For specific calculations, it is useful to consider that the heavy rare-earth elements Gd, Tb, Dy and Ho exhibit a magneto-crystalline anisotropy such that the in-plane directions are easy axes. The magnetic moments are localized in layers that correspond to the (0001)-lattice planes of the hexagonally close packed (hcp) unit cell, so that the main degree of freedom for the magnetic order is the interlayer angle ϕ between the magnetic moments in subsequent lattice planes. To understand the occurrence of a helical magnetic order in such a geometry, it is sufficient to consider only the interaction between the next- and next-next-nearest neighbors. With these simplifications, one can express the exchange interaction energy E_{ex} and find the conditions for a minimum via $\frac{\partial E}{\partial \phi} = 0$ as follows:

$$E_{ex} = -2NS^2(J_1 \cos(\phi) + J_2 \cos(2\phi)) \tag{6.4}$$

$$\Rightarrow 0 = \sin(\phi)(J_1 + 4J_2\cos(\phi)) \Rightarrow \begin{cases} \phi = 0 & \text{FM order} \\ \phi = \pi & \text{AFM order} \\ \cos\phi = -\frac{J_1}{4J_2} & \text{Helical order if } |J_1| < 4|J_2| \text{ and } J_2 < 0 \end{cases} \tag{6.5}$$

The variables N, S and ϕ in relation (6.4) correspond to the number of magnetic moments per plane, the absolute value of the localized magnetic moments and the expectation value of the interlayer turn angle between the magnetic moments respectively. ϕ is also defined in figure 6.2(a) that schematically depicts the different types of magnetic order. Ferro- and antiferromagnetic order occur, when the first factor ($\sin\phi$) in (6.4) is zero depending on the sign of J_1. The case of helical order occurs when both conditions $J_2 < 0$ and $|J_1| < 4|J_2|$ are met i.e., the second factor in relation (6.4) is zero. The resulting phase diagram for this idealized case is shown in figure 6.2(b). It is not required that the helical turn angle is commensurate with the interlayer spacing of the atomic layers.

A crucial ingredient for the occurrence of a helical spin order is the distance-dependent exchange energy $J(r)$. The rare-earth elements exhibit such an interaction, which originates from the combination of large, but localized, magnetic moments of the $4f$-electrons and the delocalized $5d6s$-valence electrons. The spatial overlap between the electron wavefunctions in the $4f$-orbitals between the atoms is very small so that the direct exchange interaction can be neglected. The spin-polarization of the surrounding (5d6s)-valence electrons provides a mechanism for the indirect coupling of the localized magnetic moments on adjacent lattice sites. This situation can be approximated with a point-like magnetic moment embedded in a free-electron gas. This simplified model is known as the RKKY-interaction named after Ruderman, Kittel, Kasuya and Yosida[295–297] and was initially conceived to study the influence of nuclear magnetic moments embedded in a free electron gas.[295] The RKKY model results in an oscillating real space magnetic susceptibility $\chi(r)$:

$$\chi(r) = \frac{2k_F^3\chi_P}{\pi} F(2k_F r) \tag{6.6}$$

$$\text{with} \quad F(x) = \frac{\sin(x) - x\cos(x)}{x^4} \propto -\frac{\cos(2k_F r)}{r^3} \text{ for large r} \tag{6.7}$$

with a radial dependence that is plotted in figure 6.2(c). The oscillation originates from the fact that the paramagnetic (PM) susceptibility $\chi(k)$ in a Sommerfeld model is wavevector-dependent and decreases for $k > 2k_F$ so that highly localized, magnetic disturbances are not perfectly screened by the surrounding free electron gas.[46] The Fourier-transformed, real-space magnetic susceptibility $\chi(r)$ of the electron gas then oscillates in the vicinity of the disturbance, which translates into a distance-dependent effective exchange coupling $J(r)$, that falls off with $1/r^3$. The RKKY interaction between localized magnetic moments, embedded in delocalized electron gas, corresponds to the Friedel oscillations in the electron density around a localized charge.[46] This RKKY interaction is only an idealized model because the magnetic moments in the $4f$-orbitals are not perfectly localized and the $5d6s$ electrons have a band-structure that deviates from the quadratic dispersion of a free electron gas. Calculations of the rare-earth bandstructures find that the resulting $\chi(k)$ has its maximum at $k = 0$ for the c/a ratio in $_{64}$Gd, whereas it shifts to a finite $k > 0$ for smaller c/a-ratios that are realized in the hexagonal unit cells of the other heavy rare-earth materials $_{65}$Tb-$_{69}$Tm.[294] A maximum in $\chi(k)$ at $k = 0$ corresponds to FM order, whereas a maximum of $\chi(k)$ at $k > 0$ corresponds to a helical AFM state with a spatial period $\lambda = 2\pi/k$. The decreasing c/a-ratio in the rare-earth series is called lanthanide contraction and results from the imperfect shielding properties of electrons in the $4f$-orbitals so that the $5d6s$-valence electrons are located closer to the core.[294] This relation between the inter-atomic spacing and the resulting different types of magnetic order already

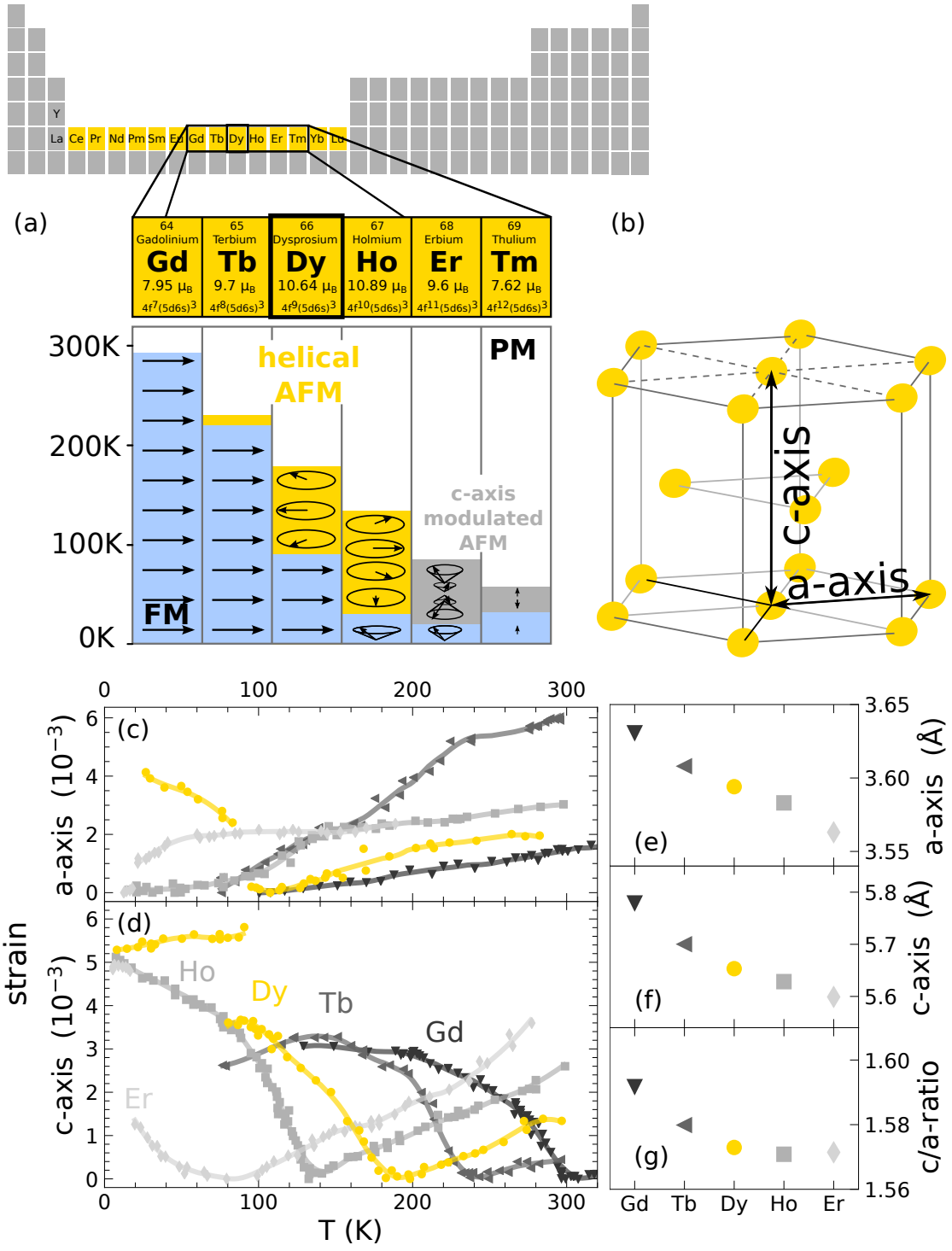

Figure 6.3: Overview of relevant properties of the heavy rare-earth elements $_{64}$Gd - $_{68}$Er: (a) zoom into the lanthanide series of the periodic table that includes the magnetic moment per atom, the electron configuration and a sketch of the different temperature-dependent magnetic orderings of these elements adapted from the thesis of Holger Ott.[290] (b) Schematic depiction of the hexagonally close packed (hcp) - unit cell that is the building block of the crystal lattice of the heavy rare-earths. Panels (c) and (d) summarize the temperature-dependent strain of the a- and c-axis of this unit cell for bulk specimen as reported in the literature by Darnell et al. [291–293] (solid lines added as guide to the eye). All materials exhibit a pronounced negative thermal expansion of the c-axis below the magnetic ordering temperature. Panels (e),(f),(g) summarize the absolute a- and c-axis lattice constant as well as their ratio at 300 K for these elements. This illustrates the lanthanide contraction, which is thought to be an important ingredient for the multifarious types of magnetic order due to the distance-dependent RKKY-interaction within these chemically very similar materials.[294]

indicates the intimate coupling between the magnetization and strain effects in this class of materials. Indeed, the heavy rare-earths exhibit so-called giant magnetostriction effects, where lattice strains larger than 10^{-3} are observed upon magnetization changes.[298] The magnetostriction in rare-earth elements profits from the large magnetic moments and the high spin-orbit coupling in these elements, but their magnetic ordering occurs, except for Gd, only at cryogenic temperatures. By alloying with magnetic 3d elements, for example Fe, the Curie-temperature of the compounds is raised and room-temperature giant magnetostriction effects become available for applications.[43, 299, 300]

There exist various general references for the properties of rare-earth materials that are only briefly mentioned here in chronological order for guidance in further reading. The general magnetic properties of the rare-earth elements based on neutron diffraction studies are provided in the review by Koehler[301] and the book of Elliott[302]. The book of Coqublin[303] focuses on the underlying electronic structure effects and the book of Jensen and Mackintosh[304] provides theoretical modeling approaches for the experimentally observed properties. A book by Engdahl[43] contains the phenomenological introduction to giant magnetostriction effects and a review publication by Dörr[208] discusses the magnetostriction in rare-earth elements and alloys with a focus on theoretical modeling. A further detailed review on the rare-earth properties is beyond the scope of this work and I will refer only to the most relevant properties, i.e. the magnetic phase diagram and the temperature-dependent strain of dysprosium.

The magnetic phase diagram of bulk dysprosium in an external magnetic field along the magnetic easy directions ($\langle 11\bar{2}0\rangle$ or hexagonal a-axis) has been explored in various experiments.[305–308] Theoretical studies often treat rare-earths in general [309–312] and have evolved to the point that ab-initio simulations reproduce the main features of the experimental observations[310–312]. The experiments explore the magnetization[305, 306], magnetocaloric effect[306] and structural distortions[307] as well as the wavevector-dependent magnetic ordering by neutron diffraction[308]. These investigations report phase diagrams with various levels of detail and figure 6.4 reproduces the basic phase diagram for dysprosium that is adapted from one of the first reports[305] by Herz and Kronmüller from 1978. This diagram contains the generic features and magnetic phases of the $H-T$ diagrams of heavy rare-earth materials[311]. Panels (b)-(e) of 6.4 provide a schematic real-space depiction of the magnetic order of the $4f$-magnetic moments for the different phases. In absence of an external field, Dy undergoes a second order phase transition from the PM to AFM state upon cooling below approximately 180 K and a transition from the AFM to FM order at approximately 85 K. The PM-AFM phase transition is a second order phase transition where structural and magnetic properties vary continuously, whereas the AFM-FM transition is of first order and thus exhibits a hysteresis and discontinuous changes in magnetic and structural properties. The helical turn angle of the localized magnetic moments between the hexagonal lattice planes in Dy decreases continuously from approximately 43.2° to 26.5° upon cooling from $T_{\text{Néel}} = 180\,\text{K}$ to $T_{\text{C}} = 85\,\text{K}$ where it jumps to 0° in the FM phase.[313]

Temperature-dependent X-ray diffraction experiments on rare-earth elements show strong anomalies of the thermal expansion response that occur in the magnetic phases. The first observations of this effect date back to the works by Darnell and Moore[292, 293, 314] who investigated the spontaneous magnetostriction in single-crystalline phases of rare-earth elements in 1963. In the same year, Legvold and coworkers reported giant forced magnetostriction effects upon applying an external field to Dy and Ho single crystals that lead to strains larger than $4\cdot10^{-3}$ along the out-of-plane and larger than $8\cdot10^{-3}$ in the in-plane direction[298]. A summary of different temperature-dependent lattice strains and the underlying structural phases from different experiments on bulk and powder specimen[293, 307, 308, 315] is given in figure 6.5. The data from different experiments are reproduced to show the reported spread in experimental observations around the common trend. All publications report a change of slope in the thermal expansion at the PM-AFM phase-transition and one observes a negative thermal expansion of the

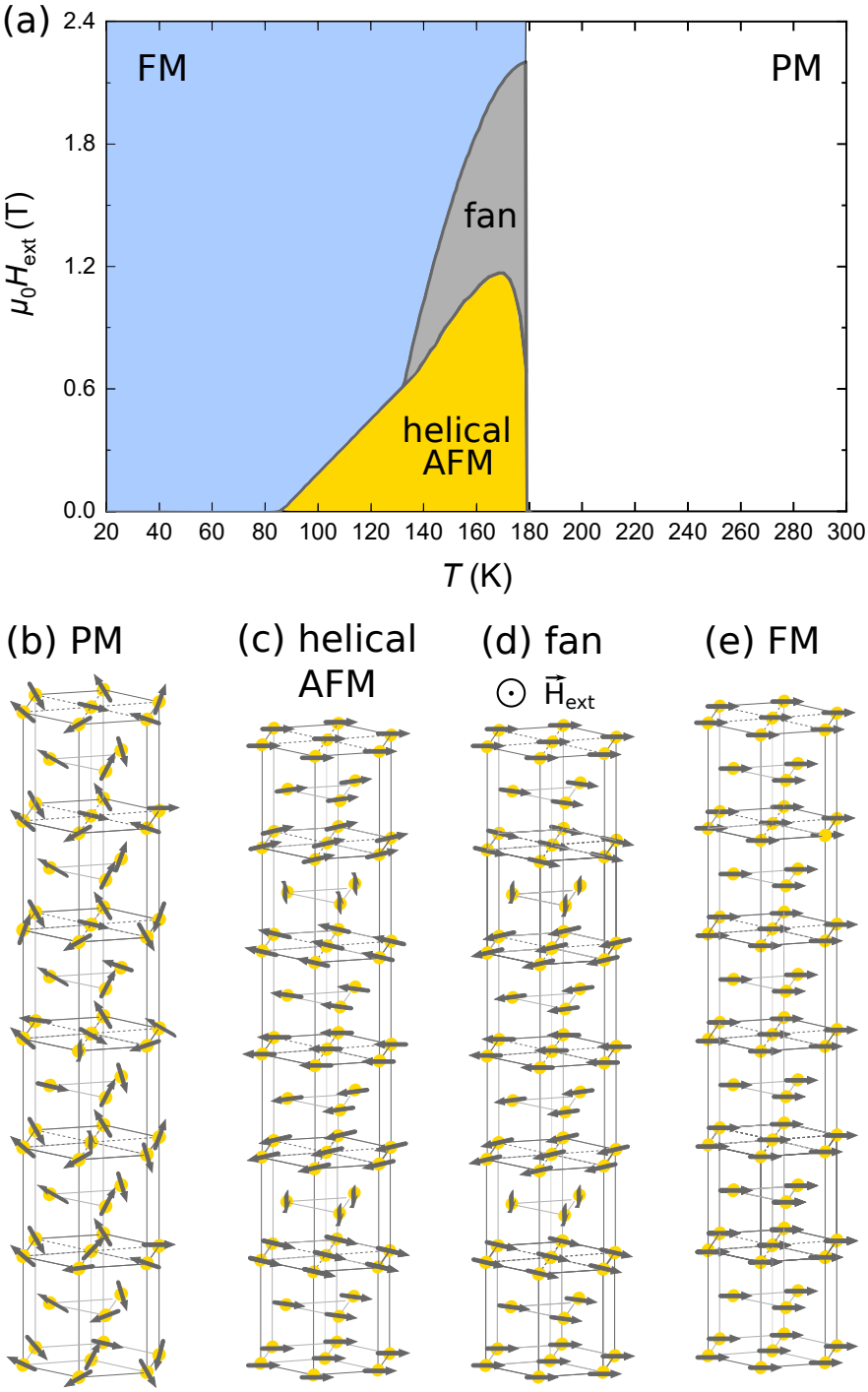

Figure 6.4: Magnetic phase diagram of dysprosium: Panel (a) depicts the $H-T$-diagram for bulk Dy that has been adapted from the study by Herz and Kronmüller [305] where the magnetization was measured for various external fields along the magnetic easy direction (hexagonal a-axis). In the absence of an external field Dy undergoes a PM-AFM phase-transition at approximately 180 K and a AFM-FM phase transition at 85 K. The application of an external field along the a-axis (in-plane easy direction) stabilizes the FM-phase for a larger range of temperatures and distorts the helical AFM phase to a fan-structure where the magnetization oscillates around the direction of the applied field. (b)-(e) provide schematic depictions of the differently aligned localized magnetic moments from the $4f$ shells.

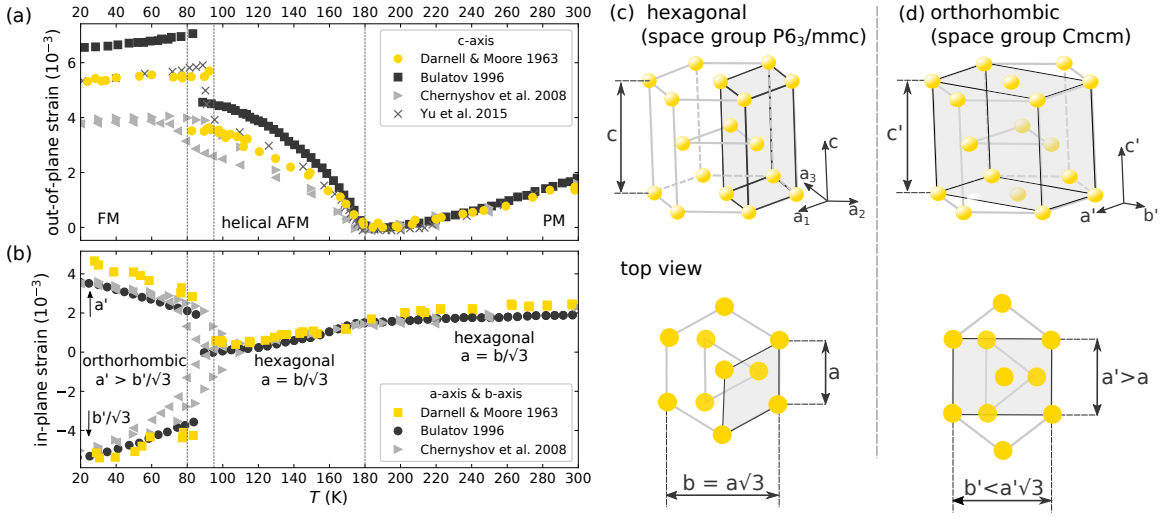

Figure 6.5: Spontaneous magnetostriction in dysprosium: The relative change of the lattice constants from various diffraction experiments is compiled in panels (a) and (b) for the hexagonal c-axis and the in-plane a-axis respectively. Changes of the strain response coincide with the magnetic ordering temperatures that are indicated as vertical dashed lines. Upon cooling below $T_{\text{Néel}} = 180\,\text{K}$, the c-axis expands while cooling. At the metamagnetic AFM-FM transition at 85 K, one observes a jump in the c-axis lattice constant and the a-axis splits into an expanding and a contracting direction indicating the structural transition from the hexagonal to orthorhombic phase. A comparison of both types of unit-cells is shown in (c) and (d).

hexagonal c-axis in the temperature region of the helical AFM phase i. e. for $85\,\text{K} < T < 180\,\text{K}$. Upon cooling below the Curie temperature, one finds a step-like increase of the c-axis, with various strains that are reported to range between $1 \cdot 10^{-3}$ and $3 \cdot 10^{-3}$. This coincides with a change of the crystal symmetry from hexagonally closed packed to orthorhombic, which is best seen by the splitting of the in-plane strain response into two branches. The upper branch corresponds to the expanding orthorombic a-axis, whereas the lower branch corresponds to the orthorhombic b-axis. In a crystal with hexagonal symmetry, the in-plane dimensions satisfy $b = \sqrt{3}a$ as indicated in panel (c) of figure 6.5. In the FM phase, the a-axis closest to the magnetization orientation expands, and the perpendicular b-axis contracts so that the symmetry of the unit cell changes to orthorhombic as indicated in panel (d) of figure 6.5. The a-axis expands along the direction of the magnetization and the unit cell contracts perpendicular to it. This is demonstrated by forced magnetostriction experiments where the external field is rotated within the basal plane.[298]

The so far presented magnetic and structural properties were obtained on bulk or powder specimen of dysprosium and not in thin films, which are used in our time-resolved UXRD investigation.[1] The dysprosium (Dy) thin films are grown on top of $(11\bar{2}0)$-oriented sapphire substrates with a hexagonal unit cell with a body-centered cubic (110)-oriented niobium (Nb) and a hexagonal (0001)-oriented Yttrium (Y) stack as buffer layer. The additional layers are introduced to reduce the lattice mismatch to the substrate. Bulk Y exhibits an approximately 1.5 % larger in-plane lattice constant compared to Dy ($a_{\text{Dy}} \approx 3.593$ versus $a_{\text{Y}} \approx 3.6474$). This leads to an expansive epitaxial in-plane strain that has been found to stabilize the helical AFM phase that has a smaller c-axis for a larger temperature region as reported by Dumesnil, Dufour and coworkers.[316–318]

[1] Nanoscopically thin films are the subject of our investigation because they allow to match the volume that is probed by X-ray diffraction to the penetration depth of the optical excitation, which is on the order of 25 nm for the rare-earth metals. Otherwise, the diffraction from the dominantly unexcited material would obscure the strain response due to the large penetration depth of the ≈ 8 keV X-rays that is on the order of a few µm.

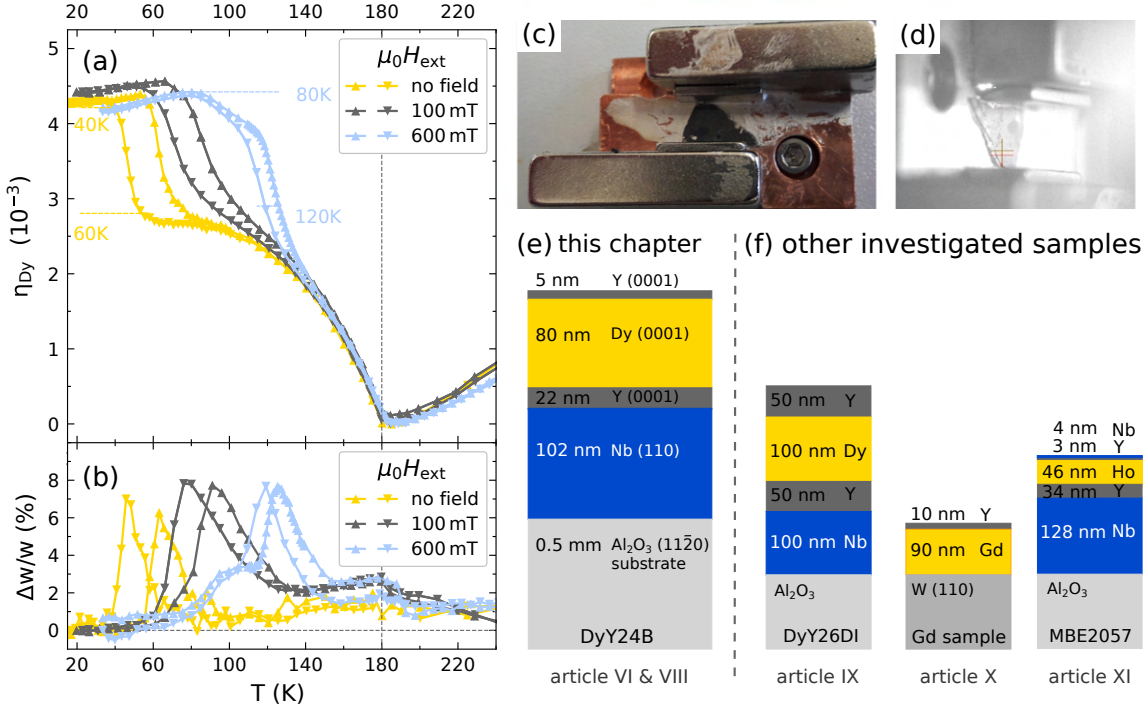

Figure 6.6: Temperature and B-field dependent lattice strain of our Dy thin film sample: The T-dependent strain in the Dy layer (a) shows a pronounced change at the AFM-PM phase transition at $T_{\text{Néel}} \approx 180\,\text{K}$. The applied in-plane field stabilizes the FM order so that the signature for the AFM-FM transition is shifted by approximately 55 K from 45 K in remanence to up to 110 K. The Dy peak width (b) shows a pronounced increase at the FM-AFM transition temperature due to the coexistence of both the FM and AFM domains within the thin film. Dashed lines indicate the additional strain contribution of approximately $1.5 \cdot 10^{-3}$ that originates from the FM order, whose transition temperature depends on the applied field. Markers indicate increasing (▲) and decreasing (▼) temperature variations, emphasizing the hysteretic behavior at the first order FM-AFM phase transition. (c) shows a photograph of the sample in the sample holder with the added permanent magnets and (d) a view of the mounted sample holder along the X-ray path. Panel (e) shows the sample layer structure of the thin film used in this investigation in comparison to the samples used in other articles that are sketched in (f).

Figure 6.6 shows the temperature-dependent c-axis strain of the Dy unit cell for the thin film sample that is used for all further experimental reports in this chapter. The sample has been prepared by Karine Dumesnil at the Institut Jean Lamour using molecular beam epitaxy. A photograph is shown in in panel (c) of figure 6.6. The description of the layered, epitaxial growth method, the characterization of the structural properties and the resulting magnetic phases have been published elsewhere.[317–320] Resonant magnetic diffraction from the helical spin-spiral at the Dy M-edge at 1293 eV from this sample is presented and discussed in the thesis of Azize Koç [321, chapter V]. The strain has been obtained by monitoring the peak shift of the Dy peak using the cw X-ray tube for temperature-dependent diffraction measurements that are shown in more detail in article VII. In general, one finds that the observed strain response in our thin film exhibits the same qualitative features as the bulk measurements from the literature. One can distinguish the onset of the helical AFM phase that is characterized by the resulting increase of the lattice strain upon cooling below $T_{\text{Néel}} = 180\,\text{K}$. The step that marks the first order metamagnetic transition from the AFM to the FM phase has a magnitude of approximately $\approx 2 \cdot 10^{-3}$ and occurs between $60 - 40\,\text{K}$ upon cooling and between $60 - 80\,\text{K}$ upon heating. The coexistence of the low temperature FM and the high temperature AFM phase in the region of the hysteresis is seen as a broadening of the diffraction peak, that is shown in panel (b) of figure 6.6. Here, I would like to emphasize the effect of the applied external

field along the in-plane direction that shifts the FM-phase to higher temperatures. The field was applied using static NdFeB magnets adjacent to the sample and the field was measured using a commercial Hall sensor. In comparison to the yellow curve that shows the strain response in absence of an applied field we observe the same behavior for the AFM phase but the step that indicates the AFM-FM transition is shifted to higher temperatures in agreement to the phase diagram introduced in figure 6.4. The maximum applied external field is just below the threshold for the onset of the fan phase reported in the literature for bulk Dy.

The hitherto presented static effects exhibit an intimate relation between the magnetic order and the underlying structural degrees of freedom. This motivates our time-domain studies of the strain response of laser-excited heavy rare-earth elements that investigate magnetostriction effects on ultrafast timescales. UXRD provides a technique that is suitable to probe both the strain and the magnetization response in laser-excited heavy rare-earth elements as shown in the PhD thesis of Azize Koç[321] in our group. Her investigations focus on the 100 ps- to multiple nanosecond-timescale in Dy and Gd. In her work, she utilizes the x-ray probe energy tunability of a synchrotron facility for resonant magnetic-diffraction from the spin-spiral wavevector as well as the stable photon flux for non-resonant diffraction studies from lattice planes. The observation of the strain response concurrent to the demagnetization requires subpicosecond time resolution that is available at the PXS. These investigations have been started during my MSc thesis[128] at the University of Potsdam. The resulting publications have developed and refined the usage of magnetic and electron-phonon Grüneisen parameters for the analysis and interpretation of the strain response in heavy rare-earth metals as detailed in article VII and article X.

Our so far published results mainly discuss the picosecond strain response in the helical AFM phase. This chapter is designed to report the experimental insights on the influence of the FM-AFM phase transition. It is interesting to study the effect of this metamagnetic transition on the observed timescale and amplitude of the magnetic stress in the strain response. To that end, I compare the picosecond strain response at temperatures just below and just above the FM-AFM phase transition for the case of an applied field as well in the absence of a field. Dashed lines in figure 6.6 indicate the chosen temperatures that I use in the subsequently discussed time-resolved experiments.

The analysis and interpretation of the observed strain response benefits from the insights on the ultrafast magnetization dynamics in heavy rare-earth materials that have been gained by other groups. Experiments on the time-resolved, helical magnetic order in heavy rare-earth materials have been discussed by Langner et al. [322] and Thielemann-Kühn et al. [225, 323] for the case of Dy and Rettig et al. [226] for Ho. The laser-induced response of the FM order in gadolinium and terbium has been discussed by various works in the group of Martin Weinelt using both (spin-resolved)-photoemission [324–328] and XMCD[329, 330] studies. A review by Bovensiepen[331] summarizes the results of surface-sensitive all-optical experiments on (0001)-oriented hcp Gd up to 2007, which are complemented by time-resolved MOKE investigations by Sultan et al. [332, 333] and time-resolved MOKE-experiments on Gd_xTb_{1-x}-alloys by Eschenlohr et al. [334]. It is interesting to note that the rare-earth containing intermetallic alloys of the elements Gd, Fe and Co were the first materials to exhibit single-shot all-optical switching.[23, 335, 336] Multi-sublattice, rare-earth-containing metallic alloys represent one of the most active material class for ultrafast current- or laser-induced-magnetization manipulation.[337] All-optical magnetization manipulation in GdFeCo alloys is one example where rare-earth elements form important constituents of functional magnetic materials. The list of functional materials can be extended to rare-earth iron garnets ($RE_3Fe_5O_{12}$), rare-earth orthoferrites ($RE_1Fe_1O_3$) that exhibit fascinating spin-wave excitations or binary rare-earth iron compounds RE_1Fe_2 that exhibit giant magnetostriction at room temperature.

The helical AFM order of laser-excited dysprosium can be probed by time-resolved, resonant magnetic diffraction from the periodic spin-spiral as shown by Thielemann-Kühn and coworkers at the femto-slicing

beamline of the BESSYII synchrotron radiation source.[225] They report that the AFM order is quenched in a two-step process that comprises a fast $220\,\mathrm{fs} \pm 70\,\mathrm{fs}$ time constant in the low-fluence regime, which increases up to 1 ps for higher fluences and a second, slower process that ranges between $12 - 30\,\mathrm{ps}$ with a trend towards a faster demagnetization at larger fluences.[225] The demagnetization signature of the FM phase of the same sample, below the Curie temperature, studied by XMCD yields a single step process with a 6 ± 2 ps timescale. The overall angular momentum dissipation rate is larger for the AFM state.[225] Similar timescales have been found by resonant X-ray diffraction for the helical AFM phase of holmium where the intrinsic demagnetization occurs within $560 \pm 90\,\mathrm{fs}$ and the time constant of the second demagnetization step was reported to be 9.5 ± 2.2 ps.[226] Rettig and coworkers furthermore find that the demagnetization of the $4f$- and the $5d$- electron states occurs nearly simultaneously. They attribute the common behavior to the strong coupling between the f and d orbitals with a $J_{\mathrm{fd}} \approx 70\,\mathrm{meV}$, which corresponds to a timescale of $\approx 10\,\mathrm{fs}$.[226] Frietsch and coworkers [327, 328] use a high harmonic generation laser source to probe the time-resolved exchange splitting of the $5d$-electron states and the magnetic linear dichroism at 36.8 eV and 40 eV of the occupied $4f$ levels on Gd and Tb respectively. For Tb, they find that both signatures decrease equally fast on a 400 fs timescale[328], whereas the $4f$ states for Gd demagnetize with a slower 14 ps timescale that clearly deviates from the subpicosecond ($\tau \approx 700\,\mathrm{fs}$) decrease of the $5d$-exchange splitting. They attribute the fast demagnetization of the $4f$-state in Tb to the strong spin-orbit coupling that is only present for a non-vanishing angular momentum ($L \neq 0$), which provides an efficient channel for the angular momentum dissipation to the lattice for the case of Tb. The slow demagnetization of the $4f$-states in Gd is taken as a sign for a transient breakdown of the intra-atomic exchange interaction between the $4f$ and $5d$ states.[327] Whether the main source of the fast demagnetization in the $4f$-states arises via the exchange coupling of the $5d$-$4f$ orbitals, as suggested in the works on Dy and Ho[225, 226] or via the spin-orbit coupling that links the $4f$-orbitals to the phonon system as suggested by Frietsch[328] is a topic of current research debate.

Time-resolved studies of the helical AFM order are scarce compared to reports on the demagnetization of FM order. Part of this may be attributed to the fact that resonant diffraction requires highly specialized setups that combine cryogenic temperatures, sub-picosecond time-resolution, energy tunability of the X-ray energy and sufficient photon flux to observe the diffraction from the spin-spiral. The time-resolved strain response of this material class was largely unexplored prior to our investigations. The early works on the temperature-dependent, spontaneous magnetostriction by Darnell already suggest that the magnetic strain should be proportional to the square of the sublattice magnetization.[293, 314] Probing the magnetic order via the detection of magnetostriction requires a separation of the magnetic strain contribution from other contributions driven by electron- and phonon-induced stresses. It could in principle be applicable regardless of the type of magnetic order i. e. for both FM or helical AFM order, which both occur in Dy. The remainder of this chapter is dedicated to experiments on the magnetic stress contribution to the picosecond strain response of a laser-excited Dy transducer.

6.2 Strain response of a laser-excited dysprosium layer

Figure 6.7 provides an overview of the RSM and the time-dependent evolution of the RSS at the Dy and Nb peak position, from which the strain response is extracted. It contrasts the time-resolved diffraction response observed in the PM-phase of the Dy transducer at $T = 250\,\mathrm{K}$ with the response in the FM of the Dy transducer at $T = 90\,\mathrm{K}$ in an applied field of $\mu_0 H_{\mathrm{ext}} = 600\,\mathrm{mT}$. The shown measurements were carried out for the same, relatively high, incident laser-excitation density of approximately 7.2 $\frac{\mathrm{mJ}}{\mathrm{cm}^2}$. This figure illustrates several aspects that are relevant for understanding and interpreting the experimentally

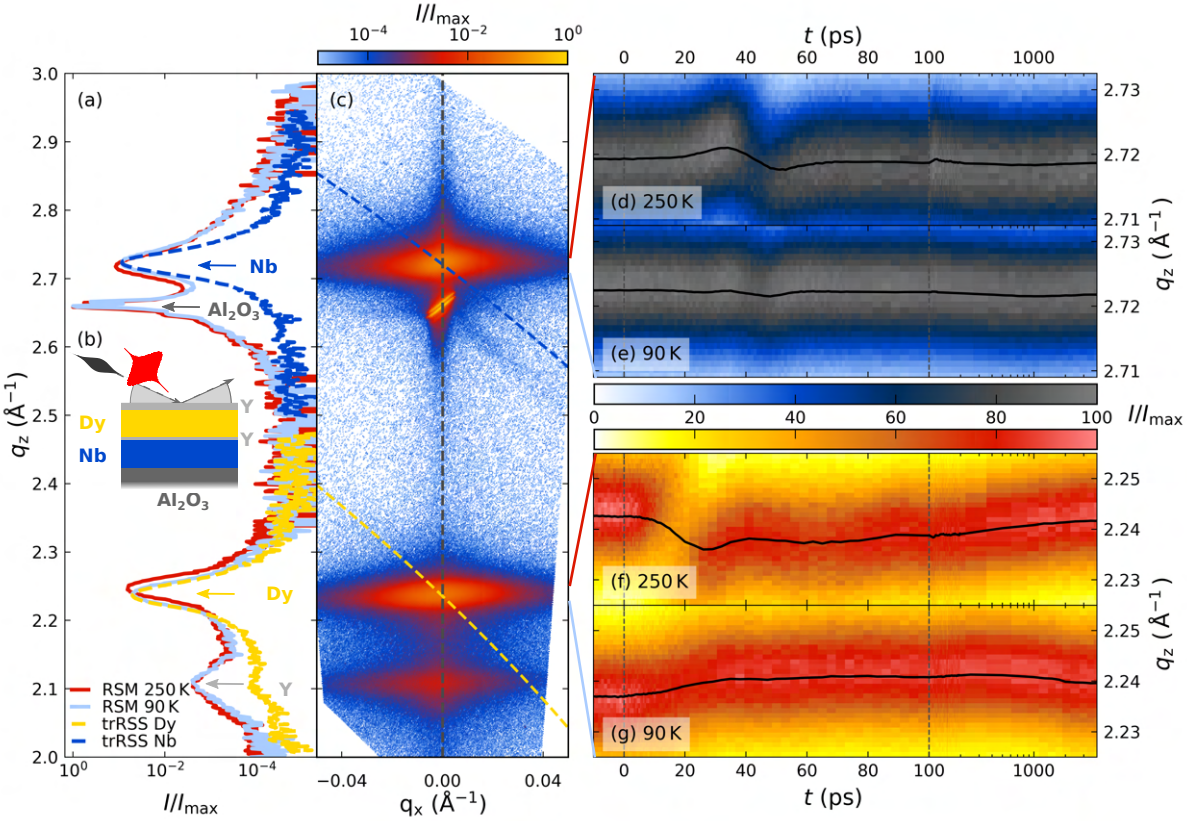

Figure 6.7: Principle of the UXRD experiment in the rare-earth heterostructure: (a) Static measurement of the X-ray diffraction intensity of our heterostructure under an applied in-plane field of 600 mT as a function of the out-of-plane reciprocal space coordinate q_z at two selected temperatures T. The diffraction curve exhibits material-specific peaks that correspond to the average lattice constant of each material in our sample. With the exception of the Dy peak, all diffraction maxima shift to higher q_z upon cooling, due to their thermal expansion. Inset (b) is a schematic depiction of the time-resolved pump-probe experiment where an X-ray pulse probes the evolution of the diffraction intensity after laser excitation. Panel (c) shows a representative reciprocal space map (RSM) at 90 K where the reciprocal space slices , monitored in the time-resolved experiments are indicated as orange and blue dashed lines at the Dy and Nb peak position respectively. Panels (f) and (g) show the evolution of the diffraction intensity in the reciprocal space slice (RSS) of the Dy layer peak at 250 K (PM phase) and 90 K (FM phase) and panels (d) and (e) display the corresponding time-resolved evolution of the RSS at the peak position of the buried Nb layer for the incident fluence $F = 7.2\,\frac{\mathrm{mJ}}{\mathrm{cm}^2}$ and the applied field of $\mu_0 H_{\mathrm{ext}} = 600\,\mathrm{mT}$. The overlaid black lines in the RSS-evolution indicate the center of mass (COM) shift of the observed diffraction intensity, from which the out-of-plane strain responses η_{Dy} and η_{Nb} are extracted.

obtained strain from a RSM that is used in the temperature-dependent measurements and a RSS used in time-resolved measurements. To clarify the differences and their implications, we have recently written an article that discusses the time-efficient reciprocal space slicing method in detail.[338] In the following, I mention the main implications because these differences are relevant for the quantitative analysis of the picosecond strain in the Nb layer of the investigated heterostructures.

By considering the temperature-dependent peak shift between 250 K (red curve) and 90 K (light blue curve) in 6.7(a), one observes that the shift is small in comparison to the peak width but nevertheless visible for all materials in the heterostructure. It can be seen that Y, Nb and Al_2O_3 all exhibit positive thermal expansion, i.e. a shift to higher q_z and thus a smaller lattice constant upon cooling. This is contrasted by the shift of the Dy peak that moves to smaller q_z and thus larger lattice constants upon cooling. This corresponds to the negative thermal expansion behavior that originates from magnetic interactions which was characterized in the previous section. The temperature-dependent strain is extracted from RSM measurements, where both the sample and the detector are scanned symmetrically such that the central pixel of the detector scans along the q_z direction by keeping $\alpha_{in} = \alpha_{out}$ as sketched in figure 3.2 in chapter 3. To that end, multiple exposures over a range of diffractometer positions are recorded, which add to a map of the reciprocal space in proximity of the symmetric diffraction peaks. To obtain the RSM shown in 6.7(c), α_{in} was scanned in 320 steps over 8° from 13.5° - 21.5° with an exposure time of 0.5 s and one scan took approximately 10.5 min. This scan was carried out using the cw-microfocus diffraction tube, which is stable over multiple days. Given that the PXS setup has an approximately 100 times smaller X-ray flux per second in comparison, it is not practical to carry out such RSM-scans for a reasonable number of delays that are necessary to probe the transient strain response in the multilayer. Instead, we make use of the 0.3° convergence of the Montel multilayer optics, which is used both in the microfocus and PXS experiments. It provides multiple α_{in} and the area detector that probes multiple α_{out} without mechanical movements of the goniometer. In this way, we probe the two selected slices of the RSM through the Dy and Nb peaks that are indicated by the orange and blue dashed line in 6.7(c). Panel 6.7(a) compares the diffraction signal of the RSS slices and the $q_x = 0$ line of the RSM, which exhibit comparable features in the near proximity of the peaks.

At this point, it is relevant to discuss that a projection of the peak shift along the q_z-direction is detected in the RSS that is probed by the fixed detector. This is due to the fact that the RSS is inclined by $\alpha_{in} = \theta_B$ with respect to the q_z-axis as shown in the simplified diffraction geometry sketched in figure 6.8(a). The dependence of this projection on the shape of the diffraction peak is illustrated in panel (b)-(d) of figure 6.8. In our recent article, we calculate the scaling factor S between the strain $\eta_{RSS} = -(\Delta q_{z,RSS})/q_{z,0}$ which is derived from the peak shift on the RSS and the strain $\eta_{RSM} = -(\Delta q_{z,RSM})/q_{z,0}$ from the shift of the peak along the q_z direction the RSM. For the simple case that the diffraction peak $I(q_x, q_z)$ can be approximated by a two-dimensional Gaussian function, where lines of equal intensity are given by ellipses with semi-axes aligned along the q_x and q_z direction, one can derive geometrically that:

$$\eta_{RSM} = \underbrace{\left(1 + \left(\frac{\sigma_z}{\sigma_x}\right)^2 \tan^2(\theta_B)\right)}_{:=S} \eta_{RSS}. \tag{6.8}$$

Therein, σ_x and σ_z are the diffraction peak widths along the q_x and q_z directions and $\alpha_{in} = \theta_B$ is the Bragg angle where we have a local intensity maximum of photons on the detector. The underlying model for the diffraction intensity:

$$I(q_x, q_z) = I_{max} e^{\left(-\frac{(q_x - g_x)^2}{2\sigma_x^2} - \frac{(q_z - g_z - \Delta q_{z,RSM})^2}{2\sigma_z^2}\right)} \tag{6.9}$$

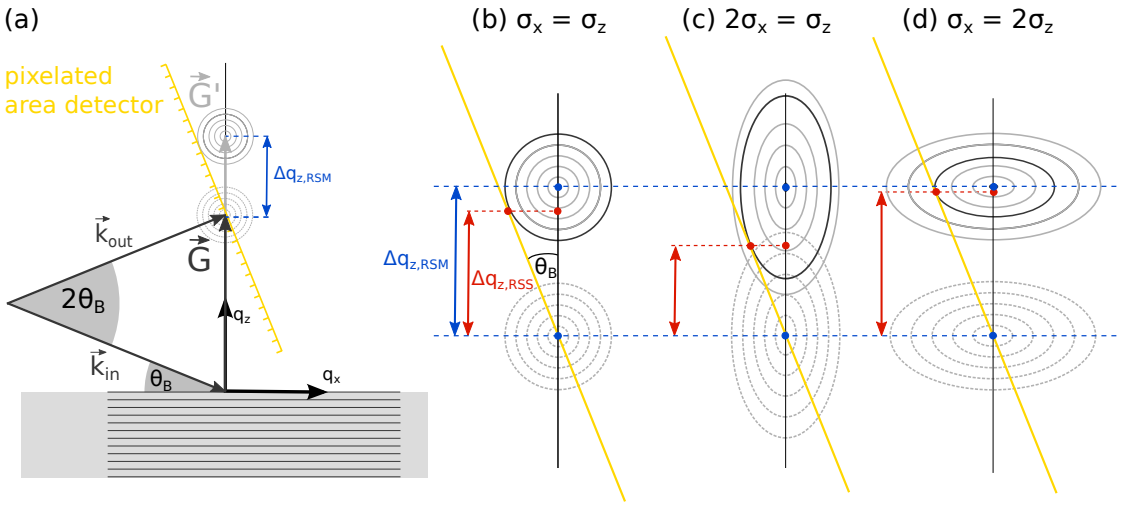

Figure 6.8: Sketch of the reciprocal space slicing scheme: All time-resolved experiments in this thesis that report the picosecond strain probed by ultrafast x-ray diffraction make use of the reciprocal space slicing (RSS) approach that is depicted schematically in panel (a). It utilizes the convergence of the PXS that provides X-rays with multiple α_{in} and an area detector that probes multiple diffraction angles α_{out} without any mechanical movements of the goniometer. The detector is approximated as a straight line in reciprocal space with α_{in} and α_{out} chosen such that the maximum intensity occurs on the center pixel of the detector. As the peak shifts by $\Delta q_{\mathrm{z,RSM}}$ as a result of out-of-plane strain, one observes the projection $\Delta q_{\mathrm{z,RSS}}$ of this shift in the RSS defined by the area-detector. The maximum of the shifted peak on the detector occurs where the RSS is tangent to the contour lines of equal diffraction intensity that are modeled by ellipses. The ratio $\Delta q_{\mathrm{z,RSM}}/\Delta q_{\mathrm{z,RSS}}$ thus depends on the width of the diffraction peaks along the in-plane (σ_x) and out-of-plane (σ_z) dimension as shown by the varying size of the red arrow. Note that the peak shift chosen in the sketch corresponds to a contractive out-of-plane strain, but the resulting ratio is identical for shifts to smaller q_z.

can account for the effect that the peak width may differ along the in-plane and out-of-plane reciprocal space direction due to direction-dependent coherence lengths, mosaicity and strain gradients that may occur within the probed films. The parameters g_{x} and g_{z} in equation (6.9) denote the reference peak positions in reciprocal space and $\Delta q_{\mathrm{z,RSM}}$ signifies the strain-induced peak shift that would be observed by reciprocal space mapping experiments. In the symmetric diffraction geometry, one has that $g_{\mathrm{x}} \approx 0$. More complex shapes of $I(q_{\mathrm{x}}, q_{\mathrm{z}})$ arise when broadening effects from the resolution area of the instrument are on the same order, or larger, as the intrinsic shape of the layer peak. This is discussed in a recent related article from our group[338], but omitted here. For small diffraction angles, where $\tan^2(\theta_{\mathrm{B}}) \approx 0$ or diffraction peaks where $\sigma_{\mathrm{x}} \gg \sigma_{\mathrm{z}}$, on finds that the correction factor $S \approx 1$. This can be seen from relation (6.8) and figure 6.8. For these cases one finds that strain seen by the RSS method nearly equals the strain that would be observed in full RSM measurements.

In this work, I analyze diffraction peaks where broadening mechanisms due to imperfections are larger than the resolution area of the instrument so that equation (6.8) provides a reasonable approximation.[2] For the diffraction peaks in the FePt-samples and the gold-nickel layers, we have $\sigma_{\mathrm{x}} \geq \sigma_{\mathrm{z}}$ in addition to relatively small θ_{B} so that the modeling predicts η_{RSS} to be within 10 % of η_{RSM}. Table 6.1 provides a summary of the calculated RSS strain scaling factors S and its contributions that are extracted from RSM of the diffraction peaks. One example for the determination of the widths σ_{x} and σ_{z} is given in 6.9 for the Dy and Nb peak of the sample that is discussed in this chapter. Figure 6.9 shows a region of

[2] This can be seen by comparing the shape and size of the RSM of the substrate peak with the layer peaks for example in figure 6.7(c). In relation to the resolution area of the PXS-setup the reciprocal space of the substrate can often be approximated as a delta function so that its diffraction intensity yields the instrument function.

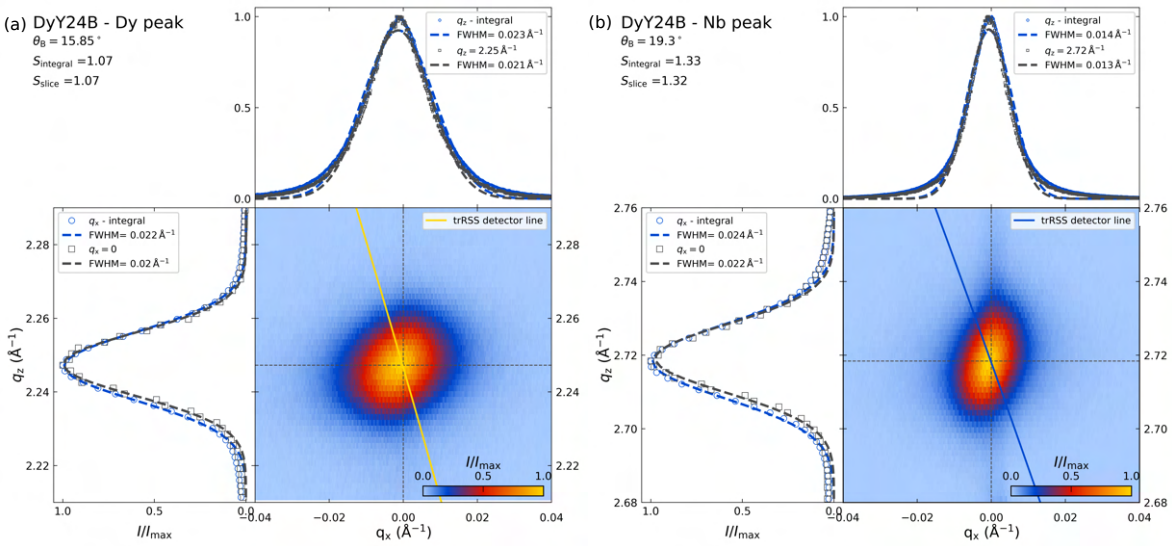

Figure 6.9: Analysis of the Dy and Nb diffraction peak widths: Panel (a) and (b) contrast the diffraction intensity of the RSM in the vicinity of the Dy and Nb peaks respectively. While the Dy diffraction peak is nearly circular in reciprocal space, the Nb peak is broader along the q_z direction in comparison to the q_x-direction. Numerical values for the full-width at half maximum values (FWHM) σ_x and σ_z are extracted from fitting Gaussian functions to the intensity distribution along reciprocal space slices that are indicated by grey dashed lines as well as for integrals along q_z and q_x of the displayed region of interest. The resulting RSS-correction factors S_{slice} and $S_{integral}$ indicated in the top left are almost equal for both methods that are used to determine the peak width.

interest around the diffraction peaks of the Dy and Nb layers on an equally scaled q_x and q_z-axis with a linear color-code to provide an undistorted picture of the shape of the diffraction peaks at the PXS-setup. The comparison shows that $\sigma_z > \sigma_x$, which leads to $S = 1.33$ so that the RSS strain underestimates the total strain by approximately one third. The inhomogeneous strain along the out-of-plane direction due to picosecond strain pulses is expected to transiently enhance S during the measurement. A detailed, quantitative analysis of the picosecond strain pulses in the RSS-scheme is, as of yet, still open because the findings will most likely depend on the equilibrium shape of the diffraction peak shape and the strain pulse amplitude. As an estimation for the worst case scenario, one can consider the transient peak width increase seen for highest excitation fluence used in the RSS experiments. For Dy, this corresponds to a factor of 2 increase and for Nb to a factor of 1.5 increase in σ_z while assuming σ_x to be constant. The resulting $S_{Dy,max} \approx 1.3$ and $S_{Nb,max} \approx 1.75$ provide an order of magnitude estimate of this effect but an experimental verification for a transiently varying S was so far not attempted.

Our analysis of the static diffraction peaks yields that the RSS-technique is expected to underestimate the average strain in the Dy-layer by approximately 7 %, whereas the Nb strain, extracted from the RSS measurement scheme, is expected to be approximately 32 % smaller than the true strain that would be observed in time-resolved full RSM-measurements. The factor S is not taken into account in any graph of this thesis or the publications, because I was not aware of its potential importance until recently. An overview given in table 6.1 shows that the necessary corrections of the strain amplitude are on the order of 10 % or less and thus often masked by fluctuations in the laser-excitation fluence. For the Nb peaks, this analysis predicts significant changes in the time-dependent strain amplitude, which may be even enhanced by transient peak width increases. This mainly affects the quantitative values for the strain reported in article VII, article XI and article III, in which we track the picosecond strain pulses that are launched by magnetic transducers into Nb-detection layers. The main findings of these articles are qualitative reports on the timing, shape and fluence-dependence of the picosecond strain pulses that

Table 6.1: Reciprocal space slicing correction-factors. Summary of the contributions to the RSS factor S for the diffraction peaks that are analyzed in this work. The peak widths σ_x and σ_z have been extracted from slices through the RSM of the static diffraction peaks as exemplified in figure 6.9. One finds for all cases except the Nb peaks that $S < 1.1$ so that $\eta_{\mathrm{RSS}} \approx \eta_{\mathrm{RSM}}$ holds. For the Nb diffraction peaks, we have that $\sigma_z > \sigma_x$ so that the η_{RSS} may underestimate η_{RSM} by $30\,\% - 40\,\%$, depending on the sample.

unit	peak	diffraction angle °	q_z-width $\mathrm{Å}^{-1}$	q_x-width $\mathrm{Å}^{-1}$	width ratio	width factor	angle factor	RSS-factor
sample	symbol	θ_B	σ_z	σ_x	$\frac{\sigma_z}{\sigma_x}$	$\left(\frac{\sigma_z}{\sigma_x}\right)^2$	$\tan^2(\theta_B)$	S
DyY24B	Dy	15.85	0.022	0.023	0.96	0.91	0.08	1.07
	Nb	19.30	0.022	0.013	1.62	2.64	0.12	1.32
TbFe42	$TbFe_2$	17.35	0.017	0.050	0.34	0.11	0.10	1.01
	Nb	19.20	0.030	0.017	1.79	3.20	0.12	1.39
NiAu 3.3	Au	18.70	0.073	0.598	0.12	0.01	0.11	1.00
	Ni	25.70	0.079	0.501	0.16	0.03	0.23	1.01
FePt film	FePt	24.58	0.077	0.128	0.60	0.36	0.21	1.08
FePt grains	FePt	24.33	0.067	0.133	0.50	0.25	0.20	1.05

traverse the Nb-layer, which remain valid. An indication of the importance of the RSS factor in Nb is seen in article III, where the amplitude of the picosecond strain pulses predicted by the simulation is much larger than the experimentally observed strain response using the RSS-scheme. A similar effect was observed in article XI, where the modeled strain amplitude response in Nb was scaled down to match the data. In the remainder of this chapter, I continue to report η_{RSS} as measured in order to be consistent with the publications. The subsequent discussion is focused on qualitative changes of the strain response in systematic measurement series that vary the temperature, excitation fluence and external magnetic field, which would not be feasible with this level of detail without the time-efficient RSS-scheme.

An example for the extensive characterization of the picosecond strain response of the Dy transducer is given in figure 6.10, which surveys the fluence-dependent response in different magnetic phases of the Dy layer. The strain response in the PM phase at 250 K shown in panel (a) shows an expansive strain that scales linearly with the incident laser fluence as the corresponding strain amplitude for representative delays shown in panel (e) confirms. The strain response in the PM-phase is purely expansive, and the linear behavior is in agreement with the positive, constant Grüneisen parameter for the electron-phonon system, that marks the proportionality between the deposited energy density and the driving stress in dysprosium. The strain reaches its maximum 30 ps after the laser excitation, which corresponds to the time it takes for the picosecond strain pulse to traverse the distance between the sample surface and the Dy layer at the speed of sound. The subsequent damped oscillation in the strain signal originate from the partial reflections of the strain pulses from interfaces as described in article VII and its supplementary. Many details are also provided in the MSc thesis[229] of Maximilian Mattern who carried out simulations of the strain response in this heterostructure with my guidance and assistance in the modeling. The laser-induced strain decreases on a nanosecond timescale due to the energy flow out of the sample. The thermal transport within a very similar heterostructure in different magnetic phases is discussed in article IX, which finds that heat flow in the magnetic phase is reduced due to energy that is stored in magnetic excitations.

The competition between the electron-phonon-stresses and the magnetic stresses within the Dy transducer becomes evident by the reduced expansion that occurs when the sample temperature is lowered so that the Dy layer is initially in the AFM state. This is shown in panels (b) and (c) of figure 6.10 that display the fluence-dependent strain response at 160 K and 130 K, respectively. The strain response changes to be almost entirely contractive in the FM state at 40 K as shown in panel (d). For low fluences,

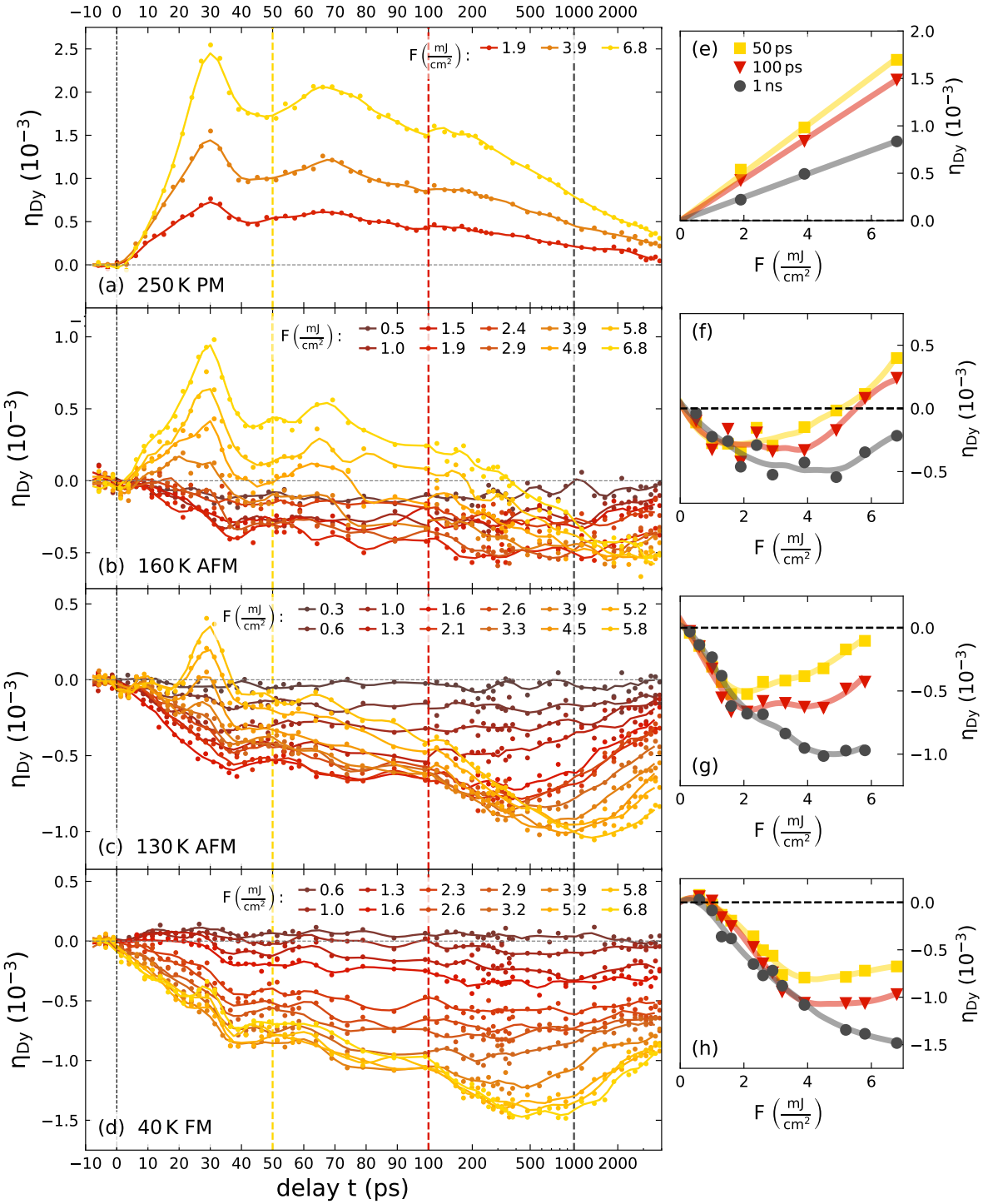

Figure 6.10: Temperature dependence of the strain response of a laser excited thin Dy film (a) Strain response at 250 K in the PM phase of Dy transducer, where the strain is linear with respect to the excitation fluence as shown in (e). (b)-(d) depict the strain response in the AFM and FM phase of Dy at 160 K, 130 K and 40 K respectively whereas (f) and (g) point out the non-linear behavior of the lattice strain with respect to the excitation fluence F for the same representative times as in (e). Solid lines are spline interpolations that serve as guide to the eye.

the Dy layer also contracts upon laser excitation in the AFM-phase, but there exists a crossover to an expansive behavior. Panels (f)-(h) that show the fluence-dependent strain for the three representative times at 50 ps, 100 ps and 1 ns, demonstrate the saturation of this contraction, at a laser fluence F that depends on the initial sample temperature T. The closer T is to $T_{\text{Néel}}$, the lower is the fluence at which the slope of the curve changes to positive strain with increasing the laser fluence. This indicates a saturation of the magnetic stress contribution, which furthermore results in an increasing energy transfer to the electron and phonon degrees of freedom. Below this temperature-dependent saturation threshold, one clearly observes that contractive magnetic stresses dominate the strain response of the Dy transducer. In article VII, we show that the magnetic stress in the AFM phase rises with very similar timescales observed in experiments reported by Thielemann-Kühn et al. [225]. This points to the possibility to probe the magnetic order by the time-dependent amplitude of the magnetostrictive stress.

The increase of the magnetic contraction after 30 ps that occurs at high fluences is indicative of a spatial saturation of the spin-stress contribution at the laser-excited front of the Dy transducer. A likely scenario is that heat diffusion to the initially unexcited areas of the thin film leads to the energy transfer to magnetic degrees of freedom at the back of the Dy layer. This spatially dependent saturation of the magnetic excitations within the Dy layer is confirmed by the analysis of the picosecond strain pulses triggered by the contraction in dysprosium in article VII.

6.3 Modeling of the strain response

In article VII, we develop a model for the strain response of the Dy transducer for different states of magnetic order within the transducer. The model captures both the strain within the transducer and the picosecond strain pulses detected in the buried Nb layer. Its main ingredients are:

- a calibration of the geometrical, elastic and thermophysical parameters of the electron-phonon system and the deposited energy density in the PM phase of the Dy transducer at 250 K.
- the addition of a contractive magnetic stress that has the same spatial dependence as the expansive electron-phonon-stress for experiments where $T_{\text{start}} \ll T_{\text{Neel}}$.
- a rise of the magnetic stress on two timescales: one instantaneous- and one 15 ps-timescale, in agreement with the ultrafast demagnetization in Dy reported by Thielemann-Kühn et al. [225]. We assume that 25% of the laser-induced energy density is transferred instantaneously to spin excitations by electron-spin coupling and 25% of the energy is transferred on the second timescale by phonon-spin coupling.
- In accordance with the ratio of the Grüneisen parameters calibrated in near-equilibrium conditions, we assume that the contractive magnetic stress per deposited energy density is three times larger than the expansive stress from electron-phonon excitations.
- a saturation threshold of the magnetic stress reflects the finite size of the energy reservoir of spin excitations. The saturation of the spin stress is indicative of a maximal spin disorder, and the threshold value is parametrized as a function of the start temperature of the experiment.

More details on the implementation are provided in article VII and elaborated in the MSc thesis of Maximilian Mattern.[229] In the following depictions I aim to illustrate the spatio-temporal stress and strain response that results from this modeling using the linear-chain of masses and springs approach that I previously introduced in chapter 4.5.2. I present the simulation response of a hypothetical sample that consists only of the Dy transducer and the Nb detection layer and omit the Y capping layer for conceptual clarity. Figures 6.11-6.13 show the modeled strain response of this system for a relatively high excitation

fluence and different start temperatures ranging between 250 K - 40 K. The result of the model in the PM-phase of the Dy transducer at 250 K provided in figure 6.11 shows the strain response in absence of magnetic stresses. This simulation is used to calibrate the film thickness, excitation fluence, spatial shape of the electron-phonon-stress and the heat diffusion within the hetero-structure in absence of magnetic stress contributions. Each spherical mass in the depiction represents approximately 10 nm of the material and the displacement is strongly enhanced for visualization purposes.

The change of the laser-induced strain response due to the presence of magnetic stresses is illustrated in figures 6.12-6.13. The contractive magnetic stress is symbolized by the laser-induced removal of red spacer sticks that represent the repulsive magnetostrictive stress within the Dy transducer. The finite length of these spacer sticks is temperature-dependent and increases upon cooling below $T_{\mathrm{Neel}} = 180\,K$. This depiction captures the saturation of the spin-stress that is the essential ingredient for the unconventional picosecond strain pulses discussed in article VII. The visualization of the simulation result captures the change from an initial expansion to a contraction of the Dy transducer and the resulting change in shape of the picosecond strain pulses within the Nb detection layer. The depiction focuses on the strain response within the initial 100 ps, where remagnetization effects of the Dy layer are neglected. The strain response in the magnetically ordered state changes upon cooling further and further below the ordering temperature because the relative amplitude of the spin-stress-contribution to the total laser-induced stress increases. These depictions are inserted to supplement the findings from article VII by a graphical depiction of the complex strain fields within the Dy transducer that lead to the average strain response that qualitatively matches the data in the publication.

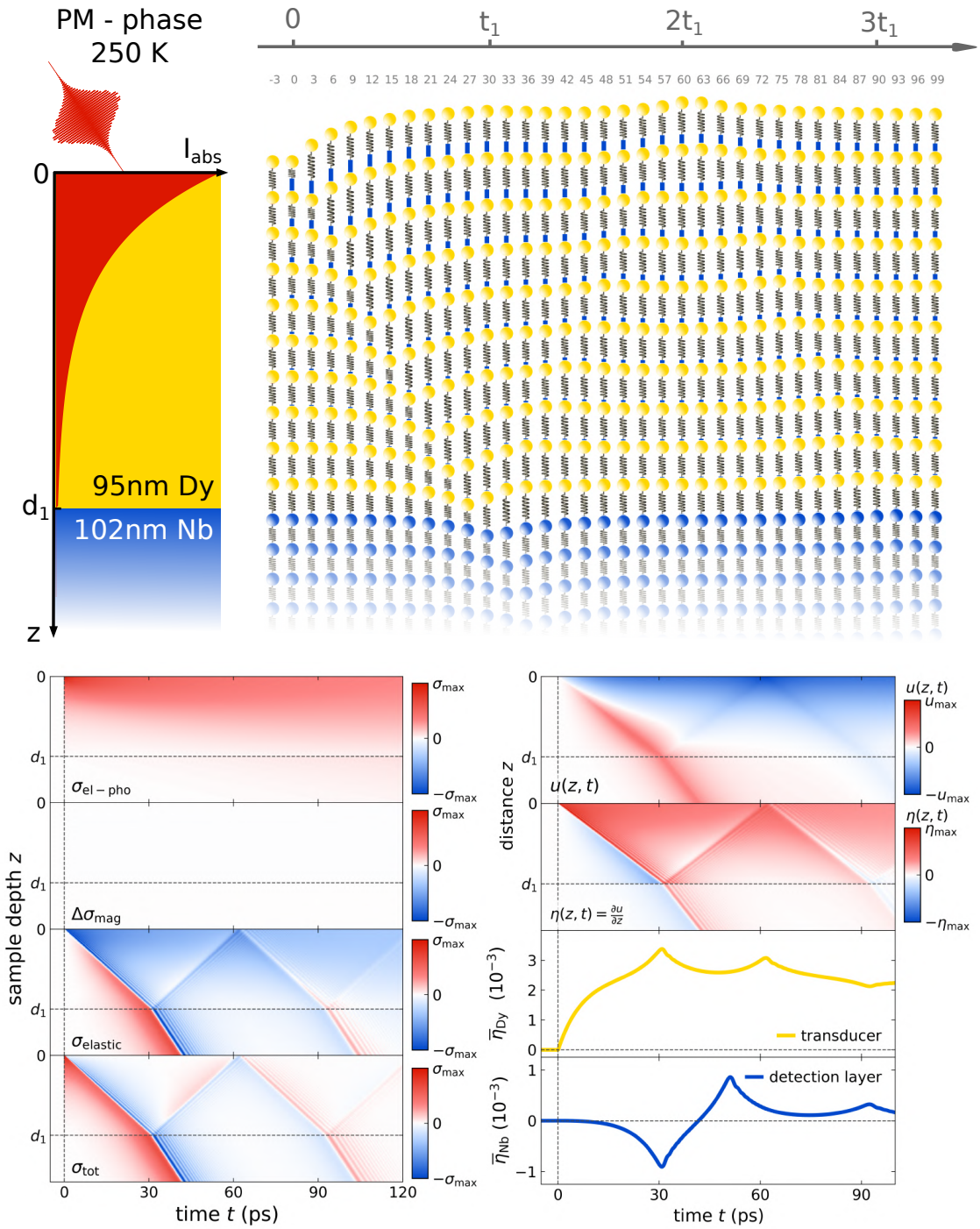

Figure 6.11: Modeled spatial and temporal stress and strain response for a Dy transducer in the PM phase at 250 K. The top row shows a sample sketch and the approximate laser excitation profile next to the linear-chain model response at selected time-slices. Inserted blue sticks represent the phonon-stress contribution. The panels in the bottom half of this depiction show the spatio-temporal stress contributions on the left side. The resulting displacement and strain field are shown on the right side alongside the average strain response within the Dy transducer and the Nb detection layer that are compared to the strain response extracted from UXRD experiments.

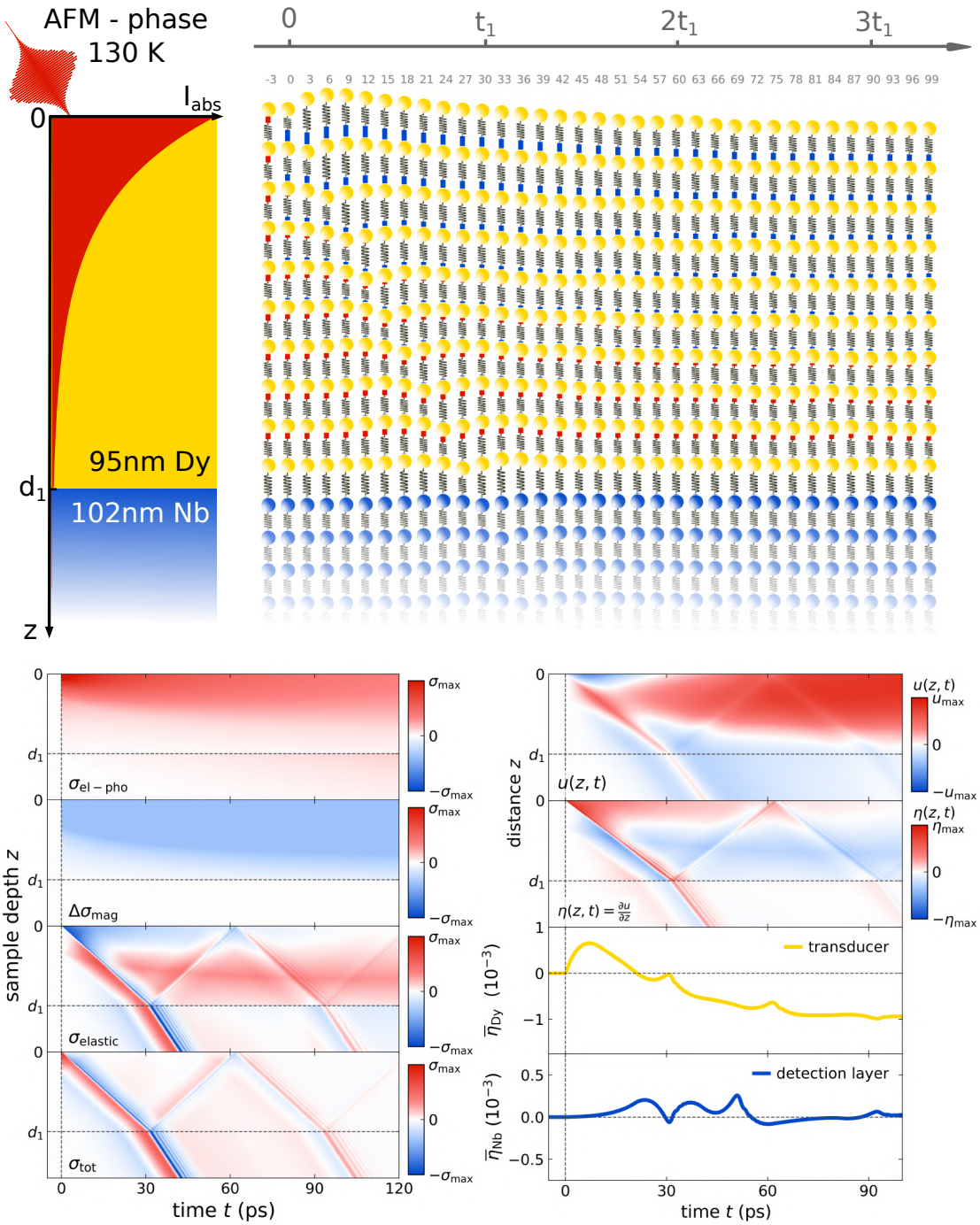

Figure 6.12: Modeled spatial and temporal stress and strain response for a Dy transducer in the AFM phase at 130 K. Same plot layout as in figure 6.11. The additional magnetic stress that occurs upon cooling below the magnetic ordering temperautre partially counteracts the expansive electron-phonon-stress. The saturation of the spin-stress in combination with the inhomogeneous excitation profile leads to an expansion of the transducer at the surface and a contraction near the Dy-Nb interface. This spatially dependent stress profile leads to the complex shape of the picosecond strain pulse that propagates into the Nb detection layer at the speed of sound.

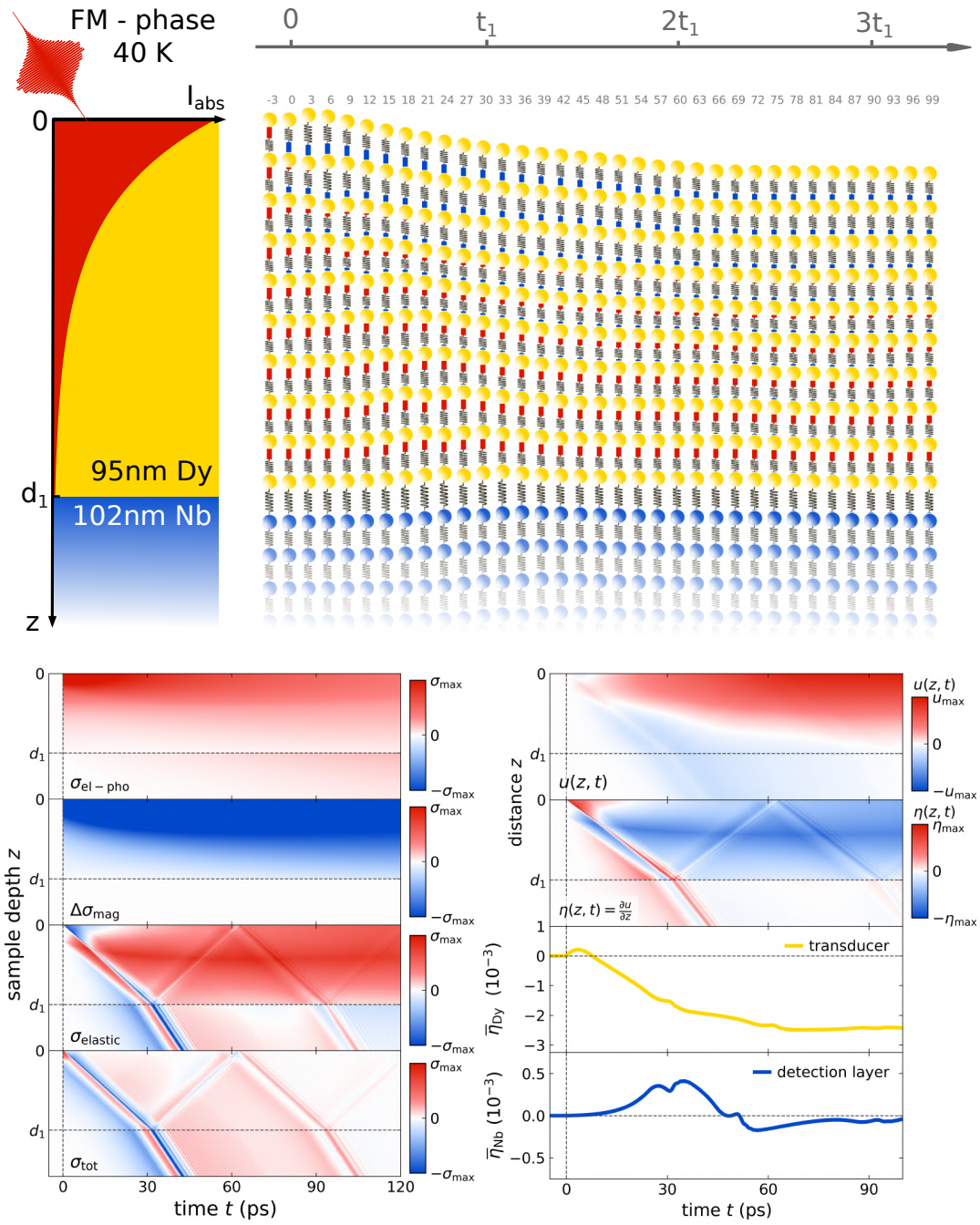

Figure 6.13: Modeled spatial and temporal stress and strain response for a Dy transducer in the FM phase at 40 K. Same plot layout as in figure 6.11. For this low temperature, we find that the large magnetic stress dominates the strain response. It leads to a nearly homogeneous contraction of the transducer upon laser excitation. The launched picosecond strain pulse deviates significantly from the bipolar strain pulse in the PM phase in the sense that an expansion precedes a contraction. Its shape is however not as sharp, since the magnetic stress does not rise instantaneously and is partially balanced by expansive electron-phonon-stresses.

6.4 Signatures of the metamagnetic FM-AFM phase transition

The so-far published results focus on the strain response in the AFM phase. The remainder of this chapter is dedicated to extending these findings by a qualitative discussion of the strain response in the FM phase, including in particular an analysis of the role of the first order FM-AFM phase transition. I furthermore investigate the possibility of manipulating the strain response by an applied external field and explore the possibility of observing the time-dependent magnetic order in the Dy layer by the two-pulse excitation scheme that was introduced in the previous chapter.

In the following section, I discuss the effect of the FM-AFM phase transition on the strain response of the Dy transducer. The signature of this metamagnetic transition in the static, temperature-dependent measurement shown in figure 6.6 is the step-like expansive strain of $1.8 \cdot 10^{-3}$ that occurs upon cooling below 60 K. The applied field of $\mu_0 H = 600\,\mathrm{mT}$ stabilizes the FM phase and shifts the transition to approximately 120 K. This allows investigating of the effect of the phase transition at the same temperature by studying the strain response in the range between 60 to 120 K with and without the applied field under otherwise similar excitation conditions. This type of experiment can be complemented by measurements just below and just above T_C. The reported experiments monitor both the average strain response of the transducer and the large amplitude, GHz frequency strain pulses that are launched by the laser-induced stress. The goal of the additional experiments is to investigate and discuss the extent to which an external magnetic field can influence the picosecond strain response by forced magnetostriction.

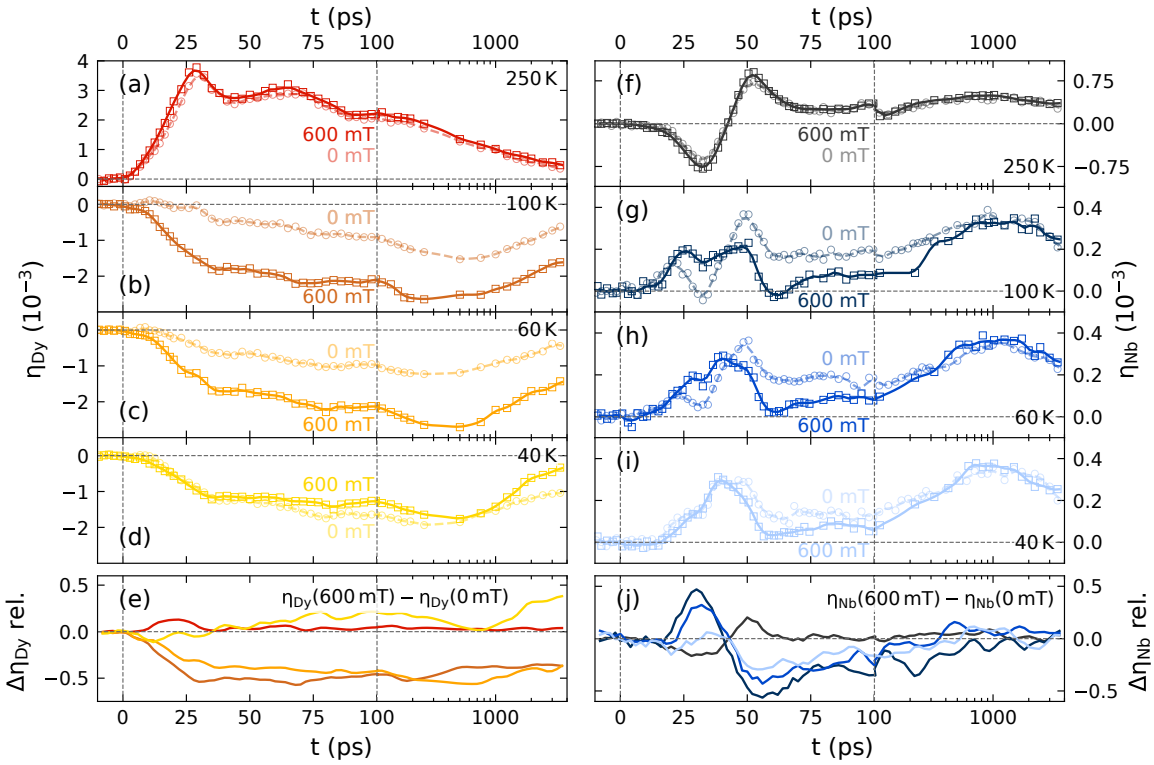

Figure 6.14: UXRD results with and without B-field: Panels (a)–(d) show the time-dependent Dy strain with and without external in-plane field for a relatively high excitation fluence of $\mathrm{F} = 7.2\,\mathrm{mJ/cm^2}$ at different initial temperatures. Panels (f)–(i) depict the corresponding strain response of the buried Nb layer. The interpolated lines serve as guide to the eye. (e) and (j) display the relative difference $\Delta\eta_{\mathrm{rel}} = (\eta(600\,\mathrm{mT}) - \eta(0\,\mathrm{mT}))/\max(|\eta(600\,\mathrm{mT})|)$ of the interpolated strain response for Dy and Nb respectively. The color code corresponds to the temperatures according to panels (a)-(d) and (f)-(i) and vertical dashed lines mark the axis break that allows showing the picosecond coherent phonon response and the nanosecond incoherent strain response in one graph.

Figure 6.14 compares the average strain of the Dy transducer (panels (a)-(e)) and the strain in the Nb detection layer (panels (f)-(j)) with and without an applied external field along the in-plane direction of $\mu_0 H_{\mathrm{ext}} \approx 600\,\mathrm{mT}$ at different temperatures. The field was applied using permanent magnets placed adjacent to the sample because we currently have no setup that allows for UXRD-measurements at cryogenic conditions in a variable in-plane field. Thus, the sample holder needs to be changed in between the measurement series to switch between measurements with and without an external magnetic field. To reproduce the excitation conditions in both cases, we use the expansive strain response in the PM phase at 250 K as a calibration. Fig 6.14(a) and (f) show that the observed strain responses in Dy and Nb nearly coincide. When comparing the average contraction of the Dy layer at 100 K and 60 K for samples with and without an external field, we observe an additional contraction of the Dy layer of approximately $1 \cdot 10^{-3}$, which rises within 30 ps and lasts up to 3.5 ns. For the picosecond strain response in the Nb layer shown in panel (g) and (h), we find that the bipolar strain feature between 20 ps and 50 ps is suppressed in the applied field. As shown in article VI, this feature results from the expansion at the top of the Dy transducer, which occurs when the magnetic stress contribution is not large enough to counteract the expansive electron-phonon-stress that rises on a (sub-) picosecond timescale. The fast rise of the additional contraction and the change of shape of the triggered strain pulse underline that the additional magnetic stress in the FM-phase needs to rise on a similar timescale as the electron-phonon-stress. This additional contractive stress arises due to the release of the forced magnetostriction upon demagnetization. From the picosecond strain response we see that this demagnetization needs to be on a similar timescale as the energy transfer to the electron-phonon system in order to counter-balance this expansive contribution. At 40 K, when the Dy layer is in the FM-state, one finds that the initial contraction of the Dy layer is almost equivalent, with only small deviations between experiments with- and without an external field, up to 1 ns. The recovery of the strain to near zero that indicates the remagnetization is observed to occur faster in the applied field, which is indicative of a faster remagnetization. This may be the case because the field provides a preferred in-plane orientation for the alignment of magnetic moments, which could speed up the domain growth and coalescence that is required for the remagnetization process.[3] Panels (e) and (j) display the relative change of the strain response with and without the applied field. I display the difference between the spline interpolations to improve the visibility because the fluctuations add when taking the difference between two measured strain signals. It shows that the effect of the FM-AFM phase transition is an additional strain of approximately $1 \cdot 10^{-3}$ that stays nearly constant after 30 ps. This is remarkable because the individual strain signatures in the Dy layer exhibit non-trivial shapes that evolve nearly parallel after the initial contraction.

The existence of an additional magnetic stress that arises due to the forced magnetostriction contribution on ultrafast timescales can be corroborated by comparing the measurements at temperatures above and below the FM-AFM phase transition. Figure 6.15 reports such experiments under otherwise equivalent excitation conditions where panels (a) and (d) provide the strain response above and below the phase transition in Dy and Nb without an applied field. Panels (b) and (e) repeat this experiment with the magnetic field of $\mu_0 H_{\mathrm{ext}} = 600\,\mathrm{mT}$. The measurements that start at $T < T_{\mathrm{C}}$ exhibit an additional contraction, which is slightly larger for the experiment with 600 mT applied in-plane. The prominent bipolar strain feature in the strain response of the Nb layer is suppressed for $T < T_{\mathrm{C}}$. This corresponds to the absence of the expansion at the top of the Dy transducer, due to the additional magnetic stress of the FM-AFM phase

[3] It is an interesting question whether the transient state of the laser-excited FM-ordered Dy layer forms a spin-helix subsequent to the laser-excitation or if it goes from a demagnetized FM state directly back to an ordered FM state. Probing the strain response is not conclusive in this regard and an answer requires time-resolved resonant magnetic diffraction that probes the periodicity of the spin-helix. However the occurence of a transient multi-domain state with different helix periodicities might complicate the interpretation even in that case.

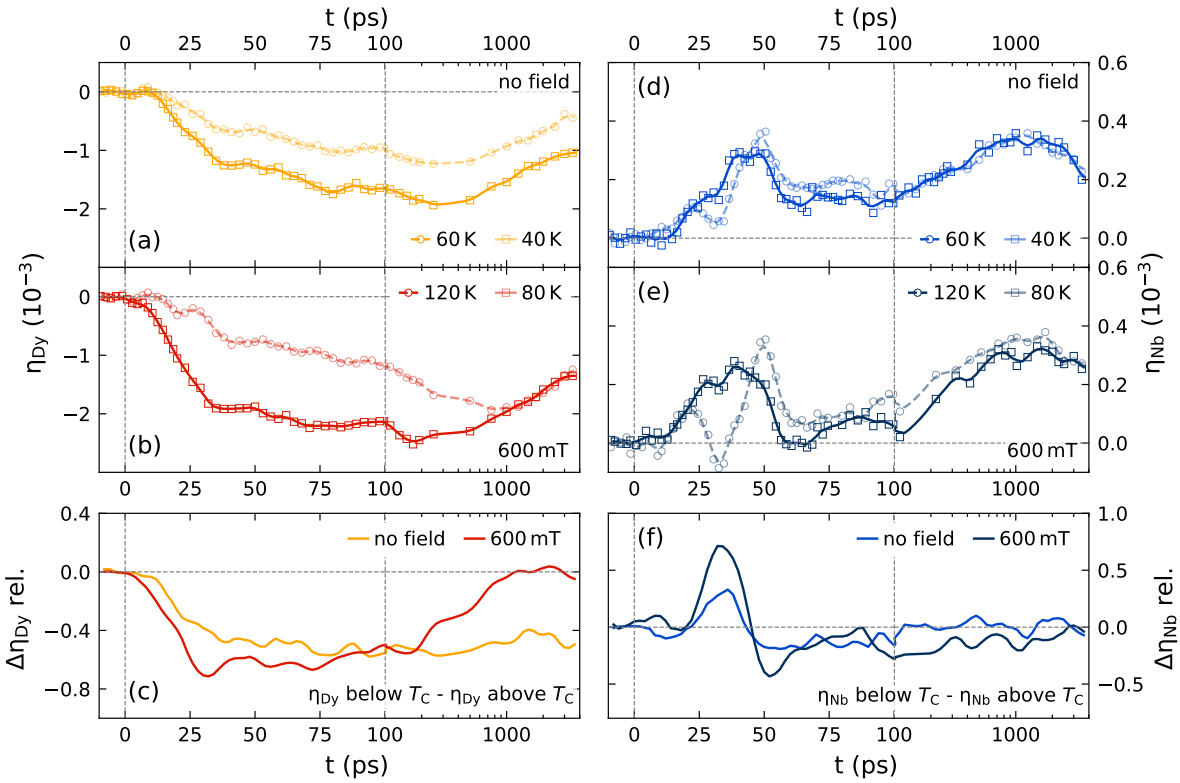

Figure 6.15: UXRD results above and below T_C: Panels (a) and (d) display the field-free strain response above (60 K) and below (40 K) the Curie temperature for the Dy transducer and the Nb detection layer respectively for $F = 7.2\,\mathrm{mJ/cm^2}$. Panels (b) and (e) show the same for the case of an applied field where the temperatures 120 K (above T_C) and 80 K (below T_C) are chosen according to the shifted phase transition as indicated in figure 6.6(a). Panels (c) and (f) display the relative difference $\Delta\eta_{rel} = (\eta_{below,Tc} - \eta_{below,Tc})/\max(|\eta_{below,Tc}|)$ of the interpolated strain response above and below the FM-AFM transition.

transition. The relative difference of the strain response shown in 6.15(c) and (f) shows the additional strain in the Dy layer and the suppressed bipolar strain wave in the Nb layer, very similar to the extracted response shown in 6.14(e) and (j).

Fluence-dependent measurements in the FM-phase are shown in figure 6.16. They provide an overview of the average strain of the Dy transducer that occurs when the film is excited across the metamagnetic phase transition up to the point of saturation of the magnetic stress. The focus of the depiction is on the variation of the picosecond strain response seen in the Nb detection layer and the time-depending variation in the average contraction of the Dy transducer for the case of an applied field of $\mu_0 H_{ext} = 600\,\mathrm{mT}$.

At this point, I would like to note that the additional stress due to the field-dependent metamagnetic phase transition temperature provides an interesting approach for the manipulation of picosecond strain pulses by an external field. The manipulation of the laser-induced strain response is usually achieved via the change of the excitation parameters wavelength, excitation fluence and pulse duration, which are usually able to tune the amplitude and the rise time of the shape of the strain but only rarely the sign. Having a transducer that contracts upon laser-excitation happens to be a relatively rare behavior. From the thermodynamic perspective discussed in chapter 4, this negative thermal expansion requires an increase of the entropy with decreasing volume. The spontaneous magnetostriction in the heavy rare-earth materials is one mechanism that is found to work on ultrafast timescales. The competition between the expansive phonon-stress and the contractive spin-stress leads to a cancellation of the fast rising stress component in Dy. The resulting strain observed in the Nb detection layer is not an inverted bipolar strain pulse but a

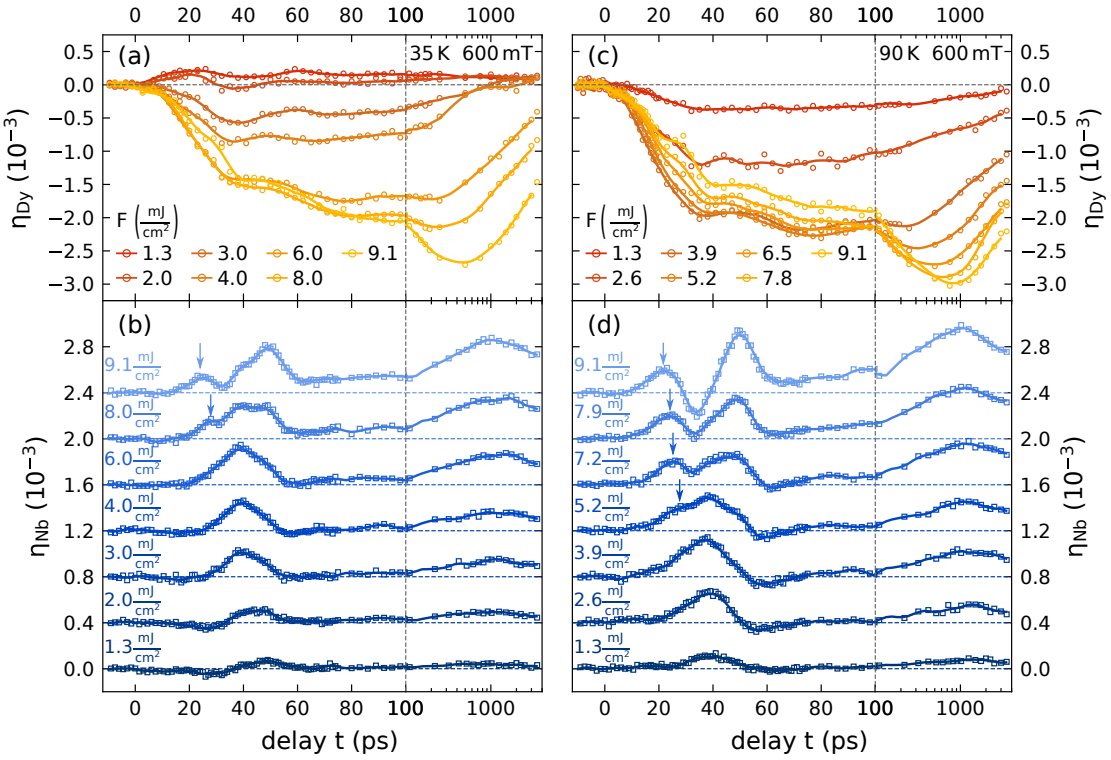

Figure 6.16: Strain response at the FM-AFM phase transition in Dy: Excitation fluence-dependent strain response η of the Dy transducer (a) and the Nb detection layer (b) for $T = 35\,\mathrm{K}$ for an in-plane B-field of 600 mT. The linear to logarithmic axis break at 100 ps (vertical, grey, dashed line) allows the simultaneous depiction of the changes in the picosecond strain pulse and the nanosecond thermal expansion response. The experimental results for varying the excitation fluence at a fixed start temperature $T = 90\,\mathrm{K}$ are depicted in the same way in (c) and (d). Spline-interpolated, solid lines serve as a guide to the eye and the Nb strain responses are offset for clarity. Vertical arrows in (b) and (d) mark the onset of the bipolar strain pulse feature that correlates with the saturation of the contractive stress at the top of the Dy layer.

nearly unipolar feature, that indicates a slowly rising, contractive stress, as modeled in the supplementary of article VII.

Versatile transducer applications that utilize the release of forced magnetostriction on ultrafast timescales can be envisioned. Figure 6.17 provides a sketch of a series of desirable scenarios where the transducer response upon laser-excitation depends on the applied magnetic field. The realization of this scenario requires giant forced magnetostriction in combination with ultrafast demagnetization. In an ideal scenario, these schemes could be realized at room temperature and in relatively soft magnetic materials in order to alleviate experimental complications of working at very high fields and ultralow temperatures. With regard to giant-room temperature magnetostriction, it is interesting to investigate the alloys Terfenol-D ($Tb_xDy_{1-x}Fe_2$ with $x \approx 0.3$) or Galfenol (FeGa) and Samfenol (SmFe). The ultrafast demagnetization response of these alloys is not as extensively investigated as is the case for the elemental metals Ni, Fe, Co and Gd but some accounts of the picosecond and subpicosecond magnetization evolution exist. [36, 339–341] Rare-earth containing alloys often exhibit a two step demagnetization process where the first step occurs on the subpicosecond timescale and the second step on a few ps to tens of picosecond timescales.[339, 341, 342]

These scenarios may lead to picosecond strain pulses that are tunable in amplitude and sign depending on the magnetic state of the transducer. This could potentially allow for engineering inverted bipolar strain

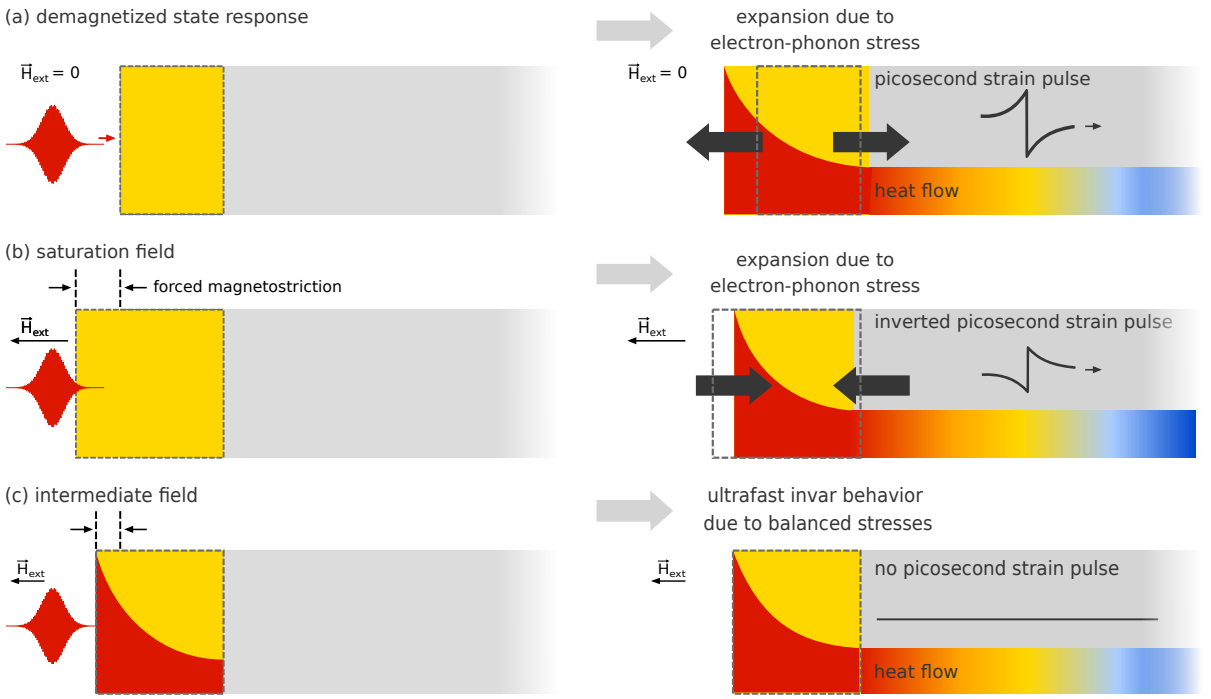

Figure 6.17: Scenarios for the use of forced magnetostriction for tunable transducers: Given that most metals expand upon laser-excitation, it would be interesting to control the ultrafast strain response of a transducer by an external field. This figure shows the hypothetical strain response of an idealized magnetostrictive transducer for different pre-strained states that are achieved by forced magnetostriction. The resulting picosecond strain pulse varies in amplitude and sign, based on the applied external field $\vec{H}_{\mathrm{ext}}$. While the demagnetized transducer would respond by an expansion if electron-phonon-stresses prevail (case (a)), it could respond by a contraction due to the release of the magnetostrictive pre-stress via ultrafast demagnetization (case (b)), which would lead to an inverted strain pulse. If the external field is chosen such that electron-phonon stresses and magnetostrictive stresses cancel, one could even observe ultrafast invar-behavior (case (c)), which would yield a localized, ultrafast source of incoherent phonons in the absence of high amplitude, picosecond strain pulses.

pulses with high strain amplitudes. In such a strain pulse, one would observe a leading tensile part that is followed by a compressive tail. Such pulses may exhibit interesting non-linear propagation properties because they are expected to become shorter while propagating, since the speed of large amplitude strain is often larger for the compressive part in comparison to the tensile. Furthermore, it would be interesting to have an ultrafast invar material, where all fs-laser-induced stresses add to zero. This would provide an ultrafast heat source that does not automatically launch picosecond strain pulses. This could, for example, help to distinguish the influence of incoherent and coherent phonons in the excitation of perpendicular standing spin-waves in an adjacent material.[109] Tunable picosecond strain pulses that could be useful for the investigation and manipulation of fundamental material properties such as band-gaps, magnetization states and optical properties on ps-timescales within a separated detection layer. Even more flexible solutions would be possible if a selective excitation of spin stresses and phonon-stresses in the transducer were possible. At the current stage this appears to be difficult because the fs laser excitation of metals inevitably leads to electron excitations that couple to magnetic excitations and phonons via intrinsic, material specific processes. Dedicated excitation schemes of magnons in semiconductors and insulators such as GaMnAs may be more suitable but the forced magnetostriction coefficient is not as large as in the rare-earth containing alloys. The development of such a flexible transducer for variable picosecond strain pulses thus requires further research on ultrafast magnetostriction and material design. The data presented in this section show that the additional, field-induced magnetostrictive stress rises on the same timescale as the demagnetization. This is a pre-requisite for the manipulation of the picosecond strain response of

the transducer using external magnetic fields.

6.5 Probing magnetic order by a two-pulse excitation scheme

So far I have shown that optical excitation of spin-ordered rare-earths triggers a complex response of the crystal lattice, because expansive stresses from electron and phonon excitations compete with a sizable contractive stress induced by spin disorder. UXRD experiments can access the layer-specific strain response of the Dy film adjacent to a non-magnetic detection layer upon fs laser-excitation. In article VII, we have shown that the picosecond strain pulse and the thermal transport show signatures of a sizable energy transfer to magnetic excitations in the rare-earth. The modeled rise times of the magnetic stress are in close agreement with the recently reported demagnetization timescales. This indicates that the strain response can serve as a proxy for the time-dependent magnetic ordering in both AFM and FM rare-earths. This section is designed to experimentally extend these findings using a two-pulse excitation scheme, wherein the first laser pulse changes the magnetic state, while the second pump pulse triggers a lattice response that strongly depends on the degree of disorder of the spin system.

Figure 6.18 provides an overview of the strain response in this type of experiment for a pump-pump delay $\Delta t = 100\,\mathrm{ps}$ and different excitation fluences. A brief schematic of the experiment is given in 6.18(c) and the layer specific strain response for the Dy layer in panel (a) and (b) respectively. It can be seen that the strain response in the Dy transducer for a fluence of $3\,\frac{\mathrm{mJ}}{\mathrm{cm}^2}$ and $5\,\frac{\mathrm{mJ}}{\mathrm{cm}^2}$ at 35 K changes from pure contraction to a strong expansion for the case that a first pulse has at least partially demagnetized the Dy layer. The strain pulse in the Nb layer directly reflects the change from a contraction of the Dy layer to an expansion by the appearance of the bipolar strain pulse feature. For the case of $F(\mathrm{p}_1) = 8\,\frac{\mathrm{mJ}}{\mathrm{cm}^2}$, one finds that the strain response to p_2 in the buried Nb layer shows no initial expansion, and only a contraction which is indicative of a near complete total demagnetization.

The experiments shown in panel (d) and (e) are designed to directly show the varying response of the Dy transducer for a fixed excitation fluence of the second pulse. In this series, which was carried out at 60 K and 600 mT in-plane field, I varied only the fluence of the first pulse as indicated by the values next to the curves. The difference between the strain response upon two-pulse excitation and single-pulse excitation reflects the varying amplitude of the Dy strain depending on the fluence of the pre-pulse. In principle, this shows a tunable transducer response based on the spontaneous release of magnetostriction in the Dy layer that varies between expansion and contraction depending of the amplitude of p_1. These experiments may serve as proof of principle that magnetic stresses can be large and fast enough to counteract the electron-phonon-stresses that dominate the strain response in common, non-magnetic metals. The second demagnetization timescale that is on the order of $\approx 15\,\mathrm{ps}$ is however too long to induce a clean inverted bipolar strain wave. A complete invar effect is not observed due to the different time-dependencies of the electron-phonon-stress that attains its final level within the first few picoseconds and the magnetic stress that rises also on the longer timescale of the second demagnetizaton and heat transport within the layer. An exploration of other materials that combine magnetostriction with a one-step demagnetization or sample geometries may allow for a nearly homogeneous excitation of the transducer.

I finish this chapter by showing results of our first exploratory measurements on the effect of the pulse to pulse time variation for our two pulse experiments on the Dy transducer. Figure 6.19 shows a measurement at 90 K and an external field of 600 mT where Δt is varied and the fluence of $F(\mathrm{p}_1) = 5\,\frac{\mathrm{mJ}}{\mathrm{cm}^2}$ and $F(\mathrm{p}_2) = 1.7\,\frac{\mathrm{mJ}}{\mathrm{cm}^2}$ are kept fixed. The recovery of the magnetic stress is seen by the reduced amplitude of the initial expansion in the Dy strain that starts at approximately 100 ps. Our measurements show the versatility of the two-pulse excitation scheme for studying saturable magnetic stresses regardless of

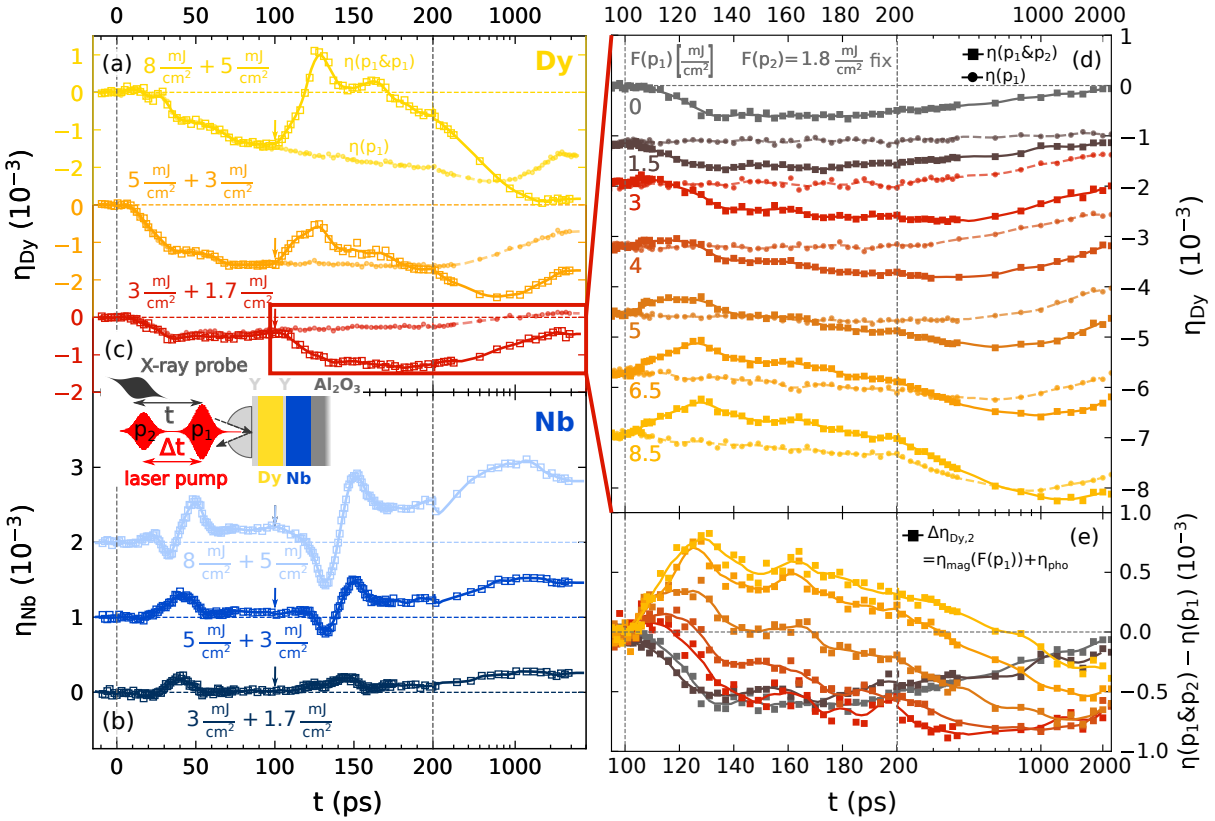

Figure 6.18: Representative strain response upon two-pulse excitation in Dy: (a) strain in the Dy transducer and (b) Nb detection-layer. Arrows indicate the timing of the second pulse. Inset (c) shows a schematic sketch of the experiment and sample structure. Dashed lines with filled symbols show the single pulse excitation results and solid lines with open symbols the two-pulse excitation and the arrows indicate time zero for the second pulse. The experiment was carried out at $T = 35\,\mathrm{K}$ with 600 mT in-plane field applied and a pulse to pulse delay of $\Delta t = 100\,\mathrm{ps}$. Note that the strain response shape both in the Dy transducer- and the Nb detection-layer change in the presence of a pre-pulse. Panel (d) shows a fluence scan of the first pulse $\mathrm{p_1}$ in a two-pulse experiment where the fluence of the second is fixed to $F(\mathrm{p_2}) = 1.8\,\frac{\mathrm{mJ}}{\mathrm{cm^2}}$. This experiment was carried out at 60 K and 600 mT in-plane field. Filled circles and dashed lines again indicate the average Dy-strain $\eta_{\mathrm{Dy},1}$ from a single pulse and filled squares with solid lines indicate the strain response to two pulses $\eta_{\mathrm{Dy},1+2}$. The extracted strain contribution of the second pulse $\Delta\eta_{\mathrm{Dy},2} = \eta_{\mathrm{Dy},1+2} - \eta_{\mathrm{Dy},1}$ depends on the amplitude of the first pulse as shown in panel (e). Lines are spline-interpolated guides to the eye and the curves are offset for clarity. Depending on the fluence of $\mathrm{p_1}$, the strain response of the Dy transducer changes from an initial contraction to an expansion. This is mainly attributed to the saturation in the spin stress contribution by the first pulse.

the type of magnetic order. In the aforementioned experiments, we have conducted the experiments in the FM-phase of the Dy transducer, but I expect very similar effects in the AFM-phase. A quantitative analysis of the average strain in the Dy-transducer is complicated by the inhomogeneous excitation of the transducer. The spatial gradient in the demagnetization adds a delayed contraction due to the energy transport to the backside of the Dy layer. The picosecond strain pulses that are launched in the Dy transducer may yield a clearer picture of the recovery of the magnetization within the Dy layer. The strain pulses reflect the stress at the moment of the second excitation. The previous results have shown that the spatially dependent stress in the Dy transducer is translated to a time-dependent average strain in the Nb detection layer via the propagation of the picosecond strain pulses. In the first measurement series, I did not record the Nb response due to time constraints. The reported two-pulse experiments provide a first orientation of the strain response in the experimental parameter space, which is extended by the fluence $F(\mathrm{p_2})$ and the relative timing Δt of the second pulse. This can be used for future measurements that study details of the spatial and temporal recovery of the magnetic stress within the rare-earth transducer.

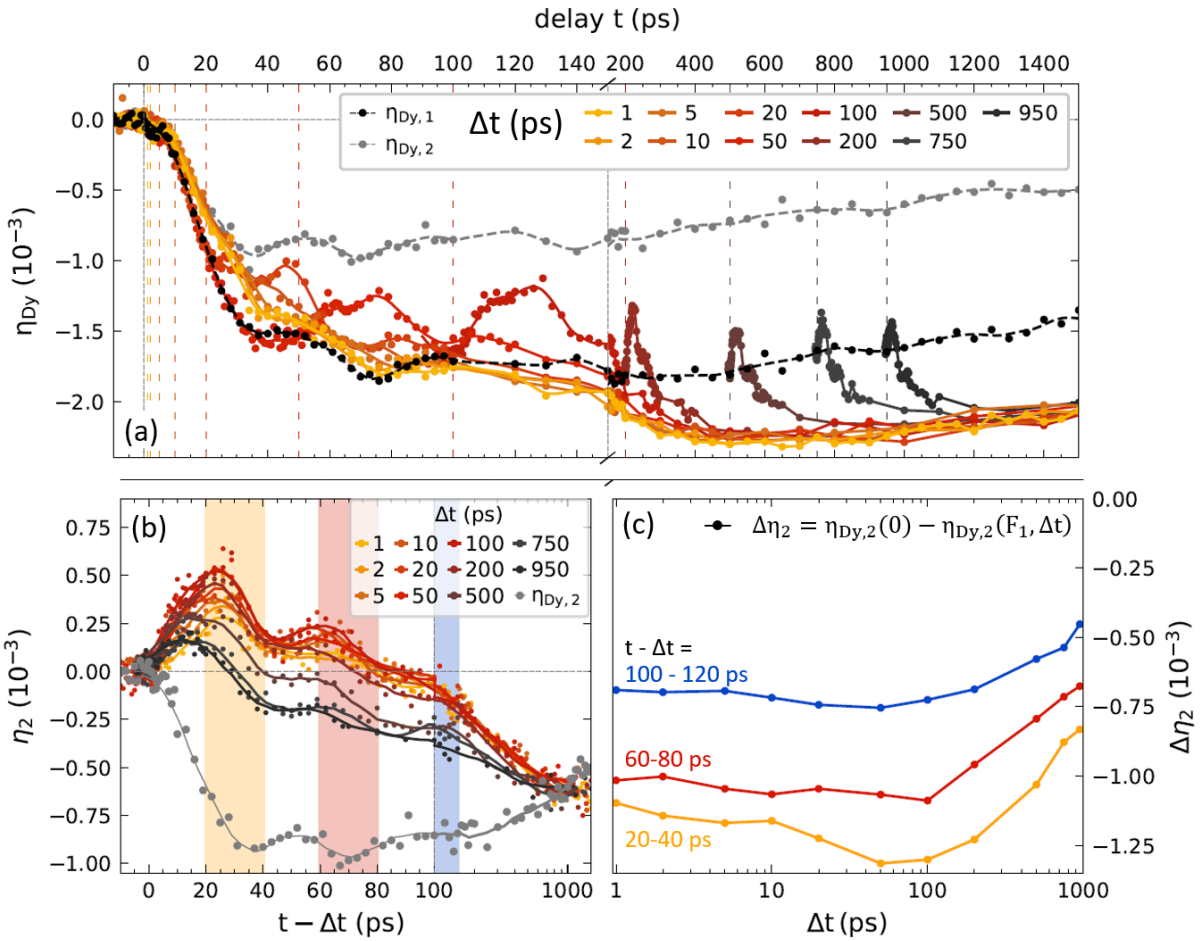

Figure 6.19: Pump-pump delay scan in a two-pulse experiment: This experiment was carried out at 90 K and 600 mT in-plane field: (a) strain in the Dy transducer with one pulse p_1 with $F = 5\,\frac{mJ}{cm^2}$ (black) and p_2 with $F = 1.7\,\frac{mJ}{cm^2}$ (grey) and color-coded for two pulses $p_1 + p_2$ with different temporal pulse to pulse separations Δt. Panel (b) displays the strain contribution of the second pulse $\Delta\eta_{Dy,2} = \eta_{Dy,1+2} - \eta_{Dy,1}$ on the shifted time-axis $t - \Delta t$. Solid lines are spline-interpolated guides to the eye. Panel (c) shows the difference between the strain evolution with and without pre-excitation averaged over the different shaded regions in (b) ($\Delta\eta_2 = \eta_2(F_1 = 0) - \eta_2(F_1, \Delta t)$). It indicates that the onset of the recovery of the magnetic stress occurs at 100 ps, which heralds a recovery of the magnetic order within the Dy transducer.

The magnetic order paramter for the helical antiferromagnets is given by the square of the sublattice magnetization. A time-resolved probe of this order parameter and the strain response under identical excitation conditions is currently lacking. Such an experiment would facilitate the direct comparison of the excitation and recovery of magnetic order in the AFM and FM phase. The presented experiments suggest that the time-dependent magnetostrictive stress amplitude may serve as a proxy to the magnetic order and a combined study of the magnetic order parameter and the magnetostrictive strain contribution may lead to quantitative comparison of these two phenomena.

CHAPTER SEVEN

Summary and Conclusion

This final part summarizes the findings from the presented experimental results and published articles. A section with possible future experiments and open questions is provided as outlook.

7.1 Effects of magnetization on the strain dynamics

This work shows that the presence of magnetic order in metallic films affects their laser-induced picosecond strain response, which thus contains signatures of the magnetic order. The observed effects could be classified as ultrafast magnetostriction and magneto-caloric effects in analogy to the related phenomena that occur in near-equilibrium conditions. Ultrafast magneto-caloric effects subsume changes in the energy transfer processes between excited electrons and phonons that result from the additional energy and entropy transfer to magnetic excitations. Magnetostriction effects comprise the stress on the lattice that results from changes in magnetic order. The three main scientific highlights of this thesis are:

- the analysis of energy transfer processes in heterostructures that contain only few atomic layers published in article II,
- the development of a versatile two-pulse excitation scheme for the identification of magnetic stress contributions demonstrated in article VI and
- the comprehensive analysis of the spatial and temporal dependence of the and magnetic stress profile in a rare-earth transducer based on the shape of the emitted picosecond strain pulses shown in article VII .

An identification of energy transfer processes in laser-excited heterostructures requires a time-resolved, nanoscopic, material-specific probing mechanism that serves as ultrafast thermometer. Tracking and analyzing the laser induced expansion is one possible approach, which is applicable in many different solids and configurations. In this work I demonstrate the application of UXRD to extract strain responses with (sub)-picosecond time-resolution in laser-excited thin films, nano-particles, heterostructures and especially layers buried within structures that are opaque to visible light. The employed laser-based diffraction setup allows for systematic measurement series in tailored sample conditions that yield the quantitative change in the average lattice constant of a material that is straightforward to extract from the data. This avoids the necessary calibration of material-specific photo-acoustic coefficients that are required for quantitative interpretations of spectroscopic techniques. Ultrafast diffraction experiments with bulk sensitivity and similar time-resolution would require large scale research facilities such as free electron lasers or dedicated slicing schemes at synchrotron beamlines, where beamtime access is often limited. The combination of picosecond ultrasonics experiments with X-rays at a table-top source represents a versatile bulk-sensitive technique that extends the capabilities of established all-optical setups and

complements surface sensitive ultrafast electron diffraction setups. The observed strain response in metals originates from a superposition of stress contributions by electrons, phonons and magnetic excitations. The response to the time-dependent total stress can be obtained numerically using an established linear chain of masses and springs that accounts for elastic stress contributions by picosecond strain pulses in addition to the laser induced external stresses. The shape of the strain pulses encodes the spatial and temporal form of the driving external stress profile and their timing can serve as a calibration of the thin film thicknesses. The modeled external stress σ_{ext} allows deriving an energy density distribution between electrons, phonons and magnetic excitations. Measurements of the ultrafast expansion of a thin film FePt sample compared to granular FePt highlight the importance of the morphology for the strain response. Depending on the constraints for the ultrafast in-plane motion it is important to account for transverse stresses that occur due to the Poisson effect only in nano-grains and not in homogeneously excited thin films. A double pulse excitation approach demonstrates the presence of a nearly instantaneous, contractive magnetic-stress contribution in FePt experimentally. The first pulse triggers magnetic excitations and the second pulse probes the strain response of the transiently demagnetized state as a function of the fluence and relative timing of the first excitation pulse. The two-pulse excitation approach can in general be employed to extract the contribution and recovery of saturable stresses that arise in materials that exhibit phase-transitions, which renders it a very versatile technique.

The analysis of the strain response contains signatures of energy transfer processes to magnetic excitations in heterostructures. Because energy itself is not an experimentally accessible observable one needs to infer magneto-caloric effects from the change of the strain response for different magnetic orders in the transducer. We find that the thermal expansion of the sensor layers buried below a magnetically ordered dysprosium or holmium transducer are reduced when the rare-earth layer exhibits magnetic order prior to its laser-excitation. This can be rationalized by a delayed heat flow through the laser excited rare-earth layer, due to energy transfer to magnetic excitations. Magnetic-stress contributions are a direct consequence of the energy transfer to magnetic excitations according to the Grüneisen concept. The magnetic stress contribution in laser-excited rare-earth layers is found to be so large, that it changes the transducer response from an expansion in the PM phase to an overall contraction in the helical AFM and FM phase. The analysis of the resulting picosecond strain pulses in article VII shows that the rise of the magnetic stress exhibits the same rise times that have been reported for the demagnetization of laser-excited dysprosium. This shows that the magnetic stress contribution to the picosecond strain response can be used a proxy for the magnetic order even for non-collinear magnetic order. A procedure for the analysis of the de- and remagnetization in laser-excited rare-earth transducers using two-pulse excitation experiments is outlined. It indicates a recovery of the magnetostrictive stress in the FM-phase of Dy to start at approximately 100 ps after laser-excitation. This approach can be developed to further investigate the long lasting non-equilibrium between magnetic excitations and phonons that I extracted in the analysis of the first systematic report of the strain response in laser-excited rare-earth elements in 2016. The reported field-dependent strain response shown in this thesis indicates the potential use of magnetostrictive transducers for tunable picosecond strain generation by the release of the magnetic stress upon laser-excitation. In general, this work applies the concept of a Grüneisen parameter to the analysis of the ultrafast strain response in metal transducers. The proportionality between the laser induced stress and the density stored within electron, phonon and magnetic subsystems of solids is found to be a useful modeling approach across various materials. It is especially useful in non-equilibrium situations where the internal equilibration of the subsystems may not be a valid assumption. Multiple illustrations and examples are designed to make the Grüneisen approach accessible to the reader.

7.2 Outlook on future investigations

Picosecond ultrasonics experiments that employ X-ray diffraction as probing mechanism yield a quantitative measure of the material-specific strain response within laser-excited heterostructures. The presented experiments are far from exhaustive in regard to the capabilities of the setup. The presented discussion in the context of sub-system specific Grüneisen parameters provides a framework for the interpretation of the strain response in materials that exhibit magnetic order. The following list summarizes experiments that could address open questions using the here-presented technique if suitable sample structures are provided where at least one layer exhibits a sufficient degree of crystallinity.

- The combination of experimental techniques that contribute independent probing mechanisms for electron excitations, phonons and magnetic excitations in one setup promises to provide a detailed picture of the energy transfer processes within laser-excited materials. An extension of the PXS setup by an optical MOKE and optical reflectivity detection routine is currently commissioned in our group, so that the electron, magnetization and structural response can be obtained under identical excitation conditions. This will allow for quantitative tests of the widely used microscopic two-temperature model[72] or three-temperature models for the magnetization dynamics. This could be applied to study the demagnetization amplitude in laser-excited thin ferromagnetic films made of, for example, Ni, Fe, Co, Gd or FePt in relation to the phonon-temperature extracted from the strain response. Further examinations of the remagnetization could investigate the relation between the recovery of the MOKE signal to the time-dependent difference between the phonon temperature and the Curie temperature.
- Studies of magnons triggered by picosecond strain pulses could also benefit from the combination of MOKE and UXRD in one setup because it allows for quantitative comparisons. The magneto-acoustic coefficient is an important quantity in time-domain studies of magnons, because it links the strain amplitude to the effective field that acts on the magnetization. UXRD-experiments provide the ability to observe and calibrate the strain amplitude from coherent and incoherent phonons (hypersound and heat) and thus quantify the magneto-acoustic coupling strength that is otherwise taken as fit parameter. Interesting materials for such experiments are technologically relevant materials such as iron-garnets that exhibit very low magnon damping or materials with large magnetostriction such as Galfenol and Terfenol-D where large magnetization precession amplitudes can be expected. This would extend the presented work in article III, where we see clear indications of picosecond strain pulses in the MOKE signal but refrain from a quantitative relation due to different excitation conditions. In order to separate the contributions of heat and strain pulses, it would be very beneficial to separate the transducer from the magnetic layer by an insulating acoustic delay line similar to our experiments in article III. This setup furthermore allows us to study damping processes of picosecond strain pulses that traverse a magnetically ordered layer, which would extend insights on critical phenomena based on ultrasonics experiments in the MHz regime to the GHz regime of laser-induced hypersound pulses.
- The double-pulse excitation technique that I applied to identify the spin-stress contribution in FePt can be used to find similar effects in many other materials with various types of magnetic order. In principle, one expects magnetostrictive contributions to be present in every magnetically ordered material due to the distance-dependent exchange interaction strength. Probing the time-dependent amplitude of the magnetostrictive contributions to the strain response yields a scenario for the investigation of antiferromagnets and materials with non-collinear magnetic order. This type of order is difficult to access via spectroscopic techniques, which require a net magnetization. Even more generally, one can use two-pulse excitation scenarios to investigate saturable stress contributions in

general as they frequently arise in the context of phase-transitions. One generic example in this regard is the metamagnetic phase transition of the AM-FM phase in FeRh that exhibits a large structural response. Additionally it could also be investigated if phase-transitions can be accelerated by a second, delayed excitation. In general, one can employ the double pulse-excitation to study the strain response of transient, non-equilibrium phases that may not be accessible in conventional heating experiments.

- Studies of the strain response yield general insights into energy transfer processes within solids. UXRD experiments are especially suitable for time domain studies of the various mechanisms that lead to negative thermal expansion. The unequivocal identification of the laser-generated high-frequency strain pulses and the calibration of their amplitude renders the presented technique suitable for the exploration of materials that could serve as tunable picosecond transducers. Invar-like behavior on ultrafast timescales is an interesting special case that is not yet achieved experimentally. If realized, such an ultrafast invar material could serve as a source for incoherent phonons (heat) without the occurrence of picosecond strain pulses in time-resolved experiments. This would help to disentangle the effects of incoherent and coherent phonons in laser-excited heterostructures that frequently intermix. It is also interesting to investigate how materials that exhibit volume invar behavior upon equilibrium heating respond to fs-laser excitation. A non-zero picosecond strain response could arise due to transient non-thermal energy distribution between the electron, phonon and spin subsystems in tailored FeNi, FePd, FePt alloys that are known for their invar behavior[44, 218].
- Many interesting transducer materials used in magnetostrictive applications such as Galfenol and Terfenol-D are polycrystalline alloys. They are thus expected to exhibit only a limited degree of long-range order so that the corresponding diffraction signals may be too weak for direct studies of their response. The presented analysis of the picosecond strain pulses that enter a buried detection layer shows that their shape is determined by the stress profile in the transducer. An extension of the presented experiments to non-crystalline transducers on top of a crystalline detection layers is thus possible. This expands the applicability of the presented diffraction technique to studies of strain pulses from transducers that lack crystalline order but nevertheless host interesting physical phenomena such as superconductivity, ferroelectricity, topological phases and strongly-correlated electrons. All of these phenomena are expected to leave signatures in the emitted picosecond strain waves.
- Tracking the strain response via UXRD furthermore provides access to the thermal transport processes in nanoscale heterostructures. Modeling the recovery of the strain response quantifies potential thermal boundary resistances, or helps distinguishing the contributions of phonons and electrons as heat carriers. Calibrating and modeling thermal transport effects across thin film interfaces and confined geometries becomes more and more important due to the permanent miniaturization of the constituents in future information technology.

The sub-picosecond time-resolution of the presented experiments allows for studies of the strain response and thermal transport in films thinner than 20 nm. This time-resolution in diffraction experiments is only matched by large scale facilities such as free-electron lasers or synchrotron facilities with special operation modes where limited beam access often restricts systematic or exploratory investigations. Picosecond strain responses are a general feature in laser-excited materials and the analysis of their shape may shed light on the sub-system specific coupling mechanisms that are the origin of their functional behavior.

Chapter Eight

Articles

Article I

Watching the vibration and cooling of ultrathin gold nanotriangles by ultrafast x-ray diffraction

Alexander von Reppert, Radwan Mohamed Sarhan, Felix Stete, Jan-Etienne Pudell, Natalia Del Fatti, Aurélien Crut, Joachim Koetz, Ferenz Liebig, Claudia Prietzel, and Matias Bargheer

The Journal of Physical Chemistry C 120, 28894-28899 (2016)

We study the vibrations of ultrathin gold nanotriangles upon optical excitation of the electron gas by ultrafast x-ray diffraction. We quantitatively measure the strain evolution in these highly asymmetric nano-objects, providing a direct estimation of the amplitude and phase of the excited vibrational motion. The maximal strain value is well reproduced by calculations addressing pump absorption by the nanotriangles and their resulting thermal expansion. The amplitude and phase of the out-of-plane vibration mode with 3.6 ps period dominating the observed oscillations are related to two distinct excitation mechanisms. Electronic and phonon pressures impose stresses with different time dependences. The nanosecond relaxation of the expansion yields a direct temperature sensing of the nano-object. The presence of a thin organic molecular layer at the nanotriangle/substrate interfaces drastically reduces the thermal conductance to the substrate.

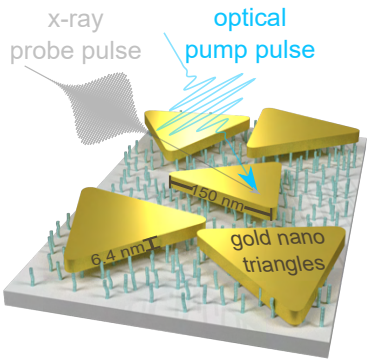

THE JOURNAL OF PHYSICAL CHEMISTRY C

Article

pubs.acs.org/JPCC

Watching the Vibration and Cooling of Ultrathin Gold Nanotriangles by Ultrafast X-ray Diffraction

A. von Reppert,[†] R. M. Sarhan,[†,∥] F. Stete,[†,∥] J. Pudell,[†] N. Del Fatti,[‡] A. Crut,[‡] J. Koetz,[§] F. Liebig,[§] C. Prietzel,[§] and M. Bargheer*[,†,⊥]

[†]Institut für Physik & Astronomie, Universität Potsdam, Karl-Liebknecht-Str. 24-25, 14476 Potsdam, Germany

[‡]FemtoNanoOptics Group, Institut Lumière Matière, Université de Lyon, CNRS-Université Lyon 1, 69622 Villeurbanne, France

[§]Institut für Chemie, Universität Potsdam, Karl-Liebknecht-Str. 24-25, 14476 Potsdam, Germany

[∥]Humboldt-Universität zu Berlin, School of Analytical Sciences Adlershof (SALSA), Albert-Einstein-Str. 5-9, 10099 Berlin, Germany

[⊥]Helmholtz Zentrum Berlin, Albert-Einstein-Str. 15, 12489 Berlin, Germany

ABSTRACT: We study the vibrations of ultrathin gold nanotriangles upon optical excitation of the electron gas by ultrafast X-ray diffraction. We quantitatively measure the strain evolution in these highly asymmetric nano-objects, providing a direct estimation of the amplitude and phase of the excited vibrational motion. The maximal strain value is well reproduced by calculations addressing pump absorption by the nanotriangles and their resulting thermal expansion. The amplitude and phase of the out-of-plane vibration mode with 3.6 ps period dominating the observed oscillations are related to two distinct excitation mechanisms. Electronic and phonon pressures impose stresses with different time dependences. The nanosecond relaxation of the expansion yields a direct temperature sensing of the nano-object. The presence of a thin organic molecular layer at the nanotriangle/substrate interfaces drastically reduces the thermal conductance to the substrate.

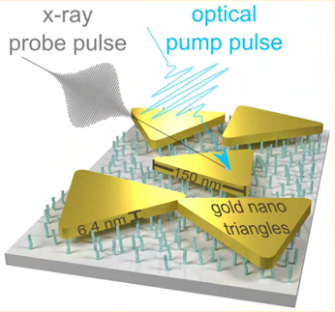

INTRODUCTION

Metallic nanoparticles have been in the focus of intensive research over decades,[1] in part because they may potentially help to realize large bandwidth optical nanoelectromechanical systems or similar small and fast devices.[2] From the perspective of physical chemistry, colloidal particles present versatile and accessible nano-objects, which can be grown as spheres, rods, cubes, pyramids, platelets, or prisms, just to name a few examples. Special shapes are useful for tailoring the plasmon-resonance and catalytic activity of the particles or to optimize them for surface-enhanced Raman scattering. Investigations of the ultrafast thermal and vibrational dynamics of such nanostructures[3−6] are often justified by applications like photothermal therapy or catalysis.[7] The strong interest in these phenomena also lies in the fundamental questions of how heat transport and vibrational response are altered on the nanoscale, when surface effects may start to play a role, making the validity of continuum descriptions questionable.[8−12] Recently the focus of ultrafast studies has shifted from spherical particles over nanorods toward truly asymmetric structures such as prisms.[4,13−15] These particles often exhibit special crystalline structures with well-defined orientation,[16] which influence not only the growth and stability but also the optical and acoustic properties.[17]

The vibrational dynamics of nano-objects have been studied by a myriad of ultrafast optical pump−probe experiments looking at absorption, reflection, or scattering of ensembles.[3,4,6] Because the polydispersity of the samples leads to a dephasing of the observed vibrations, more recently such experiments were carried out on individual nano-objects.[18,19] Although much has been learned by optical techniques and the simulations using continuum mechanics or molecular dynamics, a thorough discussion of purely optical measurements is required to obtain information about the amplitude and phase with which individual vibrational modes are excited.[4,5,20,21] Ultrafast structural tools such as ultrafast X-ray or electron diffraction are the most direct ways to study changes of the crystal lattice induced by laser excitation. Although diffraction on the femtosecond time scale started to become available 20 years ago, only very few studies of nanoparticle dynamics with dynamics faster than 100 ps have been reported.[22−24] An experiment at the free-electron laser has monitored the breathing[25] and melting[26] of a single few hundred nanometers large ellipsoidal nanocrystal. Studying asymmetric and much thinner objects has, however, remained a challenge, and, in general, ultrafast single-particle studies using X-rays can exclusively be performed at free-electron laser facilities.[10] Demonstrating the possibility to use a laser-based femtosecond X-ray source for ultrafast structural measurements on ensembles of nanoparticles is therefore a major breakthrough.

We present such ultrafast X-ray diffraction (UXRD) experiments that precisely determine the average out-of-plane

Received: November 18, 2016
Revised: November 25, 2016
Published: November 27, 2016

DOI: 10.1021/acs.jpcc.6b11651
J. Phys. Chem. C 2016, 120, 28894−28899

strain $\varepsilon(t)$ of an ensemble of <111> oriented gold nanotriangles (NTs) as a function of the time delay t after the excitation. On the basis of the sound velocity v_{111} = 3.528 nm/ps along the [111] direction,[27] the oscillation period of T = 3.6 ps corresponding to the fastest out-of-plane vibration mode yields a particle thickness $d_0 = v_{111} \cdot T/2$ = 6.4 nm, consistent with particle shape characterized by thorough TEM measurements. The amplitude of the first oscillation and the maximal expansion $\varepsilon_{max} = 3 \times 10^{-3}$ of the particle after ~20 ps are consistent with a 1D acoustic model, where the expansion mode of the film is excited by a time-dependent pressure $\sigma(t)$ imposed by hot electrons and phonons. The pump−pulse absorption is calculated by a complete 3D numerical optical model.[19,28,29] A careful analysis by electron microscopy is used to prove that the NTs shape is robust under the experimental conditions. From the measured lattice strain, ε, one can directly read the temperature change ΔT_0 via

$$\epsilon = \int_{T_0}^{T_0+\Delta T_0} \alpha_{Au}(T)\, dT \quad (1)$$

using the expansion coefficient $\alpha_{Au}(T)$ measured in thermal equilibrium. The cooling on the nanosecond time scale evidences the rather good thermal insulation given by the ~1 nm thick organic layer that was used for functionalizing the surface of the silicon substrate.

EXPERIMENTAL SECTION

Very thin gold NTs were prepared in a one-step synthesis in the presence of mixed AOT/phospholipid vesicles via a process that can be described by an Ostwald ripening growth mechanism.[31] To reduce the polydispersity of the product, the anisotropic nanoparticles were separated by using a combined polyelectrolyte/AOT micelle depletion flocculation.[31] The NTs were deposited on a silicon wafer functionalized by 3-mercaptopropyltrimethoxysilane (3-MPTMS).[32] The NTs were attached to the thiol group at a distance of ~1 nm above the Si surface. AFM investigations of >40 nanoplatelets reveal an average thickness of 8.5 ± 1.5 nm. Subtracting 1 nm of the 3-MPTMS layer, this is in full agreement with the 6.4 nm platelet thickness derived from the UXRD data. Figure 1 shows a thorough characterization of the sample by electron microscopy. The sideview (Figure 1a) of two individual NTs with 6.7 and 8.2 nm thickness illustrates the thickness of ~7.5 ± 1.5 nm. While the base length of the NTs is ~150 nm with a large size distribution (Figure 1d), the distribution of the platelet-thickness is rather sharp. The zoom into the NTs (Figure 1b)) can be Fourier-transformed to determine the periodicity of the lattice structure. Figure 1c proves the <111> orientation of the entire triangle.[30] Figure 1e confirms that the NTs are intact after UXRD experiments performed at a base temperature T_0 = 24 K with a pump wavelength of 400 nm and a fluence of F = 2.9 mJ/cm^2. Figure 1f,g shows the permanent deformation of the NTs under similar fluence conditions at room temperature. The UXRD experiments[33−35] subsequently discussed in this paper were conducted under the nondestructive conditions T_0 = 24 K and F = 2.9 mJ/cm^2. The pump pulses had a duration of ~80 fs, and the pulse length of the hard X-ray probe pulses at 8 keV derived from a laser-driven plasma source reduced the time resolution of the setup to ~200 fs.[34,35] Figure 2 illustrates the static XRD characterization of the sample in the geometry of the UXRD setup.[34] Figure 2b shows the reciprocal space map of the pristine sample, whereas the integrated X-ray diffraction intensity as a function of the Bragg angle θ in Figure 2a also reports a comparison to the diffraction from a sample after excessive irradiation with optical pump-pulses at 300 K. The reshaping of the Bragg peak indicating the permanent deformation of the gold particles at high fluence excitation at room temperature is clearly visible also in the reciprocal space map (not shown). The very weak and broad reflection from the gold (1 1 1) lattice planes (Figure 2b) renders the UXRD data acquisition extremely difficult, especially because the fluence must be reduced such that no sample damage occurs during several hours of optical pumping. Figure 2c compares the shifted Bragg peaks after 2.1 and 19 ps in the UXRD experiment with the Bragg peak at negative pump−probe delay. At low temperature and with the applied fluence the shape of these peaks is unchanged during the acquisition of the UXRD data.

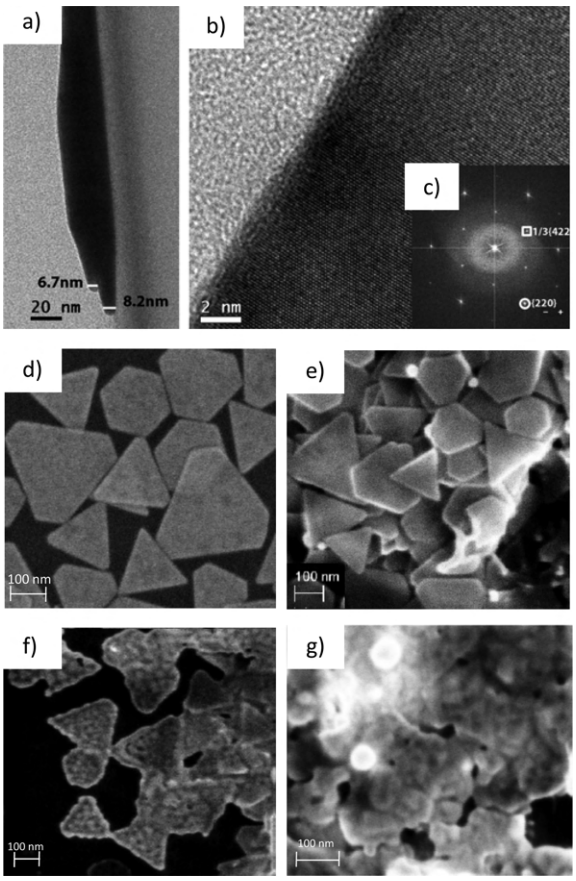

Figure 1. TEM and SEM pictures of the gold nanotriangle sample. (a) TEM sideview of gold-NTs. (b) High-resolution TEM and (c) its Fourier transform show 1/3{422} and {220} reflections characteristic of NTs with <111> orientation.[30] (d) SEM micrograph showing the polydisperse nature of the nanoplatelets. (e) SEM micrograph of the sample after the pump−probe experiment at T_0 = 24 K with F = 2.9 mJ/cm^2. (f) SEM micrograph of the sample after treatment with F = 3 mJ/cm^2 at room temperature. (g) Same for F = 5 mJ/cm^2. Triangles deform or melt together and reshape to spheres.

DOI: 10.1021/acs.jpcc.6b11651
J. Phys. Chem. C 2016, 120, 28894−28899

The Journal of Physical Chemistry C Article

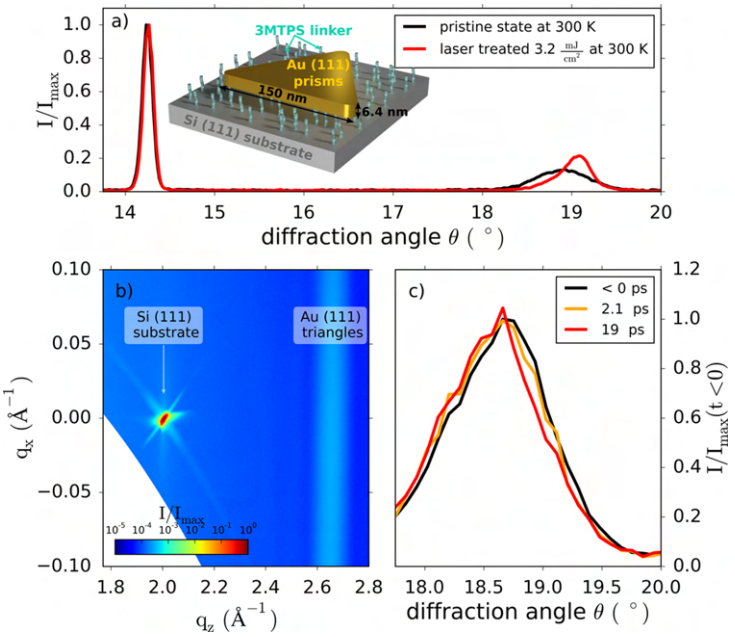

Figure 2. (a) Integrated X-ray intensity as a function of the Bragg angle θ for the pristine sample (black) and for a sample spot that was excessively irradiated at room temperature (red). Inset: Schematic of the ideal situation where all gold-NTs are attached to the surface with equally long organic spacer molecules. (b) Reciprocal space map showing the sharp Si substrate peak and the very weak and broad reflection of the gold NTs. The diffraction does not correspond to a Debye−Scherrer ring but to a single-crystal diffraction with a large mosaic spread of about ±5° originating from the nonperfect sample that also contains stacked NTs. (c) Integrated X-ray diffraction intensity for three different time delays at a fluence of 2.9 mJ/cm^2 that does not permanently modify the sample. We essentially observe a peak shift to smaller angles, indicating the ultrafast out-of-plane expansion.

RESULTS AND DISCUSSION

Figure 3 shows the lattice strain $\varepsilon(t)$ as a function of the time delay t after excitation of the gold NTs at T_0 = 24 K with 400 nm pulses. The fluence F = 2.9 mJ/cm^2 is given by the light intensity on the sample surface at the incidence angle of 40°. The femtosecond pulse excitation leads to an oscillation of the measured out-of-plane strain with a period of T = 3.6 ps, which is consistent with the fundamental breathing mode of a film with thickness 6.4 nm. The strain reaches a first maximum of ε = 2.3 ± 0.3 × 10^{-3} after ∼2 ps. The signal oscillates and reaches a maximum of ε_{max} = 3 ± 0.3 × 10^{-3} after ∼20 ps. The lattice slowly contracts on a nanosecond time scale as the heat flows out of the nanoparticle.

To interpret the observed maximum expansion ε_{max}, we calculated the temperature rise of a gold NT originating from the absorption of 400 nm pulses under 40° incidence. We computed the absorption cross-section using a finite-element approach accounting for the inhomogeneous nano-object environment induced by its deposition on a silicon substrate,[19,28,29] yielding σ_{abs} = 1200 nm^2 for NTs with 6.4 nm thickness and 150 nm side length. Neglecting heat transfer to the environment on short time scale, the temperature rise of a thermalized gold NT ΔT_0 = 285 K at T_0 = 24 K is calculated by numerical integration of

$$\sigma_{abs}F/(\rho_{Au}V) = \int_{T_0}^{T_0+\Delta T_0} c_{Au}(T)\,dT \quad (2)$$

where ρ_{Au} = 19.3 g/cm^3 is the density, $c_{Au}(T)$ is the strongly temperature-dependent heat capacity of gold, and V is the volume of the particle. From eq 1 we calculate an expansion of $\varepsilon^{calc} = 3 \times 10^{-3}$, in excellent agreement with the data. For room temperature, the calculation yields the same result. This can be understood by invoking the Grüneisen parameter of gold, γ, which is a temperature-independent[36,37] measure of the thermal stress $\sigma = \gamma \cdot Q$ upon deposition of an energy density Q.[37] The heat expansion coefficient $\alpha(T)$ and heat capacity $c(T)$ share the same temperature dependence, both for the electronic contribution and for the phonon contribution, which are given by their quantum nature. Therefore, the electronic and phononic Grüneisen parameters of gold $\gamma_e \sim \alpha_e(T)/c_e(T)$ and $\gamma_p \sim \alpha_p(T)/c_p(T)$ are independent of temperature.

To quantitatively describe the oscillation of the signal at short times, we have to account for the fact that the optical excitation first heats up the electron gas, yielding a corresponding electron stress σ_e driving the out-of-plane expansion of the NT. We estimate an electronic temperature rise of T_e(100 fs) = 4000 K from the electronic specific heat of $c_e(T) = \gamma_s T$, where $\gamma_s = 3.7 \times 10^{-6}$J/(gK) is the Sommerfeld-coefficient of gold.[38] The electron pressure $\sigma_e(t) = \gamma_e Q_e(t) = \gamma_e Q^e_{max} e^{-t/\tau_e}$ relaxes with the characteristic electron−phonon coupling time τ_e. With the same time constant, the phonon pressure $\sigma_p(t) = \gamma_p Q^p_{eq}(1 - e^{-t/\tau_e})$ rises until the electron and phonon temperatures have equilibrated. The electron−phonon coupling time in gold in the low perturbation limit is 1 ps at room temperature and 0.6 ps at 24 K.[39,40] However, under strong excitation conditions, the electronic heat capacity c_e rises with temperature, and equilibration times can exceed 5 ps under our conditions.[38,41,42] At t = 20 ps, we can safely assume that the electron and phonon system have reached a mutual

DOI: 10.1021/acs.jpcc.6b11651
J. Phys. Chem. C 2016, 120, 28894−28899

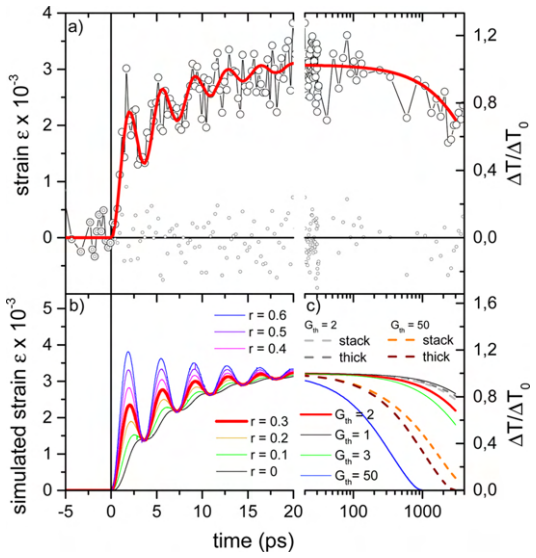

Figure 3. (a) Time-dependent strain measured by UXRD (open circles) together with the best fits from the models (red lines). The time axis is split according to the two models. The small dots represent the difference of the data and the simulation indicating only little contributions from additional vibrational modes. The relative error 3×10^{-4} of the strain measurement is estimated from the variation of data for $t < 0$ and around the maximum. (b) Model simulation according to eq 4 with a single oscillator driven by the phononic and electronic stresses according to eq 3. $r = \gamma_e/\gamma_p$ is ratio of the electronic and phononic Grüneisen parameters. (c) Results from the 3D heat-transport simulations. The thin lines are obtained for a single Au triangle separated from Si by a layer with a thermal interface conductance G_{th} in MW/(m^2 K). The fat red line indicates the best fit that is reproduced in panel a. The dashed lines are cross-checks for heat transport out of three stacked NTs (see the text).

thermal equilibrium so that a single temperature suffices to describe both systems.

The UXRD data provide a unique access to the phase and amplitude of the oscillations, which are both sensitive to the exact form of the total driving stress, which is given by the following functional form[42−44]

$$\sigma(t) = \sigma_e(t) + \sigma_p(t) = \sigma_\infty H(t)\left(1 + \left(\frac{\gamma_e}{\gamma_p} - 1\right)e^{-t/\tau_e}\right) \tag{3}$$

where $H(t)$ denotes the Heaviside function. The maximum stress $\sigma_\infty = C_{eff}\cdot\varepsilon(20\text{ ps})$ can be deduced from the measured strain and the effective elastic modulus C_{eff} along the [111] direction. To model the early time vibrations (Figure 3a), we consider the homogeneous increase of the particle thickness $d(t)$ as the only relevant vibrational mode with frequency ω_0 and damping rate η. It is excited by the time-dependent stress $\sigma(t)$ stated in eq 3. The explicit differential equation used to describe the time-dependent out-of-plane strain $\varepsilon(t) = \frac{d(t) - d_0}{d_0}$ of the particles is then

$$\frac{d^2\varepsilon}{dt^2} + 2\eta\frac{d\varepsilon}{dt} + \omega_0^2\varepsilon = P\sigma(t) \tag{4}$$

The constant prefactor P on the right-hand side is due to dimensional reasons as it relates the driving stress $\sigma(t)$ to an acceleration of the strain. The equation of motion can be solved using the Green's function of the damped harmonic oscillator $G(t, t') = H(t - t')\frac{i}{\omega_- - \omega_+}(e^{i\omega_+(t-t')} - e^{i\omega_-(t-t')})$, where $\omega_\pm = i\eta \pm \sqrt{\omega_0^2 - \eta^2}$. The time-dependent strain can then simply be found via integration

$$\varepsilon(t) = P\int_{-\infty}^{t'} G(t, t')\sigma(t')\,dt' \propto \int_{-\infty}^{t'} G(t, t')\sigma(t')\,dt' \tag{5}$$

The magnitude of the prefactor P is dictated by the strain that is attained after the oscillations are damped out. We vary $P\cdot\sigma_\infty$ to match the signal at t = 20 ps and adjust the ratio r of the Grüneisen parameters to $r = \gamma_e/\gamma_p = 0.3$ and the damping constant η = 0.15 ps^{-1} to match the amplitude of the first oscillations. The time constant τ_e = 6.5 ps is found to be close to those previously measured in similar strong perturbation conditions.[38] Figure 3a shows the measured data (open circles) together with the fit according to this model (red line) up to 20 ps. The black dots in Figure 3 represent the difference $\varepsilon_{exp}(t) - \varepsilon_{sim}(t)$ of the data and the simulation. They give an estimate of how much vibrational modes with lower frequency contribute to the out-of-plane expansion of the NTs. Because of the lateral size distribution, we expect that contributions by low-frequency modes rapidly dephase and thus are below the noise level. The left panel of Figure 3b shows simulations with a ratio $r = \gamma_e/\gamma_p$ varied from 0 to 0.6. The best fit is obtained for r = 0.3, a value that is smaller than the theoretical ratio expected for bulk gold r = 0.5[42] but consistent with other experiments performed on acoustic vibrations of small noble-metal nanoparticles.[43] We note that for $0 < r < 1$ the phase of the oscillation is delayed more and more as r approaches zero. For $r > 1$ the oscillations would start somewhat earlier. Therefore, both the amplitude and the phase of the observed UXRD signal allow us to assess the temporal form of the driving stress $\sigma(t)$.

For larger time delays (right panel), we plot the data on a logarithmic time axis and the red line represents the results of a 3D finite-element model of NT cooling, accounting for both 3D heat diffusion and thermal resistance at the triangle/substrate interface. We simulated a 6.4 nm thick gold triangle with initial temperature $T_i = T_0 + \Delta T$, which is attached to a Si substrate with a fixed temperature of T_0 = 24 K at the backside. Initial heating of the absorbing substrate was neglected as it weakly affects the cooling dynamics of the triangle due to the high thermal conductivity of silicon. We take the temperature-dependent bulk values[45−47] of the heat capacity $c_{Au/Si}$ and thermal conductivity $\kappa_{Au/Si}$ for Si and Au and account for the 1 nm thick organic layer by imposing a thermal interface conductance of G_{th} = 2 MW/(m^2 K) between Au and Si. This numerical value yields the best fit to the data in the model where a single gold particle is separated from the Si surface by an organic layer. For an epitaxial Au film on Si, one would expect an interface conductance of 50 to 150 MW/(m^2 K), which would lead to a much faster cooling.[48] For convenience, heat diffusion simulations with varying interface conductance are shown in Figure 3c for t > 20 ps as thin solid lines. The best fit G_{th} = 2 MW/(m^2 K) is shown as a thick line. To estimate the systematic error originating from the model, we also simulated the heat flow out of a "stack" of three gold NTs, which, in addition to the finite Au/Si thermal interface conductance G_{th}, have the same interface conductance between each gold

DOI: 10.1021/acs.jpcc.6b11651
J. Phys. Chem. C 2016, 120, 28894−28899

particle. As a further crosscheck, we have plotted results for "thick" NTs with a triple thickness and with only one interface with G_{th} from the gold to Si. All three models require the heat flow out of the particles to be strongly reduced by the 1 nm organic layer in comparison with a direct contact of Au on Si to achieve a good fit. The interface conductance is considerably lower than the values above 50 MW/(m^2 K) derived for Au–water interfaces with various surface functionalizations[49] and for the interface conductance of Au to Quartz across a self-assembled monolayer.[50,51] The attempt to rationalize the reduced heat flow by a low thermal conductivity of the 1 nm thick 3-MPTMS layer would require a value of 2×10^{-3}W/mK typical of dilute gases. We can therefore conclude that the slow cooling dynamics observed experimentally mostly originates from a low thermal conductance at the Au–Si interface.

CONCLUSIONS

Ultrafast X-ray diffraction measurements on an ensemble of 6.4 nm thick gold NTs directly and quantitatively measure the out-of plane expansion dynamics after optical excitation at 400 nm. The primary oscillatory motion can be explained by a single damped out-of-plane breathing mode with a period of T = 3.6 ps. The phase and amplitude of the UXRD signal are sensitive measures of the functional form $\sigma(t)$ of the time-dependent stress from hot electrons and phonons. The cooling time of several nanoseconds is dictated by the 1 nm thin organic layer that connects the gold-NTs to the silicon substrate. We can rationalize the observations by numerical models. In comparison with the situation expected for a thin gold layer on Si, our experiments demonstrate a slight modification of the relative ratio of the electronic and phononic Grüneisen parameters and a surprisingly strong reduction of heat conduction by a thin organic functional layer. Future UXRD studies on monodisperse asymmetric Au nanoparticles might also be able to quantify the contributions of other vibrational modes and can finally lead to a microscopic understanding of their reshaping under laser excitation. We believe that this pioneering experiment studying the dynamics of nanoparticles with a laser-based femtosecond X-ray source may trigger a broad range of novel experiments, for example, studying the nanoparticle temperature in photocatalytic experiments or during the magnetic heating of nanoparticles for catalysis. We emphasize that the heat-transport characteristics can be obtained by our method via synchrotron-based time-resolved X-ray diffraction, which is accessible for users from any field of natural sciences.

AUTHOR INFORMATION

Corresponding Author

*E-mail: bargheer@uni-potsdam.de. Tel: +49 (0)331 977 4272. Fax: +49 (0)331 977 5493.

ORCID

M. Bargheer: 0000-0002-0952-6602

Notes

The authors declare no competing financial interest.

ACKNOWLEDGMENTS

R.M.S. and F.S. acknowledge financial support by the DFG via the graduate school SALSA, J.P. is supported by the DFG via BA 2281/8-1, and F.L. is supported via KO 1387/14-1.

REFERENCES

(1) Tchebotareva, A.; Ruijgrok, P.; Zijlstra, P.; Orrit, M. Probing the Acoustic Vibrations of Single Metal Nanoparticles by Ultrashort Laser Pulses. *Laser Photonics Reviews* **2010**, *4*, 581–597.

(2) Chen, K.; Razinskas, G.; Feichtner, T.; Grossmann, S.; Christiansen, S.; Hecht, B. Electromechanically Tunable Suspended Optical Nanoantenna. *Nano Lett.* **2016**, *16*, 2680–2685.

(3) Crut, A.; Maioli, P.; Del Fatti, N.; Vallée, F. Time-Domain Investigation of the Acoustic Vibrations of Metal Nanoparticles: Size and Encapsulation Effects. *Ultrasonics* **2015**, *56*, 98–108.

(4) Crut, A.; Maioli, P.; Del Fatti, N.; Vallée, F. Acoustic Vibrations of Metal Nano-Objects: Time-Domain Investigations. *Phys. Rep.* **2015**, *549*, 1–43.

(5) Huang, W.; Qian, W.; El-Sayed, M. A. Coherent Vibrational Oscillation in Gold Prismatic Monolayer Periodic Nanoparticle Arrays. *Nano Lett.* **2004**, *4*, 1741–1747.

(6) Hartland, G. V. Coherent Excitation of Vibrational Modes in Metallic Nanoparticles. *Annu. Rev. Phys. Chem.* **2006**, *57*, 403–430.

(7) Blum, O.; Shaked, N. Prediction of Photothermal Phase Signatures from Arbitrary Plasmonic Nanoparticles and Experimental Verification. *Light: Sci. Appl.* **2015**, *4*, e322.

(8) Cahill, D. G.; Ford, W. K.; Goodson, K. E.; Mahan, G. D.; Majumdar, A.; Maris, H. J.; Merlin, R.; Phillpot, S. R. Nanoscale Thermal Transport. *J. Appl. Phys.* **2003**, *93*, 793–818.

(9) Cahill, D. G.; Braun, P. V.; Chen, G.; Clarke, D. R.; Fan, S.; Goodson, K. E.; Keblinski, P.; King, W. P.; Mahan, G. D.; Majumdar, A.; et al. Nanoscale Thermal Transport. II. 2003–2012. *Appl. Phys. Rev.* **2014**, *1*, 011305.

(10) Hartland, G. V.; Shang Lo, S. Spectroscopy Beyond the Single-Particle Limit. *Science* **2013**, *341*, 36–37.

(11) Sauceda, H. E.; Mongin, D.; Maioli, P.; Crut, A.; Pellarin, M.; Del Fatti, N.; Vallée, F.; Garzón, I. L. Vibrational Properties of Metal Nanoparticles: Atomistic Simulation and Comparison with Time-Resolved Investigation. *J. Phys. Chem. C* **2012**, *116*, 25147–25156.

(12) Juvé, V.; Crut, A.; Maioli, P.; Pellarin, M.; Broyer, M.; Del Fatti, N.; Vallée, F. Probing Elasticity at the Nanoscale: Terahertz Acoustic Vibration of Small Metal Nanoparticles. *Nano Lett.* **2010**, *10*, 1853–1858.

(13) Major, T. A.; Lo, S. S.; Yu, K.; Hartland, G. V. Time-Resolved Studies of the Acoustic Vibrational Modes of Metal and Semiconductor Nano-objects. *J. Phys. Chem. Lett.* **2014**, *5*, 866–874.

(14) Mahmoud, M. A.; O'Neil, D.; El-Sayed, M. A. Shape- and Symmetry-Dependent Mechanical Properties of Metallic Gold and Silver on the Nanoscale. *Nano Lett.* **2014**, *14*, 743–748.

(15) Fedou, J.; Viarbitskaya, S.; Marty, R.; Sharma, J.; Paillard, V.; Dujardin, E.; Arbouet, A. From Patterned Optical Near-Fields to High Symmetry Acoustic Vibrations in Gold Crystalline Platelets. *Phys. Chem. Chem. Phys.* **2013**, *15*, 4205–4213.

(16) Köth, A.; Appelhans, D.; Prietzel, C.; Koetz, J. Asymmetric Gold Nanoparticles Synthesized in the Presence of Maltose-Modified Poly(ethyleneimine). *Colloids Surf., A* **2012**, *414*, 50–56.

(17) Goubet, N.; Yan, C.; Polli, D.; Portalès, H.; Arfaoui, I.; Cerullo, G.; Pileni, M.-P. Modulating Physical Properties of Isolated and Self-Assembled Nanocrystals through Change in Nanocrystallinity. *Nano Lett.* **2013**, *13*, 504–508.

(18) Zijlstra, P.; Orrit, M. Single Metal Nanoparticles: Optical Detection, Spectroscopy and Applications. *Rep. Prog. Phys.* **2011**, *74*, 106401.

(19) Crut, A.; Maioli, P.; Del Fatti, N.; Vallée, F. Optical Absorption and Scattering Spectroscopies of Single Nano-Objects. *Chem. Soc. Rev.* **2014**, *43*, 3921–3956.

(20) Del Fatti, N.; Voisin, C.; Chevy, F.; Vallée, F.; Flytzanis, C. Coherent Acoustic Mode Oscillation and Damping in Silver Nanoparticles. *J. Chem. Phys.* **1999**, *110*, 11484–11487.

(21) Bonacina, L.; Callegari, A.; Bonati, C.; van Mourik, F.; Chergui, M. Time-Resolved Photodynamics of Triangular-Shaped Silver Nanoplates. *Nano Lett.* **2006**, *6*, 7–10.

DOI: 10.1021/acs.jpcc.6b11651
J. Phys. Chem. C 2016, 120, 28894–28899

(22) Ruan, C.-Y.; Murooka, Y.; Raman, R. K.; Murdick, R. A. Dynamics of Size-Selected Gold Nanoparticles Studied by Ultrafast Electron Nanocrystallography. *Nano Lett.* **2007**, *7*, 1290−1296.
(23) Plech, A.; Kürbitz, S.; Berg, K.-J.; Graener, H.; Berg, G.; Grésillon, S.; Kaempfe, M.; Feldmann, J.; Wulff, M.; von Plessen, G. Time-Resolved X-Ray Diffraction on Laser-Excited Metal Nanoparticles. *Europhys. Lett.* **2003**, *61*, 762−768.
(24) Plech, A.; Kotaidis, V.; Grésillon, S.; Dahmen, C.; von Plessen, G. Laser-Induced Heating and Melting of Gold Nanoparticles Studied by Time-Resolved X-Ray Scattering. *Phys. Rev. B: Condens. Matter Mater. Phys.* **2004**, *70*, 195423.
(25) Clark, J. N.; Beitra, L.; Xiong, G.; Higginbotham, A.; Fritz, D. M.; Lemke, H. T.; Zhu, D.; Chollet, M.; Williams, G. J.; Messerschmidt, M.; et al. Ultrafast Three-Dimensional Imaging of Lattice Dynamics in Individual Gold Nanocrystals. *Science* **2013**, *341*, 56−59.
(26) Clark, J. N.; Beitra, L.; Xiong, G.; Fritz, D. M.; Lemke, H. T.; Zhu, D.; Chollet, M.; Williams, G. J.; Messerschmidt, M. M.; Abbey, B.; et al. Imaging Transient Melting of a Nanocrystal using an X-Ray Laser. *Proc. Natl. Acad. Sci. U. S. A.* **2015**, *112*, 7444−7448.
(27) Neighbours, J. R.; Alers, G. A. Elastic Constants of Silver and Gold. *Phys. Rev.* **1958**, *111*, 707−712.
(28) Davletshin, Y. R.; Lombardi, A.; Cardinal, M. F.; Juvé, V.; Crut, A.; Maioli, P.; Liz-Marzán, L. M.; Vallée, F.; Del Fatti, N.; Kumaradas, J. C. A Quantitative Study of the Environmental Effects on the Optical Response of Gold Nanorods. *ACS Nano* **2012**, *6*, 8183−8193.
(29) Pertreux, E.; Lombardi, A.; Florea, I.; Spuch-Calvar, M.; Gómez-Graña, S.; Ihiawakrim, D.; Hirlimann, C.; Ersen, O.; Majimel, J.; Tréguer-Delapierre, M.; et al. Surface Plasmon Resonance of an Individual Nano-Object on an Absorbing Substrate: Quantitative Effects of Distance and 3D Orientation. *Adv. Opt. Mater.* **2016**, *4*, 567−577.
(30) Germain, V.; Li, J.; Ingert, D.; Wang, Z. L.; Pileni, M. P. Stacking Faults in Formation of Silver Nanodisks. *J. Phys. Chem. B* **2003**, *107*, 8717−8720.
(31) Liebig, F.; Thünemann, A.; Koetz, J. Ostwald Ripening Growth Mechanism of Gold Nanotriangles in Vesicular Template Phases. *Langmuir* **2016**, *32*, 10928−10935.
(32) Xie, W.; Walkenfort, B.; Schlücker, S. Label-Free SERS Monitoring of Chemical Reactions Catalyzed by Small Gold Nanoparticles Using 3D Plasmonic Superstructures. *J. Am. Chem. Soc.* **2013**, *135*, 1657−1660.
(33) Schick, D.; Shayduk, R.; Bojahr, A.; Herzog, M.; von Korff Schmising, C.; Gaal, P.; Bargheer, M. Ultrafast Reciprocal-Space Mapping with a Convergent Beam. *J. Appl. Crystallogr.* **2013**, *46*, 1372−1377.
(34) Schick, D.; Bojahr, A.; Herzog, M.; von Korff Schmising, C.; Shayduk, R.; Leitenberger, W.; Gaal, P.; Bargheer, M. Normalization Schemes for Ultrafast X-Ray Diffraction Using a Table-Top Laser-Driven Plasma Source. *Rev. Sci. Instrum.* **2012**, *83*, 025104.
(35) Schick, D.; Bojahr, A.; Herzog, M.; Gaal, P.; Vrejoiu, I.; Bargheer, M. Following Strain-Induced Mosaicity Changes of Ferroelectric Thin Films by Ultrafast Reciprocal Space Mapping. *Phys. Rev. Lett.* **2013**, *110*, 095502.
(36) Nix, F. C.; MacNair, D. The Thermal Expansion of Pure Metals: Copper, Gold, Aluminum, Nickel, and Iron. *Phys. Rev.* **1941**, *60*, 597−605.
(37) McLean, K. O.; Swenson, C. A.; Case, C. R. Thermal Expansion of Copper, Silver, and Gold Below 30 K. *J. Low Temp. Phys.* **1972**, *7*, 77−98.
(38) Del Fatti, N.; Arbouet, A.; Vallée, F. Femtosecond Optical Investigation of Electron-Lattice Interactions in an Ensemble and a Single Metal Nanoparticle. *Appl. Phys. B: Lasers Opt.* **2006**, *84*, 175−181.
(39) Groeneveld, R. H. M.; Sprik, R.; Lagendijk, A. Femtosecond Spectroscopy of Electron-Electron and Electron-Phonon Energy Relaxation in Ag and Au. *Phys. Rev. B: Condens. Matter Mater. Phys.* **1995**, *51*, 11433−11445.
(40) Arbouet, A.; Voisin, C.; Christofilos, D.; Langot, P.; Del Fatti, N.; Vallée, F.; Lermé, J.; Celep, G.; Cottancin, E.; Gaudry, M.; et al. Electron-Phonon Scattering in Metal Clusters. *Phys. Rev. Lett.* **2003**, *90*, 177401.
(41) Kiel, M.; Möhwald, H.; Bargheer, M. Broadband Measurements of the Transient Optical Complex Dielectric Function of a Nanoparticle/Polymer Composite upon Ultrafast Excitation. *Phys. Rev. B: Condens. Matter Mater. Phys.* **2011**, *84*, 165121.
(42) Nicoul, M.; Shymanovich, U.; Tarasevitch, A.; von der Linde, D.; Sokolowski-Tinten, K. Picosecond Acoustic Response of a Laser-Heated Gold-Film Studied with Time-Resolved X-Ray Diffraction. *Appl. Phys. Lett.* **2011**, *98*, 191902.
(43) Voisin, C.; Del Fatti, N.; Christofilos, D.; Vallée, F. Time-Resolved Investigation of the Vibrational Dynamics of Metal Nanoparticles. *Appl. Surf. Sci.* **2000**, *164*, 131−139.
(44) Wright, O. B. Ultrafast Nonequilibrium Stress Generation in Gold and Silver. *Phys. Rev. B: Condens. Matter Mater. Phys.* **1994**, *49*, 9985−9988.
(45) Ho, C. Y.; Powell, R. W.; Liley, P. E. Thermal Conductivity of the Elements. *J. Phys. Chem. Ref. Data* **1972**, *1*, 279−421.
(46) Flubacher, P.; Leadbetter, A.; Morrison, J. The Heat Capacity of Pure Silicon and Germanium and Properties of their Vibrational Frequency Spectra. *Philos. Mag.* **1959**, *4*, 273−294.
(47) Geballe, T. H.; Giauque, W. F. The Heat Capacity and Entropy of Gold from 15 to 300K. *J. Am. Chem. Soc.* **1952**, *74*, 2368−2369.
(48) Duda, J. C.; Yang, C.-Y. P.; Foley, B. M.; Cheaito, R.; Medlin, D. L.; Jones, R. E.; Hopkins, P. E. Influence of Interfacial Properties on Thermal Transport at Gold:Silicon Contacts. *Appl. Phys. Lett.* **2013**, *102*, 081902.
(49) Ge, Z.; Cahill, D. G.; Braun, P. V. Thermal Conductance of Hydrophilic and Hydrophobic Interfaces. *Phys. Rev. Lett.* **2006**, *96*, 186101.
(50) Losego, M.; Grady, M.; Sottos, N.; Cahill, D.; Braun, P. Effects of Chemical Bonding on Heat Transport Across Interfaces. *Nat. Mater.* **2012**, *11*, 502−506.
(51) O'Brien, P.; Shenogin, S.; Liu, J.; Chow, P.; Laurencin, D.; Mutin, P.; Yamaguchi, M.; Keblinski, P.; Ramanath, G. Bonding-Induced Thermal Conductance Enhancement at Inorganic Heterointerfaces Using Nanomolecular Monolayers. *Nat. Mater.* **2012**, *12*, 118−122.

DOI: 10.1021/acs.jpcc.6b11651
J. Phys. Chem. C 2016, 120, 28894−28899

Article II

Layer specific observation of slow thermal equilibration in ultrathin metallic nanostructures by femtosecond x-ray diffraction

Jan-Etienne Pudell, Alexei A. Maznev, Marc Herzog, Matthias Kronseder, Christian H. Back, Gregory Malinowski, Alexander von Reppert, and Matias Bargheer

Nature Communications 9, 3335 (2018)

Ultrafast heat transport in nanoscale metal multilayers is of great interest in the context of optically induced demagnetization, remagnetization and switching. If the penetration depth of light exceeds the bilayer thickness, layer-specific information is unavailable from optical probes. Femtosecond diffraction experiments provide unique experimental access to heat transport over single digit nanometer distances. Here, we investigate the structural response and the energy flow in the ultrathin double-layer system: gold on ferromagnetic nickel. Even though the excitation pulse is incident from the Au side, we observe a very rapid heating of the Ni lattice, whereas the Au lattice initially remains cold. The subsequent heat transfer from Ni to the Au lattice is found to be two orders of magnitude slower than predicted by the conventional heat equation and much slower than electron-phonon coupling times in Au. We present a simplified model calculation highlighting the relevant thermophysical quantities.

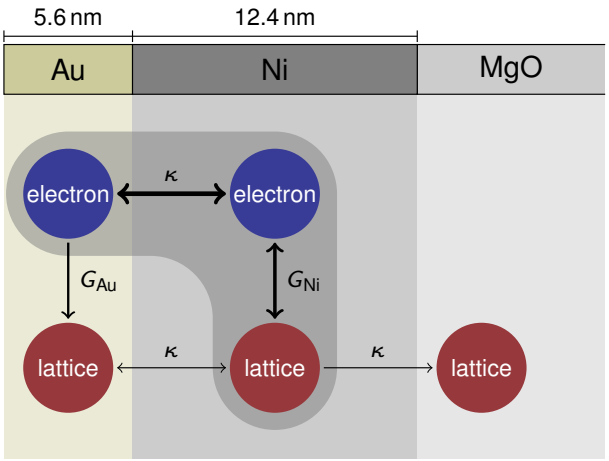

nature COMMUNICATIONS

ARTICLE

DOI: 10.1038/s41467-018-05693-5 OPEN

Layer specific observation of slow thermal equilibration in ultrathin metallic nanostructures by femtosecond X-ray diffraction

J. Pudell[1], A.A. Maznev[2], M. Herzog[1], M. Kronseder[3], C.H. Back[3,4], G. Malinowski[5], A. von Reppert[1] & M. Bargheer[1,6]

Ultrafast heat transport in nanoscale metal multilayers is of great interest in the context of optically induced demagnetization, remagnetization and switching. If the penetration depth of light exceeds the bilayer thickness, layer-specific information is unavailable from optical probes. Femtosecond diffraction experiments provide unique experimental access to heat transport over single digit nanometer distances. Here, we investigate the structural response and the energy flow in the ultrathin double-layer system: gold on ferromagnetic nickel. Even though the excitation pulse is incident from the Au side, we observe a very rapid heating of the Ni lattice, whereas the Au lattice initially remains cold. The subsequent heat transfer from Ni to the Au lattice is found to be two orders of magnitude slower than predicted by the conventional heat equation and much slower than electron–phonon coupling times in Au. We present a simplified model calculation highlighting the relevant thermophysical quantities.

[1] Institut für Physik & Astronomie, Universität Potsdam, Karl-Liebknecht-Str. 24-25, 14476 Potsdam, Germany. [2] Department of Chemistry, Massachusetts Institute of Technology, Cambridge, MA 02139, USA. [3] Physics Department, Technical University Munich, 85748 Garching, Germany. [4] Institut für Experimentelle und Angewandte Physik, Universität Regensburg, 93040 Regensburg, Germany. [5] Institut Jean Lamour (UMR CNRS 7198), Université Lorraine, Vandœuvre-lès-Nancy 54506, France. [6] Helmholtz-Zentrum Berlin for Materials and Energy GmbH, Wilhelm-Conrad-Röntgen Campus, BESSY II, Albert-Einstein-Str. 15, 12489 Berlin, Germany. Correspondence and requests for materials should be addressed to A.v.R. (email: reppert@uni-potsdam.de) or to M.B. (email: bargheer@uni-potsdam.de)

Ultrafast heating and cooling of thin metal films has been studied extensively to elucidate the fundamentals of electron–phonon interactions[1–7] and heat transport at the nanoscale[8–13]. The energy flow in metal multilayers following optical excitation attracted particular attention in the context of heat-assisted magnetic recording[14,15] and all-optical magnetic switching[16–18]. The role of temperature in optically induced femtosecond demagnetization is intensely discussed, particularly with regard to multipulse switching scenarios[19]. Two- or three-temperature models (TTMs) are often used to fit the experimental observations[20]. The microscopic three-temperature model (M3TM)[20], which uses Elliot–Yafet spin-flip scattering as the main mechanism for ultrafast demagnetization is often contrasted against superdiffusive spin transport[21]. Such electron transport is closely related to ultrafast spin-Seebeck effects[22,23], which require a description with independent majority and minority spin temperatures. The heat flow involving electrons, phonons, and spins has been found to play a profound role in ultrafast magnetization dynamics[24,25]. The description of the observed dynamics in TTMs or the M3TM are challenged by ab initio theory which explicitly holds the nonequilibrium distribution responsible for the very fast photoinduced demagnetization[26,27]. The presence of multiple subsystems (lattice, electrons, and spins), e.g., in ferromagnetic metals[5,28], poses a formidable challenge for experimental studies of their coupling and thermal transport on ultrafast time scales when these subsystems are generally not in equilibrium with each other[26,27,29]. Temperature dynamics in metal films are typically monitored using optical probe pulses via time-domain thermoreflectance (TDTR)[12]. This technique has been a workhorse of nanoscale thermal transport studies, but experiences significant limitations when applied to ultrathin multilayers with individual layer thicknesses falling below the optical skin depth, which are in the focus of ultrafast magnetism research[22–24,30–32]. Optical probes are generally sensitive to electronic and lattice temperatures, although in some cases the lattice temperature[13] or the spin temperature[24] may be deduced. In order to understand the thermal energy flow, it is highly desirable to directly access the temperature of the lattice, which provides the largest contribution to the specific heat. Ultrafast X-ray diffraction is selectively sensitive to the crystal lattice, and material-specific Bragg angles enable measurements of multiple layers even when they are thinner than the optical skin depth and/or buried below opaque capping layers[33–35]. The lattice constant variations of each layer can be measured with high absolute accuracy, making it possible to determine the amount of deposited heat in metal bilayers that was debated recently[30–32]. The great promise of ultrafast X-ray diffraction (UXRD) for nanoscale thermal transport measurements and ultrafast lattice dynamics has already been demonstrated in experiments with synchrotron-based sources[33–36]. However, limited temporal resolution of these experiments (~100 ps) only allowed to study heat transport on a relatively slow (nanosecond) time scale and over distances >100 nm. Ultrafast nanoscale thermal transport research will greatly benefit from femtosecond X-ray sources. While free electron laser facilities are in very high demand, an alternative is offered by laser-based plasma sources of femtosecond X-rays[37,38], which lack the coherence and high flux of a free electron laser but are fully adequate for UXRD measurements[6,39,40]. As an example, a recent experiment on 6 nm thick Au nanotriangles[39] confirmed the $\tau^0_{Au} = 5$ ps electron–phonon equilibration time generally accepted for high fluence excitation of Au[3,6,41,42]. For similar fluences ultrafast electron diffraction reported $\tau^0_{Ni} = 0.75$ to 1 ps for Ni thin films between room temperature and Curie temperature T_C[7,43].

In this report, we demonstrate that the use of a femtosecond X-ray probe enables thermal transport measurements over a distance as small as ~5 nm in a Au/Ni bilayer with thickness $d_{Au} = 5.6$ nm and $d_{Ni} = 12.4$ nm grown on MgO. By monitoring the dynamics of the lattice constants of Au and Ni, we find that the Ni lattice fully expands within about 2 ps, while the Au lattice initially remains cold even if a significant fraction of the excitation light is absorbed by the electronic subsystem in Au. The Au lattice then heats up slowly, reaching the maximum temperature about 80 ps after the optical excitation. The observed thermal relaxation of the bilayer structure is two orders of magnitude slower than 1 ps predicted by the heat equation and also much slower than the usual electron–phonon equilibration time $\tau^0_{Au} =$ 1–5 ps (see Table 1)[3,41,42]. We explain this surprising result in a model (see Fig. 1) based on the keen insight into the physics of the thermal transport in Au–Pt bilayers offered in recent studies[11,13], which showed that nonequilibrium between electrons and lattice in Au persists for a much longer time in a bilayer than in a single Au film. We find, furthermore, that on the spatial scale of our experiment thermal transport by phonons in metals can no longer be neglected. Our results underscore challenges for thermal transport modeling on the nanometer scale. On the other hand, they demonstrate the great potential of the UXRD for monitoring thermal transport under experimental conditions typical for studies of ultrafast magnetism[20,44].

Results

Experiment. We use femtosecond laser pulses at 400 and 800 nm to excite the electron system of Au and Ni through the Au top layer. The sample structure and the calculated absorption profiles are shown in Fig. 1. We note that for 400 nm pulses the absorbed energy density $\rho^Q_{Au,Ni}$ in Au and Ni is similar, whereas for 800 nm almost no light is absorbed in Au. The much higher absorption of 400 nm light in Au is a result of the larger real part of the refractive index[31,32]. For our 5.6 nm thick Au film, the destructive interference of light reflected at the interfaces additionally contributes to the suppressed absorption at 800 nm.

The strains $\varepsilon_{Au,Ni}$ determined via Bragg's law from UXRD data (Fig. 2b, c) can be converted to lattice temperature changes $\Delta T_{Au,Ni}$ and energy density changes $\rho^Q_{Au,Ni}$ via

$$\varepsilon_{Au,Ni} = \alpha^{uf}_{Au,Ni} \Delta T_{Au,Ni} \quad (1)$$

$$\varepsilon_{Au,Ni} = \frac{\alpha^{uf}_{Au,Ni}}{C_{Au,Ni}} \rho^Q_{Au,Ni} \quad (2)$$

Table 1 Thermophysical parameters of Au and Ni

Parameter	Gold	Nickel
Lattice specific heat, C^{ph} (10^6 Jm^{-3} K^{-1})	2.5[54]	3.8[55]
Sommerfeld constant, γ^S (Jm^{-3} K^{-2})	67.5[2]	1074[2]
Electron–phonon coupling constant, g (10^{16} Wm^{-3} K^{-1})	1–4[2]	36–105[2]
e-ph coupling time isolated layers @1000 K, τ^0 (ps)	1.7–6.7	1–3
e-ph coupling time equilibrated electrons @1000 K, τ (ps)	26–107	1–3
Thermal conductivity, κ (Wm^{-1} K^{-1})	318[56]	90[56]
Thermal conductivity (lattice), κ^{ph} (Wm^{-1} K^{-1})	5[56]	9.6[56]
Expansion coefficient with Poisson correction, α^{uf} (10^{-5} K^{-1})	3.16[57]	2.8[57]

Literature values for material parameters relevant for modeling the heat transfer after laser excitation. For C^{ph} we use the parameters at room temperature. The e-ph coupling time ranges are calculated for 1000 K to show that for an equilibrated electron system, the e-ph coupling time in Ni is much shorter than in Au

NATURE COMMUNICATIONS | DOI: 10.1038/s41467-018-05693-5 ARTICLE

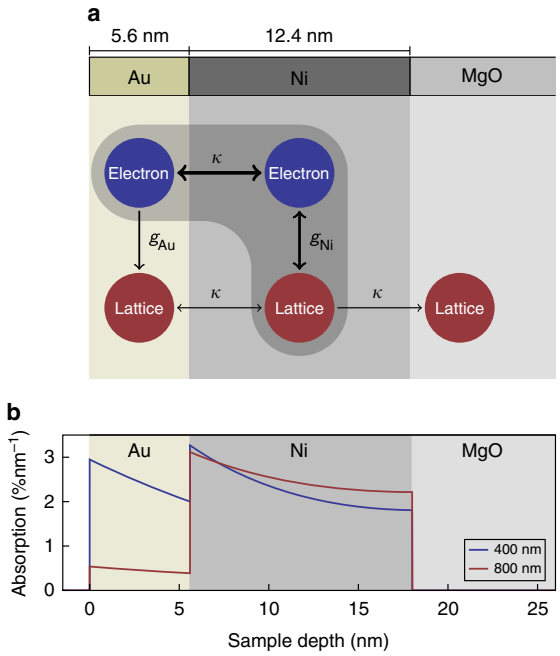

Fig. 1 Schematic of heat reservoirs in the sample structure. **a** Layer stacking of the metallic heterostructure: Au on Ni deposited on an MgO substrate. Each layer has a phonon heat reservoir. The metal layers additionally have an electronic heat reservoir. The heat contained in the Ni spin system is included in the electron system. The electron–phonon coupling constants g_{Au} and g_{Ni} parametrize the local energy flow among electrons and phonons within each layer, whereas the thermal conductivity κ indicates spatial heat transport. **b** Calculated optical absorption profiles in the metallic bilayer

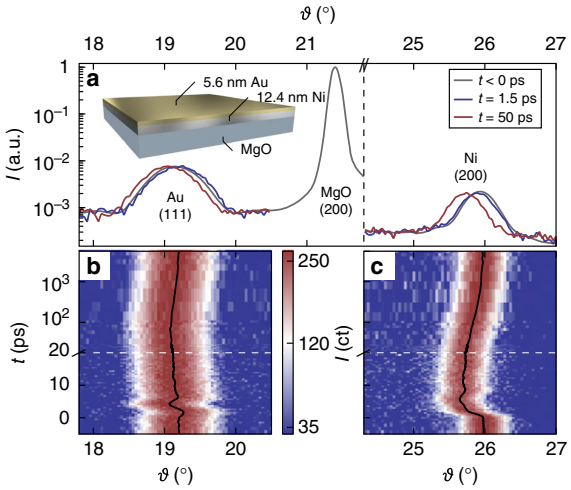

Fig. 2 Experimental data. **a** X-ray diffraction pattern of the sample (see inset) evidencing the crystalline orientation of the Au and Ni nanolayers. Colored lines visualize transient shifts of the Bragg peaks at selected times. Their full time evolution is shown in panels (**b**) for Au and **c** for Ni along with the respective peak center positions (black line). The white dashed line indicates the axis break from linear to logarithmic time scale

using effective out-of-plane expansion coefficients $\alpha^{uf}_{Au,Ni}$ and specific heats $C_{Au,Ni}$, which are generally temperature dependent. For our experimental conditions temperature-independent coefficients are good approximations. The effective expansion coefficients $\alpha^{uf}_{Au,Ni}$ take into account the crystalline orientation of the films and the fact that on ultrafast (uf) timescales the film can exclusively expand out-of plane, since the uniform heating of a large pump-spot region leads to a one-dimensional situation, as in-plane forces on the atoms by the thermal stresses vanish. For details about $\alpha^{uf}_{Au,Ni}$ and a description how heat in electrons and phonons drive the transient stress via macroscopic Grüneisen coefficients see the Methods section.

We now discuss the information that can be directly inferred from the measured transient strains (Fig. 3) in the laser-excited metallic bilayer without any advanced modeling. For convenience, we added two right vertical axes to Fig. 3a, b showing the layer-specific temperature and energy density according to Eqs. (1) and (2). Initially Ni expands, while the Au layer gets compressed by the expansion of the Ni film. Around 3 ps Au shows a pronounced expansion, when the compression wave turns into an expansion wave upon reflection at the surface. Less pronounced signatures of the strain wave are observed in Ni as well. A surprisingly long time of about 80 ps is required to reach the maximum expansion of Au by transport of heat from the adjacent Ni until $T_{Au} \approx T_{Ni}$. For times $t > 100$ ps, cooling by heat transfer to the substrate dominates the signal. In Fig. 3c we show the heat energy ΔQ_{MgO} flowing through a unit area A into the

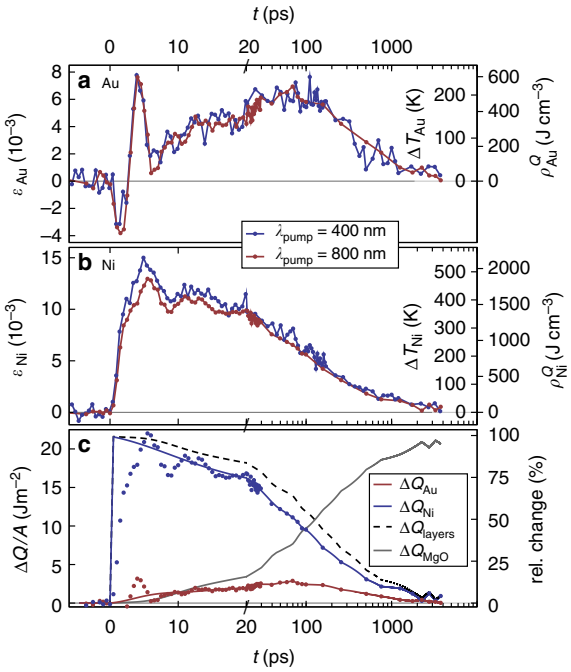

Fig. 3 Transient energy densities and temperatures. Transient lattice strain ε in the Au film (**a**) and the Ni film (**b**) as measured by UXRD after excitation with 400 nm (blue) and 800 nm (red) light pulses. The right axis label the temperature change ΔT and the energy density ρ^Q calculated from ε. **c** Red and blue dots show the energy per unit area $\Delta Q/A$ obtained from (**a**, **b**) by multiplication with $d_{Au,Ni}$. The red and blue lines show thermal dynamics with acoustic oscillations removed, yielding the true energy per unit area $\Delta Q/A$. The black dashed line shows the sum of these energies. The gray line is the thermal energy that has been transported into the substrate

substrate, which we can directly calculate from the measured energy densities via

$$\Delta Q_{\mathrm{MgO}}(t)/A = -d_{\mathrm{Au}}\Delta\rho^{\mathrm{Q}}_{\mathrm{Au}}(t) - d_{\mathrm{Ni}}\Delta\rho^{\mathrm{Q}}_{\mathrm{Ni}}(t). \quad (3)$$

$\Delta\rho^{\mathrm{Q}}_{\mathrm{Ni,Au}}(t) = \rho^{\mathrm{Q}}_{\mathrm{Ni,Au}}(t) - \rho^{\mathrm{Q}}_{\mathrm{Ni,Au}}(0)$ are the changes of the energy densities $\rho^{\mathrm{Q}}_{\mathrm{Ni}}$ and $\rho^{\mathrm{Q}}_{\mathrm{Au}}$ with respect to the initially deposited energy densities. Even when the temperatures are equilibrated at $t > 100$ ps, $\rho^{\mathrm{Q}}_{\mathrm{Ni}}$ and $\rho^{\mathrm{Q}}_{\mathrm{Au}}$ differ strongly because of the different specific heat of Au and Ni. Figure 3c confirms that within the first 20 ps the heat energy $\Delta Q_{\mathrm{Au}} = d_{\mathrm{Au}}\Delta\rho^{\mathrm{Q}}_{\mathrm{Au}}$ flowing from Ni into Au is similar to the amount ΔQ_{MgO} transported into the substrate. At about 150 ps half of the energy deposited in the film has been transported into the substrate. However, leaking a fraction of the thermal energy to the insulating substrate does not explain why the ultrathin Au layer is not much more rapidly heated via electronic heat transport typical of metals.

Modeling. Inspired by the recent studies using TDTR[11,13] we set up a modified two-temperature model graphically represented in Fig. 1b to rationalize the slow Au heating observed in Fig. 3a. We first justify this simplified modeling. The high electron conductivity—potentially including ballistic and superdiffusive electrons—rapidly equilibrates the electron systems of Ni and Au. The fact that the Au layer is equally compressed in the first 2 ps irrespective of the excitation wavelengths is an experimental proof of the rapid equilibration of electron temperatures. Otherwise the high electron pressure in Au after 400 nm excitation (cf. Fig. 1c) would counterbalance the compression caused by the Ni expansion[6]. As Ni has a much larger Sommerfeld constant (Table 1) the electronic specific heat $C^{\mathrm{e}} = \gamma^{\mathrm{S}}T$ is dominated by Ni and the ratio of energy densities $\rho^{\mathrm{Q}}_{\mathrm{Ni}}/\rho^{\mathrm{Q}}_{\mathrm{Au}} \approx 10$ is large at 1 ps. A significant electronic interface resistance[45] that would prevent a rapid equilibration of electron temperatures in Au and Ni is clearly incompatible with our measurements at 400 nm. If the electrons did not equilibrate much faster than 1 ps and effectively remove the heat deposited in the electron system of Au, we would not observe the same strong compression of the Au lattice, since electronic pressure would instantaneously force the Au to expand[6,7,40,43]. In the diffuse-mismatch model, the electronic interface conductance of metals increases linearly with the temperature and can be calculated from the Sommerfeld constant and the Fermi velocity[45]. Immediately after excitation, the electron temperature reaches several thousand Kelvin, which leads to a subpicosecond thermalization of the electrons in simulations, including the interface resistance.

The electron–phonon coupling constant in Ni is much larger than in Au (Table 1). Consequently, nearly all photon energy initially absorbed in the electronic system is funneled into the Ni lattice, even when one third of the absorbed energy is initially deposited in the electronic system of Au with 400 nm excitation. In contrast, the electron–phonon coupling times $\tau^0_{\mathrm{Au,Ni}} = C^{\mathrm{e}}_{\mathrm{Au,Ni}}/g_{\mathrm{Au,Ni}}$ for Au and Ni are not very different if the films are not in contact, because the large electronic specific heat $C^{\mathrm{e}}_{\mathrm{Ni}}$ of Ni cancels its large electron–phonon coupling constant g_{Ni} (see Table 1). However, in the bilayer, the electrons in Au and Ni rapidly form an equilibrated heat bath with $C^{\mathrm{e}}_{\mathrm{tot}} \approx C^{\mathrm{e}}_{\mathrm{Ni}}$. Now only the electron–phonon coupling constant determines the coupling time: $\tau_{\mathrm{Ni}} = C^{\mathrm{e}}_{\mathrm{tot}}/g_{\mathrm{Ni}} \ll C^{\mathrm{e}}_{\mathrm{tot}}/g_{\mathrm{Au}} = \tau_{\mathrm{Au}}$.

We start the numerical modeling when a quasi-equilibrium temperature in the combined system $C_{\mathrm{com}} = C^{\mathrm{e}}_{\mathrm{Au}} + C^{\mathrm{e}}_{\mathrm{Ni}} + C^{\mathrm{ph}}_{\mathrm{Ni}} \approx C^{\mathrm{e}}_{\mathrm{Ni}} + C^{\mathrm{ph}}_{\mathrm{Ni}} \approx C_{\mathrm{Ni}}$ is established after electron–phonon equilibration in Ni around $\tau_{\mathrm{Ni}} = C^{\mathrm{e}}_{\mathrm{tot}}/g_{\mathrm{Ni}} \approx C^{\mathrm{e}}_{\mathrm{Ni}}/g_{\mathrm{Ni}} \approx 1$ ps. Since $C^{\mathrm{ph}}_{\mathrm{Ni}} \gg C^{\mathrm{e}}_{\mathrm{Ni}} \gg C^{\mathrm{e}}_{\mathrm{Au}}$ and $d_{\mathrm{Ni}} > d_{\mathrm{Au}}$, we refer to the combined system as C_{Ni} in the equations. Since the energy stored in each layer is proportional to their thickness and the energy transfer rate from electrons to phonons in Au is proportional to the Au volume $V_{\mathrm{Au}} \propto d_{\mathrm{Au}}$, the differential equations describing this special TTM represented in Fig. 1b read

$$d_{\mathrm{Au}}C^{\mathrm{ph}}_{\mathrm{Au}}\frac{\partial T^{\mathrm{ph}}_{\mathrm{Au}}}{\partial t} = d_{\mathrm{Au}}g_{\mathrm{Au}}\left(T_{\mathrm{Ni}} - T^{\mathrm{ph}}_{\mathrm{Au}}\right) \quad (4)$$

$$d_{\mathrm{Ni}}C_{\mathrm{Ni}}\frac{\partial T_{\mathrm{Ni}}}{\partial t} = d_{\mathrm{Au}}g_{\mathrm{Au}}\left(T^{\mathrm{ph}}_{\mathrm{Au}} - T_{\mathrm{Ni}}\right). \quad (5)$$

Note that the two temperatures in this model are the temperature of the Au lattice, $T^{\mathrm{ph}}_{\mathrm{Au}}$ and the temperature of the combined system, which is denoted as T_{Ni}, keeping in mind that this Ni temperature equals the Au electron temperature. For small temperature changes over which the specific heats are approximately constant, the solution to this system of equations is an exponential decay of $T_{\mathrm{Ni}} \sim e^{-t/\tau}$ and a concomitant rise of the Au lattice temperature $T_{\mathrm{Au}} \sim (1 - e^{-t/\tau})$ on the characteristic timescale

$$\tau = \frac{1}{g_{\mathrm{Au}}\left(\frac{1}{C_{\mathrm{Au}}} + \frac{d_{\mathrm{Au}}}{d_{\mathrm{Ni}}}\frac{1}{C_{\mathrm{Ni}}}\right)}. \quad (6)$$

Due to the small film thickness and the rapid electronic heat diffusion, we do not assume any gradient in the temperatures of each film. At about 1 ps after excitation we define the initial conditions as $T_{\mathrm{Ni}}(1\,\mathrm{ps}) = T^{\mathrm{i}}_{\mathrm{Ni}}$ and $T^{\mathrm{i}}_{\mathrm{Au}} \approx 0$. The final temperature after equilibrating the temperatures of the two thin films, neglecting heat transport to the substrate is

$$T^{\mathrm{f}} = T^{\mathrm{i}}\frac{d_{\mathrm{Ni}}C_{\mathrm{Ni}}}{d_{\mathrm{Au}}C^{\mathrm{ph}}_{\mathrm{Au}} + d_{\mathrm{Ni}}C_{\mathrm{Ni}}}. \quad (7)$$

This very simple model (dashed lines of Fig. 4a) for the transient quasi-equilibrium temperatures agrees very well with the data. In particular, the exponential rise of T_{Au} and the exponential decay of T_{Ni} converge around 80 ps. Deviations at longer times originate mainly from heat transport into the MgO substrate, which is not included in the model (dashed lines).

The only fitting parameters of our model are the initial temperature T^{i} and the electron–phonon coupling constant of Au. With our simple model we get the best fit using $g_{\mathrm{Au}} = 6.5 \times 10^{16}\,\mathrm{W\,m^{-3}\,K^{-1}}$, which is somewhat larger than the range from 1 to $4 \times 10^{16}\,\mathrm{W\,m^{-3}\,K^{-1}}$ reported in the literature[2,3]. If—as an example—we reduce the electron–phonon coupling constant to the value of $4 \times 10^{16}\,\mathrm{W\,m^{-3}\,K^{-1}}$, the calculated equilibration of T_{Au} and T_{Ni} is much too slow. Including electronic interface resistance would make it even slower. The missing energy transfer rate, however, can be easily rationalized by phonon heat conductivity κ^{ph}. If we fully disregarded electronic heat conduction in Au, the literature value for $\kappa^{\mathrm{ph}}_{\mathrm{Au}}$ given in Table 1 would lead to an equilibration of Au and Ni temperature exclusively via phonons three times faster than we observe. The phonon heat transport is probably much less efficient than this prediction because of additional interface resistances for phonon heat transport and because the mean free path of phonons is on the order of the layer thickness[8,10]. However, we do not attempt to quantify κ^{ph} and g_{Au} here. We only note qualitatively that to conform to the expected values of electron–phonon coupling in Au, the phonon heat conduction must become important in nanoscale multilayers, even though

NATURE COMMUNICATIONS | DOI: 10.1038/s41467-018-05693-5 ARTICLE

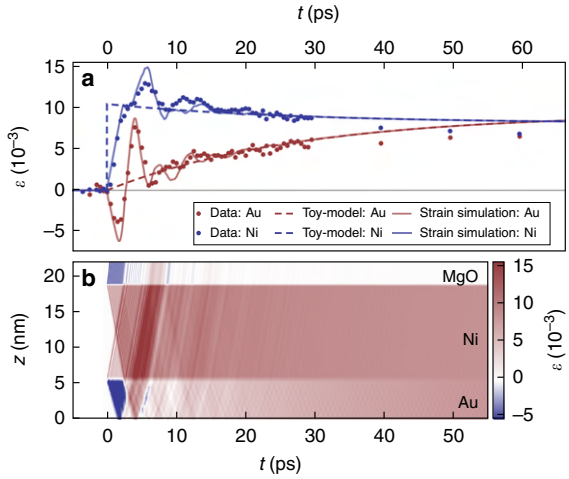

Fig. 4 Comparison of models with the experimental data. **a** Dots indicate the measured strain ε. The dashed lines represent the strain calculated from the average heating of the layers according to the model visualized in Fig. 1b. Solid lines are simulations, which are based on this model and additionally include the strain waves triggered by the impulsive excitation (see Methods section). Heat transport to the substrate is not included. **b** Color-coded strain ε as a function of sample depth and time t, which is simulated assuming a spatially homogeneous transient thermal stress in each layer which is proportional to the dashed lines in (**a**). Spatial averaging of the strain $\varepsilon(t)$ in each layer yields the solid lines in panel (**a**)

normally the heat conduction in metals is dominated by electrons ($\kappa \gg \kappa^{ph}$ see Table 1). Phonon heat transport is not included in our numerical calculations, because in fact the heat diffusion equation is not valid at such small length scales below the phonon mean free path. Similarly, a complex theoretical modeling would be required to simulate the heat transport to the substrate, e.g., by heat transfer from Ni electrons to MgO phonons at the interface[46]. Figure 3c provides a benchmark of the experimentally determined phonon heat transport into the substrate.

Discussion

In summary, the modified TTM model (Eqs. (4) and (5)) captures the essence of heat transport between ultrathin metal films: the electrons in Au and Ni are rapidly equilibrated. This is evidenced by the fact that 400 and 800 nm excitation both initially only heat Ni, regardless of the energy absorbed in Au. For 400 nm excitation we showed an intricate process of shuttling heat energy back and forth between the layers: the electrons first rapidly transport energy from Au into Ni (e–e equilibration $\ll$ 1 ps) before they transport some of the heat back from the Ni phonons to the Au phonons. Finally, the heat flows back through Ni toward the substrate. Heat transport by phonons can account for a fraction of the Au heating. The energy transported from the Ni phonons via Ni and Au electrons into the Au lattice is throttled by the weak electron–phonon coupling in Au. We believe that our results will have an important impact on ultrafast studies of the spin-Seebeck effect, superdiffusive electron transport as well as optical demagnetization and remagnetization. Precise measurements of the total heat in the system after few picoseconds will help to determine the actually required laser fluence in ultrafast demagnetization studies, which currently diverge by an order of magnitude in the literature[44,47]. The lattice is not only discussed as the sink of angular momentum in the ultrafast demagnetization: with its dominant heat capacity the lattice constitutes the heat bath which controls the speed of reordering of the spin systems at high fluence[20,44]. Our detailed account of heat flow in Ni after photo-excitation must influence the interpretation of MOKE data, which were fitted in previous studies[20,48] by using a value for the specific heat of the Ni phonon system which is a factor of two below the Dulong–Petit value.

We have demonstrated the power of UXRD in probing nanoscale heat transport in an ultrathin metallic bilayer system which is relevant to current magnetic recording developments such as heat-assisted magnetic recording. To understand the all-optical-[15] and helicity-dependent[49] switching in ferrimagnets and two different timescales observed in the demagnetization of transition metals[20,44] or rare earths[50,51], precise calibration of the lattice temperature is crucial. We are convinced that the direct access to the lattice, the layer-specific information for layers thinner than the optical skin depth, the conceptual simplicity of the arguments and the experimental geometry make the paper particularly useful for comparisons to previous[20,30–32,44] and future work on optical manipulation of spins.

Methods

Sample growth and UXRD. Ni/Au stacks with different Ni and Au thicknesses were grown by molecular beam epitaxy onto a MgO(001) substrate at 100 °C. The MgO(001) substrates were degassed at 350 °C for 10 min. The pressure during growth never exceeded 6^{-10} mbar. We measured the layer thicknesses d_{Au} = 5.6 nm and d_{Ni} = 12.4 nm of the investigated sample by X-ray reflectivity. The 24 lattice planes of Au yield a symmetric (111) Bragg reflection (Fig. 2a) at $\vartheta = 19.29°$, well separated from the symmetric (200) Ni peak at 25.92° originating from 70 lattice planes. The lattice strains $\varepsilon_{Ni,Au}(t) = -\cot(\vartheta(t))\Delta\vartheta(t)$ perpendicular to the sample surface are directly retrieved from the time-resolved Bragg-peak positions $\vartheta(t)$ (Fig. 2b, c)[5839,40]. These UXRD data were recorded at our laser-driven plasma X-ray source at the University of Potsdam, that emits 200 fs X-ray pulses with a photon energy of 8 keV. The sample was excited by p-polarized 400 and 800 nm laser pulses of about 100 fs duration with a pulse energy of 0.3 mJ and a diameter of 1.5 mm (FWHM). Since the angle between the pump pulse and the Bragg-reflecting X-ray probe pulse is fixed in the setup, we take into accout the modified angle of incidence of the optical pulse of 44° (51°) with respect to the surface normal for the Ni (Au) reflection to calculate the incident fluence of 9 (8) mJ/cm^2 and an absorbed fluence of 3 (2.9) mJ/cm^2 for our bilayer system using a matrix formalism, which also yields the absorption profiles at 400 and 800 nm excitation shown in Fig. 1c[52]. The above values are for 800 nm excitation, and the 400 nm data in Fig. 3 are scaled up for better comparison of the two different excitation conditions.

Correction of the thermal expansion coefficient. The effective expansion coefficient $\alpha^{uf}_{Au,Ni}$ valid for heating a thin epitaxial layer is based on the lattice constants and strains predicted from equilibrium thermal expansion coefficients, corrected according to the Poisson effect[53]. In cubic materials with (100) surface orientation the ratio of the observed ultrafast (uf) strain and the strain $\varepsilon^{eq} = \alpha^{eq}(T)\Delta T$ along the (100) direction calculated from equilibrium value (eq) is $\varepsilon/\varepsilon^{eq} = \alpha^{uf}(T)/\alpha^{eq}(T) = 1 + 2C_{12}/C_{11} = 2.2$ for Ni and would be 2.6 for Au. For the Au (111) cubic crystal surface, the above equation is still valid if the elastic constants are calculated in the rotated coordinate system, in which the x-axis is [111]. We find that the newly obtained C_{11} and C_{12} coincidentally yield the same correction factor of 2.2 for Au (111) as for Ni (100).

Strain waves prove ultrafast electron-equilibration. The pronounced compression and expansion of the Au layer (see Fig. 4a) clearly originates from the laser-induced stress generated in Ni. In order to show that our modified TTM predicting negligible energy density in Au immediately after the excitation can quantitatively explain the signal oscillations, we have used the transient temperatures $T_{Ni,Au}(t)$ from our TTM as input parameters for a full thermo-elastic simulation using the udkm1Dsim toolbox, which are represented as solid lines in Fig. 4a[59]. For convenience, Fig. 4b shows the spatio-temporal strain map from which the solid lines in Fig. 4a are calculated by spatial averaging over the layer for each time delay. Multiple reflections of strain waves at the interfaces are strongly damped by transmission to the substrate.

Macroscopic Grüneisen coefficients. Several recent ultrafast X-ray diffraction and electron diffraction experiments on thin metal films have highlighted two contributions of electrons and phonons to the transient stress σ, which drives the observed strain waves. A very useful concept uses the macroscopic Grüneisen coefficient Γ^e and Γ^{ph}, which relate the energy densities ρ^Q to the stress $\sigma = \Gamma\rho$. While in Au the electronic Grüneisen constant $\Gamma^e_{Au} = 1.5$ is about half of its phonon counterpart $\Gamma^{ph}_{Au} = 3.0$, in Ni $\Gamma^e_{Ni} = 1.5$ is only slightly different from $\Gamma^{ph}_{Ni} = 1.7$[6,7]. For our analysis the distinction of the origin of pressure in Ni is not very relevant, since the redistribution of energy from electrons to phonons only increases the

stress by 15%. In Au the electron pressure is negligible in our bilayer system, since due to the large electronic specific heat of Ni and the subpicosecond equilibration among the electrons, all the energy is accumulated in Ni. The ab initio modeling discussed in connection to the recent UXRD study on Fe points out that both electron–phonon coupling parameters and phonon Grüneisen coefficients depend on the phonon mode[5,29]. While in that study the scattering of X-rays from individual phonon modes selected by the scattering geometry may require a mode-specific analysis, we believe that measuring the lattice expansion via a Bragg-peak shift looks at an average response of the lattice to all phonon modes, and hence a mode-averaged analysis is reasonable if there is no selective excitation of modes with extraordinarily different Grüneisen coefficients.

Data availability. The data that support the findings of this study are available from the corresponding authors on reasonable request.

Received: 22 November 2017 Accepted: 18 May 2018
Published online: 20 August 2018

References

1. Waldecker, L., Bertoni, R., Ernstorfer, R. & Vorberger, J. Electron–phonon coupling and energy flow in a simple metal beyond the two-temperature approximation. *Phys. Rev. X* **6**, 021003 (2016).
2. Lin, Z., Zhigilei, L. V. & Celli, V. Electron–phonon coupling and electron heat capacity of metals under conditions of strong electron–phonon nonequilibrium. *Phys. Rev. B* **77**, 75133 (2008).
3. Hohlfeld, J. et al. Electron and lattice dynamics following optical excitation of metals. *Chem. Phys.* **251**, 237–258 (2000).
4. Sun, C.-K., Vallée, F., Acioli, L., Ippen, E. P. & Fujimoto, J. G. Femtosecond investigation of electron thermalization in gold. *Phys. Rev. B* **48**, 12365–12368 (1993).
5. Henighan, T. et al. Generation mechanism of terahertz coherent acoustic phonons in Fe. *Phys. Rev. B* **93**, 220301 (2016).
6. Nicoul, M., Shymanovich, U., Tarasevitch, A., von der Linde, D. & Sokolowski-Tinten, K. Picosecond acoustic response of a laser-heated gold-film studied with time resolved x-ray diffraction. *Appl. Phys. Lett.* **98**, 191902 (2011).
7. Wang, X. et al. Electronic Grüneisen parameter and thermal expansion in ferromagnetic transition metal. *Appl. Phys. Lett.* **92**, 121918 (2008).
8. Cahill, D. G. et al. Nanoscale thermal transport. *J. Appl. Phys.* **93**, 793 (2003).
9. Siemes, M. E. et al. Quasiballistic thermal transport from nanoscale interfaces observed using ultrafast coherent soft x-ray beams. *Nat. Mater.* **9**, 26–30 (2010).
10. Maznev, A. A. & Johnson, J. A. Onset of nondiffusive phonon transport in transient thermal grating decay. *Phys. Rev. B* **84**, 1–8 (2011).
11. Wang, W. & Cahill, D. G. Limits to thermal transport in nanoscale metal bilayers due to weak electron–phonon coupling in Au and Cu. *Phys. Rev. Lett.* **109**, 1–5 (2012).
12. Cahill, D. G. et al. Nanoscale thermal transport II. *Appl. Phys. Rev.* **1**, 011305 (2014).
13. Gyung-Min Choi, R. B., Wilson & Cahill, D. G. Indirect heating of Pt by short-pulse laser irradiation of Au in a nanoscale Pt/Au bilayer. *Phys. Rev. B* **89**, 064307 (2014).
14. Challener, W. A. et al. Heat-assisted magnetic recording by a near-field transducer with efficient optical energy transfer. *Nat. Photonics* **3**, 220–224 (2009).
15. Xu, Y. et al. Ultrafast magnetization manipulation using single femtosecond light and hot-electron pulses. *Adv. Mater.* **29**, 1703474 (2017).
16. Stanciu, C. D. et al. All-optical magnetic recording with circularly polarized light. *Phys. Rev. Lett.* **99**, 47601 (2007).
17. Kirilyuk, A., Kimel, A. V. & Rasing, Th Ultrafast optical manipulation of magnetic order. *Rev. Mod. Phys.* **82**, 2731–2784 (2010).
18. Mangin, S. et al. Engineered materials for all-optical helicity-dependent magnetic switching. *Nat. Mater.* **13**, 286–292 (2014).
19. El Hadri, M. S. et al. Two types of all-optical magnetization switching mechanisms using femtosecond laser pulses. *Phys. Rev. B* **94**, 064412 (2016).
20. Koopmans, B. et al. Explaining the paradoxical diversity of ultrafast laser-induced demagnetization. *Nat. Mater.* **9**, 259–265 (2010).
21. Battiato, M., Carva, K. & Oppeneer, P. M. Superdiffusive spin transport as a mechanism of ultrafast demagnetization. *Phys. Rev. Lett.* **105**, 027203 (2010).
22. Schellekens, A. J., Kuiper, K. C., De Wit, R. & Koopmans, B. Ultrafast spin-transfer torque driven by femtosecond pulsed-laser excitation. *Nat. Commun.* **5**, 4333 (2014).
23. Alekhin, A. et al. Femtosecond spin current pulses generated by the nonthermal spin-dependent seebeck effect and interacting with ferromagnets in spin valves. *Phys. Rev. Lett.* **119**, 017202 (2017).
24. Choi, G.-M., Moon, C.-H., Min, B.-C., Lee, K.-J. & Cahill, D. G. Thermal spin-transfer torque driven by the spin-dependent seebeck effect in metallic spin-valves. *Nat. Phys.* **11**, 576 (2015).
25. Kimling, J. & Cahill, D. G. Spin diffusion induced by pulsed-laser heating and the role of spin heat accumulation. *Phys. Rev. B* **95**, 014402 (2017).
26. Carva, K., Battiato, M. & Oppeneer, P. M. Ab initio investigation of the Elliott–Yafet electron–phonon mechanism in laser-induced ultrafast demagnetization. *Phys. Rev. Lett.* **107**, 207201 (2011).
27. Carva, K., Battiato, M., Legut, D. & Oppeneer, P. M. Ab initio theory of electron–phonon mediated ultrafast spin relaxation of laser-excited hot electrons in transition-metal ferromagnets. *Phys. Rev. B* **87**, 184425 (2013).
28. Reid, A. H. et al. Beyond a phenomenological description of magnetostriction. *Nat. Commun.* **9**, 388 (2018).
29. Maldonado, P., Carva, K., Flammer, M. & Oppeneer, P. M. Theory of out-of-equilibrium ultrafast relaxation dynamics in metals. *Phys. Rev. B* **96**, 174439 (2017).
30. Eschenlohr, A. et al. Ultrafast spin transport as key to femtosecond demagnetization. *Nat. Mater.* **12**, 332–336 (2013).
31. Khorsand, A. R., Savoini, M., Kirilyuk, A. & Rasing, Th Optical excitation of thin magnetic layers in multilayer structures. *Nat. Mater.* **13**, 101–102 (2014).
32. Eschenlohr, A. et al. Reply to "Optical excitation of thin magnetic layers in multilayer structures". *Nat. Mater.* **13**, 102–103 (2014).
33. Highland, M. et al. Ballistic-phonon heat conduction at the nanoscale as revealed by time-resolved X-ray diffraction and time-domain thermoreflectance. *Phys. Rev. B* **76**, 075337 (2007).
34. Shayduk, R. et al. Nanoscale heat transport studied by high-resolution time-resolved x-ray diffraction. *New J. Phys.* **13**, 093032 (2011).
35. Koc, A. et al. Ultrafast x-ray diffraction thermometry measures the influence of spin excitations on the heat transport through nanolayers. *Phys. Rev. B* **96**, 014306 (2017).
36. Sheu, Y. M. et al. Thermal transport in a semiconductor heterostructure measured by time-resolved X-ray diffraction. *Phys. Rev. B* **78**, 045317 (2008).
37. Schick, D. et al. Normalization schemes for ultrafast x-ray diffraction using a table-top laser-driven plasma source. *Rev. Sci. Instrum.* **83**, 025104 (2012).
38. Zamponi, F. et al. Femtosecond hard x-ray plasma sources with a kilohertz repetition rate. *Appl. Phys. A* **96**, 51–58 (2009).
39. von Reppert, A. et al. Watching the vibration and cooling of ultrathin gold nanotriangles by ultrafast x-ray diffraction. *J. Phys. Chem. C.* **120**, 28894–28899 (2016).
40. von Reppert, A. et al. Persistent nonequilibrium dynamics of the thermal energies in the spin and phonon systems of an antiferromagnet. *Struct. Dyn.* **3**, 054302 (2016).
41. Hartland, G. V. Measurements of the material properties of metal nanoparticles by time-resolved spectroscopy. *Phys. Chem. Chem. Phys.* **6**, 5263–5274 (2004).
42. Del Fatti, N., Arbouet, A. & Vallée, F. Femtosecond optical investigation of electron–lattice interactions in an ensemble and a single metal nanoparticle. *Appl. Phys. B* **84**, 175–181 (2006).
43. Wang, X. et al. Temperature dependence of electron–phonon thermalization and its correlation to ultrafast magnetism. *Phys. Rev. B* **81**, 220301 (2010).
44. Roth, T. et al. Temperature dependence of laser-induced demagnetization in Ni: a key for identifying the underlying mechanism. *Phys. Rev. X* **2**, 021006 (2012).
45. Gundrum, B. C., Cahill, D. G. & Averback, R. S. Thermal conductance of metal–metal interfaces. *Phys. Rev. B* **72**, 245426 (2005).
46. Sokolowski-Tinten, K. et al. Electron–lattice energy relaxation in laser-excited thin-film Au-insulator heterostructures studied by ultrafast mev electron diffraction. *Struct. Dyn.* **4**, 054501 (2017).
47. Atxitia, U., Chubykalo-Fesenko, O., Walowski, J., Mann, A. & Münzenberg, M. Evidence for thermal mechanisms in laser-induced femtosecond spin dynamics. *Phys. Rev. B* **81**, 174401 (2010).
48. Kim, J.-W., Vomir, M. & Bigot, J.-Y. Ultrafast magnetoacoustics in nickel films. *Phys. Rev. Lett.* **109**, 166601 (2012).
49. Alebrand, S., Hassdenteufel, A., Steil, D., Cinchetti, M. & Aeschlimann, M. Interplay of heating and helicity in all-optical magnetization switching. *Phys. Rev. B Condens. Matter Mater. Phys.* **85**, 1–5 (2012).
50. Frietsch, B. et al. Disparate ultrafast dynamics of itinerant and localized magnetic moments in gadolinium metal. *Nat. Commun.* **6**, 8262 (2015).
51. Rettig, L. et al. Itinerant and localized magnetization dynamics in antiferromagnetic ho. *Phys. Rev. Lett.* **116**, 257202 (2016).
52. Yariv, A. & Yeh, P. *Optical waves in Layered Media*. (Wiley, New York, 1988).
53. Lee, H. J. et al. Optically induced lattice dynamics probed with ultrafast X-ray diffraction. *Phys. Rev. B* **77**, 132301 (2008).
54. Takahashi, Y. & Akiyama, H. Heat capacity of gold from 80 to 1000 k. *Thermochim. Acta* **109**, 105–109 (1986).
55. Meschter, P. J., Wright, J. W., Brooks, C. R. & Kollie, T. G. Physical contributions to the heat capacity of nickel. *J. Phys. Chem. Solids* **42**, 861–871 (1981).

56. Stojanovic, N., Maithripala, D. H. S., Berg, J. M. & Holtz, M. Thermal conductivity in metallic nanostructures at high temperature: electrons, phonons, and the wiedemann-franz law. *Phys. Rev. B* **82**, 075418 (2010).
57. Nix, F. C. & MacNair, D. The thermal expansion of pure metals: copper, *gold*, aluminum, *nickel*, and iron. *Phys. Rev.* **60**, 597–605 (1941).
58. Schick, D. et al. Ultrafast reciprocal-space mapping with a convergent beam. *J. Appl. Crystallogr.* **46**, 1372-1377 (2013).
59. Schick, D. et al. udkm1Dsim—A simulation toolkit for 1D ultrafast dynamics in condensed matter. *Comput. Phys. Commun.* **185**, 651-660 (2014)

Acknowledgments

We acknowledge the BMBF for the financial support via 05K16IPA and the DFG via BA 2281/8-1. The contribution by A.A.M. was supported by the US Department of Energy Grant no. DE-FG02-00ER15087. We thank Daniel Schick for help regarding the calculations using the optical matrix formalism.

Author contributions

J.P. and A.v.R. conducted and analyzed the experiments. M.K. and. C.H.B. grew the nanostructures. A.A.M. and A.v.R contibuted key ideas to the interpretation, G.M. provided context to ultrafast magnetism. J.P., A.v.R. and M.H. did the simulations and modeling. J.P. initiated and M.B. supervised and coordinated the project. All authors contributed to the writing of the manuscript.

Additional information

Competing interests: The authors declare no competing interests.

Article III

Tracking picosecond strain pulses in heterostructures that exhibit giant magnetostriction

Steffen Peer Zeuschner, Tymur Parpiiev, Thomas Pezeril, Arnaud Hillion, Karine Dumesnil, Abdelmadjid Anane, Jan-Etienne Pudell, Lisa Willig, Matthias Rössle, Marc Herzog, Alexander von Reppert, and Matias Bargheer

Structural Dynamics 6, 024302 (2019)

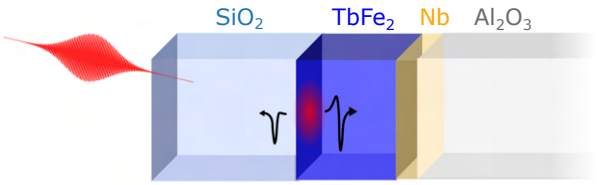

We combine ultrafast x-ray diffraction (UXRD) and time-resolved Magneto-Optical Kerr Effect (MOKE) measurements to monitor the strain pulses in laser-excited $TbFe_2$/Nb heterostructures. Spatial separation of the Nb detection layer from the laser excitation region allows for a background-free characterization of the laser-generated strain pulses. We clearly observe symmetric bipolar strain pulses when the excited TbFe2 surface terminates the sample and a decomposition of the strain wavepacket into an asymmetric bipolar and a unipolar pulse, when a SiO_2 glass capping layer covers the excited $TbFe_2$ layer. The inverse magnetostriction of the temporally separated unipolar strain pulses in this sample leads to a MOKE signal that linearly depends on the strain pulse amplitude measured through UXRD. Linear chain model simulations accurately predict the timing and shape of UXRD and MOKE signals that are caused by the strain reflections from multiple interfaces in the heterostructure.

Structural Dynamics

Tracking picosecond strain pulses in heterostructures that exhibit giant magnetostriction

Cite as: Struct. Dyn. **6**, 024302 (2019); https://doi.org/10.1063/1.5084140
Submitted: 04 December 2018 . Accepted: 26 February 2019 . Published Online: 20 March 2019

S. P. Zeuschner, T. Parpiiev, T. Pezeril, A. Hillion, K. Dumesnil, A. Anane, J. Pudell, L. Willig, M. Rössle, M. Herzog, A. von Reppert, and M. Bargheer

Structural Dynamics ARTICLE scitation.org/journal/sdy

Tracking picosecond strain pulses in heterostructures that exhibit giant magnetostriction

Cite as: Struct. Dyn. **6**, 024302 (2019); doi: 10.1063/1.5084140
Submitted: 4 December 2018 · Accepted: 26 February 2019 ·
Published Online: 20 March 2019

S. P. Zeuschner,[1,2] T. Parpiiev,[3] T. Pezeril,[3] A. Hillion,[4] K. Dumesnil,[4] A. Anane,[5] J. Pudell,[2] L. Willig,[2] M. Rössle,[1] M. Herzog,[2] A. von Reppert,[2,a)] and M. Bargheer[1,2]

AFFILIATIONS

[1]Helmholtz-Zentrum Berlin, Wilhelm-Conrad-Röntgen-Campus, BESSY II, Albert-Einstein-Straße 15, 12489 Berlin, Germany
[2]Institute of Physics and Astronomy, University of Potsdam, Karl-Liebknecht-Straße 24-25, 14476 Potsdam, Germany
[3]Institut des Molécules et Matériaux du Mans (UMR CNRS 6283), Université du Maine, 72085 Le Mans Cedex, France
[4]Institut Jean Lamour (UMR CNRS 7198), Université de Lorraine, 54000 Nancy, France
[5]Unité Mixte de Physique, CNRS, Thales, Univ. Paris-Sud, Université Paris-Saclay, 91767, Palaiseau, France

[a)]reppert@uni-potsdam.de

ABSTRACT

We combine ultrafast X-ray diffraction (UXRD) and time-resolved Magneto-Optical Kerr Effect (MOKE) measurements to monitor the strain pulses in laser-excited $TbFe_2$/Nb heterostructures. Spatial separation of the Nb detection layer from the laser excitation region allows for a background-free characterization of the laser-generated strain pulses. We clearly observe symmetric bipolar strain pulses if the excited $TbFe_2$ surface terminates the sample and a decomposition of the strain wavepacket into an asymmetric bipolar and a unipolar pulse, if a SiO_2 glass capping layer covers the excited $TbFe_2$ layer. The inverse magnetostriction of the temporally separated unipolar strain pulses in this sample leads to a MOKE signal that linearly depends on the strain pulse amplitude measured through UXRD. Linear chain model simulations accurately predict the timing and shape of UXRD and MOKE signals that are caused by the strain reflections from multiple interfaces in the heterostructure.

I. INTRODUCTION

The generation, propagation, and detection of laser-induced strain waves contain rich physics that has been studied extensively since the seminal work of Thomsen *et al.*, which exploited photoelasticity for detection.[1,2] Ingenious all-optical probing schemes for GHz to THz phonons have since then been used to investigate strain waves in multiple materials,[3–6] vibrational modes of nanoparticles,[7] shear waves,[8] nonlinear propagation effects,[9,10] and acoustic solitons.[11,12] Strain waves that originate from coherent phonon excitation can attain transient stresses on the order of GPa, which have been shown to interact with other phenomena such as phase transitions,[13,14] quantum well bandgaps,[15] piezo-[16]/ferroelectricity,[17] and magnetism.[18–22] Such interactions are not only of fundamental interest but may also become relevant for applications as soon as the understanding allows for controllability.[23,24]

In order to study the response to pure strain pulses, it is beneficial to spatially separate the laser excited transducer from the probed layer. The inherent limitation given by the finite optical penetration of the visible light in the transducer is often circumvented by backside probing schemes.[10,21] The development of (sub)-picosecond hard X-ray diffraction has opened the possibility to directly obtain the time-resolved strain amplitude[25–28] with penetration depths in the few μm regime. The separation of the layer peaks in reciprocal space allows for material specific probing of the energy flow[29,30] and strain evolution[31,32] in nanoscopic, crystalline heterostructures.

The envisioned manipulation of the polarization and magnetization states in ferroic materials via strain relies on a strong coupling between spin or electronic degrees of freedom and the atomic lattice.[23,33] In this regard, rare-earth-based alloys such as Terfenol ($TbFe_2$) have attracted attention due to the discovery of "giant magnetostriction,"[34,35]

Structural Dynamics ARTICLE scitation.org/journal/sdy

i.e., lattice strains in excess of 10^{-3} caused by magnetization change. Among the binary rare-earth alloys, $TbFe_2$ exhibits the largest magnetostriction.[36] It combines the large exchange interaction of the 3*d* orbital in Iron (Fe) with the large magnetic moment of $9\mu_B$ per Tb atom and the large spin-orbit coupling associated with 4*f* orbitals. The exchange coupling results in a ferrimagnetic alignment of the Fe and Tb moments with the Curie point ($T_C \approx 700$ K) considerably above room temperature.[37] $TbFe_2$ crystallizes in a cubic C_{15} Laves phase structure, where the $\langle 111 \rangle$-direction is the magnetic easy axis, which can be modeled by the cubic crystalline anisotropy constants $K_1 = -1.2 \times 10^8$ erg/cm^3 and $K_2 = 2.08 \times 10^7$ erg/cm^3.[38] The resulting high coercivity is often reduced for application purposes by introducing Dy ($\langle 001 \rangle$ easy axis) to obtain the ternary alloy Terfenol-D ($Tb_xDy_{1-x}Fe_2$). The desired low coercivity with large magnetostriction that is favorable for magneto-acoustic transduction applications can be tailored by different ratios *x*, where $x = 0.27$ is found to be optimal at room temperature.[39] Despite the potentially rich, coupled magnetization, and lattice dynamics in this magnetostrictive ferrimagnet, there have been only a few reports[8,23] that aim at quantifying and correlating the strain evolution and its coupling to the magnetization by time-resolved measurements in binary rare-earth alloys.

Here, we display the different capabilities of table-top ultrafast X-ray diffraction (UXRD) and all-optical methods to probe the strain propagation and evolution in a layered magnetostrictive heterostructure. Femtosecond laser pulses are used to excite the rare-earth alloy $TbFe_2$, which serves as a transducer for strain waves into adjacent layers. UXRD measurements observe the arrival and shape of the strain waves in a thin, buried detection layer. From this, we extract the stress profile that generates the strain wave in the inhomogeneously excited $TbFe_2$ layer. The timings of the observed experimental features are rationalized by modeling the strain propagation in this multilayer sample using a 1-dimensional linear chain model of masses and springs. The modeling is shown to be particularly useful when the transducer is capped by a transparent layer so that the conventional symmetric bipolar strain pulse is split into an asymmetric bipolar pulse travelling into the transducer and a unipolar strain pulse that is reflected at the sample-surface after a time determined by the transparent layer thickness. Complementary to the UXRD data, we employ an all-optical polarization sensitive measurement that probes the strain propagation in a transparent silica (SiO_2) acoustic delay line. Time-resolved magneto-optical-Kerr-effect (MOKE) measurements are shown to be a very sensitive probe for the arrival of the multiple strain echoes at the top of the laser-excited $TbFe_2$ layer, which can be used to complement the bulk sensitive UXRD.

II. EXPERIMENTAL DETAILS

We investigate laser-excited samples that consist of (110) oriented Terfenol ($TbFe_2$) layers grown by MBE on $(11\bar{2}1)$ oriented Sapphire (Al_2O_3) with a buried Niobium (Nb) (110) buffer layer as previously described.[38,40] The basic sample structure is only capped by a 2 nm thin protective Titanium (Ti) layer, which does not significantly contribute to the experimental transients. We therefore refer to sample 1 as uncapped. The second sample was instead capped with an 885 nm thick amorphous silica (SiO_2) layer. The UXRD measurements are carried out at a laser-driven, plasma-based diffraction setup (PXS) that supplies 200 fs X-ray pulses at Cu K_α-energy.[41] The table-top laser-pump X-ray-probe setup uses *p*-polarized excitation pulses at a central wavelength of 800 nm, with a 1 kHz repetition rate and a full width at half maximum spot size of a 2-dimensional Gaussian function of 1.4 mm × 1.5 mm for the laser pulses and 0.3 mm × 0.3 mm spot size of the X-ray pulses. Using the top-hat approximation with the $1/e$ width for the laser excitation profile and the pulse energy, we calculate the fluence for the $TbFe_2$ and Nb experiments, respectively. The pump-fluence at the Nb angle is approximately 4% larger compared to the $TbFe_2$ experiments since the 1.6° larger diffraction angle leads to a smaller laser footprint, whereas the Fresnel reflection coefficient for the *p*-polarized laser light decreases by approximately 1.4%.

A representative reciprocal-space map (RSM) of the uncapped sample structure obtained at the PXS alongside the static X-ray diffraction curve and the temporal evolution of the material specific Bragg peaks are displayed in Fig. 1. In the probed RSM volume, we find three separated peaks with their maximum intensity at the out-of-plane reciprocal space coordinate $q_z = 2.42$ Å^{-1}, 2.64 Å^{-1}, and 2.69 Å^{-1}, which are attributed to $TbFe_2$ (220), Al_2O_3 $(11\bar{2}1)$, and Nb (110), respectively, according to their bulk lattice plane spacings. The layer thicknesses set by the sample growth are 500 nm $TbFe_2$ on top of 50 nm Nb and 330 μm Al_2O_3 as schematically depicted in Fig. 1(e).

The $TbFe_2$ diffraction peak is significantly broadened along the in-plane reciprocal space coordinate q_x compared to the instrument function limited Al_2O_3 substrate peak. This is a hallmark for microcrystalline domains that in this case exhibit a large mosaic spread of 1.5° around the bulk diffraction angle,[40] very similar to previously reported UXRD experiments on ferroelectric samples.[42,43] The presence of such structural imperfections in the $TbFe_2$ becomes evident by comparison to the diffraction peak of the Nb layer, which exhibits a much smaller width in q_x. The blue and orange lines in Fig. 1(b) represent the reciprocal space slices that are probed in our setup for two fixed angles of incidence (AOI) ω that are chosen to be selectively sensitive to the $TbFe_2$ and Nb lattice strains, respectively.

The combination of an optic that focuses X-rays onto the sample with a convergence of $\Delta\omega \approx 0.3°$ (Montel optic from Layertec) and an X-ray area pixel detector (Dectris PILATUS-100k) allows for swift data acquisition that avoids time-consuming mesh scans of the AOI (ω) and the diffraction angle (θ). Each pixel of the X-ray area detector is mapped to reciprocal space coordinates q_x and q_z using the mapping routine described in a previous publication,[42] which is applicable in the thin film regime. Using this fixed angle detection scheme, the flux of 10^6 photons/s incident on the sample is sufficient to probe the evolution of the material specific diffraction peaks and the laser excited heterostructure with subpicosecond time resolution within few hours. The X-ray diffraction curves of the unexcited sample at the Nb and $TbFe_2$ AOI are indicated by orange and blue solid lines in Fig. 1(a) and their time evolution is represented by Figs. 1(c) and 1(d) for Nb and $TbFe_2$, respectively. The dashed lines in Figs. 1(c) and 1(d) indicate the temporal evolution of the peak center that is extracted by fitting the diffraction signal with a Gaussian line profile at each delay. This extracted Bragg peak position in reciprocal space is inversely proportional to the lattice constant *d* of the material via $q_{z,\mathrm{Fit}}(t) = \frac{2\pi}{d_{\mathrm{Fit}}(t)}$. UXRD thus probes the time-resolved strain $\varepsilon(t)$, defined as the change of the average lattice constant *d* relative to the unexcited sample $\varepsilon = \frac{d(t) - d(t<0)}{d(t<0)}$. The presented UXRD measurements were carried out without the external magnetic field. The application of static magnetic fields on the order of $\mu_0 H = 500$ mT in- and out-of-plane only leads

Structural Dynamics ARTICLE scitation.org/journal/sdy

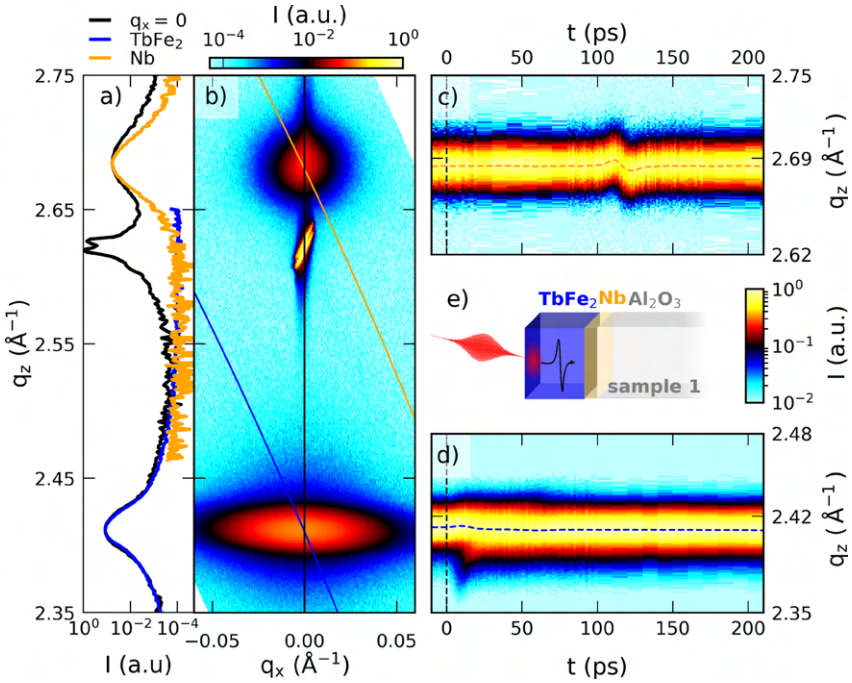

FIG. 1. Characterization of sample 1 via X-ray diffraction: (a) slice of the reciprocal space map shown in (b) at $q_x = 0$ (black line). The blue and orange lines in (a) correspond to the probed reciprocal slice when using the convergent beam of the X-ray focusing optic and area detector at the lab-based diffraction setup at a fixed angle of incidence. (c) and (d) depict the temporal evolution of the Nb and TbFe$_2$ peak at 13.3 mJ/cm^2, respectively, with the fitted peak position indicated by dashed lines. (e) Schematic depiction of the uncapped sample structure.

to minor modification of the UXRD signals consistent with a slightly increased sound velocity.

III. ANALYSIS AND DISCUSSION OF THE RESULTS

A. Signatures from the sample without SiO_2 capping

Before discussing the transient strain of the SiO_2 capped Terfenol ($TbFe_2$) structures, it is instructive to rationalize the signals seen in the UXRD experiment on the uncapped sample 1 that is schematically depicted in Fig. 1(e) for a fluence of 12.7 mJ/cm^2 and 13.3 mJ/cm^2 for the $TbFe_2$ and Nb, respectively. At first we discuss the strain evolution in the directly excited, approximately 500 nm thick $TbFe_2$ layer shown in Fig. 2(a). The blue data points show the experimentally obtained strain from Gaussian fits to the diffraction curves. The representative fits and raw time-resolved data from Figs. 1(c) and 1(d) are shown in Fig. S1 of the supplementary material. Beyond 20 ps, we observe an expansion that manifests in a shift of the diffraction peaks to smaller q_z. Within the first 20 ps, one observes a transient shift of the majority of the Bragg peak to larger q_z, which coincides with the appearance of a shoulder at smaller q_z. Between 40 and 80 ps, we detect a pronounced, triangular shaped strain increase and subsequent decrease in addition to an overall rising background.

No background is observed in the strain response of the 50 nm thin, buried Nb layer displayed in Fig. 2(b). The strain in the Nb layer is close to zero up to 4 ns (not shown), except for the very pronounced, nearly symmetric bipolar strain pulse that starts with a contraction at approximately 90 ps, reverses sign at 117 ps, and ceases at approximately 150 ps. The diffraction peak evolution of the thin Nb layer displayed in Fig. 1(c) exhibits a large peak shift that corresponds to a

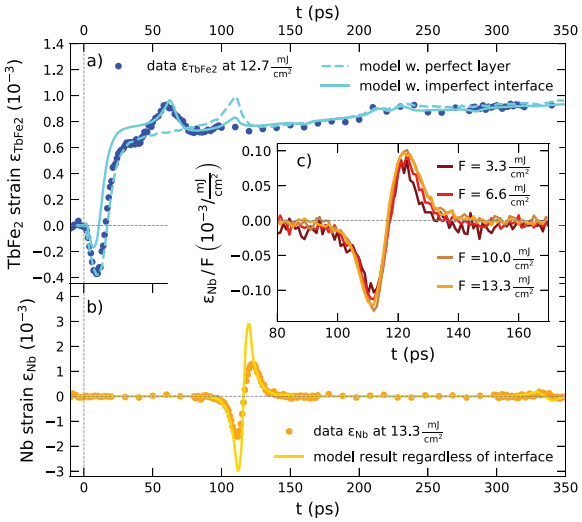

FIG. 2. Transient strain signatures of sample 1 without SiO_2 capping: (a) and (b) display transient strains extracted from the average peak shift via Gaussian lineshape fits and the simulated strain response using the udkm1Dsim toolbox as lines. The dashed line in (a) corresponds to a model with a full single-crystalline $TbFe_2$ layer whereas the solid line takes a disordered $TbFe_2$ layer at the $TbFe_2$/Nb interface into account. Inset (c) depicts the transient strain pulse in the Nb layer normalized to the different excitation fluences.

Structural Dynamics ARTICLE scitation.org/journal/sdy

strain amplitude of 1.5‰, which is only present during a short time window. The inset (c) in Fig. 2 shows the strain oscillation in Nb for different pump fluences, normalized to the fluence of the laser pulses. Since the transient strain curves nearly coincide, our data evidence a linear fluence dependence for this strain oscillation feature in Nb up to 13.3 mJ/cm^2.

The interpretation of the UXRD data from the thick $TbFe_2$ layer is based on the insights into ultrafast lattice response of photoexcited thin films studied by UXRD, which were previously discussed by Schick *et al.*[44] The laser illumination leads to the excitation of coherent and incoherent phonons, which superimpose in the strain response of the absorbing layer.[2] The strain pulse composed of the coherent excitation of phonons subsequently propagates at the longitudinal acoustic phonon velocity whereas the thermal energy leaves the excited layer by a slower diffusion process.

Our experiment represents the limiting case of an inhomogeneously excited transducer since the $TbFe_2$ layer thickness is approximately 25 times larger than the 19.9 nm light intensity penetration depth at 800 nm, which we obtain from ellipsometry measurements using a commercial setup and analyzing software (SENTECH), as discussed in Sec. III of the supplementary material. The appearance of a marked shoulder in the $TbFe_2$ diffraction signal on the lower q_z side for the main diffraction in Fig. 1(d) signals the existence of a highly strained surface layer on top of the nearly unperturbed $TbFe_2$. Schick *et al.*[44] have analyzed in detail that the exponential stress profile originating from inhomogeneous laser heating leads to an initial compression of the majority of the layer. Since the Gaussian fit is most sensitive to the central region of the diffraction peak, we observe the leading compressive strain front as a shift of the Bragg peak maximum to larger angles in the first 15 ps. When the free surface expansion propagates into the material at the speed of sound, the strong expansive component finally shifts the Bragg peak maximum to smaller angles. We attribute the remaining slope to the heat transport that equilibrates the inhomogeneous temperature profile within the $TbFe_2$ layer on a timescale of hundreds of picoseconds to several nanoseconds.

The strain response of the Nb layer seen in Fig. 2(b) confirms that the thermal transport occurs mainly within the $TbFe_2$ layer since we observe no thermal expansion that would appear as a background within our 4 ns measurement window. The bipolar strain pulse marks the delayed passage of the coherently excited phonon wave packet, which is launched at the sample-air interface, through the buried Nb layer. The detected diffraction peak shift of the 50 nm thick detection layer thus shows a background-free signal of the strain pulse, consisting of a compressive leading edge, which is followed by an expansive trailing edge as it is known from previous picosecond acoustic investigations.[2,45] The smaller layer thickness leads to higher average strain signals and sharper features as compared to the strain detected in the thick transducer layer.

The signature of the exit of the bipolar strain pulse from the probed $TbFe_2$ layer is an increase in the average layer strain followed by a decrease back to the thermal expansion background since the leading compressive edge exits while the trailing expansive part is still in the layer. In our experiment, we observe a pronounced delay between the exit of the strain wave from the $TbFe_2$ layer, at approximately 40 ps and its arrival in the adjacent Nb at 90 ps. This 50 ps delay of the signatures can only be rationalized if the strain pulse traverses a $TbFe_2$ layer that does not contribute significantly to the X-ray diffraction signal. Using $v_{sound} = 3.94$ nm/ps, known for polycrystalline $TbFe_2$,[46] this corresponds to a layer with a thickness of approximately 187 nm $TbFe_2$ that has a considerably different texture. Structural inhomogeneities are in-line with the mosaic peak broadening and the comparably small X-ray diffraction intensity of the $TbFe_2$ peak. The existence of a structurally imperfect interface layer at the $TbFe_2$-Nb interface is further supported by Atomic Force microscopy measurements that observed that the rare-earth alloy layer growth proceeds first as separated 3-dimensional islands that only coalesce to form a continuous film for thicknesses on the order of 100 nm and above.[38] The large in-plane lattice-constant mismatch of 11.6% between the underlying Nb template and the $TbFe_2$ is reduced by a thin FeNb layer but is probably the origin for the large mosaicity and for the limited coherence length along the growth direction,[47] which amounts to 50 nm in the present $TbFe_2$ film.

Modeling the excitation and propagation of picosecond acoustic strain pulses is achieved by solving the partial differential equation for the time-dependent local strain in which the given spatio-temporal stress profile acts as source term.[2,44,48] The thin film geometry reduces this to a 1-dimensional problem as the laser excitation spot is much larger than the film thickness of the nanostructure and the probed X-ray spot. Numerical solutions for the strain evolution in nanoscopic layers are frequently applied in nanoscopic heterostructure geometries where multiple interface reflections complicate analytical solutions.[32,48,49] In Figs. 2(a) and 2(b), we compare the UXRD data to simulation results obtained with the udkm1Dsim toolbox package that we used to calculate the time-resolved strain response based on a linear chain model of masses and springs. Although details of the software are given in the reference publication,[50] we briefly outline the workflow of the modeling. Upon input of the thermophysical material properties and the known sample geometry that are listed in Table I of the supplementary material, we first calculate the absorbed optical energy density and temperature profiles according to the heat diffusion equation[51] with unit cell resolution. The resulting spatio-temporal temperature profile represents the thermoelastic stress that drives a linear chain of masses and springs, where the masses represent individual unit cells. In the last simulation step, the obtained time-resolved strains are used as an input for the computation of the time-dependent dynamical X-ray diffraction signal.[52] The resulting diffraction peaks are fitted with a Gaussian line profile to yield the strain signal displayed as lines in Figs. 2(a) and 2(b).

The dashed line in Fig. 2(a) shows the modeled strain of a structurally perfect 436 nm thick $TbFe_2$ layer on top of a 50 nm Nb layer attached to an Al_2O_3 substrate. The simulation data represented by the solid line assume only 249 nm structurally perfect $TbFe_2$ on top of a 187 nm $TbFe_2$ layer with substantial disorder. The improved fit of the model regarding the triangular feature beginning at 40 ps substantiates the evidence for a structurally different $TbFe_2$ layer at the Nb interface. The total $TbFe_2$ layer thickness is determined by the arrival time of the bipolar strain pulse in Nb using the directionally averaged speed of sound of $v_{sound} = 3.94$ nm/ps for polycrystalline $TbFe_2$,[46] due to the lack of exact elastic constants for single-crystalline $TbFe_2$. Despite the agreement between the simulated and experimental strains in the $TbFe_2$ layer, the simulation substantially overestimates the bipolar strain pulse amplitude in the Nb layer. This may be accounted for by taking into account a slowly rising stress profile in $TbFe_2$ and acoustic damping as well as scattering of the coherent phonons at the interface.[53–55]

Structural Dynamics ARTICLE scitation.org/journal/sdy

B. Signals in the SiO_2 capped sample

The central experimental result of this work is summarized in Fig. 3. Here, we combine the experimental results from a sample capped by an amorphous SiO_2 layer as sketched in the inset of Fig. 3(e). Figure 3(a) shows the spatio-temporal strain profile that is obtained within the linear chain model for the second sample structure with the stacking sequence 882 nm SiO_2 / 342 nm $TbFe_2$ / 50 nm Nb / Al_2O_3 substrate, which is solved by the udkm1Dsim toolbox.[50] Red and blue colors correspond to regions of expansive and compressive strain, respectively. One observes that the expansion of the laser-heated region slowly spreads as the heat diffuses within the $TbFe_2$ layer. Now, the bipolar strain pulse that is launched towards the substrate is clearly asymmetric, where a large-amplitude leading compressive part is followed by a smaller expansive tail. In addition, a unipolar compression pulse propagates in the SiO_2 capping layer towards the surface where it is converted into an expansion. The simulated strain in Fig. 3(a) clarifies that for a very thin capping layer, the expansive unipolar wave reflected at the surface would superimpose with the small expansive tail of the asymmetric bipolar wave to form the symmetric bipolar wave observed in sample 1, see Fig. 2. Multiple reflections of the strain pulses occur at the material interfaces indicated by horizontal dashed lines where the reflection and transmission arise due to the acoustic impedance mismatch.[2,56,57] A direct comparison of the simulation results is presented in Sec. IV of the supplementary material.

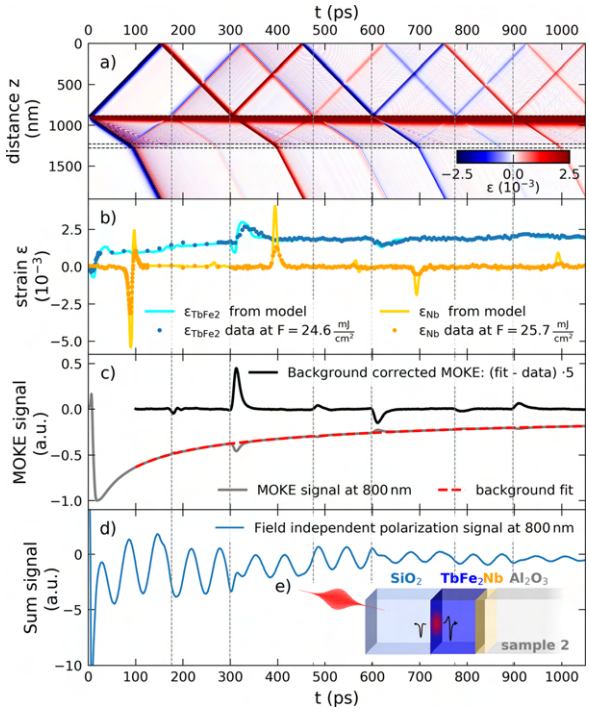

FIG. 3. Time-resolved signals from the SiO_2 capped sample structure: (a) spatio-temporal strain simulation result that highlights the occurrence of multiple echoes from bipolar and unipolar strain pulses. Horizontal dashed lines indicate the layer interfaces of the schematic sample geometry displayed in (e). (b) Comparison of the strain signal from UXRD measurements and udkm1Dsim toolbox simulations. (c) Time-resolved all-optical MOKE signal S: $[S(H_{up}) - S(H_{down})]$. The background subtracted signal shows pronounced peaks when strain pulses traverse the SiO_2/$TbFe_2$ interface, which are marked by vertical dashed lines. The field-independent polarization change $[S(H_{up}) + S(H_{down})]$ shown in (d) is dominated by oscillations of the time-resolved Brillouin scattering signal of the strain pulses within the SiO_2 capping.

The occurrence of multiple unipolar strain pulse echoes that traverse the $TbFe_2$ and Nb layers at different timings is readily seen in the UXRD data presented in Fig. 3(b). The modeled average strain shown as solid lines accurately predicts the timing and shape of the observed features but the amplitude of the Nb strain is substantially overestimated. This may indicate a finite electron-phonon-coupling time and scattering of the coherent phonons in $TbFe_2$ from structural imperfections, which are both not captured in the current modeling. The presented UXRD data were obtained under identical excitation conditions as the experiments on the uncapped sample except for the larger pump-fluence 24.6 mJ/cm^2, which leads to an increase in the detected strain amplitudes.

In the following, we discuss the results of time-resolved MOKE measurements, which probe the change of the polarization state of the probe light upon reflection due to the permanent magnetization of the sample. The measurement displayed in Fig. 3(c) was carried out close to the polar MOKE geometry with an external out-of-plane magnetic field of $\mu_0 H = 800$ mT using 200 fs laser pulses at a central wavelength of approximately 800 nm, a repetition rate of 250 kHz, and a pump fluence of approximately 2.7 mJ/cm^2. In these measurements, the difference of the polarization changes for opposite external field orientations $[S(H_{up}) - S(H_{down})]$ is probed using the reflection of 800 nm probe-light-pulses analyzed by a half-wave plate in combination with a Wollaston-prism and a balanced photo-diode. Lock-in detection using an acousto-optical modulation of the pump beam intensity at 50 kHz was employed. The resulting polar MOKE signal displayed as a solid grey line essentially probes the out-of-plane magnetization component of the $TbFe_2$ layer within the 19.9 nm optical penetration depth and is probably sensitive to the Fe sub-lattice.[58] Subtraction of the slowly varying thermal background approximated by a double-exponential decay (red line) from the MOKE signal (grey line) reveals multiple sharp peaks in the residual black curve. By comparison with the linear chain model results in Fig. 3(a), it becomes obvious that the observed features occur at the time when the longitudinal strain pulse echoes traverse the top few nanometers of the $TbFe_2$ layer given by the penetration depth of the probe pulse. Note that the sign of the peaks correlates with the sign of the (unipolar) strain-pulse echoes and that even the small reflections from the $TbFe_2$/Nb interface produce observable MOKE signatures at around 180, 485, and 790 ps.

Figure 3(d) displays the time-resolved polarization analysis signal of the reflected 800 nm probe beam independent of the magnetization state, which is obtained from the sum signal $[S(H_{up}) + S(H_{down})]$ of the balanced detection. Similar time-resolved Brillouin scattering experiments have shown that the observed oscillations originate from the interference of the reflected light from the traveling strain pulse in the transparent SiO_2 medium and the static interfaces.[59,60] Pronounced phase jumps in this Brillouin signal occur when the strain pulses invert their sign due to the reflection at the SiO_2/air interface.[56,61]

Consequently, the strain propagation as modeled by the 1-dimensional-linear chain model accurately predicts the timings of all

Structural Dynamics ARTICLE scitation.org/journal/sdy

the experimental signals we observed in this heterostructure. We have employed a single temperature model for the driving stress on the lattice. This certainly oversimplifies the equilibration process of the electron-, lattice-, and spin-subsystems to occur instantaneously. A detailed analysis of the dynamics prior to the equilibration is beyond the scope of the current investigation as it requires the knowledge of the thermophysical properties for each sub-system as well as the coupling constants of this largely unexplored material.

C. Experimental results from the buried detection layer

In the henceforth presented data analysis, we put the focus on the qualitative and quantitative information that can be directly extracted from the UXRD signal in the buried Nb detection layer. In Fig. 4(a), we see that the normalized, background-subtracted MOKE signal originating from $TbFe_2$ matches the normalized Nb strain when shifted by 84 ps, which is the longitudinal acoustic propagation time through the $TbFe_2$ layer. This agreement proves a linear relation between the lattice strain and the observed MOKE signal. The slight discrepancies at 485 and 790 ps probably originate from the fact that the MOKE signal results from a superposition of the strain pulses reflected at the surface and at the $TbFe_2$/Nb interface, which traverse the top $TbFe_2$ layer simultaneously [see Fig. 3(a)]. Since only part of the reflection at the $TbFe_2$/Nb interface is again reflected at the $TbFe_2/SiO_2$ interface, the Nb layer senses a different strain wave composition. It will be important for future experiments investigating the interaction of shear waves with the magnetization to accurately identify also the small longitudinal acoustic pulse echoes in such multilayered structures. Previous picosecond acoustic investigations in magnetic samples have observed that strain pulses can exert a torque on the sample magnetization $\vec{M}$ via a transient modification of the crystalline anisotropy, often resulting in a damped precessional motion of $\vec{M}$.[18,62,63] Although a torque on the magnetization by the strain pulse is expected, the absence of precessional oscillations challenges the theoretical interpretation of the observed MOKE signal based on the Landau-Lifshitz-Gilbert model. Crystalline defects in the $TbFe_2$, resulting in small magnetic domains,[63] in combination with a magneto-crystalline anisotropy and damping could drastically suppress the coherent precessional signal. The signal might have contributions from a modulation of the reflectivity driven by the photoelastic effect;[21] however, the reflectivity signal does not exhibit significant spikes at the echo positions. In any case, the striking resemblance of the detected strain pulses in the Nb layer to extracted features in the MOKE measurements demonstrates a high sensitivity of MOKE for probing strain pulses arriving at the $TbFe_2$ surface.

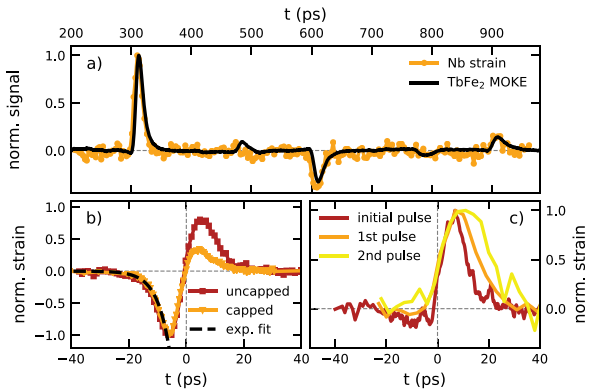

FIG. 4. Analysis of the strain pulse signatures: (a) comparison of the coherent phonon strain contribution seen in the MOKE and UXRD signal, scaled to the maximum amplitude and shifted to overlap in time. (b) Comparison of the initial asymmetric bipolar strain pulse in the capped sample 2 and the symmetric bipolar strain in the uncapped sample 1, to an exponential fit with a time-constant of 4.56 ps. (c) Evolution of the strain pulse after passing the SiO_2 layer multiple times.

In Fig. 4(b), we compare the initial bipolar strain pulses from the capped and uncapped samples, normalized to their compressive part. We observe that the leading, compressive parts coincide, whereas the expansive parts in the SiO_2 capped sample 2 are strongly reduced. The black dashed line indicates a single exponential fit to the falling edge of the compressive strain with a time constant of 4.6 ps, which translates to a spatial extension of approximately 18 nm using $v_{sound} = 3.94$ nm/ps. This value provides an estimation of the spatial extension of the driving stress profile.[3,64] This matches the optical penetration depth obtained from ellipsometry, which shows that potential hot-electron diffusion does not substantially increase the excitation profile length.

The evolution of the unipolar strain pulse within the SiO_2 capping is shown in Fig. 4(c), where we compare the first and second unipolar strain echoes that traverse the Nb layer at 396 ps and 695 ps to the initial pulse launched into the SiO_2 capping. The latter is extracted from the difference between the bipolar strain pulses observed on the capped and uncapped samples. In this analysis, we assume that the laser generated stress profile is identical in the capped and uncapped $TbFe_2$ samples and that the difference of the initially detected bipolar strain pulse seen in Fig. 4(b) originates solely from partial reflection of the expansion at the top $TbFe_2$ interface. The FWHM of the detected strain signals increases from 9 to 16 and 21 ps. The modeling does not include any broadening mechanisms and reports echoes with a constant width of 8 ps FWHM. Anharmonic interactions in the lattice potential have been shown to change the shape and broaden high amplitude coherent phonon wavepackets.[65] Contributions from the SiO_2 surface roughness should also be taken into account.

IV. CONCLUSION

In this work, we have combined multiple techniques to follow the trajectory of strain pulses that are generated by femtosecond laser pulses exploiting the giant magnetostriction material Terfenol ($TbFe_2$) as a transducer. MOKE measurements in $TbFe_2$ are shown to provide a surface sensitive method to probe strain pulses at the top of the metallic $TbFe_2$ that is complementary to bulk sensitive X-ray diffraction.

Probing the strain pulse in a thin, buried detection layer adjacent to an optically opaque transducer via UXRD allows for a characterization of the coherent strain pulse separately from heat expansion without frontside-pump backside-probe schemes. By detecting the strain pulse in the buried and perfect Nb layer, we demonstrate how UXRD can clearly locate the structurally imperfect fraction of the $TbFe_2$ layer in this opaque heterostructure. Contrary to all-optical methods, UXRD provides a quantitative measure of the average lattice strain that does not require detailed knowledge of photo elastic coefficients and optical properties. In combination with 1-dimensional-linear chain models, UXRD can provide quantitative information on realistic strains with unit cell resolution, which can be

Structural Dynamics ARTICLE scitation.org/journal/sdy

used as input for modeling strain-assisted magnetization switching approaches.[23] The obtained maximum strain amplitude in $TbFe_2$ of 2‰ is well below the deterministic switching limit of a few percent strain, but the local heating substantially lowers the anisotropy[66] as it is known from heat-assisted magnetic recording schemes.

The combination of MOKE and UXRD outlines a potential path towards an experimental calibration of the magneto-elastic coefficient, i.e., the magnetization change per strain amplitude for picosecond acoustic pulses. Such a quantity is not only relevant for testing fundamental research that models magneto-elastic couplings but also represents a valuable input for application-oriented research.

We believe that probing the strain-pulse in a buried detection layer is a versatile method for studying the stress generation profile as it separates coherent from incoherent phonon excitations. It will be especially useful in situations where multiple mechanisms with different spatial or temporal characteristics superimpose in the strain generation process as it is the case in (anti-)ferromagnetic[67,68] materials. The use of an acoustic delay line further introduces the possibility to study the evolution of the strain pulse shape and to calibrate the magnetization response to unipolar compression and expansion pulses. This will support important future steps towards a full understanding of the demagnetization process especially in high-anisotropy, giant magnetostriction materials. A combination of time-resolved probes that monitor different degrees of freedom within the same experiment will foster the understanding of the intricate couplings between electron-, spin-, and lattice systems in solids, which forms the basis for many useful devices.

SUPPLEMENTARY MATERIAL

See supplementary material for the details of the time evolution of the $TbFe_2$ and Nb Bragg peaks (S1) and the material parameters used in the modeling (S2). Furthermore, we provide the complex index of refraction and the resulting optical properties that were extracted from spectroscopic ellipsometry on the uncapped $TbFe_2$ sample (S3) as well as a section that compares the modeling results for the strain propagation in the capped and uncapped samples (S4).

ACKNOWLEDGMENTS

We gratefully acknowledge the BMBF for the financial support via 05K16IPA and the DFG via BA 2281/8-1 and BA 2281/11-1, the Open Access Publishing Fund of University of Potsdam, and Agence Nationale de la Recherche under Grant No. ANR-14-CE26-0008. We are thankful to Marwan Deb and Gregory Malinowski for stimulating discussions.

REFERENCES

[1]C. Thomsen *et al.*, "Coherent phonon generation and detection by picosecond light pulses," Phys. Rev. Lett. **53**, 989–992 (1984).
[2]C. Thomsen, H. T. Grahn, H. J. Maris, and J. Tauc, "Surface generation and detection of phonons by picosecond light pulses," Phys. Rev. B **34**, 4129–4138 (1986).
[3]O. B. Wright and K. Kawashima, "Coherent phonon detection from ultrafast surface vibrations," Phys. Rev. Lett. **69**, 1668–1671 (1992).
[4]T. Saito, O. Matsuda, and O. B. Wright, "Picosecond acoustic phonon pulse generation in nickel and chromium," Phys. Rev. B **67**(20), 205421 (2003).
[5]Y. Sugawara *et al.*, "Watching ripples on crystals," Phys. Rev. Lett. **88**, 185504 (2002).
[6]O. B. Wright, "Ultrafast nonequilibrium stress generation in gold and silver," Phys. Rev. B **49**, 9985–9988 (1994).
[7]G. V. Hartland, "Coherent vibrational motion in metal particles: Determination of the vibrational amplitude and excitation mechanism," J. Chem. Phys. **116**, 8048–8055 (2002).
[8]T. Pezeril, "Laser generation and detection of ultrafast shear acoustic waves in solids and liquids," Opt. Laser Technol. **83**, 177–188 (2016).
[9]A. Bojahr *et al.*, "Second harmonic generation of nanoscale phonon wave packets," Phys. Rev. Lett. **115**, 195502 (2015).
[10]C. Klieber, V. E. Gusev, T. Pezeril, and K. A. Nelson, "Nonlinear acoustics at GHz frequencies in a viscoelastic fragile glass former," Phys. Rev. Lett. **114**, 065701 (2015).
[11]H.-Y. Hao and H. J. Maris, "Experiments with acoustic solitons in crystalline solids," Phys. Rev. B **64**, 64302 (2001).
[12]P. J. S. van Capel and J. I. Dijkhuis, "Time-resolved interferometric detection of ultrashort strain solitons in sapphire," Phys. Rev. B **81**, 144106 (2010).
[13]P. Ruello, S. Zhang, P. Laffez, B. Perrin, and V. Gusev, "Laser-induced coherent acoustical phonons mechanisms in the metal-insulator transition compound $NdNiO_3$: Thermal and nonthermal processes," Phys. Rev. B **79**, 94303 (2009).
[14]S. H. Kim, B. J. Kim, T. Y. Jeong, Y. S. Lee, and K. J. Yee, "Coherent phonon spectroscopy of the phase transition in VO_2 single crystals and thin films," J. Appl. Phys. **117**, 163107 (2015).
[15]A. V. Akimov, A. V. Scherbakov, D. R. Yakovlev, C. T. Foxon, and M. Bayer, "Ultrafast band-gap shift induced by a strain pulse in semiconductor heterostructures," Phys. Rev. Lett. **97**(3), 037401 (2006).
[16]M. R. Armstrong *et al.*, "Observation of terahertz radiation coherently generated by acoustic waves," Nat. Phys. **5**, 285–288 (2009).
[17]C. K. Schmising *et al.*, "Coupled ultrafast lattice and polarization dynamics in ferroelectric nanolayers," Phys. Rev. Lett. **98**, 257601 (2007).
[18]J.-W. Kim, M. Vomir, and J.-Y. Bigot, "Ultrafast magnetoacoustics in nickel films," Phys. Rev. Lett. **109**, 166601 (2012).
[19]J. V. Jäger *et al.*, "Picosecond inverse magnetostriction in galfenol thin films," Appl. Phys. Lett. **103**, 032409 (2013).
[20]V. N. Kats *et al.*, "Ultrafast changes of magnetic anisotropy driven by laser-generated coherent and noncoherent phonons in metallic films," Phys. Rev. B **93**, 214422 (2016).
[21]L. Thevenard *et al.*, "Effect of picosecond strain pulses on thin layers of the ferromagnetic semiconductor (Ga,Mn)(As,P)," Phys. Rev. B **82**, 104422 (2010).
[22]M. Deb *et al.*, "Picosecond acoustic-excitation-driven ultrafast magnetization dynamics in dielectric Bi-substituted yttrium iron garnet," Phys. Rev. B **98**, 174407 (2018).
[23]O. Kovalenko, T. Pezeril, and V. V. Temnov, "New concept for magnetization switching by ultrafast acoustic pulses," Phys. Rev. Lett. **110**, 266602 (2013).
[24]A. V. Scherbakov *et al.*, "Ultrafast control of light emission from a quantum-well semiconductor microcavity using picosecond strain pulses," Phys. Rev. B **78**, 241302(R) (2008).
[25]C. Rose-Petruck *et al.*, "Picosecond-milliangstrom lattice dynamics measured by ultrafast X-ray diffraction," Nature **398**, 310–312 (1999).
[26]A. M. Lindenberg *et al.*, "Time-resolved x-ray diffraction from coherent phonons during a laser-induced phase transition," Phys. Rev. Lett. **84**, 111–114 (2000).
[27]D. A. Reis *et al.*, "Probing impulsive strain propagation with x-ray pulses," Phys. Rev. Lett. **86**, 3072–3075 (2001).
[28]T. Henighan *et al.*, "Generation mechanism of terahertz coherent acoustic phonons in Fe," Phys. Rev. B **93**, 220301(R) (2016).
[29]M. Highland *et al.*, "Ballistic-phonon heat conduction at the nanoscale as revealed by time-resolved x-ray diffraction and time-domain thermoreflectance," Phys. Rev. B **76**, 075337 (2007).
[30]A. Koc *et al.*, "Ultrafast x-ray diffraction thermometry measures the influence of spin excitations on the heat transport through nanolayers," Phys. Rev. B **96**, 014306 (2017).
[31]M. Bargheer *et al.*, "Coherent atomic motions in a nanostructure studied by femtosecond X-ray diffraction," Science **306**, 1771–1773 (2004).
[32]J. Pudell *et al.*, "Layer specific observation of slow thermal equilibration in ultrathin metallic nanostructures by femtosecond X-ray diffraction," Nat. Commun. **9**, 3335 (2018).

Structural Dynamics ARTICLE scitation.org/journal/sdy

[33]W. Eerenstein, N. D. Mathur, and J. F. Scott, "Multiferroic and magnetoelectric materials," Nature **442**, 759–765 (2006).
[34]A. E. Clark and H. S. Belson, "Giant room-temperature magnetostrictions in $TbFe_2$ and $DyFe_2$," Phys. Rev. B **5**, 3642–3644 (1972).
[35]N. C. Koon, A. I. Schimdler, and F. L. Carter, "Giant magnetostriction in cubic rare earth-iron compounds of the type RFe_2," Phys. Lett. A **37**, 413–414 (1971).
[36]A. Clark and D. Crowder, "High temperature magnetostriction of $TbFe_2$ and $Tb_{.27}Dy_{.73}Fe_2$," IEEE Trans. Magn. **21**, 1945–1947 (1985).
[37]K. H. J. Buschow and R. P. van Stapele, "Magnetic properties of some cubic rare-earth-iron compounds of the type RFe_2 and $R_xY_{1-x}Fe_2$," J. Appl. Phys. **41**, 4066–4069 (1970).
[38]A. Mougin, C. Dufour, K. Dumesnil, and P. Mangin, "Strain-induced magnetic anisotropy in single-crystal RFe_2 (110) thin films (R = Dy, Er, Tb, $Dy_{0.7}$ $Tb_{0.3}$, Sm, Y)," Phys. Rev. B **62**, 9517–9531 (2000).
[39]R. Bergstrom *et al.*, "Morphotropic phase boundaries in ferromagnets: $Tb_{1-x}Dy_xFe_2$ alloys," Phys. Rev. Lett. **111**, 017203 (2013).
[40]V. Oderno, C. Dufour, K. Dumesnil, P. Mangin, and G. Marchal, "Epitaxial growth of (110) $DyFe_2$, $TbFe_2$ and $Dy_{0.7}Tb_{0.3}Fe_2$ thin films by molecular beam epitaxy," J. Cryst. Growth **165**, 175–178 (1996).
[41]D. Schick *et al.*, "Normalization schemes for ultrafast x-ray diffraction using a table-top laser-driven plasma source," Rev. Sci. Instrum. **83**, 025104 (2012).
[42]D. Schick *et al.*, "Ultrafast reciprocal-space mapping with a convergent beam," J. Appl. Crystallogr. **46**, 1372–1377 (2013).
[43]D. Schick *et al.*, "Following strain-induced mosaicity changes of ferroelectric thin films by ultrafast reciprocal space mapping," Phys. Rev. Lett. **110**, 095502 (2013).
[44]D. Schick *et al.*, "Ultrafast lattice response of photoexcited thin films studied by X-ray diffraction," Struct. Dyn. **1**, 064501 (2014).
[45]P. Ruello and V. E. Gusev, "Physical mechanisms of coherent acoustic phonons generation by ultrafast laser action," Ultrasonics **56**, 21–35 (2015).
[46]A. E. Clark, H. S. Belson, and R. E. Strakna, "Elastic properties of rare-earth-iron compounds," J. Appl. Phys. **44**, 2913–2914 (1973).
[47]A. Mougin *et al.*, "Strain in single-crystal RFe_2 (110) thin films (R = Y, Sm, Gd, Tb, $Dy_{0.7}Tb_{0.3}$, Dy, Er, Lu)," Phys. Rev. B **59**, 5950–5959 (1999).
[48]M. Nicoul, U. Shymanovich, A. Tarasevitch, D. von der Linde, and K. Sokolowski-Tinten, "Picosecond acoustic response of a laser-heated gold-film studied with time-resolved x-ray diffraction," Appl. Phys. Lett. **98**, 191902 (2011).
[49]M. Herzog *et al.*, "Analysis of ultrafast X-ray diffraction data in a linear-chain model of the lattice dynamics," Appl. Phys. A **106**, 489–499 (2012).
[50]D. Schick *et al.*, "udkm1Dsim—A simulation toolkit for 1D ultrafast dynamics in condensed matter," Comput. Phys. Commun. **185**, 651–660 (2014).
[51]I. A. Veres, T. Berer, and P. Burgholzer, "Numerical modeling of thermoelastic generation of ultrasound by laser irradiation in the coupled thermoelasticity," Ultrasonics **53**, 141–149 (2013).
[52]S. A. Stepanov *et al.*, "Dynamical x-ray diffraction of multilayers and superlattices: Recursion matrix extension to grazing angles," Phys. Rev. B **57**, 4829–4841 (1998).
[53]M. Hase, Y. Miyamoto, and J. Tominaga, "Ultrafast dephasing of coherent optical phonons in atomically controlled $GeTe/Sb_2Te_3$ superlattices," Phys. Rev. B **79**, 174112 (2009).
[54]M. Hase and M. Kitajima, "Interaction of coherent phonons with defects and elementary excitations," J. Phys. Condens. Matter **22**, 073201 (2010).
[55]G. Chen *et al.*, "Increased phonon scattering by nanograins and point defects in nanostructured silicon with a low concentration of germanium," Phys. Rev. Lett. **102**(19), 196803 (2009).
[56]D. Royer and E. Dieulesaint, *Elastic Waves in Solids I* (Springer, 1996), Chap. I.
[57]A. I. H. Persson, H. Enquist, A. Jurgilaitis, B. P. Andreasson, and J. Larsson, "Real-time observation of coherent acoustic phonons generated by an acoustically mismatched optoacoustic transducer using x-ray diffraction," J. Appl. Phys. **118**, 185308 (2015).
[58]A. R. Khorsand *et al.*, "Element-specific probing of ultrafast spin dynamics in multisublattice magnets with visible light," Phys. Rev. Lett. **110**, 107205 (2013).
[59]M. Lejman *et al.*, "Ultrafast acousto-optic mode conversion in optically birefringent ferroelectrics," Nat. Commun. **7**, 12345 (2016).
[60]A. Bojahr *et al.*, "Brillouin scattering of visible and hard X-ray photons from optically synthesized phonon wavepackets," Opt. Express **21**, 21188 (2013).
[61]E. Pavlenko *et al.*, "Azobenzene-functionalized polyelectrolyte nanolayers as ultrafast optoacoustic transducers," Nanoscale **8**, 13297 (2016).
[62]A. V. Scherbakov *et al.*, "Coherent magnetization precession in ferromagnetic (Ga,Mn)As induced by picosecond acoustic pulses," Phys. Rev. Lett. **105**, 117204 (2010).
[63]T. L. Linnik *et al.*, "Theory of magnetization precession induced by a picosecond strain pulse in ferromagnetic semiconductor (Ga,Mn)As," Phys. Rev. B **84**, 214432 (2011).
[64]J. Pudell *et al.*, "Ultrafast negative thermal expansion driven by spin-disorder," Phys. Rev. B (to be published).
[65]A. Bojahr, M. Herzog, D. Schick, I. Vrejoiu, and M. Bargheer, "Calibrated real-time detection of nonlinearly propagating strain waves," Phys. Rev. B **86**, 144306 (2012).
[66]A. Clark, R. Abbundi, and W. Gillmor, "Magnetization and magnetic anisotropy of $TbFe_2$, $DyFe_2$, $Tb_{0.27}Dy_{0.73}Fe_2$ and $TmFe_2$," IEEE Trans. Magn. **14**, 542–544 (1978).
[67]A. von Reppert *et al.*, "Persistent nonequilibrium dynamics of the thermal energies in the spin and phonon systems of an antiferromagnet," Struct. Dyn. **3**, 054302 (2016).
[68]A. von Reppert *et al.*, "Ultrafast laser generated strain in granular and continuous FePt thin films," Appl. Phys. Lett. **113**, 123101 (2018).

Article III – Supplemental Material

Supplementary Material for

Tracking picosecond strain pulses in heterostructures that exhibit giant magnetostriction

S. P. Zeuschner[1,5], T. Parpiiev[2], T. Pezeril[2], A. Hillion[3], K. Dumesnil[3], M. Anane[4], J. Pudell[5], L. Willig[5], M. Rössle[1], M. Herzog[5], A. von Reppert[5]*, M. Bargheer[1,5]

[1]*Helmholtz-Zentrum Berlin, Wilhelm-Conrad-Röntgen-Campus, BESSY II, Albert-Einstein-Straße 15, 12489 Berlin, Germany*

[2]*Institut des Molécules et Matériaux du Mans (UMR CNRS 6283), Université du Maine, 72085 Le Mans cedex, France*

[3]*Institut Jean Lamour (UMR CNRS 7198), Université de Lorraine, 54000 Nancy, France*

[4]*Unité Mixte de Physique CNRS/Thales (UMR CNRS 137), 91767 Palaiseau, France*

[5]*Institute of Physics and Astronomy, University of Potsdam, Karl-Liebknecht-Straße 24-25, 14476 Potsdam, Germany*

* reppert@uni-potsdam.de

1) Time evolution of the $TbFe_2$ and Nb Bragg peaks

The timeresolved strain that is analyzed in the main text is extracted from Gaussian fits to the diffraction signal. In Fig S1a) and S1b) we explicitly show the Gaussian Fits to the (220)-diffraction peak of $TbFe_2$ and the (110)-diffraction peak of Nb for representative delays for the uncapped sample. The time-resolved Bragg-peak evolution is depicted in Fig. 1 c) and d) of the main text. Fig. S1a) underlines that the Gaussian fit is mostly sensitive to the main diffraction peak, which represents the majority of the probed $TbFe_2$ layer, whereas the pronounced shoulder at low q_z side, which originates from the already expanded surface layer is not captured by the model. This explains the compression of the $TbFe_2$ layer that is observed in the first 20ps of Fig 2a) of the main text. Due to the much smaller thickness of only 50nm for the buried detection layer we observe that the Nb peak shifts much more homogeneously without the appearance of marked shoulders as can be seen in Fig. S1b). This effect has been discussed to some detail by Schick et al.[1]

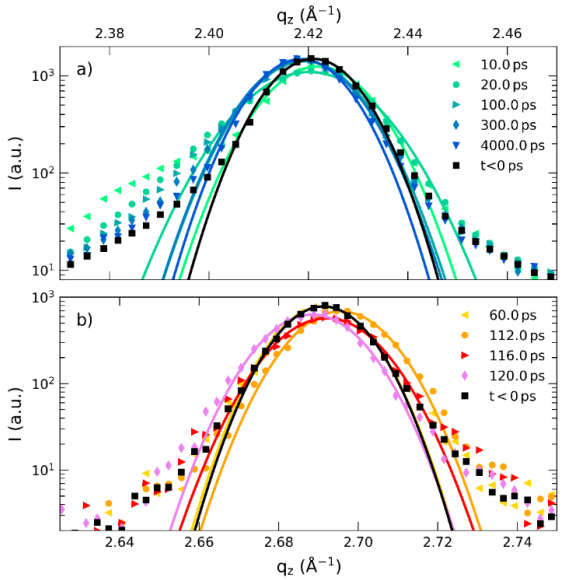

Figure S1: Diffraction data of the $TbFe_2$ (a) and Nb (b) layers at representative time delays alongside Gaussian line shape fits as solid lines.

2) Material properties as used in the modeling:

In the discussion of our experiments we refer to the udkm1Dsim toolbox[2], that calculates the time-resolved strain and the resulting X-ray diffraction from a linear chain model that is driven by a spatiotemporal stress, which results from the thermal expansion. In this process the model numerically solves the 1D - heat diffusion equation. This modelling requires the thermophysical properties of all sample materials. The used simulation parameters are given in Table S1 as a reference. In the modeling we employed temperature independent values.

Table S1: Material properties used in the udkm1Dsim toolbox simulation and evaluation.

Property/Material	**SiO_2**	**$TbFe_2$**	**Nb**	**Al_2O_3**
Lattice constant (Å) c-axis (out of plane) b-axis (in plane) a-axis (in plane)	 amorphous --- 	cubic 10.39 [4,5] 10.39 [4,5] 7.35 [45]	cubic 4.67 [6] 3.30 [6] 4.67 [6]	hexagonal 4.76 [7] 12.80 [7] 8.24 [7]
Sound velocity ($nm \cdot ps^{-1}$)	5.9 [8]	3.94 [9]	5.083 [10]	11.075 [7]
Linear thermal expansion coefficient (10^{-6} K^{-1})	0.55 [11]	23.7 [12]	7.6 [13]	6.6 [14]
Heat capacity ($J \cdot kg^{-1} \cdot K^{-1}$)	740 [15]	330 [16]	264.78 [17]	778.73 [18]
Density ($g \cdot cm^{-3}$)	2.2 [8]	9.17 [19]	8.57 [17]	4.05 [7]
Heat conductivity ($W \cdot m^{-1} \cdot K^{-1}$)	1.38 [17]	5*	58.3 [20]	40 [7]
Unit cell orientation out of plane	---	(220)	(110)	(11-20)
Molar mass ($g \cdot mol^{-1}$)	60.1	270.6	92.9	101.96
Acoustic impedance ($\rho \cdot v_{sound}$) ($g \cdot cm^{-3} \cdot nm \cdot ps^{-1}$)	12.98	38.24	43.56	44.853
Optical penetration depth (nm, measured by ellipsometry)	∞	18	24	∞
Simulated q_z ($Å^{-1}$)	-	2.421	2.694	2.643

*Due to the lack of reliable heat conductivity data for $TbFe_2$ and the interface conductivity we treated it as a free parameter in our modeling. For a value of 5 $Wm^{-1}K^{-1}$ we observed a good fit to our data. This value is approximately half of what is reported for Terfenol-D ($Tb_{0.3}Dy_{0.7}Fe_{1.92}$)[3]

3) Complex index of refraction of $TbFe_2$ as determined from ellipsometry measurements

An important property in the interpretation of our measurements is the light penetration depth α of the 800nm optical pump and probe pulses employed in our MOKE and UXRD measurements. This parameter is used to estimate the spatial dependence of the light intensity $I(z)$ in a Lambert-Beer law according to: $I(z) = I_0 e^{-\frac{z}{\alpha}}$. The penetration depth was estimated from the complex refractive index $\widetilde{N} = n + i\kappa$ of the material using $\alpha = \frac{\lambda}{4\pi\kappa}$. To that end we determined $\widetilde{N}$ by ellipsometry measurements on the uncapped sample by using a commercial setup (SENTEC) that supplies photons in the energy range from 0.48 eV (2600nm) to 5.4 eV (230nm). In the following analysis we have neglected any influence from the 2nm Ti capping as it is much smaller than the employed wavelength.

In this experiment one observes the different reflection amplitudes r_p and r_s for p- and s- polarized light. From the observed ratio $\frac{r_p}{r_s} = \psi e^{i\Delta}$ one extracts the amplitude factor ψ and the relative phase difference Δ. The software packet SpectraRay/3 was used to fit these two observables using a model of multiple Lorentz-oscillators of different strengths, damping and resonance frequencies.

The resulting dielectric function $\varepsilon(\omega)$ from the superposition of the different Lorentz-Oscillator models is then translated to the complex refractive index via the relation $\widetilde{N} = \sqrt{\varepsilon(\omega)}$, which neglects any magnetic contributions to the optical properties. The resulting real and imaginary part of the refractive index of $TbFe_2$ are displayed in Fig S2a) and S2b), respectively. From this we calculate the optical penetration depth α at normal incidence as well as for the AOI used in the x-Ray diffraction experiment (Fig S2c)). The predicted reflection coefficient of 0.43 is larger than the ratio of 0.34 that between the incident and reflected power that we observe in the UXRD experiments.

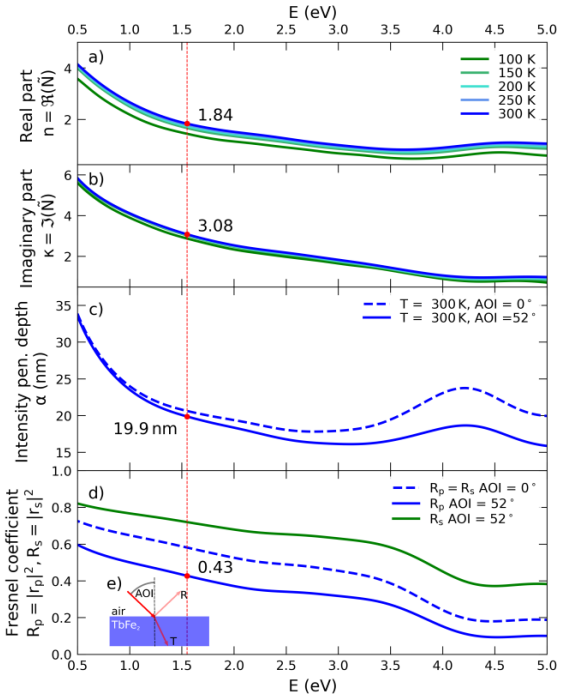

Figure S2: a) and b) show the real and imaginary part of the reflective index of the uncapped $TbFe_2$ layer respectively. The resulting optical penetration depth at 300K is shown in c) for normal incidence and 52° angle of incidence of 52°, which corresponds to the set AOI of the UXRD experiments. The resulting reflection coefficient derived from the Fresnel Equations is depicted in d). Inset e) schematically depicts the sample geometry of the ellipsometry setup. The red dashed line indicates the photon energy of the pump photon energy and the probe photon energy in the MOKE and UXRD setup, where the points mark the values used for the analysis in the main text.

4) Comparison of the spatiotemporal strain simulation of the capped and uncapped structure

In Figure 3a) of the main text we show the spatiotemporal strain profile for the laser-excited Terfenol sample with SiO_2 capping. For completeness we present here a comparison of the simulation for the uncapped and capped Terfenol samples in Fig. S3 and S4 respectively. There one can directly see origin of the asymmetry of the strain pulse in the SiO_2 capped case: The expansive stress that is generated by the laser excitation in the $TbFe_2$ layer creates a coherent strain wave packet that is partially transmitted as compressive strain pulse into the transparent capping layer, whereas it is completely reflected at the $TbFe_2$-air interface for the uncapped sample.

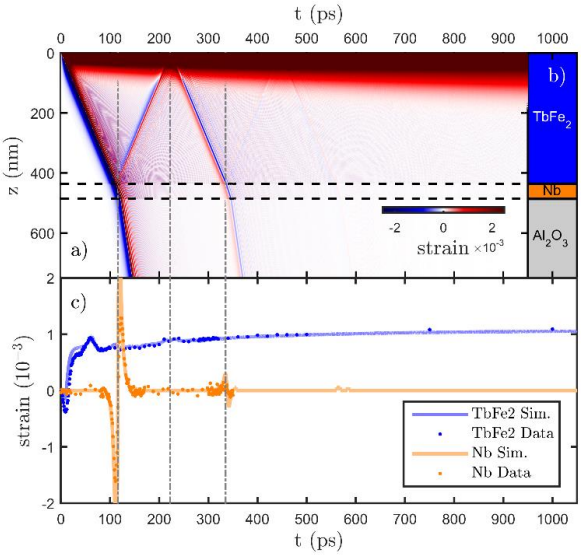

Fig S3: a) Spatio-temporal strain profile from the udkm1Dsim toolbox, where horizontal dashed lines indicate the sample structure b). The simulated and measured UXRD signals are compared in c) as solid lines and points respectively.

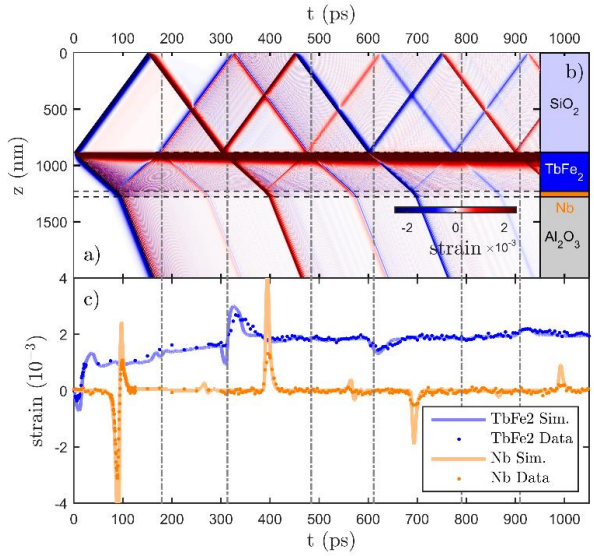

Fig S4: Same as Fig. S3 but showing the result for the SiO_2 capped sample. The presence of the SiO_2 capping leads to multiple partial strain pulse reflections at the acoustically mismatched SiO_2/$TbFe_2$ interface.

5) References

1. Schick, D. *et al.* Ultrafast lattice response of photoexcited thin films studied by X-ray diffraction. *Struct. Dyn.* **1,** (2014).
2. Schick, D. *et al.* udkm1Dsim - A Simulation Toolkit for 1D Ultrafast Dynamics in Condensed Matter. *Comput. Phys. Commun.* **185,** 651–660 (2014).
3. MatWeb, material property data for Terfenol.
4. Buschow, K. H. J. Intermetallic compounds of rare-earth and 3d transition metals. *Reports Prog. Phys.* **40,** 1179–1256 (1977).
5. Mougin, A. *et al.* Strain in single-crystal RFe2 (110) thin films (R = Y , Sm, Gd, Tb, Dy0.7Tb0.3, Dy, Er, Lu). *Phys. Rev. B* **59,** 5950–5959 (1999).
6. Straumanis, M. E. & Zyszczynski, S. Lattice parameters, thermal expansion coefficients and densities of Nb, and of solid solutions Nb–O and Nb–N–O and their defect structure. *J. Appl. Crystallogr.* **3,** 1–6 (1970).
7. Dobrovinskaya, E. R., Lytvynov, L. A. & Pishchik, V. *Sapphire. Material, Manufacturing, Applications*. (Springer, 2009).
8. Simmons, G. & Wang, H. *Single crystal elastic constants and calculated aggregate properties: a handbook*. (M.I.T. Press, 1971).
9. Clark, A. E., Belson, H. S. & Strakna, R. E. Elastic properties of rare-earth-iron compounds. *J. Appl. Phys.* **44,** 2913–2914 (1973).
10. Carroll, K. J. Elastic Constants of Niobium from 4.2° to 300°K. *J. Appl. Phys.* **36,** 3689–3690 (1965).
11. Wong, C. P. & Bollampally, R. S. Thermal conductivity, elastic modulus, and coefficient of thermal expansion of polymer composites filled with ceramic particles for electronic packaging. *J. Appl. Polym. Sci.* **74,** 3396–3403 (1999).
12. Zeuschner, S. P. Magnetostriction and timeresolved X-ray diffraction on TbFe2. (Universität Potsdam, 2017).
13. von Reppert, A. Ultrafast Magnetostriction in Dysprosium studied by Femtosecond X-Ray diffraction. (University of Potsdam, 2015).
14. Lucht, M. *et al.* Precise measurement of the lattice parameters of Sapphire in the temperature range 4.5 K -250 K using the Moessbauer wavelength standard. *J. Appl. Cryst* **36,** 1075–1081 (2003).
15. Lord, R. C. & Morrow, J. C. Calculation of the Heat Capacity of α Quartz and Vitreous Silica from Spectroscopic Data. *J. Chem. Phys.* **26,** 230–232 (1957).
16. Germano, D. J., Butera, R. A. & Gschneidner, K. A. Heat capacity and thermodynamic functions of theRFe2 compounds (R =Gd, Tb, Dy, Ho, Er, Tm, Lu) over the temperature region 8 to 300 K. *J. Solid State Chem.* **37,** 383–389 (1981).
17. Haynes, W. M. *CRC Handbook of Chemistry and Physics*. (Taylor & Francis, 2012).
18. Ginnings, D. C. & Furukawa, G. T. Heat Capacity Standards for the Range 14 to 1200 K. *J. Am. Ceram. Soc.* **43,** (1953).
19. Clark, A. E. *Alloys and Intermetallics*. *Handbook on the Physics and Chemistry of Rare Earths* **2,** (Elsevier, 1979).

20. Ho, C. Y., Powell, R. W. & Liley, P. E. Thermal Conductivity of the Elements. *J. Phys. Chem. Ref. Data* **1,** 279–421 (1972).

21. Parpiiev, T. Ultrafast magneto-acoustics in magnetostrictive materials. (Le Mans Université, 2018).

Article IV

Ultrafast laser generated strain in granular and continuous FePt thin films

Alexander von Reppert, Lisa Willig, Jan-Etienne Pudell, Matthias Rössle, Wolfram Leitenberger, Marc Herzog, Fabian Ganss, Olav Hellwig, and Matias Bargheer

Applied Physics Letters 113, 123101 (2018)

We employ ultrafast x-ray diffraction to compare the lattice dynamics of laser-excited continuous and granular FePt films on MgO (100) substrates. Contrary to recent results on free-standing granular films, we observe in both cases a pronounced and long-lasting out-of-plane expansion. We attribute this discrepancy to the in-plane expansion, which is suppressed by symmetry in continuous films. Granular films on substrates are less constrained and already show a reduced out-of-plane contraction. Via the Poisson effect, out-of-plane contractions drive in-plane expansion and vice versa. Consistently, the granular film exhibits a short-lived out-of-plane contraction driven by ultrafast demagnetization which is followed by a reduced and delayed expansion. From the acoustic reflections of the observed strain waves at the film-substrate interface, we extract a 13% reduction of the elastic constants in thin 10 nm FePt films compared to bulk-like samples.

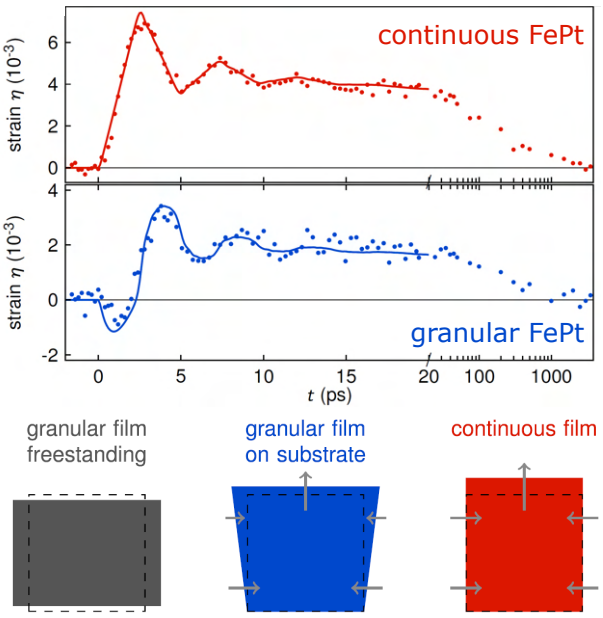

Applied Physics Letters

Ultrafast laser generated strain in granular and continuous FePt thin films

Cite as: Appl. Phys. Lett. **113**, 123101 (2018); https://doi.org/10.1063/1.5050234
Submitted: 28 July 2018 . Accepted: 02 September 2018 . Published Online: 18 September 2018

A. von Reppert, L. Willig, J.-E. Pudell, M. Rössle, W. Leitenberger, M. Herzog, F. Ganss, O. Hellwig, and M. Bargheer

AIP Publishing

APPLIED PHYSICS LETTERS **113**, 123101 (2018)

Ultrafast laser generated strain in granular and continuous FePt thin films

A. von Reppert,[1] L. Willig,[1] J.-E. Pudell,[1] M. Rössle,[2] W. Leitenberger,[1] M. Herzog,[1] F. Ganss,[3] O. Hellwig,[3,4] and M. Bargheer[1,2,a)]
[1]*Institut für Physik und Astronomie, Universität Potsdam, Karl-Liebknecht-Str. 24-25, 14476 Potsdam, Germany*
[2]*Helmholtz-Zentrum Berlin für Materialien und Energie GmbH, Wilhelm-Conrad-Röntgen Campus, BESSY II, Albert-Einstein-Str. 15, 12489 Berlin, Germany*
[3]*Institut für Physik, Technische Universität Chemnitz, Reichenhainer Str. 70, 09126 Chemnitz, Germany*
[4]*Institut für Ionenstrahlphysik und Materialforschung, Helmholtz-Zentrum Dresden-Rossendorf, Bautzner Landstrasse 400, 01328 Dresden, Germany*

(Received 28 July 2018; accepted 2 September 2018; published online 18 September 2018)

We employ ultrafast X-ray diffraction to compare the lattice dynamics of laser-excited continuous and granular FePt films on MgO (100) substrates. Contrary to recent results on free-standing granular films, we observe in both cases a pronounced and long-lasting out-of-plane expansion. We attribute this discrepancy to the in-plane expansion, which is suppressed by symmetry in continuous films. Granular films on substrates are less constrained and already show a reduced out-of-plane contraction. Via the Poisson effect, out-of-plane contractions drive in-plane expansion and vice versa. Consistently, the granular film exhibits a short-lived out-of-plane contraction driven by ultrafast demagnetization which is followed by a reduced and delayed expansion. From the acoustic reflections of the observed strain waves at the film-substrate interface, we extract a 13% reduction of the elastic constants in thin 10 nm FePt films compared to bulk-like samples. https://doi.org/10.1063/1.5050234

The $L1_0$ ordered phase of FePt is a prominent example of a highly anisotropic material with a simple unit cell, which can be easily stabilized in nanoscale thin films.[1,2] Its technological relevance originates from the large uniaxial magnetic anisotropy (K_u),[2,3] which makes FePt the material of choice for heat-assisted magnetic recording (HAMR) schemes.[4,5] Established bulk characterization methods for thermophysical properties, i.e., elastic constants (C_{ij}), heat capacity (C_p), thermal conductivity (κ), and thermal expansion coefficients (α), are mostly inapplicable in such nanoscale thin film materials. The envisioned applications nevertheless substantiate the need for a thorough characterization of all involved properties.

Ideally, the inaccessible properties of the material could be calculated on an *ab-initio* basis. The so far simulated properties relevant to the HAMR process range from the Curie temperature variation in granular films[6,7] over *ab-initio* models for mode specific electron phonon coupling constants[8] up to full multiscale models for the magnetization dynamics.[9] Apart from recent mode specific calculations of the phonon Grüneisen constants[10] (Γ) and extensive work on the elastic constants,[11–13] predictions for C_p, κ, and α are lacking, which hints at the complexity of full *ab-initio* theoretical approaches.

Experimental methods tailored to be applicable in the thin-film regime have been developed alongside the improved thin film growth techniques. Specifically, for FePt, time-domain thermoreflectance in combination with 1D thermal transport models has been used to extract the heat conductivity and thermal boundary resistances.[14,15] Even an estimate for the diverging magnetic specific heat has been obtained.[16] The out-of-plane elastic constant C_{33} has been determined by picosecond ultrasonics from the coherent phonon propagation monitored by an all-optical pump-probe method[17] and electromagnetic-acoustic resonance.[18] Diffraction studies on $L1_0$ FePt compounds report a strong anisotropy in the thermal expansion upon equilibrium heating where the dominant in-plane expansion heralds anisotropic stresses.[19,20]

A recent time-resolved investigation has combined the direct access to the structural dynamics of FePt nanograins via ultrafast electron diffraction (UED) with direct measurements of the Fe magnetization by resonant soft X-ray diffraction.[10] This study connected the obtained experimental interpretation with the insight of *ab-initio* theory to study the complex coupled dynamics initiated by the simultaneous action of electronic, magnetic, and phononic stress contributions.[10] The ultrafast demagnetization and potentially anisotropic electron and phonon stresses were found to drive a pronounced out-of-plane contraction that decays to zero within 20 ps. For this experiment, the FePt nanograins embedded in a carbon matrix were transferred from the substrate to an ultrathin metal grid suitable for UED and the out-of-plane lattice motion was derived from asymmetric diffraction peaks. Ultrafast X-ray diffraction (UXRD) in the symmetric Bragg reflection geometry is an established method for measurements of the lattice expansion of thin films and heterostructures that are supported by a substrate.[21,22] A synchrotron-based UXRD study[23] on continuous FePt films has reported an out-of-plane expansion upon photo-excitation; however, the time resolution was insufficient to observe the acoustic vibrations.[10]

Here, we present laser-based UXRD experiments on FePt in the $L1_0$ phase on MgO substrates with a time resolution of approximately 200 fs. We compare the lattice

a)bargheer@uni-potsdam.de

response of a continuous crystalline FePt thin film to the nano-granular FePt samples in a carbon matrix relevant for magnetic recording. Both samples are investigated as-grown onto the MgO (100) substrates. In contrast to the out-of-plane contraction in free-standing granular FePt films, observed by UED in the transmission geometry on a transmission electron microscopy (TEM) grid,[10] we observe an ultrafast out-of-plane expansion within 2.5 ps limited by the sound velocity. From the observed coherent phonon oscillations period of 4.6 ps and a precise measurement of the film thickness $d = 9.7$ nm by X-ray reflectivity (XRR), we derive an out-of-plane longitudinal acoustic sound velocity of 4.2 nm/ps which is in line with the previously reported elastic constants[17] and with the periods observed by UED.[10] We discuss that the out-of-plane structural dynamics strongly varies for different film morphologies because out-of-plane contractions are coupled to in-plane expansion by the Poisson effect. Our study thus illustrates the capabilities of laboratory-based UXRD for determining the elastic constants in ultrathin samples. From a conceptually simple one-dimensional linear chain (LC) model, we furthermore obtain the different stresses that drive the out-of-plane response in granular and thin-film media.

We compare granular and continuous FePt films that are both in the $L1_0$ phase and grown onto MgO (100) oriented substrates. The continuous film was prepared by magnetron-sputtering Fe and Pt from a composite FePt target onto a substrate preheated to 500 °C. The granular film was sputtered from a FePt-carbon composite target with approximately 30 vol. % C onto a substrate preheated to 650 °C. The c-axis and magnetization are oriented out-of-plane. XRR was carried out to characterize the film thicknesses at the KMC3-XPP endstation[24] at the BESSY II synchrotron radiation facility. Using programs from the reflpak suite,[25] the XRR data in Figs. 1(a) and 1(c) were analyzed and fitted by the resulting electron density depicted in Figs. 1(e) and 1(f). The insets (b) and (d) depict the inferred sample structures. The Kiessig fringes of the granular film decay quickly, confirming the increased surface roughness known from cross sectional TEM images of comparable samples.[2,26]

Scanning electron microscopy (SEM) images of similarly prepared samples (not shown) display that the granular film consists of segregated FePt-nanograins with a size distribution centered at approximately 10 nm embedded in amorphous carbon that magnetically decouples the grains. This is confirmed by the magnetic hysteresis measurements shown in Fig. 1(g) carried out using a commercial SQUID-vibrating sample magnetometer (Quantum Design). The granular sample exhibits a large coercive field of approximately $\mu_0 H = 5$ T, which is desirable for HAMR, whereas the thin film switches at a considerably reduced field of $\mu_0 H = 0.4$ T via domain wall motion, which is inhibited in granular samples.[27] The saturation magnetization for the granular film is reduced by a factor of 0.7 as compared to the continuous film, which agrees with the volume filling factor of FePt in the non-magnetic carbon estimated from SEM images.

Using UXRD, we monitor the Bragg peak shift in the symmetric Bragg diffraction geometry and thus the out-of-plane lattice expansion of the two different crystalline

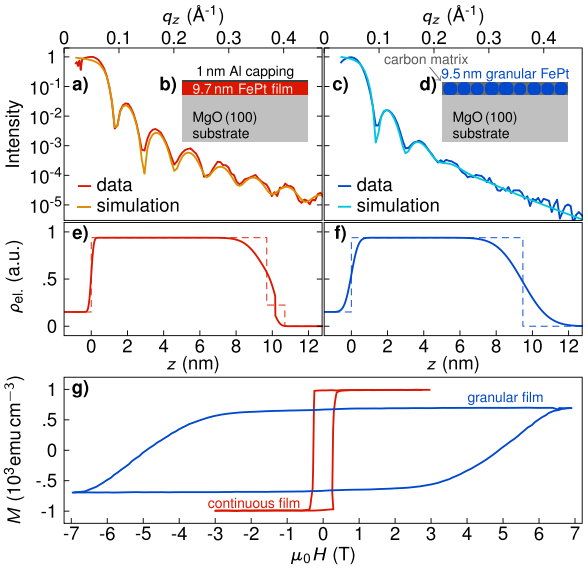

FIG. 1. Sample characterization: X-ray reflectivity data of the continuous (a) and granular (c) film. Orange and cyan colored lines indicate the fit result obtained by assuming the electron densities shown in (e) and (f). Sample structures derived from the electron density without roughness [dashed lines in (e) and (f)] are schematically shown in the insets (b) and (d). The magnetization hysteresis in (g) shows a strongly enhanced coercivity and a reduced saturation magnetization of the granular film compared to the continuous film.

specimens with sub-picosecond time resolution at a laboratory-based diffraction setup.[28] Figure 2(a) displays the Bragg diffraction curve of the unexcited granular and continuous film samples and the inset (b) schematically shows the diffraction and pump-probe geometry. The MgO (002) substrate peak is located at $\theta = 21.45°$, and the (002) FePt-peaks appear approximately at $\theta = 24.6°$. We optically excite the samples with p-polarized pump pulses with a central wavelength of 800 nm and a pulse duration of 100 fs. From the 0.2 mJ pulse energy at a 1 kHz repetition rate with a 1.4 mm × 1.5 mm (FWHM) beam profile incident under $\beta = 45°$ relative to the surface normal, we calculate an incident fluence of 6 mJ cm^{-2}. Using a transfer matrix algorithm for the optical absorption calculation[29] and literature values for the optical properties,[30] we find that a fraction of 25% of the incident energy is absorbed in the continuous FePt material. The hard X-ray probe-pulses with a duration of 200 fs are generated by a laser driven X-ray source, monochromatized, and focused onto the sample using a Montel optic[31] with a convergence of approximately 0.3°. This produces a flux of approximately 10^6 photons/s at the sample in the energy range of Cu-K α_1/α_2 X-ray characteristic line emission. To obtain the time-resolved strain from the diffracted intensity I, the detector images are mapped to the out-of-plane reciprocal space coordinate q_z as described previously.[32] $I(q_z)$ is then fitted by a Gaussian line profile, in order to extract the position of the (002) Bragg peaks $q_{z,\mathrm{fit}}(t)$ for each delay t between pump and probe pulses. Using $q_z(t) = 4\pi/c(t)$, we obtain the evolution of the average FePt lattice plane spacing $c(t)$ in real space. The resulting strain $\varepsilon(t) = (c(t) - c_0)/c_0$, using $c_0 = c(t < 0)$, is depicted in Figs. 2(c) and 2(d).

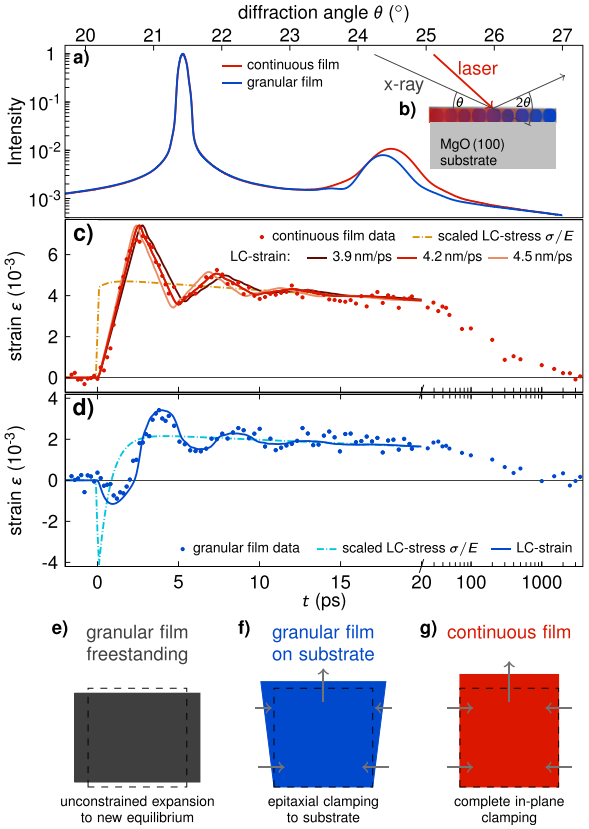

FIG. 2. X-ray diffraction and simulations: (a) Characterization of the samples using X-ray diffraction in the reflection geometry shown in the inset (b). Data points in (c) and (d) show the strain extracted from the shift of the FePt (002) Bragg peaks of the continuous and granular film in reciprocal space. Solid lines in (c) and (d) represent the transient strains that result from the applied time dependent stresses (dashed lines), in a linear chain (LC) model. The lattice dynamics in the first 10 ps of the granular film differ significantly from the strain observed in a continuous film. An initially contractive stress is required to obtain a qualitative agreement between simulation and measurement. (e)–(g) Schematic of clamping mechanisms that we believe to affect the out-of-plane expansion for the three different growth cases: (e) free-standing (f) granular film on a substrate and (g) continuous film on a substrate.

We first discuss the transient strain of the continuous FePt film [Fig. 2(c)]. An out-of-plane lattice expansion of up to 0.7% rises to its maximum within 2.8 ± 0.2 ps. Subsequently, an oscillation with a period of $T = 4.6 \pm 0.2$ ps superimposes the strain relaxation that originates from the flow of thermal energy to the substrate. From the measured T and d, we obtain the longitudinal acoustic sound velocity $v_s = 2d/T = 4.2 \pm 0.2$ nm/ps.[33,34]

We observe a considerable out-of-plane expansion of approximately 0.4% at $t = 20$ ps for the continuous thin film after the coherent strain wave oscillations end due to repeated partial transmission into the substrate. At such large delays, the observed strain ε scales linearly with the quasi-thermal stress σ according to Hooke's law $\sigma = E\varepsilon$. In metal films, the observed strain originates from a stress that is a superposition of the contributions from energy deposition into the electron and lattice system.[33,35–37] In the particular case of magnetically ordered materials, additional stress originating from the excitation of the spin system has been reported.[10,21] Assuming thermal equilibration of these contributing subsystems, the observed strain ε directly indicates the transient temperature rise ΔT via $\varepsilon = \alpha \Delta T$. For such a simplified analysis, we can extract an effective linear thermal expansion coefficient α, which incorporates all contributing stresses, e.g., electron and phonon pressure, magnetostriction, and the coupling of in- and out-of-plane strain by the Poisson effect by a very coarse estimation of the temperature rise. Considering the dominant contribution of the phonons to the specific heat of approximately[16] $C_p = 3.5 \times 10^6$ J m^{-3} K^{-1}, we estimate from the absorbed laser fluence F_a and the film thickness d: $\Delta T = F_a/(dC) \approx 147$ K. This yields an estimate for the effective linear thermal expansion coefficient,[38] which is applicable only on timescales where the electron-spin-phonon system is in a quasi-equilibrium while in-plane strain propagation is still negligible: $\alpha = \varepsilon/\Delta T \approx 2.7 \times 10^{-5}$ K^{-1}. The observed decaying strain for times $t > 20$ ps is attributed to a cooling of the FePt film by phonon heat transport to the insulating substrate, in agreement with previous synchrotron studies.[23] In our coarse approximation, we refer to a quasi-equilibrium, since recent theoretical developments in the modeling of time-resolved experiments that go beyond two or three temperature models indicate that such an equilibration process may take many tens of picoseconds due to mode dependent electron phonon couplings[8,10,37] or potentially weak spin-lattice coupling.[21]

In order to further interpret the measurement on the epitaxial thin film, we simulate the results in a 1-dimensional LC model of coupled masses and springs. The simulations are carried out using the strain calculation module from the udkm1Dsim toolbox simulation package.[39] We calculate the response to a time-dependent expansive stress that is assumed to be homogenous across the FePt thin films motivated by the optical penetration depth[30] for 800 nm light in FePt of approximately 24.2 nm, which is large compared to the 9.7 nm film thickness. The dashed-dotted line in Fig. 2(c) shows the total time-dependent stress that leads to the observed transient strain, with multiple acoustic reflections shown as solid lines. It is rather close to a step function with a rising edge given by the laser pulse duration. A slight additional rise and decay can be attributed to a conversion of electronic to phononic stress and the onset of heat transport to the substrate, respectively. For convenience, we have added the simulated strain as solid lines to Fig. 2(c) assuming different longitudinal acoustic sound velocities v_s from which we can obtain the elastic constant $C_{33} = \rho v_s^2 \approx 267$ GPa using $v_s = 4.2$ nm/ps. We use the density $\rho = 15\,113$ kg/m^3 of FePt calculated from atomic weights and the known unit cell dimensions of the conventional tetragonal unit cell of parameters $c = 3.72$ Å and $a = 3.85$ Å of FePt.[20] The derived C_{33} value lies just at the lower bound of the range of 242 – 371 GPa from theoretical considerations.[11–13] It agrees well with the observed reduction of the elastic constant of FePt specimen from 309 to about 250 GPa, when the thickness is less than 40 nm.[17] The temperature dependence of the elastic constants observed under equilibrium heating[18] supports an even further decrease in the transient bulk modulus resulting from a laser-induced temperature increase. The surprisingly small $v_s = 2.2$ nm/ps reported for the free standing

grains[10] might be due to a missing factor of 2 since for spheres, the expected period $T = d/v_s$ must be calculated using the diameter d of the laser excited particles instead of their radius.

Now, we discuss the dynamics in our nano-granular film. The oscillation period is nearly identical to the continuous film, as expected for the same layer thickness. The in-plane dynamics of the granular film occur with a similar period because the average grain size equals the thickness. Its out-of-plane contraction within the first 2.5 ps [Fig. 2(d)] confirms the ultrafast contractive stress contribution that was reported for the free-standing granular film.[10] The contractive stress component was shown to originate from the release of magnetostriction due to the transient demagnetization of the FePt.[10] The timescale of the demagnetization varies depending on the experimental conditions but is usually fitted by an exponential decay with time constants smaller than 0.5 ps.[10,26,27] The magnetization recovers within several tens of picoseconds, depending on the excitation fluence.[10,26] For larger time delays ($t > 2.5$ ps), we definitely observe a long-lasting lattice expansion, which has only about half the amplitude of the continuous film. The contractive stress driven by spin-excitations is still operative due to the slow remagnetization, but the phonon-driven heat expansion prevails. As we argue below, the crossover from compressive to tensile strain is due to partial constraints to the in-plane motion of the nanograins. The contraction observed in the free standing film is thus probably stopped as soon as the in-plane grain expansion is inhibited by the epitaxial pinning to the MgO substrate and the surrounding carbon matrix, which is also pinned to the substrate. In the case of the continuous epitaxial film, such in-plane constraints completely inhibit the compressive strain at early delays.

For the epitaxial continuous film, the 1D LC model is an excellent approximation for the first 20 ps, since in-plane motion is prohibited by symmetry. In the nano-granular sample, this symmetry is broken and various anisotropic driving stresses can occur so that a modeling of the three-dimensional response of particles with anisotropic elastic properties embedded in a carbon matrix would be required. The inhomogeneous size distribution with unknown coupling strength to the substrate further challenges *ab-initio* treatment. Here, we analyze the strain response of the FePt granular sample grown on a substrate, because it connects the previous research on free-standing nanograins[10] and epitaxial thin films[23] and since it is the relevant geometry used in HAMR media. For a simplified simulation of the observed out-of-plane strain, we assume the effective out-of-plane stress shown in Fig. 2(d) as a dashed-dotted line, which includes contributions from an in-plane expansion that leads to an out-of-plane contractive stress via Poisson's ratio. We speculate that the crossover from a contractive to an expansive out-of-plane stress within about 1 ps is due to the fact that the in-plane expansion concomitant with the out-of-plane contraction is hindered by epitaxial clamping to the substrate and the carbon matrix. This contribution of the Poisson effect adds to the out-of-plane contraction driven by ultrafast spin disordering.[10]

Figures 2(e)–2(g) schematically show our current understanding of the pronounced differences for free-standing grains vs. continuous epitaxial films of FePt, with nano-granular films on a substrate as an intermediate case. While the nearly free-standing grains, which are more loosely embedded in a carbon matrix on a TEM grid, can contract out-of-plane because they can expand in-plane, the continuous film cannot expand in-plane. This suppresses the contraction out-of-plane and an expansion due to electron and phonon stresses prevails. For the nano-granular film on the substrate, the in-plane expansion is still somewhat suppressed due to the carbon matrix and due to epitaxial strain resulting from the pinning to the substrate.

In conclusion, we have shown that laser-excited FePt in the $L1_0$ phase essentially expands out-of-plane, if the continuous film or the nano-grains are epitaxially attached to a substrate. From the observed strain-wave oscillations, we obtain the out-of-plane sound velocity and thus the elastic constant C_{33}, well in line with the reported decrease for films of few nm thickness.[17] Our experiments showcase the capabilities of table-top UXRD to monitor transient stresses via the resulting coherent strain waves. The subpicosecond time-resolution of the experiments reveal a markedly different response of the granular sample compared to the continuous film. This proves the relevance of different balances of the in-plane stresses for the out-of-plane lattice dynamics. Few previous experimental studies assume that the related Poisson effect enhances the amplitude of ultrafast generated strain in continuous films;[21,38,40] however, an unambiguous general proof for this enhancement is so far missing.

The complexity of the anisotropic nanogranular samples calls for modeling approaches that go beyond harmonic oscillator models[8,16] or the 1D approximation that is frequently applied in laser-excited bulk materials or continuous thin films since the seminal work of Thomson *et al.*[41] We envision that time-resolved studies of various properties of nanoparticles could be cross-fertilized by the development of three-dimensional model calculations since they are often intricately linked to the lattice via changes in their band structure.

We acknowledge the BMBF for the financial support via 05K16IPA and the DFG via BA 2281/8-1 and BA 2281/11-1.

[1]S. Wicht, S. Wee, O. Hellwig, V. Mehta, S. Jain, D. Weller, and B. Rellinghaus, J. Appl. Phys. **119**, 115301 (2016).
[2]O. Mosendz, S. Pisana, J. Reiner, B. Stipe, and D. Weller, J. Appl. Phys. **111**, 07B729 (2012).
[3]D. Weller, A. Moser, L. Folks, M. Best, W. Lee, M. Toney, M. Schwickert, J.-U. Thiele, and M. Doerner, IEEE Trans. Magn. **36**, 10 (2000).
[4]D. Weller, O. Mosendz, G. Parker, S. Pisana, and T. S. Santos, Phys. Status Solidi A **210**, 1245 (2013).
[5]D. Weller, G. Parker, O. Mosendz, A. Lyberatos, D. Mitin, N. Y. Safonova, and M. Albrecht, J. Vac. Sci. Technol., B **34**, 060801 (2016).
[6]O. Hovorka, S. Devos, Q. Coopman, W. J. Fan, C. J. Aas, R. F. L. Evans, X. Chen, G. Ju, and R. W. Chantrell, Appl. Phys. Lett. **101**, 052406 (2012).
[7]S. Pisana, S. Jain, J. Reiner, G. Parker, C. Poon, O. Hellwig, and B. Stipe, Appl. Phys. Lett. **104**, 162407 (2014).
[8]P. Maldonado, K. Carva, M. Flammer, and P. M. Oppeneer, Phys. Rev. B **96**, 174439 (2017).
[9]N. Kazantseva, D. Hinzke, U. Nowak, R. W. Chantrell, U. Atxitia, and O. Chubykalo-Fesenko, Phys. Rev. B **77**, 184428 (2008).
[10]A. H. Reid, X. Shen, P. Maldonado, T. Chase, E. Jal, P. W. Granitzka, K. Carva, R. K. Li, J. Li, L. Wu, T. Vecchione, T. Liu, Z. Chen, D. J. Higley,

N. Hartmann, R. Coffee, J. Wu, G. L. Dakovski, W. F. Schlotter, H. Ohldag, Y. K. Takahashi, V. Mehta, O. Hellwig, A. Fry, Y. Zhu, J. Cao, E. E. Fullerton, J. Stöhr, P. M. Oppeneer, X. J. Wang, and H. A. Dürr, Nat. Commun. **9**, 388 (2018).
[11]J. Kim, Y. Koo, and B.-J. Lee, J. Mater. Res. **21**, 199 (2006).
[12]M. Müller, P. Erhart, and K. Albe, J. Phys.: Condens. Matter **19**, 326220 (2007).
[13]N. Zotov and A. Ludwig, Intermetallics **16**, 113 (2008).
[14]A. Chernyshov, D. Treves, T. Le, F. Zong, A. Ajan, and R. Acharya, J. Appl. Phys. **115**, 17B735 (2014).
[15]A. Giri, S. H. Wee, S. Jain, O. Hellwig, and P. E. Hopkins, Sci. Rep. **6**, 32077 (2016).
[16]J. Kimling, J. Kimling, R. Wilson, B. Hebler, M. Albrecht, and D. G. Cahill, Phys. Rev. B **90**, 224408 (2014).
[17]N. Nakamura, A. Uranishi, M. Wakita, H. Ogi, M. Hirao, and M. Nishiyama, Appl. Phys. Lett. **98**, 101911 (2011).
[18]N. Nakamura, N. Yoshimura, H. Ogi, and M. Hirao, J. Appl. Phys. **114**, 093506 (2013).
[19]R. Nicula, O. Crisan, A. Crisan, I. Mercioniu, M. Stir, and F. Vasiliu, J. Alloys Compd. **622**, 865 (2015).
[20]Y. Tsunoda and H. Kobayashi, J. Magn. Magn. Mater. **272**, 776 (2004).
[21]A. von Reppert, J. Pudell, A. Koc, M. Reinhardt, W. Leitenberger, K. Dumesnil, F. Zamponi, and M. Bargheer, Struct. Dyn. **3**, 054302 (2016).
[22]A. Von Reppert, R. Sarhan, F. Stete, J. Pudell, N. Del Fatti, A. Crut, J. Koetz, F. Liebig, C. Prietzel, and M. Bargheer, J. Phys. Chem. C **120**, 28894 (2016).
[23]D. Xu, C. Sun, D. Brewe, S.-W. Han, P. Ho, J. Chen, S. Heald, X. Zhang, and G. Chow, J. Appl. Phys. **115**, 243907 (2014).
[24]M. Reinhardt and W. Leitenberger, J. Large-Scale Res. Facil. **2**, 89 (2016).
[25]P. A. Kienzle, K. V. O'Donovan, J. F. Ankner, N. Berk, and C. Majkrzak, "NCNR Reflectometry Software," (2006).
[26]J. Mendil, P. Nieves, O. Chubykalo-Fesenko, J. Walowski, T. Santos, S. Pisana, and M. Münzenberg, Sci. Rep. **4**, 3980 (2014).
[27]T. Shima, K. Takanashi, Y. K. Takahashi, and K. Hono, Appl. Phys. Lett. **81**, 1050 (2002).
[28]D. Schick, A. Bojahr, M. Herzog, C. V. K. Schmising, R. Shayduk, W. Leitenberger, P. Gaal, and M. Bargheer, Rev. Sci. Instrum. **83**, 025104 (2012).
[29]L. Le Guyader, A. Kleibert, F. Nolting, L. Joly, P. Derlet, R. Pisarev, A. Kirilyuk, T. Rasing, and A. Kimel, Phys. Rev. B **87**, 054437 (2013).
[30]Z. H. Cen, B. X. Xu, J. F. Hu, J. M. Li, K. M. Cher, Y. T. Toh, K. D. Ye, and J. Zhang, Opt. Express **21**, 9906 (2013).
[31]M. Bargheer, N. Zhavoronkov, R. Bruch, H. Legall, H. Stiel, M. Woerner, and T. Elsaesser, Appl. Phys. B **80**, 715 (2005).
[32]D. Schick, R. Shayduk, A. Bojahr, M. Herzog, C. von Korff Schmising, P. Gaal, and M. Bargheer, J. Appl. Crystallogr. **46**, 1372 (2013).
[33]M. Nicoul, U. Shymanovich, A. Tarasevitch, D. von der Linde, and K. Sokolowski-Tinten, Appl. Phys. Lett. **98**, 191902 (2011).
[34]D. Schick, M. Herzog, A. Bojahr, W. Leitenberger, A. Hertwig, R. Shayduk, and M. Bargheer, Struct. Dyn. **1**, 064501 (2014).
[35]S. Nie, X. Wang, H. Park, R. Clinite, and J. Cao, Phys. Rev. Lett. **96**, 25901 (2006).
[36]K. Sokolowski-Tinten, X. Shen, Q. Zheng, T. Chase, R. Coffee, M. Jerman, R. K. Li, M. Ligges, I. Makasyuk, M. Mo, A. H. Reid, B. Rethfeld, T. Vecchione, S. P. Weathersby, H. A. Dürr, and X. J. Wang, Struct. Dyn. **4**, 054501 (2017).
[37]T. Henighan, M. Trigo, S. Bonetti, P. Granitzka, D. Higley, Z. Chen, M. P. Jiang, R. Kukreja, A. Gray, A. H. Reid, E. Jal, M. C. Hoffmann, M. Kozina, S. Song, M. Chollet, D. Zhu, P. F. Xu, J. Jeong, K. Carva, P. Maldonado, P. M. Oppeneer, M. G. Samant, S. S. P. Parkin, D. A. Reis, and H. A. Dürr, Phys. Rev. B **93**, 220301 (2016).
[38]J. Pudell, A. A. Maznev, M. Herzog, M. Kronseder, C. H. Back, G. Malinowski, A. von Reppert, and M. Bargheer, Nat. Commun. **9**, 3335 (2016).
[39]D. Schick, A. Bojahr, M. Herzog, C. von Korff Schmising, R. Shayduk, and M. Bargheer, Comput. Phys. Commun. **185**, 651 (2014).
[40]H. J. Lee, J. Workman, J. S. Wark, R. D. Averitt, A. J. Taylor, J. Roberts, Q. McCulloch, D. E. Hof, N. Hur, S.-W. Cheong, and D. J. Funk, Phys. Rev. B **77**, 132301 (2008).
[41]C. Thomsen, H. T. Grahn, H. J. Maris, and J. Tauc, Phys. Rev. B **34**, 4129 (1986).

Applied Physics Letters ERRATUM scitation.org/journal/apl

Erratum: "Ultrafast laser generated strain in granular and continuous FePt thin films" [Appl. Phys. Lett. 113, 123101 (2018)]

Cite as: Appl. Phys. Lett. **117**, 049902 (2020); doi: 10.1063/5.0022340
Submitted: 21 July 2020 · Accepted: 22 July 2020 ·
Published Online: 30 July 2020

A. von Reppert,[1] L. Willig,[1] J.-E. Pudell,[1] M. Rössle,[2] W. Leitenberger,[1] M. Herzog,[1] F. Ganss,[3] O. Hellwig,[3,4] and M. Bargheer[1,2,a)]

AFFILIATIONS

[1]Institut für Physik und Astronomie, Universität Potsdam, Karl-Liebknecht-Str. 24-25, 14476 Potsdam, Germany
[2]Helmholtz-Zentrum Berlin für Materialien und Energie GmbH, Wilhelm-Conrad-Röntgen Campus, BESSY II, Albert-Einstein-Str. 15, 12489 Berlin, Germany
[3]Institut für Physik, Technische Universität Chemnitz, Reichenhainer Str. 70, 09126 Chemnitz, Germany
[4]Institut für Ionenstrahlphysik und Materialforschung, Helmholtz-Zentrum Dresden-Rossendorf, Bautzner Landstrasse 400, 01328 Dresden, Germany

[a)]bargheer@uni-potsdam.de

https://doi.org/10.1063/5.0022340

In the original article,[1] a simple miscalculation led to an error in the estimated laser induced temperature change, $\Delta T = \frac{F_a}{dC}$, which should yield $\Delta T = 442\,\mathrm{K}$ instead of $\Delta T = 147\,\mathrm{K}$ stated in this paper. All values entered in this formula, i.e., the incident Fluence of $F = 6\,\mathrm{mJ/cm^2}$, the absorbed energy fraction in FePt of approximately 25%, the film thickness $d = 9.7\,\mathrm{nm}$, and the estimated heat capacity of $C = 3.5 \times 10^6\ \frac{\mathrm{J}}{\mathrm{m^3}}$, are stated correctly in the text. The correct estimation leaves the main findings of the manuscript unchanged but the estimated thermal expansion coefficient on picosecond timescales α has to be corrected by the same factor 3 to yield $\alpha = \frac{\varepsilon}{\Delta T} = \frac{4\times10^{-3}}{442\,\mathrm{K}} \approx 9.05 \times 10^{-6}\ \frac{1}{\mathrm{K}}$.

REFERENCE

[1]A. von Reppert, L. Willig, J.-E. Pudell, M. Rössle, W. Leitenberger, M. Herzog, F. Ganss, O. Hellwig, and M. Bargheer, Appl. Phys. Lett. **113**, 123101 (2018).

Article V

Finite-size effects in ultrafast remagnetization dynamics of FePt

Lisa Willig, Alexander von Reppert, Marwan Deb, Fabian Ganss, Olav Hellwig, and Matias Bargheer

Physical Review B 100, 224408 (2019)

We investigate the ultrafast magnetization dynamics of FePt in the L10 phase after an optical heating pulse, as used in heat-assisted magnetic recording. We compare continuous and nano-granular thin films and emphasize the impact of the finite size on the remagnetization dynamics. The remagnetization speeds up significantly with increasing external magnetic field only for the continuous film, where domain-wall motion governs the dynamics. The ultrafast remagnetization dynamics in the continuous film are only dominated by heat transport in the regime of high magnetic fields, whereas the intrinsic timescale required for cooling is prevalent in the granular film for all magnetic field strengths. These findings highlight the necessary conditions for studying the intrinsic heat transport properties in magnetic materials.

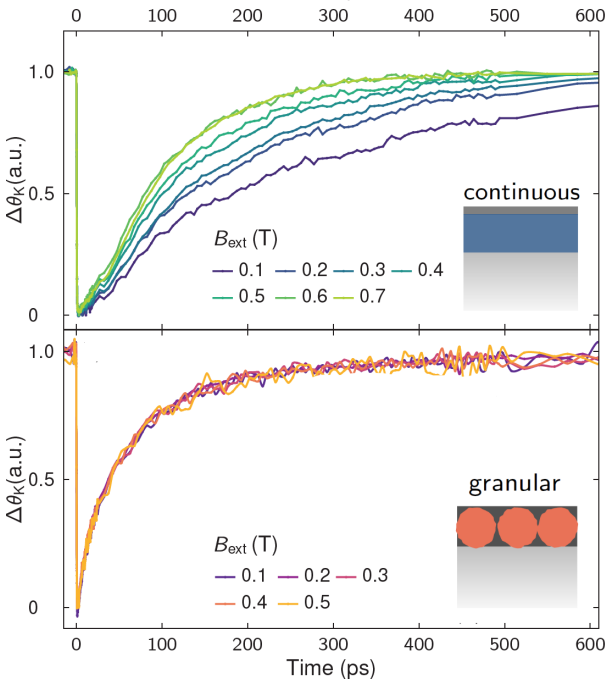

PHYSICAL REVIEW B **100**, 224408 (2019)

Finite-size effects in ultrafast remagnetization dynamics of FePt

L. Willig,[1,2] A. von Reppert,[1] M. Deb,[1] F. Ganss,[3] O. Hellwig,[3,4] and M. Bargheer[1,2,*]

[1]*Institut für Physik & Astronomie, Universität Potsdam, Karl-Liebknecht-Str. 24-25, 14476 Potsdam, Germany*

[2]*Helmholtz Zentrum Berlin, Albert-Einstein-Str. 15, 12489 Berlin, Germany*

[3]*Institut für Physik, Technische Universität Chemnitz, Reichenhainer Str. 70, 09126 Chemnitz, Germany*

[4]*Institut für Ionenstrahlphysik und Materialforschung, Helmholtz-Zentrum Dresden-Rossendorf, Bautzner Landstrasse 400, 01328 Dresden, Germany*

(Received 16 September 2019; revised manuscript received 20 November 2019; published 9 December 2019)

We investigate the ultrafast magnetization dynamics of FePt in the $L1_0$ phase after an optical heating pulse, as used in heat-assisted magnetic recording. We compare continuous and nano-granular thin films and emphasize the impact of the finite size on the remagnetization dynamics. The remagnetization speeds up significantly with increasing external magnetic field only for the continuous film, where domain-wall motion governs the dynamics. The ultrafast remagnetization dynamics in the continuous film are only dominated by heat transport in the regime of high magnetic fields, whereas the timescale required for cooling is prevalent in the granular film for all magnetic field strengths. These findings highlight the necessary conditions for studying the intrinsic heat transport properties in magnetic materials.

DOI: 10.1103/PhysRevB.100.224408

I. INTRODUCTION

The fascinating field of ultrafast magnetization dynamics has developed rapidly from the first demonstration of femtosecond demagnetization [1] toward all-optical switching [2,3], magnetization reversal by ultrashort electron pulses [4], and heat-assisted magnetic recording (HAMR) [5–7]. Future light-based data-recording applications motivate an understanding of the fundamental light-matter-interactions in magnetic materials with nanoscale bit dimensions, which are a key to satisfy the increasing demand for high-density information storage technology.

Information storage devices using the HAMR scheme have demonstrated that data densities beyond $1.4\,\mathrm{Tb/in^2}$ are feasible since long-term data stability of nanoscopic bits can be achieved by using materials with large perpendicular anisotropy [8,9]. FePt in the highly ordered $L1_0$ phase is a promising material since it combines a large uniaxial magnetocrystalline anisotropy $K_u \cong 7 \times 10^6\,\mathrm{J/m^3}$, with a relatively low Curie temperature ($T_C \leqslant 750\,\mathrm{K}$) and the possibility to grow nanograins with diameters down to 3 nm by commercially viable sputtering techniques [9].

Besides nanoscopic bit volumes for high information density, it is of the utmost importance to write and read information at the fastest possible speed and with the highest efficiency. This has triggered many research projects studying the ultrafast magnetization response of thin films to rapid heating via pulses of optical photons, photoinduced hot electrons, or few-picosecond-long electrical currents [1,10–12]. Much of the fundamental research has focused on the timescales and mechanisms of the spin-angular momentum transfer during the demagnetization process [13–15]. The subsequent field-assisted remagnetization has received less experimental attention despite its equal importance for future working devices [16].

Magnetization switching in continuous thin films under thermal equilibrium requires the nucleation, propagation, and, finally, coalescence of reversed magnetic domains. The substantial laser heating used in the HAMR-scheme adds the need for understanding nanoscale thermal transport and potential changes of material properties such as the magnetic anisotropy that occurs upon heating close to and above T_C, as in fascinating all-optical switching experiments, which report toggle switching of the magnetization in the absence of an external field [10].

Current modeling approaches for the remagnetization dynamics [11,17–19] often employ a three-temperature model for the equilibration of electron-, phonon-, and spin-temperatures where the local spin temperature defines a stochastic magnetic field that enters in an atomistic Landau-Lifshitz-Gilbert (LLG) equation. Extending the atomistic LLG model to micromagnetic simulations of the macrospin evolution using the Landau Lifshitz-Bloch equation computes the magnetization dynamics on the relevant picosecond to nanosecond timescale even for macroscopic specimens [11,18]. The incorporation of temperature-dependent material parameters [19,20], quantized spin-states [18], and the proper quantum-thermodynamics noise-distribution function [21] further improve the comparison to experiments. However, spatial confinement effects and interfaces that alter the domain propagation and the thermal transport are often not implemented in the modeling.

Here we present an experimental comparison of the magnetization dynamics of equally thin continuous and nanogranular FePt after medium- to high-fluence femtosecond laser excitation. The observed remagnetization process speeds up

*bargheer@uni-potsdam.de;
http://www.udkm.physik.uni-potsdam.de.

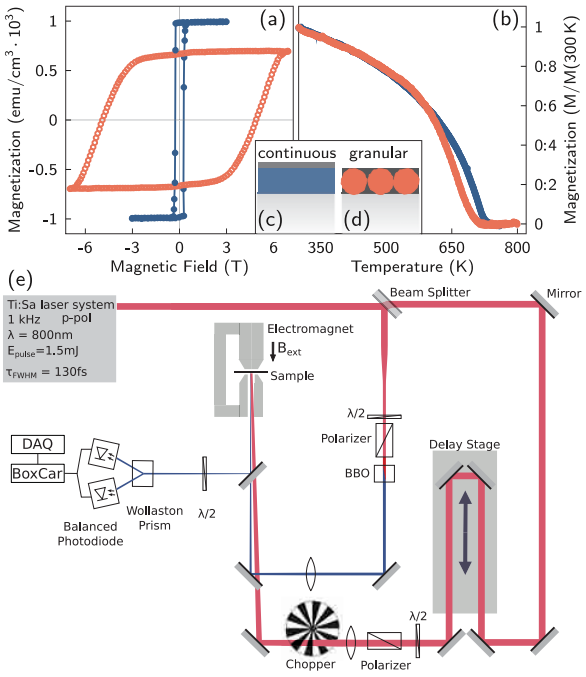

FIG. 1. Static magnetic properties of the FePt samples and sketch of the TR-MOKE setup. (a) Magnetization hysteresis loops and (b) temperature dependence of the magnetization of the granular (open symbols) and continuous (plain symbols) samples. For (b) a stabilizing field of 65 mT was applied for the continuous film, while the granular film was measured in remanence. The magnetic field in (a) and (b) was applied perpendicular to the plane of the samples. Sketch of (c) the continuous and (d) the granular FePt samples. (e) Sketch of the TR-MOKE setup.

by a factor of three with increasing external field for the continuous film. This effect is significantly reduced for the nanogranular FePt and for medium fluences the timescale of remagnetization is independent of the external field. We argue that domain-wall propagation is irrelevant in the grains which are magnetically decoupled by the surrounding amorphous carbon matrix. In the continuous film, the remagnetization rate saturates for high external fields of about 0.7 T and it approaches the timescale observed in the granular film, where the remagnetization speed is limited by the heat dissipation rate. We discuss the influence of the carbon matrix, which rapidly absorbs about 30% of the deposited energy and partially stores it for about 1 ns.

The investigated continuous and granular FePt films are grown in the ordered $L1_0$ phase onto MgO (100)-oriented substrates, which aligns the easy magnetic axis out of plane. The interpretation of the magnetization dynamics is facilitated by the fact that spin transport out of the thin films can be excluded. A more detailed description of the growth conditions and the structural properties of the samples can be found in Ref. [22]. In particular, we mention that the granular film consists of segregated FePt nanograins embedded in amorphous carbon with a size distribution of FePt particles centered at approximately 8 ± 2 nm [see Fig. 1(d)]. The continuous film of FePt is capped by a 1-nm Al layer, which is oxidized to Al_2O_3 [see Fig. 1(c)]. The static magnetic properties of the samples were characterized using a superconducting quantum interference device—vibrating sample magnetometer under an external magnetic field (B_{ext}) applied normal to the sample plane. The measured hysteresis loops of the continuous and granular films are shown in Fig. 1(a). Their square shape shows that the magnetic easy axis is oriented perpendicular to the plane of the films. The coercive field of the granular film is around 5 T, which is very large compared to the coercive field of the continuous film of approximately 0.4 T. This is due to the different magnetization reversal mechanisms. Domain-wall nucleation and propagation governs the continuous film, whereas the magnetization dynamics in the nanoparticles are dominated by quasicoherent magnetization reversal [23]. In addition, we observed a reduction of the saturation magnetization (M_S) by 30% in the granular film, which can be related to the volume occupied by the nonmagnetic carbon matrix in that film together with a small contribution related to the well-known effect of finite size [24,25] on M_S. The temperature dependence of the saturation magnetization was also measured in a wide range of temperatures between 300 and 850 K [see Fig. 1(b)]. The laser-induced ultrafast magnetization dynamics was investigated using the time-resolved magneto-optical Kerr effect (TR-MOKE) setup sketched in Fig. 1 (e). The pump and probe pulses were generated from an amplified Ti:Sapphire laser system delivering 130-fs pulses centered at 800 nm at the repetition rate of 1 kHz. The pump beam is kept at the fundamental of the amplifier at 800 nm and excites the sample under a small angle from the surface normal to the sample ($\cong 2^\circ$), while the probe beam is frequency doubled to 400 nm with a nonlinear beta-barium-borate crystal and incident onto the sample at almost perpendicular incidence ($\cong 1^\circ$). A chopper reduces the repetition rate of the pump pulses to 500 Hz, enabling pulse-to-pulse comparison of the pumped and unexcited states of the sample at the full 1-kHz repetition rate. Both light pulses are linearly polarized and focused through one of the pole shoes of an electromagnet onto the sample on a spot of 1000 μm for the pump and 300 μm for the probe. The reflected probe pulses allow measuring the differential change of the polar Kerr rotation ($\Delta\theta_K$) using a polarization bridge consisting of a $\lambda/2$ wave plate, a Wollaston prism, and a balanced photodiode. The detected signal is analyzed via a Boxcar integrator and a data acquisition (DAQ) card. The B_{ext} of the electromagnet is applied perpendicular to the surface of the sample.

II. RESULTS AND DISCUSSION

Figure 2 shows the TR-MOKE measured for the continuous [Fig. 2(a)] and the granular [Fig. 2(b)] samples as a function of B_{ext} at a pump fluence of $F_{pump} = 5\,mJ/cm^2$. To compare the field effect on the ultrafast magnetization dynamics, $\Delta\theta_K(t)$ signals were scaled by the $\Delta\theta_K$ amplitude corresponding to the maximum demagnetization. In both samples, the pump laser pulses induce a subpicoseond demagnetization process, which is independent of B_{ext}. We focus on the remagnetization process following this ultrafast demagnetization. Interestingly, a clear difference in the effect of B_{ext}

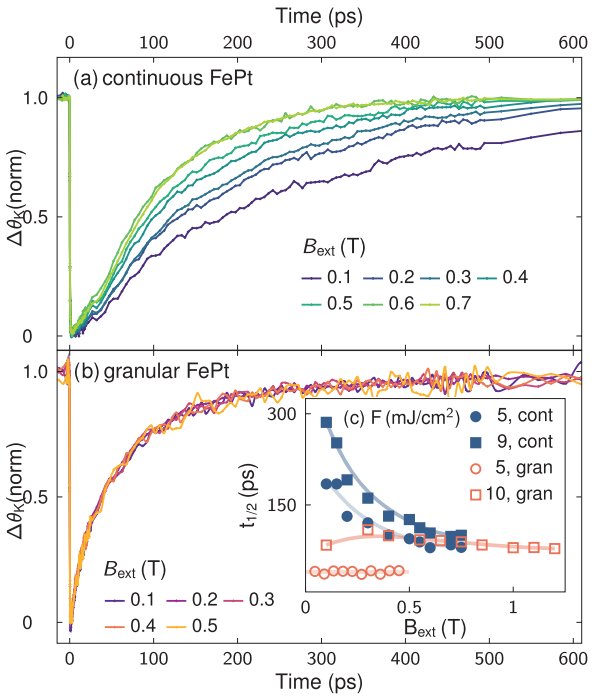

FIG. 2. Magnetic field dependence of laser induced magnetization dynamics. (a), (b) Normalized Kerr rotation $\Delta\theta_K$ measured in the (a) continuous and (b) granular samples at different applied magnetic fields for a fixed pump fluence of 5 mJ/cm^2. The inset (c) shows the magnetic-field dependence of the time $t_{1/2}$ at which half of the demagnetization amplitude has recovered for this pump fluence of 5 mJ/cm^2 and an approximately doubled fluence of 9 and 10 mJ/cm^2 for the continuous and granular sample, respectively. Solid lines are a guide to the eye.

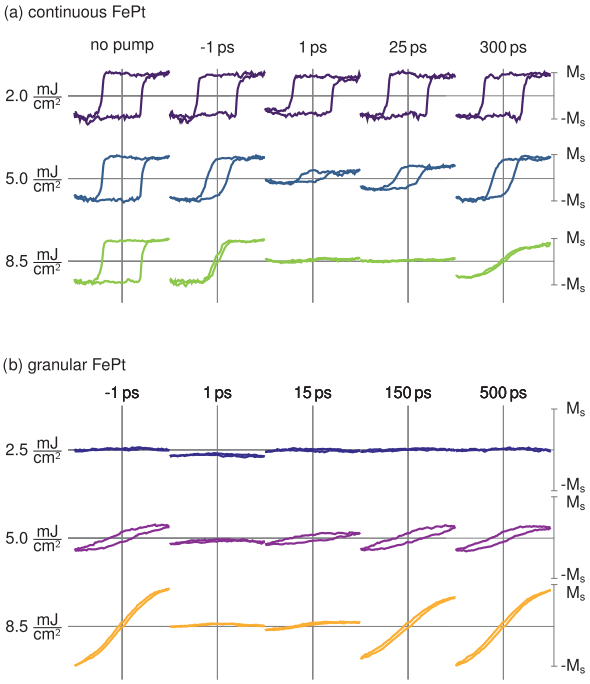

FIG. 3. Hysteresis measured in the continuous (a) and granular (b) samples at different pump fluence and delay between the pump and the probe pulses. In all measurements, the applied B_{ext} ranges between ± 0.75 T. The vertical scaling is fixed for all hysteresis curves and the saturation magnetization is normalized as described in the text (a) to the hysteresis loop without pump and (b) by the signal observed at the highest fluence.

on this remagnetization is observed for the continuous and granular films. Indeed, the remagnetization of the continuous film speeds up significantly when the external field increases from 0.1 to 0.7 T [see Fig 2 (a)], while the remagnetization of the granular one is independent of B_{ext} [see Fig. 2 (b)]. To study this phenomenon in more detail, we measured the TR-MOKE at high pump fluence of $F_{pump} = 10$ mJ/cm^2 and over a wide range of B_{ext} up to 1.2 T. The results of this study are summarized in Fig. 2(c). For both samples and at the two F_{pump} values of 5 mJ/cm^2 and 10 mJ/cm^2, we show the field dependence of the time $t_{1/2}$ corresponding to the time in which half of the demagnetization amplitude has recovered. Interestingly, the effect of B_{ext} on the remagnetization becomes more pronounced in the continuous film at higher fluence and it reaches a saturation around 0.6 and 0.7 T, while the remagnetization of the granular film remains weakly sensitive to B_{ext}, even though the range of applied fields is nearly twice as large. It is straightforward to assign the large field dependence of the continuous film to domain-wall propagation that is well-known to govern the magnetization dynamics in continuous thin films and very sensitive to the amplitude of B_{ext} [26–28]. On the other hand, the domain-wall propagation is irrelevant in nanosized magnets where the remagnetization should be governed by the cooling of the grain. Furthermore, we show that $t_{1/2}$ in the continuous film converges under high B_{ext} to a value of $\cong$100 ps, similar to the one characterizing the granular film at high fluence. Such saturation can be explained by the fact that the remagnetization in the continuous film at high fields is essentially governed by the dissipation of heat which cools the FePt spin system. Indeed, when the external field is large enough, it can keep the entire film essentially in a monodomain state such that domain-wall propagation does not play a role. Figure 2(a) clearly shows that in the continuous film we can interpret the observed magnetization change essentially by cooling of the spin system to the phonons only if a high magnetic field is applied. For lower fields, the remagnetization dynamics are considerably slowed down because, despite the same cooling, the spin system reorders in domains which lead to a reduced macroscopic magnetization which should not be misinterpreted as a hot spin system. Therefore, to study the intrinsic heat-transport properties in magnetic materials, it is necessary to investigate the magnetization dynamics in nanosized structures or under a high external magnetic field.

To quantify the vertical axis of the TR-MOKE traces and to study the ultrafast magnetization dynamics in more detail, we performed hysteresis measurements on both samples using a maximum field of 0.75 T at different pump fluences and delays between the pump and the probe pulses (Fig. 3). The two samples exhibit very different fluence and time-dependent

hysteresis loops. Let us first focus on the continuous film for which the amplitude of the hysteresis was normalized to the one measured without excitation [Fig. 3(a)]. The excitation at a low fluence of $F_{pump} = 2.0\,mJ/cm^2$ shows that the absorbed energy of the pump pulse induces only a very small decrease in the saturation magnetization at short timescales ($t = 1$ ps) without any change of the coercive field. At a medium fluence of $F_{pump} = 5.0\,mJ/cm^2$, the saturation magnetization is reduced significantly, and the coercive field is smaller compared to the one measured without excitation. At high fluence of $F_{pump} = 8.5\,mJ/cm^2$, the hysteresis is fully closed over a significant amount of time of at least 25 ps. For the granular sample, no hysteresis loop is observed at the low fluence of $F_{pump} = 2.5\,mJ/cm^2$ [Fig. 3(b)], since the coercive field [cf. Fig. 1 (a)] is larger than the maximum applied field of 0.75 T. At this low fluence, the transient hysteresis at the time delay of 1 ps shows the same reduction of the magneto-optical signal for the full B_{ext} field range. This vertical shift indicates a reduced transient magnetization. No grains are switched in their magnetization when B_{ext} is reversed and we only access the upper hysteresis branch of the granular film. A clear open hysteresis is observed at negative time delays for a medium fluence of $F_{pump} = 5.0\,mJ/cm^2$ and, by further increasing F_{pump}, its amplitude becomes more and more pronounced and its coercivity is continuously reduced. The increasing hysteresis amplitude with increasing F_{pump} implies a larger fraction of switched particles. This phenomenon is related to the size distribution of the FePt grains, which leads to a large spread in the temperature changes proportional to the inhomogeneous light absorption that varies between 10 and 30% according to finite element simulations of the field enhancement effects in the optical absorption [29]. This inhomogeneous distribution of heat cannot be washed out by electronic heat transport through the insulating carbon matrix, which rapidly cools down the FePt particles but does not transport the heat efficiently from grain to grain. Only the grains which experience a temperature rise close to the Curie temperature T_C participate in the switching. We estimate that more than 90% of the particles are switched at $8.5\,mJ/cm^2$, since for $11\,mJ/cm^2$ the demagnetization only increases marginally. As a good approximation, we thus calibrate the vertical axis in Fig. 3(b) by the amplitude of the hysteresis loop measured at negative delay with high fluence since this value is the saturation magnetization of the granular film. This calibration in Fig. 3(b) emphasizes that more and more particles switch with increasing F_{pump}. We mention that at the time delay of 1 ps and for $F_{pump} = 8.5\,mJ/cm^2$ the hysteresis measured in both—continuous and granular—films are flat and have zero amplitude, which indicates that for both films the temperature exceeds T_C and therefore they are in the paramagnetic phase. On the other hand, we observe that for time delays larger than $\cong$15 ps for the granular film and $\cong$25 ps for the continuous one the hysteresis amplitudes gradually increase (Fig. 3), nicely visualizing the remagnetization dynamics of the films.

To better illustrate the remagnetization dynamics as a function of the pump fluence, TR-MOKE measurements at selected F_{pump} are shown for the continuous and the granular film in Figs. 4(a) and 4(b), respectively. The data were recorded for an applied field of 0.75 T. In both cases, an increasing pump fluence causes the remagnetization to slow

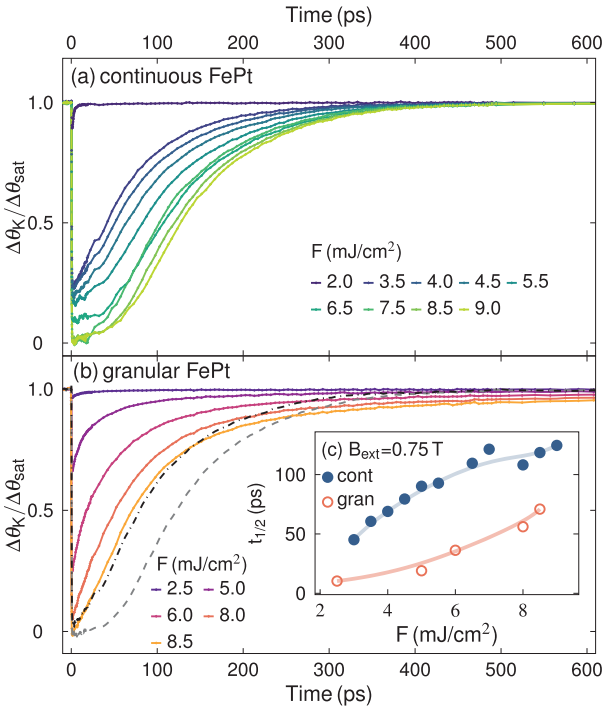

FIG. 4. Pump fluence dependence of laser-induced ultrafast magnetization dynamics. (a), (b) $\Delta\theta_K$ measured in the (a) continuous and (b) granular samples as a function of the pump fluence at high external magnetic field of $B_{ext} = 0.75$ T. The dashed dotted and dashed lines in (b) are the $\Delta\theta_K$ signal induced in continuous film by F_{pump} of 4.5 and $8.5\,mJ/cm^2$, respectively. The inset (c) shows the pump fluence dependence of the time $t_{1/2}$ at which half of the demagnetization amplitude has recovered for 0.75 T with the solid lines as guide to the eye.

down. In addition, with the exception of the lowest fluence measurement of both samples, the granular film recovers significantly faster than the continuous film at equal incident fluence values. To illustrate this feature, Fig. 4(c) shows the pump fluence dependencies of the time $t_{1/2}$ of the continuous and granular film. To directly visualize the faster recovery of the granular film, we plot by a dash-dotted line in Fig. 4(b) the $\Delta\theta_K(t)$ measured for the continuous film at $F_{pump} = 4.5\,mJ/cm^2$. The early dynamics of the granular film are similar to this dash-dotted line when excited at almost twice the fluence. For $8.5\,mJ/cm^2$ excitation of the continuous film the dynamics are much slower (dashed line), suggesting a significantly reduced light absorption in the granular film. However, for both fluences the continuous film approaches the saturation magnetization faster than the granular one beyond 300-ps time delay [see Fig. 4(b)]. The similarity between the initial remagnetization of the continuous film and the granular one when exposed to twice the incident fluence suggests that a difference in the absorption for two films plays a role on the observed behavior. To examine the validity of this hypothesis, we have employed a transfer matrix calculation to estimate the optical absorption profile for the two samples [30]. We have used in our

numerical calculation experimental values for the optical constants of the continuous (n= 3.30 +2.63i) and granular (n= 2.98 +1.78i) FePt films [29,31], which are measured in samples with comparable thickness, size of particles, and carbon matrix. We note that the smaller extinction coefficient of the granular film (i.e., the imaginary part) not only indicates that it absorbs less energy compared to the continuous FePt layer. It also reveals that the absorption in the FePt grains is considerably larger than in the carbon, since otherwise the effective medium should have an increased imaginary part. The continuous FePt layer absorbs approximately $A_{\mathrm{cont}} \cong 33\%$ of the incident fluence F_{pump}, while the granular one absorbs approximately $A_{\mathrm{gran}} \cong 27\%$ in the effective medium that consists of FePt immersed in amorphous carbon. Thus, the absorbed light energy heating the electron system of the granular FePt is only about $A_{\mathrm{gran}}/A_{\mathrm{cont}} = 81\%$ of the continuous film. Instead of scaling the incident fluence values by this relative absorption factor, we describe the second factor of similar magnitude which changes the dynamics in the continuous and granular film.

Heat conduction to the surrounding carbon matrix is a second factor which reduces the energy density in the FePt grains. A four-temperature model was recently proposed to capture this energy transfer for the nanogranular FePt-carbon composite [32]. Due to the comparable specific heat per volume of both materials, we estimate that the fraction of energy that will flow from FePt grains ($c_{\mathrm{V}} = 3.8 \times 10^6\,\mathrm{J/m^3K}$) to the carbon matrix is roughly proportional to its volume fraction of 0.3. Since the Debye temperature of amorphous carbon is considerably above room temperature [33], c_{V} increases from $c_{\mathrm{V}} = 2$ to $3.5 \times 10^6\,\mathrm{J/m^3K}$ between room temperature and 800 K and thus becomes comparable to the FePt value for our strong excitation regime. Hence, combining the two arguments, after heat flow to the carbon matrix, the average FePt unit cell of the granular film contains only a fraction $\cong$70% of the absorbed energy, which is, moreover only $\cong$81% of the absorbed energy in the continuous film. This reconciles that about only half (57%) of the incident fluence is needed in the continuous film to trigger the same magnetization dynamics as in the granular one.

Finally, we address the observation that for long timescales beyond 300 ps, the continuous film always approaches the saturation magnetization faster than the granular film, although it has absorbed twice the energy. The relatively weak van-der-Waals bonds of carbon was shown to exhibit a significantly reduced interface conductance as compared to metal-oxide interfaces with strong binding [34]. Therefore, the carbon matrix should store the heat energy longer than the FePt and it can serve as an additional heat bath, which heats the FePt grains on long timescales up to 1 ns and beyond. The temperature gradient across the interface has then reversed compared to the initial situation, where carbon cools the FePt particles after they have been optically heated to very high temperatures.

III. CONCLUSION

We have compared the laser-induced magnetization dynamics of a continuous and a granular FePt thin film with a similar thickness of about 10 nm under various excitation fluences and external magnetic fields. Our experimental results show that the granular nature of the film influences the observed dynamics in several ways. First of all, the laser energy absorbed by the grains shows a broad distribution, where the average FePt unit cell in the continuous sample absorbs about twice the energy compared to the granular sample. Moreover, the carbon matrix changes the dynamics in three ways: (i) It rapidly takes up approximately 30% of the absorbed energy and thus initially speeds up the remagnetization; (ii) it gives heat back to FePt after cooling and therefore slows down the remagnetization at later times; and (iii) the grain boundaries prevent domain-wall motion and therefore strongly reduce the impact of an external field on the remagnetization dynamics. We believe that this, thorough comparison of the two morphologies of the $L1_0$ phase of FePt, is useful as a reference for the laser-induced magnetization dynamics, especially on the timescale of remagnetization and cooling.

ACKNOWLEDGMENTS

We acknowledge the BMBF for the financial support via 05K16IPA and the DFG via BA 2281/11-1. M.D. thanks the Alexander von Humboldt foundation for financial support. We thank Gabriel Sellge for the static M(T) characterization of the samples.

[1] Beaurepaire, Merle, Daunois, and Bigot, Ultrafast Spin Dynamics in Ferromagnetic Nickel, Phys. Rev. Lett. **76**, 4250 (1996).

[2] C. D. Stanciu, F. Hansteen, A. V. Kimel, A. Kirilyuk, A. Tsukamoto, A. Itoh, and Th. Rasing, All-Optical Magnetic Recording with Circularly Polarized Light, Phys. Rev. Lett. **99**, 047601 (2007).

[3] C-H. Lambert, S. Mangin, B. S. D. Ch. S. Varaprasad, Y. K. Takahashi, M. Hehn, M. Cinchetti, G. Malinowski, K. Hono, Y. Fainman, M. Aeschlimann, and E. E. Fullerton, All-optical control of ferromagnetic thin films and nanostructures, Science (New York) **345**, 1337 (2014).

[4] Y. Yang, R. B. Wilson, J. Gorchon, C.-H. Lambert, S. Salahuddin, and J. Bokor, Ultrafast magnetization reversal by picosecond electrical pulses, Sci. Adv. **3**, e1603117 (2017).

[5] W. A. Challener, C. Peng, A. V. Itagi, D. Karns, W. Peng, Y. Peng, X. Yang, X. Zhu, N. J. Gokemeijer, Y.-T. Hsia, G. Ju, R. E. Rottmayer, M. A. Seigler, and E. C. Gage, Heat-assisted magnetic recording by a near-field transducer with efficient optical energy transfer, Nat. Photonics **3**, 303 (2009).

[6] D. Weller, G. Parker, O. Mosendz, A. Lyberatos, D. Mitin, N. Y. Safonova, and M. Albrecht, FePt heat assisted magnetic recording media, J. Vac. Sci. Technol., B: Nanotechnol. Microelectron.: Mater., Process., Meas., Phenom. **34**, 060801 (2016).

[7] G. Varvaro, A. Maria Testa, D. Peddis, and S. Laureti, in *Ultrahigh-Density Magnetic Recording. Storage Materials and Media Designs*, 1st ed., edited by F. Casoli and G. Varvaro (Pan Stanford Publishing, Singapore, 2016), Chap. 8, pp. 385–456.

[8] K. Hono, Y. K. Takahashi, G. Ju, J.-U. Thiele, A. Ajan, X. Yang, R. Ruiz, and L. Wan, Heat-assisted magnetic recording media materials, MRS Bull. **43**, 93 (2018).

[9] D. Weller, O. Mosendz, G. Parker, S. Pisana, and T. S. Santos, $L1_0$ FePtX-Y media for heat-assisted magnetic recording, Phys. Status Solidi A **210**, 1245 (2013).

[10] J. Gorchon, C.-H. Lambert, Y. Yang, A. Pattabi, R. B. Wilson, S. Salahuddin, and J. Bokor, Single shot ultrafast all optical magnetization switching of ferromagnetic Co/Pt multilayers, Appl. Phys. Lett. **111**, 042401 (2017).

[11] J. Mendil, P. Nieves, O. Chubykalo-Fesenko, J. Walowski, T. Santos, S. Pisana, and M. Münzenberg, Resolving the role of femtosecond heated electrons in ultrafast spin dynamics, Sci. Rep. **4**, 3980 (2014).

[12] J. Zhao, B. Cui, Z. Zhang, B. Ma, and Q. Y. Jin, Ultrafast heating effect on transient magnetic properties of $L1_0$-FePt thin films with perpendicular anisotropy, Thin Solid Films **518**, 2830 (2010).

[13] B. Koopmans, G. Malinowski, F. Dalla Longa, D. Steiauf, M. Fähnle, T. Roth, M. Cinchetti, and M. Aeschlimann, Explaining the paradoxical diversity of ultrafast laser-induced demagnetization, Nat. Mater. **9**, 259 (2009).

[14] J.-Y. Bigot, M. Vomir, and E. Beaurepaire, Coherent ultrafast magnetism induced by femtosecond laser pulses, Nat. Phys. **5**, 515 (2009).

[15] M. Battiato, K. Carva, and P. M. Oppeneer, Superdiffusive Spin Transport as a Mechanism of Ultrafast Demagnetization, Phys. Rev. Lett. **105**, 027203 (2010).

[16] N. Kazantseva, U. Nowak, R. W. Chantrell, J. Hohlfeld, and A. Rebei, Slow recovery of the magnetization after a sub-picosecond heat pulse, Europhys. Lett. **81**, 27004 (2008).

[17] R. Chimata, A. Bergman, L. Bergqvist, B. Sanyal, and O. Eriksson, Microscopic Model for Ultrafast Remagnetization Dynamics, Phys. Rev. Lett. **109**, 157201 (2012).

[18] P. Nieves and O. Chubykalo-Fesenko, Modeling of Ultrafast Heat- and Field-Assisted Magnetization Dynamics in FePt, Phys. Rev. Appl. **5**, 014006 (2016).

[19] A. Lyberatos and G. J. Parker, Model of ballistic-diffusive thermal transport in HAMR media, Jpn. J. Appl. Phys. **58**, 045002 (2019).

[20] P. Scheid, G. Malinowski, S. Mangin, and S. Lebègue, *Ab initio* study of electronic temperature effects on magnetic materials properties, Phys. Rev. B **99**, 174415 (2019).

[21] J. Barker and G. E. W. Bauer, Quantum thermodynamics of complex ferrimagnets, Phys. Rev. B **100**, 140401(R) (2019).

[22] A. von Reppert, L. Willig, J.-E. Pudell, M. Rössle, W. Leitenberger, M. Herzog, F. Ganss, O. Hellwig, and M. Bargheer, Ultrafast laser generated strain in granular and continuous FePt thin films, Appl. Phys. Lett. **113**, 123101 (2018).

[23] K. Hono and Y. K. Takahashi in *Ultrahigh-Density Magnetic Recording. Storage Materials and Media Designs*, 1st ed., edited by F. Casoli and G. Varvaro (Pan Stanford Publishing, Singapore, 2016) Chap. 5, pp. 245–277.

[24] A. Lyberatos, D. Weller, and G. J. Parker, Finite size effects in $L1_0$-FePt nanoparticles, J. Appl. Phys. **114**, 233904 (2013).

[25] O. Hovorka, S. Devos, Q. Coopman, W. J. Fan, C. J. Aas, R. F. L. Evans, X. Chen, G. Ju, and R. W. Chantrell, The Curie temperature distribution of FePt granular magnetic recording media, Appl. Phys. Lett. **101**, 052406 (2012).

[26] R. P. Cowburn, J. Ferré, S. J. Gray, and J. A. C. Bland, Domain wall mobility in ultrathin epitaxial Ag/Fe/Ag(001) films, Appl. Phys. Lett. **74**, 1018 (1999).

[27] P. J. Metaxas, J. P. Jamet, A. Mougin, M. Cormier, J. Ferré, V. Baltz, B. Rodmacq, B. Dieny, and R. L. Stamps, Creep and Flow Regimes of Magnetic Domain-Wall Motion in Ultrathin Pt/Co/Pt Films with Perpendicular Anisotropy, Phys. Rev. Lett. **99**, 217208 (2007).

[28] A. Hubert and R. Schäfer, *Magnetic Domains: The Analysis of Magnetic Microstructures*, (Springer, Berlin, 2011).

[29] P. W. Granitzka, E. Jal, L. Le Guyader, M. Savoini, D. J. Higley, T. Liu, Z. Chen, T. Chase, H. Ohldag, G. L. Dakovski, W. F. Schlotter, S. Carron, M. C. Hoffman, A. X. Gray, P. Shafer, E. Arenholz, O. Hellwig, V. Mehta, Y. K. Takahashi, J. Wang, E. E. Fullerton, J. Stöhr, A. H. Reid, and H. A. Dürr, Magnetic switching in granular FePt layers promoted by near-field laser enhancement, Nano Lett. **17**, 2426 (2017).

[30] L. Le Guyader, A. Kleibert, F. Nolting, L. Joly, P. M. Derlet, R. V. Pisarev, A. Kirilyuk, Th. Rasing, and A. V. Kimel, Dynamics of laser-induced spin reorientation in Co /$SmFeO_3$ heterostructure, Phys. Rev. B **87**, 054437 (2013).

[31] Z. H. Cen, B. X. Xu, J. F. Hu, J. M. Li, K. M. Cher, Y. T. Toh, K. D. Ye, and J. Zhang, Optical property study of FePt-C nanocomposite thin film for heat-assisted magnetic recording, Opt. Express **21**, 9906 (2013).

[32] A. H. Reid, X. Shen, P. Maldonado, T. Chase, E. Jal, P. W. Granitzka, K. Carva, R. K. Li, J. Li, L. Wu, T. Vecchione, T. Liu, Z. Chen, D. J. Higley, N. Hartmann, R. Coffee, J. Wu, G. L. Dakovski, W. F. Schlotter, H. Ohldag, Y. K. Takahashi, V. Mehta, O. Hellwig, A. Fry, Y. Zhu, J. Cao, E. E. Fullerton, J. Stöhr, P. M. Oppeneer, X. J. Wang, and H. A. Dürr, Beyond a phenomenological description of magnetostriction, Nat. Commun. **9**, 388 (2018).

[33] J. Krumhansl and H. Brooks, The lattice vibration specific heat of graphite, J. Chem. Phys. **21**, 1663 (1953).

[34] W.-P. Hsieh, A. S. Lyons, E. Pop, P. Keblinski, and D. G. Cahill, Pressure tuning of the thermal conductance of weak interfaces, Phys. Rev. B **84**, 184107 (2011).

Article VI

Spin stress contribution to the lattice dynamics of FePt

Alexander von Reppert, Lisa Willig, Jan-Etienne Pudell, Steffen Peer Zeuschner, Gabriel Sellge, Fabian Ganss, Olav Hellwig, Jon Ander Arregi, Vojteč Uhlíř, Aurélien Crut, and Matias Bargheer

Science Advances 6, eaba1142 (2020)

Invar-behavior occurring in many magnetic materials has long been of interest to materials science. Here, we show not only invar behavior of a continuous film of FePt but also even negative thermal expansion of FePt nanograins upon equilibrium heating. Yet, both samples exhibit pronounced transient expansion upon laser heating in femtosecond x-ray diffraction experiments. We show that the granular microstructure is essential to support the contractive out-of-plane stresses originating from in-plane expansion via the Poisson effect that add to the uniaxial contractive stress driven by spin disorder. We prove the spin contribution by saturating the magnetic excitations with a first laser pulse and then detecting the purely expansive response to a second pulse. The contractive spin stress is reestablished on the same 100-ps time scale that we observe for the recovery of the ferromagnetic order. Finite-element modeling of the mechanical response of FePt nanosystems confirms the morphology dependence of the dynamics.

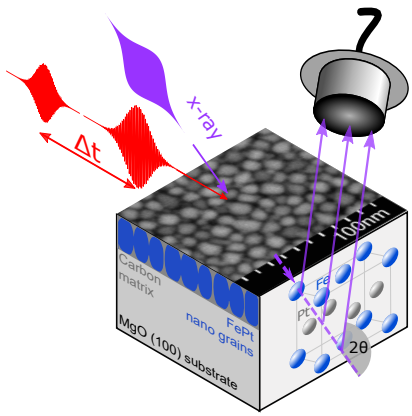

SCIENCE ADVANCES | RESEARCH ARTICLE

PHYSICS

Spin stress contribution to the lattice dynamics of FePt

A. von Reppert[1], L. Willig[1,2], J.-E. Pudell[1,2], S. P. Zeuschner[1,2], G. Sellge[3,4], F. Ganss[3], O. Hellwig[3,4], J. A. Arregi[5], V. Uhlíř[5,6], A. Crut[7], M. Bargheer[1,2]*

Invar-behavior occurring in many magnetic materials has long been of interest to materials science. Here, we show not only invar behavior of a continuous film of FePt but also even negative thermal expansion of FePt nanograins upon equilibrium heating. Yet, both samples exhibit pronounced transient expansion upon laser heating in femtosecond x-ray diffraction experiments. We show that the granular microstructure is essential to support the contractive out-of-plane stresses originating from in-plane expansion via the Poisson effect that add to the uniaxial contractive stress driven by spin disorder. We prove the spin contribution by saturating the magnetic excitations with a first laser pulse and then detecting the purely expansive response to a second pulse. The contractive spin stress is reestablished on the same 100-ps time scale that we observe for the recovery of the ferromagnetic order. Finite-element modeling of the mechanical response of FePt nanosystems confirms the morphology dependence of the dynamics.

INTRODUCTION

Invar materials exhibit almost zero thermal expansion over a wide temperature range (*1*). Although the discovery of a 10-fold reduction of the thermal expansion of the $Fe_{0.65}Ni_{0.35}$ alloy compared to its pure elements (*2*) dates back to 1897, its origin remained an active area of solid-state research over the next century (*3*–*5*). Invar behavior requires a mechanism that counteracts the thermal expansion resulting from anharmonic phonon-phonon interactions. For magnetic invar materials, it is found that the required contractive stress originates from an increased volume for the spin-ordered state compared to the disordered state that can now be predicted in different ab initio approaches (*4*, *5*). Quantitative, time-resolved studies of the structural dynamics have recently started to explore the response of the lattice to magnetic stresses (*6*–*12*), which are attributed to the transfer of angular momentum (*6*, *7*), energy (*8*, *12*), and entropy (*9*) from and to the spin system. In this context, it is interesting to ask how invar materials respond to laser-induced heating on the picosecond time scale and to determine the lattice dynamics induced by counteracting contributions of phonon and spin stresses.

One approach for the separation of the magnetic response from the ever-present phonon contribution to the lattice dynamics in laser-excited metals is to compare the structural response above and below the magnetic ordering temperature (*8*–*10*). This is sometimes prohibited by irreversible modifications of the material under heating. A demagnetized state can also be created transiently by femtosecond laser excitation (*13*, *14*) and characterized by applying a pump-probe sequence, where a second pump pulse excites the nonequilibrium state generated by the first pump pulse. Double-pulse excitation experiments not only have been used to demonstrate intriguing coherent control of the magnetization (*15*–*17*) and lattice dynamics (*18*, *19*) but they also revealed that the induced magnetization dynamics, (*20*) total transient demagnetization (*21*), and magnetic anisotropy (*22*) critically depend on the pulse-to-pulse separation.

Invar behavior is found in many Fe-containing alloys (*1*, *23*). The magnetic recording medium FePt in the fully ordered $L1_0$ phase is receiving particular attention due to its large uniaxial magnetic anisotropy energy ($K_u > 4.5$ J/cm^3) (*24*), which sustains nanoscopic magnetically stable bits with perpendicular magnetization. The envisioned heat-assisted magnetic recording scheme (*25*) aims at improving the magnetic information densities to exceed 2 Tb/in^2 in commercial products of the near future (*26*). The possibility to grow magnetic, oriented nanograins with a high degree of structural order makes this material an ideal candidate for studying the lattice using time-resolved diffraction techniques. In a recent ultrafast x-ray diffraction (UXRD) study, we have found a short-lived lattice contraction along the short out-of-plane *c* axis of the tetragonal unit cell of a nanogranular FePt film on a substrate, whereas continuous epitaxial thin films merely expanded under otherwise identical excitation conditions (*27*). Previously, ultrafast electron diffraction experiments had reported a transient *c*-axis contraction and in-plane expansion for freestanding FePt nanograins (*11*). Spin-polarized density functional theory consistently predicts this tetragonal distortion when comparing the spin-ordered ferromagnetic ground state to the paramagnetic phase with full spin disorder (*11*). In the same paper, a strongly anisotropic phonon stress was predicted, seven times larger in-plane than out-of-plane (*11*). In all three cases the material is the $L1_0$ phase of FePt. Therefore, the variability of the measured ultrafast dynamics suggests that the morphology and substrate-induced strain must have an important influence on the lattice dynamics at ultrafast time scales.

Here, we use fluence-dependent UXRD experiments on granular FePt thin films to show experimentally that the initial contraction originates from spin entropy, as it saturates for high fluence when the spin system is disordered. Weak excitation pulses trigger an initial contraction driven by spin stress, but expansive lattice stresses prevail after about 3 ps. The direct connection of spin disorder with the contractive stress is revealed by double-pulse excitation scenarios. When a strong first excitation pulse has essentially disordered the

[1]Institute of Physics and Astronomy, University of Potsdam, Karl-Liebknecht-Str. 24-25, 14476 Potsdam, Germany. [2]Helmholtz-Zentrum Berlin für Materialien und Energie GmbH, Wilhelm-Conrad-12 Röntgen Campus, BESSY II, Albert-Einstein-Str. 15, 12489 Berlin, Germany. [3]Institut für Physik, Technische Universität Chemnitz, Reichenhainer Str. 70, 09126 Chemnitz, Germany. [4]Institut für Ionenstrahlphysik und Materialforschung, Helmholtz-Zentrum Dresden-Rossendorf, Bautzner Landstrasse 400, 01328 Dresden, Germany. [5]CEITEC BUT, Brno University of Technology, Purkyňova 123, 612 00 Brno, Czechia. [6]Institute of Physical Engineering, Brno University of Technology, Technická 2, 616 69 Brno, Czechia. [7]FemtoNanoOptics Group, Institut Lumière Matière, Université de Lyon, CNRS-Université Lyon 1, 69622 Villeurbanne, France.
*Corresponding author. Email: bargheer@uni-potsdam.de

spin system, a second excitation pulse applied after a short delay only triggers expansion.

However, if the second pulse arrives about 100 ps later, the spin order has partially recovered, and the second pulse yields a contraction. This time scale for the recovery of the contractive stress is dictated by thermal transport and identical to the time scale of remagnetization observed in time-resolved magneto-optical Kerr effect (tr-MOKE) measurements. We model the coupled out-of-plane and in-plane lattice response of the nanograins using finite-element modeling (FEM) by varying the amplitude of the uniaxial contractive stress component $\sigma_{\perp}^{sp}$ associated with the spin disorder, which is the essential parameter for describing the two-pulse experiments. To provide a solid experimental basis for our interpretation, we compare granular films composed of FePt grains in a carbon matrix to continuous films, where the in-plane expansion on the picosecond time scale is forbidden by symmetry.

RESULTS

Time-resolved and static expansion

We first discuss the lattice response of FePt to laser excitation and equilibrium heating. Figure 1 (A and B) compares the lattice response of a granular and a continuous film of similar thickness to 100-fs pump laser pulses for incident laser fluences ranging from F_{in} = 1.4 to 11 mJ/cm^2 (see Materials and Methods for details). To show that lattice expansion beyond 3 ps is approximately proportional to F_{in} and thus to the energy density, we have normalized the observed out-of-plane strain $\eta_{\perp}$ to the incident laser fluence. Because the phonon system hosts most of the energy density at this time, the strain per fluence is approximately the same, and variations are due to energy absorbed in the spin system. The central finding for the granular film (Fig. 1A) is the pronounced contraction in the first 2 ps. Its absolute value is maximized for medium laser fluences, and the contraction disappears upon increasing the laser fluence further (see Supplementary Materials for the unscaled data). This already hints at the spin disorder as the driving mechanism of the contraction. The UXRD results in Fig. 1B show that the contraction is essentially absent for the continuous FePt film at all fluences. The small delay of the expansion observed in Fig. 1B for low laser fluences suggests that expansive and contractive out-of-plane stresses have different time dependences. Although the thermal expansion of bulk FePt solid solutions of different composition has been studied (*28*–*31*), static characterization of the out-of-plane expansion for continuous and granular $L1_0$-ordered thin films approaching the Curie temperature $T_C \approx 700$ K was, so far, not available. Our results in Fig 1C show that the out-of-plane dimension of $L1_0$-FePt behaves invar-like for the continuous film and even exhibits negative thermal expansion (NTE) for the granular FePt sample. The in-plane thermal expansion coefficient of FePt matches the value 1×10^{-5} K^{-1} of the MgO substrate (see Supplementary Materials), so that epitaxial stresses on the thin film upon equilibrium heating are expected to be small (*11*, *29*, *31*). Figure 1 thus directly contrasts that the FePt out-of-plane strain $\eta_{\perp}$ exhibits a pronounced difference between equilibrium heating, which shows NTE and invar behavior for granular and continuous FePt films, respectively, and ultrafast laser heating, where FePt mainly expands out-of-plane showing a positive strain $\eta_{\perp} = \Delta c/c$. We attribute the differences in $\eta_{\perp}(t)$ for the nanogranular and continuous FePt to the different magnitudes of in-plane strain $\eta_{\parallel}(t)$. The probed region is almost homogeneously heated as the excitation spot is three times

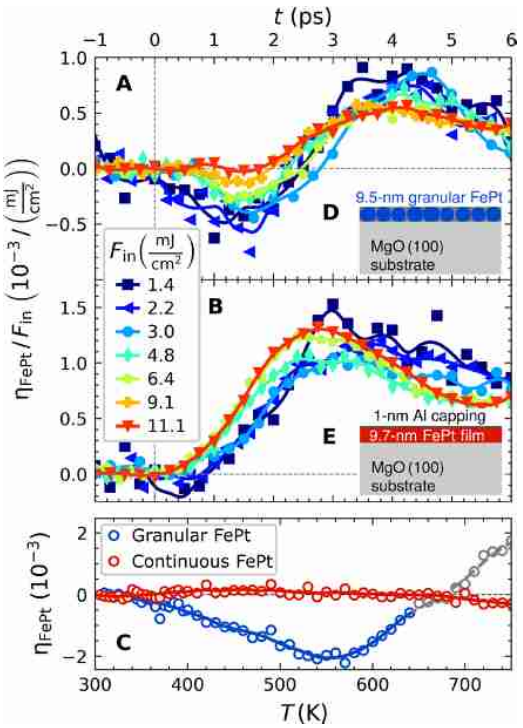

Fig. 1. Comparison of granular and continuous FePt film responses to laser excitation and equilibrium heating. (**A**) Normalized transient out-of-plane strain $\eta_{\perp}$ in FePt derived from the Bragg peak shift in UXRD experiments involving excitation of the granular FePt film with various incident fluences F_{in}. The observed strain is normalized to F_{in}. (**B**) Same for the continuous film. (**C**) Out-of-plane strain $\eta_{\perp}$ upon equilibrium heating for both samples. Points above 650 K are grayed out, because the Bragg peak intensity decrease by 20% of the granular sample may indicate a slight sample degradation. Solid lines serve as guide to the eye. The insets (**D**) and (**E**) schematically depict the sample structures.

larger than the probe pulses. Any in-plane stresses are therefore balanced by the adjacent unit cells for the continuous FePt film. The in-plane strain propagation from the edge of the excitation region to the probed region at the sound velocity sets the 100-ns time scale (much longer than those investigated in the time-resolved experiments) on which this in-plane fixation is relieved. For the granular FePt film, the inhomogeneity at the carbon-FePt interface enables transverse stresses and strains even on picosecond time scales, whereas they are forbidden by symmetry in the continuous film case. Under static heating conditions, both the substrate and the thin film can relax in-plane, which creates additional contractive elastic stresses out-of-plane via the Poisson effect. Thus, the static out-of-plane NTE of the granular film is reduced to an invar behavior in the continuous film, for which the in-plane expansion of FePt and hence the Poisson effect are limited by the epitaxial clamping to the substrate.

Double-pulse excitation: Spin stress tuning

The results of a double-pulse excitation scheme displayed in Fig. 2A confirm that the spin excitations drive the contraction in the granular FePt film. In these experiments, we use a first strong laser pulse (p_1) to saturate the spin excitations and a second, weaker laser pulse (p_2) for triggering subsequent dynamics with a delay Δt. The ultrashort

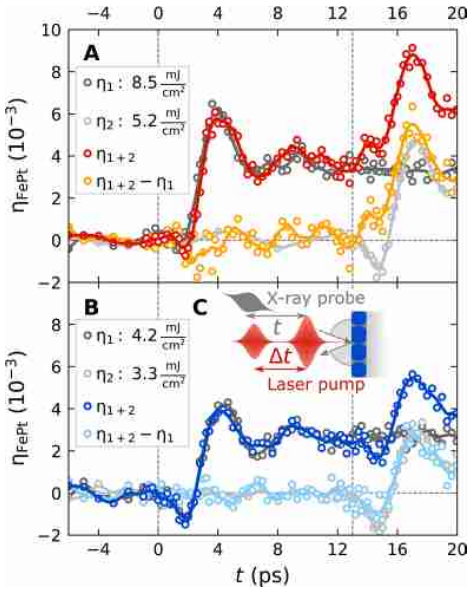

Fig. 2. UXRD with double-pulse excitation. (**A**) Transient strain $\eta(t)$ of the granular FePt film from UXRD with single- and double-pulse excitation. The first pulse at $t = 0$ has a fluence of $F_{in,1} = 8.5$ mJ/cm^2, and the second pulse at 13 ps is weaker ($F_{in,2} = 5.2$ mJ/cm^2). The nonequilibrium strains $\eta_{ne}(t) = \eta_{1+2}(t) - \eta_1(t)$ (orange) are derived by subtracting the dark gray curve from the red curve. This strain is induced by the photoexcitation in the nonequilibrium conditions set by the first pulse. (**B**) Same for weaker pump pulses $F_{in,1} = 4.2$ mJ/cm^2 and $F_{in,2} = 3.3$ mJ/cm^2, which only partially demagnetize the film. (**C**) Relative timing of the double-pulse excitation experiments.

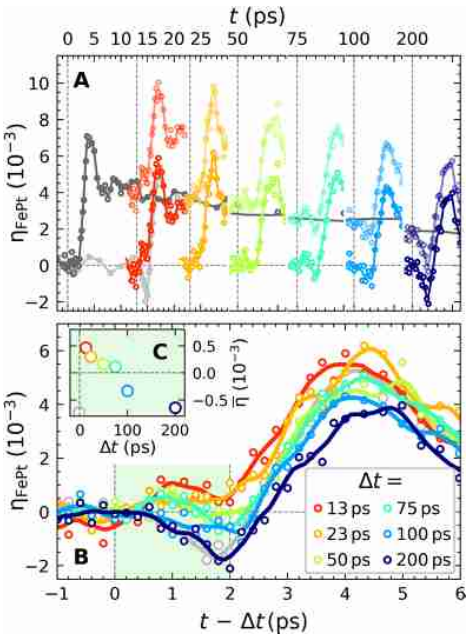

Fig. 3. Recovery of the spin entropy–driven lattice contraction. (**A**) Dark gray: transient strain $\eta_1(t)$ from UXRD with single-pulse excitation at $t = 0$ ($F_{in,1} = 8.5$ mJ/cm^2) for the granular film. Light-colored data: strain $\eta_{1+2}(t)$ observed for double-pulse excitation with the same first pulse and a second pulse with fluence ($F_{in,2} = 5.2$ mJ/cm^2) after $\Delta t = 13$, 23, 50, 75, 100, and 200 ps. The bright-colored data represent $\eta_{ne}(t) = \eta_{1+2}(t) - \eta_1(t)$. (**B**) Comparison of $\eta_{ne}(t - \Delta t)$ from (A) to the strain $\eta_2(t)$ obtained for excitation only with the second pulse (gray). (**C**) Average strain $\eta_{ne}(t - \Delta t)$ within the first 2 ps.

x-ray probe pulse detects the lattice dynamics $\eta_\perp(t)$ that is induced by this double-pulse excitation, as schematically depicted in Fig 2C. The dark gray data from Fig. 2A show the UXRD signal that characterizes the strain $\eta_1(t)$ due to a single strong pulse with $F_{in,1} = 8.5$ mJ/cm^2 at $t = 0$, which almost exclusively leads to expansion of the FePt film. In contrast, the light gray data representing the strain $\eta_2(t)$ generated by a weaker single pulse with $F_{in,2} = 5.2$ mJ/cm^2 arriving at $\Delta t = 13$ ps show a pronounced contraction at the onset of the second pulse, consistent with the fluence series in Fig. 1A. When both pulses excite the sample with the delay set to $\Delta t = 13$ ps, we observe the strain $\eta_{1+2}(t)$ (red data points). The orange points represent the additional strain $\eta_{ne}(t) = \eta_{1+2}(t) - \eta_1(t)$, which is induced by the photoexcitation of the sample in the nonequilibrium conditions previously set by the first pulse. It mainly differs from $\eta_2(t)$ (light gray curve in Fig. 2A) in the first 2 ps after the second laser pulse arrives. Clearly, there is no contraction at $t = 15$ ps just after the second pulse, if the sample was pre-excited with the first pulse. We conclude that the first pulse has essentially saturated the spin excitations. Figure 2B confirms this interpretation by reducing the fluences to $F_{in,1} = 4.2$ mJ/cm^2 and $F_{in,2} = 3.3$ mJ/cm^2 with the same timing. Now, $\eta_{ne}(t)$ shows approximately half of the contraction at $t = 15$ ps compared to $\eta_2(t)$ (light gray data) because the first pulse does not fully saturate the spin excitations.

Our double-pulse scheme also allows monitoring the recovery of the contractive stress by adjusting the timing between the excitation pulses for constant $F_{in,1}$ and $F_{in,2}$. Figure 3A depicts the results from Fig. 2A for tuning the double-pulse time delay Δt. Again, the gray line shows the strain induced only by the first pump pulse with $F_{in,1} = 8.5$ mJ/cm^2. Within 200 ps, the cooling of the FePt lattice reduces the transient strain from $\eta_\perp = 4 \times 10^{-3}$ to the half value. The light-colored lines show the strain $\eta_{1+2}(t)$ observed for double-pulse excitation, and the bright colors show the nonequilibrium strain $\eta_{ne}(t) = \eta_{1+2}(t) - \eta_1(t)$. Figure 3B reproduces these data on a time axis where $t = 0$ indicates the arrival of the second pulse and compares $\eta_{ne}(t - \Delta t)$ to $\eta_2(t)$ (light gray), i.e., the response to the second pulse with and without pre-excitation. For a pulse delay of $\Delta t = 200$ ps, $\eta_{ne}(t - \Delta t)$ and $\eta_2(t)$ nearly coincide in the first 3 ps, indicating a reordering of the spin system within this time scale. For time delays shorter than $\Delta t = 75$ ps, the lattice expansion prevails. The red line ($\Delta t = 13$ ps) transforms continuously into the dark blue line ($\Delta t = 200$ ps) with increasing time delay, indicating the emergence of the contractive stress as the spin system can be disordered again by the second pulse.

Magnetization dynamics and energy density

To corroborate our findings about the spin stress contribution to the lattice dynamics, we analyze the magnetic system. The spin stress contribution to the strain response must vanish if the magnetic system is in a state close to its maximal entropy that can be reached either thermally or via laser-induced demagnetization. According to recent FEM simulations of the field enhancement effects in the optical absorption of a similar nanogranular sample (*32*), the temperature change due to the inhomogeneous optical absorption of the irregularly shaped FePt nano-islands varies between 10 and

30%. For $F_{in,1}$ = 8.5 mJ/cm², we therefore estimate the temperature rise to be in the range ΔT = 300 to 700 K. The majority of the nanogranular FePt will be transiently heated above the Curie temperature, which is about $T_C \approx$ 650 to 700 K for the current particle size (*33*).

Figure 4A contains tr-MOKE data for three selected fluences. We assume nearly full demagnetization for the incident fluence of 11 mJ/cm², as the signal does not increase beyond this fluence. Consistent with literature, this sets the initial demagnetization for the pulses (8.5 mJ/cm²) used in the UXRD experiment from Figs. 3A and 2A at 85%. Because of the large out-of-plane anisotropy and the single-domain character of the grains (no domain wall propagation), we can use the tr-MOKE signal recorded with an external field of ±0.7 *T* as an estimation of the time-dependent average magnetization $M(t)$ of the sample (*34*). The static magnetization curve $M(T)$ of the granular FePt sample is depicted in Fig 4B. To relate the UXRD and tr-MOKE signal, we calculate an estimate for the spin contribution to the heat capacity (Fig. 4C) according to the mean field theory relation (*35*) $C_{sp} \propto \frac{\partial M^2}{\partial T} = M\frac{\partial M}{\partial T}$, which agrees reasonably well with recent theoretical predictions represented by the dashed line (*36*).

The colored dashed lines in Fig. 4 (A to C) indicate how the MOKE signal, which is proportional to $M(t)$, is related to the auxiliary temperature $T(t)$ of the spin system for the specific time $t = \Delta t$ of the UXRD experiment. This temperature is used to estimate the energy density $\Delta\rho^Q_{sp} = \int_T C_{sp}(T')\,dT'$, which would be required to fully saturate the heat capacity $C_{sp}(T)$ of the spin system. In a first-order analysis, the individual stresses from electrons, phonons, and spins $\sigma_{e,ph,sp} = \Gamma_{e,ph,sp}\rho^Q_{e,ph,sp}$ are directly proportional to the heat energy densities $\rho^Q_{e,ph,sp}$, and the dimensionless macroscopic Grueneisen coefficients $\Gamma_{e,\,ph,\,sp}$ describe the efficiency for generating stress from energy in each of the three systems (*8*).

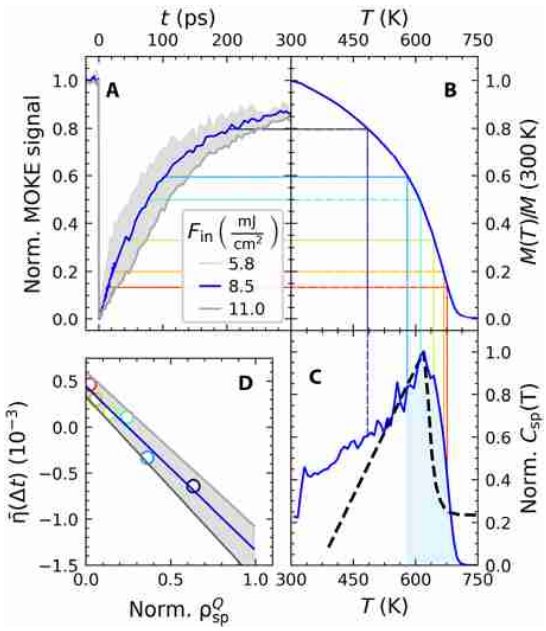

Fig. 4. Semiquantitative approximation of the remaining spin energy from tr-MOKE measurements. (**A**) Transient MOKE data for the granular FePt film for various fluences, normalized (Norm.) to their maximum demagnetization. (**B**) Equilibrium magnetization $M(T)$ measurement for a similarly prepared granular FePt film obtained by vibrating sample magnetometry (VSM). (**C**) Spin-specific heat as derived via $C_{sp} \approx M\frac{\partial M}{\partial T}$ (blue line) from $M(T)$ and calculations (*36*) (thick black dashed line). The colored dashed lines connect the graphs at selected times for which partial recovery of the spin entropy–driven contraction is observed (compare Fig 3). (**D**) Average strain $\bar{\eta}(\Delta t)$ in the first 2 ps after the second pulse (green area in Fig. 3B) as a function of the energy density $\Delta\rho^Q_{sp}(\Delta t)$ that this second pulse can still introduce into the spin system. The light blue shaded area in (C) visualizes $\Delta\rho^Q_{sp}$ for the case of T(100 ps) = 580 K, which gives rise to the light blue circle in (D).

To combine UXRD and tr-MOKE, we reproduce on the vertical axis of Fig. 4D the average lattice strain $\bar{\eta}$ from Fig. 3C, while the horizontal axis quantifies the fraction of the energy density $\Delta\rho^Q_{sp}(\Delta t)$ that the second pulse can still introduce into the spin system according to (Fig. 4C). For simplicity, we assume that after a short time delay Δt = 15 ps, the FePt is still nearly fully demagnetized (Fig. 4A), and almost no energy density $\Delta\rho^Q_{sp}$ can be deposited into the spin system. Hence, the second pulse only induces expansion, i.e., positive $\bar{\eta}(\Delta t)$ in Fig. 4D by exciting electrons and phonons. With increasing Δt, the contractive stress $\sigma_{sp} = \Gamma_{sp}\Delta\rho^Q_{sp}$ increases. The slope of Fig. 4D is proportional to the macroscopic Grueneisen constant Γ_{sp} of the spin system, which must, in fact, be negative to support the observed NTE or invar behavior (*3*, *37*).

Modeling

We experimentally find that the spin stress contribution recovers on a 100-ps time scale, consistent with the remagnetization of the grains. As domain wall propagation is not relevant within the nanoscopic grains on this time scale, the dynamics are governed by thermal transport to the carbon matrix and the substrate. Figure 4C illustrates that the energy density ρ^Q_{sp} and the associated spin entropy density $S_{sp} \propto \rho^Q_{sp}/T$ that can be induced by a second excitation after a given time delay Δt are finite. Statistical mechanics limits the maximum spin entropy to $S_{sp} = Nk_B \ln(2J+1)$, where J is the angular momentum per magnetic atom. This saturation provides the necessary mechanism for the reduced contractive stress contribution at high fluences in the otherwise linear stress-strain relations. NTE generally requires an increasing entropy with decreasing volume (*23*).

The main features of the fluence-dependent responses observed for the continuous and granular films (Fig. 1) and of the two-pulse excitation experiments (Figs. 2 and 3) can be qualitatively understood in the light of a simplified equation of motion [see Materials and Methods for the full three-dimensional (3D) equation]

$$\rho\frac{\partial^2 u_\perp}{\partial t^2} = \frac{\partial}{\partial z}\left(\underbrace{C_{33}\frac{\partial u_\perp}{\partial z}}_{\text{elast.}\sigma_\perp} + \underbrace{2C_{31}\eta_\parallel}_{\text{elast.}\sigma_\perp^{\text{Poi}}} - \underbrace{\sigma_\perp^{\text{sp}}}_{<0} - \underbrace{\sigma_\perp^{e-\text{ph}}}_{>0}\right) \quad (1)$$

At equilibrium, negative strain $\eta_\perp = \frac{\partial u_\perp}{\partial z} < 0$ occurs only if a contractive spin stress $\sigma_\perp^{sp}$ and the elastic Poisson stress contribution $\sigma_\perp^{Poi}(t) \sim \eta_\parallel(t)$ induced by in-plane strain $\eta_\parallel$ add constructively to overcome the expansive out-of-plane stress $\sigma_\perp^{e-ph}$ imposed by hot electrons and phonons. Equation 1 is valid in the case of a thin FePt needle, i.e., a cylinder with radius much smaller than height ($r \ll d$), because this allows us to assume that in-plane strains $\eta_\parallel$ are relaxed and equal in x and y directions. The main reason for writing Eq. 1 is to see that it can be further simplified for the continuous film because $\sigma_\perp^{Poi}$ is absent at ultrafast time scales for which $\eta_\parallel = 0$ for symmetry reasons. Thus, on ultrafast time scales, Eq. 1 with $\sigma_\perp^{Poi} = 0$ is exact, and the Poisson stress makes the out-of-plane response of the granular film response substantially different.

We complement this simple analysis of the FePt deformation dynamics by FEM simulations using the actual FePt nanostructure dimensions and considering 3D, nonsimplified equations of motion (see Materials and Methods and Supplementary Materials for technical details). The results for the granular FePt film are shown in Fig. 5, while those obtained for continuous films and free grains can be found in the Supplementary Materials. In each case, various values of the relative amplitude A^{sp} of the spin stress contribution were used to mimic its variation in the context of fluence dependence (Fig. 1—saturation of the contraction) and two-pulse excitation (Figs. 2 and 3—time-dependent recovery of the spin stress). A complete reproduction of the measured time-resolved signals is challenging, as it would require to precisely take into account the morphological dispersion of the FePt grains and the heat transfer to the carbon. Nevertheless, enable a good qualitative reproduction of the strain dynamics measured for granular FePt films, as can be seen by comparing the measured strain (Figs. 1A and 3B) with the simulated strain in Fig. 5B.

Figure 5A illustrates the electron-phonon, spin, and Poisson stress contributions, which drive the out-of-plane strain dynamics of granular films (Eq. 1). As expected, in the absence of the contractive spin stress ($A^{sp} = 0$), the total stress almost always remains positive. The computed out-of-plane strain dynamics correspond to oscillations of the FePt nanostructure configuration around an expanded equilibrium, with a total absence of out-of-plane compression throughout the motion (Fig. 5B). These computed strain dynamics agree well with experimental strain data where the spin contribution is strongly reduced via the use of high-fluence light pulses (Figs. 1 to 3). Conversely, a sufficient amplitude of A^{sp} (e.g., $A^{sp} = 0.2$, as in Fig. 5A) creates a negative average value of the computed total stress enabling out-of-plane FePt contractions (Fig. 5B), in agreement with the experimental observation of a contraction at the beginning of the dynamics. Moreover, the computed strains shown in Fig. 5B qualitatively reproduce both the maximal contraction at 1.7 ps and maximal expansion at 4.5 ps, observed in the context of both low-fluence single-pump experiments (Fig. 1A) and double-pulse excitation with large delay between pump pulses, i.e., recovered spin order (Fig. 3B). The FePt deformation computed at these two instants is illustrated for $A^{sp} = 0.2$ in Fig. 5. For the same range of A^{sp}, our FEM modeling of a continuous film (see Supplementary Materials) reproduces the absence of a contraction and the 0.5-ps phase shift observed in Fig. 1B for increasing fluence. Conversely, the Poisson effect is enhanced for free FePt grains (see Supplementary Materials) because the in-plane displacement is unconstrained. Our simulations qualitatively reproduce the large out-of-plane contractions observed previously (*11*).

A systematic variation of the simulation parameters shows that a reasonable agreement with the experimental data can be obtained only by assuming an anisotropic electron-phonon stress, with nonequal out-of-plane and in-plane amplitudes $\sigma_{\perp}^{e-ph,0} = A^{ani}\,\sigma_{\parallel}^{e-ph,0}$. However, the optimal value of the anisotropy parameter $A^{ani} \approx 3$ used for the simulations shown in Fig. 5 is more than twice smaller than predicted (*11*). Including an in-plane expansion resulting from spin stress (*11*) would even reduce A^{ani} further. Although the overall agreement between simulations and experiments is good, the simulations systematically underestimate the expansion beyond 3 ps observed experimentally. This may be compensated for by adding expansive stress in the carbon shell resulting from heat transfer from the FePt, which would decrease the Poisson stress $\sigma_{\perp}^{Poi}$ acting on FePt on long time scales.

Our modeling shows that the difference in the response of free grains, a granular film, and the continuous film mainly originates from the different in-plane boundary conditions, which suppress or partially allow the Poisson effect. We can reproduce the essential conclusion drawn from the double-pulse experiment (Fig. 3) that the initial out-of-plane contraction is driven by spin stress.

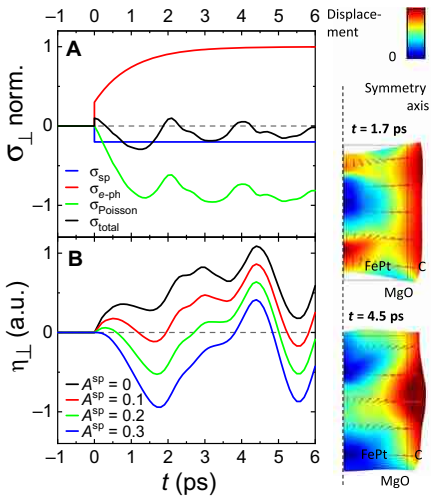

Fig. 5. FEM modeling of the mechanical response of a granular FePt film. (**A**) Time-dependent out-of-plane stresses $\sigma_{\perp}(t)$ acting on FePt for $A^{sp} = 0$ (no spin stress, solid lines) and $A^{sp} = 0.2$ (dashed lines). The Poisson stress component was deduced from the computed in-plane strains. (**B**) Average out-of-plane strain $\eta_{\perp}(t)$ in arbitrary units (a.u.) computed for various ratios A^{sp} of the spin and electron-phonon stress amplitudes. The computed FePt deformation at instants corresponding to maximal initial contraction and expansion for $A^{sp} = 0.2$ are illustrated at the right.

CONCLUSION

In conclusion, we have shown that laser-generated spin entropy drives a pronounced but short-lived lattice contraction of nanogranular FePt films in the $L1_0$ phase. In a double-pulse excitation scenario, the absence of a contraction after the second laser pulse quantifies the contractive stress contribution of the spin excitations, as they saturate when the FePt temperature approaches T_C. Fluence-dependent transient MOKE data confirm that the relaxation of the magnetization occurs on the same time scale as the spin entropy–driven contraction reappears.

Our elastic continuum modeling clarifies the important role of the Poisson effect in establishing the transient contraction of the granular film, which is not observed for the continuous film. We are confident that this double-pulse excitation scenario can be developed into a versatile tool for investigating coupled systems with many degrees of freedom, when a phase transition leads to the saturation for one of the driving stresses of the lattice response.

MATERIALS AND METHODS

X-ray and MOKE experiments

We performed laser-based UXRD pump-probe experiments with an x-ray pulse duration (*38*) of approximately 200 fs on two FePt thin films in the ordered $L1_0$ phase grown on MgO (001) oriented substrates. We observe the time-dependent evolution of the (002)

FePt diffraction peak, from which we deduce the time-resolved out-of-plane lattice strain of the FePt layer $\eta_\perp(t)$. The samples are excited by p-polarized pump pulses with a duration of 100 fs at a central wavelength of 800 nm, which are incident under 45° relative to the surface normal. The laser spot size of approximately 1.6 mm by 1.3 mm (full width at half maximum) ensures that a homogeneously excited sample area is probed by the x-rays that have rhombical 0.3 mm–by–0.3 mm profile (*39*). The tr-MOKE setup (*34*) uses comparable excitation parameters. For experimental details, see Supplementary Materials. Static x-ray diffraction measurements at different sample temperatures were recorded using a commercial diffraction setup (Rigaku SmartLab 9 kW system).

Sample preparation

A continuous FePt thin film was prepared by magnetron-sputtering Fe and Pt from a composite FePt target onto a substrate preheated to 500°C. Similarly, a granular FePt film was prepared at a slightly higher substrate temperature of 650°C by adding approximately 30 volume % of carbon to the sputtering target. X-ray reflectivity measured the sample thicknesses to be about d = 9.5 nm, where the continuous film is covered with an additional 1-nm layer of oxidized Al (*27*). According to scanning electron microscopy images of similarly prepared samples (see Supplementary Materials), the size distribution of the FePt nanograins segregated in a carbon matrix within the granular film is centered at approximately 8 nm. This nano-morphology yields a very large coercive field of approximately $\mu_0 H$ = 5 T, whereas the coercive field of the continuous film $\mu_0 H$ = 0.4 T is substantially smaller because of the possibility of domain wall motion that cannot occur in the nanogranular samples (*40*). The sample structures are schematically depicted as insets (C) and (D) in Fig. 1, and their properties and the measurement technique have been described in a previous publication (*27*).

FEM modeling

Finite-element simulations were performed using the Structural Mechanics Module of the COMSOL commercial software. It determines the spatiotemporal variations of displacement $u_i(x_1, x_2, x_3, t)$ by the numerical, approximation-free resolution of the continuum mechanics equation of motion in all Cartesian directions x_i

$$\rho\frac{\partial^2 u_i}{\partial t^2} = \sum_{j=1}^{3}\frac{\partial}{\partial x_j}\left(\sum_{k,l=1}^{3} C_{ijkl}\eta_{kl} - \sigma_{ij}^{ext}\right) \text{ with the strain } \eta_{kl} = \frac{1}{2}\left(\frac{\partial u_k}{\partial x_l} + \frac{\partial u_l}{\partial x_k}\right)$$

The simulation system was composed of a FePt cylinder with the radius r = 4 nm and d=10 nm height encapsulated by a cylindrical carbon shell of 2-nm thickness and same height supported on a MgO substrate. Note that the choice of such an axially symmetric geometry allowed us to perform 2D simulations, which are computationally much less expensive than 3D ones. Perfect mechanical contact was assumed at all internal interfaces of the system. Vanishing in-plane displacement was imposed on the lateral surface of the simulation domain, 6 nm away from its symmetry axis, to describe the absence of lateral contraction in films. Stress-free and low-reflecting boundary conditions were, respectively, used at the top of the FePt–carbon film and at the bottom of the MgO substrate.

Table 1. Elastic parameters used in the modeling.

	FePt	C	MgO
ρ (kg/m^3)	14,700	2000	3580
Y (GPa)	237	200	249
ν	0.31	0.2	0.18

FePt elastic anisotropy was neglected, and all materials were described by their density ρ, Young modulus Y, and Poisson ratio ν as listed in Table 1.

The time-dependent displacement fields $u_i(t)$ induced in this system by its sudden excitation were computed in the time domain, and the average out-of-plane strain in FePt $\eta_\perp(t) = \frac{\partial u_z(t)}{\partial z}$ was deduced by spatial integration.

The laser-induced excitation was described by a time-dependent diagonal matrix obtained by summing the contributions of an expansive, anisotropic electron-phonon stress with components $\sigma_{xx}^{e-ph}(t) = \sigma_{yy}^{e-ph}(t) = A^{ani}\sigma_{zz}^{e-ph}(t) = A^{ani}\sigma^{e-pho,0}\left(1 + \left(\frac{\gamma_e}{\gamma_{ph}} - 1\right)e^{-\frac{t}{\tau}}\right)\Theta(t)$ accounting for energy dissipation from electrons to phonons after selective excitation of the former by light (*41*) and an instantaneously rising contractive uniaxial spin stress $\sigma_{zz}^{sp}(t) = \sigma_\perp^{sp,0}\Theta(t)$, where Θ is the Heaviside function. A τ = 1 ps electron-phonon coupling time and a $\frac{\gamma_e}{\gamma_{ph}}$ = 0.3 ratio of electron and phonon Grüneisen constants were used in the modeling. We approximate both the contractive spin stress and the expansive electron stress as instantaneous, i.e., much shorter than the 200 fs time resolution of our UXRD experiment. This is consistent with recent ultrafast electron calorimetry, which has shown that the energy transfer to the spin system in nickel is effective within the first 20 fs (*42*).

SUPPLEMENTARY MATERIALS

Supplementary material for this article is available at http://advances.sciencemag.org/cgi/content/full/6/28/eaba1142/DC1

REFERENCES AND NOTES

1. E. F. Wasserman, Invar: Moment-volume instabilities in transition metals and alloys. *Handbook Ferromagn. Mater.* **5**, 237–322 (1990).
2. C. E. Guillaume, Recherches sur les aciers au nickel. Dilatations aux températures élevées; résistance électrique. *C. R. Acad. Sci.* **125**, 18 (1897).
3. R. J. Weiss, The origin of the `Invar'effect. *Proc. Phys. Soc.* **82**, 281 (1963).
4. M. Van Schilfgaarde, I. A. Abrikosov, B. Johansson, Origin of the invar effect in iron-nickel alloys. *Nature* **400**, 46–49 (1999).
5. S. Khmelevskyi, I. Turek, P. Mohn, Large negative magnetic contribution to the thermal expansion in iron-platinum alloys: Quantitative theory of the invar effect. *Phys. Rev. Lett.* **91**, 037201 (2003).
6. C. Dornes, Y. Acremann, M. Savoini, M. Kubli, M. J. Neugebauer, E. Abreu, L. Huber, G. Lantz, C. A. F. Vaz, H. Lemke, E. M. Bothschafter, M. Porer, V. Esposito, L. Rettig, M. Buzzi, A. Alberca, Y. W. Windsor, P. Beaud, U. Staub, D. Zhu, S. Song, J. M. Glownia, S. L. Johnson, The ultrafast Einstein–de Haas effect. *Nature* **565**, 209–212 (2019).
7. E. Jal, V. López-Flores, N. Pontius, T. Ferté, N. Bergeard, C. Boeglin, B. Vodungbo, J. Lüning, N. Jaouen, Structural dynamics during laser-induced ultrafast demagnetization. *Phys. Rev. B.* **95**, 184422 (2017).
8. A. von Reppert, J. Pudell, A. Koc, M. Reinhardt, W. Leitenberger, K. Dumesnil, F. Zamponi, M. Bargheer, Persistent nonequilibrium dynamics of the thermal energies in the spin and phonon systems of an antiferromagnet. *Struct. Dyn.* **3**, 054302 (2016).
9. J. Pudell, A. von Reppert, D. Schick, F. Zamponi, M. Rössle, M. Herzog, H. Zabel, M. Bargheer, Ultrafast negative thermal expansion driven by spin disorder. *Phys. Rev. B.* **99**, 094304 (2019).
10. C. von Korff Schmising, A. Harpoeth, N. Zhavoronkov, Z. Ansari, C. Aku-Leh, M. Woerner, T. Elsaesser, M. Bargheer, M. Schmidbauer, I. Vrejoiu, D. Hesse, M. Alexe, Ultrafast magnetostriction and phonon-mediated stress in a photoexcited ferromagnet. *Phys. Rev. B.* **78**, 060404 (2008).
11. A. H. Reid, X. Shen, P. Maldonado, T. Chase, E. Jal, P. W. Granitzka, K. Carva, R. K. Li, J. Li, L. Wu, T. Vecchione, T. Liu, Z. Chen, D. J. Higley, N. Hartmann, R. Coffee, J. Wu, G. L. Dakovski, W. F. Schlotter, H. Ohldag, Y. K. Takahashi, V. Mehta, O. Hellwig, A. Fry, Y. Zhu, J. Cao, E. E. Fullerton, J. Stöhr, P. M. Oppeneer, X. J. Wang, H. A. Dürr, Beyond a phenomenological description of magnetostriction. *Nat. Commun.* **9**, 388 (2018).

12. A. Koc, M. Reinhardt, A. von Reppert, M. Rössle, W. Leitenberger, M. Gleich, M. Weinelt, F. Zamponi, M. Bargheer, Grueneisen-approach for the experimental determination of transient spin and phonon energies from ultrafast x-ray diffraction data: Gadolinium. *J. Phys. Condens. Matter* **29**, 264001 (2017).
13. E. Beaurepaire, J.-C. Merle, A. Daunois, J.-Y. Bigot, Ultrafast spin dynamics in ferromagnetic nickel. *Phys. Rev. Lett.* **76**, 4250–4253 (1996).
14. J. Kimling, J. Kimling, R. B. Wilson, B. Hebler, M. Albrecht, D. G. Cahill, Ultrafast demagnetization of FePt:Cu thin films and the role of magnetic heat capacity. *Phys. Rev. B.* **90**, 224408 (2014).
15. T. Kampfrath, A. Sell, G. Klatt, A. Pashkin, S. Mährlein, T. Dekorsy, M. Wolf, M. Fiebig, A. Leitenstorfer, R. Huber, Coherent terahertz control of antiferromagnetic spin waves. *Nat. Photonics* **5**, 31–34 (2011).
16. F. Hansteen, A. Kimel, A. Kirilyuk, T. Rasing, Nonthermal ultrafast optical control of the magnetization in garnet films. *Phys. Rev. B.* **73**, 014421 (2006).
17. J. W. Kim, M. Vomir, J. Y. Bigot, Controlling the spins angular momentum in ferromagnets with sequences of picosecond acoustic pulses. *Sci. Rep.* **5**, 8511 (2014).
18. M. Sander, J. E. Pudell, M. Herzog, M. Bargheer, R. Bauer, V. Besse, V. Temnov, P. Gaal, Quantitative disentanglement of coherent and incoherent laser-induced surface deformations by time-resolved x-ray reflectivity. *Appl. Phys. Lett.* **111**, 261903 (2017).
19. D. C. Heinecke, O. Kliebisch, J. Flock, A. Bruchhausen, K. Köhler, T. Dekorsy, Selective excitation of zone-folded phonon modes within one triplet in a semiconductor superlattice. *Phys. Rev. B* **87**, 075307 (2013).
20. T. Cheng, J. Wu, T. Liu, X. Zou, J. Cai, R. W. Chantrell, Y. Xu, Dual-pump manipulation of ultrafast demagnetization in TbFeCo. *Phys. Rev. B.* **93**, 064401 (2016).
21. K. Bühlmann, R. Gort, G. Salvatella, S. Däster, A. Fognini, T. Bähler, C. Dornes, C. A. F. Vaz, A. Vaterlaus, Y. Acremann, Ultrafast demagnetization in iron: Separating effects by their nonlinearity. *Struct. Dyn.* **5**, 044502 (2018).
22. J. Y. Shi, M. Tang, Z. Zhang, L. Ma, L. Sun, C. Zhou, X. F. Hu, Z. Zheng, L. Q. Shen, S. M. Zhou, Y. Z. Wu, L. Y. Chen, H. B. Zhao, Impact of ultrafast demagnetization process on magnetization reversal in $L1_0$ FePt revealed using double laser pulse excitation. *Appl. Phys. Lett.* **112**, 082403 (2018).
23. G. D. Barrera, J. A. O. Bruno, T. H. K. Barron, N. L. Allan, Negative thermal expansion. *J. Phys. Condens. Matter* **17**, R217–R252 (2005).
24. O. Mosendz, S. Pisana, J. W. Reiner, B. Stipe, D. Weller, Ultra-high coercivity small-grain FePt media for thermally assisted recording (invited). *J. Appl. Phys.* **111**, 07B729 (2012).
25. D. Weller, G. Parker, O. Mosendz, A. Lyberatos, D. Mitin, N. Y. Safonova, M. Albrecht, Review article: FePt heat assisted magnetic recording media. *J. Vac. Sci. Technol.* **34**, 060801 (2016).
26. K. Hono, Y. K. Takahashi, G. Ju, J.-U. Thiele, A. Ajan, X. Yang, R. Ruiz, L. Wan, Heat-assisted magnetic recording media materials. *MRS Bull.* **43**, 93–99 (2018).
27. A. von Reppert, L. Willig, J.-E. Pudell, M. Rössle, W. Leitenberger, M. Herzog, F. Ganss, O. Hellwig, M. Bargheer, Ultrafast laser generated strain in granular and continuous FePt thin films. *Appl. Phys. Lett.* **113**, 123101 (2018).
28. K. Sumiyama, M. Shiga, M. Morioka, Y. Nakamura, Characteristic magnetovolume effects in Invar type Fe-Pt alloys. *J. Phys. F Met. Phys.* **9**, 1665–1677 (1979).
29. Y. Tsunoda, H. Kobayashi, Temperature variation of the tetragonality in ordered PtFe alloy. *J. Magn. Magn. Mater.* **272–276**, 776–777 (2004).
30. R. Nicula, O. Crisan, A. D. Crisan, I. Mercioniu, M. Stir, F. Vasiliu, Thermal stability, thermal expansion and grain-growth in exchange-coupled Fe–Pt–Ag–B bulk nanocomposite magnets. *J. Alloys Compd.* **622**, 865–870 (2015).
31. P. Rasmussen, X. Rui, J. E. Shield, Texture formation in FePt thin films via thermal stress management. *Appl. Phys. Lett.* **86**, 191915 (2005).
32. P. W. Granitzka, E. Jal, L. Le Guyader, M. Savoini, D. J. Higley, T. Liu, Z. Chen, T. Chase, H. Ohldag, G. L. Dakovski, W. F. Schlotter, S. Carron, M. C. Hoffman, A. X. Gray, P. Shafer, E. Arenholz, O. Hellwig, V. Mehta, Y. K. Takahashi, J. Wang, E. E. Fullerton, J. Stöhr, A. H. Reid, H. A. Dürr, Magnetic switching in granular FePt layers promoted by near-field laser enhancement. *Nano Lett.* **17**, 2426–2432 (2017).
33. O. Hovorka, S. Devos, Q. Coopman, W. J. Fan, C. J. Aas, R. F. L. Evans, X. Chen, G. Ju, R. W. Chantrell, The Curie temperature distribution of FePt granular magnetic recording media. *Appl. Phys. Lett.* **101**, 052406 (2012).
34. L. Willig, A. Von Reppert, M. Deb, F. Ganss, O. Hellwig, M. Bargheer, Finite-size effects in ultrafast remagnetization dynamics of FePt. *Phys. Rev. B.* **100**, 224408 (2019).
35. J. M. D. Coey, *Magnetism and Magnetic Materials* (Cambridge Univ. Press, 2012).
36. A. Lyberatos, G. J. Parker, Model of ballistic-diffusive thermal transport in HAMR media. *Jpn. J. Appl. Phys.* **58**, 045002 (2019).
37. T. H. K. Barron, J. G. Collins, G. K. White, Thermal expansion of solids at low temperatures. *Adv. Phys.* **29**, 609–730 (1980).
38. D. Schick, A. Bojahr, M. Herzog, C. von Korff Schmising, R. Shayduk, W. Leitenberger, P. Gaal, M. Bargheer, Normalization schemes for ultrafast x-ray diffraction using a table-top laser-driven plasma source. *Rev. Sci. Instrum.* **83**, 025104 (2012).
39. M. Bargheer, N. Zhavoronkov, R. Bruch, H. Legall, H. Stiel, M. Woerner, T. Elsaesser, Comparison of focusing optics for femtosecond x-ray diffraction. *Appl. Phys. B.* **80**, 715–719 (2005).
40. T. Shima, K. Takanashi, Y. K. Takahashi, K. Hono, Preparation and magnetic properties of highly coercive FePt films. *Appl. Phys. Lett.* **81**, 1050–1052 (2002).
41. A. von Reppert, R. M. Sarhan, F. Stete, J. Pudell, N. Del Fatti, A. Crut, J. Koetz, F. Liebig, C. Prietzel, M. Bargheer, Watching the vibration and cooling of ultrathin gold nanotriangles by ultrafast x-ray diffraction. *J. Phys. Chem. C* **120**, 28894–28899 (2016).
42. P. Tengdin, W. You, C. Chen, X. Shi, D. Zusin, Y. Zhang, C. Gentry, A. Blonsky, M. Keller, P. M. Oppeneer, H. Kapteyn, Z. Tao, M. Murnane, Critical behavior within 20 fs drives the out-of-equilibrium laser-induced magnetic phase transition in nickel. *Sci. Adv.* **4**, eaap9744 (2018).
43. D. Schick, R. Shayduk, A. Bojahr, M. Herzog, C. von Korff Schmising, P. Gaal, M. Bargheer, Ultrafast reciprocal-space mapping with a convergent beam. *J. Appl. Cryst.* **46**, 1372–1377 (2013).

Acknowledgments

Funding: We acknowledge the BMBF for the financial support via 05K16IPA and the DFG via BA 2281/8-1 and BA2281/11-1. Part of the work was carried out with the support of CEITEC Nano Research Infrastructure (MEYS CR, LM2018110). This work has received funding from the European Union's Horizon 2020 research and innovation program under the Marie Skłodowska-Curie program, and it is cofinanced by the South Moravian Region under grant agreement no. 665860. We acknowledge the precharacterization of the crystalline thin films at the XPP-KMC3 synchrotron radiation beamline D13.2 at the BESSY II electron storage ring operated by the Helmholtz-Zentrum Berlin. **Author contributions:** A.v.R. and M.B. conceived the experiment A.v.R., J.-E.P., and S.P.Z. performed the time-resolved x-ray experiments and analysis. F.G., G.S., and O.H. grew and characterized the samples. J.A.A. and V.U. performed and analyzed the T-dependent x-ray diffraction experiment. A.C. performed the FEM simulations. L.W. and A.v.R. performed the MOKE experiments and analysis. A.v.R. and M.B coordinated writing of the paper with contributions from all coauthors. **Competing interests:** The authors declare that they have no competing interests. **Data and materials availability:** All data needed to evaluate the conclusions in the paper are present in the paper and/or the Supplementary Materials. Additional data related to this paper may be requested from the authors.

Submitted 5 November 2019
Accepted 22 May 2020
Published 8 July 2020
10.1126/sciadv.aba1142

Citation: A. von Reppert, L. Willig, J.-E. Pudell, S. P. Zeuschner, G. Sellge, F. Ganss, O. Hellwig, J. A. Arregi, V. Uhlíř, A. Crut, M. Bargheer, Spin stress contribution to the lattice dynamics of FePt. *Sci. Adv.* **6**, eaba1142 (2020).

ScienceAdvances

Spin stress contribution to the lattice dynamics of FePt

A. von Reppert, L. Willig, J.-E. Pudell, S. P. Zeuschner, G. Sellge, F. Ganss, O. Hellwig, J. A. Arregi, V. Uhlír, A. Crut and M. Bargheer

Sci Adv **6** (28), eaba1142.
DOI: 10.1126/sciadv.aba1142

Science Advances (ISSN 2375-2548) is published by the American Association for the Advancement of Science, 1200 New York Avenue NW, Washington, DC 20005. The title *Science Advances* is a registered trademark of AAAS.

Article VI – Supplemental Material

Science Advances
AAAS

advances.sciencemag.org/cgi/content/full/6/28/eaba1142/DC1

Supplementary Materials for

Spin stress contribution to the lattice dynamics of FePt

A. von Reppert, L. Willig, J.-E. Pudell, S. P. Zeuschner, G. Sellge, F. Ganss, O. Hellwig, J. A. Arregi, V. Uhlíř, A. Crut, M. Bargheer*

*Corresponding author. Email: bargheer@uni-potsdam.de

Published 8 July 2020, *Sci. Adv.***6**, eaba1142 (2020)
DOI: 10.1126/sciadv.aba1142

This PDF file includes:

citation fluence dependent strain of ranular and continuous FePt

he fluence series of the time-resolved -ray diffraction using single pulse e citation for both the granular and the continuous FePt film is displayed in figure S1: Figure S1 a) and b) show that the e pansion ma imum increases with increasing fluence. he contractive strain that occurs within the first 2ps that is observed in the granular film saturates at a contraction of appro imately $2 \cdot 10^{-3}$. his threshold behavior already indicates a magnetic origin of the driving stress, as saturation of the spin contribution to the stress is predicted for a full demagneti ation. he bottom panels c) and d) display the data normali ed to the incident fluence as presented in the main te t.

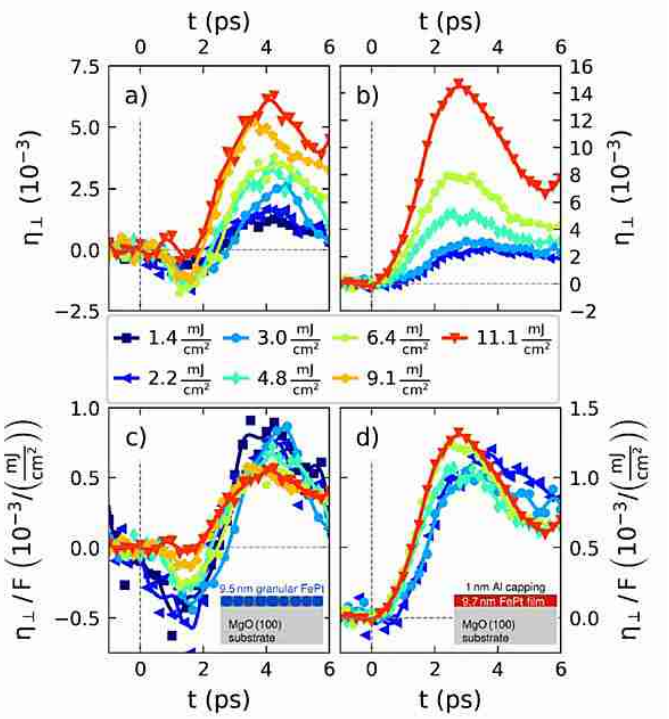

Fi ure S : omparison of the fluence dependent lattice dynamics of the t o FePt thin films after laser e citation a) and b) display the time dependent strain for the granular and continuous FePt film respectively. he data normali ed to fluence are displayed in the low panel c) and d) below, where the insets display the schematic sample structure.

Temperature dependent thermal e pansion of the ranular and continuous FePt thin film

he static diffraction curve as well as the temperature dependent e periments on the FePt thin films that have been conducted on the samples after the time-resolved e periments were finished are depicted in figure S2. he static diffraction e periments were carried out at a Riga u W SmartLab system using a 4-circle goniometer that uses the characteristic Cu-$K_{\alpha 1}$ radiation (λ ($K_{\alpha 1}$) 1.54) of a rotating anode -ray tube for diffraction. he sample was ept in an inert gas atmosphere inside a carbon dome chamber, while it was heated up to 800 . he diffraction curve in Fig S2a) e hibits sharp and intense MgO substrate pea s and smaller diffraction pea s, which can be attributed to

the FePt thin films. In order to e tract the thermal e pansion strain $\eta_{\perp,\mathrm{eq}}$ of the FePt thin films and the MgO substrate, we observed the FePt (002) and the MgO (004) shift as a function of the sample temperature. From similar e periments we e tract the in-plane strain upon e uilibrium heating $\eta_{||,\mathrm{eq}}$ by monitoring the pea shift of the FePt (220) and the MgO (440) diffraction pea .

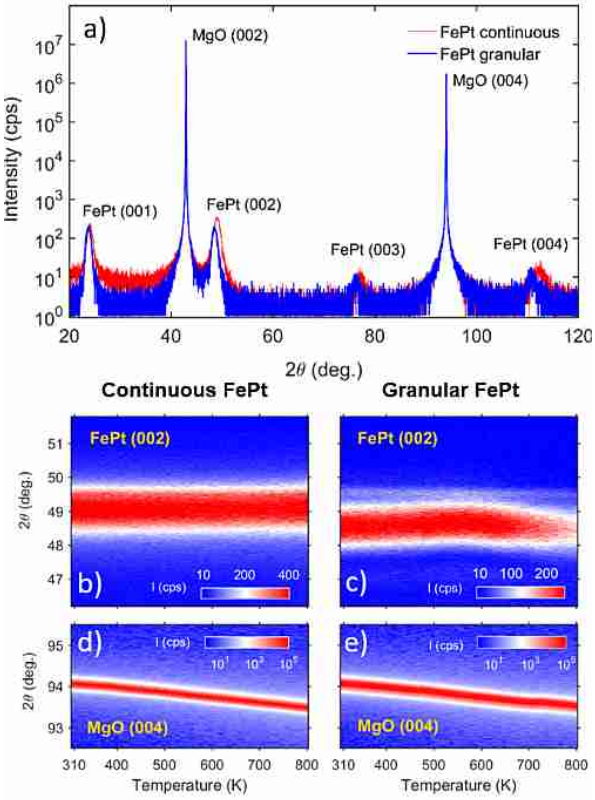

Fi ure S Static ray diffraction results: a) Roc ing curves of the granular and continuous FePt thin films. he temperature dependence for the FePt (002) reflection for the continuous (b)) and the granular(c)) FePt e hibit only a very small shift, whereas the MgO substrates in c) and d) shift considerably to lower diffraction angles. he intensity decrease for the granular FePt above 650 indicates a modification of the structure, which prohibits reliable time-resolved e periments at temperatures above c

he out-of-plane ($\eta_{\perp,\mathrm{eq}}$) and in-plane strains ($\eta_{||,\mathrm{eq}}$) that we obtain from the pea shifts by pea fits to the temperature dependent diffraction data under e uilibrium heating are displayed in figure S . Figure S a) uantifies that the continuous film e hibits invar behavior ($\alpha_{\perp,\mathrm{FePt,cont}} \approx 0$) along the out-of-plane direction from 00 00 whereas the granular FePt e hibits a negative thermal e pansion with an e pansion coefficient of $\alpha_{\perp,\mathrm{FePt,gran,1}} \approx -9 \cdot 10^{-6}\,\frac{1}{\mathrm{K}}$ between 00 and 550 , which switches to a large positive thermal e pansion of $\alpha_{\perp,\mathrm{FePt,gran,2}} \approx 23 \cdot 10^{-6}\,\frac{1}{\mathrm{K}}$ between 580 and 650 . ualitatively similar observations have been made in the magnetovolume effect of FePt alloys with different composition by Sumiyama et al.[28]. Above 650 we observe a decrease of the - ray diffraction pea intensity of the granular FePt film that can be seen in Fig S2c). his

could be due to an irreversible carbon interdiffusion into the sample structure as the pea intensity remains reduced by 15 even after the sample has cooled to room temperature. his illustrates that e periments at elevated temperatures above $T > T_c \approx 700$ modify the sample whereas transient heating above c on a picosecond timescale is reversible since no change of the Bragg pea intensity was observed after laser pulse e citation. he thermal e pansion coefficient e tracted from the MgO (004) pea shift is appro imately $\alpha_{\perp,\mathrm{MgO}} \approx 9.3 \cdot 10^{-6} \frac{1}{\mathrm{K}}$ in reasonable agreement with literature. [1] he in-plane thermal e pansion coefficient of both FePt morphologies that can be e tracted from Figure S b) appro imately matches the thermal e pansion of the MgO substrate $\alpha_{\parallel,\mathrm{FePt}} \approx 9 \cdot 10^{-6} \frac{1}{\mathrm{K}}$.

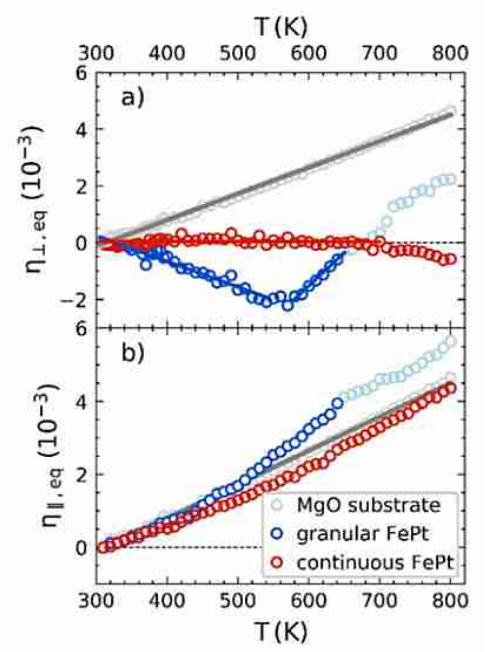

Fi ure S Static thermal e pansion of the ranular and continuous FePt thin film: a) Out-of-plane and b) in-plane strain e tracted from the -dependent pea shifts under e uilibrium heating, where the solid lines indicate linear fits for the thermal e pansion coefficients. he pea center position for a) the FePt (002) / MgO (004) and b) the FePt (220) Bragg pea were obtained by a Gaussian fits to the data from Figure S2.

S ima es of similarly prepared FePt samples

Figure S4 shows a scanning electron micrograph (SEM) image of a similarly prepared granular FePt sample as the one employed in our study. he bright parts are the FePt grains whereas the blac parts correspond to the amorphous carbon. he images illustrate the appro imate si e distribution, which is centered around 8nm islands with an appro imate 2nm carbon separation.

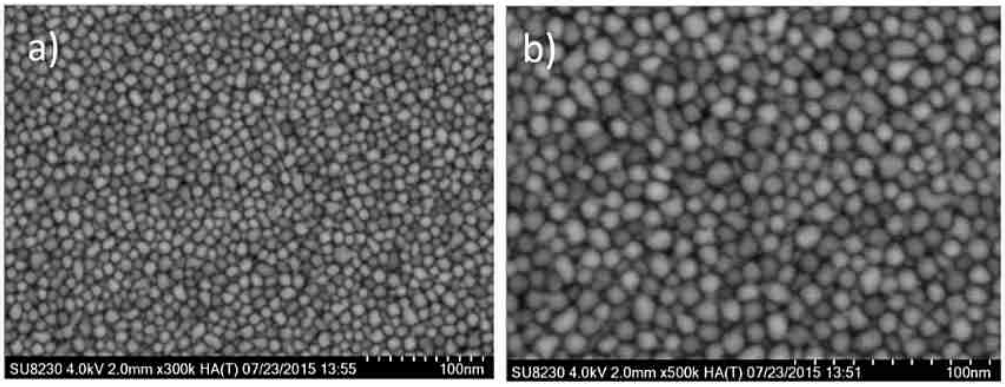

Fi ure S : Scannin lectron icroscope ima es of similarly prepared FePt samples, that illustrate the appro imate si e distribution for the granular specimen studied in the main te t. Bright areas correspond to the FePt islands with an average diameter of appro imately 8nm. he dar spacing in between the grains is due to the carbon nanolayer, which has an average thic ness on the order of 2nm.

F modelin

FEM simulations were performed for both granular and continuous FePt films. o facilitate the comparison with the literature results reported for granular, matri -free FePt films deposited on a EM grid, the ideal case of a free FePt grain was also considered. Figure S5 shows the geometry of the FEM simulations, indicating the boundary conditions used in each case. Vanishing in-plane displacement at the cylinder lateral surface was assumed for continuous films bound to a substrate, while in-plane motion of the FePt surface was allowed in the granular film (at the FePt/C interface) and free nanoparticle cases.

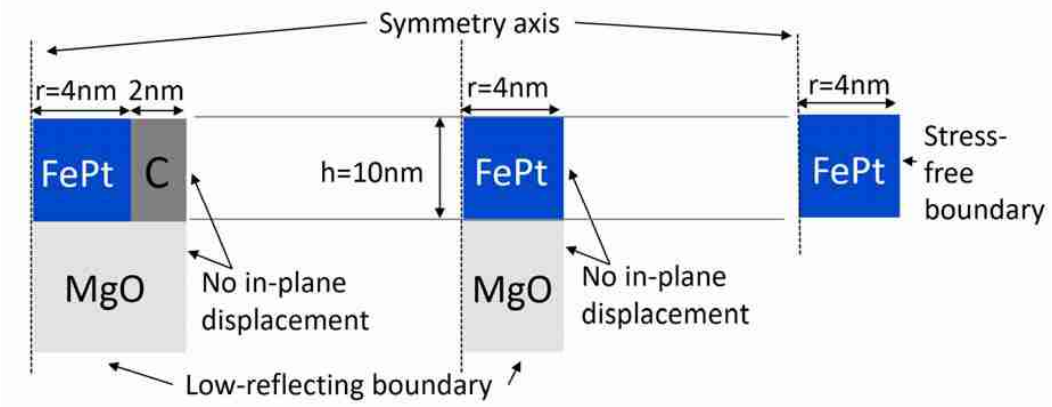

Fi ure S : eometry of the F simulations performed for three different FePt nanosystems: granular film (left), continuous film (middle) and free grain (right).

Fig. S6 shows the results of the FEM simulations for the continuous film (Fig. S6 a b) and for a free FePt grain (Fig. S6 c d), which complement those obtained for the granular film presented in Fig. 5 of the main te t of the paper.

 he simulations performed for the continuous film noticeably show a variation (by about 0.5 ps) with the amplitude of the spin stress contribution of the time at which the strain is ma imal (Fig. S6 b), which is in agreement with e perimental observations (Fig. 1b and S1b). he FEM results obtained for free grains (Fig. S6 d) are in ualitative agreement with the observations reported in the conte t of ultrafast electron-diffraction e periments[11].

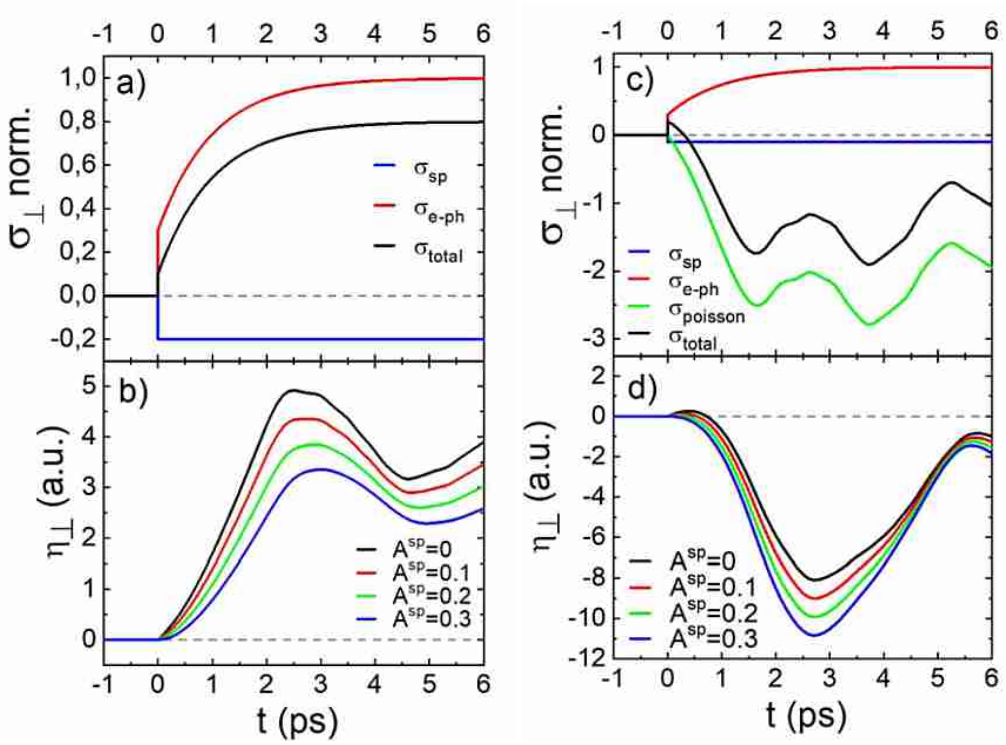

Fi ure S6: F modelin of the mechanical response of a continuous FePt film and a free FePt rain: a) time-dependent out of plane stresses $\sigma_{\perp}(t)$ acting on the FePt film for A^{sp} 0.2 (solid lines). he dashed line shows the ero line corresponding to $\sigma_{sp} = 0$ for A^{sp} 0 b) Average out of plane strain $\eta_{\perp}(t)$ in arbitrary units (a.u.) computed for various ratios A^{sp} of the spin and electron-phonon stress amplitudes. c-d) same a- b) for a free grain.

aser based plasma ray source and femtosecond ray diffractometer

 he principal components of the laser-based femtosecond plasma -ray source (P S) have remained unchanged since their installation nine years ago. [8] he input to the P S are 50 fs laser pulses at a center wavelength of 800 nm with a pulse energy of 5 mJ at 1 H

repetition rate that are focused by a 2 inch 0 off-a is parabolic mirror with a focal length of f 10 cm into a vacuum chamber. At the focus, a 15 m thic Cu band is transported fast enough to offer a fresh spot to each laser pulse impinging at a repetition rate of 1 H . he entrance and e it windows of the chamber are protected from the Cu plasma debris by moving plastic bands. he emitted -rays are focused and monochromati ed to the K_α doublet by a Montel multilayer optic with a convergence of 0. and a focal spot si e of 200 00 m FWHM at a distance d 1000 mm from the P S point source. he -ray pulses contain only about 500-1000 photons per pulse on the sample. ey to the good signal to noise ratio are the gated CMOS 2D pi el detector and a careful optimi ation of the stability of the entire setup including the pump-laser. he -rays are guided through evacuated tubes in order to avoid absorption and scattering by air molecules. he detector rests on the 2Θ arm of the 2-circle goniometer and detects scattered -rays in the vicinity of the selected Bragg reflections, that are evaluated as reciprocal space mapping with a convergent beam[4] .

Each data point in Figs. 1a,b), 2 and too an ac uisition time of about 120 s for the granular film and 0 s for the continuous film.

REFERENCES AND NOTES

1. E. F. Wasserman, Invar: Moment-volume instabilities in transition metals and alloys. *Handbook Ferromagn. Mater.* **5**, 237–322 (1990).

2. C. E. Guillaume, Recherches sur les aciers au nickel. Dilatations aux températures élevées, résistance électrique. *C. R. Acad. Sci.* **125**, 18 (1897).

3. R. J. Weiss, The origin of the 'Invar' effect. *Proc. Phys. Soc.* **82**, 281 (1963).

4. M. Van Schilfgaarde, I. AAbrikosov, B. Johansson, Origin of the invar effect in iron-nickel alloys. *Nature* **400**, 46–49 (1999).

5. S. Khmelevskyi, I. Turek, P. Mohn, Large negative magnetic contribution to the thermal expansion in iron-platinum alloys: Quantitative theory of the invar effect. *Phys. Rev. Lett.* **91**, 037201 (2003).

6. C. Dornes, Y. Acremann, M. Savoini, M. Kubli, M. J. Neugebauer, E. Abreu, L. Huber, G. Lantz, C. A. F. Vaz, H. Lemke, E. M. Bothschafter, M. Porer, V. Esposito, L. Rettig, M. Buzzi, A. Alberca, Y. W. Windsor, P. Beaud, U. Staub, D. Zhu, S. Song, J. M. Glownia, S. L. Johnson, The ultrafast Einstein–de Haas effect. *Nature* **565**, 209–212 (2019).

7. E. Jal, V. López-Flores, N. Pontius, T. Ferté, N. Bergeard, C. Boeglin, B. Vodungbo, J. Lüning, N. Jaouen, Structural dynamics during laser-induced ultrafast demagnetization. *Phys. Rev. B* **95**, 184422 (2017).

8. A. von Reppert, J. Pudell, A. Koc, M. Reinhardt, W. Leitenberger, K. Dumesnil, F. Zamponi, M. Bargheer, Persistent nonequilibrium dynamics of the thermal energies in the spin and phonon sys of an antiferromagnet. *Struct. Dyn.* **3**, 054302 (2016).

9. J. Pudell, A. von Reppert, D. Schick, F. Zamponi, M. Rössle, M. Herzog, H. Zabel, M. Bargheer, Ultrafast negative thermal expansion driven by spin disorder. *Phys. Rev. B* **99**, 094304 (2019).

10. C. von Korff Schmising, A. Harpoeth, N. Zhavoronkov, Z. Ansari, C. Aku-Leh, M. Woerner, T. Elsaesser, M. Bargheer, M. Schmidbauer, I. Vrejoiu, D. Hesse, M. Alexe, Ultrafast magnetostriction and phonon-mediated stress in a photoexcited ferromagnet. *Phys. Rev. B* **78**, 060404 (2008).

11. A. H. Reid, X. Shen, P. Maldonado, T. Chase, E. Jal, P. W. Granitzka, K. Carva, R. K. Li, J. Li, L. Wu, T. Vecchione, T. Liu, Z. Chen, D. J. Higley, N. Hartmann, R. Coffee, J. Wu, G. L. Dakovski, W. F. Schlotter, H. Ohldag, Y. K. Takahashi, V. Mehta, O. Hellwig, A. Fry, Y. Zhu, J. Cao, E. E. Fullerton, J. Stöhr, P. M. Oppeneer, X. J. Wang, H. A. Dürr, Beyond a phenomenological description of magnetostriction. *Nat. Commun.* **9**, 388 (2018).

12. A. Koc, M. Reinhardt, A. von Reppert, M. Rössle, W. Leitenberger, M. Gleich, M. Weinelt, F. Zamponi, M. Bargheer, Grueneisen-approach for the experimental determination of transient spin phonon energies from ultrafast x-ray diffraction data: Gadolinium. *J. Phys. Condens. Matter* **29**, 264001 (2017).

13. E. Beaurepaire, J.-C. Merle, A. Daunois, J.-Y. Bigot, Ultrafast spin dynamics in ferromagnetic nickel. *Phys. Rev. Lett.* **76**, 4250–4253 (1996).

14. J. Kimling, J. Kimling, R. B. Wilson, B. Hebler, M. Albrecht, D. G. Cahill, Ultrafast demagnetization of FePt:Cu thin films and the role of magnetic heat capacity. *Phys. Rev. B* **90**, 224408 (2014).

15. T. Kampfrath, A. Sell, G. Klatt, A. Pashkin, S. Mährlein, T. Dekorsy, M. Wolf, M. Fiebig, A. Leitenstorfer, R. Huber, Coherent terahertz control of antiferromagnetic spin waves. *Nat. Photonics* **5**, 31–34 (2011).

16. F. Hansteen, A. Kimel, A. Kirilyuk, T. Rasing, Nonthermal ultrafast optical control of the magnetization in garnet films. *Phys. Rev. B* **73**, 014421 (2006).

17. J. W. Kim, M. Vomir, J. Y. Bigot, Controlling the spins angular momentum in ferromagnets with sequences of picosecond acoustic pulses. *Sci. Rep.* **5**, 8511 (2014).

18. M. Sander, J. E. Pudell, M. Herzog, M. Bargheer, R. Bauer, V. Besse, V. Temnov, P. Gaal, Quantitative disentanglement of coherent and incoherent laser-induced surface deformations by time-resolved x-ray reflectivity. *Appl. Phys. Lett.* **111**, 261903 (2017).

19. D. C. Heinecke, O. Kliebisch, J. Flock, A. Bruchhausen, K. Köhler, T. Dekorsy, Selective excitation of zone-folded phonon modes within one triplet in a semiconductor superlattice. *Phys. Rev. B* **87**, 075307 (2013).

20. T. Cheng, J. Wu, T. Liu, X. Zou, J. Cai, R. W. Chantrell, Y. Xu, Dual-pump manipulation of ultrafast demagnetization in TbFeCo. *Phys. Rev. B* **93**, 064401 (2016).

21. K. Bühlmann, R. Gort, G. Salvatella, S. Däster, A. Fognini, T. Bähler, C. Dornes, C. A. F. Vaz, A. Vaterlaus, Y. Acremann, Ultrafast demagnetization in iron: Separating effects by their nonlinearity. *Struct. Dyn.* **5**, 044502 (2018).

22. J. Y. Shi, M. Tang, Z. Zhang, L. Ma, L. Sun, C. Zhou, X. F. Hu, Z. Zheng, L. Q. Shen, S. M. Zhou, Y. Z. Wu, L. Y. Chen, H. B. Zhao, Impact of ultrafast demagnetization process on magnetization reversal in $L1_0$ FePt revealed using double laser pulse excitation. *Appl. Phys. Lett.* **112**, 082403 (2018).

23. G. D. Barrera, J. A. O. Bruno, T. H. K. Barron, N. L. Allan, Negative thermal expansion. *J. Phys. Condens. Matter* **17**, R217–R252 (2005).

24. O. Mosendz, S. Pisana, J. W. Reiner, B. Stipe, D. Weller, Ultra-high coercivity small-grain FePt media for thermally assisted recording (invited). *J. Appl. Phys.* **111**, 07B729 (2012).

25. D. Weller, G. Parker, O. Mosendz, A. Lyberatos, D. Mitin, N. Y. Safonova, M. Albrecht, Review article: FePt heat assisted magnetic recording media. *J. Vac. Sci. Technol. B* **34**, 060801 (2016).

26. K. Hono, Y. K. Takahashi, G. Ju, J.-U. Thiele, A. Ajan, X. Yang, R. Ruiz, L. Wan, Heat-assisted magnetic recording media materials. *MRS Bull.* **43**, 93–99 (2018).

27. A. von Reppert, L. Willig, J.-E. Pudell, M. Rössle, W. Leitenberger, M. Herzog F. Ganss, O. Hellwig, M. Bargheer, Ultrafast laser generated strain in granular and continuous FePt thin films. *Appl. Phys. Lett.* **113**, 123101 (2018).

28. K. Sumiyama, M. Shiga, M. Morioka, Y. Nakamura, Characteristic magnetovolume effects in Invar type Fe-Pt alloys. *J. Phys. F Met. Phys.* **9**, 1665–1677 (1979).

29. Y. Tsunoda, H. Kobayashi, Temperature variation of the tetragonality in ordered PtFe alloy. *J. Magn. Magn. Mater.* **272–276**, 776–777 (2004).

30. R. Nicula, O. Crisan, A. D. Crisan, I. Mercioniu, M. Stir, F. Vasiliu, Thermal stability, thermal expansion and grain-growth in exchange-coupled FePt–Ag–B bulk nanocomposite magnets. *J. Alloys Compd.* **622**, 865–870 (2015).

31. P. Rasmussen, X. Rui, J. E. Shield, Texture formation in FePt thin films via thermal stress management. *Appl. Phys. Lett.* **86**, 191915 (2005).

32. P. W. Granitzka, E. Jal, L. Le Guyader, M. Savoini, D. J. Higley, T. Liu, Z. Chen, T. Chase, H. Ohldag, G. L. Dakovski, W. F. Schlotter, S. Carron, M. C. Hoffman, A. X. Gray, P. Shafer, E. Arenholz, O. Hellwig, V. Mehta, Y. K. Takahashi, J. Wang, E. E. Fullerton, J. Stöhr, A. H. Reid, H. A. Dürr, Magnetic switching in granular FePt layers promoted by near-field laser enhancement. *Nano Lett.* **17**, 2426–2432 (2017).

33. O. Hovorka, S. Devos, Q. Coopman, W. J. Fan, C. J. Aas, R. F. L. Evans, X. Chen, G. Ju, R. W. Chantrell, The Curie temperature distribution of FePt granular magnetic recording media. *Appl. Phys. Lett.* **101**, 052406 (2012).

34. L. Willig, A. Von Reppert, M. Deb, F. Ganss, O. Hellwig, M. Bargheer, Finite-size effects in ultrafast remagnetization dynamics of FePt. *Phys. Rev. B* **100**, 224408 (2019).

35. J. M. D. Coey, *Magnetism and Magnetic Materials* (Cambridge Univ. Press, 2012).

36. A. Lyberatos, G. J. Parker, Model of ballistic-diffusive thermal transport in HAMR media. *Jpn. J. Appl. Phys.* **58**, 045002 (2019).

37. T. H. K. Barron, J. G. Collins, G. K. White, Thermal expansion of solids at low temperatures. *Adv. Phys.* **29**, 609–730 (1980).

38. D. Schick, A. Bojahr, M. Herzog, C. von Korff Schmising, R. Shayduk, W. Leitenberger, P. Gaal, M. Bargheer, Normalization schemes for ultrafast x-ray diffraction using a table-top laser-driven plasma source. *Rev. Sci. Instrum.* **83**, 025104 (2012).

39. M. Bargheer, N. Zhavoronkov, R. Bruch, H. Legall, H. Stiel, M. Woerner, T. Elsaesser, Comparison of focusing optics for femtosecond x-ray diffraction. *Appl. Phys. B* **80**, 715–719 (2005).

40. T. Shima, K. Takanashi, Y. K. Takahashi, K. Hono, Preparation and magnetic properties of highly coercive FePt films. *Appl. Phys. Lett.* **81**, 1050–1052 (2002).

41. A. von Reppert, R. M. Sarhan, F. Stete, J. Pudell, N. Del Fatti, A. Crut, J. Koetz, F. Liebig, C. Prietzel, M. Bargheer, Watching the vibration and cooling of ultrathin gold nanotriangles by ultrafas x-ray diffraction *J. Phys. Chem. C*, **120**, 28894–28899 (2016).

42. P. Tengdin, W. You, C. Chen, X. Shi, D. Zusin, Y. Zhang, C. Gentry, A. Blonsky, M. Keller, P. M. Oppeneer, H. Kapteyn, Z. Tao, M. Murnane, Critical behavior within 20 fs drives the out-of-equilibrium laser-induced magnetic phase transition in nickel. *Sci. Adv.* **4,** eaap9744 (2018).

43. D. Schick, R. Shayduk, A. Bojahr, M. Herzog, C. von Korff Schmising, P. Gaal, M. Bargheer, Ultrafast reciprocal-space mapping with a convergent beam. *J. Appl. Cryst.* **46**, 1372–1377 (2013).

Article VII

Unconventional picosecond strain pulses resulting from the saturation of magnetic stress within a photoexcited rare-earth layer

Alexander von Reppert, Maximilian Mattern, Jan-Etienne Pudell, Steffen Peer Zeuschner, Karine Dumesnil, and Matias Bargheer

Structural Dynamics 7, 024303 (2020)

We present a picosecond ultrasonics study that employs time-resolved x-ray diffraction to measure the strain of a transducer with a strongly spin-dependent lattice response. The detection of the strain in a layer adjacent to the transducer allows for a separation of the generated strain pulses and the thermal expansion in the time domain. Both contributions are affected significantly by energy transfer processes to magnetic excitations within the (anti)-ferromagnetic transducer. We model the observed response in order to extract a spatio-temporal evolution of the contractive magnetic stress that acts in addition to the expansive electron-phonon stresses extracted from the paramagnetic material response. The magnetic stress contribution is found to rise on the same timescales that were previously observed in demagnetization experiments of heavy rare-earth materials. The addition of saturation effects in the energy deposition and heat diffusion within the magnetic transducer are key to model the experimental results. Our findings indicate that the magnetic excitations act as a saturable heat reservoir that generates substantial contractive stress. This could be further developed into a tunable, opto-mechanical transducer, if a selective excitation of the spin system is achieved.

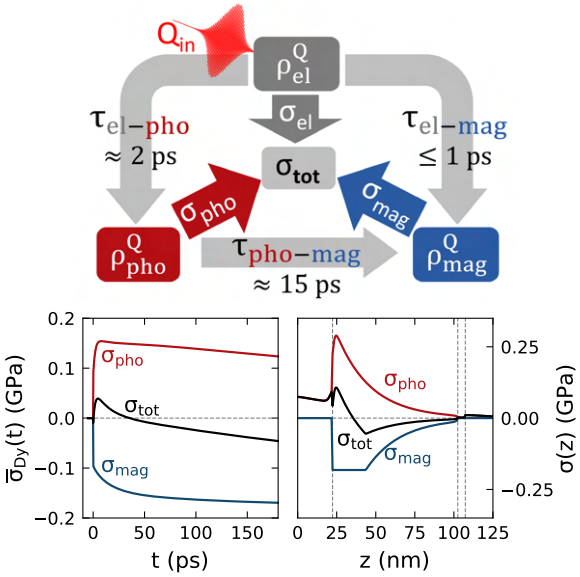

Structural Dynamics

Unconventional picosecond strain pulses resulting from the saturation of magnetic stress within a photoexcited rare earth layer

Cite as: Struct. Dyn. **7**, 024303 (2020); https://doi.org/10.1063/1.5145315
Submitted: 17 January 2020 . Accepted: 09 March 2020 . Published Online: 27 March 2020

A. von Reppert, M. Mattern, J.-E. Pudell, S. P. Zeuschner, K. Dumesnil, and M. Bargheer

Structural Dynamics ARTICLE scitation.org/journal/sdy

Unconventional picosecond strain pulses resulting from the saturation of magnetic stress within a photoexcited rare earth layer

Cite as: Struct. Dyn. **7**, 024303 (2020); doi: 10.1063/1.5145315
Submitted: 17 January 2020 · Accepted: 9 March 2020 ·
Published Online: 27 March 2020

A. von Reppert,[1] M. Mattern,[1] J.-E. Pudell,[1,2] S. P. Zeuschner,[1,2] K. Dumesnil,[3] and M. Bargheer[1,2,a)]

AFFILIATIONS

[1]Institut für Physik & Astronomie, Universität Potsdam, Karl-Liebknecht-Str. 24-25, 14476 Potsdam, Germany
[2]Helmholtz Zentrum Berlin, Albert-Einstein-Str. 15, 12489 Berlin, Germany
[3]Institut Jean Lamour (UMR CNRS 7198), Université Lorraine, 54000 Nancy, France

[a)]**Author to whom correspondence should be addressed:** bargheer@uni-potsdam.de

ABSTRACT

Optical excitation of spin-ordered rare earth metals triggers a complex response of the crystal lattice since expansive stresses from electron and phonon excitations compete with a contractive stress induced by spin disorder. Using ultrafast x-ray diffraction experiments, we study the layer specific strain response of a dysprosium film within a metallic heterostructure upon femtosecond laser-excitation. The elastic and diffusive transport of energy to an adjacent, non-excited detection layer clearly separates the contributions of strain pulses and thermal excitations in the time domain. We find that energy transfer processes to magnetic excitations significantly modify the observed conventional bipolar strain wave into a unipolar pulse. By modeling the spin system as a saturable energy reservoir that generates substantial contractive stress on ultrafast timescales, we can reproduce the observed strain response and estimate the time- and space dependent magnetic stress. The saturation of the magnetic stress contribution yields a non-monotonous total stress within the nanolayer, which leads to unconventional picosecond strain pulses.

I. INTRODUCTION

Experiments that probe the strain response of the atomic lattice that results from the light-matter interaction of a femtosecond optical pulse with an opto-acoustic transducer material can be subsumed as picosecond ultrasonics.[1,2] They yield fundamental insights into physical processes within the laser-excited thin film, such as electron-phonon coupling,[3–5] hot electron propagation,[6,7] and electron–hole pair generation.[8,9] This is possible because the lattice strain is the deterministic, elastic response to a physical stress that itself contains the time- and length-scales of the energy transfer processes within the transducer region. Research in this field has developed from studying the elementary processes in metals[3,4] and semiconductors[8,10] to the point that various thermal and non-thermal mechanisms for the stress generation have been distinguished.[11]

Picosecond ultrasonics within magnetic materials offers a route to study spin-lattice interactions in the time domain. An additional motivation comes from the prospect that strain assisted magnetization manipulation could lead to faster, potentially field-free data storage techniques, with increased storage densities.[12,13] Recent experiments have shown that electronically generated surface-acoustic-waves are able to switch the magnetization by nanosecond strain pulses.[14,15] Precession of the magnetization due to traversing picosecond strain pulses that transiently modify the crystal field anisotropy has been observed in many common and technologically relevant magnets such as nickel,[16,17] GaMnAs,[18,19] galfenol,[20] and doped yttrium–iron–garnet.[21,22] The inverse effect, i.e., lattice stress that originates from the change of the magnetic state, is less explored by time-resolved investigations although examples, such as the metamagnetic phase-transition in FeRh[23,24] and the change in the tetragonality of FePt[25,26] and $SrRuO_3$,[27] exist. For static and low frequency applications, it is known that metallic, magnetostrictive transducers complement the frequently used piezoelectric ceramics with the advantage of increased conductivity and ductility.[28] The class of heavy rare earth elements exhibits an exceptionally large magnetostriction[29] where the stress that can be generated by spin disorder is not only contractive but also dominates over the expansive phonon contribution as we have confirmed by

Structural Dynamics ARTICLE scitation.org/journal/sdy

probing the structural response of laser-excited gadolinium,[30] holmium,[31] and dysprosium (Dy).[32,33] Ultrafast x-ray diffraction (UXRD) is a suitable tool for quantitatively probing the strain generation and propagation as well as the accompanying heat flow in crystalline heterostructures that are either inseparable or potentially opaque to all-optical probing schemes.[34–36]

Here, we present the ultrafast lattice response of a laser-excited Dy thin film within a metallic heterostructure, where we use a buried niobium (Nb) layer for separating strain pulses from the lattice expansion that results from heat diffusion. We systematically analyze the lattice dynamics as a function of the temperature-dependent magnetic order and the laser excitation energy density. The strain-pulse observed in the Nb detection layer changes upon cooling well below $T_{Néel}$ from a bipolar compression-expansion feature that is characteristic of a fast expansive stress to an almost unipolar expansion that results from a slowly rising contractive stress within the transducer. By modeling the strain response of the heterostructure, we obtain separated spatio-temporal stress-profiles for both the expansive phonon stress and the contractive magnetic stress. The stress within the Dy layer changes from expansive to contractive because the energy conversion to the spin system is saturated only in the strongly excited near surface region. To reproduce the observed low-temperature strain-response within a one dimensional elastic model, we have to assume a contractive stress contribution that rises nearly instantaneously and counteracts the quasi-instantaneous expansive, thermoelastic stress from hot phonons and electrons. In addition, a second contractive contribution is needed that rises with an ≈15 ps time constant. These timescales match the sub-picosecond electron-spin coupling and the subsequent phonon-spin coupling that were reported by previous demagnetization experiments in heavy rare earth elements.[37–39] For high excitation densities, we observe an additional increase in the spin-stress on a longer timescale. We attribute this to phonon mediated energy transport processes from surface-near regions of complete demagnetization to regions with partial magnetic order deeper in the sample, which have been photoexcited less. The energy transfer to the magnetic system removes energy from the phonon system. The storage of heat in spin disorder in Dy is documented by a reduced thermal expansion of the buried Nb detection layer, which only accepts heat from electrons and phonons.

The presented experiments extend our previous works[32,33] that mainly discuss the evolution of the average Dy layer strain on timescales $t > 45$ ps, by an analysis of the initial picosecond strain response for $t < 180$ ps. The main experimental novelty is the use of a dedicated non-magnetic and non-excited detection layer that allows for a clear separation of elastic waves and thermal expansion following the diffusion of heat. In addition, we now discuss a spatially resolved model for the magnetic stress evolution and its saturation within the Dy layer, which is at the origin of the unconventional picosecond strain response.

This paper consists of three main parts: in Sec. II, we present the sample characterization and the temperature dependent lattice expansion of the transducer and detection layer and introduce the concept of Grüneisen constants that are central to the following analysis. Section III contains the main experimental findings on the temperature and excitation energy dependent strain within the transducer and detection layer studied by UXRD. Section IV is devoted to the modeling of the spatiotemporal stress profile and corroborates the experimental findings.

II. STATIC PROPERTIES

In the following, we provide a brief overview over the relevant properties that are later probed by time-resolved experiments. We depict a representative x-ray diffraction pattern and discuss the material specific thermal expansion response that shows fingerprints of the magnetic phase-transition within the Dy layer. We introduce the thermodynamic concept of a Grüneisen constant that relates the energy density for phonons and magnetic excitations to their stress on the crystal lattice.

A. Sample characterization by x-ray diffraction

The static and temperature dependent characterization of the Dy sample by x-ray diffraction is provided in Fig. 1. In the inset of Fig. 1(b), we display a schematic of the investigated metallic heterostructure. It consists of a 80 nm (0001)-oriented Dy transducer layer grown in between two yttrium (Y) hcp-(0001) layers (22 nm on top of and 5 nm below Dy) on-top of a 102 nm niobium (Nb) body centered cubic (110)-oriented film that enables the crystalline growth on a sapphire (Al_2O_3) hcp-(11–20) substrate[40] and serves as an additional strain detection layer. X-ray diffraction, using a microfocus Cu − K_α radiation source, yields a reciprocal space projection that is depicted in Fig. 1(c), where the four different diffraction maxima that correspond to the material specific lattice constants are clearly separated along the out-of-plane reciprocal-space coordinate q_z. These Bragg-peaks are seen as diffraction intensity maxima in Fig. 1(a), where we show the

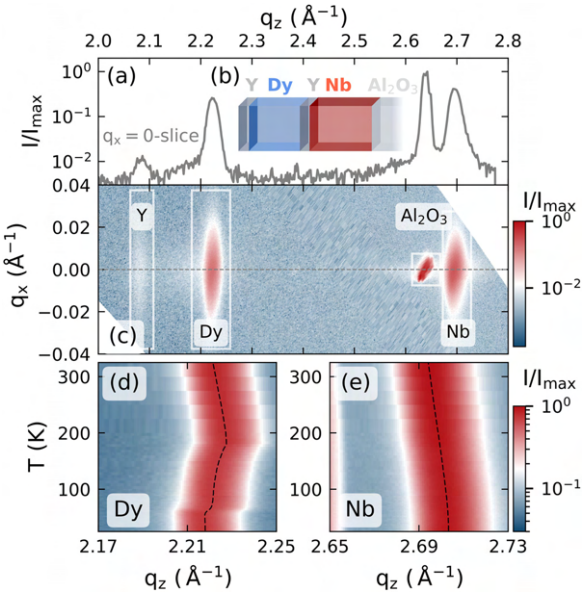

FIG. 1. Static x-ray diffraction results: (a) x-ray diffraction intensity of the sample structure that is schematically depicted in the inset (b). The material specific Bragg peaks are labeled in the reciprocal space map shown in (c). The temperature dependent peak-shifts that contrast the negative thermal expansion in the FM and AFM phase of dysprosium to the monotonous peak shift of the PM niobium are depicted in (d) and (e), respectively.

Structural Dynamics ARTICLE scitation.org/journal/sdy

slice of the reciprocal space at $q_x = 0$. In the main experiments, we observe the time-dependent shift of the Dy and Nb diffraction peaks after laser-excitation and extract the resulting average lattice strain η of these materials in a laser-pump, x-ray diffraction-probe scheme, with a time-resolution of approximately 200 fs as described previously.[35,41,42]

An important reference for our interpretation of the lattice response upon laser-excitation is the equilibrium thermal expansion and contraction during heating of the sample structure. The temperature dependent peak-shift that we extract by heating from 25 K to 350 K is depicted in Figs. 1(d) and 1(e) for Dy and Nb, respectively, where the dashed lines indicate the peak center positions as obtained by Gaussian fits. The monotonous shift of the niobium peak to smaller q_z represents the common positive thermal expansion behavior. This contrasts with the thermal expansion seen in the dysprosium peak that exhibits a pronounced negative thermal expansion (NTE) between 40 K and 180 K as well as a change between expansion and contraction at 180 K.

B. Temperature-dependent material properties

The temperature dependent lattice strain $\eta = (c(T) - c_0)/c_0$ of the c-axis with $c_0 = c(T = 250\,\mathrm{K})$ in the hcp unit cell of the investigated thin Dy film is depicted in Fig. 2. For comparison, we relate it to the lattice constant change[43] [Fig. 2(a)] and to the heat capacity[44] of bulk Dy [Fig. 2(b)]. Changes in the thermal expansion are known to coincide with changes within the magnetic order and magnetic

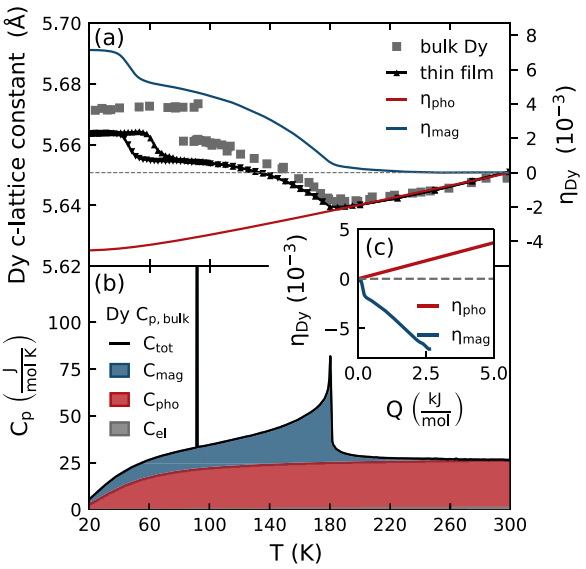

FIG. 2. Subsystem separation of (a) the static strain and (b) heat capacity contributions in Dy: The temperature-dependent c-axis of Dy and the heat capacity show a pronounced change at the AFM-PM phase transition at $T_{Néel} \approx 180$ K. The FM-AFM phase transition that occurs at $T_{Curie} \approx 90$ K for bulk Dy is shifted to lower temperatures in the used thin film sample. The inset in (c) shows the strain per deposited energy, which results from the separation of the strain and heat capacity into the contributions of phonon and spin excitations, which are indicated in red and blue, respectively.

contributions to the strain can exceed 10^{-3}.[29,45] Elemental Dy has one of the highest magnetic moments of 10.64 μ_B per atom, which order ferromagnetically (FM) below $T_{Curie,bulk} \approx 90$ K and antiferromagnetically (AFM) between T_{Curie} and $T_{Néel} \approx 180$ K above which Dy becomes paramagnetic (PM).[46–48] The large magnetic moment originates mainly from the localized magnetic moments of the partially filled 4*f*-electron orbitals that interact via the delocalized 5d6s-conduction band electrons by the Ruderman -Kittel -Kasuya -Yosida (RKKY)-mechanism.[47,48] The magnetic easy axis in the FM phase lies along the *a*-axis in the basal plane of the hexagonal unit cell and the AFM phase exhibits a helical spin ordering that is characterized by a finite turn angle between the magnetic moments for neighboring unit cells along the *c*-axis direction.[46]

Magnetostriction in rare earth elements is often discussed within the so-called standard model of magnetostriction pioneered by Callen and Callen.[49,50] This formalism takes both single-ion and two-ion interactions into account.[50,51] Single-ion contributions originate from the interaction of the crystal field with the anisotropic 4*f*-orbitals, which leads to a lattice deformation upon magnetization change due to the intrinsic spin–orbit coupling.[51,52] The case of vanishing orbital momentum, that is realized in Gadolinium, demonstrates the importance of the exchange-striction mechanism that explains the occurrence of magnetostriction even for spherically symmetric charge distributions.[51] Exchange-striction is a two-ion contribution that originates from a distance-dependent magnetic interaction energy (here provided by the oscillatory RKKY-interaction[53]) that in turn affects the equilibrium position of the magnetic ions based on their alignment.[51,52] A unified, potentially even microscopic model that explains the temperature and field dependent magnetostriction for the entire class of heavy rare earth elements does not exist.[51,52]

C. Grüneisen concept

In the discussion of the time-resolved strain, we employ a macroscopic, thermodynamic approach that approximates the laser-generated stresses to be directly proportional to the energy densities deposited in the corresponding subsystems. We introduce the main idea at first for the static thermal expansion of Dy. The origin of our approach dates back to 1912 when Grüneisen recognized that the contributions of the lattice vibrations to the volumetric thermal expansion coefficient $\beta(T)$ of elemental solids and their heat capacity $C_V(T)$ at constant volume V share the same temperature dependence, so that their ratio can be simplified to a dimensionless, nearly temperature-independent parameter.[54] The concept of this Grüneisen constant Γ has been employed continuously and was further generalized for the discussion of the thermal expansion in solids.[55–57] The thermodynamic derivation yields the macroscopic Γ as[55]

$$\Gamma = KV\frac{\beta(T)}{C_V(T)}, \tag{1}$$

wherein K represents the bulk modulus. This approach can be extended to account for different excitations that contribute energy reservoirs r in a solid by introducing dedicated Γ_r.[55] The generalization to the case of anisotropic expansion requires the use of anisotropic linear thermal expansion coefficients $\alpha_i(T)$ and anisotropic Grüneisen constants Γ_i as well as the proper directional elastic constants c_{ij} (Ref. 55) as exemplified for the rare earth Holmium.[58] For simplicity,

Structural Dynamics ARTICLE scitation.org/journal/sdy

we consider the elastic strain response to be purely one-dimensional. This is justified if the probed region is homogeneously excited along the lateral dimension, so that its picosecond response shows no in-plane strain. We thus limit the discussion to the out-of-plane response of the materials so that we will drop the directional indices for the out-of-plane stress $\sigma_3 = c_{33}\eta_3$ in the following. For sufficiently small ΔT, Eq. (1) can be transformed to the linear relation

$$\sigma_r = \Gamma_r \rho_r^Q \tag{2}$$

between the stress σ_r and the laser-induced energy density $\rho_r^Q(\Delta T) = \int_T^{T+\Delta T} C_r(T')\mathrm{d}T'$, wherein the subscript, r, denotes one of the energy reservoirs. For the case of Dy, we separate the total strain response to stress contributions from electronic excitations (r = el), phonons (r = pho), and magnetic excitations (r = mag).

In Fig. 2, we demonstrate the separation of the subsystem contributions to the equilibrium lattice strain and heat capacity in Dy from which we subsequently extract the ratio of the Grüneisen parameters for the combined electron-phonon and magnetic excitations. Using the heat capacity of the chemically equivalent non-magnetic heavy rare earth Lutetium, scaled according to the Debye temperature of Dy, provides an estimate for the combined electron and phonon contribution to the specific heat.[59] This is indicated by the red shading in Fig. 2(b). The estimated electronic contribution to the heat capacity C corresponds to the very small gray shaded area in Fig. 2(b), which we obtain from a Sommerfeld model [$C_{el} = \gamma_{Dy} T$ with $\gamma_{Dy} = 4.9$ mJ/(mol K)].[60] Electronic excitations thus only store a sizeable energy fraction at high electron temperatures that are attained only directly after laser-excitation. For that reason, we label the combined electron-phonon subsystem in the following as phonon contribution (r = pho) unless stated otherwise.

Assuming a constant Grüneisen parameter for the phonon contribution, we obtain an estimate for the thermal expansion of non-magnetic Dy (η_{pho}) that we represent by the red line in Fig. 2(a). By subtracting η_{pho} and C_{pho} from the measured lattice strain and the combined heat capacity, we obtain the contribution of magnetic excitations to the strain and heat capacity, which are indicated by the blue line in Fig. 2(a) and blue shaded area in Fig. 2(b), respectively. From this separation, we can directly extract the strain per deposited energy for the phonon and magnetic subsystem, which is displayed in the inset in Fig. 2(c). Indeed, the linear slope of the magnetic strain in Fig. 2(c) reconfirms the linear relation of stress and energy density of Eq. (2) for the spin system. The linear strain-energy-density relation for the phonon strain is in agreement with previous analysis of the thermal expansion of solids[55,61] and in particular, the non-magnetic rare earth Lutetium[62] where Grüneisen parameters Γ are found that are nearly constant over an extended range of temperatures even when $C(T)$ and $\beta(T)$ are T-dependent. Recently, this was extended to the separated magnetic and nonmagnetic contributions of the thermal expansion of Dy.[32,33] The slope of the resulting curves is proportional to the Grüneisen parameter since the relevant elastic constant c_{33} changes by less than 10% across the displayed temperature region.[63] The ratio of the Grüneisen constants $\Gamma_{mag}/\Gamma_{pho} \approx -3$ indicates that magnetic excitations in Dy are three times more efficient in the stress generation per deposited energy as compared to phonons.

As opposed to the AFM-PM transition that is of second order, the FM-AFM transition is a first order phase transition with a latent heat of 50.7 J/mol.[44] In our thin film sample, we see that this phase transition occurs between 60 K and 75 K upon heating. We attribute the shift and broadening of the phase transition to epitaxial strains. The FM-AFM phase transition leads to orthorhombic in-plane distortions that are clamped near the interfaces. Since a measurement of the temperature-dependent heat capacity of the Dy transducer within our heterostructure is not possible, we can only specify that the observed negative strain per deposited energy of the spin system is potentially even larger in the region of the FM-AFM transition. Note, however, that this contraction results mainly from the FM-AFM phase transition, since within the FM phase the lattice expands for rising temperatures.

The presented subsystem separation can be applied to gadolinium[30] and holmium,[31] which exhibit similarly large negative Grüneisen parameters for magnetic excitations. Heavy rare earth metals are an interesting class of materials for lattice dynamics since their magnetic heat capacity C_{mag} and the associated entropy of magnetic excitations $\delta S_{mag} = \Delta Q_{mag}/T$ are comparable to the phonon contribution over a large temperature region.[31,55,58] This renders Dy a suitable candidate for experiments that investigate the magnetic contributions, that lead to the NTE response, within a time-resolved experiment.

III. TIME-RESOLVED EXPERIMENTS

The main experimental results of our study are summarized in Figs. 3 and 4, which display representative picosecond strain responses for both the Dy transducer and the buried Nb detection layer at different starting temperatures T and excitation energy densities F. In our UXRD experiments, the sample is subjected to 110 fs-long, p-polarized laser pulses with a central wavelength of 800 nm at a repetition rate of 1 kHz. The laser excitation profile corresponds to a 2D-Gaussian contour with approximately $1.6 \times 1.2\,\mathrm{mm}^2$ full width at half maximum along its principal axis. The optical pump-pulses are incident under 36° for measuring the Dy response and 40° for the Nb measurements where the angle is given relative to the surface plane of the sample. The x-ray probe-pulses are generated using a laser-based plasma x-ray source,[64] monochromatized to Cu-K_α-radiation, and focused onto the sample using a Montel optic[65] with a diamond shaped $300 \times 300\ \mu\mathrm{m}^2$ beam focus on the sample. The sample temperature is monitored via a thermocouple adjacent to the sample and all reported fluence values are provided as incident energy density that is calculated from the incident laser power and the beam footprint.

A. Temperature dependent UXRD experiments

First, we discuss the results displayed in Fig. 3, where a fixed energy density of 7.2 mJ/cm^2 is used to excite the sample for different initial temperatures, sampling the different magnetic orders. The results obtained in the PM phase at $T = 250$ K are displayed by red open symbols and represent the non-magnetic response of the investigated metallic heterostructure. We find an expansion of the Dy layer that reaches its maximum within 30 ps, which corresponds to the time it takes to propagate strain from the air/Y interface through the Dy layer to the Dy/Y interface. After traversing the 5 nm Y interlayer, this expansion enters the Nb layer at approximately 31.5 ps. This expansion pulse is preceded by a compression that results from the fast rise of the spatially inhomogeneous expansive stress. The resulting bipolar shape of the propagating strain pulse is well known in picosecond

Structural Dynamics ARTICLE scitation.org/journal/sdy

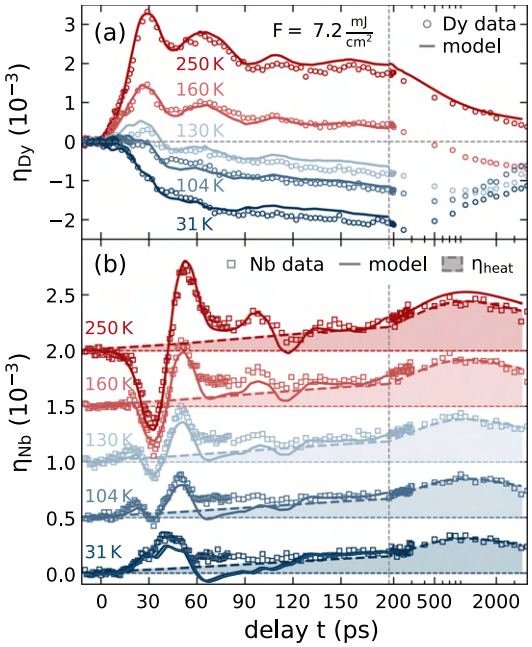

FIG. 3. Temperature-dependent strain response of (a) the Dy transducer and (b) the Nb detection layer for a fixed excitation energy density of $F = 7.2$ mJ/cm^2. Open symbols represent the average strain of the layers extracted from the Bragg peak shift observed by UXRD. Solid lines represent the simulated UXRD response obtained from a one-dimensional elastic model subjected to time-dependent phonon and magnetic stresses that are detailed in the modeling Sec. IV. The shaded region in (b) indicates the estimated thermal contribution to the Nb strain. The linear to logarithmic axis break (vertical, dashed line) allows the simultaneous comparison of the picosecond strain pulse and the subsequent thermal expansion. Nb curves are offset for clarity.

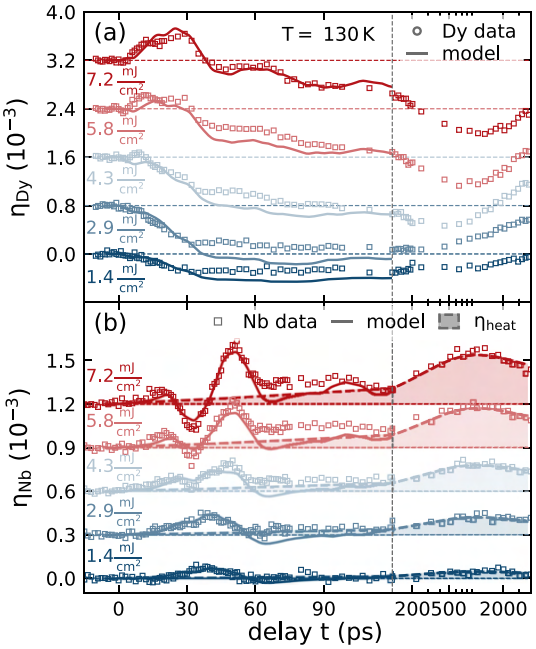

FIG. 4. Same depiction as in Fig. 3 used for the excitation energy density dependent strain response of (a) the Dy transducer and (b) the Nb detection layer for the fixed $T = 130$ K. All curves are offset for clarity. The initial transducer response changes from contraction to expansion as the excitation energy is increased, which coincides with the appearance of the delayed bipolar strain feature in the coherent phonon response of the buried detection layer.

acoustics; however, optical detection schemes often probe the wave returning back to the surface after a reflection.[1,2,5]

UXRD experiments can monitor the bipolar strain pulse traversing a buried detection layer: The classical bipolar wave first leads to a negative average strain in this layer and before it turns positive, a zero average strain indicates equal expansive and contractive parts in this layer.[35,66] The nearly bipolar shape of the Nb strain in Fig. 3(b) within the first 75 ps is characteristic of a symmetric strain pulse that is generated by a total stress that rises fast compared to the strain-propagation time through the laser-excited transducer. Echos of the laser-generated picosecond strain pulses that occur due to the partial reflection at the layer interfaces lead to a damped oscillation of the average strain in the Dy transducer and a second bipolar feature in the Nb detection layer between 80 ps and 125 ps.

In addition to these signatures of the coherent phonon wave packets, we observe a slowly increasing strain that originates from the excitation of incoherent phonons in the materials. This thermal expansion contribution of the excited Dy transducer is observed to decay on a nanosecond timescale by heat diffusion toward the substrate. This diffusion leads to a transient thermal expansion in the Nb detection layer that exhibits its maximum at approximately 1 ns after the excitation. To highlight the contribution of heat transport to the Nb expansion, we added dashed lines and shaded areas to Fig. 3(b). These lines are all scaled copies $A(T)\bar{\eta}_{\mathrm{heat}}(t)$ of the transient average strain $\bar{\eta}_{\mathrm{heat}}(t)$ in the Nb layer, which fit the 250 K data. This line could be drawn through the data by averaging out any coherent oscillations, but here we used the simulated expansion according to a Fourier heat law model discussed below. The temperature dependent factor $A(T)$ is determined by scaling the temperature-independent $\bar{\eta}_{\mathrm{heat}}(t)$ to the Nb data between 200 ps and 3 ns. $A(T)$ decreases significantly with temperature T, indicating that part of the energy density is stored in magnetic excitations that become accessible below $T_{\mathrm{Néel}}$ within the Dy transducer. The details of the modeling including a plot of $A(T)$ are discussed in Sec. IV.

Looking at the short timescale, we find that the magnetic excitations accessible upon lowering the temperature transform the transducer response continuously from a rapid expansion to a relatively slow contraction [Fig. 3(a)]. The coherent phonon oscillations in Dy become significantly weaker. In the Nb-detection layer [Fig. 3(b)], this coherent picosecond strain wave is observed to change from a large bipolar shape with a leading compression to a weaker unipolar expansion. At intermediate temperatures, a bipolar strain wave with reduced amplitude compared to the PM phase is preceeded by an expansion, which we attribute to contractive stress at the back side of the Dy layer, which absorbs the smallest energy density.

Structural Dynamics ARTICLE scitation.org/journal/sdy

B. Excitation density dependent strain-response

This hypothesis was checked by the excitation-density dependent measurements that we depict in Fig. 4. We repeated the UXRD experiment for a systematic variation of excitation fluences at a fixed initial sample temperature of $T = 130\,\mathrm{K}$ in the AFM phase of Dy. The increase in the deposited energy in the heterostructure can be seen directly as an increase in the transient thermal expansion of the Nb detection layer beyond 100 ps. The shaded area in Fig. 4(b) again indicates our estimate of the incoherent strain contribution that we obtain by scaling the strain $\bar{\eta}_{\mathrm{heat}}(t)$ from the PM phase to approximate the data between 0.2 and 3 ns. The resulting amplitude $A(130\,\mathrm{K}, F)$ scales super-linearly with F, indicating a saturation of the energy transfer to magnetic excitations (cf. Sec. IV E). Note that the magnetic contribution to the specific heat C_{mag} above $T_{\mathrm{Néel}}$ is small but finite [Fig. 2(b)]. According to the equilibrium analysis, the Grüneisen constant Γ_{mag} has the same value above $T_{\mathrm{Néel}}$, as the slope in Fig. 2(c) remains constant toward the end. Similar to the temperature dependent experiments, we find a strong qualitative change of the picosecond strain response in our heterostructure. For low excitation energies $F < 4.3\ \mathrm{mJ/cm^2}$, we observe an average contraction of the Dy transducer that goes along with the unipolar expansion of the Nb layer. For $F > 4.3\ \mathrm{mJ/cm^2}$, we observe an initial expansion of the Dy transducer that changes to an average contraction at delays much larger than the 30 ps that it takes for strain propagation through the layer.

The strain pulse measured in the Nb detection layer [Fig. 4(b)] exhibits a unipolar expansion feature for low excitation energy densities. For higher fluences, this expansion is superimposed by a bipolar strain response expected for the excitation of phonons, i.e., the dominant signal in the PM phase. However, here we confirm that the bipolar strain pulse is preceded by an expansion. Since this leading expansion is rationalized by a contractive stress at the backside of the Dy transducer, the high fluence data directly show that the magnetic excitations at the back side of the Dy transducer are not saturated. The simultaneous expansion at the Dy front side, however, triggers the bipolar waveform which is observed in the detection layer with a delay given by the sound propagation. This waveform confirms a saturation of the magnetic excitation in the Dy front part, because it is the trailing part of the strain pulse, which is considerably changed by the increasing fluence. The fraction of the transducer, where expansive stress from the combined electron-phonon system dominates over the contractive stress, extends over a thicker part of the layer for higher excitation energy densities.

Before discussing the resulting quantitative findings and the modeling approach, we briefly summarize the experimental conclusions that can be drawn directly from the presented UXRD data. For low excitation energies and temperatures, we observe that the magnetic rare earth transducer contracts on average as opposed to the expansion that is observed in the PM phase. For intermediate temperatures, we can infer that the front of the transducer expands while its backside contracts. This behavior can be rationalized by a spatially dependent saturation of the magnetic stress that originates from the inhomogeneous energy deposition profile. We find that the strain propagation maps the stress profile onto a nearly background-free, time-dependent signal of the average strain in the buried Nb detection layer. Since heat diffusion takes longer than strain waves, detecting the propagated strain wave in the detection layer separates the strain contribution of coherent and incoherent phonons, which are superimposed within the photoexcited Y and Dy layer. The additional layer thus provides a nanometric depth-resolution of the UXRD experiments using hard x-rays, which otherwise exhibit an extinction length on the order of few μm. The heat transport observed via the thermal expansion of the adjacent Nb layer is found to be reduced below the magnetic ordering temperatures. This can be directly seen in the area under the curve for the average strain in Nb [Fig. 4(b)], which is smaller at low temperatures. This is quantitatively depicted in Fig. S1(c) of the supplementary material.

IV. MODELING SPATIO-TEMPORAL STRESS

Our modeling approach is designed to identify the ingredients that are necessary to rationalize the observed temperature- and excitation fluence-dependent strain-response of the magnetic rare earth transducer. To that end, we model a time- and space dependent driving stress $\sigma_{\mathrm{tot}}(z,t) = \sigma_{\mathrm{pho}}(z,t) + \sigma_{\mathrm{mag}}(z,t)$ generated by energy transfer to magnetic excitations that acts in addition to the electron-phonon stress calibrated by the response in the PM phase. The measured average strain $\bar{\eta}$ for $t > 100$ ps only encodes the average stress in the Nb layer originating from the heat diffusion. The qualitative analysis of the strain wave detected in Nb for $t < 100$ ps already indicated that we are able to extract temporal variations $\sigma(z,t)$ of the spatial stress profile in the Dy by modeling the strain wave launched into the Nb detection layer. As shown in Figs. 3 and 4, we find qualitative and quantitative agreement between our model and data.

In the following, we first discuss the general assumptions of our modeling approach before we specify the simulation steps and assumptions for the modeled electron-phonon stress and the magnetic stress contributions.

A. General model assumptions

We assume the energy transfer processes between the stress-contributing subsystems schematically shown in Fig. 5(a), with coupling-times that correspond to the stress rise-times depicted in Fig. 5(b). The spatial stress profiles in the Dy layer are exemplified in Fig. 5(c) for the parameters $T = 130\,\mathrm{K}$ and $F = 7.2\ \mathrm{mJ/cm^2}$ that are representative of the AFM sample response. The total energy provided by the laser pulse is distributed between electron-phonon excitations that exert an expansive stress and magnetic-excitations that exert a contractive stress within the Dy layer. The energy is assumed to be deposited with the same inhomogeneous spatial profile to phonon- and magnetic excitations. The magnetic excitations however induce a contractive stress whose amplitude is three times larger than the expansive stress that is generated by electron-phonon excitations with the same energy density, according to the static Grüneisen analysis [Fig. 2(c)]. We keep as many simulation parameters as possible constant throughout the modeling. This includes the three coupling times illustrated in Fig. 5, the ratio of the initial energy redistribution from electrons to spins and phonons, and the maximum value for the spin energy density given by the saturation value $\rho_{\mathrm{mag}}^{\mathrm{sat}}$. We assume that the spatial energy distribution in the magnetic subsystem follows the profile of the phonon energy-density obtained by modeling the PM phase. This profile changes in time according to the heat diffusion, and we implicitly assume that the coupling of energy from phonons to spins is effective enough to prevent different spatial profiles of the contributing excitations. However, when the magnetic energy density exceeds the saturation value $\rho_{\mathrm{mag}}^{\mathrm{sat}}$, we truncate it. This truncation yields the

Structural Dynamics ARTICLE scitation.org/journal/sdy

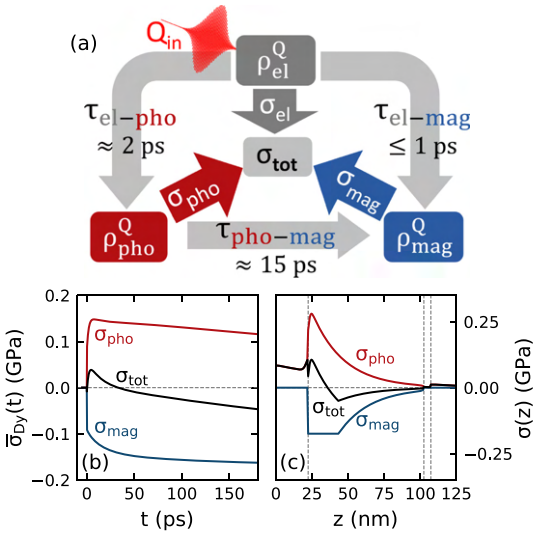

FIG. 5. (a) Schematic stress contributions used in the modeling approach. Arrows and labels indicate the modeled energy transfer processes between the subsystems and the assumed coupling-timescales τ. The resulting time-dependence of the spatially averaged stress contributions in Dy (b) and the used stress profile 100 fs after excitation (c) are shown exemplarily for $T = 130$ K and $F = 7.2$ mJ/cm^2. Vertical dashed lines in (c) indicate interfaces of the Y/Dy/Y/Nb heterostructure. This illustrates that the total stress evolution is a superposition of the expansive electron-phonon stress and the contractive magnetic stress both in the space- and time-domain.

non-monotonous spatial variation of the total driving stress as a function of temperature and excitation fluence. The temporal variation owes to the fact that the fraction of energy coupled rapidly to the phonon system is larger than into the magnetic system. Therefore, the additional 15 ps spin-phonon coupling time leads to a slow rise of the spin excitation and a decay of the phonon excitation.

We limit the modeling time to 180 ps since we expect remagnetization effects to significantly contribute to the strain at later times via magnetostriction. A full description would require a detailed model for the recovery of the magnetic order including both thermal transport and nucleation, growth, and coalescence of magnetic domains. This is beyond the scope of our one-dimensional thermodynamical approach. We furthermore refrain from a time- and space-dependent three-temperature model that has been previously used to rationalize the demagnetization of the magnetic specimen,[67,68] because it would require many, potentially temperature dependent, material constants for all layers in our heterostructure that are not known with the required accuracy. To what extend a three temperature model would capture the demagnetization and remagnetization of both the itinerant (5*d*6*s*) conduction band electrons and the localized 4*f* electrons in heavy rare earth metals is a matter of current research debate.[39,69,70]

B. Simulated spatio-temporal stress contributions

The modeled time-dependent stress profiles, separated into the expansive, contractive and the total stress contributions are displayed in Figs. 6(a)–6(o). The first row [Figs. 6(a)–6(e)] shows the expansive electron-phonon stress (σ_{pho}). In the PM-phase (250 K), σ_{pho} is identical to the total stress (σ_{tot}), shown in the third row. For the low temperature magnetic phases, the energy transfer to magnetic excitations reduces the amplitude of σ_{pho} [Figs. 6(b)–6(e)] without changing the relative spatio-temporal form, and at the same time, it creates the magnetic-stress contribution (σ_{mag}) shown in the second row [Figs. 6(f)–6(j)]. The resulting total stress σ_{tot} [Figs. 6(k)–6(o)] strongly depends on the initial temperature and excitation energy. This is supported by the modeled spatiotemporal stress profile and strain response for the excitation energy density dependent experiments at $T = 130$ K that we display in Sec. S5 of the supplementary material. The modeled strain response [Figs. 6(p)–6(t)] contains the propagating strain pulses that are launched at gradients of the driving stress in addition to the strain contribution of the local driving stress.

While the saturation level of the magnetic stress changes for the *T*-dependent measurements, *F*-dependent measurements vary the deposited energy density for a fixed maximum magnetic stress. In both cases, we observe that the absolute value of the total stress that acts on the lattice is reduced in comparison to the competing contributions from magnetic- and phonon excitations. Even though the total stress is contractive at the end of most simulation scenarios, the maximum contraction is attained slower than the magnetic stress rise time due to the time-dependent balance of phonon and magnetic stresses. The reappearance of the bipolar strain pulse in the detection layer response for high excitation energies thus occurs since the total stress at the top Y/Dy interface is dominated by an unbalanced electron-phonon stress.

C. Simulation steps

We use the modular UDKM1DSIM[71] MATLAB library to model the time-dependent energy density, strain, and x-ray reflectivity of the non-magnetic heterostructure response. The solid, dark-red line in Figs. 3(a) and 3(b) corresponds to the strain that we obtain from the simulated transient x-ray diffraction peak shift. In the first step, we calculate the time-dependent temperature changes upon laser excitation using a one-dimensional Fourier heat diffusion model from the thermophysical properties of the materials in the PM phase that we list in Sec. S3 of the supplementary material. The resulting spatiotemporal energy density is subsequently translated to a stress that acts as the driving force on a linear chain of masses and springs, which calculates the time-resolved layer strain with unit-cell resolution. The final simulation step employs a transfer matrix algorithm that yields the Bragg-peak evolution of the strained sample according to dynamical x-ray diffraction theory. Section S3 of the supplementary material shows a flow chart of the simulation steps including the relevant equations. The good quantitative agreement between UXRD data and simulation indicates that our model is a suitable representation of the sample properties and non-magnetic processes (i.e., layer thicknesses, optical excitation parameters, stress profiles, and rise-times) in the PM phase of Dy. We keep all the parameters given in Table I of the supplementary material fixed throughout the modeling, even in the FM and AFM phase, since these parameters describe the electron-phonon system. Section IV E describes how we added the contractive negative stress according to Eq. (2) for excitation in the AFM and FM phase.

Structural Dynamics ARTICLE scitation.org/journal/sdy

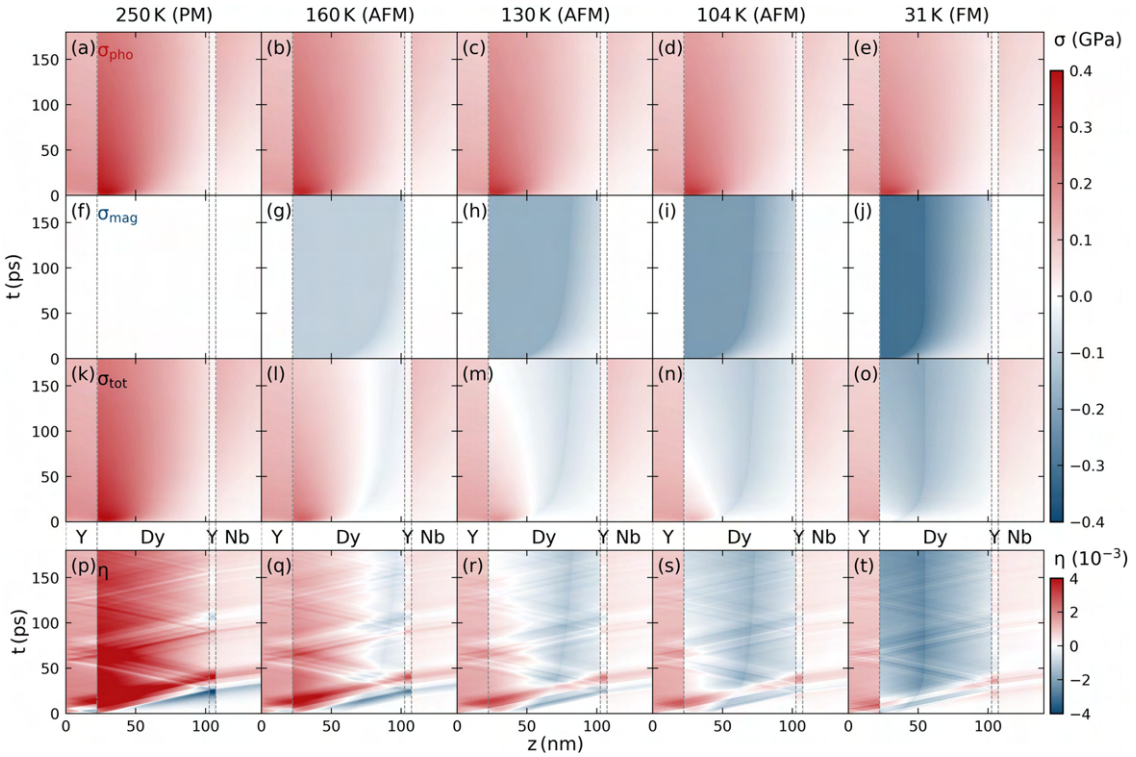

FIG. 6. Modeled spatiotemporal stress and strain response in our heterostructure for a fixed excitation with $F = 7.2$ mJ/cm^2 at different starting temperatures. The phonon-stress contributions (a)–(e) and the magnetic-stress contributions (f)–(j) in the first and second row add to the total stress provided in the third row (k)–(o). This illustrates the temperature and time-dependent energy transfer and the saturation effects due to the finite amount of energy that can be transferred to magnetic excitations. The resulting strain response of a linear chain of masses and springs model that contains contributions from both coherent and incoherent phonons is shown at the bottom (p)–(t). These strain maps are used to simulate the time-dependent Bragg peak shift that yields the modeled Dy and Nb strain response in Fig. 3. Vertical dashed lines indicate the interfaces within the Y/Dy/Y/Nb heterostructure.

D. Electron-phonon stress contribution

Both the Dy and the Nb strain responses in the PM-phase are used to calibrate the electron-phonon stress contribution. The electron-phonon coupling is included by a 2 ps time-constant of the expansive stress and a ratio between the Grüneisen constants $\Gamma_{el}/\Gamma_{pho} = 0.5$ for both the Y and Dy layers. These parameters are chosen to fit the observed expansion of the Dy layer and the coherent phonon oscillation amplitude of the PM response and are fixed for the subsequent modeling. To illustrate the effect of the stress rise time on the shape of the strain pulse seen by UXRD in the detection layer, we present the elastic-response-simulations of the average strain within a simplified structure that contains only a transducer and a detection layer in Sec. S2 of the supplementary material. To recover the observed direct rise of the Dy strain after laser excitation, we have to assume a reduced absorption and thermal expansion in the 21 nm thick Y capping layer, which would otherwise compress the adjacent Dy. Although the estimated expansion of the Y layer is reduced by 40% compared to the literature value, we stress that this parameter is kept fixed for all subsequent simulations that focus on the T-dependent magnetic response. One possible explanation for this deviation could be a partial oxidation of the capping layer since the metallic sample was kept at ambient conditions prior to the measurements.

To match the slow nanosecond decay of the Dy strain as well as the delayed rise of the expansion in the Nb layer, we use an effective thermal conductivity value for the Dy layer that is reduced by approximately 40% compared to the bulk literature value to account for thermal interface resistance effects. Using the material-specific elastic constants, we can then transform the energy densities ρ_r into an estimated spatiotemporal profile of the driving stress $\sigma_r = \Gamma_r \rho_r$ according to the Grüneisen concept [Figs. 6(a) and 6(k)]. This stress drives the elastic response shown in Fig. 6(p). The modeled strain matches both the Dy transducer and Nb detection layer response qualitatively and quantitatively over the entire 3.5 ns simulation time as shown in Fig. 3.

E. Magnetic stress contribution

To minimize the number of parameters for the simulations in the AFM and FM phase, we not only keep all thermophysical parameters describing the e-ph system fixed. We also use the shape of the

Structural Dynamics ARTICLE scitation.org/journal/sdy

spatiotemporal phonon stress-profile $\eta_{\text{heat}}(z,t)$ extracted in the PM phase. We reduce its amplitude in all layers (Y, Dy and Nb) according to the fraction of the energy that is transferred to magnetic excitations that is shown in Fig. 7 as red squares. The blue squares represent $1-\eta_{\text{heat}}$, which is proportional to the fraction of energy that is stored in the magnetic system of Dy on the few ns timescale. The lines in Fig. 7 show the relative weight of the energy densities in the phonon (red) and magnetic system (blue) in our model. We find a qualitative agreement with the data if locally a fraction of 25% of the excitation energy is deposited instantaneously into the magnetic system to account for subpicosecond electron-spin couplings and additionally a second energy fraction of 25% of the excitation energy is subsequently transferred from phonon to magnetic excitations by the phonon-spin coupling. Only when this energy transfer locally exceeds the maximum energy density $\rho^{\text{sat}}_{\text{mag}}$ in the spin system, we truncate the energy transfer from phonons to spins. Thus, to account for the experimentally observed reduced energy transport to the adjacent layer in the magnetic phase of Dy, we reduce the energy density in the Nb and Y layers and add the removed fraction to the Dy layer where the energy is distributed between magnetic and phonon excitation. We use $\rho^{\text{sat}}_{\text{mag}}$ as a free parameter in the modeling and find the best agreement with our data with $\rho^{\text{sat}}_{\text{mag}}(T_{\text{start}}) = 0.81 \int_{T_{\text{start}}}^{\infty} C_{\text{mag}}(T')\mathrm{d}T'$, using the literature bulk values for $C_{\text{mag}}(T')$. We believe that either the thin film value for $C_{\text{mag}}(T')$ is smaller compared to the bulk value, or only a reduced fraction of the magnetic heat capacity of the thin film is accessible upon ultrafast laser excitation. Our model reproduces the trends of the experimentally observed reduced energy flow in Fig. 7 as a function of the starting temperature and the fluence correctly. The energy fraction that is not detected in Nb persists in the magnetic excitations of Dy that act as a saturable heat sink. The saturation can be seen by the reduced energy fraction in the magnetic excitations closer to $T_{\text{Néel}}$ and the decrease in the magnetic energy fraction for higher excitation densities. The blue lines representing the fraction of heat in the magnetic system around 180 ps in our model report a systematically larger value than the blue squares derived from the experiment of the Nb strain between 0.2 and 3 ns. This is in line with the previous analysis of persistent magnetic excitations in Dy decaying within a few ns.[32]

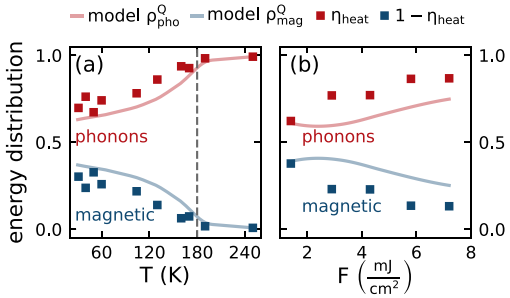

FIG. 7. Estimated energy distribution between magnetic- and phonon excitations within the rare earth transducer for the presented temperature- (a) and excitation energy dependent (b) measurements at fixed $F = 7.2$ mJ/cm^2 and $T = 130$ K, respectively. Data points correspond to the fitted amplitude $A(T, F)$ of the thermal expansion $A(T,F)\eta_{\text{heat}}(t)$ of the Nb detection layer (shaded areas in Figs. 3 and 4), normalized to the PM phase value $A(250\,\text{K})$. Solid lines represent the energy distribution at the last time step $t = 180$ ps of the spatiotemporal stress–strain simulation. The fraction of deposited energy in the spin system decreases when approaching $T_{\text{Néel}}$ from low temperatures as well as for higher fluences.

We use energy transfer times that are in agreement with recent ultrafast demagnetization studies in AFM-dysprosium[38] and holmium.[39] The resonant diffraction studies independently report both a subpicosecond demagnetization, which is attributed to electron-spin coupling and a second demagnetization timescale on the order of 15 ps, which is attributed to phonon-spin coupling. Systematic modeling of our data yields that both timescales are necessary to capture the early time strain response of the transducer. A substantial fraction of the magnetic stress needs to be present within the first ps to balance the otherwise expansive electron-phonon response. However, our modeling shows that not all energy is instantaneously transferred to magnetic excitations since the resulting stress would drive a contraction that is significantly faster than the observed response.

In addition to these two intrinsic demagnetization timescales, we observe a contraction of the Dy transducer for larger pump-probe delays. This effect is most pronounced at high excitation densities and T close to and above $T_{\text{Néel}}$. Our simulations show that this can be rationalized by two energy transport effects within the inhomogeneously excited heterostructure. First there is thermal diffusion of phonon excitations within the inhomogeneously heated Dy. This transports energy from the near surface region where spin-excitations are saturated into the depth of the transducer, where the spin energy density is below the saturation threshold. The coupling of energy from phonons to the spins decreases the expansive phonon stress and increases the contractive magnetic stress contribution. The transport of phonon heat out of the Dy layer into the Nb reduces the expansion further. This allows us to model the spatial spin-stress profile. Although the quantitative link between the magnetic stress and the sublattice magnetization in the time-domain is largely unexplored, we can argue qualitatively that the saturation of the spin-stress will be linked to regions of complete demagnetization. For static thermal expansion experiments, it has been reported that the magnetostrictive stress is proportional to the square of the sublattice-magnetization.[43,72] Thus, we can speculate that the modeled magnetic stress profile is qualitatively similar to the demagnetization profile. More precisely, we assume that the observed magnetic stress profile reflects the demagnetization of the 4*f*-electrons of the heavy rare earth. These anisotropic orbitals carry large, localized magnetic moments that distinguish rare earth materials from 3*d*-transition metals that exhibit by far smaller magnetostriction.

The color code of Fig. 6 provides a qualitative overview over the temperature dependent stress contributions that we focus on in the current report. For a more quantitative comparison, we refer the reader to Sec. S5 of the supplementary material. There we show outlines of the modeled spatial stress profiles at 6 ps, 45 ps, and 180 ps alongside the time dependence of the modeled stress contributions for both the *T*- and *F*-dependent experiments.

Our current modeling provides a plausible scenario for the driving stress. A satisfactory agreement between the data and modeling definitively requires three energy transfer timescales to the spin system. The first energy transfer to the magnetic excitations has to rise equally fast or faster than the electron-phonon stress to cancel the expansive electron-phonon stress in the first few ps. The second timescale has to be in the range of 10–20 ps to model the contraction of the Dy layer and the unipolar expansion wave observed in the Nb layer.

Structural Dynamics ARTICLE scitation.org/journal/sdy

The third process on a timescale larger than 40 ps is given by thermal transport within the Dy layer. This is the simplest possible temporal behavior of the stress that is consistent with our data.

So far, we have also treated the FM and AFM response equally although there exists an additional first order phase-transition in the low temperature phase and the demagnetization of the ferromagnetic phase was reported to occur slower than in the antiferromagnetic Dy.[38] We attribute the reasonable agreement for the FM phase at $T = 31$ K to the use of a large excitation energy density that drives mainly spin excitations with the calibrated Grüneisen constant of the AFM phase. These magnetic-excitations seem to dominate the magnetostrictive response at high excitation energy densities compared to the potential contribution of the latent heat that is necessary to undergo the metamagnetic FM-AFM transition. A detailed study of the magnetostriction at the FM-AFM transition is deferred to future investigations.

V. CONCLUSION

The presented picosecond strain dynamics in a laser-excited heterostructure containing a rare-earth transducer shows strong magnetic contributions to the lattice response. Both the picosecond strain pulse and the thermal transport are affected by energy transfer processes to magnetic excitations. The transient strain observed in a buried detection layer directly shows the saturation of the contractive magnetic stress component, which occurs when an increasing fraction of the Dy layer is excited across its magnetic phase transition. The spatially varying sign of the stress within the Dy layer triggers unconventional strain pulses, which exhibit a leading expansive part in front of the conventional bipolar strain pulse. Our modeling yields an estimate for the time- and space-dependent profile of the additional magnetic stress contribution to the lattice dynamics. The magnetic excitations act as a saturable heat reservoir, which stores a significant fraction of the excitation energy and exerts a contractive stress that dominates over the phonon contribution. We expect this finding to be generic for the magnetic phase in the class of heavy rare earth materials in the periodic table of elements $_{64}$Gd–$_{69}$Tm. The observed energy transfer timescales are in agreement with recent demagnetization experiments. This indicates that the magnetostrictive response can be used to probe the time-dependent evolution of the sublattice magnetization.

Our investigation demonstrates the capabilities of UXRD experiments in a transducer-detector geometry to observe non-trivial spatial stress profiles. We emphasize that extracting the stress profile in the transducer by UXRD from an adjacent crystalline detection layer can be applied to investigate non-crystalline transducer films. The combination of picosecond acoustics experiment, UXRD detection, and elastic modeling can be used to study the strain generation by energy transfer to other degrees of freedom. This comprises, in particular, phase-transition effects such as studies of ferroelectric and charge order transition as well as investigations of other magnetostrictive materials, which may hold hitherto unknown functionalities.

SUPPLEMENTARY MATERIAL

See the supplementary material for a complete overview of the UXRD results (Sec. S1) and simulations (Sec. S2) that illustrate the effect of the stress rise time, stress profile length, and the detection layer thickness for the strain response in a simplified transducer-detector heterostructure. Section S3 provides an overview of the mathematical relations relevant for the strain simulation and a list of the relevant thermophysical material properties, including a description of the Poisson correction factor for the Grüneisen constant. Section S4 shows a detailed plot of the spatiotemporal stress contributions for the T- and F-dependent modeling that comprises stress-profiles at selected times and the time dependent average stress within the Dy layer.

ACKNOWLEDGMENTS

We gratefully acknowledge the BMBF for the financial support via No. 05K16IPA and the DFG via Nos. BA 2281/8-1 and BA 2281/11-1. We acknowledge the pre-characterization of the crystalline thin lms at the XPP-KMC3 synchrotronradiation beamline D13.2 at the BESSY II electron storage ring operated by the Helmholtz-Zentrum Berlin.

REFERENCES

[1]C. Thomsen, H. T. Grahn, H. J. Maris, and J. Tauc, "Surface generation and detection of phonons by picosecond light pulses," Phys. Rev. B **34**, 4129–4138 (1986).
[2]O. Matsuda, M. C. Larciprete, R. Li Voti, and O. B. Wright, "Fundamentals of picosecond laser ultrasonics," Ultrasonics **56**, 3–20 (2015).
[3]M. Nicoul, U. Shymanovich, A. Tarasevitch, D. von der Linde, and K. Sokolowski-Tinten, "Picosecond acoustic response of a laser-heated gold-film studied with time-resolved x-ray diffraction," Appl. Phys. Lett. **98**, 191902 (2011).
[4]O. B. Wright, "Ultrafast nonequilibrium stress generation in gold and silver," Phys. Rev. B **49**, 9985–9988 (1994).
[5]T. Saito, O. Matsuda, and O. B. Wright, "Picosecond acoustic phonon pulse generation in nickel and chromium," Phys. Rev. B **67**, 205421 (2003).
[6]G. Tas and H. J. Maris, "Electron diffusion in metals studied by picosecond ultrasonics," Phys. Rev. B **49**, 15046–15054 (1994).
[7]M. Lejman, V. Shalagatskyi, O. Kovalenko, T. Pezeril, V. V. Temnov, and P. Ruello, "Ultrafast optical detection of coherent acoustic phonons emission driven by superdiffusive hot electrons," J. Opt. Soc. Am. B **31**, 282 (2014).
[8]O. B. Wright, O. Matsuda, B. Perrin, and V. E. Gusev, "Ultrafast carrier diffusion in gallium arsenide probed with picosecond acoustic pulses," Phys. Rev. B **64**, 3–6 (2001).
[9]E. S. Young, A. V. Akimov, R. P. Campion, A. J. Kent, and V. Gusev, "Picosecond strain pulses generated by a supersonically expanding electron-hole plasma in GaAs," Phys. Rev. B **86**, 1–13 (2012).
[10]O. B. Wright and V. E. Gusev, "Acoustic generation in crystalline silicon with femtosecond optical pulses," Appl. Phys. Lett. **66**, 1190–1192 (1995).
[11]P. Ruello and V. E. Gusev, "Physical mechanisms of coherent acoustic phonons generation by ultrafast laser action," Ultrasonics **56**, 21–35 (2015).
[12]O. Kovalenko, T. Pezeril, and V. V. Temnov, "New concept for magnetization switching by ultrafast acoustic pulses," Phys. Rev. Lett. **110**, 266602 (2013).
[13]W. Li, B. Buford, A. Jander, and P. Dhagat, "Acoustically assisted magnetic recording: A new paradigm in magnetic data storage," IEEE Trans. Magn. **50**, 37–40 (2014).
[14]L. Thevenard, I. S. Camara, S. Majrab, M. Bernard, P. Rovillain, A. Lemaître, C. Gourdon, and J.-Y. Duquesne, "Precessional magnetization switching by a surface acoustic wave," Phys. Rev. B **93**, 134430 (2016).
[15]I. S. Camara, J. Y. Duquesne, A. Lemaître, C. Gourdon, and L. Thevenard, "Field-free magnetization switching by an acoustic wave," Phys. Rev. Appl. **11**, 1 (2019).
[16]J.-W. Kim, M. Vomir, and J.-Y. Bigot, "Ultrafast magnetoacoustics in nickel films," Phys. Rev. Lett. **109**, 166601 (2012).
[17]J. W. Kim, M. Vomir, and J. Y. Bigot, "Controlling the spins angular momentum in ferromagnets with sequences of picosecond acoustic pulses," Sci. Rep. **5**, 1–7 (2014).

Structural Dynamics ARTICLE scitation.org/journal/sdy

[18]A. V. Scherbakov, A. S. Salasyuk, A. V. Akimov, X. Liu, M. Bombeck, C. Brüggemann, D. R. Yakovlev, V. F. Sapega, J. K. Furdyna, and M. Bayer, "Coherent magnetization precession in ferromagnetic (Ga,Mn)As induced by picosecond acoustic pulses," Phys. Rev. Lett. **105**, 1–4 (2010).
[19]M. Bombeck, J. V. Jäger, A. V. Scherbakov, T. Linnik, D. R. Yakovlev, X. Liu, J. K. Furdyna, A. V. Akimov, and M. Bayer, "Magnetization precession induced by quasitransverse picosecond strain pulses in (311) ferromagnetic (Ga,Mn)As," Phys. Rev. B **87**, 1–5 (2013).
[20]J. V. Jäger, A. V. Scherbakov, T. L. Linnik, D. R. Yakovlev, M. Wang, P. Wadley, V. Holy, S. A. Cavill, A. V. Akimov, A. W. Rushforth, and M. Bayer, "Picosecond inverse magnetostriction in galfenol thin films," Appl. Phys. Lett. **103**, 032409 (2013).
[21]Y. Hashimoto, D. Bossini, T. H. Johansen, E. Saitoh, A. Kirilyuk, and T. Rasing, "Frequency and wavenumber selective excitation of spin waves through coherent energy transfer from elastic waves," Phys. Rev. B **97**, 1–5 (2018); arXiv:1710.08087.
[22]M. Deb, E. Popova, M. Hehn, N. Keller, S. Mangin, and G. Malinowski, "Picosecond acoustic-excitation-driven ultrafast magnetization dynamics in dielectric Bi-substituted yttrium iron garnet," Phys. Rev. B **98**, 174407 (2018); arXiv:1807.00610.
[23]S. O. Mariager, F. Pressacco, G. Ingold, A. Caviezel, E. Möhr-Vorobeva, P. Beaud, S. L. Johnson, C. J. Milne, E. Mancini, S. Moyerman, E. E. Fullerton, R. Feidenhans'l, C. H. Back, and C. Quitmann, "Structural and magnetic dynamics of a laser induced phase transition in FeRh," Phys. Rev. Lett. **108**, 87201 (2012).
[24]F. Quirin, M. Vattilana, U. Shymanovich, A.-E. El-Kamhawy, A. Tarasevitch, J. Hohlfeld, D. von der Linde, and K. Sokolowski-Tinten, "Structural dynamics in FeRh during a laser-induced metamagnetic phase transition," Phys. Rev. B **85**, 20103 (2012).
[25]A. H. Reid, X. Shen, P. Maldonado, T. Chase, E. Jal, P. W. Granitzka, K. Carva, R. K. Li, J. Li, L. Wu, T. Vecchione, T. Liu, Z. Chen, D. J. Higley, N. Hartmann, R. Coffee, J. Wu, G. L. Dakovski, W. F. Schlotter, H. Ohldag, Y. K. Takahashi, V. Mehta, O. Hellwig, A. Fry, Y. Zhu, J. Cao, E. E. Fullerton, J. Stöhr, P. M. Oppeneer, X. J. Wang, and H. A. Dürr, "Beyond a phenomenological description of magnetostriction," Nat. Commun. **9**, 388 (2018).
[26]A. von Reppert, L. Willig, J.-E. Pudell, M. Rössle, W. Leitenberger, M. Herzog, F. Ganss, O. Hellwig, and M. Bargheer, "Ultrafast laser generated strain in granular and continuous FePt thin films," Appl. Phys. Lett. **113**, 123101 (2018).
[27]C. von Korff Schmising, A. Harpoeth, N. Zhavoronkov, Z. Ansari, C. Aku-Leh, M. Woerner, T. Elsaesser, M. Bargheer, M. Schmidbauer, I. Vrejoiu, D. Hesse, and M. Alexe, "Ultrafast magnetostriction and phonon-mediated stress in a photoexcited ferromagnet," Phys. Rev. B **78**, 60404 (2008).
[28]E. D. T. De Lacheisserie, *Magnetostriction: Theory and Applications of Magnetoelasticity* (CRC, 1993).
[29]F. Darnell, "Temperature dependence of lattice parameters for Gd, Dy, and Ho," Phys. Rev. **130**, 1825–1828 (1963).
[30]A. Koc, M. Reinhardt, A. von Reppert, M. Rössle, W. Leitenberger, M. Gleich, M. Weinelt, F. Zamponi, and M. Bargheer, "Gruneisen-approach for the experimental determination of transient spin and phonon energies from ultrafast x-ray diffraction data: Gadolinium," J. Phys.: Condens. Matter **29**, 264001 (2017).
[31]J. Pudell, A. von Reppert, D. Schick, F. Zamponi, M. Rössle, M. Herzog, H. Zabel, and M. Bargheer, "Ultrafast negative thermal expansion driven by spin disorder," Phys. Rev. B **99**, 094304 (2019); arXiv:pudell2019a.
[32]A. von Reppert, J. Pudell, A. Koc, M. Reinhardt, W. Leitenberger, K. Dumesnil, F. Zamponi, and M. Bargheer, "Persistent nonequilibrium dynamics of the thermal energies in the spin and phonon systems of an antiferromagnet," Struct. Dyn. **3**, 054302 (2016).
[33]A. Koc, M. Reinhardt, A. von Reppert, M. Rössle, W. Leitenberger, K. Dumesnil, P. Gaal, F. Zamponi, and M. Bargheer, "Ultrafast x-ray diffraction thermometry measures the influence of spin excitations on the heat transport through nanolayers," Phys. Rev. B **96**, 014306 (2017); arXiv:1701.05918.
[34]J. Pudell, A. Maznev, M. Herzog, M. Kronseder, C. Back, G. Malinowski, A. von Reppert, and M. Bargheer, "Layer specific observation of slow thermal equilibration in ultrathin metallic nanostructures by femtosecond x-ray diffraction," Nat. Commun. **9**, 3335 (2018); arXiv:1803.04034.
[35]S. P. Zeuschner, T. Parpiiev, T. Pezeril, A. Hillion, K. Dumesnil, A. Anane, J. Pudell, L. Willig, M. Rössle, M. Herzog, A. von Reppert, and M. Bargheer, "Tracking picosecond strain pulses in heterostructures that exhibit giant magnetostriction," Struct. Dyn. **6**, 024302 (2019).
[36]Y. Gao, Z. Chen, Z. Bond, A. Loether, L. E. Howard, S. LeMar, S. White, A. Watts, B. C. Walker, and M. F. DeCamp, "Reconstructing longitudinal strain pulses using time-resolved x-ray diffraction," Phys. Rev. B **88**, 525A (2013).
[37]A. Eschenlohr, M. Sultan, A. Melnikov, N. Bergeard, J. Wieczorek, T. Kachel, C. Stamm, and U. Bovensiepen, "Role of spin-lattice coupling in the ultrafast demagnetization of gd 1- x tb x alloys," Phys. Rev. B **89**, 214423 (2014).
[38]N. Thielemann-Kühn, D. Schick, N. Pontius, C. Trabant, R. Mitzner, K. Holldack, H. Zabel, A. Föhlisch, and C. Schüßler-Langeheine, "Ultrafast and energy-efficient quenching of spin order: antiferromagnetism beats ferromagnetism," Phys. Rev. Lett. **119**, 197202 (2017); arXiv:1703.03689.
[39]L. Rettig, C. Dornes, N. Thielemann-Kühn, N. Pontius, H. Zabel, D. L. Schlagel, T. A. Lograsso, M. Chollet, A. Robert, M. Sikorski, S. Song, J. M. Glownia, C. Schüßler-Langeheine, S. L. Johnson, and U. Staub, "Itinerant and localized magnetization dynamics in antiferromagnetic Ho," Phys. Rev. Lett. **116**, 257202 (2016).
[40]K. Dumesnil, C. Dufour, P. Mangin, G. Marchal, and M. Hennion, "Magnetic structure of dysprosium in epitaxial Dy films and in Dy/Er superlattices," Phys. Rev. B **54**, 6407–6420 (1996).
[41]D. Schick, M. Herzog, A. Bojahr, W. Leitenberger, A. Hertwig, R. Shayduk, and M. Bargheer, "Ultrafast lattice response of photoexcited thin films studied by x-ray diffraction," Struct. Dyn. **1**, 064501 (2014).
[42]D. Schick, R. Shayduk, A. Bojahr, M. Herzog, C. von Korff Schmising, P. Gaal, and M. Bargheer, "Ultrafast reciprocal-space mapping with a convergent beam," J. Appl. Crystallogr. **46**, 1372–1377 (2013).
[43]F. J. Darnell and E. P. Moore, "Crystal structure of dysprosium at low temperatures," J. Appl. Phys. **34**, 1337–1338 (1963).
[44]V. Pecharsky, K. Gschneidner, and D. Fort, "Superheating and other unusual observations regarding the first order phase transition in Dy," Scr. Mater. **35**, 843–848 (1996).
[45]S. Legvold, J. Alstad, and J. Rhyne, "Giant magnetostriction in dysprosium and holmium single crystals," Phys. Rev. Lett. **10**, 509–511 (1963).
[46]W. C. Koehler, "Magnetic properties of rare earth metals and alloys," J. Appl. Phys. **36**, 1078–1087 (1965).
[47]R. Elliott, *Magnetic Properties of Rare Earth Metals* (Springer Science & Business Media, 1972).
[48]J. Jensen and A. R. Mackintosh, *Rare Earth Magnetism* (Clarendon, Oxford, 1991).
[49]E. R. Callen and H. B. Callen, "Static magnetoelastic coupling in cubic crystals," Phys. Rev. **129**, 578–593 (1963).
[50]E. Callen and H. B. Callen, "Magnetostriction, forced magnetostriction, and anomalous thermal expansion in ferromagnets," Phys. Rev. **139**, A455–A471 (1965).
[51]M. Doerr, M. Rotter, and A. Lindbaum, "Magnetostriction in rare-earth based antiferromagnets," Adv. Phys. **54**, 1–66 (2005).
[52]L. Benito, J. Arnaudas, M. Ciria, C. de La Fuente, and A. del Moral, "The magnetostriction of Tb, Dy and Ho revisited," J. Phys.: Condens. Matter **16**, 7151 (2004).
[53]W. Nolting and A. Ramakanth, *Quantum Theory of Magnetism* (Springer Science & Business Media, 2009).
[54]E. Grüneisen, "Theorie des festen zustandes einatomiger elemente," Ann. Phys. **344**, 257–306 (1912).
[55]T. Barron, J. Collins, and G. K. White, "Thermal expansion of solids at low temperatures," Adv. Phys. **29**, 609–730 (1980).
[56]J. Chen, L. Hu, J. Deng, and X. Xing, "Negative thermal expansion in functional materials: Controllable thermal expansion by chemical modifications," Chem. Soc. Rev. **44**, 3522–3567 (2015); arXiv:1612.08814.
[57]M. T. Dove and H. Fang, "Negative thermal expansion and associated anomalous physical properties: Review of the lattice dynamics theoretical foundation," Rep. Prog. Phys. **79**, 066503 (2016).
[58]G. K. White, "Phase transitions and the thermal expansion of holmium," J. Phys.: Condens. Matter **1**, 6987–6992 (1989).
[59]L. D. Jennings, R. E. Miller, and F. H. Spedding, "Lattice heat capacity of the rare earths. Heat capacities of yttrium and lutetium from 15–350K," J. Chem. Phys. **33**, 1849–1852 (1960).

Structural Dynamics ARTICLE scitation.org/journal/sdy

[60]W. M. Haynes, *CRC Handbook of Chemistry and Physics*, CRC Handbook of Chemistry and Physics, 93rd ed. (Taylor & Francis, 2012).
[61]T. Barron, "Grüneisen parameters for the equation of state of solids," Ann. Phys. **1**, 77–90 (1957).
[62]J. J. Tonnies, K. A. Gschneidner, and F. H. Spedding, "Elastic moduli and thermal expansion of lutetium single crystals from 4.2 to 300k," J. Appl. Phys. **42**, 3275–3283 (1971).
[63]S. B. Palmer and E. W. Lee, "The elastic constants of dysprosium and holmium," Proc. R. Soc. A **327**, 519–543 (1972).
[64]D. Schick, A. Bojahr, M. Herzog, C. v K. Schmising, R. Shayduk, W. Leitenberger, P. Gaal, and M. Bargheer, "Normalization schemes for ultrafast x-ray diffraction using a table-top laser-driven plasma source," Rev. Sci. Instrum. **83**, 025104 (2012).
[65]M. Bargheer, N. Zhavoronkov, R. Bruch, H. Legall, H. Stiel, M. Woerner, and T. Elsaesser, "Comparison of focusing optics for femtosecond x-ray diffraction," Appl. Phys. B: Lasers Opt. **80**, 715–719 (2005).
[66]C. Rose-Petruck, R. Jimenez, T. Guo, A. Cavalleri, C. W. Siders, F. Rksi, *et al.*, "Picosecond -milliångström lattice dynamics measured by ultrafast X-ray diffraction," Nature **398**(6725), 310–312 (1999).
[67]E. Beaurepaire, J.-C. Merle, A. Daunois, and J.-Y. Bigot, "Ultrafast spin dynamics in ferromagnetic nickel," Phys. Rev. Lett. **76**, 4250–4253 (1996).
[68]B. Koopmans, G. Malinowski, F. Dalla Longa, D. Steiauf, M. Fähnle, T. Roth, M. Cinchetti, and M. Aeschlimann, "Explaining the paradoxical diversity of ultrafast laser-induced demagnetization," Nat. Mater. **9**, 259–265 (2010).
[69]B. Frietsch, J. Bowlan, R. Carley, M. Teichmann, S. Wienholdt, D. Hinzke, U. Nowak, K. Carva, P. M. Oppeneer, and M. Weinelt, "Disparate ultrafast dynamics of itinerant and localized magnetic moments in gadolinium metal," Nat. Commun. **6**, 8262 (2015).
[70]K. Bobowski, M. Gleich, N. Pontius, C. Schüßler-Langeheine, C. Trabant, M. Wietstruk, B. Frietsch, and M. Weinelt, "Influence of the pump pulse wavelength on the ultrafast demagnetization of Gd(0 0 0 1) thin films," J. Phys. Condens. Matter **29**, 234003 (2017).
[71]D. Schick, A. Bojahr, M. Herzog, R. Shayduk, K. C. von Schmising, and M. Bargheer, "udkm1Dsim—A simulation toolkit for 1D ultrafast dynamics in condensed matter," Comput. Phys. Commun. **185**, 651 (2014).
[72]C. Kittel, "Model of exchange-inversion magnetization," Phys. Rev. **120**, 335–342 (1960).

Article VII – Supplemental Material

Supplementary material to: Unconventional picosecond strain pulses resulting from the saturation of magnetic stress within a photoexcited rare earth layer

A. von Reppert,[1] M. Mattern,[1] J.-E. Pudell,[1,2] S. P. Zeuschner,[1,2] K. Dumesnil,[3] and M. Bargheer[1,2,*]

[1]*Institut für Physik & Astronomie, Universität Potsdam, Karl-Liebknecht-Str. 24-25, 14476 Potsdam, Germany*
[2]*Helmholtz Zentrum Berlin, Albert-Einstein-Str. 15, 12489 Berlin, Germany*
[3]*Institut Jean Lamour (UMR CNRS 7198), Université Lorraine, 54000 Nancy, France*

(Dated: February 24, 2020)

S1. OVERVIEW OF EXPERIMENTAL RESULTS

In Fig. S1 we present a complete overview of the temperature and excitation energy dependent UXRD measurements from which a selection is shown in Fig. 3 and Fig. 4 of the main manuscript. The data are presented without offset to allow for direct comparison. The insets (Fig. S1(c) and Fig. S1(f)) show the Nb detection layer strain averaged for over $t > 200$ ps. This model-independent measure for the thermal expansion indicates the reduced energy transport from the Dy film to the Nb detection layer at $T < T_{\text{Néel}} = 180$ K (see S1(c)). The saturation of the energy transfer to the finite energy reservoir of magnetic excitations is heralded by the non-linear fluence dependence that is pointed out by the grey dashed line in Fig. S1(f) and further discussed in the main text.

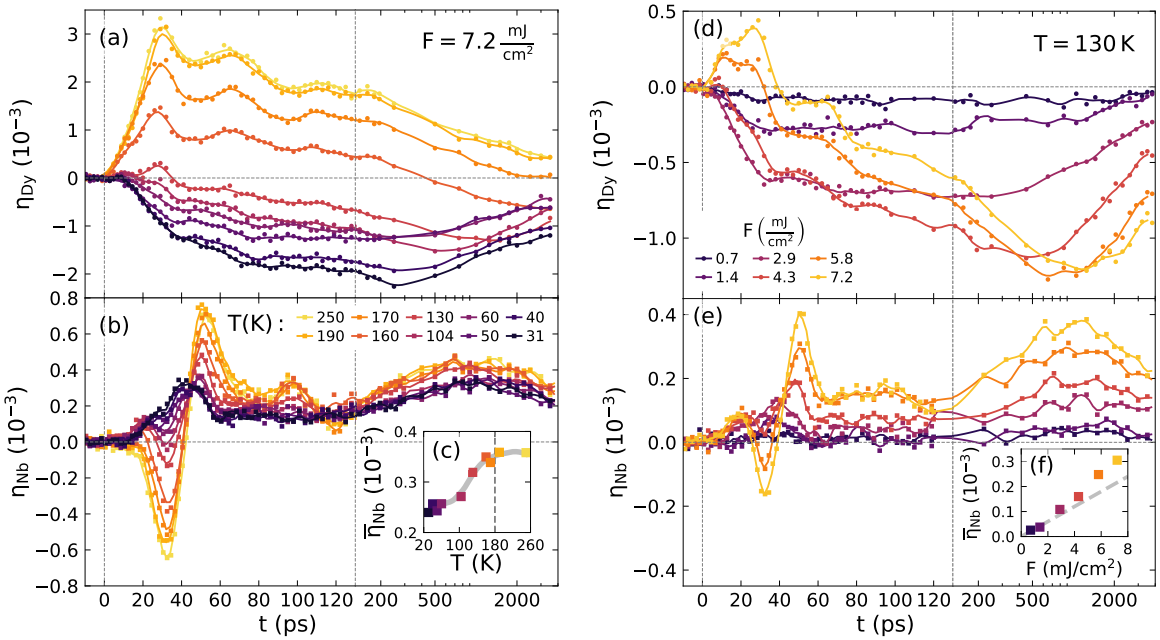

FIG. S1. **Overview of experimental results:** Temperature-dependent strain response η of the Dy transducer (a) and the Nb detection layer (b) for a fixed excitation fluence of $F = 7.2\,\text{mJ/cm}^2$. The linear to logarithmic axis break at 130 ps (vertical, grey, dashed line) allows the simultaneous depiction of the changes in the picosecond strain pulse and the nanosecond thermal expansion response. Inset (c) shows the average thermal expansion of the Nb detection layer from 200 ps to 4000 ps. Solid lines serve as guide to the eye. The experimental results for varying the excitation fluence at a fixed start temperature $T = 130$ K are depicted in the same way in (d)–(f). The dashed line in (f) highlights the small non-linear increase of the thermal expansion of the Nb detection layer.

* bargheer@uni-potsdam.de; http://www.udkm.physik.uni-potsdam.de

S2. SIMPLIFIED MODEL SIMULATIONS

In this section we discuss the modeled strain response for an idealized transducer-detection layer sample that is depicted in Fig. S2(a). We present the characteristics of the picosecond strain response that relate to the rise time τ and the profile length ξ of the driving stress as well as the layer thicknesses d_1 and d_2. We compare the simulations to selected experimental data to illustrate the influence of these parameters on the expected picosecond strain response, as it is briefly discussed in the main text.

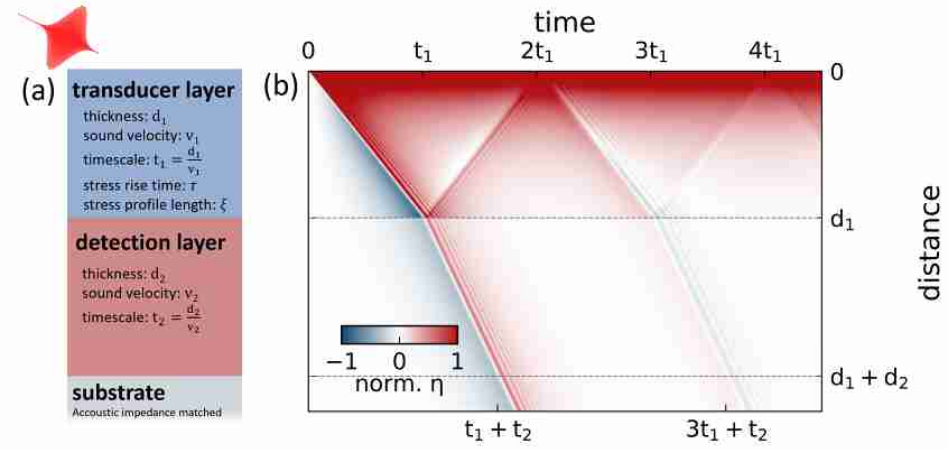

FIG. S2. **Strain response of a simplified transducer-detection layer system:** (a) Schematic visualization of the structure, which consists of an absorbing transducer ($d_1 \approx 95$ nm, $v_1 \approx 3$ nm/ps) adjacent to a non-absorbing layer ($d_2 \approx 103$ nm, $v_2 \approx 5$ nm/ps on top of a semi-infinite substrate with good acoustic impedance matching to the film. (b) A typical spatio-temporal strain $\eta(z,t)$ profile that results from an instantaneous ($\tau = 0$, expansive stress ($\sigma > 0$) with an exponentially decaying profile ($\xi = 25$ nm) within the transducer layer. Tick marks indicate significant points in time that result from the characteristic timescales $t_1 = d_1/v_1$ and $t_2 = d_2/v_2$. In the following we discuss the strain response averaged over the transducer- (η_1) and detection-layer (η_2).

The presented model simulations illustrate the influence of the driving stress characteristics τ, ξ on the strain response. We deliberately omit the complications that arise from the multiple reflections at additional interfaces, thermal transport and the sensitivity function for hard x-ray diffraction experiments. The presented simulations are obtained using the phonon class of the modular UDKM1DSIM[1] MATLAB library that simulates the strain response of a linear chain of masses and springs for different idealized scenarios for the driving stress sigma $\sigma(z,t)$ with unit cell resolution. The mechanical properties of the transducer and detection layer system have been chosen to match our sample structure where the Y interlayers are replaced by Dy. We emphasize that the observed response can be generalized to any two-layer system by introducing the natural timescales $t_1 = d_1/v_1 \approx 30.6$ ps and $t_2 = d_2/v_2 \approx 20.2$ ps that it takes to propagate strain through the layers at the speed of sound.

A. Signatures of the stress rise time

Fig. S3 shows the effect of different rise times τ for the driving stress $\sigma(t) = \sigma_\infty(1-\exp(-t/\tau))$ on the average strain response of the transducer layer $\eta_1(t)$ and detection layer $\eta_2(t)$. The spatial profile is fixed throughout this simulation series to be an exponential stress profile $\sigma(z) = \sigma_{\max}\exp(-z/\xi)$ with a decay-length $\xi = 25\,\mathrm{nm}$. The direct comparison between the expansive stress (Fig. S3(a)–(d)) and contractive stress (Fig. S3(e)–(h)) shows that the simulated strain results for both the transducer and detection layer are identical except for a change of sign. We relate the simulation of η_1 and η_2 to the two representative data sets at 250 K and 31 K for η_{Dy} and η_{Nb} that are shown in Fig. 3 of the main manuscript.

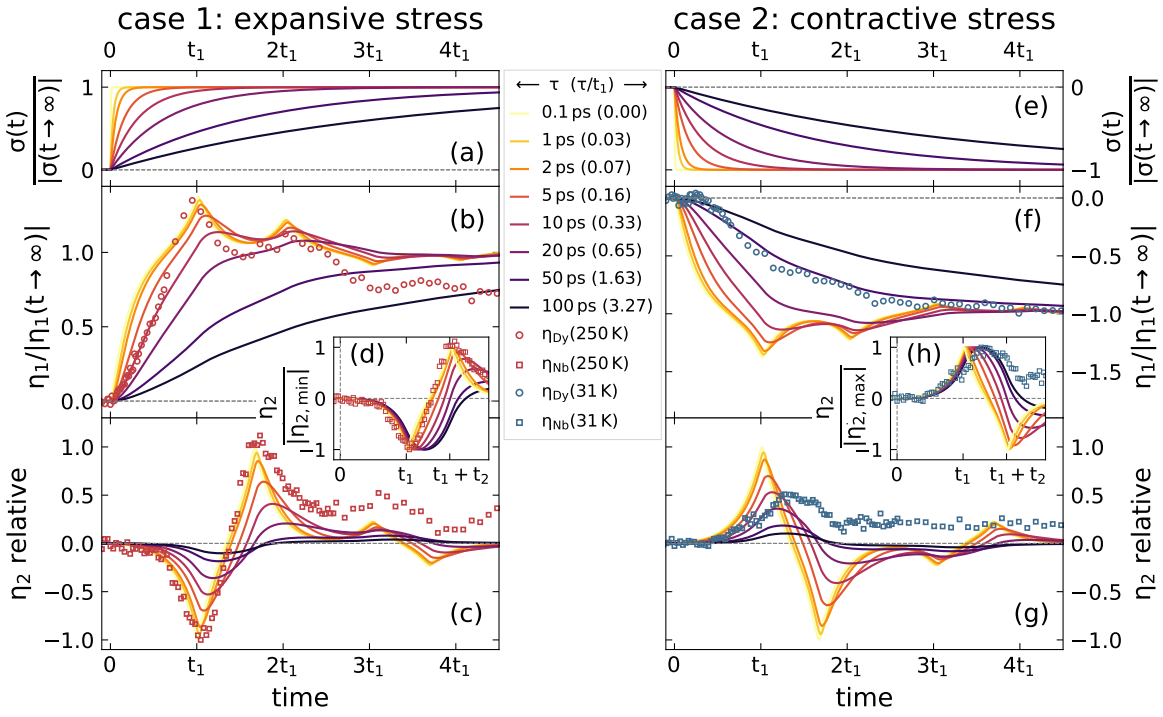

FIG. S3. **Effects of the stress rise time τ on the picosecond strain response:** We compare the cases of an expansive stress (a)–(d) and a contractive stress (e)–(g) within the transducer. The top panels (a) and (e) depict the time-dependence of the stress. The middle panels (b) and (f) show the simulated average strain in the transducer layer normalized to the value attained for large delays. The bottom panels (c) and (g) display the corresponding average strain in the buried detection layer relative to the maximum strain amplitude for the fast rising stress. The insets (d) and (h) compare the shape of the simulated curves by normalizing to the maximum contraction and expansion respectively. The experimentally observed strain responses for $T = 250\,\mathrm{K}$ is best described by a fast rising expansive stress whereas the sample response at 31 K resembles that of a slowly contracting transducer.

A qualitative comparison with the shape of the experimental results shows that the response within the paramagnetic phase of Dy ($T = 250\,\mathrm{K}$, $F = 7.2\,\mathrm{mJ/cm^2}$) can be rationalized by fast rising expansive stress $\tau < 5\,\mathrm{ps}$ that launches a pronounced bipolar strain pulse into the adjacent detection layer. Deviations of the simulated η_1 and $\eta_{\mathrm{Dy}}(250\,\mathrm{K})$ for small delays $t < t_1$ can be rationalized by the neglected Y capping layer of the real sample structure. For $t > t_1$ η_{Dy} exhibits a decay that is not reproduced in the simulations since we neglect thermal transport to adjacent layers.

The experimentally observed contraction for the magnetically ordered phase of Dy ($T = 31\,\mathrm{K}$ $F = 7.2\,\mathrm{mJ/cm^2}$) shows the best agreement with a slowly rising total stress that increases with $\tau > 40\,\mathrm{ps}$. The reduced amplitude and the nearly uni-polar shape of the strain pulse launched into the detection layer is incompatible with a fast rising total stress. The absence of pronounced peaks in the slowly rising contraction of the Dy transducer at t_1 and t_2 corroborates this finding.

This brief, qualitative analysis of the stress rise times provides a first rough overview over the signal interpretation. To quantitatively capture the measurement results we require a more complex model that is outlined in the main manuscript.

B. Signatures of the stress profile length and layer thicknesses

To calibrate the expansive electron-phonon stress and the layer thicknesses we employ the results of the strain response of non-magnetic heterostructure in the PM phase of Dy at 250 K. Fig. S4 illustrates the influence of the spatial shape of the stress profile $\sigma(z)$ that is parametrized as $\sigma(z) = \sigma_{\max} \exp(-z/\xi)$ and the thickness of the detection layer d_2. Compared to the simplified simulation series one finds that the measured response in the PM phase of Dy is best described by $\xi \approx 25$ nm and $d_2 \approx 100$ nm. The full simulation of the PM phase presented in Fig. 3 of the main manuscript includes the additional Y-layers, heat diffusion and a simulation of the X-ray diffraction signal that are omitted here for clarity.

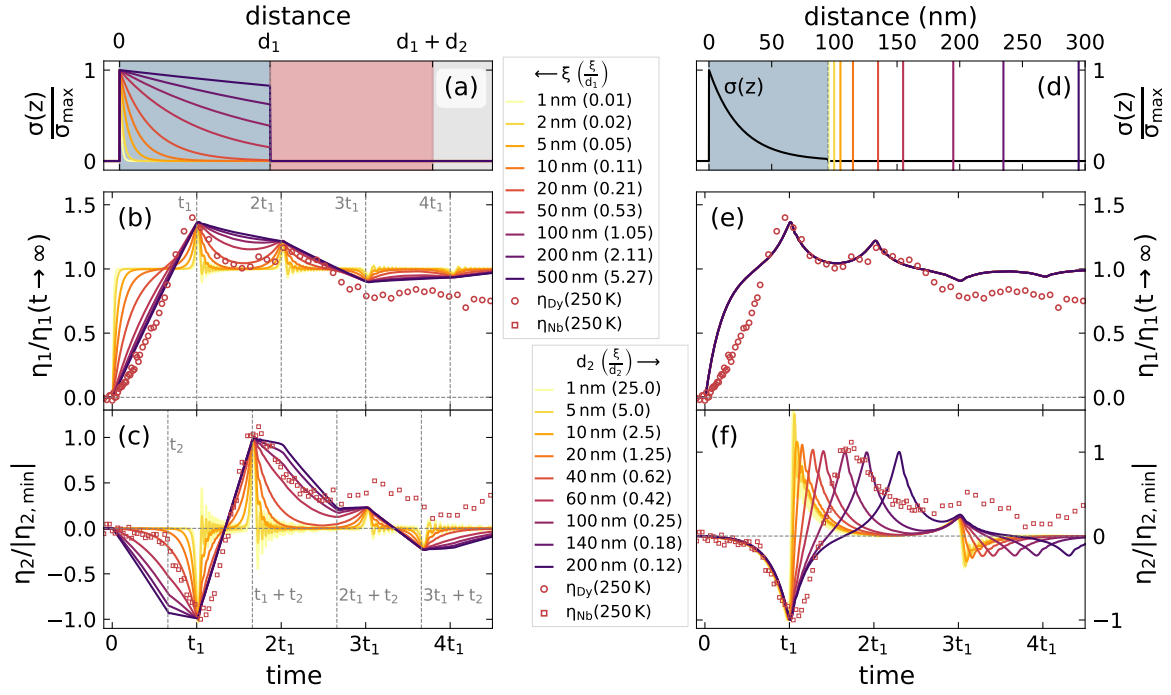

FIG. S4. **Influence of the stress profile $\sigma(z)$ and detection layer thickness d_2 on the observed strain response η:** (a)–(c) Simulated dependence of strain in the bilayer on the exponential stress profile length ξ for an instantaneous stress $\tau \to 0$. Panel (a) depicts the different stress profiles within the transducer layer. Panels (b) and (c) show the temporal shape of the average transducer and detection layer strain respectively. Dashed lines and tick marks relate characteristic strain signatures to the natural timescales t_1 and t_2 of the sample. Panels (d)–(f) show the influence of the detection layer thickness d_2 on the strain signal. Colored lines in (d) indicated the different detection layer thicknesses in relation to the stress-profile within the transducer. While the transducer strain response shown in (e) is not affected by d_2 , the timing of the second part of the bipolar strain pulse shifts.

S3. MODELING DETAILS

In subsection S3 A we provide an overview over the implementation and mathematical relations of the simulation that are described textually in the main manuscript. In subsection S3 B we provide the relevant thermophysical parameters for the materials within the heterostructure. In subsection S3 C we discuss a Gedankenexperiment that illustrates the effect of different boundary conditions on the observed strain for equilibrium heating and ultrafast laser heating of thin film samples.

A. Sequence of the simulation steps

For the modeling we use the modular UDKM1DSIM toolbox package that developed by Schick et al.[1]. We only introduce an additional magnetic stress contribution (a force term in the linear chain model for the strain evolution) according to the linear dependence of stress and energy density in the magnetic subsystem. In Fig S5 a schematic block diagram that summarizes the simulation steps for the PM and AFM simulations together with the mathematical relations for the strain calculation provided in the following paragraphs.

The complexity of the required model leads to the fact that there is no single analytical equation but rather a set of thermophysical - relations that we evaluate numerically on a unit-cell grid. We discuss first the central equations for the modeling of the PM phase response and subsequently for the AFM phase.

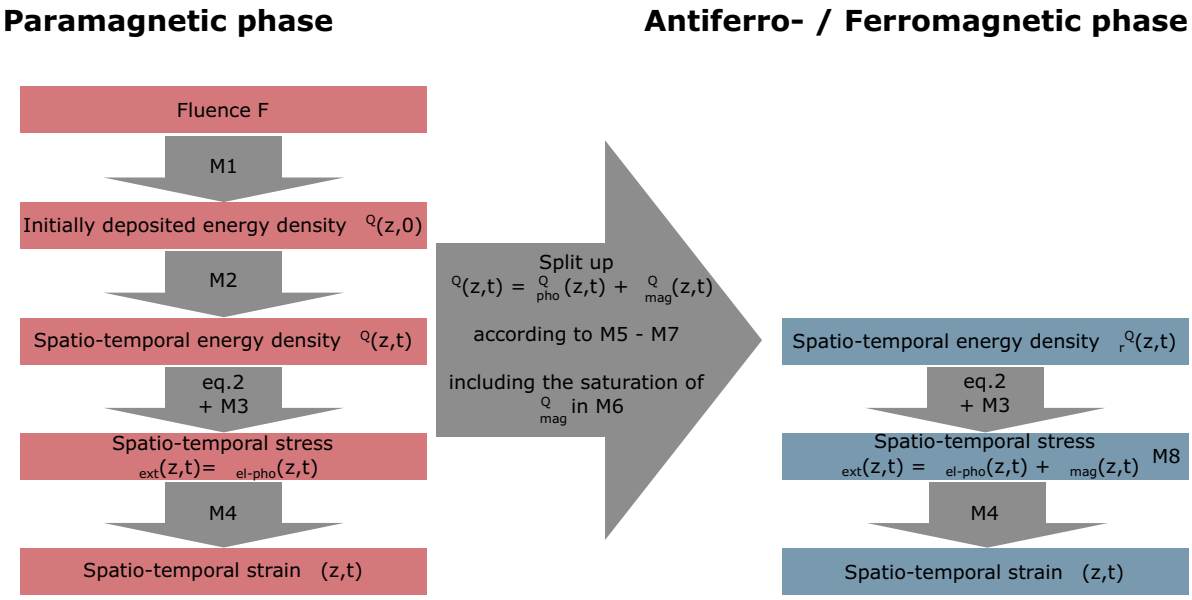

FIG. S5. **Schematic block diagram for the simulation steps:** The left side shows the simulation of the PM-phase strain response using the UDKM1DSIM toolbox. The right side shows the modification to model the AFM phase response by the additional stress that arises from the energy transfer to magnetic excitations.

1. *Paramagnetic-phase simulation*

First we provide the relations for simulating the electron-phonon stress at 250 K (following the left side of the block diagram in Fig. S5).

Step 1: The initial temperature jump to $T_{\mathrm{start}} + \Delta T(z)$ after laser-excitation is calculated from:

$$\rho_{\mathrm{tot}}^{\mathrm{Q}} = \int_{T_{\mathrm{start}}}^{T_{\mathrm{start}}+\Delta T(z)} C(T')\mathrm{d}T' = \frac{F}{\xi} e^{-\frac{z}{\xi}} \tag{M1}$$

with the heat capacity $C(T)$, optical penetration depth ξ, and absorbed fluence F.

Step 2: The subsequent spatio-temporal-energy flow is approximated using a 1D heat diffusion equation. The heat transport in Dy, Y and Nb proceeds via electrons and phonons. The electronic conductivity contributes a larger fraction, but the fast

electron-phonon coupling allows us to approximate the transport by a one-temperature-model. For the combined electron-phonon temperature $T(z,t)$ we use:

$$C\rho\frac{\partial T}{\partial t} = \frac{\partial}{\partial z}\left(\kappa\frac{\partial T}{\partial z}\right), \tag{M2}$$

with the heat capacity C, density ρ and heat conductivity κ.

Step 3: The conversion between the local energy density and strain is done using the Grüneisen relation between stress and energy density given in the main manuscript (eq. 2 of the main text), and the electron-phonon coupling is implemented as a change in the stress by an empirical electron-phonon time-constant $\tau_{\mathrm{el-pho}}$:

$$\sigma_{\mathrm{el-pho}}(t,z) = \Gamma_{\mathrm{pho}}\rho^{\mathrm{Q}}_{\mathrm{pho}}(t,z) + \Gamma_{\mathrm{el}}\rho^{\mathrm{Q}}_{\mathrm{el}}(t,z) = \Gamma_{\mathrm{pho}}\rho^{\mathrm{Q}}_{\mathrm{tot}}(t,z)(1-e^{-\frac{t}{\tau_{\mathrm{el-pho}}}}) + \Gamma_{\mathrm{el}}\rho^{\mathrm{Q}}_{\mathrm{tot}}(t,z)(e^{-\frac{t}{\tau_{\mathrm{el-pho}}}}). \tag{eq. 2}$$

Thus the stress only depends on the ratio of their different Grüneisen constants $\frac{\Gamma_{\mathrm{el}}}{\Gamma_{\mathrm{pho}}}$:

$$\sigma_{\mathrm{el-pho}}(t,z) = \sigma_{\mathrm{pho}}(t,z)H(t)\left(1+\left(\frac{\Gamma_{\mathrm{el}}}{\Gamma_{\mathrm{pho}}}-1\right)e^{-\frac{t}{\tau_{\mathrm{el-pho}}}}\right). \tag{M3}$$

where $H(t)$ is a Heaviside function and $\sigma_{\mathrm{pho}}(t,z) = \Gamma_{\mathrm{ph}}\rho^{\mathrm{Q}}_{\mathrm{tot}}(t,z)$ is the value attained after electron-phonon equilibration. The ratio $\frac{\Gamma_{\mathrm{el}}}{\Gamma_{\mathrm{pho}}} \approx 0.5$ and $\tau_{\mathrm{el-pho}} = 2\,\mathrm{ps}$ are used in all simulations.

Step 4: The resulting stress $\sigma_{\mathrm{ext}} = \sigma_{\mathrm{el-pho}}$ enters as an external forcing into the 1D - elastic wave equation of the atomic displacement u.:

$$\rho\frac{\partial^2 u_{\mathrm{i}}}{\partial t^2} = \frac{\partial}{\partial z}(c_{33}\frac{\partial u}{\partial z} + \sigma_{\mathrm{ext}}) \tag{M4}$$

This continuum elasticity relation is solved numerically using a linear chain of masses and springs model as provided by the modular UDKM1DSIM toolbox. Due to the homogeneous laser excitation we neglect any shear forces so that the local out-of-plane strain $\eta(z,t)$ follows then directly from the local displacement $u(z,t)$ according to $\eta = \frac{\partial u}{\partial z}$.

2. *AFM-phase simulation*

The simulation of the strain response in the magnetic phase is similar to the non-magnetic sample. The main difference is that an additional stress term (σ_{mag}) appears in equation M4.

The magnetic stress generation is subject to the following constraints: Energy conservation requires $\int \rho^{\mathrm{Q}}_{\mathrm{tot}}(t,z)\mathrm{d}z$ to be the same for all simulated experiments with the same excitation fluence. This yields the relation:

$$\int \rho^{\mathrm{Q}}_{\mathrm{tot}}(t,z)\mathrm{d}z = \int \left(\rho^{\mathrm{Q}}_{\mathrm{pho}}(t,z) + \rho^{\mathrm{Q}}_{\mathrm{mag}}(t,z)\right)\mathrm{d}z, \tag{M5}$$

with

$$\begin{aligned}
\rho^{\mathrm{Q}}_{\mathrm{pho}}(t,z) &= f_{\mathrm{pho}}(t)\rho^{\mathrm{Q}}_{\mathrm{pho,PM}}(t,z) \\
\rho^{\mathrm{Q}}_{\mathrm{mag}}(t,z) &= \begin{cases} f_{\mathrm{mag}}(t)\rho^{\mathrm{Q}}_{\mathrm{pho,PM}}(t,z) & \text{if} \quad f_{\mathrm{mag}}(t)\rho^{\mathrm{Q}}_{\mathrm{pho,PM}}(t,z) \le \rho^{\mathrm{Q}}_{\mathrm{mag,max}}(T_{\mathrm{start}}) \\ \rho^{\mathrm{Q}}_{\mathrm{mag,max}}(T_{\mathrm{start}}) & \text{if} \quad f_{\mathrm{mag}}(t)\rho^{\mathrm{Q}}_{\mathrm{pho,PM}}(t,z) > \rho^{\mathrm{Q}}_{\mathrm{mag,max}}(T_{\mathrm{start}}) \\ 0 & \text{if z is in } \mathrm{Y}, \mathrm{Nb}, \mathrm{Al_2O_3} \end{cases}
\end{aligned} \tag{M6}$$

where the time-dependent energy transfer to magnetic excitations is modeled with two time-scales according to:

$$f_{\mathrm{mag}}(t) = \left(A_1 H(t) + A_2\left(1-e^{-\frac{t}{\tau_2}}\right)\right). \tag{M7}$$

The parameters $A_1 = A_2 = 0.255$ and $\tau_2 = 15\,\mathrm{ps}$ are used in all AFM and FM simulations. The total external stress thus has two contributions in the magnetic phase:

$$\sigma_{\mathrm{ext}}(t,z) = \sigma_{\mathrm{el-pho}}(t,z) + \sigma_{\mathrm{mag}}(t,z) = \Gamma_{\mathrm{pho}}\rho^{\mathrm{Q}}_{\mathrm{pho}}(t,z) + \Gamma_{\mathrm{el}}\rho^{\mathrm{Q}}_{\mathrm{el}}(t,z) + \Gamma_{\mathrm{mag}}\rho^{\mathrm{Q}}_{\mathrm{mag}}(t,z), \tag{M8}$$

B. List of Thermo-physical simulation parameters

Carrying out strain simulations using the UDKM1DSIM toolbox [1] requires the thermophysical and elastic properties of the materials within the sample as input. An overview of the simulation parameters at $T = 250$ K is provided in Tab. I. References are given and where not otherwise specified the values are taken from the CRC Handbook of Chemistry and Physics, 93rd Edition, by Haynes Haynes [2]. Values that are marked by an asterisk (⋆) are adjusted for the simulation to match the observed result. In that case the corresponding literature value is provided in parentheses. Especially the properties of the Y cap layer needed to be altered to find a satisfactory fit with the measured data. The reduction of the absorption and thermal expansion of this cap layer is attributed to a (partial) oxidation of this layer since the sample was kept at ambient conditions prior to the measurements.

TABLE I. **Material properties used for the strain simulation.**

property / material	**Y**	**Dy**	**Nb**	**Al_2O_3**
number of simulated unit cells	37 (22 nm) 8 (5 nm)	142 (80 nm)	220 (103 nm)	1890 (900 nm)
unit cell orientation	(0001)	(0001)	(110)	(11−20)
crystal structure	hcp	hcp	bcc	hcp
lattice constant (Å)				
c-axis out-of-plane	6.03 (5.73⋆)	5.65	4.67	4.76
a-axis in-plane	3.65	3.59	4.67	12.80
b-axis in-plane	3.65	3.59	3.30	8.24
order of reflex	2	2	1	2
q_z-position in simulation ($Å^{-1}$)	2.083	2.225	2.694	2.643
elastic constants (GPa)	from [3]	from [4]	from [5]	from [6]
c_{33}	77.8	78.3	246.7	498.1
c_{13}	20.0	22.5	133.7	110.9
c_{11}	79.0	74.2	246.7	496.8
c_{12}	28.7	25.5	133.7	163.6
density ρ (g/cm^{-3})	4.47	8.6	8.57	4.05
out-of-plane sound velocity v (nm/ps)	4.15	3.10	5.08	11.14
acoustic impedance (g/cm^{-3} nm/ps)	18.54	26.50	43.56	44.853
molar mass (g/mol)	88.91	162.5	92.91	101.96
lin. therm. expansion ($10^{-6}\,K^{-1}$)				
thin film: out-of-plane $\alpha_\perp$	7.14⋆ (11.9)	18.27	7.6	–
bulk: out-of-plane $\alpha_\perp$	19.7 [7]	20.3 [7]	7.6 [8]	6.6 [9]
bulk: in-plane $\alpha_\parallel$	6.2 [7]	4.7 [7]	7.6 [8]	–
Poisson correction factor for Γ_{pho}: $1+\frac{c_{13}}{c_{33}}\frac{2\alpha_\parallel}{\alpha_\perp}$	1.1	1.1	2.4	–
Poisson correction factor for Γ_{mag}: $1-\frac{c_{13}^2}{(c_{11}+c_{12})c_{33}}$	-	0.87	-	-
specific heat C_p ($J\,kg^{-1}K^{-1}$)	291.49 [10]	167.3 [11]	270.88 [2]	657.22 [12]
thermal conductivity κ ($W\,m^{-1}K^{-1}$)	24.8 [13]	6.7⋆ (11.1 [13])	53.0 [13]	58.33 [14]
optical penetration depth (nm)	72⋆ (24)	22⋆ (24)	25	∞

C. Effect of boundary conditions in equlibrium- and laser-heating experiments

Within the analysis of our experiment we use the Grüneisen coefficients that were extracted from equilibrium heating conditions where the sample is in equilibrium with the adjacent cryostat. In these equilibrium heating experiments the sample temperature is equilibrated over minutes so that the materials are given enough time to expand both in-plane and out-of-plane. On the contrary in the laser-excitation experiments the probed sample area is excited homogeneously by the laser-pulse and we probe the strain on a sub-nanosecond to nanosecond timescale that is too short for the in-plane strains to develop due to the strain propagation at the speed of sound. The following section provides the equations that we use to approximate the effect of the boundary conditions for ultrafast and equilibrium heating in our sample. Fig S6 displays a schematic Gedankenexperiment

that illustrates that the absence of in-plane motion on ultrafast timescales increases the out-of-plane expansion of electron-phonon stresses. The same effect decreases the out-of-plane contraction by magnetic stresses on ultrafast timescales. The following formulas are designed to provide a quantitative estimate of the resulting difference between the Grüneisen constant extracted from equilibrium measurements and the Grüneisen constant that is applicable in the time-resolved experiments under in-plane fixation conditions.

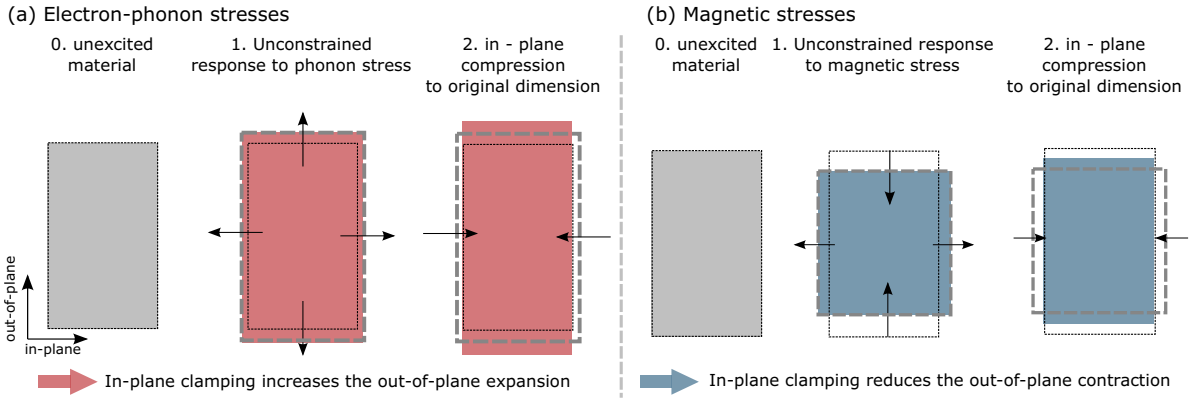

FIG. S6. **Gedankenexperiment on the effect of in-plane fixation on the out-of-plane strain:** The first step shows the equilibrium response of the thin film without in-plane constraints and the second step illustrates the result of the in-plane fixation. (a) Effect for the expansive stress of electrons and phonons, where the out-plane strain increases. (b) Effect on the magnetic stress that is dominated by a uniaxial contraction along the out-of-plane c-axis and a small in-plane expansion. Here the in-plane fixation leads to a smaller contraction compared to the equilibrium response.

The general linear relation between stress σ and strain η from linear elastic theory is tensor like and is stated in equation P1 with the help of the stiffness tensor c_{ijkl}.

$$\sigma_{ij} = \sum_{kl} c_{ijkl}\eta_{kl} \tag{P1}$$

Using the symmetry properties of a hexagonal system and applying the compressed Voigt notation (1 = 11, 2 = 22, 3 = 33, 4 = 23, 5 = 31, 6 = 12) equation (P1) can be simplified to the six relations (P2) with the five independent material parameters $c_{11}, c_{33}, c_{12}, c_{13}$ and c_{44} ($c_{66} = 0.5(c_{11} - c_{12})$).[15]

$$\underbrace{\begin{pmatrix}\sigma_1\\ \sigma_2\\ \sigma_3\\ \sigma_4\\ \sigma_5\\ \sigma_6\end{pmatrix}}_{\text{stress}} = \underbrace{\begin{pmatrix} c_{11} & c_{12} & c_{13} & 0 & 0 & 0\\ c_{12} & c_{11} & c_{13} & 0 & 0 & 0\\ C_{13} & C_{13} & C_{33} & 0 & 0 & 0\\ 0 & 0 & 0 & c_{44} & 0 & 0\\ 0 & 0 & 0 & 0 & c_{44} & 0\\ 0 & 0 & 0 & 0 & 0 & c_{66}\end{pmatrix}}_{\text{elastic constants } c_{ij}} \underbrace{\begin{pmatrix}\eta_1\\ \eta_2\\ \eta_3\\ \eta_4\\ \eta_5\\ \eta_6\end{pmatrix}}_{\text{strain}} \tag{P2}$$

In the experiments presented here I neglect any shear strain effects. This reduces the system to the three coupled equations stated in (P3). The off-diagonal elements c_{13} couple the in-plane strains η_1 and η_2 to the out-of-plane strain η_3. This manifests itself by an in-plane strain response to a uniaxial out-of-plane stress σ_3, which is quantified by Poisson's number $\nu = -\frac{\eta_1}{\eta_3} = \frac{c_{13}}{c_{11}+c_{12}}$.

$$\begin{pmatrix}\sigma_1\\ \sigma_2\\ \sigma_3\end{pmatrix} = \begin{pmatrix} c_{11} & c_{12} & c_{13}\\ c_{12} & c_{11} & c_{13}\\ c_{13} & c_{13} & c_{33}\end{pmatrix} \begin{pmatrix}\eta_1\\ \eta_2\\ \eta_3\end{pmatrix} \tag{P3}$$

This transverse strain (i. e. Poisson effect) is at the origin of the necessary modification of the Grüneisen constant that has been extracted from equilibrium measurements for the simulation of ultrafast strain responses. For a given temperature change ΔT the unconstrained equilibrium heating the strains will be $\eta_1^{\text{eq}} = \eta_2^{\text{eq}} = \alpha_{\parallel}\Delta T$ and $\eta_3^{\text{free}} = \alpha_{\perp}\Delta T$ (Step 1 in Fig. S6(a)).

Under laser-excitation the in-plane expansion is constrained due to the homogeneous excitation of the sample where the in-plane strain relaxation is limited to the timescales of hundreds of nanoseconds by the speed of sound and the excitation spotsize. To account for this we can calculate the additional out-of-plane strain η_3' that results from the in-plane stress $\sigma_1' = \sigma_2'$ that is necessary to compress the material to its initial dimensions (Step 2 in Fig. S6(a)). The corresponding system of equation is:

$$\begin{pmatrix} \sigma_1' \\ \sigma_2' \\ 0 \end{pmatrix} = \begin{pmatrix} c_{11} & c_{12} & c_{13} \\ c_{12} & c_{11} & c_{13} \\ c_{13} & c_{13} & c_{33} \end{pmatrix} \begin{pmatrix} \eta_1' \\ \eta_2' \\ \eta_3' \end{pmatrix} \tag{P4}$$

Solving relation (P4) for η_3' leads to :

$$\eta_3' = -\frac{C_{13}}{C_{33}}(\eta_1' + \eta_2') = \frac{C_{13}}{C_{33}}(2\alpha_\parallel \Delta T) \tag{P5}$$

The corresponding correction factor for unconstrained equilibrium heating and constrained ultrafast-heating is the ratio of the clamped (η_3^{clamped}) and free expansion (η_3^{free}):

$$\frac{\eta_3^{\text{clamped}}}{\eta_3^{\text{free}}} = \frac{\eta_3^{\text{free}} + \eta_3'}{\eta_3^{\text{free}}} = 1 + \frac{C_{13}}{C_{33}} \frac{2\alpha_\parallel}{\alpha_\perp}. \tag{P6}$$

The resulting, so-called Poisson correction factor for the thermoelastic expansion due to electron and phonon excitations $1 + \frac{C_{13}}{C_{33}} \frac{2\alpha_\parallel}{\alpha_\perp}$ is provided in table I for all materials.

1. *Special case for the (110)-oriented - Niobium layer*

For the Nb (110)-oriented cubic crystal surface, the above discussion remains valid but the elastic constants need to be calculated in the rotated coordinate system, where the new z-axis coincides with the [110]-direction. For the in-plane directions we choose the cartesian coordinate system with the x-axis pointing along the [1-10]- and the y axis along the [001]-direction.

The different representations of the stiffness tensor c in two different coordinate systems are related via:

$$\widetilde{c}_{ijkl} = c_{pqrs}(\vec{e}_p \cdot \widetilde{\vec{e}}_i)(\vec{e}_q \cdot \widetilde{\vec{e}}_j)(\vec{e}_r \cdot \widetilde{\vec{e}}_k)(\vec{e}_s \cdot \widetilde{\vec{e}}_l) \tag{P7}$$

The new relations in the contracted Voigt notation are:

$$\begin{pmatrix} \sigma_1 \\ \sigma_2 \\ \sigma_3 \\ \sigma_4 \\ \sigma_5 \\ \sigma_6 \end{pmatrix} = \begin{pmatrix} \widetilde{c}_{33} & \widetilde{c}_{12} & \widetilde{c}_{13} & 0 & 0 & 0 \\ \widetilde{c}_{12} & \widetilde{c}_{22} & \widetilde{c}_{13} & 0 & 0 & 0 \\ \widetilde{c}_{13} & \widetilde{c}_{13} & \widetilde{c}_{33} & 0 & 0 & 0 \\ 0 & 0 & 0 & \widetilde{c}_{44} & 0 & 0 \\ 0 & 0 & 0 & 0 & \widetilde{c}_{55} & 0 \\ 0 & 0 & 0 & 0 & 0 & \widetilde{c}_{44} \end{pmatrix} \begin{pmatrix} \eta_1 \\ \eta_2 \\ \eta_3 \\ \eta_4 \\ \eta_5 \\ \eta_6 \end{pmatrix} \tag{P8}$$

It contains the 7 different material constants given in table II.

$\widetilde{c}_{33}$ (GPa)	$\widetilde{c}_{12}$ (GPa)	$\widetilde{c}_{13}$ (GPa)	$\widetilde{c}_{22}$ (GPa)	$\widetilde{c}_{44}$ (GPa)	$\widetilde{c}_{55}$ (GPa)
221.45	138.7	162.85	245.6	29.3	53.4

TABLE II. Elements of the transformed stiffness tensor

The resulting Poisson correction factor for the thermoelastic expansion of (110)-oriented Nb is thus turns out to be $1 + \frac{\widetilde{c}_{13}}{\widetilde{c}_{33}} \frac{2\alpha_\parallel}{\alpha_\perp} \approx 2.4$

2. Special case for magnetic stress in the Dy layer

The effect of the in-plane fixation on the contractive magnetic strain has to be estimated using a different formula since it is to a first approximation driven by a uniaxial stress along the c-axis [16]. Due to the Poisson effect, such a uniaxial out-of-plane stress leads not only to an out-of-plane contraction but also to an in-plane expansion. This requires a similar scaling factor between the magnetic Grüneisen coefficient that is determined from unconstrained equilibrium measurements when it is used to simulate time-resolved experiments under in-plane fixation conditions. The corresponding two step scheme for the calculation of the correction factor is displayed in Fig. S6(b). Explicitly we substitute $\eta_1' = \eta_2' = -\nu\eta_{3,\mathrm{mag}}$ into equation (P4) where $\nu = \frac{c_{13}}{c_{11}+c_{12}}$ and again solve the system of equations for η_3', which yields.

$$\eta_{3,\mathrm{mag}}' = -2\nu\frac{c_{13}}{c_{33}}\eta_{3,\mathrm{mag}}^{\mathrm{free}} \tag{P9}$$

$$\Rightarrow \frac{\eta_{3,\mathrm{mag}}^{\mathrm{clamped}}}{\eta_{3,\mathrm{mag}}^{\mathrm{free}}} = \frac{\eta_{3,\mathrm{mag}}^{\mathrm{free}} + \eta_{3,\mathrm{mag}}'}{\eta_{3,\mathrm{mag}}^{\mathrm{free}}} = 1 - 2\nu\frac{c_{13}}{c_{33}} = 1 - \frac{\mathrm{c}_{13}^2}{(\mathrm{c}_{11}+\mathrm{c}_{12})\mathrm{c}_{33}} \tag{P10}$$

Inserting the elastic constants known for Dysprosium[4] into relation (P10) leads to the estimate that approximately 13% less contraction is observed under laser excitation as compared to unconstrained equilibrium heating. This correction factor for the magnetic Grüneisen factor in Dysprosium is added to table I.

S4. SPATIO-TEMPORAL STRESS MAPS

Here we provide a complete overview of the modeled stress maps that are driving the linear chain of masses and springs model to obtain the simulated UXRD strain response via the UDKM1DSIM toolbox [1]. The resulting strain simulations for the Dy transducer and the Nb detection layer are shown as solid lines in Fig. 3 and 4 of the main text for the temperature and excitation energy dependent experiments respectively. For completeness we also reproduce Fig. 6 of the main text since it allows for the direct comparison of the similarities and differences in the modeled stress response between temperature- and excitation energy density dependent measurements.

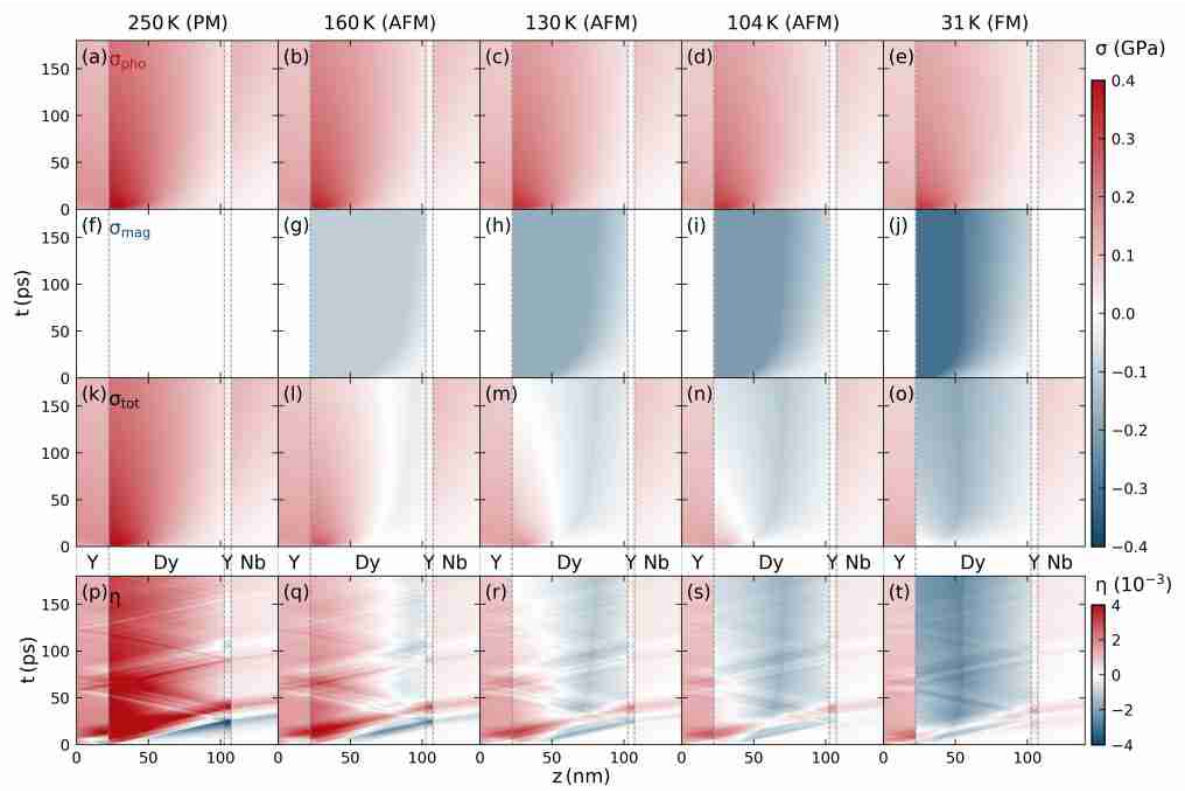

FIG. S7. **Separated stress contributions σ for the temperature dependent simulations.** Top row shows the electron-phonon stress σ_{pho}, second row the stress contributions σ_{mag} by magnetic excitations and the third row shows the total stress σ_{tot} as the sum of both contributions. Note that the compensation point that separates areas of dominantly expansive and dominantly compressive stress in the transducer shifts more and more towards the top of the Dy layer. The simulated strain dynamics that include both the coherent and incoherent strain response is depicted in the bottom row ((p)–(t)). Strain pulses that propagate at the speed of sound and get reflected at the material interfaces (indicated by dashed lines), superimposing the slowly varying strain proportional to the thermal stress.

Fig. S7 visualizes the trend in the picosecond stress for different starting temperatures but fixed pulse energy for the excitation. The observed changes in the total stress originate from the temperature dependent maximal energy density that can be deposited in the spin system. The top row of Fig. S7((a)–(e)) displays the electron-phonon stress (σ_{pho}) that varies slightly in amplitude due to the energy transfer to magnetic excitations. The second row ((f)–(j)) shows the temperature dependent contribution of the magnetic excitations (σ_{mag}) where the homogeneous color at the top of the Dy transducer indicates the saturated spin-stress. The closer the starting temperature is to $T_{Néel}$, the smaller is the maximal magnetic stress amplitude and the larger is the fraction of the transducer with fully saturated spin stress. The resulting total stress is depicted in the third row ((k)–(o)). It shows that the Dy transducer has an expansive stress at the top and a contractive stress at its bottom interface. The strain response (last row (p)–(t)), simulated using the UDKM1DSIM[1] toolbox, is driven by the presented total stress. The homogeneous strain contribution that can be attributed to the thermal expansion i.e. incoherent phonons is superimposed by picosecond strain pulses i.e. coherent phonon wavepackets that are reflected at the interfaces.

Although the color code of Fig. S7 provides a qualitative overview over the temperature dependent stress contributions, a more quantitative comparison is possible when the spatial stress profiles are compared for selected simulation times. To

that end we provide the time dependent average stress in the Dy transducer as well as the spatial energy distribution profiles depicted in Fig. S8(a)–(e) and (f)–(j) respectively. The modeled spatial stress profiles are shown at 6, 45, and 180 ps alongside the time dependence of the contractive and expansive stress contributions. The selected times for the spatial profiles are chosen such that the contributions from the 2 ps – electron-phonon and instantaneous el-spin coupling, the 15 ps – spin-phonon coupling and the heat diffusion process can be judged separately.

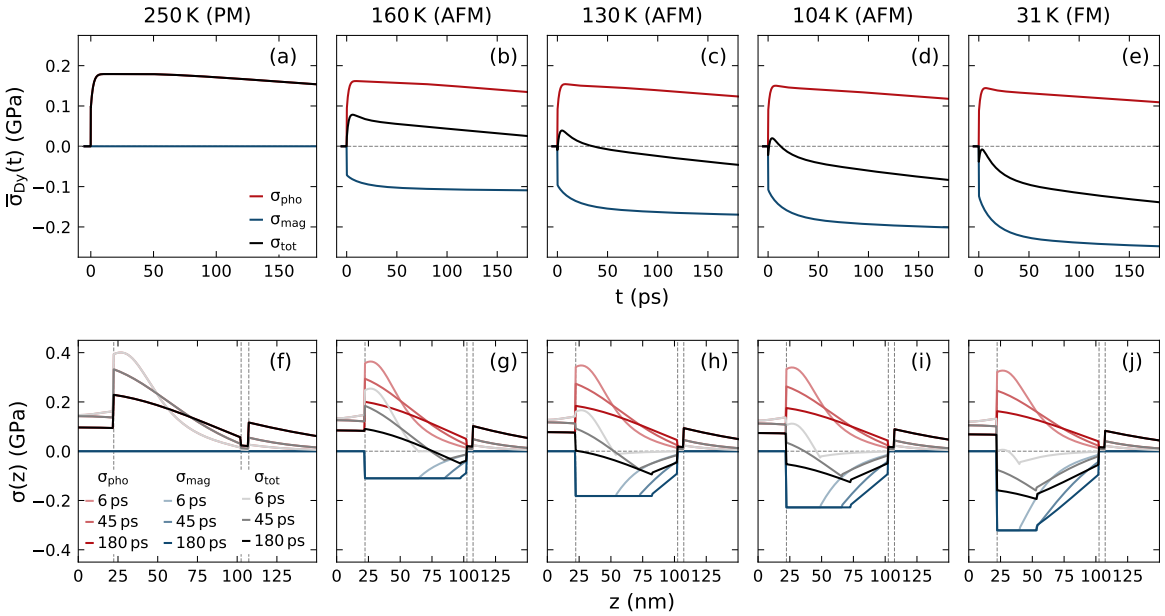

FIG. S8. **Stress contributions for the T-dependent modeling.** The top row ((a)–(e)) shows the time-dependence of the average stress in the sample for the electron-phonon, magnetic and total stress. The phonon response consists of an instantaneous step followed by a 2 ps rise time that is designed to mimic the electron-phonon coupling. The subsequent slow decay originates from thermal transport of energy to adjacent layers. The stress by magnetic excitations exhibits an instantaneous rise, an approx. 15 ps rise and an additional slow rise as deeper and deeper parts of the dysprosium layer experience spin excitation by thermal transport. The lower panel ((f)–(j)) shows the spatial form of the driving stress with discontinuous slopes arising from the initial spin-saturation.

The stress maps that correspond to the modeled excitation-energy dependent experiments at a fixed starting temperature of $T = 130$ K are presented in Fig. S9. In this series of experiments the maximal energy that can be deposited into magnetic excitations is constant while the energy deposited by the excitation pulses is increased, which is complementary to the previously discussed temperature dependent experiments. For low excitation energy densities we find that the total stress within the transducer is contractive throughout the entire layer since the larger Grüneisen constant of the spin excitations dominates the stress response. The saturation of σ_{mag} for high excitation densities leads to an expansive stress at the top of the transducer. This results in the recovery of the bipolar strain pulse feature observed in the strain response via UXRD for higher excitation energy densities. The bipolar strain response is however preceded by an expansion that is triggered by the contraction at the backside of the Dy transducer.

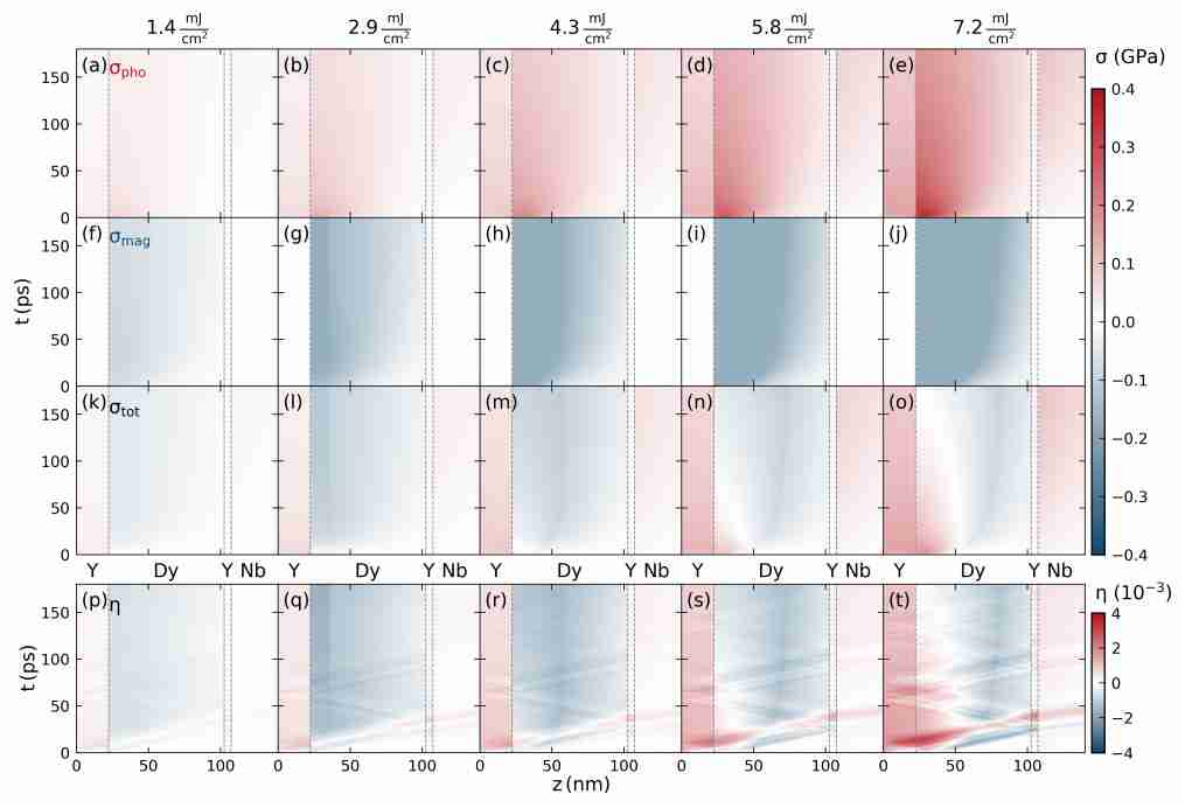

FIG. S9. **Separated stress contributions for the excitation fluence dependent simulations at $T = 130$ K.** Same plot layout as Fig. S7.

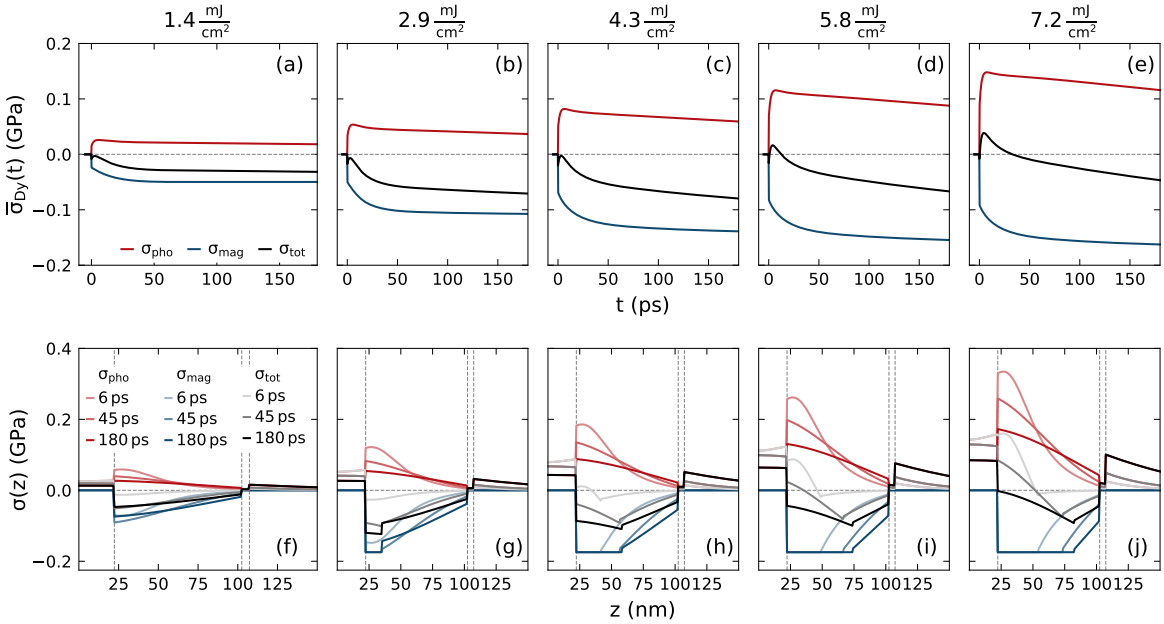

FIG. S10. **Separated stress contributions for the excitation fluence dependent simulations at $T = 130$ K.** Same plot layout as Fig. S8

[1] D. Schick, A. Bojahr, M. Herzog, R. Shayduk, K. C. von Schmising, and M. Bargheer, udkm1DsimA simulation toolkit for 1D ultrafast dynamics in condensed matter, Computer Physics Communications **185**, 10.1016/j.cpc.2013.10.009 (2014).

[2] W. M. Haynes, *CRC Handbook of Chemistry and Physics, 93rd Edition*, CRC Handbook of Chemistry and Physics (Taylor & Francis, 2012).

[3] J. F. Smith and J. A. Gjevre, Elastic constants of yttrium single crystals in the temperature range 4.2–400k, Journal of Applied Physics **31**, 645 (1960).

[4] S. B. Palmer and E. W. Lee, The elastic constants of dysprosium and holmium, Proceedings of the Royal Society of London. Series A. Mathematical and Physical Sciences **327**, 519 (1972).

[5] K. J. Carroll, Elastic constants of niobium from 4.2 to 300k, Journal of Applied Physics **36**, 3689 (1965).

[6] W. E. Tefft, Elastic constants of synthetic single crystal corundum, Journal of research of the National Bureau of Standards. Section A, Physics and chemistry **70A**, 277 (1966).

[7] F. H. Spedding, J. J. Hanak, and A. H. Daane, High temperature allotropy and thermal expansion of the rare-earth metals, Journal of the Less Common Metals **3**, 110 (1961).

[8] R. Roberge, Lattice parameter of niobium between 4.2 and 300 K, Journal of the Less Common Metals **40**, 161 (1975).

[9] M. Lucht, M. Lerche, H.-C. Wille, Y. V. Shvyd'ko, H. D. Rüter, E. Gerdau, and P. Becker, Precise measurement of the lattice parameters of a-al2o3 in the temperature range 4.5–250 k using the mössbauer wavelength standard, Journal of Applied Crystallography **36**, 1075 (2003).

[10] L. D. Jennings, R. E. Miller, and F. H. Spedding, Lattice heat capacity of the rare earths. heat capacities of yttrium and lutetium from 15–350k, The Journal of Chemical Physics **33**, 1849 (1960).

[11] V. K. Pecharsky, K. a. Gschneidner Jr., and D. Fort, Superheating and other unusual observations regarding the first order phase transition in Dy, Scripta Materialia **35**, 843 (1996).

[12] D. C. Ginnings and G. T. Furukawa, Heat capacity standards for the range 14 to 1200k, Journal of the American Chemical Society **75**, 522 (1953).

[13] C. Y. Ho, R. W. Powell, and P. E. Liley, Thermal Conductivity of the Elements, Journal of Physical and Chemical Reference Data **1**, 279 (1972).

[14] E. R. Dobrovinskaya, L. A. Lytvynov, and V. Pishchik, *Sapphire. Material, Manufacturing, Applications* (Springer, 2009).

[15] D. Royer and E. Dieulesaint, *Elastic waves in solids: Including nonlinear dynamics*, 3rd ed., Advanced texts in physics (Springer, Berlin, 2000).

[16] P. C. Landry, Variation of the helicomagnetic turn angle in dysprosium, Physical Review **156**, 578 (1967).

Article VIII

Persistent nonequilibrium dynamics of the thermal energies in the spin and phonon systems of an antiferromagnet

Alexander von Reppert, Jan-Etienne Pudell, Azize Koç, Matthias Reinhardt, Wolfram Leitenberger, Karine Dumesnil, Flavio Zamponi, and Matias Bargheer

Structural Dynamics 3, 054302 (2016)

We present a temperature and fluence dependent ultrafast x-ray diffraction study of a laser-heated antiferromagnetic dysprosium thin film. The loss of antiferromagnetic order is evidenced by a pronounced lattice contraction. We devise a method to determine the energy flow between the phonon and spin system from calibrated Bragg peak positions in thermal equilibrium. Reestablishing the magnetic order is much slower than the cooling of the lattice, especially around the Néel temperature. Despite the pronounced magnetostriction, the transfer of energy from the spin system to the phonons in Dy is slow after the spin-order is lost.

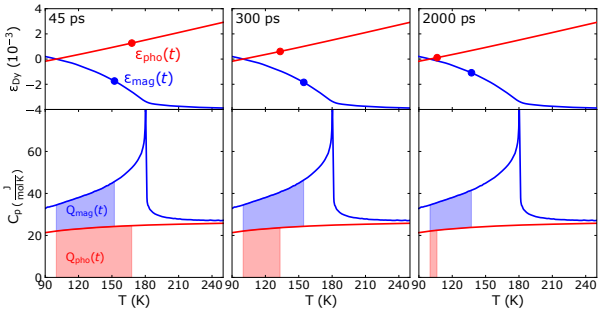

Structural Dynamics

Persistent nonequilibrium dynamics of the thermal energies in the spin and phonon systems of an antiferromagnet

Cite as: Struct. Dyn. 3, 054302 (2016); https://doi.org/10.1063/1.4961253
Submitted: 03 June 2016 . Accepted: 04 August 2016 . Published Online: 07 September 2016

A. von Reppert, J. Pudell, A. Koc, M. Reinhardt, W. Leitenberger, K. Dumesnil, F. Zamponi, and M. Bargheer

ACA

AIP Publishing

STRUCTURAL DYNAMICS **3**, 054302 (2016)

Persistent nonequilibrium dynamics of the thermal energies in the spin and phonon systems of an antiferromagnet

A. von Reppert,[1] J. Pudell,[1] A. Koc,[2] M. Reinhardt,[2] W. Leitenberger,[1]
K. Dumesnil,[3] F. Zamponi,[1] and M. Bargheer[1,2,a)]
[1]*Institut für Physik and Astronomie, Universität Potsdam, Karl-Liebknecht-Str. 24-25, 14476 Potsdam, Germany*
[2]*Helmholtz Zentrum Berlin, Albert-Einstein-Str. 15, 12489 Berlin, Germany*
[3]*Institut Jean Lamour (UMR CNRS 7198), Université Lorraine, Boulevard des Aiguillettes B.P. 239, F-54500 Vandoeuvre les Nancy Cédex, France*

(Received 3 June 2016; accepted 4 August 2016; published online 7 September 2016)

We present a temperature and fluence dependent Ultrafast X-Ray Diffraction study of a laser-heated antiferromagnetic dysprosium thin film. The loss of antiferromagnetic order is evidenced by a pronounced lattice contraction. We devise a method to determine the energy flow between the phonon and spin system from calibrated Bragg peak positions in thermal equilibrium. Reestablishing the magnetic order is much slower than the cooling of the lattice, especially around the Néel temperature. Despite the pronounced magnetostriction, the transfer of energy from the spin system to the phonons in Dy is slow after the spin-order is lost.
[http://dx.doi.org/10.1063/1.4961253]

INTRODUCTION

The unexpectedly fast magnetization loss in magnetic thin films upon photoexcitation observed two decades ago[1] stimulated extensive research aiming at ultrafast data storage and related applications. Experiments using different schemes for probing the changes induced in magnetic systems by optical light pulses have been employed. They range from visible magneto-optical Kerr effect (MOKE),[2,3] extreme ultraviolet MOKE,[4] x-ray magnetic circular dichroism[5–8] over photoelectron spectroscopy[9–11] to ultrafast x-ray diffraction (UXRD)[12] and resonant x-ray scattering.[13] The discussions are mainly focused on the transfer of angular momentum or the loss of spin-order in the framework of two- or three-temperature models. Antiferromagnets are believed to support even faster local angular momentum changes, since the average spin remains zero.[7,14] The multifarious behavior of transition metals and 4f magnetic materials, however, have eluded so far the effort to be described by a unique physical picture.[3,15,16] The demagnetization aspects at ultrashort timescales are an exciting first step of the full magnetization dynamics. The remagnetization is another fundamental issue, especially in the perspective of possible technological applications, which has received less attention. Few authors have approached the problem of how fast and through which intermediate steps the remagnetization occurs.[13,17–20] Different models have been developed to simulate the dynamics on longer timescales.[21–24] Some of them point out the important role of fluctuations and domain formation close to the phase transition. In particular, resonant x-ray diffraction experiments from the dysprosium spin-spiral have shown that some disorder of the spin system persists more than 10 ns, especially for high fluence excitation.[13]

However, a characterization of the influence of the temperature and excitation density on the remagnetization dynamics is still missing. In fact, a detailed account of the energy in the phonon and spin systems at the different stages of the remagnetization has not been reported.

[a)]bargheer@uni-potsdam.de. URL: http://www.udkm.physik.uni-potsdam.de

Dysprosium (Dy) is a thoroughly characterized material[25–28] with a pronounced magnetostrictive expansion of the lattice constant c. The 4f electrons, coupled via the 5d electrons (i.e., RKKY coupling), are responsible for its magnetic properties.[27,28] All magnetic materials show magnetostriction, i.e., a change of the lattice constant that depends on the magnetization $M(T)$. Only a single UXRD study has so far explored the magnetostrictive strain on ultrafast timescales,[12] although the existing UXRD setups have been constantly improved and allow for measuring minute lattice strains on ultrafast timescales.[29] In general, the lattice strain occurs as a response to stress imposed by a modified energy density. This is particularly evident, when the Grüneisen concept is used, e.g., for separating the electron and phonon contribution to photoinduced stress.[30,31] Although the extension to magnetic systems was suggested,[30] this powerful approach has not been realized.

Here, we analyze temperature- and excitation-fluence-dependent UXRD data from an 80 nm Dy thin film to characterize the nonequilibrium spin and lattice dynamics triggered by ultrafast heating of the electron system by a near-infrared laser pulse. The central and surprising result of our analysis can be directly read from the experimental data: The lattice contraction originating from the spin-disorder persists on the nanosecond timescale when the lattice heat is already dissipated to the substrate. The Bragg peak shift is a direct measure of the time-dependent strain $\varepsilon(t) = \Delta c(t)/c$ in the out-of-plane lattice constant c which is linearly related to the deposited heat Q_{tot} in the film. From these two measured variables $\epsilon(t)$ and Q_{tot}, we determine the transient energy densities $Q_{\text{P}}(t)$ and $Q_{\text{S}}(t)$ in the phonon and spin excitations, respectively, from a numerically robust analysis. Our model adopts the linear relation of these energy densities to the experimentally observed lattice strain via separate nearly temperature independent constants for the phonon and spin systems (see Eq. (1)). Therefore, our analysis in a "two-thermal-energies-model" (TTEM) is independent of modifications of the spatial excitation profile. In comparison with a "two-temperatures-model" (TTM),[1,32] our TTEM has the advantage that the energy contained in random motion of the phonon and spin excitations is a well-defined quantity even in strong nonequilibrium-situations, where the temperature is not.

The electron system of the Y cap layer and the dysprosium layer are photoexcited, and the multilayer system is cooled through the substrate. Here, we examine how the thermal energy in the dysprosium layer is distributed between the phonon and the spin system.

RESULTS

Linear relation of strain to lattice- and spin-energy

The sample is an 80 nm thick (0 0 0 1) oriented Dy film grown on a sapphire substrate with a 100 nm Niobium and 10 nm Yttrium (Y) buffer layer. The structure is capped with another 18 nm thin Y layer (see Fig. 3(e)) in order to support the helical spin ordering in the thin Dy film[34] and to prevent oxidation.

We have carefully measured the lattice constant $c(T)$ of the Dy thin film as a function of temperature. The lattice strain derived from the Bragg peak position (black dots in Fig. 1(a)) shows a pronounced expansion below the Néel temperature $T_{\text{N}} = 180\,\text{K}$, which results from the antiferromagnetic spin-ordering. Fig. 1(b) shows the linear expansion coefficient $\alpha(T)$ derived from this measurement, with a pronounced negative thermal expansion below 180 K. The constant-pressure specific heat C in Fig. 1(c) is taken from the literature (black line).[33] We separated the strain $\varepsilon(T) = \varepsilon_{\text{P}}(T) + \varepsilon_{\text{S}}(T)$, its derivative $\alpha(T)$, and the heat capacity $C(T) = C_{\text{P}}(T) + C_{\text{S}}(T)$ into phonon and spin contributions (cf. Fig. 1). We determined the combined electron and phonon contribution from the specific heat of the non-magnetic rare earth lutetium,[35] which is in agreement with a simple Debye approximation. Near its maximum at T_N the spins carry more than half of the specific heat, whereas the specific heat of the electrons is negligible in the relevant temperature range. Fig. 1(a) exemplifies the separation of the strain $\varepsilon(T) = \varepsilon_{\text{P}}(T) + \varepsilon_{\text{S}}(T)$ for the initial temperature $T_{\text{i}} = 120\,\text{K}$. This is the equilibrium temperature given by the thermostate before deposition of the heat Q by the laser pulse.

In thermal equilibrium, more and more modes with frequency ω fulfill the relation $k_B T > \hbar\omega$ with rising temperature, which therefore contribute a thermally accessible degree of

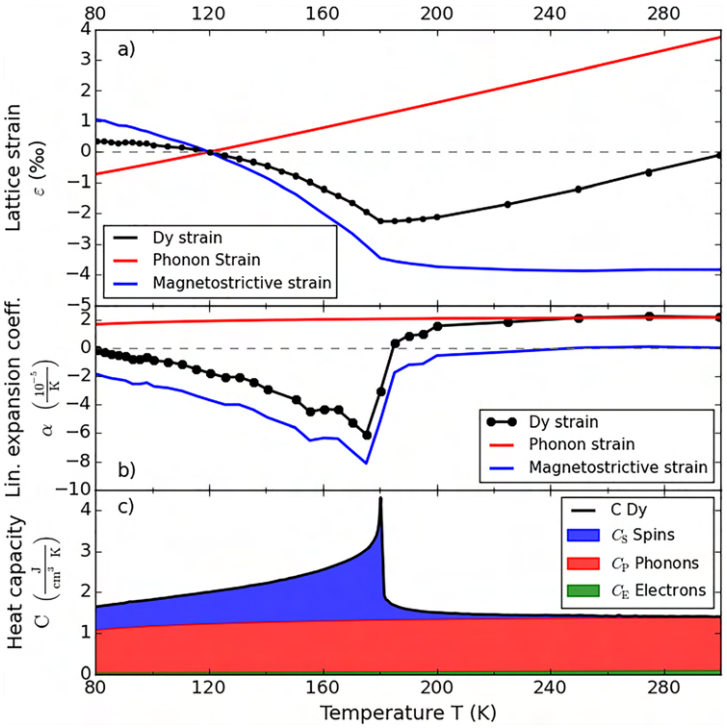

FIG. 1. Temperature dependence of the equilibrium properties of Dy. (a) Black: strain along the c-axis in the Dy film obtained by static X-Ray diffraction measurements on the hcp (0 0 0 2) reflection. The red and blue curves represent the lattice strain contributions for heating the phonons and the magnetic system. (b) Thermal expansion coefficients of Dy derived from the data in panel (a). (c) Heat capacity reported for bulk Dy[33] decomposed into C_P, C_S, and C_E.

freedom.[36] As a consequence, both the thermal expansion coefficient α and the specific heat strongly vary with the temperature T. However, if we numerically calculate the lattice strains $\varepsilon_{P,S}$ as a function of the energy densities $Q_{P,S}$, a linear relation is obtained (see solid lines in Fig. 2). While the phonon contribution simply extrapolates to high Q until the melting of the lattice is observed, the spin contribution to the energy density is limited (blue area in Fig. 1(c)). The linear relation of strain and energy suggests the definition of parameters $\beta_{P,S} = C_{P,S}(T)/\alpha_{P,S}(T)$ which measure the infinitesimal energy density required to yield an additional strain at the temperature T. These parameters are essentially inverse macroscopic Grüneisen constants $\Gamma_{P,S} = K/\beta_{P,S}$, where K is the bulk modulus of Dy.[37]

Microscopic theories define mode-specific Grüneisen constants, which may vary both in magnitude and sign.[38] However, if we assume a non-equilibrium situation which has no selective population of special modes, we can assume the lattice strain

$$\varepsilon_{P,S} = \int_{T}^{T+\Delta T} \alpha_{P,S}(T)dT = \frac{Q_{P,S}}{\beta_{P,S}} = \frac{\Gamma_{P,S} Q_{P,S}}{K} \tag{1}$$

to be proportional to the average increase of the energy density Q_P and Q_S of the phonon and spin systems, respectively. The parameters β or Γ are independent of T to a first approximation, making our non-equilibrium data analysis very robust. While $\Gamma_P \approx 0.6$ and $\Gamma_S \approx -1.8$ are dimensionless quantities, $\beta_P = 63\,\mathrm{kJ/cm^3}$ and $\beta_S = -20\,\mathrm{kJ/cm^3}$ can be interpreted as a characteristic energy densities required to expand or contract a solid. For example, the energy density $Q = 0.01 \cdot \beta$ expands or contracts the solid by 1%, depending on the sign of β. The weak temperature dependence of the bulk modulus $K \approx 41\,\mathrm{GPa} = 41\,\mathrm{kJ/cm^3}$ adds some subtle difference near the phase transition. We note that

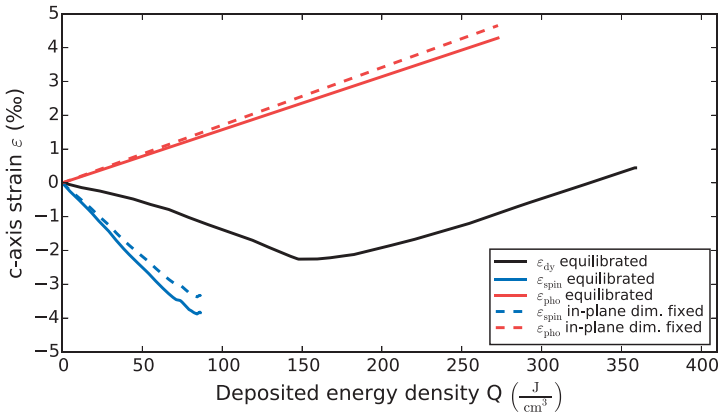

FIG. 2. Lattice strain as a function of the total heat Q_{tot} (black), for $T_{\text{Start}} = 120\,\text{K}$. The red and blue curves show the separation into strain driven by heat in the phonons Q_P and in spin excitations Q_S. Although the black line is strongly curved, the separation into spin and phonon contributions yields a linear dependence. Note that the maximum heat in the spin system is given by the blue area in Fig. 1(c), i.e., the spin contribution to the specific heat C_S. The dashed lines show the result after taking into account that, on ultrafast timescales, the lattice cannot expand in plane.

for the same amount of energy the lattice contraction resulting from the spin excitation is three times larger than the expansion due to phonon heating, also above T_N. Even above T_N, where the spin-contribution to the specific heat is strongly reduced (Fig. 1(c)), the negative thermal expansion driven by spin excitations persists (Fig. 1(b)).

Ultrafast x-ray diffraction data

We now describe the UXRD data of Dy after ultrafast heating of the electrons in Y and Dy by a 100 fs, 800 nm laser pulse. The optical penetration depth of 24 nm was determined by ellipsometry. The lattice response is probed by diffraction of 250 fs Cu-K_α pulses originating from a tabletop Plasma-X-Ray source.[29,39] Fig. 3(a) shows the transient strain $\varepsilon(t)$ for different pump fluences F of the excitation pulse at the initial temperature $T_i = 160\,\text{K} < T_N$. The incident fluence F is determined as the average intensity divided by the pumped area on the sample in the top-hat approximation, and the pump pulse is about four times larger than the probe pulse. For small fluences, the Dy lattice contracts within less than 30 ps given by the timescale of sound propagation through 18 nm Y and 80 nm Dy. In contrast, for high fluences, we first see a rapid Dy lattice expansion that relaxes on a few-nanosecond timescale. To visualize this threshold behavior, Fig. 3(b) shows the lattice strain $\varepsilon(t = 45\,\text{ps})$ as a function of the fluence. Below $F_{\text{th}} = 2\,\text{mJ/cm}^2$, a higher fluence leads to a more thorough disordering of the spin system and a concomittant lattice contraction. Above this threshold, additional energy leads to a linear expansion indicative of preferential excitation of phonons. For lower starting temperatures, a higher threshold fluence is required. The excitation of the spin system saturates due to the abrupt decrease of the specific heat of the spin system at T_N.

Fig. 3(c) shows the temperature dependence of the photoinduced Dy strain for a fixed fluence of 6.8 mJ/cm^2. For $T_i > T_N$, we observe the expected rapid phonon heat driven expansion superimposed with oscillations originating from coherent acoustic phonons (reflection of the strain waves at the interfaces of the multilayer) followed by a slow recovery of the lattice constant as heat flows towards the substrate. The red dashed line indicates the excellent agreement of a heat transport simulation according to the Fourier heat law through the layered system which we map on the strain axis by reading the experimentally determined strain in Fig. 1(a) at the calculated average temperature. For the heat diffusion we used the specific heat[40] $C_p = 162.3\,\text{J/kg K}$ and the heat conductivity[41] $\kappa = 11.7\,\text{W/mK}$ reported in the literature (for details see Ref. 42). We note that the negative slope of the data from 0.1 to 1 ns (Fig. 3(c)) is exactly the same for all initial temperatures (gray dashed lines). Since for $T_i = 200\,\text{K}$ this slope is dictated only by the phonon

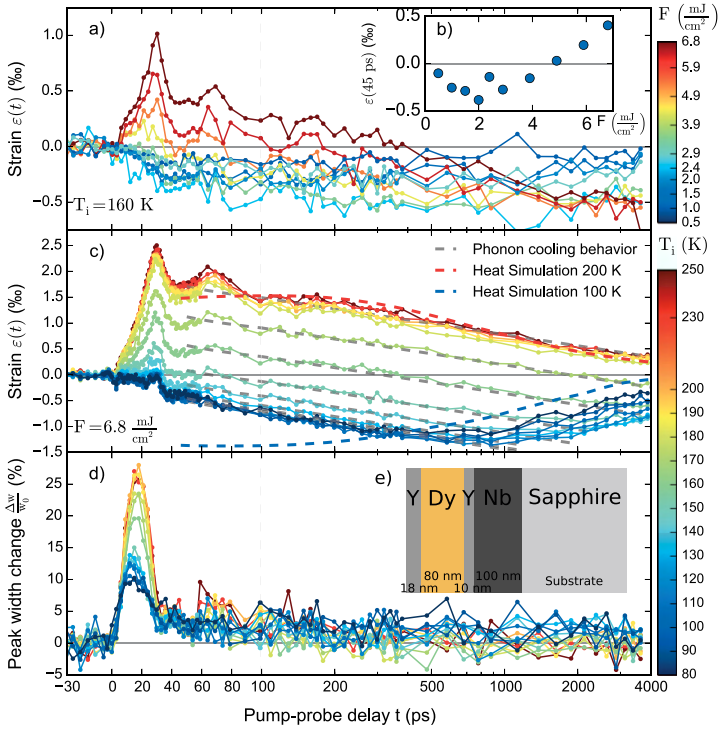

FIG. 3. UXRD data. (a) Time resolved lattice strain $\varepsilon(t)$ for $T_i = 160$ K for different excitation fluences. (b) $\varepsilon(45\,\text{ps})$ as a function of fluence. The initial strain rises linearly above the threshold fluence $F_{th} = 2$ mJ/cm^2. (c) Lattice strain $\varepsilon(t)$ and (d) the relative peak width change for different initial temperatures at fixed excitation fluence $F = 6.8$ mJ/cm^2. Dashed lines in (c) indicate the expected lattice strain according to simulations of the heat conduction. (e) Layering sequence of the sample.

heat transport, we conclude that this is the case for all temperatures. The blue dashed line shows the strain resulting from a heat transport simulation for $T_i = 100$ K. The lattice contraction resulting from the increased spin excitation is captured by the simulations, since it is encoded in the negative thermal expansion coefficient. However, in contrast to the observed minimum around 500 ps, the simulation predicts a contracted lattice right after the excitation, because solving the Fourier-law for heat diffusion assumes the material parameters for thermal equilibrium, i.e., where the phonons and the magnetic system have the same temperature.

The Bragg peak width change (Fig. 3(d)) shows that in both the paramagnetic and the antiferromagnetic phases the width starts rising about 1 ps after the excitation. A simple masses and springs model[43] confirms that the quasi-instantaneous stress originating from phonon heating yields a strong expansion wave with an exponential spatial profile starting at the surface. This wave travels into the Dy layer, and the maximum peak width is reached after about 18 ps when half the Dy layer is expanded. The width returns to near the initial value after 35 ps, when this strain front traverses the Dy-Y interface. This is consistent with the observation that at this time the average lattice constant determined from the peak shift (Fig. 3(c)) of Dy experiences a rapid contraction, as the expansion wave is transmitted towards the substrate. It is relevant to argue why the average lattice constant does not change in the first 35 ps for start temperatures between 80 and 130 K, although the peak width very strikingly shows an immediate inhomogeneous lattice deformation. The strong average expansion of Dy triggered by phonon heating must be cancelled by substantial contractive wavefronts starting at the Dy-Y interfaces due to the quasi-instantaneous loss of the magnetic order and the strong magnetostrictive coupling. The average cancellation suggests that at $t = 35$ ps about 25% of the energy heat up

the magnetic system, while less than 75% heat up the phonon system according to the two Grüneisen constants.

The data in Fig. 3(c) confirm the threshold behavior: The laser induced average lattice strain remains unchanged from $T_i = 80$ to 130 K in agreement with the nearly temperature-independent Grüneisen constants. Then, the observed initial strain gradually increases up to $T_\mathrm{i} = 180$ K, where it saturates.

Data analysis in a two-thermal-energy-model

The description of the UXRD data clearly showed that assuming a thermal equilibrium between the spin and phonon system on the nanosecond timescale is incompatible with the observations. Therefore, we analyze the flow of thermal energy among the spin and phonon systems within a model, where Q_S and Q_P are a function of time and space. We explicitly avoid a microscopic simulation in order to emphasize which conclusion can be drawn from the data under the assumption that the lattice strain is proportional to the energies in the two subsystems according to Eq. (1). To simplify the analysis, we start at times $t = 45$ ps where we may safely neglect a separate contribution of electrons, assuming them to be in thermal equilibrium with the phonons since electron-phonon coupling times in metals are expected on the order of few picoseconds at maximum.[7,10]

As a first step in our analysis, we calibrate the total energy densities $Q_\mathrm{tot,i}$ deposited by the laser excitation. At $T_\mathrm{i} = 250$ K, all available energy Q_tot^{250K} heats up the lattice, leading to a temperature increase of about 90 K corresponding to $\varepsilon = 0.2\%$. According to ellipsometric measurements of the sample, the optical absorption varies by less than 5%, so the total amount of energy deposited is $Q_\mathrm{tot}^{T} = Q_\mathrm{tot}^{250K}$ for all temperatures.

In the following, we discuss the measured data in terms of a nonequilibrium "two-thermal-energies-model" (TTEM) that satisfies energy conservation (Eq. (2)) and the linear superposition of magnetostrictive and thermoelastic strains (Eq. (3))

$$Q_\mathrm{tot}(t) = Q_\mathrm{S}(t) + Q_\mathrm{P}(t), \tag{2}$$

$$\varepsilon_\mathrm{tot}(t) = \varepsilon_\mathrm{S}(Q_\mathrm{S}(t)) + \varepsilon_\mathrm{P}(Q_\mathrm{P}(t)). \tag{3}$$

This approach circumvents problems with the definition of temperature in nonequilibrium situations, the lack of literature data for the spin-phonon coupling constant and the separated contributions of the spin and phonon system to the heat conductivities, which would be necessary to obtain predictions from the differential equations of a standard TTM.[1,32] We assume that the excitation pulse instantaneously deposits the previously calibrated initial energy density $Q_\mathrm{tot,i}$ in the Y cap layer and the top of the Dy layer via the very fast coupling of hot electrons to phonons and spins.[7] The deposited energy is rapidly divided into the initial phonon energy density $Q_\mathrm{P,i}$ and the initial energy $Q_\mathrm{S,i}$ in magnetic excitations. Each energy density (stress) manifests itself as a lattice strain $\varepsilon_\mathrm{P,S}(Q_\mathrm{P,S})$, which superimpose to yield the measured strain. For analyzing the time resolved data, we take into account the effect of in-plane clamping of the lattice expansion according to Poisson's ratio (dashed lines in Fig. 2) as detailed in Ref. 42. Since both Grüneisen parameters are approximately constant as a function of temperature (see Fig. 1(c)), a linear relation between imparted energy and lattice strain emerges. This makes the analysis applicable even though the spin- and the phonon system may not be internally thermalized to one temperature $T_\mathrm{S,P}$ over the film depth.

First, we solve the system of equations, Eqs. (2) and (3), for the initial time $t_i = 45$ ps, where the electron and phonon system are equilibrated but no energy has flown to the substrate. From the two measured variables $Q_\mathrm{tot}(t_i)$ and $\varepsilon_\mathrm{tot}(t_i)$, we calculate the energy in the spin $Q_\mathrm{S}(t_i)$ and the phonon system $Q_\mathrm{P}(t_i)$. This procedure is visualized in Figs. 4(a) and 4(d). The total energy density $Q_\mathrm{tot}(t_i)$ (red + blue area in Fig. 4(d)) in the sample is calibrated from the measurements in the paramagnetic phase, i.e., at $T_\mathrm{i} = 250$ K where the energy exclusively excites phonons, so that the deposited energy can therefore directly be found via Eq. (1) from the measured lattice strain ($\varepsilon_\mathrm{tot}(t_i) = \varepsilon_\mathrm{P}(t_i)$).

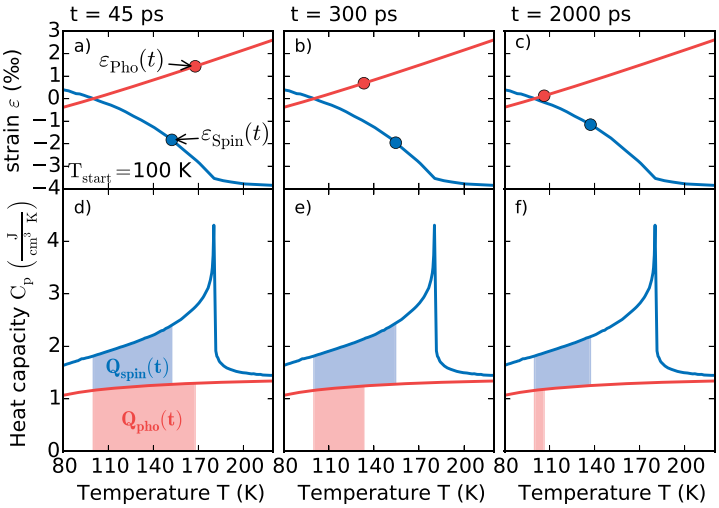

FIG. 4. Visualization of the TTEM at $T_i = 100$ K for three different time delays. The measured total strain $\varepsilon_{\mathrm{tot}}(t)$ and the total heat energy Q_{tot} allow deriving the individual phonon and spin contributions to the strain and the heat. The upper panels (a)–(c) show the separation of strain contributions according to Fig. 1(a) and the lower panels (d)–(f) show the transient heat as an area under the specific heat curve according to Fig. 1(c). Note that for the analysis only the energy densities are required. From the figures one can read that, e.g., after 2 ns, the Q_S would correspond to an equilibrium spin temperature of 140 K whereas Q_P corresponds to an equilibrium phonon temperature of 108 K. Although the temperature definitely has a strong gradient across the film, the analysis of the average heat $Q_{P;S}$ is robust, because of the linear relation $\varepsilon_{P;S} \sim Q_{P;S}$.

For excitation with $F = 6.8$ mJ/cm^2, this TTEM yields $Q_{\mathrm{S,i}}$ and $Q_{\mathrm{P,i}}$ and their fraction of the total energy is depicted in Fig. 5(b). It shows that essentially 35% of the energy is initially deposited in the spin system for $T_{\mathrm{i}} \ll T_{\mathrm{N}}$. Here, we assume that only the deposition of energy in each subsystem immediately leads to the stress according to the higher energy density, which causes the corresponding strain at delays larger than the time needed to the sound wave to propagate through Dy. We can safely assume that no energy has left the Dy layer by thermal transport shortly after excitation.

To obtain a solution of the system of equations for arbitrary times t as visualized in Fig. 4, we make two alternative approximations for the evolution of $Q_{\mathrm{tot}}(t)$ in the dysprosium layer. $Q_{\mathrm{tot}}(t)$ is reduced by phononic and electronic heat conduction to the substrate. As a lower boundary, we assume that the total heat flows out of the film as fast as if all energy would be stored in the phonons, i.e., $Q^T_{\mathrm{tot}}(t) = Q^{250K}_{\mathrm{tot}}(t)$. The direct flow of excitations from the magnetic system in the Dy layer to the adjacent nonmagnetic materials is not possible so that coupling energy in the spin system to phonons is the only channel of magnetic energy dissipation. Therefore, this assumption overestimates the heat flow to the substrate when a substantial fraction of $Q^T_{\mathrm{tot}}(t)$ is in spin excitations and we obtain the lower curves in Fig. 5(a). The data analysis within the first approximation indicates that close to T_{N} the energy in the spin system dissipates very slowly. To estimate an upper bound (Fig. 5(a)) we use the second approximation $Q^T_{\mathrm{tot}}(t) = Q^T_{\mathrm{S,i}} + Q^T_{\mathrm{P,i}}(Q^{250\mathrm{K}}_{\mathrm{tot}}(t)/Q^{250\mathrm{K}}_{\mathrm{tot,i}})$. It assumes that only the fraction of energy initially deposited in the phonon system can flow out of the film. This clearly overestimates the total energy in the Dy layer for long times t after the excitation, because the energy initially deposited in the magnetic system cannot leave the Dy layer and Q_{tot} can never drop below $Q_{\mathrm{S,i}}$. This approximation is especially suitable for initial conditions where $Q_{\mathrm{S,i}} \ll Q_{\mathrm{P,i}}$, i.e., at high temperatures. Fig. 5(a) shows the result of the TTEM data analysis for five representative temperatures using both approximations for $Q_{\mathrm{tot}}(t)$. The heat dissipation from the phonon system is much faster than for the spin system. At very early times some transfer of thermal energy from the phonons into the spin system is observed. Referring to Fig. 4, we can observe that the main findings in Fig. 5 are already seen in the raw data. The upper panel of Fig. 4 illustrates that

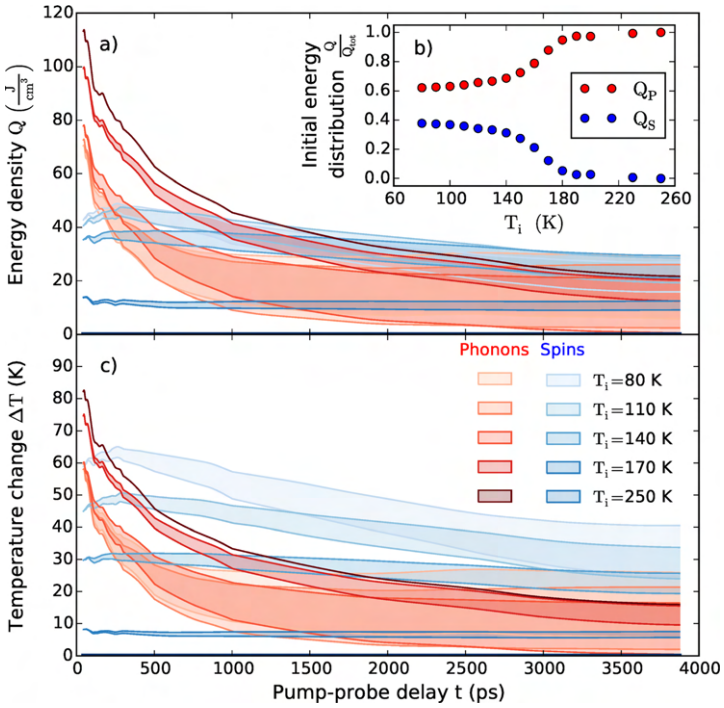

FIG. 5. TTEM results extracted from the experimental data at a fluence of $F = 6.8\text{mJ/cm}^2$. (a) Energy in the phonon- and spin excitations derived from the data as described in the text. Q_P^{80K} and Q_P^{110K} are hard to distinguish. (b) Initial energy distribution between phonons and spins at 45 ps. (c) Temperature changes obtained from (a) via the corresponding heat-capacities $C_{S,P}(T)$ (Fig. 1(b)). The resulting temperatures indicate a long-lasting non-equilibrium between phonons and spins. In panel (c), no temperature change of the spin system is plotted for $T_i = 250\,\text{K}$ because its heat capacity is zero $C_S(250\,\text{K}) = 0$.

transient heat in the spin system leads to a contraction and transient heat in the phonon system leads to an expansion. The Grüneisen coefficients tell us that the energy in the spin system is three times more effective in straining the lattice than the energy contained in phonons. For the illustrated initial temperature of $T_i = 100\,\text{K}$, we observe at 45 ps that about three times more energy is required in the phonon system to nearly balance the contraction resulting from energy in the spin excitations. $\epsilon_p(45\,\text{ps})$ is slightly smaller than $\epsilon_s(45\,\text{ps})$, consistent with the slight contraction seen in Fig. 3(c). Around 300 ps, the phonon energy Q_p has greatly decreased (Fig. 4(e)) by conduction of heat to the substrate, while $Q_s(300\,\text{ps}) \sim Q_s(45\,\text{ps})$. Therefore, the contractive strain ϵ_s prevails and leads to the pronounced contraction seen in Fig. 3(c) around 300 ps. At 2 ns, there is almost no positive transient strain ϵ_p due to phonons left (Fig. 4(c)) because $Q_p \sim 0$, and also Q_s is greatly reduced (see Fig. 4(f)). In the raw data, this is seen as the recovery of the negative strain, which slowly approaches zero on this nanosecond timescale.

DISCUSSION

Our analysis derives the flow of heat among the spin and lattice system directly from experimental data. In order to make it comparable to a conventional TTM, we present time-resolved temperature changes derived from the above TTEM using the static temperature-dependent heat capacity in Fig. 1(c). Initially, the temperature in the phonon system is higher than the temperature of the spin system, especially when T_i approaches T_N. While the phonons in Dy cool rapidly to the substrate, T_S rises slightly within the first 200 ps even when the average temperature of the spin system is already higher than the average phonon temperature.

Such behavior may be rationalized by a spatial nonequilibrium or—equivalently—by a nonequilibrium population of modes in microscopic theories. The subsequent cooling of the spin-system is found to be much slower. When the initial temperature T_i approaches T_N from below, the timescale for reordering (i.e., cooling) of the magnetic system dramatically increases: essentially, a decoupling of the two heat reservoirs from each other is observed. For example, for a starting temperature $T_i = 170\,\mathrm{K}$, $\Delta T_S \simeq 8\,\mathrm{K}$ remains constant for 4 ns although initially $\Delta T_P \simeq 70\,\mathrm{K}$. From the experimental findings, we can give at least three indications that not only the two "temperatures" T_S and T_P are different, but that each of the subsystems is in a non-equilibrium situation. (i) As discussed above, the heat flow between spins and phonons is not controlled by the temperature difference. (ii) The heat simulation for $T_i = 250\,\mathrm{K}$ which matches the experimental data predicts a strong temperature gradient in the Dy layer. Definitely, the phonons are spatially not in equilibrium over the sample thickness of 80 nm for more than 1 ns. (iii) The detected increase in the peak width in the first 35 ps while no peak shift is observed in the anti-ferromagnetic phase, which clearly calls for different spatial profiles of the excitations in the phonon and spin system. Probably, in the laser-heated region of the Dy layer $T_P > T_S$ while at the back interface to Y $T_P < T_S$. Potentially, the local excited mode spectrum cannot be approximated by a Bose-distribution with two temperatures at all.

CONCLUSION

In conclusion, we have discussed UXRD data in the rare earth Dy to obtain clear evidence that the phonon and spin systems are mutually not in thermal equilibrium for several nanoseconds after optical excitation. We demonstrate a method to extract the transient energy densities $Q_S(t)$ and $Q_P(t)$ deposited in the spins and the phonons from the UXRD data. In the antiferromagnetic phase, approximately 35% of the energy heats up and disorders the spin system, leading to a rapid contraction of the lattice. Although the spins can exclusively dissipate their heat to phonons and electrons in Dy, the cooling rate of the magnetic system that finally leads to a reordering of the spin-system depends only weakly on the transient phonon temperature.

We hope that our experimental analysis will inspire theoreticians to model the spatiotemporal coupled excitations in rare earth metals and we believe that it is an important contribution in the context of the debate about ultrafast angular-momentum transfer to the lattice. Our observations are indicative for a rapid disorder in the spin system—inducing a contractive force, indicating a very strong spin-lattice interaction in the ordered phase. On the other hand the transfer of energy from the magnetic system to the phonons is very slow (on the nanosecond timescale), in particular, close to the phase-transition, giving strong evidence for a critical behavior. This suggests a rather weak spin-phonon coupling for (partially) disordered spins.

ACKNOWLEDGMENTS

We acknowledge the BMBF for the financial support via 05K12IP1 and the ellipsometric characterization by L. Willig and M. Roessle.

[1]E. Beaurepaire, J.-C. Merle, A. Daunois, and J.-Y. Bigot, "Ultrafast spin dynamics in ferromagnetic nickel," Phys. Rev. Lett. **76**, 4250 (1996).
[2]A. Kirilyuk, A. V. Kimel, and Th. Rasing, "Ultrafast optical manipulation of magnetic order," Rev. Mod. Phys. **82**, 2731–2784 (2010).
[3]B. Koopmans, G. Malinowski, F. Dalla Longa, D. Steiauf, M. Fahnle, T. Roth, M. Cinchetti, and M. Aeschlimann, "Explaining the paradoxical diversity of ultrafast laser-induced demagnetization," Nat. Mater. **9**, 259–265 (2010).
[4]S. Mathias, C. La-O-Vorakiat, P. Grychtol, P. Granitzka, E. Turgut, J. M. Shaw, R. Adam, H. T. Nembach, M. E. Siemens, S. Eich *et al.*, "Probing the timescale of the exchange interaction in a ferromagnetic alloy," Proc. Natl. Acad. Sci. U.S.A. 109, 4792–4797 (2012).
[5]A. Eschenlohr, M. Battiato, P. Maldonado, N. Pontius, T. Kachel, K. Holldack, R. Mitzner, A. Föhlisch, P. M. Oppeneer, and C. Stamm, "Ultrafast spin transport as key to femtosecond demagnetization," Nat. Mater. **12**, 332–336 (2013).
[6]M. Wietstruk, A. Melnikov, C. Stamm, T. Kachel, N. Pontius, M. Sultan, C. Gahl, M. Weinelt, H. A. Dürr, and U. Bovensiepen, "Hot-electron-driven enhancement of spin-lattice coupling in Gd and Tb 4*f* ferromagnets observed by femtosecond x-ray magnetic circular dichroism," Phys. Rev. Lett. **106**, 127401 (2011).
[7]C. Trabant, "Ultrafast photoinduced phase transitions in complex materials probed by time-resolved resonant soft x-ray diffraction," Ph.D. thesis, Universität Potsdam, 2014.

[8]C. von Korff Schmising, B. Pfau, M. Schneider, C. M. Günther, M. Giovannella, J. Perron, B. Vodungbo, L. Müller, F. Capotondi, E. Pedersoli, N. Mahne, J. Lüning, and S. Eisebitt, "Imaging ultrafast demagnetization dynamics after a spatially localized optical excitation," Phys. Rev. Lett. **112**, 217203 (2014).
[9]R. Carley, K. Dobrich, B. Frietsch, C. Gahl, M. Teichmann, O. Schwarzkopf, P. Wernet, and M. Weinelt, "Femtosecond laser excitation drives ferromagnetic gadolinium out of magnetic equilibrium," Phys. Rev. Lett. **109**, 057401 (2012).
[10]U. Bovensiepen, "Coherent and incoherent excitations of the Gd(0001) surface on ultrafast timescales," J. Phys.: Condens. Matter **19**, 083201 (2007).
[11]B. Frietsch, J. Bowlan, R. Carley, M. Teichmann, S. Wienholdt, D. Hinzke, U. Nowak, K. Carva, P. M. Oppeneer, and M. Weinelt, "Disparate ultrafast dynamics of itinerant and localized magnetic moments in gadolinium metal," Nat. Commun. **6**, 8262 (2015).
[12]C. von Korff Schmising, M. Bargheer, M. Kiel, N. Zhavoronkov, M. Woerner, T. Elsaesser, I. Vrejoiu, D. Hesse, and M. Alexe, "Accurate time delay determination for femtosecond X-ray diffraction experiments," Appl. Phys. B **88**, 1–4 (2007).
[13]M. C. Langner, S. Roy, A. F. Kemper, Y.-D. Chuang, S. K. Mishra, R. B. Versteeg, Y. Zhu, M. P. Hertlein, T. E. Glover, K. Dumesnil, and R. W. Schoenlein, "Scattering bottleneck for spin dynamics in metallic helical antiferromagnetic dysprosium," Phys. Rev. B **92**, 184423 (2015).
[14]A. V. Kimel, A. Kirilyuk, A. Tsvetkov, R. V. Pisarev, and Th. Rasing, "Laser-induced ultrafast spin reorientation in the antiferromagnet $TmFeO_3$," Nature **429**, 850–853 (2004).
[15]M. Battiato, K. Carva, and P. M. Oppeneer, "Superdiffusive spin transport as a mechanism of ultrafast demagnetization," Phys. Rev. Lett. **105**, 027203 (2010).
[16]G. P. Zhang, W. Hubner, G. Lefkidis, Y. Bai, and T. F. George, "Paradigm of the time-resolved magneto-optical Kerr effect for femtosecond magnetism," Nat. Phys. **5**, 499–502 (2009).
[17]T. Kise, T. Ogasawara, M. Ashida, Y. Tomioka, Y. Tokura, and M. Kuwata-Gonokami, "Ultrafast spin dynamics and critical behavior in half-metallic ferromagnet: Sr_2FeMoO_6," Phys. Rev. Lett. **85**, 1986–1989 (2000).
[18]X. J. Liu, Y. Moritomo, A. Nakamura, H. Tanaka, and T. Kawai, "Critical behavior of a photodisordered spin system in doped manganite," Phys. Rev. B **64**, 100401 (2001).
[19]T. Ogasawara, K. Ohgushi, Y. Tomioka, K. S. Takahashi, H. Okamoto, M. Kawasaki, and Y. Tokura, "General features of photoinduced spin dynamics in ferromagnetic and ferrimagnetic compounds," Phys. Rev. Lett. **94**, 087202 (2005).
[20]S. Muhammad, "Ultrafast magnetization dynamics of lanthanide metals and alloys," Ph.D. thesis, Freie Universität Berlin, 2012.
[21]A. Manchon, Q. Li, L. Xu, and S. Zhang, "Theory of laser-induced demagnetization at high temperatures," Phys. Rev. B **85**, 064408 (2012).
[22]J. Kimling, J. Kimling, R. B. Wilson, B. Hebler, M. Albrecht, and D. G. Cahill, "Ultrafast demagnetization of FePt: Cu thin films and the role of magnetic heat capacity," Phys. Rev. B **90**, 224408 (2014).
[23]U. Atxitia and O. Chubykalo-Fesenko, "Ultrafast magnetization dynamics rates within the Landau-Lifshitz-Bloch model," Phys. Rev. B **84**, 144414 (2011).
[24]N. Kazantseva, U. Nowak, R. W. Chantrell, J. Hohlfeld, and A. Rebei, "Slow recovery of the magnetisation after a sub-picosecond heat pulse," Europhys. Lett. **81**, 27004 (2008).
[25]F. J. Darnell and E. P. Moore, "Crystal structure of dysprosium at low temperatures," J. Appl. Phys. **34**, 1337–1338 (1963).
[26]W. C. Koehler, "Magnetic properties of rare-earth metals and alloys," J. Appl. Phys. **36**, 1078–1087 (1965).
[27]B. Coqblin, *The Electronic Structure of Rare-Earth Metals and Alloys: The Magnetic Heavy Rare-Earths* (Academic Press, 1977), p. xvi.
[28]J. Jensen and A. R. Mackintosh, *Rare Earth Magnetism - Structures and Excitations* (Clarendon Press, 1991).
[29]D. Schick, A. Bojahr, M. Herzog, C. von Korff Schmising, R. Shayduk, W. Leitenberger, P. Gaal, and M. Bargheer, "Normalization schemes for ultrafast x-ray diffraction using a table-top laser-driven plasma source," Rev. Sci. Instrum. **83**, 025104 (2012).
[30]S. Nie, X. Wang, H. Park, R. Clinite, and J. Cao, "Measurement of the electronic Grüneisen constant using femtosecond electron diffraction," Phys. Rev. Lett. **96**, 025901 (2006).
[31]M. Nicoul, U. Shymanovich, A. Tarasevitch, D. von der Linde, and K. Sokolowski-Tinten, "Picosecond acoustic response of a laser-heated gold-film studied with time-resolved x-ray diffraction," Appl. Phys. Lett. **98**, 191902 (2011).
[32]S. I. Anisimov, B. L. Kapeliovitch, and T. L. Perel'man, "Electron emission from metal surfaces exposed to ultrashort laser pulses," Sov. Phys. - JETP **2**, 375–377 (1974).
[33]V. K. Pecharsky, K. A. Gschneidner, Jr., and D. Fort, "Superheating and other unusual observations regarding the first order phase transition in Dy," Scr. Mater. **35**, 843–848 (1996).
[34]K. Dumesnil, C. Dufour, Ph. Mangin, G. Marchal, and M. Hennion, "Magnetoelastic and exchange contributions to the helical-ferromagnetic transition in dysprosium epitaxial films," Europhys. Lett. **31**, 43 (1995).
[35]L. D. Jennings, R. E. Miller, and F. H. Spedding, "Lattice heat capacity of the rare earths. Heat capacities of yttrium and lutetium from 15–350 °k," J. Chem. Phys. **33**, 1849–1852 (1960).
[36]N. W. Ashcroft and N. D. Mermin, *Solid State Physics* (Cengage Learning, 2011).
[37]S. B. Palmer and E. W. Lee, "The elastic constants of dysprosium and holmium," Proc. R. Soc. Lond., Ser. A **327**, 519–543 (1972).
[38]O. B. Wright, "Ultrafast nonequilibrium stress generation in gold and silver," Phys. Rev. B **49**, 9985–9988 (1994).
[39]F. Zamponi, Z. Ansari, C. von Korff Schmising, P. Rothhardt, N. Zhavoronkov, M. Woerner, T. Elsaesser, M. Bargheer, T. Trobitzsch-Ryll, and M. Haschke, "Femtosecond hard x-ray plasma sources with a kilohertz repetition rate," Appl. Phys. A **96**, 51–58 (2009).
[40]B. Y. Mueller and B. Rethfeld, "Thermodynamic model of ultrafast magnetization dynamics," Phys. Rev. B **90**, 144420 (2014).
[41]C. Y. Ho, R. W. Powell, and P. E. Liley, "Thermal conductivity of the elements," J. Phys. Chem. Ref. Data **1**, 279–421 (1972).

[42]A. von Reppert, "Ultrafast magnetostriction in dysprosium studied by femtosecond X-Ray diffraction," M.S. thesis, Universität Potsdam, 2015.
[43]D. Schick, A. Bojahr, M. Herzog, R. Shayduk, C. von Korff Schmising, and M. Bargheer, "UDKM1DSIM—A simulation toolkit for 1D ultrafast dynamics in condensed matter," Comput. Phys. Commun. **185**, 651–660 (2014).

Article IX

Ultrafast x-ray diffraction thermometry measures the influence of spin excitations on the heat transport through nanolayers

Azize Koç, Matthias Reinhardt, Alexander von Reppert, Matthias Rössle, Wolfram Leitenberger, Karine Dumesnil, Peter Gaal, Flavio Zamponi, and Matias Bargheer

Physical Review B 96, 014306 (2017)

We investigate the heat transport through a rare earth multilayer system composed of yttrium (Y), dysprosium (Dy), and niobium (Nb) by ultrafast x-ray diffraction. This is an example of a complex heat flow problem on the nanoscale, where several different quasiparticles carry the heat and conserve a nonequilibrium for more than 10 ns. The Bragg peak positions of each layer represent layer-specific thermometers that measure the energy flow through the sample after excitation of the Y top layer with fs-laser pulses. In an experiment-based analytic solution to the nonequilibrium heat transport problem, we derive the individual contributions of the spins and the coupled electron-lattice system to the heat conduction. The full characterization of the spatiotemporal energy flow at different starting temperatures reveals that the spin excitations of antiferromagnetic Dy speed up the heat transport into the Dy layer at low temperatures, whereas the heat transport through this layer and further into the Y and Nb layers underneath is slowed down. The experimental findings are compared to the solution of the heat equation using macroscopic temperature-dependent material parameters without separation of spin- and phonon contributions to the heat. We explain why the simulated energy density matches our experiment-based derivation of the heat transport, although the simulated thermoelastic strain in this simulation is not even in qualitative agreement.

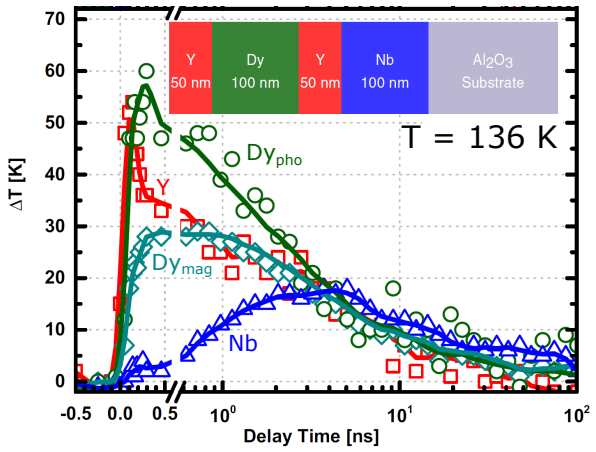

PHYSICAL REVIEW B **96**, 014306 (2017)

Ultrafast x-ray diffraction thermometry measures the influence of spin excitations on the heat transport through nanolayers

A. Koc,[1] M. Reinhardt,[1] A. von Reppert,[2] M. Rössle,[2] W. Leitenberger,[2] K. Dumesnil,[3] P. Gaal,[1,4] F. Zamponi,[2] and M. Bargheer[2,1,*]

[1]*Helmholtz Zentrum Berlin, Albert-Einstein-Str. 15, 12489 Berlin, Germany*

[2]*Institut für Physik & Astronomie, Universität Potsdam, Karl-Liebknecht-Str. 24-25, 14476 Potsdam, Germany*

[3]*Institut Jean Lamour (UMR CNRS 7198), Université Lorraine, Boulevard des Aiguillettes B.P. 239, F-54500 Vandoeuvre les Nancy cédex, France*

[4]*Institut für Nanostruktur- und Festkörper Physik, Univesität Hamburg, Jungiusstr. 11,20355 Hamburg, Germany*

(Received 19 January 2017; revised manuscript received 4 May 2017; published 25 July 2017)

We investigate the heat transport through a rare earth multilayer system composed of yttrium (Y), dysprosium (Dy), and niobium (Nb) by ultrafast x-ray diffraction. This is an example of a complex heat flow problem on the nanoscale, where several different quasiparticles carry the heat and conserve a nonequilibrium for more than 10 ns. The Bragg peak positions of each layer represent layer-specific thermometers that measure the energy flow through the sample after excitation of the Y top layer with fs-laser pulses. In an experiment-based analytic solution to the nonequilibrium heat transport problem, we derive the individual contributions of the spins and the coupled electron-lattice system to the heat conduction. The full characterization of the spatiotemporal energy flow at different starting temperatures reveals that the spin excitations of antiferromagnetic Dy speed up the heat transport into the Dy layer at low temperatures, whereas the heat transport through this layer and further into the Y and Nb layers underneath is slowed down. The experimental findings are compared to the solution of the heat equation using macroscopic temperature-dependent material parameters without separation of spin and phonon contributions to the heat. We explain why the simulated energy density matches our experiment-based derivation of the heat transport, although the simulated thermoelastic strain in this simulation is not even in qualitative agreement.

DOI: 10.1103/PhysRevB.96.014306

I. INTRODUCTION

Heat transport at the nanoscale has become an important problem of contemporary physics [1–3]. The field is driven largely by the need to improve heat transport characteristics in integrated circuits operating at high clock rates [4]. The design length scales approach the physical limits, where wave fundamental properties of phonon-heat conduction play an important role [5,6]. Research on the functionality of interfaces in nanoelectronics is prevalent, and the heat transport characteristics of interfaces depend strongly, e.g., on the roughness of the interface, which is often hard to control in the fabrication process [1,2,7]. In many insulators and semiconductors the heat capacity is dominated by phonons, whereas electrons only contribute significantly at high temperatures. The heat transport in metals in contrast is dominated by the conduction band electrons and the excitation of phonons typically reduces the heat transport, because they act as scatterers for electrons [8]. In some magnetic materials with strong exchange interactions and large magnetic moments the spin correlations can contribute more than half of the specific heat over large temperature ranges [9–11]. One classical example is the rare earth dysprosium, which we are investigating in this article. Similar to phonon excitations, the magnetic excitations are known to reduce the heat conductivity when it is dominated by the electrons [12]. On the other hand, heat conduction by magnons may dominate in antiferromagnets [13]. The transport of heat across interfaces in nanostructures with magnetic and nonmagnetic layers is far beyond what can be safely simulated on an *ab initio* basis. The additional degree of freedom given by the quasiparticles of the magnetic excitations presents a very complex problem [14]. Additional to the basic understanding of heat transport at the nanoscale [15], fundamental studies of ultrafast magnetism regarding the possibility of all optical magnetic switching [16–19] or the role of spin currents [20,21] will profit from a detailed knowledge about transient temperatures and temperature gradients in such systems. Ultrafast x-ray diffraction has only recently become a tool to measure the transient temperatures in multilayers [22] and to assign contributions from electrons and phonons to thermal transport [23].

In this paper we present the results of time-resolved ultrafast x-ray diffraction (UXRD) studies on a complex thin film heterostructure with the layering sequence Y/Dy/Y/Nb/sapphire. We simultaneously measured the relative Bragg peak shifts of all layers as a direct measure of transient strain $\varepsilon(t)$ after optical excitation of the top Y layer. Using the Grüneisen coefficients derived from the thermal expansion, experimentally measured on the same structure, we extract the time dependent energy densities $\rho^Q_Y, \rho^Q_{Dy}, \rho^Q_{Nb}$ in each layer. When only electrons and phonons carry the heat, the transient temperatures $T_{Y,Nb,Dy}(t) \sim \varepsilon_{Y,Nb,Dy}(t)$ can be direcly read from the measured strains $\varepsilon_{Y,Nb,Dy}(t)$. In the antiferromagnetic state of Dy, a large fraction of the energy resides in spin excitations and we show how to separate the phonon and spin contributions ($\rho^Q_{S,P}$) via an analytic decomposition of

*bargheer@uni-potsdam.de; http://www.udkm.physik.uni-potsdam.de

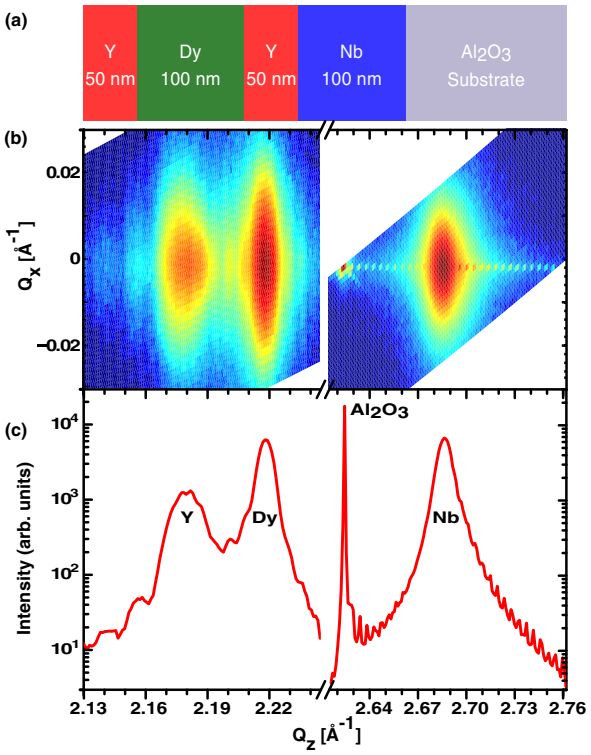

FIG. 1. (a) Schematic of the sample. (b) Reciprocal space map at $T_i = 165$ K of the sample with (0002) reflections of two Y and Dy layers, the (220) reflection of Nb layer, and the $(22\bar{4}0)$ substrate (Al_2O_3) reflection, respectively. (c) Bragg reflections along Q_z obtained by integration of the RSM.

the measured signal. The initial temperature T_i is varied from 136 K through the Néel temperature $T_N = 180$ K of Dy up to 276 K. We find that the additional presence of antiferromagnetic spin excitations in Dy below T_N speeds up the energy flow from the excited Y layer into the Dy layer, where an additional channel for heat dissipation is present. At the same time, the heat transport through Dy is slowed down as the temperature gradient is decreased when the magnetic excitations scatter the electrons, which are the main heat transporting quasiparticles. A full *ab initio* simulation of this complex heat transport problem seems impossible, since the interface resistances, depending on the perfection of the nanostructure and the coupling constants between electrons, phonons, and spin excitations, are unknown. Still, heat transport simulations using bulk values for the thermal conductivities [24,25] can be compared with our measured total energy densities, although the contributions of individual quasiparticles are neglected. We find the nonequilibrium of spins and phonons in the observable of the measured strain.

The sample shown in Fig. 1(a) is grown epitaxially and consists of a 100 nm thick (0001)-oriented Dy layer encapsulated between two 50 nm thick Y films with (0001) orientation in order to prevent oxidation and to stabilize the helical spin order of Dy [26]. A 100 nm thick Nb buffer layer connects this metallic sandwich structure to an Al_2O_3 substrate. The thickness values are derived from the Laue oscillations around individual Bragg peaks. The penetration depth of 32 nm for our excitation pulses at $\lambda = 1030$ nm wavelength was determined by ellipsometry studies, showing that mainly the upper Y layer is excited. The refractive index is nearly constant in the relevant temperature range with real part $n = 2.7 \pm 0.01$ and imaginary part $\kappa = 2.12 \pm 0.01$.

II. EXPERIMENTAL SCHEME

Time-resolved x-ray diffraction measurements were performed at the XPP experimental station at the storage ring BESSY II [27,28]. The x rays probe an ellipsoidal area with a FWHM of about 100×400 μm, which is homogeneously pumped by a laser focus of about 290×960 μm. The electron storage ring was operating in the hybrid mode, in which a "camshaft" electron bunch generates x-ray pulses of about 80 ps pulse duration at 1.25 MHz repetition rate [27]. Every sixth of these pulses is accepted by the 60 ns electronic gate of the two-dimensional hybrid pixel x-ray detector (Pilatus 100k, Dectris Inc.), which is synchronized with the 208 kHz repetition rate of the laser pump pulses. The other x-ray pulses, which are emitted in the hybrid mode of the storage ring, are rejected by the electronic gate of the detector and do not contribute to the signal. The time delay between the recorded x-ray pulses and the exciting laser pulses is adjusted by the synchronization electronics with an accuracy of about 1 ps. Reciprocal space mapping (RSM) is performed by recording the x-ray photons diffracted from the sample at various incidence angles ω around the Bragg reflections while the area detector resolves the diffraction angle 2θ [28]. The large extinction length of hard x-ray pulses at $\lambda = 0.138$ nm allows for simultaneous detection of diffraction signals from all layers of this structure that is opaque to optical light. As an example, Fig. 1(b) displays the broad RSM [29] of the thin films Y, Dy, and Nb as well as the sharp RSM of the Al_2O_3 substrate at $T_i = 165$ K. Figure 1(c) shows the diffracted intensity of the out-of-plane scattering vector Q_z obtained by integrating the RSM over the in-plane scattering vector components Q_x and Q_y. The signal broadening of the nanolayers in Q_z is due to the limited layer thickness, whereas the mosaic structure of the crystal is mainly observed as a broadening in the in-plane directions.

III. TIME-RESOLVED X-RAY DIFFRACTION DATA

We present the transient response of each nanolayer after ultrafast laser heating with a laser fluence of 2 mJ/cm^2. To extract this information from the data, we fitted each Bragg peak at any delay time with a Gaussian line profile in Q_z to determine the peak position. Transforming the average reciprocal lattice vector $Q_z(t)$ to lattice constants $c(t) = 2\pi/Q_z(t)$, we obtain the transient strain $\varepsilon(t) = \frac{c(t)-c(t<0)}{c(t<0)}$ in each layer. In Fig. 2(a) the transient strain of both Y layers as the average of the upper and bottom Y layer is shown for different base temperatures T_i. At 276 K the laser-heated Y layer shows a maximal expansion within the 100 ps time-resolution limit given by the pulse duration of the x rays at beamline. It relaxes via heat diffusion into the other thin film layers. At lower T_i the same dynamics are observed, however, the maximal strain value decreases with decreasing T_i. The indirectly heated Dy layer [Fig. 2(b)] shows

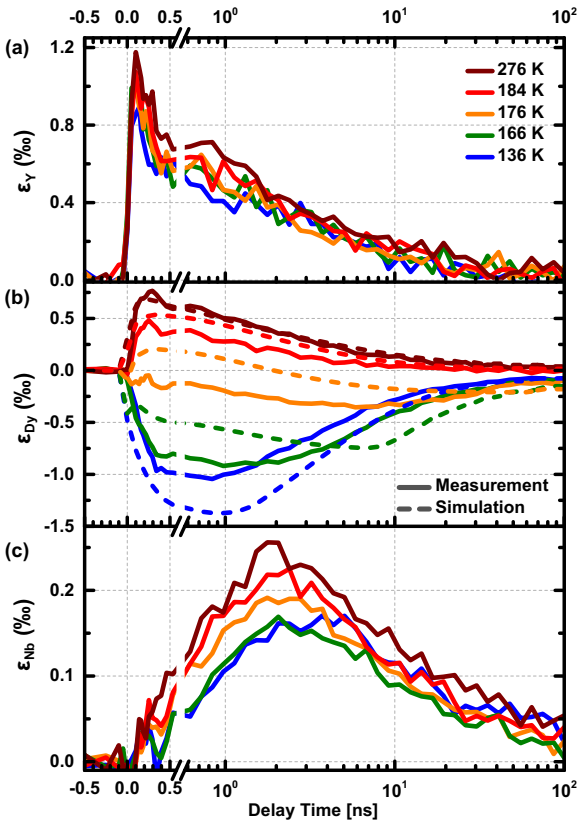

FIG. 2. Transient strain $\varepsilon(t)$ for different initial temperatures T_i after ultrafast laser heating at 3 mJ/cm^2 fluence: solid lines depict the measured transient strain of (a) the two Y layers, (b) the Dy layer ε_{Dy}, and (c) the Nb layer. The dashed lines in panel (b) represent the unsuccessful attempt to simulate the strain $\varepsilon^{av}_{Dy}(t)$ by the heat equation, i.e., without taking into account the fact that magnetic excitations and phonons contribute to the heat propagation and the strain.

very different dynamics depending on the base temperature. At 276 K the paramagnetic Dy layer expands and reaches the maximal expansion after about 300 ps. In the AFM phase below $T_{\text{Néel}}$ the Dy layer contracts upon heating. This negative thermal expansion is a signature of spin excitations in the antiferromagnetic spin order [30]. The transient strain in the Nb layer is depicted in Fig. 2(c). A maximal expansion of the Nb layer at $T_i = 276$ K is observed at about 1.8 ns. At lower base temperatures the maximal expansion shifts to larger time delays and the magnitude of the maximal expansion is reduced. The inhomogeneous spatial heat distribution in the three materials not only changes the Bragg peak positions, but also the Bragg peak width. For Dy, a maximum peak width increase of 8% is observed in the first 100 ps, when strain waves propagate from the surface through the film. The inhomogeneous thermal strain in Dy increases the peak width by less than 4%. In the Y layer the peak width change is more pronounced, since both layers above and below Dy contribute equally. Here the peak width increase rapidly decreases from 30% to 8% within 400 ps. In Nb, the peak width increase is always less than 2%.

TABLE I. β constants of Y, Nb, and Dy spin and phonons.

System	β (kJ/cm^3)
Y	69
Dy spin	−20
Dy phonon	95
Nb	206

IV. DATA ANALYSIS IN TWO-THERMAL-ENERGIES MODEL

We analyze the dynamics of the thin film system on time scales larger than the time required for propagating sound through the nanolayer system and smaller than the time for sound propagation over the in-plane length scale given by the laser-excitation spot. Therefore, we assume Hooke's law to be valid, which relates the strain ε to the stress $\sigma = C_{\text{eff}}\,\varepsilon$ via an effective elastic constant C_{eff} [31–33] that takes into account the in-plane clamping of the film to the substrate. The macroscopic Grüneisen constant $\Gamma_i = \frac{\alpha_i(T)\,C_{i,\text{eff}}}{c_i(T)}$ measures how efficiently the energy density ρ^Q_i in a subsystem i generates stress $\sigma_i = \Gamma_i \rho^Q_i$. We prefer to write an inverse parameter $\beta_i = \frac{c_i}{\alpha_i} = \frac{C_{\text{eff}}}{\Gamma_i}$ which we directly obtained from the bulk specific heat c_i per volume from the literature [9,34,35] and the expansion coefficient α_i determined from the temperature dependent XRD on the investigated thin film structure. The change of the integral heat

$$\Delta Q_i = V_i \cdot \Delta\rho^Q_i = V_i \beta_i \varepsilon_i \tag{1}$$

in a volume V_i of a system is proportional to the lattice strain ε_i. At temperatures above T_N, the increase of the energy densities $\Delta\rho^Q_{Y,Dy,Nb}$ in Y, Dy, and Nb can be directly found from Eq. (1). Essentially, the energy density of excited phonons in each material drives the lattice expansion, since the electrons carry a negligible fraction of the specific heat, when the electrons have relaxed to approximately the lattice temperature. Table I summarizes the β constants of Nb, Y, as well as the spin and phonon systems of Dy. These β values are essentially independent of temperature, as confirmed exemplarily by the constant linear slopes of the curves $\varepsilon_{P,S} \sim Q_{P,S}$ plotted in Fig. 2 of Ref. [30]. To simplify the analysis we do not separately account for the electron and phonon contributions in each metal, since the specific heat of the electron system is always very small. Above T_N the spin contribution to β_{Dy} remains constant, but the specific heat of the spins above T_N is very small.

In contrast, the specific heat of the spin system below T_N is very large. In order to measure the individual contributions of phonons and spins to the energy density and expansion of Dy at temperatures below T_N, we invoke the two-thermal-energies model (TTEM) [30] in Dy. This model assumes that the measured strain ε_{Dy} is a superposition of both thermoelastic strain ε_P and the magnetostrictive strain ε_S:

$$\Delta\rho^Q_{Dy} = \Delta\rho^Q_S + \Delta\rho^Q_P = \beta_S \cdot \varepsilon_S + \beta_P \cdot \varepsilon_P, \tag{2}$$

$$\varepsilon_{Dy} = \varepsilon_S\left(\Delta\rho^Q_S\right) + \varepsilon_P\left(\Delta\rho^Q_P\right). \tag{3}$$

Since the Grüneisen constants and the coefficients $\beta_{P,S}$ are temperature independent, these strains are a robust and linear measure of the local energy densities.

We can combine Eqs. (2) and (3) to

$$\Delta\rho^{Q}_{Dy} = \beta_p(\varepsilon_{Dy} - \varepsilon_s) + \beta_s\varepsilon_s. \tag{4}$$

Below T_N we have four heat carrying degrees of freedom in the system, namely the spin excitations in Dy and the phonon excitation in Dy, Nb, and Y. In addition to the three measured transient lattice strains $\varepsilon_{Dy,Y,Nb}$ (Fig. 2), we need a fourth equation to find the solution to the heat transport problem. We conducted temperature-dependent ellipsometry measurements proving that the absorbed energy density of the multilayer does not change considerably with temperature. Assuming that no substantial fraction of the initial heat is transported to the substrate, we can identify the total amount of energy deposited in the multilayer at any temperature $\Delta Q^{T}_{\text{tot}}$ with the value $\Delta Q^{276K}_{\text{tot}}$ measured at $T = 276$ K, where only phonons drive the Dy expansion. This is an excellent approximation for time scales below 1 ns and a very good approximation up 100 ns, because the heat transport into the sapphire substrate is similar for all temperatures.

When we write

$$\Delta Q^{T}_{Dy} = \Delta Q^{276K}_{\text{tot}} - \Delta Q^{T}_{Y} - \Delta Q^{T}_{Nb}, \tag{5}$$

we only overestimate ΔQ^{T}_{Dy} at low temperatures by the rather small fraction $\Delta Q_{\text{err}} = \Delta Q^{T}_{\text{tot}} - \Delta Q^{276K}_{\text{tot}}$ of heat that is transported into the substrate more than it would be transported at 276 K. For convenience, this error can be read from the difference of brown and blue lines in Fig. 3(b), where we use the calculated total energy Q transported into substrate to calculate a change of energy density $\Delta\rho$ that has left a 100 nm thick layer. The energy densities $\Delta\rho^{Q}_{Dy} = \Delta Q^{T}_{Dy}/V_{Dy}$ in Dy derived for several different base temperatures are plotted in Fig. 3(a). We find that with lower base temperature a larger and larger fraction of the energy is rapidly transferred from the excited Y layer into Dy.

We now solve Eq. (4) to obtain equations for the contractive strain ε_S driven by spin order and the phonon driven expansive strain ε_P, which only depend on measured quantities:

$$\varepsilon_{\text{S}} = \frac{\left(\Delta\rho^{Q}_{\text{Dy}} - \beta_P\varepsilon_{\text{Dy}}\right)}{(\beta_S - \beta_P)}, \tag{6}$$

$$\varepsilon_{\text{P}} = \varepsilon_{\text{Dy}} - \varepsilon_S. \tag{7}$$

Here, $\Delta\rho^{Q}_{Dy}$ is the experimentally determined energy density plotted in Fig. 3(a). We can now use Eq. (1) to derive the contributions to the time-dependent energy densities $\Delta\rho^{Q}_{S,P}$ in Dy. The corresponding energy densities $\Delta\rho^{Q}_{Y,Nb}$ of the adjacent layers are determined directly from the measured quantities $\varepsilon_{Y,Nb}$. The resulting energy densities in each material derived from the experiment are plotted in Fig. 3(c) and compared to a simple calculation of the heat transport according to the heat equation [36]. Assuming a small thermal interface resistance of 200 MW/m^{2}K only between Nb and sapphire, we find a very good simultaneous agreement of the experimentally derived total energy density in Dy $\Delta\rho^{Q}_{Dy} = \Delta\rho^{Q}_{P} + \Delta\rho^{Q}_{S}$ and the simulations at 276 K and 136 K. In contrast, the simulated

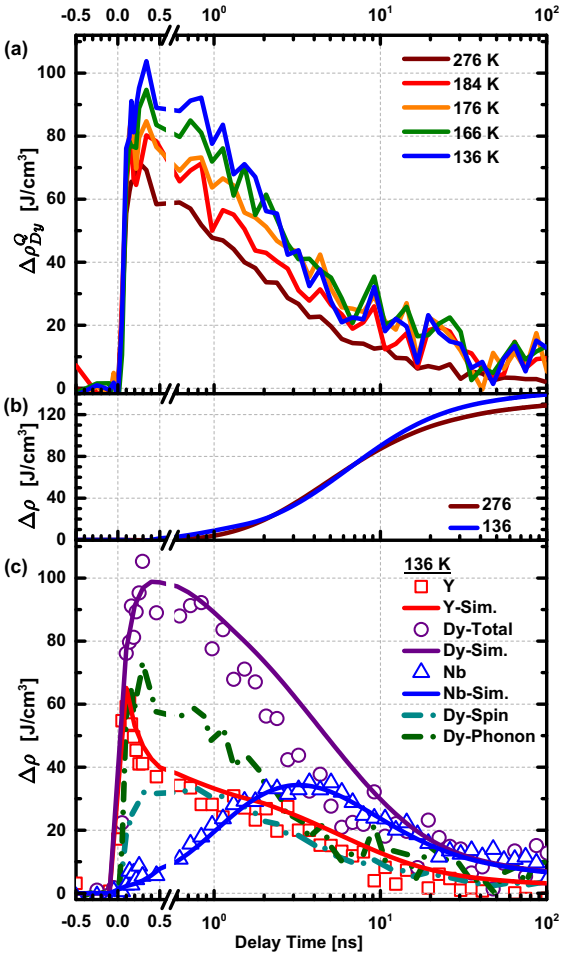

FIG. 3. (a) Transient increase of the energy density in the Dy layer ρ^{Q}_{Dy} after optical excitation derived from the measurement according to Eq. (4). (b) Simulation of the energy density transported into the substrate according to the heat equation. (c) Symbols show the experimentally determined transient energy densities $\rho^{Q}_{Y,Dy,Nb}$ in each material. Solid lines represent simulations according to heat equation. Dotted lines show the experimentally derived energy densities in the spin and phonon system of Dy $\rho^{Q}_{S,P}$.

thermal expansion $\varepsilon^{av}_{Dy}(t)$ averaged over the film thickness [dashed lines in Fig. 2(b)] considerably deviates from the measured strain ε_{Dy}, because the spin and phonon system are not even locally in thermal equilibrium. Closer to the phase transition the deviations get stronger and last longer. In the future, time-resolved resonant x-ray scattering experiments [19,37,38] on the several nanoseconds time scale may reveal the nature of the nonequilibrium.

V. DISCUSSION

Heat transport is driven by temperature gradients. We therefore plot the transient temperature changes of the spins and phonons $\Delta T_{S,P}$ in Dy and $\Delta T_{Y,Nb}$ in Fig. 4 as the

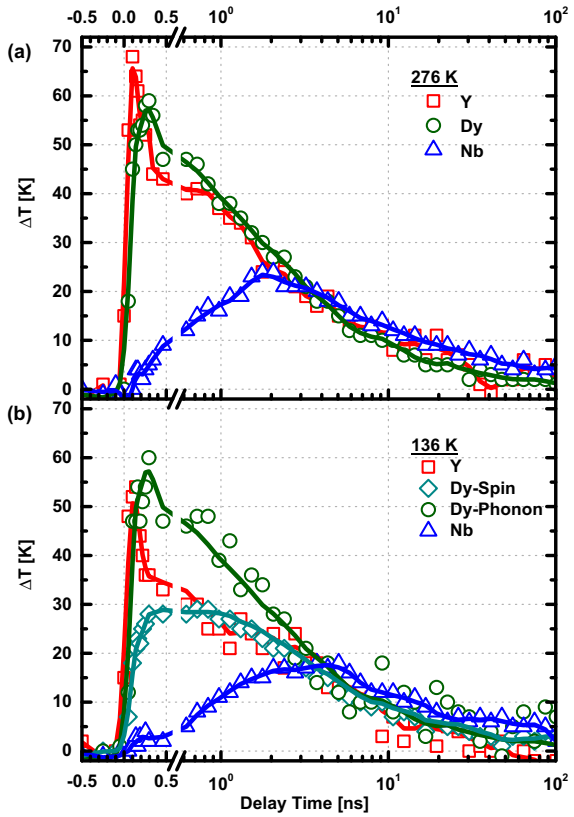

FIG. 4. Temperature change in each layer after excitation at (a) 276 K and (b) 136 K. The temperature in the spin system is only well defined at $T < T_N$. Solid lines represent running averages as a guide to the eye.

experimental solution of the heat transport problem through the three layers as a function of time for two temperatures above and below T_N. We use the specific heats c_i of the individual subsystems to calculate the temperature rise ΔT from $\Delta\rho_Q = \int_{T_0}^{T_0+\Delta T} c(T)dT$. The most striking result is that, within the time resolution of 100 ps, we measure that the Y layer is heated by $\Delta T = 50$ K at low and 68 K at high temperature, although ellipsometry proves that the same amount of energy was deposited by the light pulse. This suggests that the additional energy dissipation channel into spin excitations at low temperatures dramatically speeds up the heat transport across the Y/Dy interface.

Another robust feature seen in Fig. 4 is the delay of the temperature rise in the Nb layer, indicating a reduced heat transport through Dy. The temperature rise in the phonon system of Dy at both base temperatures is nearly the same, and therefore the heat arriving in the spin system effectively is additional to the phonon heat, explaining the observation in Fig. 3(a) that the increase of the energy density in Dy is higher at low temperature. Note that the kinetics of the temperature rise in the spin and phonon systems of Dy are clearly different.

The fact that energy density in the spin system of Dy drives a lattice contraction counteracting the expansion initiated by phonon heating explains the strong deviations of the observed lattice strain $\varepsilon_{Dy}^{av}(t) \neq \varepsilon_{Dy}$ from the simulated strain [Fig. 2(b)] when spins and phonons are not in a thermal equilibrium. The good agreement on the level of comparing the heat transport can be understood, when we identify the electrons as the main heat transporting quasiparticles. This means that a temperature-gradient in the electron system promotes the transport. Immediately after the optical excitation, the energy is essentially stored in the electron system, with a very large temperature gradient according to the small heat capacity of electrons in Dy. Within the time scale of electron-phonon and electron-spin coupling the heat transport should therefore considerably speed up with respect to the simulations using equilibrium parameters. This would then lead to an even better match of the simulations with the data in Fig. 3(a). When the electron, spin, and phonon temperatures have approached each other, the heat is essentially stored in spin excitations and phonons. Nonetheless it is the electron system that transports the energy, explaining why we simulate the heat transport essentially correct, even if the spin and phonon system have not equilibrated.

VI. CONCLUSION

We have exemplified an experimental procedure to measure the heat transport through multilayer systems with thicknesses in the nanometer range in the nontrivial case, where a considerable fraction of the heat of one material (Dy) is dynamically stored in a strongly interacting spin system. At all temperatures, the heat transport is dominated by electron transport, although electrons only contribute negligibly to the heat capacity. Below the Néel temperature, the spin system opens up an additional heat sink. While the heat transport into the phonon system is nearly unchanged, the spins extract additional energy from the adjacent laser heated Y layer and speed up the initial cooling. At the same time the spin excitations slow down the electronic heat transport by electron-magnon scattering, which is evidenced by a delayed rise of the Nb temperature, through which the heat is finally dissipated. For future investigations it would be ideal to correlate the heat flow via the spin system with direct observations of the antiferromagnetic spin system using resonant x-ray scattering [19,37,38].

Although the average heat, experimentally measured in each layer, is in rather good agreement with standard simulations using the heat equation, there are strong deviations of simulated strain from the measured values. This is because a large fraction of the energy is stored in spin excitations, which promote the contraction of the film. In general, for multilayer systems where only electrons and phonons carry the heat, the transient temperatures can be directly read from the measured strains, which may be very useful when simulations fail to predict real situations, e.g., rough interfaces. For even more complex situations, where several quasiparticles contribute to the heat transport and thermoelastic strain, we have shown how to analytically decompose the measured signal and get the correct decomposition of spin and phonon contributions to the strain and the heat. A direct experimental assessment of the heat flow is crucial for understanding the heat transport via various quasiparticles and across interfaces. We believe that such direct experimental

cross-checks of theoretical predictions yield valuable information when it comes to optimizing heat transport for real applications.

ACKNOWLEDGMENT

We acknowledge the BMBF for financial support via Grant No. 05K12IPA.

[1] D. G. Cahill, W. K. Ford, K. E. Goodson, G. D. Mahan, A. Majumdar, H. J. Maris, R. Merlin, and S. R. Phillpot, Nanoscale thermal transport, J. Appl. Phys. **93**, 793 (2003).

[2] D. G. Cahill, P. V. Braun, G. Chen, D. R. Clarke, S. Fan, K. E. Goodson, P. Keblinski, W. P. King, G. D. Mahan, A. Majumdar *et al.*, Nanoscale thermal transport. II. 2003–2012, Appl. Phys. Rev. **1**, 011305 (2014).

[3] K. M. Hoogeboom-Pot, J. N. Hernandez-Charpak, X. Gu, T. D. Frazer, E. H. Anderson, W. Chao, R. W. Falcone, R. Yang, M. M. Murnane, H. C. Kapteyn, and D. Nardi, A new regime of nanoscale thermal transport: Collective diffusion increases dissipation efficiency, Proc. Natl. Acad. Sci. USA **112**, 4846 (2015).

[4] A. A. Balandin, Nanoscale thermal management, IEEE Potentials **21**, 11 (2002).

[5] M. N. Luckyanova, J. Garg, K. Esfarjani, A. Jandl, M. T. Bulsara, A. J. Schmidt, A. J. Minnich, S. Chen, M. S. Dresselhaus, Z. Ren, E. A. Fitzgerald, and G. Chen, Coherent phonon heat conduction in superlattices, Science **338**, 936 (2012).

[6] S. Xiong, K. Sääskilahti, Y. A. Kosevich, H. Han, D. Donadio, and S. Volz, Blocking Phonon Transport by Structural Resonances in Alloy-based Nanophononic Metamaterials Leads to Ultralow Thermal Conductivity, Phys. Rev. Lett. **117**, 025503 (2016).

[7] G. Chen, D. Borca-Tasciuc, and R. G. Yang, Nanoscale heat transfer, Encycl. Nanosci. Nanotechnol. **7**, 429 (2004).

[8] N.W. Ashcroft and N.D. Mermin, *Solid State Physics* (Saunders College, Philadelphia, 1976).

[9] V. K. Pecharsky, K. A. Gschneidner, Jr., and D. Fort, Superheating and other unusual observations regarding the first order phase transition in Dy, Scr. Mater. **35**, 843 (1996).

[10] M. Griffel, R. E. Skochdopole, and F. H. Spedding, The heat capacity of gadolinium from 15 to 355 K, Phys. Rev. **93**, 657 (1954).

[11] B. C. Gerstein, M. Griffel, L. D. Jennings, R. E. Miller, R. E. Skochdopole, and F. H. Spedding, Heat capacity of holmium from 15 to 300 K, J. Chem. Phys. **27**, 394 (1957).

[12] D. W. Boys and S. Legvold, Thermal conductivities and Lorenz functions of Dy, Er, and Lu single crystals, Phys. Rev. **174**, 377 (1968).

[13] C. Hess, B. Büchner, U. Ammerahl, L. Colonescu, F. Heidrich-Meisner, W. Brenig, and A. Revcolevschi, Magnon Heat Transport in Doped La_2CuO_4, Phys. Rev. Lett. **90**, 197002 (2003).

[14] E. Beaurepaire, J.-C. Merle, A. Daunois, and J.-Y. Bigot, Ultrafast Spin Dynamics in Ferromagnetic Nickel, Phys. Rev. Lett. **76**, 4250 (1996).

[15] R. Biele, R. D'Agosta, and A. Rubio, Time-dependent Thermal Transport Theory, Phys. Rev. Lett. **115**, 056801 (2015).

[16] C. Stamm, T. Kachel, N. Pontius, R. Mitzner, T. Quast, K. Holldack, S. Khan, C. Lupulescu, E. F. Aziz, M. Wietstruk, H. A. Durr, and W. Eberhardt, Femtosecond modification of electron localization and transfer of angular momentum in nickel, Nat. Mater. **6**, 740 (2007).

[17] A. Eschenlohr, M. Battiato, R. Maldonado, N. Pontius, T. Kachel, K. Holldack, R. Mitzner, A. Foehlisch, P. M. Oppeneer, and C. Stamm, Ultrafast spin transport as key to femtosecond demagnetization, Nat. Mater. **12**, 332 (2013).

[18] B. Frietsch, J. Bowlan, R. Carley, M. Teichmann, S. Wienholdt, D. Hinzke, U. Nowak, K. Carva, P. M. Oppeneer, and M. Weinelt, Disparate ultrafast dynamics of itinerant and localized magnetic moments in gadolinium metal, Nat. Commun. **6**, 8262 (2015).

[19] L. Rettig, C. Dornes, N. Thielemann-Kühn, N. Pontius, H. Zabel, D. L. Schlagel, T. A. Lograsso, M. Chollet, A. Robert, M. Sikorski, S. Song, J. M. Glownia, C. Schüeßler-Langeheine, S. L. Johnson, and U. Staub, Itinerant and Localized Magnetization Dynamics in Antiferromagnetic Ho, Phys. Rev. Lett. **116**, 257202 (2016).

[20] J. Li, L. R. Shelford, P. Shafer, A. Tan, J. X. Deng, P. S. Keatley, C. Hwang, E. Arenholz, G. van der Laan, R. J. Hicken, and Z. Q. Qiu, Direct Detection of Pure ac Spin Current by X-ray Pump-probe Measurements, Phys. Rev. Lett. **117**, 076602 (2016).

[21] G.-M. Choi, B.-C. Min, K.-J. Lee, and D. G. Cahill, Spin current generated by thermally driven ultrafast demagnetization, Nat. Commun. **5**, 4334 (2014).

[22] H. A. Navirian, D. Schick, P. Gaal, W. Leitenberger, R. Shayduk, and M. Bargheer, Thermoelastic study of nanolayered structures using time-resolved x-ray diffraction at high repetition rate, Appl. Phys. Lett. **104**, 021906 (2014).

[23] D. B. Xu, C. J. Sun, D. L. Brewe, S.-W. Han, P. Ho, J. S. Chen, S. M. Heald, X. Y. Zhang, and G. M. Chow, Spatiotemporally separating electron and phonon thermal transport in $L1_0$ FePt films for heat assisted magnetic recording, J. Appl. Phys. **115**, 243907 (2014).

[24] Y. C. Ho, R. W. Powell, and P. E Liley, Thermal conductivity of the elements: A comprehensive review, J. Phys. Chem. Ref. Data **3**, 1 (1974).

[25] E. R. Dobrovinskaya, L. A. Lytvynov, and V. Pishchik, *"Sapphire", Micro- and Opto-Electronic Materials, Structures, and Systems* (Springer, New York, 2009).

[26] K. Dumesnil, C. Dufour, Ph. Mangin, G. Marchal, and M. Hennion, Magnetoelastic and exchange contributions to the helical-ferromagnetic transition in dysprosium epitaxial films, EPL (Europhys. Lett.) **31**, 43 (1995).

[27] H. Navirian, R. Shayduk, W. Leitenberger, J. Goldshteyn, P. Gaal, and M. Bargheer, Synchrotron-based ultrafast x-ray diffraction at high repetition rates, Rev. Sci. Instrum. **83**, 063303 (2012).

[28] M. Reinhardt, A. Koc, W. Leitenberger, P. Gaal, and M. Bargheer, Optimized spatial overlap in optical pump–x-ray probe experiments with high repetition rate using laser-induced surface distortions, J. Synchrotron Radiat. **23**, 474 (2016).

[29] D. Schick, R. Shayduk, A. Bojahr, M. Herzog, C. von Korff Schmising, P. Gaal, and M. Bargheer, Ultrafast reciprocal-space mapping with a convergent beam, J. Appl. Crystallogr. **46**, 1372 (2013).

[30] A. von Reppert, J. Pudell, A. Koc, M. Reinhardt, W. Leitenberger, K. Dumesnil, F. Zamponi, and M. Bargheer, Persistent nonequilibrium dynamics of the thermal energies in the spin and phonon systems of an antiferromagnet, Struct. Dyn. **3**, 054302 (2016).

[31] J. F. Smith and J. A. Gjevre, Elastic constants of yttrium single crystals in the temperature range 4.2–400 K, J. Appl. Phys. **31**, 645 (1960).

[32] M. Rosen and H. Klimker, Low-temperature elasticity and magnetoelasticity of dysprosium single crystals, Phys. Rev. B **1**, 3748 (1970).

[33] K. J. Carroll, Elastic constants of niobium from 4.2 to 300 K, J. Appl. Phys. **36**, 3689 (1965).

[34] L. D. Jennings, R. E. Miller, and F. H. Spedding, Lattice heat capacity of the rare earths. Heat capacities of yttrium and lutetium from 15–350 K, J. Chem. Phys. **33**, 1849 (1960).

[35] A. von Reppert, Ultrafast magnetostriction in dysprosium studied by femtosecond x-ray diffraction, Master's thesis, Universität Potsdam, 2015.

[36] D. Schick, A. Bojahr, M. Herzog, R. Shayduk, C. von Korff Schmising, and M. Bargheer, UDKM and SIM—A simulation toolkit for 1D ultrafast dynamics in condensed matter, Comput. Phys. Commun. **185**, 651 (2014).

[37] N. Thielemann-Kühn, D. Schick, N. Pontius, C. Trabant, R. Mitzner, K. Holldack, H. Zabel, A. Föhlisch, and C. Schüßler-Langeheine, Ultrafast and energy-efficient spin manipulation: Antiferromagnetism beats ferromagnetism, arXiv:1703.03689.

[38] M. C. Langner, S. Roy, A. F. Kemper, Y.-D. Chuang, S. K. Mishra, R. B. Versteeg, Y. Zhu, M. P. Hertlein, T. E. Glover, K. Dumesnil, and R. W. Schoenlein, Scattering bottleneck for spin dynamics in metallic helical antiferromagnetic dysprosium, Phys. Rev. B **92**, 184423 (2015).

Article X

Grueneisen-approach for the experimental determination of transient spin and phonon energies from ultrafast x-ray diffraction data: gadolinium

Azize Koç, Matthias Reinhardt, Alexander von Reppert, Matthias Rössle, Wolfram Leitenberger, Markus Gleich, Martin Weinelt, Flavio Zamponi, and Matias Bargheer

Journal of Physics: Condensed matter 29, 264001 (2017)

We study gadolinium thin films as a model system for ferromagnets with negative thermal expansion. Ultrashort laser pulses heat up the electronic subsystem and we follow the transient strain via ultrafast x-ray diffraction. In terms of a simple Grueneisen approach, the strain is decomposed into two contributions proportional to the thermal energy of spin and phonon subsystems. Our analysis reveals that upon femtosecond laser excitation, phonons and spins can be driven out of thermal equilibrium for several nanoseconds.

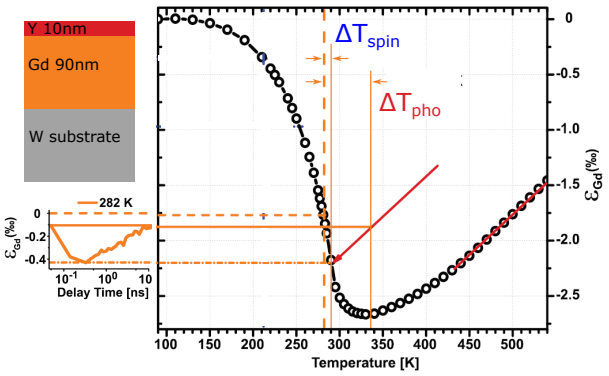

IOP Publishing Journal of Physics: Condensed Matter
J. Phys.: Condens. Matter **29** (2017) 264001 (8pp) https://doi.org/10.1088/1361-648X/aa7187

Grueneisen-approach for the experimental determination of transient spin and phonon energies from ultrafast x-ray diffraction data: gadolinium

A Koc[1], M Reinhardt[1], A von Reppert[2], M Rössle[2], W Leitenberger[2], M Gleich[3], M Weinelt[3], F Zamponi[2] and M Bargheer [1,2]

[1] Helmholtz Zentrum Berlin, Albert-Einstein-Str. 15, 12489 Berlin, Germany
[2] Institut für Physik und Astronomie, Universität Potsdam, Karl-Liebknecht-Str. 24-25, 14476 Potsdam, Germany
[3] Fachbereich Physik, Freie Universität Berlin, Arnimallee 14, 14195 Berlin, Germany

E-mail: bargheer@uni-potsdam.de

Received 20 February 2017, revised 27 April 2017
Accepted for publication 8 May 2017
Published 30 May 2017

Abstract
We study gadolinium thin films as a model system for ferromagnets with negative thermal expansion. Ultrashort laser pulses heat up the electronic subsystem and we follow the transient strain via ultrafast x-ray diffraction. In terms of a simple Grueneisen approach, the strain is decomposed into two contributions proportional to the thermal energy of spin and phonon subsystems. Our analysis reveals that upon femtosecond laser excitation, phonons and spins can be driven out of thermal equilibrium for several nanoseconds.

Keywords: ultrafast, x-ray diffraction, magnetostriction, nonequilibrium, spin, phonon, rare earth

(Some figures may appear in colour only in the online journal)

1. Introduction

Gadolinium has the highest magnetic ordering temperature among all lanthanides and is ferromagnetic from the Curie temperature $T_C = 293$ K down to 4 K, although for bulk Gd a spin-reorientation takes place at $T_{SR} = 232$ K. The magnetic moment of the lanthanides mainly arises from the 4*f* shell electrons, and the localized nature of these inner orbitals predestines these elements to test fundamental models of magnetism. Gd is a prototype system for a Heisenberg ferromagnet. Ferromagnetic order is established via the indirect RKKY exchange interaction described by an effective exchange constant J [1]. Gd stands out among the lanthanides for having the largest spin angular momentum of 7.55 μ_B and zero orbital moment. Therefore the interaction with the lattice cannot be explained by crystal field effects [1],

1.1. Thermal expansion coefficient in a Heisenberg ferromagnet

Above and below the Curie temperature, a large fraction of the thermal energy density ρ_Q in Gd is carried by spin excitations [2]. These spin excitations drive a strong negative thermal expansion below the Curie temperature [3]. An excellent theoretical analysis of the spin-phonon excitation in Heisenberg ferromagnets lead Pytte [4] to derive the thermal expansion coefficient, which is proportional to the specific heat of the phonon- and the spin system, C_P and C_S, according to

$$\alpha = \alpha_P + \alpha_S = \frac{1}{9}\frac{1}{d_0^2 K}\left(\frac{3\Gamma_P}{d_0}C_P + \frac{1}{J}\frac{\partial J}{\partial d}C_S\right). \quad (1)$$

K is the elastic modulus and d_0 the equilibrium lattice constant. Since the phonon Grueneisen constant Γ_P is nearly independent of temperature, the characteristic dip of α around the second order phase transition at T_C indicates that $\frac{\partial J}{\partial d} < 0$, i.e. it

is the exchange interaction that induces the negative thermal expansion. At low temperatures, the spin-contribution to the specific heat $C_S \sim T^{3/2}$ can be described by magnon excitations and the Grueneisen constant of the spin system can be defined as the logarithmic derivative $\Gamma_S = \frac{\partial \ln J}{\partial \ln V}$ in close analogy to the phonon system $\Gamma_P = \frac{\partial \ln \hbar\omega}{\partial \ln V}$ [5]. Both Grueneisen constants measure how efficiently the energy density $\rho^Q_{S,P}$ generates stress $\sigma_{S,P} = \Gamma_{S,P}\rho^Q_{S,P}$. Therefore they linearly relate the lattice strain $\epsilon_{S,P} \sim \sigma_{S,P} \sim \rho^Q_{S,P}$ to the energy density.

1.2. Ultrafast magnetization dynamics of Gd thin films

Spin-excitations and correlations not only govern the thermophysical characteristics of Gd. They give likewise rise to the exchange splitting of majority and minority spin bands in the valence band structure and the macroscopic magnetization [1]. Gd has become one of the most thoroughly studied model systems [6] regarding ultrafast optical manipulation of spins and GdFeCo alloys were the first sample system to demonstrate all-optical magnetic switching [7, 8].

Time-, angle- and energy-resolved photoemission spectroscopy showed that upon optical excitation the exchange splitting decreases within 2 ps [9]. The response of the majority spin band is delayed by 1 ps and is somewhat slower than the minority spin valence band [9]. In contrast to the thermal phase transition, the spin polarization of the Gd surface state remains nearly constant within the first picoseconds after laser excitation and decays only slowly within $\tau = 15 \pm 8$ ps [10]. Photoemission studies of the 4*f* magnetic linear dichroism and the 5*d* exchange splitting showed that their dynamics differ by one order of magnitude, with decay constants of about 14 versus 0.8 ps [11]. The slower picosecond time scale has been attributed to 4*f* spin-lattice coupling [12–14], which determines the spin polarization [10].

The notion of thermally driven demagnetization and all-optical switching is prevalent in the recent literature [15, 16], and already Koopmans *et al* suggested that ultrafast demagnetization could be described, disregarding highly excited electronic states, merely considering the thermalized electron system [17]. The recent experimental work mainly focuses on the ultrafast response of the spins upon optical excitation, although restoring the equilibrium is equally important for the functionality in ultrafast data storage. Therefore it is important to study how the temperatures of spin and phonon subsystems evolve as a function of time for different starting temperatures. Very recent ultrafast x-ray diffraction experiments on dysprosium already exploited the strong connection of the lattice expansion and the deposited energy in the spin- and phonon subsystems [18]. In particular, a persistent non-equilibrium was found with the spin-system remaining hotter than the phonon-system for several nanoseconds, although initially the phonon heating dominated the energy balance.

In this paper we discuss the Grueneisen approach to analyze temperature-dependent time-resolved ultrafast x-ray diffraction data in magnetostrictive systems. As a model system we study a 90 nm thin Gd(0 0 0 1) film on a W(1 1 0) substrate. At low temperatures $T \ll T_C$, our experiments show a very strong transient contraction of the lattice along the *c* axis perpendicular to the (0 0 0 1) surface plane upon laser heating. The contraction is larger than the transient thermal expansion at $T > T_C$, although a considerably larger fraction of the energy deposited in the electron system is transferred to the phonon system. The phonon system relaxes within 500 ps by heat transport to the substrate. At low temperatures the spin excitations relax on a similar timescale. Close to the Curie temperature, the lattice contraction indicates spin excitations persisting for several nanoseconds. Although the hot electrons had excited both the phonon and the spin system within a few picoseconds, the spin system is largely decoupled from the phonon system, as the equilibration times differ by an order of magnitude near T_C. At any initial temperature, the laser excitation drives spin and phonon subsystems out of equilibrium in the sense that they must be described by different temperatures, if the concept of temperature is applicable at all.

2. Experiment

The investigated sample is a $D = 90 \pm 10$ nm thick Gd film epitaxially grown at a pressure of $1 \cdot 10^{-10}$ mbar on a (1 1 0)-oriented tungsten single crystal substrate. The tungsten crystal was cleaned following the procedure described in [19]. We used homebuilt evaporators and controlled the thickness by a quartz micro balance. First a Gd seed-layer of 10 nm thickness was grown at room temperature and annealed to 400 °C. The completed 90 nm Gd film was annealed to 490 °C and showed the low-energy electron diffraction pattern of the hcp(0 0 0 1) surface. Finally we deposited a polycrystalline yttrium cap layer of 10 ± 1 nm thickness to protect the sample during transport in air to the diffraction experiments. The thickness of the sample was confirmed by acoustic pulse echoes measured by ultrafast x-ray diffraction [20].

Static and time-resolved x-ray diffraction measurements were performed at the XPP experimental station of the storage ring facility BESSY II (Helmholtz–Zentrum-Berlin) [21, 22]. Figure 1(a) shows a reciprocal space map of the Gd film, confirming its good structural quality. In the time-resolved experiments, we determined the lattice strain $\varepsilon(t) = [c(t) - c(t<0)]/c(t<0)$ from projections of the reciprocal space maps (RSM) [23] of Gd around the (0 0 0 2) reflection as shown exemplarily in figure 1(b). The 9 keV hard x-rays have an attenuation length in Gd of approximately 800 nm and thus probe the entire Gd film. Therefore, the measured Bragg peak shift yields a reliable measure of the average strain in the film. The 250 fs pump pulses have a central wavelength of 1032 nm. The penetration depth of the pump light in yttrium and Gd is about 23 nm. We emphasize that the Grueneisen concept developed below yields the same average strain, independent of the spatial profile of the deposited energy. The expansion is proportional to the total energy deposited in the spin and the phonon system. Further details of the setup are given in previous publications [21, 22].

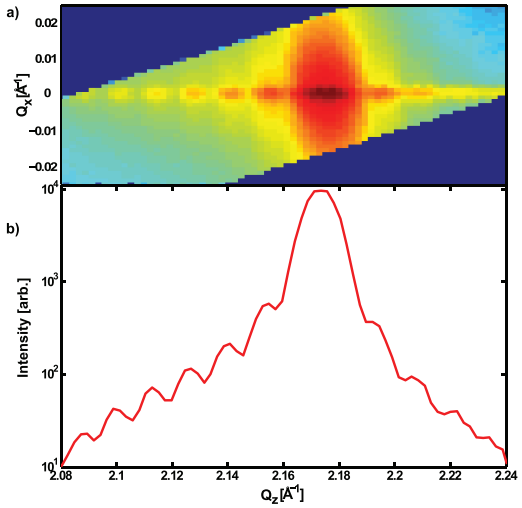

Figure 1. (a) Reciprocal space map around the 0002 reflection of Gd. (b) Projection of the RSM onto the q_z direction showing pronounced Laue oscillations which indicate a good structural quality.

3. Results

3.1. Spin and phonon Grueneisen coefficient of Gd

Figure 2(a) shows the measured temperature-dependent out-of-plane lattice constant c of our Gd(0 0 0 1) film, which we used to calculate the thermal expansion coefficient α_{Gd} depicted in figure 2(b). The strong negative thermal expansion coefficient of Gd is closely related to the specific heat contribution of the ferromagnetically ordered spin-system, as both clearly peak at 293 K. For convenience we reproduce the heat capacity C_{Gd} at constant pressure in figure 2(c) after [2]. From the relation $\Gamma = \alpha K / C_{\mathrm{Gd}}$ we evaluate the Grueneisen constants Γ_{S} and Γ_{P} shown in figure 2(d). The spin and phonon contributions follow from the appropriate decomposition of the thermal expansion coefficient $\alpha_{\mathrm{Gd}} = \alpha_{\mathrm{S}} + \alpha_{\mathrm{P}}$ and the specific heat $C_{\mathrm{Gd}} = C_{\mathrm{S}} + C_{\mathrm{P}}$. In our analysis we neglected the difference between thermal expansion driven by electrons and phonons, since it is only relevant on the few picosecond timescale, when the electron system is significantly hotter than the lattice [18, 24, 25]. The joint contribution of electrons and phonons to the specific heat was obtained by scaling the phonon contribution to the specific heat values for non-magnetic lutetium according to the Debye-temperature [26, 27]. The phonon contribution of Lu was obtained by subtracting the electron contribution $C_{\mathrm{e}}^{\mathrm{Lu}}$ according to the Sommerfeld constant [28]. The corresponding electron contribution $C_{\mathrm{e}}^{\mathrm{Gd}}$ for Gd was added to the scaled phonon $C_{\mathrm{P}}^{\mathrm{Gd}}$ value to obtain the non-magnetic contributions of Gd shown in figure 2(c) for electrons (red) and phonons (green). The thermal expansion above 350 K is approximated by the phonon driven expansion in the Debye model and extrapolated to low temperatures. In the relevant temperature range the linear expansion coefficient is essentially constant [3, 29].

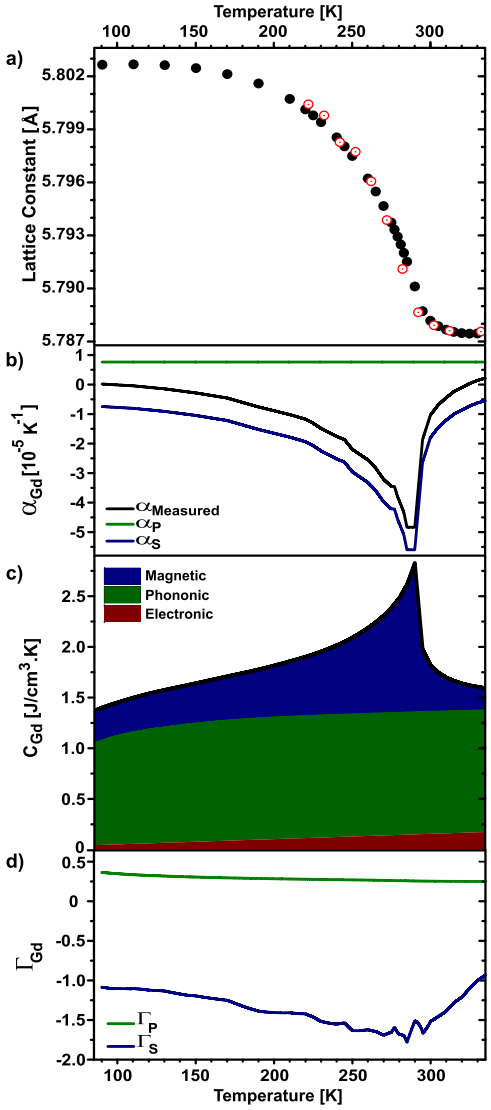

Figure 2. Temperature-dependent parameters of Gd in equilibrium: (a) out-of-plane lattice constant (black points). The red points show the out-of plane lattice constant under irradiation with a laser fluence of 1.7 mJ cm^{-2}. The red points are shifted by $\Delta T = 12$ K to show the excellent agreement with the black points. (b) thermal expansion coefficient α_{Gd}, (c) specific heat capacity c_{Gd} [2] separated into the electronic, phononic and magnetic contributions (see text), (d) Grueneisen constant Γ_{Gd} derived from the data in panels (b) and (c).

3.2. Time-resolved x-ray diffraction data

Figure 3 depicts the transient lattice strain in the Gd layer $\varepsilon(t)$ after ultrafast laser heating. For these measurements the initial temperature T_{i} of the film was tuned across the Curie temperature between 212 K and 322 K, while the excitation was kept constant at an incident fluence of 1.7 mJ cm^{-2}. In the entire paper the temperatures T_{i} are the temperatures of the sample including a $\Delta T = 12$ K heating that results from the heat deposited at the high repetition rate. This ΔT is deduced

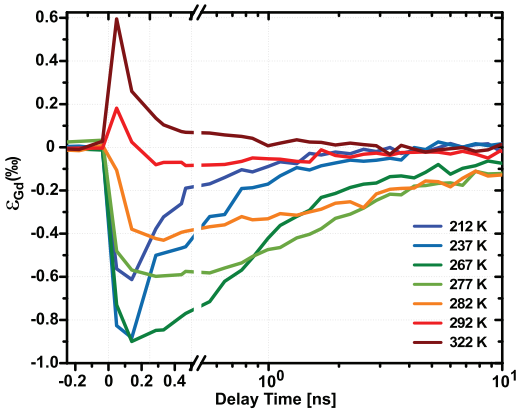

Figure 3. Transient strain $\varepsilon(t)$ in the 90 nm Gd layer for different initial temperatures T_i after ultrafast laser heating at 1.7 mJ cm^{-2} incident fluence. We note that the temperatures given in the legend are the sample temperatures, taking into account the static heat load in the sample imposed by the fluence of 1.7 mJ cm^{-2} at the high repetition rate. The temperature of the sample is increased by 12 K, and correspondingly the given T_i values are 12 K larger than the reading of the cryostat's temperature controller.

from the red points in figure 2(a), which were recorded under the same fluence conditions.

The lattice response at $T_i = 322$ K, i.e. above the Curie temperature, shows an initial expansion of the lattice as expected from phonon heating. Maximum strain is reached within the time-resolution of about 80 ps given by the x-ray pulse duration. The timescale t_{max} for expansion is given by the sound velocity [30] $v_{Gd} = 3\,\text{nm ps}^{-1}$ via $t_{max} = D/v_{Gd} = 33$ ps. The lattice expansion relaxes within about 500 ps via heat diffusion into the W substrate.

All transients recorded for an initial temperature below T_C show a lattice contraction at all time delays. This reflects the intimate coupling between interatomic distances and exchange interaction. The strongest negative expansion of about $-9 \cdot 10^{-4}$ at $T_i = 267$ K even exceeds the positive expansion measured at $T_i = 322$ K (see figure 3).

With T_i approaching T_C, the contraction decreases while the relaxation of the transient strain slows down, with considerable contraction persisting longer than 10 ns. Close to the Curie temperature at $T_i = 292$ K we observe an initial expansion followed by a contraction for delays >150 ps.

Qualitatively, our data directly prove that a substantial fraction of the energy deposited by the laser heats up the spin system, since only ρ_S^Q drives the negative expansion according to the Grueneisen constant. The contraction observed for $T_i = 292$ K in figure 3 indicates that this is also true close to the Curie temperature, when the magnetic order is almost lost. Even when the thermal expansion coefficient turns positive above T_c (see figure 2(b), the phonon driven expansion is significantly reduced by spin contributions. By a more detailed analysis below we will show that even the transient at $T_i = 322$ K is considerably influenced by a contractive stress driven by spin-excitation.

In the following we show that laser-excitation leads to a strong non-equilibrium between spin and lattice subsystems and estimate their different transient temperatures. To this end we can safely assume that within the time resolution of our setup of about 80 ps electron and phonon systems have essentially equilibrated. Therefore we can describe both subsystems by a single temperature and only consider different heating of spins and phonons. From temperature dependent ellipsometry measurements of a 10 nm thick Y capping layer on a 100 nm Dy sample [18] we know that the energy deposited by the laser pulse is independent of the initial temperature in the relevant temperature range. Unfortunately the Gd sample was too big to be mounted in the ellipsometry cryostat. First we attempt to analyze the data in an equilibrium model by assuming that spins and phonons have the same temperature at all times. This enforces the static lattice constant $c(T)$ depicted in figure 2(a) to map the transient temperature $T(t)$ via $c(t) = c(T)$. Likewise the transient strain would mimic the transient temperature via $\epsilon(t) = \epsilon(T)$.

We show for three different examples that this equilibrium approach is incorrect:

(i) Figure 4 illustrates two situations for different starting temperatures T_i. If spins and phonons were in equilibrium, the maximum transient strain of $-4.3 \cdot 10^{-4}$ observed for $T_i = 282$ K would correspond to a temperature rise of 9 K. In contrast, the maximum strain for $T_i = 212$ K is $-6.1 \cdot 10^{-4}$, which would reflect a temperature rise of 42 K. These values can be directly read from the dashed and dash-dotted orange and blue lines in figure 4. The maximum temperature change extracted from the change in $\epsilon(T)$ varies by about a factor of 5 for the two different starting temperatures, although the optical absorption coefficient is constant and consequently the same amount of energy is deposited. We can safely conclude from the observation at $T_i = 212$ K that the energy deposited by the laser pulse must at least lead to a temperature rise of $\Delta T > 42$ K. At $T_i = 282$ K the total heat capacity of Gd is at most 25 % larger than at $T_i = 212$ K. Therefore, the temperature jump would at least be 24 K, contradicting our simple equilibrium description.

(ii) Moreover, if we consider the situation at a delay of 50 ps (solid orange line in figure 4), the failure to assume $T_S = T_P$ becomes even more obvious. The lattice response shows a strain of $-1 \cdot 10^{-5}$ corresponding to a temperature rise of only 1 K. In fact this can only be explained in a non-equilibrium model by assuming a simultaneous heating of spin- and phonon systems with an almost exact cancellation $\alpha_S \Delta T_S \approx \alpha_P \Delta T_P$ of the lattice contraction and expansion. If we write this relation in terms of the energy densities it follows $-\Gamma_S \rho_S^Q = \Gamma_P \rho_P^Q = \Gamma_P(\rho_{Gd}^Q - \rho_S^Q)$. From the latter identity we can immediately conclude that the spin system initially takes the fraction $\rho_S^Q/\rho_{Gd}^Q = \Gamma_P/(\Gamma_P - \Gamma_S) = 14$ % of the total deposited energy ρ_{Gd}^Q at $T_i = 282$ K. This analysis is robust, because strain and energy density are linearly related, and it implies a similarly large difference in the temperature rise of the spin and phonon system, since the heat capacity C_S at 282 K is only 20% smaller than

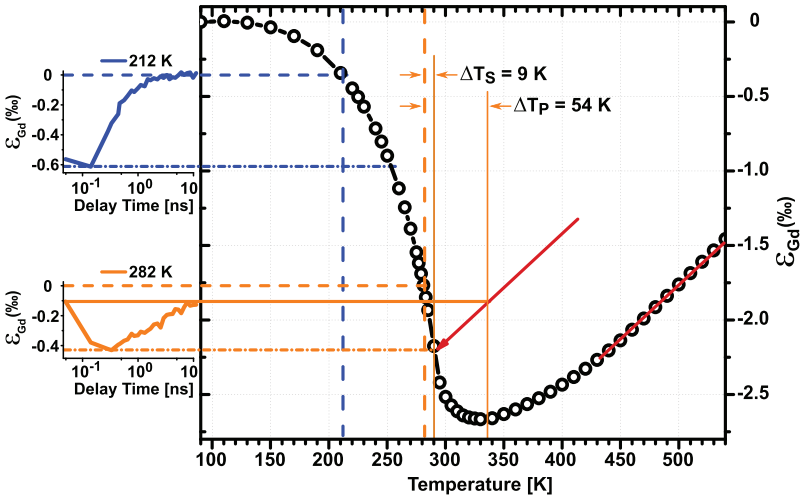

Figure 4. Illustration of the temperature rise in the Gd film after ultrafast laser excitation. The insets show the transient lattice response $\varepsilon(t)$ for two selected initial temperatures $T_i = 212$ K (blue) and 282 K (orange) reproduced from figure 3. The solid circles represent the measured lattice strain from static heating experiments (figure 2(a)) extrapolated by using high temperature literature values [3]. The thick dashed lines indicate the initial temperature T_i and the corresponding $\varepsilon = 0$. The dash-dotted lines show the maximum contraction, which yields a lower estimate of the temperature rise ΔT_S of the spin excitations. The solid lines highlight the initial non-equilibrium response that explains the tiny initial contraction at $t = 50$ ps resulting from a near cancellation of the contractive stress from heating spins by $\Delta T_S = 9$ K and the expansive stress from heating the phonon system by $\Delta T_P = 54$ K. The red line indicates the linear thermal expansion of Gd for high temperatures, where the spin contribution is negligible. The red arrow with the same slope symbolizes a fictitious exclusive cooling of the phonon system towards the equilibrium at $\Delta T_S = \Delta T_P = 9$ K. This scenario yields a lower estimate of the non-equilibrium heating. The real dynamics deviate from the red arrow (see figure 6). The total absorbed energy is larger. Additional $\Delta T_P = 6\Delta T_S$ keeps the initial strain at 50 ps constant according to the Grueneisen coefficients. In order to explain the maximal observed contraction cooling of both the spin and phonon system are then necessary.

$C_P + C_e$. Figure 5 shows the distribution of energy density ρ_S^Q and ρ_P^Q for different initial temperatures, determined 50 ps after the excitation by the analytic method described in the next section.

(iii) We get the third important estimate from the temperature rise required to rationalize the contraction of $-6.1 \cdot 10^{-4}$ for $T_i = 212$ K. In equilibrium we have to assume at least a temperature rise $\Delta T > 42$ K to account for the contraction. In non-equilibrium we can, however, also explain the observation by a larger temperature rise ΔT_S of the spin system, if we assume that the phonon system receives even more energy. We explain this situation graphically in figure 4 for the example of $T_i = 282$ K. At $t = 50$ ps, the dynamics start at a small negative strain level indicated by the solid orange line. This is the strain level given by an approximate balance of expansive and contractive stresses.

The dash-dotted orange line indicates the maximum negative strain that the transient attains at about 300 ps. At this time spin and phonon systems must at least still be heated by 9 K. In order to explain the strain balance just after excitation, we have to assume an excessive heating of the phonon system beyond the temperature of the spin system. The red line in figure 4 indicates the slope at which the phonon heating leads to strain according to the high-temperature thermal expansion. If we assume an initial temperature jump of the spin system by $\Delta T_S = 9$ K then the phonon systems must exhibit an initial temperature jump of $\Delta T_P = 54$ K to compensate the

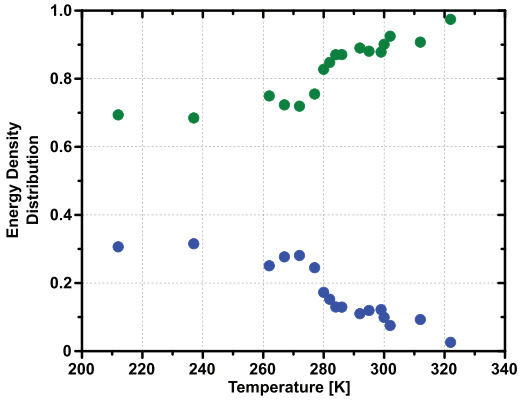

Figure 5. Fraction of energy deposited in the spin system (blue) and in the electron-phonon system (green) as a function of initial temperature T_i. Note that at $T > T_C$ less than 10% of the energy leads to spin excitations.

negative strain of the spin system. This yields a lower estimate of the energies leading to the non-equilibrium. Starting from this fictitious non-equilibrium state, the red arrow would indicate the path of the system via exclusive phonon cooling towards a fictitious equilibrium at the maximum contraction for $\Delta T_P = \Delta T_S = 9$ K. The real non-equilibrium state is determined by the analytic solution presented in the next section, where we obtain the initial temperature jumps to be $\Delta T_P = 70$ K and $\Delta T_S = 15$ K, respectively.

These three examples show that we can prove the non-equilibrium of spin and phonon subsystems directly from the UXRD transients without detailed calculations. In the following we will discuss an analytic decomposition of the transient signal for any T_i, which for example shows that at $T_i = 282$ K, the phonons are initially heated by $\Delta T_P = 70$ K, whereas the spins heat only up by $\Delta T_S = 15$ K.

4. Discussion

4.1. Data analysis in the two-thermal-energies-model (TTEM)

For an analytic decomposition of the observed lattice strain, we have derived the macroscopic Grueneisen constants $\Gamma_{P,S} = \frac{\alpha_{P,S}(T)\,K_{Gd}}{C_{P,S}(T)}$ in figure 2(d). K_{Gd} is the effective elastic constant of Gd, which depends only weakly on the temperature. The laser-induced change of the energy densities $\rho^Q_{P,S}$ generates the stresses $\sigma_{P,S} = \Gamma_{P,S}\rho^Q_{P,S}$ which superimpose to yield the proportional strain:

$$\varepsilon_{Gd} = \frac{\sigma_P + \sigma_S}{K_{Gd}} = \frac{1}{K_{Gd}}(\Gamma_P\rho^Q_P + \Gamma_S\rho^Q_S). \qquad (2)$$

We have measured $\varepsilon_{Gd}(t)$ and know the parameters $\Gamma_{S,P}$ and K_{Gd} [30]. In order to find the values of ρ^Q_S and ρ^Q_S we use $\rho^Q_{Gd}(t) = \rho^Q_P(t) + \rho^Q_S(t)$. We get $\rho^Q_{Gd}(0\,\text{ps})$ from the absorbed laser fluence, which we have calibrated carefully by measuring the transient thermal expansion of materials that have only conventional heat expansion, e.g. 100 nm Dy with a 10 nm Y layer. At room temperature Dy has no spin contribution to the thermal expansion, since the phase transition temperature $T_N = 180$ K is far below room temperature. In the current setup, it was not possible to conduct the UXRD experiment on Gd at a base temperature of 500 K. In that case it would have been possible to calibrate the deposited energy from the transient expansion of Gd at high temperatures by comparison to the static expansion as it was done for Dy [18]. For the present paper we also assume that the temperature induced change of the optical constants of Y/Gd is very similar to Y/Dy. Since for $T_i = 322$ K the energy is essentially fed into the phonon system, we take the observed dynamics also as an estimate for the phonon cooling at lower T_i.

Figure 6 summarizes the results of the analytic decomposition. Figure 6(a) shows the energy densities in the spin and phonon systems. For $T_i = 267$ K as much as 30% of the deposited energy enters the spin system. The phonon system cools faster than the spins, and already after 200 ps less than 50% of the energy resides in the phonons. For $T_i = 322$ K the contribution of the spin system starts with less than 10%. The transport of heat and the interconversion of energy between subsystems should be governed by the temperature, which is plotted in figure 6(b). The spin-temperature increase is reduced at temperatures just below T_c. This in part explains why the cooling of the spins for $T_i = 267$ K and 282 K is slowed down. For higher initial temperature, the fraction of energy initially deposited in the spin system is reduced (see figure 5), and the specific heat increases near the phase transition. Both facts

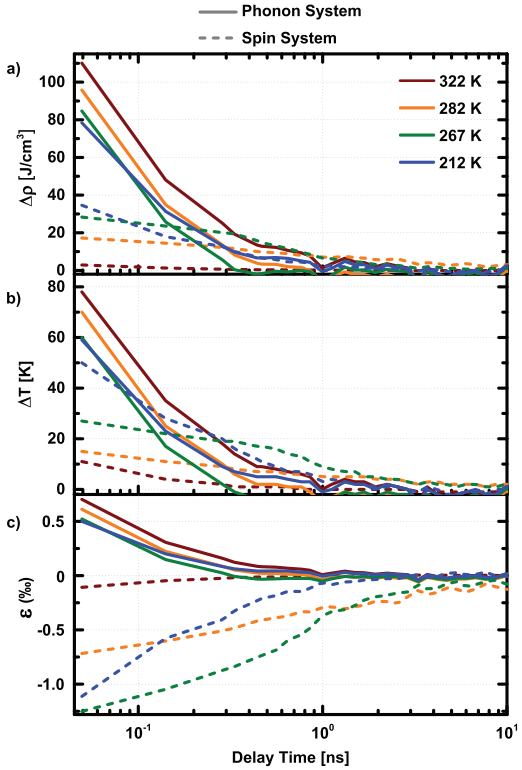

Figure 6. Result of the data analysis for selected initial temperatures. Solid and dashed lines represent the results for phonon and spin systems, respectively. (a) Transient energy density, (b) temperature change and (c) transient strain.

reduce the change of the spin temperature ΔT_S and hence it takes a longer time until the phonon temperature T_P has cooled below T_S. The main reason for the reduced energy deposition in the spin system is the decreasing spin contribution of the specific heat above T_C. Although this contribution diverges at T_C, the integral over a finite ΔT is finite and decreases when the effective end-temperature is above T_C. The phonon contribution is approximately constant in the relevant temperature range, and hence the fraction of energy exciting the phonon system increases. In the limit of very high temperatures, the ρ^Q_S must converge to zero, and 100% of the energy remain in the electron-lattice system.

4.2. Comparison of the results to recent literature

In the results for all initial temperatures $T_i < T_C$ below the phase transition, we observe the phonon system is initially heated more than the spin system. Not only is the contribution to the energy density higher ($\rho^Q_P > \rho^Q_S$, see figure 6(a), but also the temperature rise $\Delta T_P > \Delta T_S$ (see figure 6(b). The phonon system cools faster than the spin system, i.e. after a time t_{eq}, they reach equal temperatures ($\Delta T_P = \Delta T_S$), after several hundreds of picoseconds. However, the phonon system keeps cooling faster and therefore the temperature rise is inverted ($\Delta T_P < \Delta T_S$). This inversion of the temperatures observed for

all transients below T_C shows that the spin system is decoupled from the electron-phonon system on the 100 ps—1 ns timescale, although the initial transfer of energy from electrons to phonons and spins is very rapid. Note that t_{eq} is smaller for low temperatures and the inversion is more pronounced towards the phase transition. Probably fluctuations at the phase transition reduce the efficient loss of spin energy, because this at the same time requires a decreasing spin-entropy, when the spins reorder. The persistence of the spin-excitations is much more pronounced in dysprosium, where the spin reordering has been observed to take several tens of nanoseconds [18, 31]. We believe that the ordered spin system around the laser-heated spot dictates a direction along which the spins reorder in the ferromagnetic gadolinium, whereas the cooling in antiferromagnetic dysprosium lacks a preferential direction for establishing order. For a precise comparison to the ultrafast demagnetization experiments of Gd [9, 11, 32], additional measurements at the same sample temperature around 100 K would be helpful. However, in the UXRD experiments at the lowest temperature of 212 K measured in our study, the phonon temperature increase decays to half of its value within 120 ps and the spin temperature rise requires about 200 ps to decay to its half value. Taking into account the larger thermal conductivity at 100 K, the results are consistent with relaxation times of about 80 ps reported in the literature [9, 11, 32].

We emphasize that qualitatively our main conclusion can be directly drawn from the data for $T_i = 292$ K in figure 3. We start just below the phase transition, and initially the phonon driven expansion dominates the signal, whereas after about 150 ps the persistent spin excitations yield the contraction. If both systems would dissipate energy at the same rate, such a sign change of the strain should not be observed. These results clearly call for a microscopic simulation of the heat transport, which takes into account the interconversion of heat between electron-, phonon-, and spin-degrees of freedom. From a macroscopic point of view it is somewhat puzzling, that the the electrons contribute about one half of the thermal conductivity [33, 34] although they contribute only a tiny fraction to the specific heat. Our observation that the heat is transported more slowly through Dy at low temperatures is consistent with the thermal conductivity, which is reduced near the phase transition [34]. This reduction is related to increasing scattering of phonons and electrons from magnetic excitations or to changes of the band structure near the Fermi surface [35] and to the loss of RKKY interaction due to the spin disorder.

5. Conclusion

We derived the nearly temperature-independent Grueneisen coefficients of the spin- and phonon systems in the temperature range between 212 K and 322 K, $\Gamma_S \approx -1.54$ and $\Gamma_P = 0.26$ from literature values of the strongly temperature dependent specific heat C_{Gd} and the thermal expansion coefficient α_{Gd} measured in the thin film.

By analytically separating the phonon- and spin-contributions ($\rho^Q_{S,P}$) to the measured transient signal, we find that the fraction of energy deposited in the spin system decreases from 31% at 212 K to about 11% around T_c. The analysis is robust, because the measured strain ε depends linearly on both energy densities ρ^Q_S and ρ^Q_P. Even above T_c, in the absence of long-range ferromagnetic order, there is a considerable negative contribution of the spin excitations to the static and transient strain. Although the optical excitation of the valence electrons rapidly couples the energy into the phonon and spin system within few ps, the cooling and reordering of the spin system is much slower than the cooling of the phonon system.

We expect that this study triggers additional work on the experimental and theoretical level, in order to obtain a full understanding of the coupling mechanisms and the heat transport pathways in non-equilibrium situations, which are regularly met in ultrafast magnetic switching experiments.

Acknowledgment

We are grateful to financial support by the BMBF and the Helmholtz Virtual Institute *Dynamic Pathways in Multidimensional Landscapes*.

References

[1] Jensen J and Mackintosh A R 1991 *Rare Earth Magnetism—Structures and Excitations* (Oxford: Clarendon)
[2] Griffel M, Skochdopole R E and Spedding F H 1954 *Phys. Rev.* **93** 657
[3] Darnell F 1963 *Phys. Rev.* **130** 1825
[4] Pytte E 1965 *Ann. Phys., NY* **32** 377
[5] Lord A 1967 *J. Phys. Chem. Solids* **28** 517
[6] Bovensiepen U 2007 *J. Phys.: Condens. Matter* **19** 083201
[7] Stanciu C *et al* 2007 *Phys. Rev. Lett.* **98** 207401
[8] Radu I *et al* 2011 *Nature* **472** 205
[9] Carley R, Döbrich K, Frietsch B, Gahl C, Teichmann M, Schwarzkopf O, Wernet P and Weinelt M 2012 *Phys. Rev. Lett.* **109** 0574012
[10] Andres B, Christ M, Gahl C, Wietstruk M, Weinelt M and Kirschner J 2015 *Phys. Rev. Lett.* **115** 207404
[11] Frietsch B, Bowlan J, Carley R, Teichmann M, Wienholdt S, Hinzke D, Nowak U, Carva K, Oppeneer P and Weinelt M 2015 *Nat. Commun.* **6** 8262
[12] Hübner W and Bennemann K H 1996 *Phys. Rev.* B **53** 3422
[13] Melnikov A, Prima-Garcia H, Lisowski M, Gießel T, Weber R, Schmidt R, Gahl C, Bulgakova N M, Bovensiepen U and Weinelt M 2008 *Phys. Rev. Lett.* **100** 107202
[14] Wietstruk M, Melnikov A, Stamm C, Kachel T, Pontius N, Sultan M, Gahl C, Weinelt M, Dürr H A and Bovensiepen U 2011 *Phys. Rev. Lett.* **106** 127401
[15] Albisetti E *et al* 2016 *Nat. Nanotechnol.* **11** 545–51
[16] Lambert C H *et al* 2014 *Science* **345** 1337
[17] Koopmans B, Malinowski G, Dalla Longa F, Steiauf D, Fähnle M, Roth T, Cinchetti C and Aeschlimann M 2010 *Nat. Mater.* **9** 259
[18] von Reppert A, Pudell J, Koc A, Reinhardt M, Leitenberger W, Dumesnil K, Zamponi F and Bargheer M 2016 *Struct. Dyn.* **3** 054302
[19] Zakeri K, Peixoto T, Zhang Y, Prokop J and Kirschner J 2011 *Surf. Sci.* **604** L1
[20] Schick D, Herzog M, Bojahr A, Leitenberger W, Hertwig A, Shayduk R and Bargheer M 2014 *Struct. Dyn.* **1**
[21] Navirian H A, Schick D, Gaal P, Leitenberger W, Shayduk R and Bargheer M 2014 *Appl. Phys. Lett.* **104** 021906

[22] Reinhardt M, Koc A, Leitenberger W, Gaal P and Bargheer M 2016 *J. Synchrotron Radiat.* **23** 474
[23] Schick D, Shayduk R, Bojahr A, Herzog M, von Korff Schmising C, Gaal P and Bargheer M 2013 *J. Appl. Crystallogr.* **46** 1372
[24] Nicoul M, Shymanovich U, Tarasevitch A, von der Linde D and Sokolowski-Tinten K 2011 *Appl. Phys. Lett.* **98** 191902
[25] Nie S, Wang X, Park H, Clinite R and Cao J 2006 *Phys. Rev. Lett.* **96** 025901
[26] Jennings L D, Miller R E and Spedding F H 1960 *J.Chem. Phys.* **33** 1849
[27] Gerstein B C, Taylor W A, Shickell W D and Spedding F H 1969 *J.Chem. Phys.* **51** 2924
[28] Ventura G and Perfetti M 2014 *Thermal Properties of Solids at Room and Cryogenic Temperatures* (Netherlands: Springer)
[29] Barson F, Legvold S and Spedding F 1957 *Phys. Rev.* **105** 418
[30] Palmer S B, Lee E W and Islam M N 1974 *Proc. R. Soc. A* 338 341
[31] Koc A, Reinhardt M, von Reppert A, Leitenberger W, Dumesnil K, Gaal P, Zamponi F and Bargheer M 2017 (arXiv: 1701.05918)
[32] Sultan M, Melnikov A and Bovensiepen U 2011 *Phys. Status Solidi* B **248** 2323
[33] Nigh H E, Legvold S and Spedding F H 1963 *Phys. Rev.* **132** 1092
[34] Nellis W J and Legvold S 1969 *Phys. Rev.* **180** 581
[35] Döbrich K M, Bostwick A, Rotenberg E and Kaindl G 2010 *Phys. Rev.* B **81** 012401

Article XI

Ultrafast negative thermal expansion driven by spin disorder

Jan Pudell, Alexander von Reppert, Daniel Schick, Flavio Zamponi, Matthias Rössle, Marc Herzog, Hartmut Zabel, and Matias Bargheer

Physical Review B 99, 094304 (2019)

We measure the transient strain profile in a nanoscale multilayer system composed of yttrium, holmium, and niobium after laser excitation using ultrafast x-ray diffraction. The strain propagation through each layer is determined by transient changes in the material-specific Bragg angles. We experimentally derive the exponentially decreasing stress profile driving the strain wave and show that it closely matches the optical penetration depth. Below the Néel temperature of Ho, the optical excitation triggers negative thermal expansion, which is induced by a quasi-instantaneous contractive stress and a second contractive stress contribution increasing on a 12-ps timescale. These two timescales were recently measured for the spin disordering in Ho [Rettig et al., Phys. Rev. Lett. 116, 257202 (2016)]. As a consequence, we observe an unconventional bipolar strain pulse with an inverted sign traveling through the heterostructure.

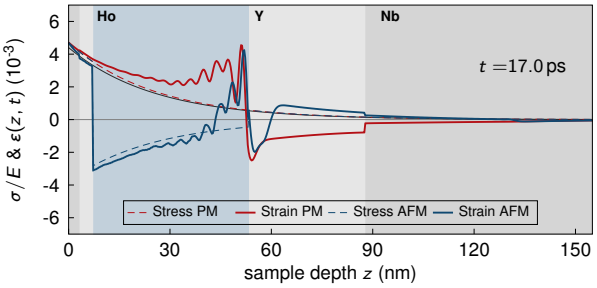

PHYSICAL REVIEW B **99**, 094304 (2019)

Ultrafast negative thermal expansion driven by spin disorder

J. Pudell,[1] A. von Reppert,[1] D. Schick,[2,3] F. Zamponi,[1] M. Rössle,[1,3] M. Herzog,[1] H. Zabel,[4] and M. Bargheer[1,3,*]

[1]*Institut für Physik und Astronomie, Universität Potsdam, Karl-Liebknecht-Strasse 24-25, 14476 Potsdam, Germany*

[2]*Max-Born-Institut Berlin, Max-Born-Straße 2a, 12489 Berlin, Germany*

[3]*Helmholtz Zentrum Berlin, Albert-Einstein-Strasse 15, 12489 Berlin, Germany*

[4]*Fakultät für Physik und Astronomie, Ruhr-Universität Bochum, 44780 Bochum, Germany*

(Received 27 July 2018; revised manuscript received 15 February 2019; published 11 March 2019)

We measure the transient strain profile in a nanoscale multilayer system composed of yttrium, holmium, and niobium after laser excitation using ultrafast x-ray diffraction. The strain propagation through each layer is determined by transient changes in the material-specific Bragg angles. We experimentally derive the exponentially decreasing stress profile driving the strain wave and show that it closely matches the optical penetration depth. Below the Néel temperature of Ho, the optical excitation triggers negative thermal expansion, which is induced by a quasi-instantaneous contractive stress and a second contractive stress contribution increasing on a 12-ps timescale. These two timescales were recently measured for the spin disordering in Ho [Rettig *et al.*, Phys. Rev. Lett. **116**, 257202 (2016)]. As a consequence, we observe an unconventional bipolar strain pulse with an inverted sign traveling through the heterostructure.

DOI: 10.1103/PhysRevB.99.094304

I. INTRODUCTION

In most of the research on ultrafast magnetism the lattice was considered only as an angular momentum sink [1–3]. Ultrafast effects on the lattice induced by demagnetization have been discussed surprisingly rarely [4–7]. Time-resolved magneto-optical Kerr measurements and optical picosecond ultrasonics are the workhorse for many researchers [1,2,8–12]. Ultrafast electron diffraction (UED) or ultrafast x-ray diffraction (UXRD) experiments that directly observe the transient lattice strain induced by ultrafast demagnetization have been discussed only sporadically [4,5,13–15]. Several ultrafast diffraction studies on the transition metals Ni and Fe [16–18] discuss the strain waves excited by electron and phonon stresses σ_e and σ_{ph}, and theory predicts relevant electron-phonon (*e*-ph) coupling constants [19] even with mode specificity [20]. Very recently, granular FePt films were studied by UXRD [21] and UED [5]. The rapid out-of-plane lattice contraction could be convincingly ascribed to changes in the tetragonality of the lattice by *ab initio* calculations of the total ground-state energy for the spin system in the paramagnetic and ferromagnetic phases [5]. To simulate the dynamic changes in a system with several degrees of freedom it is common to apply multiple-temperature models [5,9] which assume that each subsystem can be described by an individual temperature T_i, although it has been shown that different phonon modes may be out of thermal equilibrium for 100 ps [20]. Specialized techniques allow for assigning timescales to specific electronic processes and orbitals or bands [3,22–25]. This is particularly relevant in the magnetic rare earths, where the exchange interaction between the localized $4f$ spin and orbital magnetic moments is mediated by the itinerant $5d6s$ conduction electrons via the Ruderman–Kittel–Kasuya–Yosida (RKKY) interaction [26,27]. In antiferromagnetically ordered phases the question of angular momentum transfer is less relevant since the net magnetization is zero. Rare-earth elements prove to be a versatile testing ground for understanding how rapidly ultrafast demagnetization leads to stress in the crystal lattice. We selected Ho since a recent resonant hard x-ray scattering experiment measured that the demagnetization of both the localized $4f$ moments and the itinerant conduction electrons proceed on a fast 200-fs timescale attributed to electron-spin interaction and a slow 9-ps timescale for coupling phonons to the spins [22].

In this paper we use UXRD at a laser-based femtosecond plasma x-ray source (PXS) to show that the ultrafast laser excitation of Ho below its Néel temperature $T_N = 132\,\mathrm{K}$ generates negative stress that rises on the two timescales for disordering the spin system [22] and drives bipolar strain wave packets with an inverted sign compared to common materials without negative thermal expansion (NTE) [8,28]. We use the material specificity of UXRD to cross-check the individual lattice constant changes in this metallic multilayer system, which is opaque to optical probes.

In the paramagnetic (PM) phase of Ho, the analysis is simplified by the complete spin disorder, and we show that the spatial excitation profile of the driving stress can be derived by probing the bipolar strain pulse in the adjacent Y and Nb buffer layers. The spatial stress profile is approximately given by the penetration depth of the pump pulses. The UXRD experiment in the antiferromagnetic (AFM) phase reveals an instantaneous compensation of the expansive electron and phonon stress in Ho by the negative instantaneous stress component $\sigma_{sp,0}$ due to spin disorder. In addition to this subpicosecond negative-stress component, the negative stress $\sigma_{sp}(t)$ keeps rising on a 12-ps timescale. These negative-stress

*bargheer@uni-potsdam.de; http://www.udkm.physik.uni-potsdam.de

components in Ho are evidenced in the adjacent Y and Nb by the extended leading expansive edge of the propagating bipolar strain pulse, which has an opposite sign compared to excitation of Ho in the PM phase. Thus, we observe dynamic stress rising on the two timescales on which disordering of the spin helix was observed by resonant x-ray scattering [22]. However, we emphasize that the observed lattice contraction in Ho is about 20 times larger than the peak shift of the magnetic Bragg peak that was observed for very similar fluence [22] because it, in fact, measures the period of spin helix which is incommensurate with the lattice.

In a broader context, our observation of ultrafast lattice contraction in Ho is discussed as an example of a rapid entropy-driven manifestation of the NTE phenomenon, which may occur on different timescales in various materials ranging from nonmagnetic molecular nanocrystals [29] and oxides with open oxygen frameworks [30] to ferroelectrics [31] and magnetically ordered systems like Heusler alloys [32].

II. SPIN-GRÜNEISEN CONSTANT AND NTE

In laser-excited magnetic systems, the role of a nonequilibrium within and/or among the different subsystems is heavily debated. The prevalent basis of the discussions is multiple-temperature models. In thermal equilibrium, standard thermodynamic approaches emphasize the role of the entropy S by calculating the equilibrium lattice constants from the minimum of the Gibbs free energy $G = U + pV - TS$ [33,34]. For a discussion of lattice dynamics, where the change in volume V is driven by a pressure p or, for an anisotropic case, the strain ε is driven by a stress σ, we can circumvent the discussion of a (non)equilibrium temperature by considering the energy density ρ^Q.

It is common to evoke the macroscopic Grüneisen coefficients (GCs) $\Gamma_{\mathrm{e,ph}}$ for phonons and electrons, which describe the efficiency of generating stress $\sigma_{\mathrm{e,ph}} = \Gamma_{\mathrm{e,ph}}\rho^Q_{\mathrm{e,ph}}$ by a heat energy density $\rho^Q_{\mathrm{e,ph}}$ [34]. If $\Gamma_{\mathrm{e}} \neq \Gamma_{\mathrm{ph}}$, ultrafast diffraction allows inferring the time-dependent $\sigma(t)$ from the observed transient strain $\varepsilon(t)$ [16,17,35]. Hooke's law relates ε linearly to σ and hence to the energy densities $\rho^Q_{\mathrm{e,ph}}$ deposited in each subsystem. The Grüneisen concept was extended to stress resulting from spin excitations in Ni and Fe [33,36], but the experimental verification remained ambiguous [16–18]. Thermodynamic analysis affirms that the GCs generally measure how entropy S depends on strain ε [37]. While for a gas of phonons or electrons the entropy usually increases with the volume, the phenomenon of NTE generally occurs when the entropy S decreases upon expansion, i.e., $\partial S/\partial\varepsilon < 0$. There are various origins of NTE [33,34]; however, for spin-ordered phases of rare earths, the NTE along the c axis of the hexagonal lattice is very large and clearly associated with the energy density ρ^Q_{sp} of the spin system. Figure 1(a) shows the three contributions $C_{\mathrm{e,ph,sp}}(T)$ to the specific heat [38,39]. The negligible contribution of the electron system is barely visible as a gray area below the red shaded phonon contribution. The blue shaded spin contribution is very large for all temperatures below T_{N}, and close to the second-order phase transition to the PM phase it is even larger than the phonon contribution. Figure 1(b) indicates the change in the c-axis lattice constant, which is negative, when the spin contribution

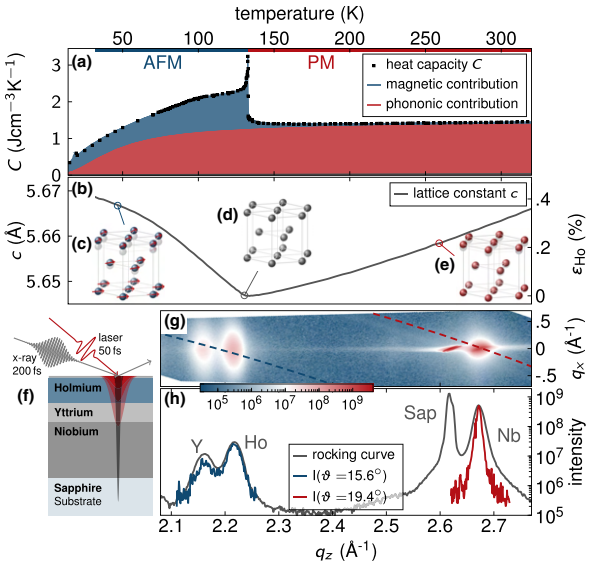

FIG. 1. (a) Specific heat of Ho [38,39] separated into the three contributions $C_{\mathrm{e,ph,sp}}(T)$, where the electron contribution $C_{\mathrm{e}}(T)$ is hardly visible and the spin contribution C_{sp} even exceeds the phonon contribution C_{ph} at some temperatures. (b) c axis of the Ho thin film as a function of temperature, showing large NTE below $T_{\mathrm{N}} = 132$ K. (c)–(e) Schematics of the hexagonal lattice illustrating the c-axis lattice change and the helical spin order below T_{N}. (f) Schematic of the layer stacking and the pump-probe geometry. (g) The RSM including separated Bragg peaks of Y, Ho, sapphire, and Nb. The slices of the RSM used for (h) and the time-resolved measurements are shown in red (Nb) and blue (Ho+Y). (h) The projection of the full RSM (gray) and measurements along the slices with a fixed angle ω (red and blue).

to the specific heat is large. Surprisingly, also in these systems exhibiting a divergent specific heat at the phase transition, the spin GC Γ_{sp} is essentially independent of T [13,14], even though the total GC [37] varies strongly with T. Separating phonon and spin contributions to the thermal expansion and the heat capacity of Ho yields $\Gamma_{\mathrm{ph}}/\Gamma_{\mathrm{sp}} \approx -0.2$ [33,37]. This implies that equal energy densities in the spin and phonon system lead to a five times larger contractive stress, which overwhelms the expansive phonon stress. The separate GC $\Gamma_{\mathrm{e,ph,sp}}$ are independent of T because the T dependences of the specific heat $C_{\mathrm{e,ph,sp}}(T)$ and the thermal expansion coefficient $\alpha_{\mathrm{e,ph,sp}}(T)$, which originate from the quantum nature of the excitations, cancel out [33,34]. This linear dependence of energy density and stress in each subsystem makes the Grüneisen concept useful and causes temperature and thermal equilibrium within each subsystem to be properties of secondary relevance to the dynamics. Nonetheless, the temperature-dependent specific heats $C_{\mathrm{e,ph,sp}}(T)$ map the multiple-thermal energy model onto classical multiple-temperature models.

III. EXPERIMENTAL DETAILS

The multilayer stack was grown by molecular beam epitaxy on sapphire in the sequence 128 nm Nb, 34 nm Y,

46 nm Ho with a thin capping layer of 4 nm Y and 3 nm Nb [see Fig. 1(f)]. X-ray reflectivity measurements confirm the total thickness of the metallic multilayer on the sapphire substrate; 200-fs hard x-ray probe pulses with a photon energy of 8 keV are derived from the PXS at the University of Potsdam [40]. The *p*-polarized 50-fs laser pulses with a diameter of 1500 μm (FWHM) excite the sample at an incidence angle of about 52°. The incident fluence of the 800-nm pump pulses is 3 mJ/cm^2; an absorbed fluence of 1.7 mJ/cm^2 is calculated according to the refractive index obtained by spectroscopic ellipsometry. The penetration depth is 21 nm at 800 nm for all temperatures. A schematic of the sample and the pump-probe geometry is given in Fig. 1(f).

The reciprocal space map (RSM) of the multilayer system including separated Bragg peaks of Y, Ho, sapphire, and Nb at room temperature is shown in Fig. 1(g). The map is obtained by recording the symmetrically and asymmetrically diffracted x rays on the area pixel detector (Dectris PILATUS 100K) as a function of the "rocking" angle ω between the sample surface and the center of the convergent femtosecond x-ray beam [40]. The gray line in Fig. 1(h) shows a projection of the full RSM onto the out-of-plane component q_z. The red and blue lines indicate typical x-ray diffraction curves derived from the dashed cuts through reciprocal space indicated by the red and blue lines in Fig. 1(g). These cuts are given by the x rays' angle of incidence ω chosen for the UXRD experiments. The center position of the Bragg reflection is obtained by fitting a Gaussian function to each layer peak.

IV. RESULTS

Figure 2 summarizes the strain in all three layers for the PM phase of Ho (red) and in the helical AFM phase of Ho around 40 K (blue). The individual data points were obtained by fitting a Gaussian function to each layer peak. In the PM phase two characteristic times are identified from the UXRD data: At $t = 17$ ps, Ho has reached the maximum expansion. This indicates the time it takes the expansive sound to travel from the surface to the Y interface. At this time the leading compressive part of the bipolar strain wave packet [8,28] has fully propagated from the Ho into the Y layer, as evidenced by the pronounced minimum in the Y strain (see Fig. 3 for an illustration of the strain wave). At $t = 26$ ps the zero crossing of the bipolar strain wave packet traverses the Y/Nb interface, which yields the pronounced minimum in the Nb strain. These characteristic time points yield the layer thicknesses given above.

The UXRD data recorded in the AFM phase of Ho directly show a delay of the contractive strain in Ho [Fig. 2(a), blue line]. The minimum of the Ho strain at about 23 ps is delayed by about 6 ps compared to the maximum in the PM phase. The signal in Y [Fig. 2(b)] confirms that also the propagating bipolar strain wave packet has a reversed sign of the strain amplitude at low temperature and a delay of about 6 ps. In the PM phase, the leading compressive part of the strain launched in Ho by thermal expansion reduces the out-of-plane lattice spacing in Y, although the Y layer is also excited by the pump pulse [28]. In the AFM phase the contractive stress in Ho dominates and reverses the sign of the bipolar

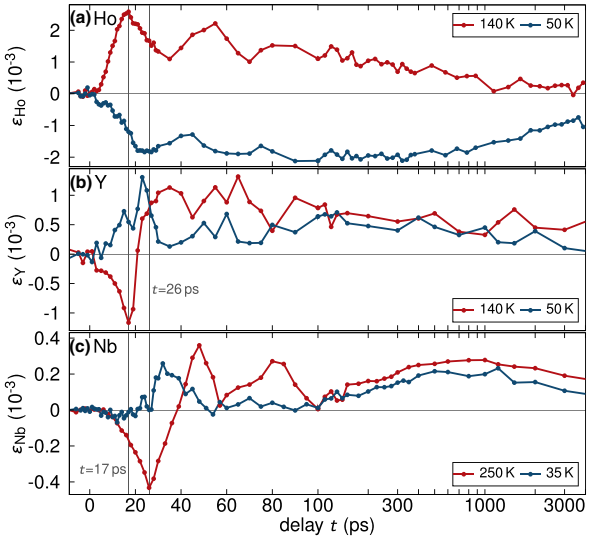

FIG. 2. Transient lattice strain ε for (a) Ho, (b) Y, and (c) Nb after laser excitation in the PM (red) and AFM (blue) phases as determined from UXRD. The thin solid line at 17 ps indicates the time it takes the maximum expansion starting at the surface to propagate to the Ho/Y interface. At this time Ho is maximally expanded, and Y is fully compressed since the expansive part of the bipolar strain is fully in the Ho layer, whereas the leading compressive part is only in the Y layer. The thin line at 26 ps indicates the same fully compressed situation for the Nb layer. In the AFM phase Ho [in (a)] has a 6-ps delay of the maximal contraction compared to the maximal PM expansion.

strain. Hence, the Ho contraction expands the adjacent Y, assisted by the small expansive stress from direct optical excitation of Y. The UXRD signal from the Nb layer is even cleaner, as a negligible amount of light is absorbed in this layer. Therefore, we repeated the experiments on Nb. The obtained signal [Fig. 2(c)] had to be scaled appropriately due to the slightly different base temperature and fluence. The tiny negative lattice constant change in Nb [Fig. 2(c)] in the first 15 ps is due to the stress generated in Y, and the crossover to the strong expansion starts around 10 ps, when the leading expansive part of the bipolar strain wave packet generated by the exponentially decaying compressive stress in Ho reaches the Nb layer. The very short wiggle of the average Nb layer strain at 26 ps heralds the rather strong but spatially narrow bipolar strain wave packet launched by the 7-nm-thick Nb/Y capping layer. The time perfectly coincides with the arrival of the wave created by surface expansion that was already observed in the PM phase. The same feature from the capping layer is also clearly observed in the Y data at 19 ps. In the PM data set, this feature is absent since the cap layer and the Ho layer both expand with similar amplitude.

For $t > 200$ ps the sound wave reflections have ceased, and we can safely interpret the expansion and contraction of each layer by the average energy densities $\rho_{e,ph,s}$. For earlier time delays, the spatially averaged thermal stress in each layer can be obtained from the data by averaging out the oscillations. For timescales shorter than the characteristic

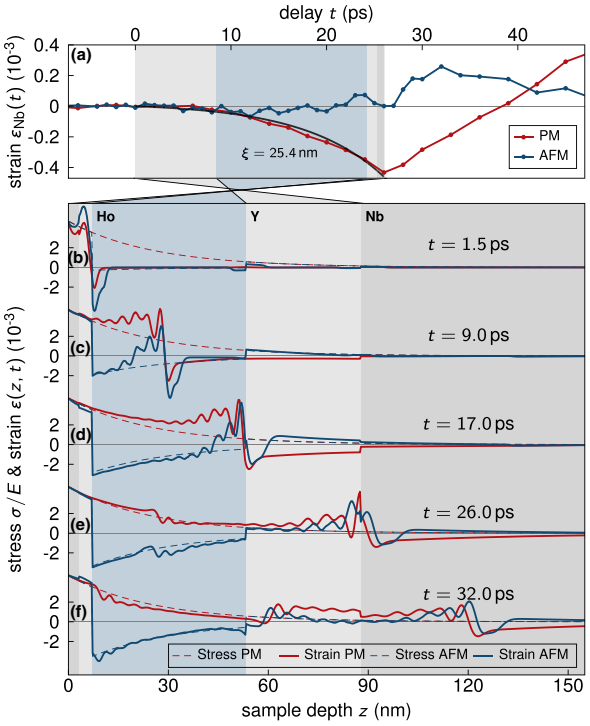

FIG. 3. (a) Zoom of the first 45 ps of the Nb data from Fig. 2(c). The black line shows an exponential fit to the strain in the PM phase, which is used to extract the driving stress via Hooke's law. (b)–(f) Stress (dashed) and strain profiles for selected delays in the heterostructure from a simulation. To avoid unimportant rapid oscillations in this graph, the temporal stress profile was smoothed by a 0.5-ps Gaussian function. The NTE stress in Ho rises with $\tau = 12$ ps. The inverted strain profile is most prominently seen in (c) and (d) in the Y and Nb layers, respectively. As an illustration, a video sequence of this temporal evolution of the stress profile and the strain wave is given in the Supplemental Material [41].

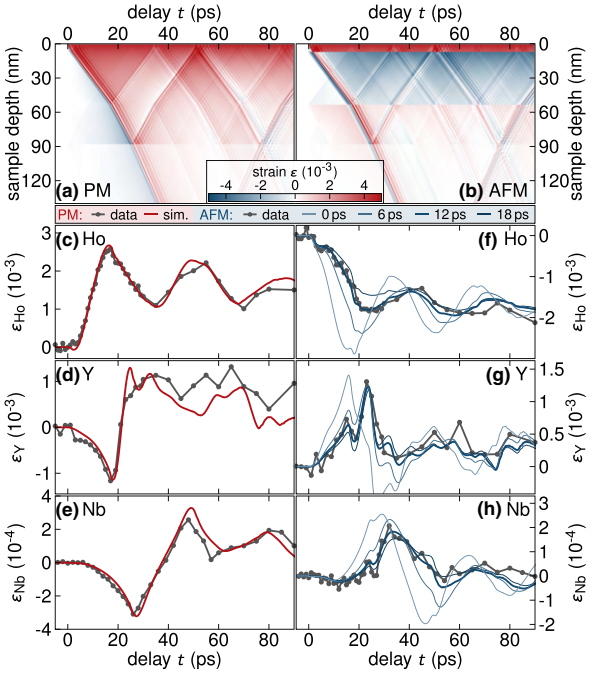

FIG. 4. The simulated spatiotemporal strain profiles show the traveling sound waves in the heterostructure in the (a) PM and (b) AFM phases. (c)–(e) Simulated strain for the PM phase in the three layers (red) is compared to the data. (f)–(h) Simulations for the AFM phase with varying time constant $\tau = 0$, 6, 12, and 18 ps. The best match to the data is obtained for $\tau = 12$ ps.

oscillation period of the layer, however, the transient stress must be obtained from modeling the elastic response of the system. The measured transient (negative) thermal expansion $\varepsilon(t) = \varepsilon_{th}(t) + \varepsilon_{sw}(t)$ is a linear superposition of the averaged thermal strain $\varepsilon_{th}(t)$ and the layer-averaged amplitude of the hypersound waves $\varepsilon_{sw}(t)$ triggered by the rapid expansion following the ultrashort pulse excitation, which reflect from the interfaces.

V. ANALYSIS

In this section we highlight the potential of UXRD for deriving the spatial form of the stress driving the observed strain [42,43]. In Fig. 3(a) we analyze the UXRD data recorded for the Nb layer in the PM state of Ho, zooming in on the pronounced compression signal of the Nb layer. The average strain ε_{Nb} shows an increasing compression slowly starting at $t = 0$ when the bipolar strain wave packet starts entering the Nb layer. Neglecting sound velocity differences in the heterostructure, an exponential spatial stress profile generates a bipolar strain pulse with a compressive leading edge that has an exponential spatial dependence as well [28].

Thus, from the measured strain in a dedicated detection layer, we can show that the spatial stress profile in fact decays exponentially with the characteristic length scale $\xi = 25$ nm which matches the value calculated from the optical constants measured by ellipsometry. For direct comparison with the data we plotted in Fig. 3(a) the stress $\sigma_{PM} = \sigma_0 e^{-z/\xi}$ onto the measured strain data using an appropriate scaling by Hooke's law. In the AFM phase (blue) the spin and phonon stress contributions approximately cancel out immediately after excitation. In Figs. 3(b)–3(f) we show the spatial stress profiles used in the further analysis of the data via simulations as dashed lines.

VI. MODELING AND DISCUSSION

Now we discuss the numerical modeling of the observed strain that is necessary to derive the transient stress changing faster than the characteristic thickness modulation time of the layers. In the PM phase of Ho we calculate the transient strain [Fig. 4(a)] by integrating the equation of motion for a linear masses-and-springs model using the UDKM1DSIM toolbox [44]. The experimentally derived exponential spatial form of the stress σ_{PM} serves as an input. Figures 4(c)–4(e) show the excellent agreement of the simulations with the measured data for all three layers in the PM phase when

using the exponentially decaying stress profile $\xi = 25$ nm derived above. For simplicity, we assume an instantaneous rise of the combined *e*-ph stress. Separate electron and phonon GCs do not improve the fit in Figs. 4(c)–4(e). We note that the energy density in each subsystem is linearly proportional to the stress and strain in each layer. The spatiotemporal strain shown in Fig. 4(a) is used as input parameter for the calculation of the x-ray diffraction pattern by dynamical x-ray diffraction theory. The positions of the simulated Bragg peaks are obtained by fitting a Gaussian function as done in the experimental data analysis. For illustration, Figs. 3(b)–3(f) depict the spatial strain profiles for selected time delays, which are cross sections of the spatiotemporal strain profiles in Figs. 4(a) and 4(b), leading to the fits in Fig. 4(c)–4(h). Figures 3(b)–3(f) contain the transient spatial stress profiles (dashed lines) used as input for the simulation. After about 30 ps [Figs. 3(e) and 3(f)] the simulated strain profile is very close to the simple stress-strain relation, with only a slight deviation due to residual hypersound waves. The observed signal oscillations (Fig. 4) due to hypersound waves reflected at the interfaces of all three layers are reproduced by the model.

To simulate the corresponding spatiotemporal strain [Fig. 4(b)] when Ho is excited in the AFM phase, we have to take into account the negative stress induced by spin disorder, which adds to the positive *e*-ph stress; the dynamics become richer and challenge the modeling. We model the transient stress $\sigma = \Gamma_{\text{e-ph}}\rho^{Q}_{\text{e-ph}} + \Gamma_{\text{sp}}\rho^{Q}_{\text{sp}}$ [Figs. 3(b)–3(f)] from the balance of thermal energy densities in the combined *e*-ph system $\rho^{Q}_{\text{e-ph}}$ and in the spin system ρ^{Q}_{s}:

$$\rho^{Q}_{\text{e-ph}}(t) = \rho^{Q}_{\text{e-ph},\infty} + \rho^{Q}_{\text{dyn}} e^{-t/\tau}, \tag{1}$$

$$\rho^{Q}_{\text{sp}}(t) = \rho^{Q}_{\text{sp},0} + \rho^{Q}_{\text{dyn}}(1 - e^{-t/\tau}), \tag{2}$$

$$\rho^{Q}_{\text{laser}} = \rho^{Q}_{\text{e-ph},\infty} + \rho^{Q}_{\text{sp},0} + \rho^{Q}_{\text{dyn}}. \tag{3}$$

In the first 70 ps in Figs. 4(f)–4(h), we may disregard heat transport and assume local conversion of energy $\rho^{Q}_{\text{e-ph}}(t)$ to $\rho^{Q}_{\text{sp}}(t)$ with a coupling time τ. In this model the energy density ρ^{Q}_{laser} imparted by the laser is partially converted to the spin system quasi-instantaneously as $\rho^{Q}_{\text{sp},0}$. ρ^{Q}_{dyn} is transferred from the *e*-ph system to the spins on the timescale τ. $\rho^{Q}_{\text{e-ph},\infty}$ is the heat remaining in the *e*-ph system until heat transport starts to become relevant. The variables $Q_{\text{e-ph}}$, Q_{sp}, and Q_{dyn} have to fulfill energy conservation and approach thermal equilibrium for $t \gg \tau$. The remaining parameter is used to match the amplitude of the signal. The partitioning into only two simulated heat reservoirs is chosen because $\rho^{Q}_{\text{e-ph}}$ and ρ^{Q}_{sp} trigger competing expansive and contractive stresses, respectively. We do not attempt to separate the electron and phonon contributions because this seperation did not improve the fit with the data in the PM phase either. The essential fitting parameter is τ, which we initially assumed coincided with the slow timescale for demagnetization of $\tau_2 = 9$ ps observed by resonant x-ray scattering (RXS) [22]. The fast timescale $\tau_1 = 0.6$ ps is beyond the time resolution we can extract from the lattice dynamics of layers with a thickness on the order of 50 nm. For the modeling we assume an instantaneous coupling of heat energy into the spin system described by $\rho^{Q}_{\text{sp},0}$ in Eq. (2), which mimics τ_1 for the spin disordering observed via RXS, which is attributed to a rapid spin-flip scattering of the optically excited conduction band electrons, enabled by the strong spin-orbit interaction in Ho [22]. Figures 4(f)–4(h) show the excellent agreement achieved simultaneously in the signals from all three layers for $\tau = 12$ ps. Especially, the initial contraction of Ho and the delayed expansion of Nb are very sensitive to variations of τ, as can be seen in the thin lines depicting the simulated signal in Figs. 4(f) and 4(h)

We would like to point out that the intense bipolar strain wave packet launched by the expansion of the capping layer at low temperatures evident from Fig. 4(b) enhances our confidence in the model since it is directly observed in the signal: The short dips in the Y strain [Fig. 4(g)] at 18 ps and in the Nb strain [Fig. 4(h)] at 26 ps indicate the arrival of the narrow compressive part of the bipolar strain pulse, independent of τ. For $\tau = 0$ ps, the maximum in the Nb strain coincides with the minimum observed in the PM phase of Ho. Thus, when all the energy transferred to the spin system arrives there instantaneously, Fig. 4(h) is a nearly perfect mirror image of Fig. 4(e). The increasing delay of the maximum in Nb for increasing τ can be assigned to the delayed NTE stress induced by spin disordering. The blue line in Fig. 3(f) shows once more that the total strain essentially follows the NTE stress profile in Ho (dashed line). Variation of the spatial stress profile of the spin excitation, e.g., to a homogeneous demagnetization profile throughout the layer, has a negligible effect on the Ho signal and does not improve the agreement with the Y and Nb signals.

Finally, we would like to discuss the observation of ultrafast negative stress on the subpicosecond timescale in the context of NTE in general.

NTE requires a specific interaction, where the energy decreases with changes in the volume [33,36]. For Ho the dominant interaction is the exchange interaction J_{exc}, and it was shown earlier that the expansion coefficient $\alpha \sim \partial J_{\text{exc}}/\partial c$ scales with the strain-induced change in the exchange interaction J_{exc} [27,45]. From a statistical physics perspective, the spin entropy $S = R\ln(2J + 1)$ must be dominated by the large angular momentum J of the localized $4f$ moments. Hence, the heat energy density ρ^{Q}_{sp} associated with the spin disordering and the concomitant stress $\sigma(t) = \Gamma_{\text{sp}}\rho^{Q}_{\text{sp}}(t)$ is also mainly connected to the localized spins. On the other hand, the RKKY interaction requires the itinerant electrons to mediate the coupling. It is not self-evident if a disordering of the optically excited itinerant electrons alone would be able to explain the full magnitude of the negative stress. In the Ho system, the recent work by Rettig *et al.* [22] confirmed that both types of electrons disorder on the same timescale; however, it will be interesting to test the situation in other systems, such as Gd, where disparate timescales have been observed [46].

VII. CONCLUSION

In conclusion, we have reported that ultrafast laser-induced disordering of the spin system of Ho proceeds on two timescales and triggers NTE via ultrafast stress mediated by

the exchange interaction. On the subpicosecond timescale already nearly half of the negative stress is present, and it fully balances the expansive stress from electrons and phonons. According to the ratio of GCs $\Gamma_{\text{e-ph}}/\Gamma_{\text{sp}} = -0.2$ this balance implies that 20% of the energy absorbed in the Ho layer has excited the spin system. Within $\tau = 12$ ps, the fraction of energy in the spin system rises to 40%. If we consider the fact that for the ferromagnetic rare earth Gd, different timescales for disordering the localized and itinerant orbitals have been observed, it is not clear on which timescale the stress should occur. We believe that this study may trigger similar investigations in other systems with NTE since it is not obvious that the thermodynamic relation predicting stress $\sigma = \Gamma\rho^{Q}$ proportional to the energy density in a subsystem will hold in time-dependent nonequilibrium situations and for any origin of the negative entropy-volume relation required for NTE.

ACKNOWLEDGMENTS

We acknowledge the BMBF for the financial support via 05K16IPA and the DFG via BA 2281/8-1 and BA 2281/11-1. We would like to thank J. Podschwadek for the MBE sample preparation

[1] E. Beaurepaire, J.-C. Merle, A. Daunois, and J.-Y. Bigot, Ultrafast Spin Dynamics in Ferromagnetic Nickel, Phys. Rev. Lett. **76**, 4250 (1996).

[2] J.-Y. Bigot, M. Vomir, and E. Beaurepaire, Coherent ultrafast magnetism induced by femtosecond laser pulses, Nat. Phys. **5**, 515 (2009).

[3] C. Stamm, T. Kachel, N. Pontius, R. Mitzner, T. Quast, K. Holldack, S. Khan, C. Lupulescu, E. F. Aziz, M. Wietstruk, H. A. Dürr, and W. Eberhardt, Femtosecond modification of electron localization and transfer of angular momentum in nickel, Nat. Mater. **6**, 740 (2007).

[4] C. V. Korff Schmising, A. Harpoeth, N. Zhavoronkov, Z. Ansari, C. Aku-Leh, M. Woerner, T. Elsaesser, M. Bargheer, M. Schmidbauer, I. Vrejoiu, D. Hesse, and M. Alexe, Ultrafast magnetostriction and phonon-mediated stress in a photoexcited ferromagnet, Phys. Rev. B **78**, 060404 (2008).

[5] A. H. Reid, X. Shen, P. Maldonado, T. Chase, E. Jal, P. W. Granitzka, K. Carva, R. K. Li, J. Li, L. Wu, T. Vecchione, T. Liu, Z. Chen, D. J. Higley, N. Hartmann, R. Coffee, J. Wu, G. L. Dakovski, W. F. Schlotter, H. Ohldag, Y. K. Takahashi, V. Mehta, O. Hellwig, A. Fry, Y. Zhu, J. Cao, E. E. Fullerton, J. Stöhr, P. M. Oppeneer, X. J. Wang, and H. A. Dürr, Beyond a phenomenological description of magnetostriction, Nat. Commun. **9**, 388 (2018).

[6] G. Malinowski, F. Dalla Longa, J. H. H. Rietjens, P. V. Paluskar, R. Huijink, H. J. M. Swagten, and B. Koopmans, Control of speed and efficiency of ultrafast demagnetization by direct transfer of spin angular momentum, Nat. Phys. **4**, 855 (2008).

[7] D. Rudolf, C. La-O-Vorakiat, M. Battiato, R. Adam, J. M. Shaw, E. Turgut, P. Maldonado, S. Mathias, P. Grychtol, H. T. Nembach, T. J. Silva, M. Aeschlimann, H. C. Kapteyn, M. M. Murnane, C. M. Schneider, and P. M. Oppeneer, Ultrafast magnetization enhancement in metallic multilayers driven by superdiffusive spin current, Nat. Commun. **3**, 1037 (2012).

[8] C. Thomsen, H. T. Grahn, H. J. Maris, and J. Tauc, Surface generation and detection of phonons by picosecond light pulses, Phys. Rev. B **34**, 4129 (1986).

[9] B. Koopmans, G. Malinowski, F. Dalla Longa, D. Steiauf, M. Fähnle, T. Roth, M. Cinchetti, and M. Aeschlimann, Explaining the paradoxical diversity of ultrafast laser-induced demagnetization, Nat. Mater. **9**, 259 (2010).

[10] M. Hofherr, P. Maldonado, O. Schmitt, M. Berritta, U. Bierbrauer, S. Sadashivaiah, A. J. Schellekens, B. Koopmans, D. Steil, M. Cinchetti, B. Stadtmüller, P. M. Oppeneer, S. Mathias, and M. Aeschlimann, Speed and efficiency of femtosecond spin current injection into a nonmagnetic material, Phys. Rev. B **96**, 100403 (2017).

[11] A. V. Kimel, A. Kirilyuk, P. A. Usachev, R. V. Pisarev, A. M. Balbashov, and T. Rasing, Ultrafast non-thermal control of magnetization by instantaneous photomagnetic pulses, Nature (London) **435**, 655 (2005).

[12] J.-W. Kim, M. Vomir, and J.-Y. Bigot, Ultrafast Magnetoacoustics in Nickel Films, Phys. Rev. Lett. **109**, 166601 (2012).

[13] A. Koc, M. Reinhardt, A. von Reppert, M. Rössle, W. Leitenberger, M. Gleich, M. Weinelt, F. Zamponi, and M. Bargheer, Grueneisen-approach for the experimental determination of transient spin and phonon energies from ultrafast x-ray diffraction data: Gadolinium, J. Phys.: Condens. Matter **29**, 264001 (2017).

[14] A. von Reppert, J. Pudell, A. Koc, M. Reinhardt, W. Leitenberger, K. Dumesnil, F. Zamponi, and M. Bargheer, Persistent nonequilibrium dynamics of the thermal energies in the spin and phonon systems of an antiferromagnet, Struct. Dyn. **3**, 054302 (2016).

[15] F. Quirin, M. Vattilana, U. Shymanovich, A.-E. El-Kamhawy, A. Tarasevitch, J. Hohlfeld, D. von der Linde, and K. Sokolowski-Tinten, Structural dynamics in FeRh during a laser-induced metamagnetic phase transition, Phys. Rev. B **85**, 020103 (2012).

[16] X. Wang, S. Nie, J. Li, R. Clinite, M. Wartenbe, M. Martin, W. Liang, and J. Cao, Electronic Grüneisen parameter and thermal expansion in ferromagnetic transition metal, Appl. Phys. Lett. **92**, 121918 (2008).

[17] X. Wang, S. Nie, J. Li, R. Clinite, J. E. Clark, and J. Cao, Temperature dependence of electron-phonon thermalization and its correlation to ultrafast magnetism, Phys. Rev. B **81**, 220301 (2010).

[18] T. Henighan, M. Trigo, S. Bonetti, P. Granitzka, D. Higley, Z. Chen, M. P. Jiang, R. Kukreja, A. Gray, A. H. Reid, E. Jal, M. C. Hoffmann, M. Kozina, S. Song, M. Chollet, D. Zhu, P. F. Xu, J. Jeong, K. Carva, P. Maldonado, P. M. Oppeneer, M. G. Samant, S. S. P. Parkin, D. A. Reis, and H. A. Dürr, Generation mechanism of terahertz coherent acoustic phonons in Fe, Phys. Rev. B **93**, 220301 (2016).

[19] Z. Lin, L. V. Zhigilei, and V. Celli, Electron-phonon coupling and electron heat capacity of metals under conditions of strong electron-phonon nonequilibrium, Phys. Rev. B **77**, 075133 (2008).

[20] P. Maldonado, K. Carva, M. Flammer, and P. M. Oppeneer, Theory of out-of-equilibrium ultrafast relaxation dynamics in metals, Phys. Rev. B **96**, 174439 (2017).

[21] A. von Reppert, L. Willig, J.-E. Pudell, M. Rössle, W. Leitenberger, M. Herzog, F. Ganss, O. Hellwig, and M. Bargheer, Ultrafast laser generated strain in granular and continuous FePt thin films, Appl. Phys. Lett. **113**, 123101 (2018).

[22] L. Rettig, C. Dornes, N. Thielemann-Kühn, N. Pontius, H. Zabel, D. L. Schlagel, T. A. Lograsso, M. Chollet, A. Robert, M. Sikorski, S. Song, J. M. Glownia, C. Schüßler-Langeheine, S. L. Johnson, and U. Staub, Itinerant and Localized Magnetization Dynamics in Antiferromagnetic Ho, Phys. Rev. Lett. **116**, 257202 (2016).

[23] N. Thielemann-Kühn, D. Schick, N. Pontius, C. Trabant, R. Mitzner, K. Holldack, H. Zabel, A. Föhlisch, and C. Schüßler-Langeheine, Ultrafast and Energy-Efficient Quenching of Spin Order: Antiferromagnetism Beats Ferromagnetism, Phys. Rev. Lett. **119**, 197202 (2017).

[24] B. Pfau, S. Schaffert, L. Müller, C. Gutt, A. Al-Shemmary, F. Büttner, R. Delaunay, S. Düsterer, S. Flewett, R. Frömter, J. Geilhufe, E. Guehrs, C. M. Günther, R. Hawaldar, M. Hille, N. Jaouen, A. Kobs, K. Li, J. Mohanty, H. Redlin, W. F. Schlotter, D. Stickler, R. Treusch, B. Vodungbo, M. Kläui, H. P. Oepen, J. Lüning, G. Grübel, and S. Eisebitt, Ultrafast optical demagnetization manipulates nanoscale spin structure in domain walls, Nat. Commun. **3**, 1100 (2012).

[25] M. Doerr, M. Rotter, and A. Lindbaum, Magnetostriction in rare-earth based antiferromagnets, Adv. Phys. **54**, 1 (2005).

[26] M. A. Ruderman and C. Kittel, Indirect exchange coupling of nuclear magnetic moments by conduction electrons, Phys. Rev. **96**, 99 (1954).

[27] F. J. Darnell, Magnetostriction in dysprosium and terbium, Phys. Rev. **132**, 128 (1963).

[28] D. Schick, M. Herzog, A. Bojahr, W. Leitenberger, A. Hertwig, R. Shayduk, and M. Bargheer, Ultrafast lattice response of photoexcited thin films studied by x-ray diffraction, Struct. Dyn. **1**, 064501 (2014).

[29] R. M. van der Veen, O.-H. Kwon, A. Tissot, A. Hauser, and A. H. Zewail, Single-nanoparticle phase transitions visualized by four-dimensional electron microscopy, Nat. Chem. **5**, 395 (2013).

[30] G. Ernst, C. Broholm, G. R. Kowach, and A. P. Ramirez, Phonon density of states and negative thermal expansion in ZrW_2O_8, Nature (London) **396**, 147 (1998).

[31] J. Chen, L. Fan, Y. Ren, Z. Pan, J. Deng, R. Yu, and X. Xing, Unusual Transformation from Strong Negative to Positive Thermal Expansion in $PbTiO_3$-$BiFeO_3$ Perovskite, Phys. Rev. Lett. **110**, 115901 (2013).

[32] S. Khmelevskyi, I. Turek, and P. Mohn, Large Negative Magnetic Contribution to the Thermal Expansion in Iron-Platinum Alloys: Quantitative Theory of the Invar Effect, Phys. Rev. Lett. **91**, 037201 (2003).

[33] T. H. K. Barron, J. G. Collins, and G. K. White, Thermal expansion of solids at low temperatures, Adv. Phys. **29**, 609 (1980).

[34] G. D. Barrera, J. A. O. Bruno, T. H. K. Barron, and N. L. Allan, Negative thermal expansion, J. Phys.: Condens. Matter **17**, R217 (2005).

[35] M. Nicoul, U. Shymanovich, A. Tarasevitch, D. von der Linde, and K. Sokolowski-Tinten, Picosecond acoustic response of a laser-heated gold-film studied with time-resolved x-ray diffraction, Appl. Phys. Lett. **98**, 191902 (2011).

[36] G. K. White, Thermal expansion at low temperatures - V. Dilute alloys of manganese in copper, J. Phys. Chem. Solids **23**, 169 (1962).

[37] G. K. White, Phase transitions and the thermal expansion of holmium, J. Phys.: Condens. Matter **1**, 6987 (1989).

[38] B. C. Gerstein, M. Griffel, L. D. Jennings, R. E. Miller, R. E. Skochdopole, and F. H. Spedding, Heat capacity of holmium from 15 to 300°K, J. Chem. Phys. **27**, 394 (1957).

[39] K. D. Jayasuriya, S. J. Campbell, and A. M. Stewart, Specific heat study of a holmium single crystal, J. Phys. F **15**, 225 (1985).

[40] D. Schick, A. Bojahr, M. Herzog, C. von Korff Schmising, R. Shayduk, W. Leitenberger, P. Gaal, and M. Bargheer, Normalization schemes for ultrafast x-ray diffraction using a table-top laser-driven plasma source, Rev. Sci. Instrum. **83**, 025104 (2012).

[41] See Supplemental Material at http://link.aps.org/supplemental/10.1103/PhysRevB.99.094304 for a video sequence of the temporal evolution of the stress profile and the strain wave in the paramagnetic and antiferromagnetic phases of holmium.

[42] P. Ruello and V. E. Gusev, Physical mechanisms of coherent acoustic phonons generation by ultrafast laser action, Ultrasonics **56**, 21 (2015).

[43] A. I. H. Persson, A. Jarnac, X. Wang, H. Enquist, A. Jurgilaitis, and J. Larsson, Studies of electron diffusion in photo-excited Ni using time-resolved x-ray diffraction, Appl. Phys. Lett. **109**, 203115 (2016).

[44] D. Schick, A. Bojahr, M. Herzog, R. Shayduk, C. von Korff Schmising, and M. Bargheer, UDKM1DSIM - A simulation toolkit for 1D ultrafast dynamics in condensed matter, Comput. Phys. Commun. **185**, 651 (2014).

[45] E. Pytte, Spin-phonon interactions in a Heisenberg ferromagnet, Ann. Phys. (NY) **32**, 377 (1965).

[46] B. Frietsch, J. Bowlan, R. Carley, M. Teichmann, S. Wienholdt, D. Hinzke, U. Nowak, K. Carva, P. M. Oppeneer, and M. Weinelt, Disparate ultrafast dynamics of itinerant and localized magnetic moments in gadolinium metal, Nat. Commun. **6**, 8262 (2015).

Bibliography

[1] C. Rovelli: *Reality is not what it seems: The journey to quantum gravity* (Penguin, 2018)

[2] Leucippus, Democritus and C. C. W. Taylor: *The atomists: Leucippus and Democritus: Fragments; a text and translation with a commentary*, volume 5 of *Phoenix Presocratics* (Univ. of Toronto Press, Toronto, 2010)

[3] A. Einstein: "Über die von der molekularkinetischen Theorie der Wärme geforderte Bewegung von in ruhenden Flüssigkeiten suspendierten Teilchen", *Annalen der Physik* 322, 549 (1905)

[4] H. Geiger and E. Marsden: "On a diffuse reflection of the α-particles", *Proceedings of the Royal Society of London. Series A. Mathematical and Physical Sciences* 82, 495 (1909)

[5] E. Rutherford: "LXXIX. The scattering of α and β particles by matter and the structure of the atom", *The London, Edinburgh, and Dublin Philosophical Magazine and Journal of Science* 21, 669 (1911)

[6] N. Bohr: "XXXVII. On the constitution of atoms and molecules", *The London, Edinburgh, and Dublin Philosophical Magazine and Journal of Science* 26, 476 (1913)

[7] G. Binnig, H. Rohrer, C. Gerber and E. Weibel: "Surface Studies by Scanning Tunneling Microscopy", *Physical Review Letters* 49, 57 (1982)

[8] F. A. Lindemann: "Über die Berechnung Molekularer Eigenfrequenzen", *Physikalische Zeitschrift* 11, 609 (1910)

[9] G. Grimvall and S. Sjödin: "Correlation of Properties of Materials to Debye and Melting Temperatures", *Physica Scripta* 10, 340 (1974)

[10] A. M. Lindenberg, S. L. Johnson and D. A. Reis: "Visualization of Atomic-Scale Motions in Materials via Femtosecond X-Ray Scattering Techniques", *Annual Review of Materials Research* 47, 425 (2017)

[11] M. Bargheer, N. Zhavoronkov, M. Woerner and T. Elsaesser: "Recent progress in ultrafast X-ray diffraction", *ChemPhysChem : a European journal of chemical physics and physical chemistry* 7, 783 (2006)

[12] T. Elsaesser and M. Woerner: "Perspective: structural dynamics in condensed matter mapped by femtosecond x-ray diffraction", *The Journal of Chemical Physics* 140, 020901 (2014)

[13] K. Sokolowski-Tinten et al.: "Femtosecond X-ray measurement of coherent lattice vibrations near the Lindemann stability limit", *Nature* 422, 287 (2003)

[14] S. Lee, G. J. Williams, M. I. Campana, D. A. Walko and E. C. Landahl: "Picosecond x-ray strain rosette reveals direct laser excitation of coherent transverse acoustic phonons", *Scientific reports* 6, 19140 (2016)

[15] C. Dornes et al.: "The ultrafast Einstein-de Haas effect", *Nature* 565, 209 (2019)

[16] V. Juvé et al.: "Ultrafast light-induced shear strain probed by time-resolved x-ray diffraction: Multiferroic BiFeO3 as a case study", *Physical Review B* 102 (2020)

[17] M. Trigo et al.: "Fourier-transform inelastic X-ray scattering from time- and momentum-dependent phonon–phonon correlations", *Nature Physics* 9, 790 (2013)

[18] J. Chen et al.: "Time- and momentum-resolved probe of heat transport in photo-excited bismuth", *Applied Physics Letters* 102, 181903 (2013)

[19] M. Sander et al.: "Spatiotemporal Coherent Control of Thermal Excitations in Solids", *Physical Review Letters* 119, 075901 (2017)

[20] M. Sander, J.-E. Pudell, M. Herzog, M. Bargheer, R. Bauer, V. Besse, V. Temnov and P. Gaal: "Quantitative disentanglement of coherent and incoherent laser-induced surface deformations by time-resolved x-ray reflectivity", *Applied Physics Letters* 111, 261903 (2017)

[21] H. D. Chopra and M. Wuttig: "Non-Joulian magnetostriction", *Nature* 521, 340 (2015)

[22] Beaurepaire, Merle, Daunois and Bigot: "Ultrafast spin dynamics in ferromagnetic nickel", *Physical Review Letters* 76, 4250 (1996)

[23] C. D. Stanciu, F. Hansteen, A. V. Kimel, A. Kirilyuk, A. Tsukamoto, A. Itoh and T. Rasing: "All-optical magnetic recording with circularly polarized light", *Physical Review Letters* 99, 047601 (2007)

[24] A. V. Kimel, A. M. Kalashnikova, A. Pogrebna and A. K. Zvezdin: "Fundamentals and perspectives of ultrafast photoferroic recording", *Physics Reports* 852, 1 (2020)

[25] A. El-Ghazaly, J. Gorchon, R. B. Wilson, A. Pattabi and J. Bokor: "Progress towards ultrafast spintronics applications", *Journal of Magnetism and Magnetic Materials* 502, 166478 (2020)

[26] M. van Kampen, C. Jozsa, J. T. Kohlhepp, P. LeClair, L. Lagae, W. J. M. de Jonge and B. Koopmans: "All-optical probe of coherent spin waves", *Physical Review Letters* 88, 227201 (2002)

[27] O. Matsuda, M. C. Larciprete, R. Li Voti and O. B. Wright: "Fundamentals of picosecond laser ultrasonics", *Ultrasonics* 56, 3 (2015)

[28] P. Ruello and V. E. Gusev: "Physical mechanisms of coherent acoustic phonons generation by ultrafast laser action", *Ultrasonics* 56, 21 (2015)

[29] A. Kirilyuk, A. V. Kimel and T. Rasing: "Ultrafast optical manipulation of magnetic order", *Reviews of Modern Physics* 82, 2731 (2010)

[30] J.-Y. Bigot and M. Vomir: "Ultrafast magnetization dynamics of nanostructures", *Annalen der Physik* 525, 2 (2013)

[31] A. Rousse, C. Rischel and J.-C. Gauthier: "Femtosecond x-ray crystallography", *Reviews of Modern Physics* 73, 17 (2001)

[32] D. Royer and E. Dieulesaint: *Elastic waves in solids: Including nonlinear dynamics* Advanced texts in physics (Springer, Berlin, 2000), 3rd edition

[33] R. Gross and A. Marx: *Festkörperphysik* De Gruyter Studium (De Gruyter, Berlin and Boston, 2018), 3rd edition

[34] J. V. Jäger et al.: "Picosecond inverse magnetostriction in galfenol thin films", *Applied Physics Letters* 103, 032409 (2013)

[35] O. Matsuda, K. Tsutsui, G. Vaudel, T. Pezeril, K. Fujita and V. Gusev: "Optical generation and detection of gigahertz shear acoustic waves in solids assisted by a metallic diffraction grating", *Physical Review B* 101, 224307 (2020)

[36] T. Parpiiev: "Ultrafast magnetoacoustics in magnetostrictive materials" PhD thesis, Le Mans Université, Le Mans (2017)

[37] B. A. Auld: *Acoustic fields and waves in solids* (Wiley, New York, NY, 1973), 2nd edition

[38] S. Azzawi, A. T. Hindmarch and D. Atkinson: "Magnetic damping phenomena in ferromagnetic thin-films and multilayers", *Journal of Physics D: Applied Physics* 50, 473001 (2017)

[39] L. Thevenard, I. S. Camara, S. Majrab, M. Bernard, P. Rovillain, A. Lemaître, C. Gourdon and J.-Y. Duquesne: "Precessional magnetization switching by a surface acoustic wave", *Physical Review B* 93, 134430 (2016)

[40] T. L. Linnik, A. V. Scherbakov, D. R. Yakovlev, X. Liu, J. K. Furdyna and M. Bayer: "Theory of magnetization precession induced by a picosecond strain pulse in ferromagnetic semiconductor (Ga,Mn)As", *Physical Review B* 84, 214432 (2011)

[41] T. L. Linnik et al.: "The effect of dynamical compressive and shear strain on magnetic anisotropy in a low symmetry ferromagnetic film", *Physica Scripta* 92, 054006 (2017)

[42] C. Kittel: "Physical Theory of Ferromagnetic Domains", *Reviews of Modern Physics* 21, 541 (1949)

[43] G. Engdahl (Editor) *Handbook of giant magnetostrictive materials* Electromagnetism (Academic Press, San Diego Calif. u.a., 2000)

[44] É. Du Trémolet de Lacheisserie: *Magnetostriction: Theory and applications of magnetoelasticity* (CRC Press, Boca Raton, 1993)

[45] C. Kittel: *Introduction to solid state physics* (Wiley, New York [u.a.], 1996), 7th edition

[46] S. Blundell: *Magnetism in condensed matter*, volume 4 of *Oxford master series in condensed matter physics* (Oxford Univ. Press, Oxford, 2014), reprint edition

[47] F. Büttner et al.: "Observation of fluctuation-mediated picosecond nucleation of a topological phase", *Nature materials* 20, 30 (2021)

[48] K. Gerlinger et al.: "Application concepts for ultrafast laser-induced skyrmion creation and annihilation", *Applied Physics Letters* 118, 192403 (2021)

[49] U. Atxitia, D. Hinzke and U. Nowak: "Fundamentals and applications of the Landau–Lifshitz–Bloch equation", *Journal of Physics D: Applied Physics* 50, 033003 (2017)

[50] F. Hansteen, A. Kimel, A. Kirilyuk and T. Rasing: "Femtosecond photomagnetic switching of spins in ferrimagnetic garnet films", *Physical Review Letters* 95, 047402 (2005)

[51] F. Hansteen: "Ultrafast optical control of magnetization in ferrimagnetic garnets" PhD thesis, Radboud University, Nijmegen (2006)

[52] Thomsen, Grahn, Maris and Tauc: "Surface generation and detection of phonons by picosecond light pulses", *Physical Review. B* 34, 4129 (1986)

[53] D. Schick, M. Herzog, A. Bojahr, W. Leitenberger, A. Hertwig, R. Shayduk and M. Bargheer: "Ultrafast lattice response of photoexcited thin films studied by X-ray diffraction", *Structural Dynamics* 1, 064501 (2014)

[54] V. P. Antropov, S. V. Tretyakov and B. N. Harmon: "Spin dynamics in magnets: Quantum effects and numerical simulations", *Journal of Applied Physics* 81, 3961 (1997)

[55] J. L. García-Palacios and F. J. Lázaro: "Langevin-dynamics study of the dynamical properties of small magnetic particles", *Physical Review B* 58, 14937 (1998)

[56] P. Nieves, D. Serantes, U. Atxitia and O. Chubykalo-Fesenko: "Quantum Landau-Lifshitz-Bloch equation and its comparison with the classical case", *Physical Review B* 90, 1 (2014)

[57] J. Barker and G. E. W. Bauer: "Semiquantum thermodynamics of complex ferrimagnets", *Physical Review B* 100, 140401 (2019)

[58] O. Chubykalo-Fesenko, U. Nowak, R. W. Chantrell and D. Garanin: "Dynamic approach for micromagnetics close to the Curie temperature", *Physical Review B* 74, 094436 (2006)

[59] U. Atxitia, P. Nieves and O. Chubykalo-Fesenko: "Landau-Lifshitz-Bloch equation for ferrimagnetic materials", *Physical Review B* 86, 196 (2012)

[60] M. O. A. Ellis, R. F. L. Evans, T. A. Ostler, J. Barker, U. Atxitia, O. Chubykalo-Fesenko and R. W. Chantrell: "The Landau–Lifshitz equation in atomistic models", *Low Temperature Physics* 41, 705 (2015)

[61] V. G. Bar'yakhtar and B. A. Ivanov: "The Landau-Lifshitz equation: 80 years of history, advances, and prospects", *Low Temperature Physics* 41, 663 (2015)

[62] M. Herzog, D. Schick, P. Gaal, R. Shayduk, C. Korff Schmising and M. Bargheer: "Analysis of ultrafast X-ray diffraction data in a linear-chain model of the lattice dynamics", *Applied Physics A* 106, 489 (2012)

[63] D. Schick, A. Bojahr, M. Herzog, R. Shayduk, C. von Korff Schmising and M. Bargheer: "udkm1Dsim - A simulation toolkit for 1D ultrafast dynamics in condensed matter", *Computer Physics Communications* 185, 651 (2014)

[64] J. N. Clark et al.: "Ultrafast three-dimensional imaging of lattice dynamics in individual gold nanocrystals", *Science (New York, N.Y.)* 341, 56 (2013)

[65] V. Juvé, A. Crut, P. Maioli, M. Pellarin, M. Broyer, N. Del Fatti and F. Vallée: "Probing elasticity at the nanoscale: Terahertz acoustic vibration of small metal nanoparticles", *Nano letters* 10, 1853 (2010)

[66] P. Maioli et al.: "Mechanical Vibrations of Atomically Defined Metal Clusters: From Nano- to Molecular-Size Oscillators", *Nano letters* 18, 6842 (2018)

[67] A. Bojahr et al.: "Second Harmonic Generation of Nanoscale Phonon Wave Packets", *Physical Review Letters* 115, 195502 (2015)

[68] A. Bojahr: "Hypersound Interaction Studied by Time-Resolved Inelastic Light and X-Ray Scattering" PhD thesis, Universität Potsdam, Potsdam (2015)

[69] S. I. Anisimov, B. L. Kapeliovich and T. L. Perel'man: "Electron emission from metal surfaces exposed to ultrashort laser pulses", *Sov. Phys. JETP* 39, 375 (1974)

[70] P. B. Allen: "Theory of thermal relaxation of electrons in metals", *Physical Review Letters* 59, 1460 (1987)

[71] Z. Lin, L. V. Zhigilei and V. Celli: "Electron-phonon coupling and electron heat capacity of metals under conditions of strong electron-phonon nonequilibrium", *Physical Review B* 77, 776 (2008)

[72] B. Koopmans, G. Malinowski, F. Dalla Longa, D. Steiauf, M. Fähnle, T. Roth, M. Cinchetti and M. Aeschlimann: "Explaining the paradoxical diversity of ultrafast laser-induced demagnetization", *Nature materials* 9, 259 (2010)

[73] M. Battiato, K. Carva and P. M. Oppeneer: "Superdiffusive spin transport as a mechanism of ultrafast demagnetization", *Physical Review Letters* 105, 027203 (2010)

[74] B. Vodungbo et al.: "Indirect excitation of ultrafast demagnetization", *Scientific Reports* 6, 18970 (2016)

[75] I. Razdolski, A. Alekhin, N. Ilin, J. P. Meyburg, V. Roddatis, D. Diesing, U. Bovensiepen and A. Melnikov: "Nanoscale interface confinement of ultrafast spin transfer torque driving non-uniform spin dynamics", *Nature communications* 8, 15007 (2017)

[76] A. Alekhin et al.: "Femtosecond Spin Current Pulses Generated by the Nonthermal Spin-Dependent Seebeck Effect and Interacting with Ferromagnets in Spin Valves", *Physical Review Letters* 119, 017202 (2017)

[77] J. Kimling, J. Kimling, R. B. Wilson, B. Hebler, M. Albrecht and D. G. Cahill: "Ultrafast demagnetization of FePt:Cu thin films and the role of magnetic heat capacity", *Physical Review B* 90, 224408 (2014)

[78] L. Waldecker, R. Bertoni, R. Ernstorfer and J. Vorberger: "Electron-Phonon Coupling and Energy Flow in a Simple Metal beyond the Two-Temperature Approximation", *Physical Review X* 6, 945 (2016)

[79] P. Maldonado, K. Carva, M. Flammer and P. M. Oppeneer: "Theory of out-of-equilibrium ultrafast relaxation dynamics in metals", *Physical Review B* 96, 173 (2017)

[80] U. Ritzmann, P. M. Oppeneer and P. Maldonado: "Theory of out-of-equilibrium electron and phonon dynamics in metals after femtosecond laser excitation", *Physical Review B* 102, 214305 (2020)

[81] T. Henighan et al.: "Generation mechanism of terahertz coherent acoustic phonons in Fe", *Physical Review B* 93, 220301 (2016)

[82] P. Maldonado et al.: "Tracking the ultrafast nonequilibrium energy flow between electronic and lattice degrees of freedom in crystalline nickel", *Physical Review B* 101 (2020)

[83] L. Waldecker, R. Bertoni, H. Hübener, T. Brumme, T. Vasileiadis, D. Zahn, A. Rubio and R. Ernstorfer: "Momentum-Resolved View of Electron-Phonon Coupling in Multilayer WSe_2", *Physical Review Letters* 119, 036803 (2017)

[84] R. B. Wilson and S. Coh: "Parametric dependence of hot electron relaxation timescales on electron-electron and electron-phonon interaction strengths", *Communications Physics* 3, 179 (2020)

[85] N. Kazantseva, U. Nowak, R. W. Chantrell, J. Hohlfeld and A. Rebei: "Slow recovery of the magnetisation after a sub-picosecond heat pulse", *EPL (Europhysics Letters)* 81, 27004 (2008)

[86] B. Rethfeld, A. Kaiser, M. Vicanek and G. Simon: "Ultrafast dynamics of nonequilibrium electrons in metals under femtosecond laser irradiation", *Physical Review B* 65, 214303 (2002)

[87] P. Tengdin et al.: "Critical behavior within 20 fs drives the out-of-equilibrium laser-induced magnetic phase transition in nickel", *Science Advances* 4, eaap9744 (2018)

[88] P. Scheid, G. Malinowski, S. Mangin and S. Lebègue: "Ab initio study of electronic temperature effects on magnetic materials properties", *Physical Review B* 99, 174415 (2019)

[89] A. Einstein and W. J. de Haas: "Experimental proof of the existence of Ampere's molecular currents" in *Proc. KNAW*, volume 181, 696 (1915)

[90] O. W. Richardson: "A Mechanical Effect Accompanying Magnetization", *Physical Review (Series I)* 26, 248 (1908)

[91] V. Shokeen, M. Sanchez Piaia, J.-Y. Bigot, T. Müller, P. Elliott, J. K. Dewhurst, S. Sharma and E. K. U. Gross: "Spin Flips versus Spin Transport in Nonthermal Electrons Excited by Ultrashort Optical Pulses in Transition Metals", *Physical Review Letters* 119, 107203 (2017)

[92] J. K. Dewhurst, P. Elliott, S. Shallcross, E. K. U. Gross and S. Sharma: "Laser-Induced Intersite Spin Transfer", *Nano letters* 18, 1842 (2018)

[93] F. Siegrist et al.: "Light-wave dynamic control of magnetism", *Nature* 571, 240 (2019)

[94] F. Willems, C. von Korff Schmising, C. Strüber, D. Schick, D. W. Engel, J. K. Dewhurst, P. Elliott, S. Sharma and S. Eisebitt: "Optical inter-site spin transfer probed by energy and spin-resolved transient absorption spectroscopy", *Nature communications* 11, 871 (2020)

[95] M. Hofherr et al.: "Ultrafast optically induced spin transfer in ferromagnetic alloys", *Science Advances* 6, eaay8717 (2020)

[96] J. V. Jäger, A. V. Scherbakov, B. A. Glavin, A. S. Salasyuk, R. P. Campion, A. W. Rushforth, D. R. Yakovlev, A. V. Akimov and M. Bayer: "Resonant driving of magnetization precession in a ferromagnetic layer by coherent monochromatic phonons", *Physical Review B* 92, 020404 (2015)

[97] M. Deb, E. Popova, M. Hehn, N. Keller, S. Mangin and G. Malinowski: "Picosecond acoustic-excitation-driven ultrafast magnetization dynamics in dielectric Bi-substituted yttrium iron garnet", *Physical Review B* 98, 444 (2018)

[98] C. S. Davies et al.: "Anomalously Damped Heat-Assisted Route for Precessional Magnetization Reversal in an Iron Garnet", *Physical Review Letters* 122, 027202 (2019)

[99] O. Kovalenko, T. Pezeril and V. V. Temnov: "New concept for magnetization switching by ultrafast acoustic pulses", *Physical Review Letters* 110, 266602 (2013)

[100] S. F. Maehrlein et al.: "Dissecting spin-phonon equilibration in ferrimagnetic insulators by ultrafast lattice excitation", *Science Advances* 4, eaar5164 (2018)

[101] A. V. Scherbakov et al.: "Coherent magnetization precession in ferromagnetic (Ga,Mn)As induced by picosecond acoustic pulses", *Physical Review Letters* 105, 117204 (2010)

[102] L. Thevenard, E. Peronne, C. Gourdon, C. Testelin, M. Cubukcu, E. Charron, S. Vincent, A. Lemaître and B. Perrin: "Effect of picosecond strain pulses on thin layers of the ferromagnetic semiconductor (Ga,Mn)(As,P)", *Physical Review B* 82, 444 (2010)

[103] M. Deb, P. Molho, B. Barbara and J.-Y. Bigot: "Controlling laser-induced magnetization reversal dynamics in a rare-earth iron garnet across the magnetization compensation point", *Physical Review B* 97, 134419 (2018)

[104] M. Deb, E. Popova, M. Hehn, N. Keller, S. Petit-Watelot, M. Bargheer, S. Mangin and G. Malinowski: "Damping of Standing Spin Waves in Bismuth-Substituted Yttrium Iron Garnet as Seen via the Time-Resolved Magneto-Optical Kerr Effect", *Physical Review Applied* 12, 677

(2019)

[105] J.-W. Kim, M. Vomir and J.-Y. Bigot: "Ultrafast magnetoacoustics in nickel films", *Physical Review Letters* 109, 166601 (2012)

[106] J. Walowski and M. Münzenberg: "Perspective: Ultrafast magnetism and THz spintronics", *Journal of Applied Physics* 120, 140901 (2016)

[107] Clarivate analytics: "Web of Science" (2020)

[108] J.-W. Kim, M. Vomir and J.-Y. Bigot: "Controlling the spins angular momentum in ferromagnets with sequences of picosecond acoustic pulses", *Scientific reports* 5, 8511 (2015)

[109] M. Deb, E. Popova, M. Hehn, N. Keller, S. Petit-Watelot, M. Bargheer, S. Mangin and G. Malinowski: "Femtosecond Laser-Excitation-Driven High Frequency Standing Spin Waves in Nanoscale Dielectric Thin Films of Iron Garnets", *Physical Review Letters* 123, 027202 (2019)

[110] I. S. Camara, J.-Y. Duquesne, A. Lemaître, C. Gourdon and L. Thevenard: "Field-Free Magnetization Switching by an Acoustic Wave", *Physical Review Applied* 11, 1 (2019)

[111] K. Hono, Y. K. Takahashi, G. Ju, J.-U. Thiele, A. Ajan, X. Yang, R. Ruiz and L. Wan: "Heat-assisted magnetic recording media materials", *MRS Bulletin* 43, 93 (2018)

[112] D. Weller, G. Parker, O. Mosendz, A. Lyberatos, D. Mitin, N. Y. Safonova and M. Albrecht: "Review Article: FePt heat assisted magnetic recording media", *Journal of Vacuum Science & Technology B, Nanotechnology and Microelectronics: Materials, Processing, Measurement, and Phenomena* 34, 060801 (2016)

[113] C. v. Korff Schmising et al.: "Ultrafast magnetostriction and phonon-mediated stress in a photoexcited ferromagnet", *Physical Review B* 78, 060404 (2008)

[114] S. O. Mariager et al.: "Structural and magnetic dynamics of a laser induced phase transition in FeRh", *Physical Review Letters* 108, 087201 (2012)

[115] F. Quirin, M. Vattilana, U. Shymanovich, A.-E. El-Kamhawy, A. Tarasevitch, J. Hohlfeld, D. von der Linde and K. Sokolowski-Tinten: "Structural dynamics in FeRh during a laser-induced metamagnetic phase transition", *Physical Review B* 85, 498 (2012)

[116] J. Janušonis, C. L. Chang, P. H. M. van Loosdrecht and R. I. Tobey: "Frequency tunable surface magneto elastic waves", *Applied Physics Letters* 106, 181601 (2015)

[117] J. Janušonis et al.: "Transient Grating Spectroscopy in Magnetic Thin Films: Simultaneous Detection of Elastic and Magnetic Dynamics", *Scientific reports* 6, 29143 (2016)

[118] T. Parpiiev et al.: "Ultrafast non-thermal laser excitation of gigahertz longitudinal and shear acoustic waves in spin-crossover molecular crystals [Fe (PM – AzA) 2 (NCS) 2]", *Applied Physics Letters* 111, 151901 (2017)

[119] T. Pezeril: "Laser generation and detection of ultrafast shear acoustic waves in solids and liquids", *Optics and Laser Technology* 83, 177 (2016)

[120] E. Jal, V. López-Flores, N. Pontius, T. Ferté, N. Bergeard, C. Boeglin, B. Vodungbo, J. Lüning and N. Jaouen: "Structural dynamics during laser-induced ultrafast demagnetization", *Physical Review B* 95, 184422 (2017)

[121] F. S. Krasniqi et al.: "Spatial Distortion of Vibration Modes via Magnetic Correlation of Impurities", *Physical Review Letters* 120, 105501 (2018)

[122] A. H. Reid et al.: "Beyond a phenomenological description of magnetostriction", *Nature Communications* 9, 388 (2018)

[123] Y. Hashimoto, D. Bossini, T. H. Johansen, E. Saitoh, A. Kirilyuk and T. Rasing: "Frequency and wavenumber selective excitation of spin waves through coherent energy transfer from elastic waves", *Physical Review B* 97, 140404 (2018)

[124] T. Hioki, Y. Hashimoto, T. H. Johansen and E. Saitoh: "Time-Resolved Imaging of Magnetoelastic Waves by the Cotton-Mouton Effect", *Physical Review Applied* 11, 061007 (2019)

[125] D. Schick: "Ultrafast Lattice Dynamics in Photoexcited Nanostructures" PhD thesis, Universität Potsdam, Potsdam (2013)

[126] D. Schick, A. Bojahr, M. Herzog, C. von Korff Schmising, R. Shayduk, W. Leitenberger, P. Gaal and M. Bargheer: "Normalization schemes for ultrafast x-ray diffraction using a table-top laser-driven plasma source", *Review of Scientific Instruments* 83, 025104 (2012)

[127] D. Schick, R. Shayduk, A. Bojahr, M. Herzog, C. von Korff Schmising, P. Gaal and M. Bargheer: "Ultrafast reciprocal-space mapping with a convergent beam", *Journal of Applied Crystallography* 46, 1372 (2013)

[128] A. von Reppert: "Ultrafast Magnetostriction in Dysprosium studied by Femtosecond X-Ray diffraction" MSc thesis, Universität Potsdam, Potsdam (2015)

[129] J. Weisshaupt, V. Juvé, M. Holtz, S. Ku, M. Woerner, T. Elsaesser, S. Ališauskas, A. Pugžlys and A. Baltuška: "High-brightness table-top hard X-ray source driven by sub-100-femtosecond mid-infrared pulses", *Nature Photonics* 8, 927 (2014)

[130] M. Bargheer, N. Zhavoronkov, R. Bruch, H. Legall, H. Stiel, M. Woerner and T. Elsaesser: "Comparison of focusing optics for femtosecond X-ray diffraction", *Applied Physics B* 80, 715 (2005)

[131] V. Holý, U. Pietsch and T. Baumbach: *High-Resolution X-Ray Scattering from Thin Films and Multilayers*, volume 149 of *Springer Tracts in Modern Physics*(Springer, Berlin and Heidelberg, 1999)

[132] J. Als-Nielsen and Des McMorrow: *Elements of modern X-ray physics* (Wiley, Chichester, 2011), second edition edition

[133] B. E. Warren: *X-ray diffraction* (Dover, New York, NY, 1990), unabridged and corrected edition

[134] A. Authier: *Dynamical theory of X-ray diffraction*, volume 11 of *IUCr monographs on crystallography* (Oxford Univ. Press, Oxford, 2008), reprint edition

[135] J. R. Helliwell and P. M. Rentzepis (Editors) *Time-resolved diffraction*, volume 2 of *Oxford series on synchrotron radiation* (Clarendon Press, Oxford, 2007), reprint edition

[136] D. Kriegner, E. Wintersberger and J. Stangl: "xrayutilities : a versatile tool for reciprocal space conversion of scattering data recorded with linear and area detectors", *Journal of Applied Crystallography* 46, 1162 (2013)

[137] M. Reinhardt and W. Leitenberger: "XPP: X-ray Pump Probe station at BESSY II", *Journal of large-scale research facilities JLSRF* 2, 1 (2016)

[138] M. Rössle, W. Leitenberger, M. Reinhardt, A. Koç, J. Pudell, C. Kwamen and M. Bargheer: "The time-resolved hard X-ray diffraction endstation KMC-3 XPP at BESSY II", *Journal of Synchrotron*

Radiation 28, 948 (2021)

[139] P. Trueb, B. A. Sobott, R. Schnyder, T. Loeliger, M. Schneebeli, M. Kobas, R. P. Rassool, D. J. Peake and C. Broennimann: "Improved count rate corrections for highest data quality with PILATUS detectors", *Journal of synchrotron radiation* 19, 347 (2012)

[140] D. Schick, A. Bojahr, M. Herzog, P. Gaal, I. Vrejoiu and M. Bargheer: "Following strain-induced mosaicity changes of ferroelectric thin films by ultrafast reciprocal space mapping", *Physical Review Letters* 110, 095502 (2013)

[141] J.-E. Pudell: "Lattice Dynamics observed with x-ray Diffraction" PhD thesis, Universität Potsdam, Potsdam (2020)

[142] J.-E. Pudell: "Ultraschnelle Magnetostriktion von antiferromagnetischem Holmium" MSc thesis, Universität Potsdam, Potsdam (2015)

[143] M. Herzog, D. Schick, W. Leitenberger, R. Shayduk, R. M. van der Veen, C. J. Milne, S. L. Johnson, I. Vrejoiu and M. Bargheer: "Tailoring interference and nonlinear manipulation of femtosecond x-rays", *New Journal of Physics* 14, 013004 (2012)

[144] M. Bargheer: "Atombewegung im Röntgenkino - Die Femtosekunden-Röntgenbeugung entschlüsselt ultraschnelle Gitterdynamik", *Physik Journal* 6, 1 (2007)

[145] J. Stingl, F. Zamponi, B. Freyer, M. Woerner, T. Elsaesser and A. Borgschulte: "Electron transfer in a virtual quantum state of LiBH4 induced by strong optical fields and mapped by femtosecond x-ray diffraction", *Physical Review Letters* 109, 147402 (2012)

[146] D. Schick et al.: "Localized excited charge carriers generate ultrafast inhomogeneous strain in the multiferroic BiFeO3", *Physical Review Letters* 112, 097602 (2014)

[147] M. Nicoul, U. Shymanovich, A. Tarasevitch, D. von der Linde and K. Sokolowski-Tinten: "Picosecond acoustic response of a laser-heated gold-film studied with time-resolved x-ray diffraction", *Applied Physics Letters* 98, 191902 (2011)

[148] R. M. Sarhan: "Plasmon-driven photocatalytic reactions monitored by surfaceenhanced Raman spectroscopy" PhD thesis, Universität Potsdam, Potsdam (2019)

[149] G. V. Hartland: "Coherent excitation of vibrational modes in metallic nanoparticles", *Annual review of physical chemistry* 57, 403 (2006)

[150] A. L. Tchebotareva, P. V. Ruijgrok, P. Zijlstra and M. Orrit: "Probing the acoustic vibrations of single metal nanoparticles by ultrashort laser pulses", *Laser & Photonics Reviews* 4, 581 (2010)

[151] A. Crut, P. Maioli, N. Del Fatti and F. Vallée: "Acoustic vibrations of metal nano-objects: Time-domain investigations", *Physics Reports* 549, 1 (2015)

[152] R. Ferrando et al.: "Structures of metal nanoparticles adsorbed on MgO(001). I. Ag and Au", *The Journal of Chemical Physics* 130, 174702 (2009)

[153] Y. Han, R. Ferrando and Z. Y. Li: "Atomic Details of Interfacial Interaction in Gold Nanoparticles Supported on MgO(001)", *The journal of physical chemistry letters* 5, 131 (2014)

[154] P. A. Kienzle, K. V. O'Donovan, J. F. Ankner, N. F. Berk and C. F. Majkrzak: "NCNR Reflectometry Software" (2017)

[155] D. I. Yakubovsky, Y. V. Stebunov, R. V. Kirtaev, G. A. Ermolaev, M. S. Mironov, S. M. Novikov, A. V. Arsenin and V. S. Volkov: "Ultrathin and Ultrasmooth Gold Films on Monolayer MoS 2",

Advanced Materials Interfaces 6, 1900196 (2019)

[156] L. Le Guyader, A. Kleibert, F. Nolting, L. Joly, P. M. Derlet, R. V. Pisarev, A. Kirilyuk, T. Rasing and A. V. Kimel: "Dynamics of laser-induced spin reorientation in Co/SmFeO 3 heterostructure", *Physical Review B* 87, 935 (2013)

[157] D. I. Yakubovsky, A. V. Arsenin, Y. V. Stebunov, D. Y. Fedyanin and V. S. Volkov: "Optical constants and structural properties of thin gold films", *Optics express* 25, 25574 (2017)

[158] P. B. Johnson and R. W. Christy: "Optical Constants of the Noble Metals", *Physical Review B* 6, 4370 (1972)

[159] A. R. Khorsand, M. Savoini, A. Kirilyuk and T. Rasing: "Optical excitation of thin magnetic layers in multilayer structures", *Nature materials* 13, 101 (2014)

[160] K. Kang and G.-M. Choi: "Thermal coupling parameters between electron, phonon, and magnon of Nickel", *Journal of Magnetism and Magnetic Materials* 514, 167156 (2020)

[161] D. Zahn et al.: "Lattice dynamics and ultrafast energy flow between electrons, spins, and phonons in a 3d ferromagnet", *arXiv-preprint* (2021)

[162] F. C. Nix and D. MacNair: "The Thermal Expansion of Pure Metals: Copper, Gold, Aluminum, Nickel, and Iron", *Physical Review* 60, 597 (1941)

[163] P. J. Meschter, J. W. Wright, C. R. Brooks and T. G. Kollie: "Physical contributions to the heat capacity of nickel", *Journal of Physics and Chemistry of Solids* 42, 861 (1981)

[164] C. Y. Ho, R. W. Powell and P. E. Liley: "Thermal Conductivity of the Elements", *Journal of Physical and Chemical Reference Data* 1, 279 (1972)

[165] W. Wang and D. G. Cahill: "Limits to thermal transport in nanoscale metal bilayers due to weak electron-phonon coupling in Au and Cu", *Physical Review Letters* 109, 175503 (2012)

[166] G.-M. Choi, B.-C. Min, K.-J. Lee and D. G. Cahill: "Spin current generated by thermally driven ultrafast demagnetization", *Nature communications* 5, 4334 (2014)

[167] Y. Shin, Y. Liu, M. Vomir and J.-W. Kim: "Higher-order acoustic phonon oscillations in Au nanoparticles controlled by a sequence of ultrashort strain pulses generated by superdiffusive hot electrons", *Physical Review B* 101, 020302 (2020)

[168] J.-E. Pudell, M. Mattern, M. Hehn, G. Malinowski, M. Herzog and M. Bargheer: "Heat Transport without Heating?—An Ultrafast X–Ray Perspective into a Metal Heterostructure", *Advanced Functional Materials* 30, 2004555 (2020)

[169] Y. Takahashi and H. Akiyama: "Heat capacity of gold from 80 to 1000 K", *Thermochimica Acta* 109, 105 (1986)

[170] T. H. Geballe and W. F. Giauque: "The Heat Capacity and Entropy of Gold from 15 to 300 K.", *Journal of the American Chemical Society* 74, 2368 (1952)

[171] T. H. K. Barron, W. T. Berg and J. A. Morrion: "On the heat capacity of crystalline magnesium oxide", *Proceedings of the Royal Society of London. Series A. Mathematical and Physical Sciences* 250, 70 (1959)

[172] L.-Y. Lu, Y. Cheng, X.-R. Chen and J. Zhu: "Thermodynamic properties of MgO under high pressure from first-principles calculations", *Physica B: Condensed Matter* 370, 236 (2005)

[173] G. Fiquet, P. Richet and G. Montagnac: "High-temperature thermal expansion of lime, periclase,

corundum and spinel", *Phys. Chem. Minerals* 27, 103 (1999)

[174] G. K. White and O. L. Anderson: "Grüneisen Parameter of Magnesium Oxide", *Journal of Applied Physics* 37, 430 (1966)

[175] C. Thomsen, J. Strait, Z. Vardeny, H. J. Maris, J. Tauc and J. J. Hauser: "Coherent Phonon Generation and Detection by Picosecond Light Pulses", *Physical Review Letters* 53, 989 (1984)

[176] Y. Beyazit, J. Beckord, P. Zhou, J. P. Meyburg, F. Kühne, D. Diesing, M. Ligges and U. Bovensiepen: "Local and Nonlocal Electron Dynamics of Au/Fe/MgO(001) Heterostructures Analyzed by Time-Resolved Two-Photon Photoemission Spectroscopy", *Physical Review Letters* 125, 076803 (2020)

[177] J.-A. Yang, S. Parham, D. Dessau and D. Reznik: "Novel Electron-Phonon Relaxation Pathway in Graphite Revealed by Time-Resolved Raman Scattering and Angle-Resolved Photoemission Spectroscopy", *Scientific Reports* 7, 40876 (2017)

[178] K. Sokolowski-Tinten et al.: "Thickness-dependent electron–lattice equilibration in laser-excited thin bismuth films", *New Journal of Physics* 17, 113047 (2015)

[179] K. Sokolowski-Tinten et al.: "Electron-lattice energy relaxation in laser-excited thin-film Au-insulator heterostructures studied by ultrafast MeV electron diffraction", *Structural Dynamics* 4, 054501 (2017)

[180] T. Vasileiadis, L. Waldecker, D. Foster, A. Da Silva, D. Zahn, R. Bertoni, R. E. Palmer and R. Ernstorfer: "Ultrafast Heat Flow in Heterostructures of Au Nanoclusters on Thin Films: Atomic Disorder Induced by Hot Electrons", *ACS nano* 12, 7710 (2018)

[181] N. Rothenbach et al.: "Microscopic nonequilibrium energy transfer dynamics in a photoexcited metal/insulator heterostructure", *Physical Review B* 100, 174301 (2019)

[182] G.-M. Choi, R. B. Wilson and D. G. Cahill: "Indirect heating of Pt by short-pulse laser irradiation of Au in a nanoscale Pt/Au bilayer", *Physical Review B* 89, 064307 (2014)

[183] S. M. Oommen and S. Pisana: "Role of the electron-phonon coupling in tuning the thermal boundary conductance at metal-dielectric interfaces by inserting ultrathin metal interlayers", *Journal of physics. Condensed matter* 085702 (2020)

[184] H. Jang, J. Kimling and D. G. Cahill: "Nonequilibrium heat transport in Pt and Ru probed by an ultrathin Co thermometer", *Physical Review B* 101, 064304 (2020)

[185] G. Tas and H. Maris: "Electron diffusion in metals studied by picosecond ultrasonics", *Physical Review. B* 49, 15046 (1994)

[186] M. Lejman, V. Shalagatskyi, O. Kovalenko, T. Pezeril, V. V. Temnov and P. Ruello: "Ultrafast optical detection of coherent acoustic phonons emission driven by superdiffusive hot electrons", *Journal of the Optical Society of America B* 31, 282 (2014)

[187] S. Eich et al.: "Band structure evolution during the ultrafast ferromagnetic-paramagnetic phase transition in cobalt", *Science Advances* 3, e1602094 (2017)

[188] M. G. Münzenberg: "Magnetization dynamics: Ferromagnets stirred up", *Nature materials* 9, 184 (2010)

[189] G. D. Barrera, J. A. O. Bruno, T. H. K. Barron and N. L. Allan: "Negative thermal expansion", *Journal of Physics: Condensed Matter* 17, R217 (2005)

[190] G. K. White: "Solids: Thermal expansion and contraction", *Contemporary Physics* 34, 193 (1993)

[191] T. Barron, J. G. Collins and G. K. White: "Thermal expansion of solids at low temperatures", *Advances in Physics* 29, 609 (1980)

[192] E. Grüneisen: "Theorie des festen Zustandes einatomiger Elemente", *Annalen der Physik* 344, 257 (1912)

[193] N. W. Ashcroft and N. D. Mermin: *Solid state physics* (Brooks/Cole Thomson Learning, South Melbourne, 2012), 4th edition

[194] M. T. Dove: *Structure and dynamics: An atomic view of materials*, volume 1 of *Oxford master series in condensed matter physics* (Oxford Univ. Press, Oxford, 2005), reprinted. edition

[195] O. Heuzé: "General form of the Mie–Grüneisen equation of state", *Comptes Rendus Mécanique* 340, 679 (2012)

[196] M. de Souza, P. Menegasso, R. Paupitz, A. Seridonio and R. E. Lagos: "Grüneisen parameter for gases and superfluid helium", *European Journal of Physics* 37, 055105 (2016)

[197] E. Grüneisen: "Zusammenhang zwischen Kompressibilität, thermischer Ausdehnung, Atomvolumen und Atomwärme der Metalle", *Annalen der Physik* 331, 393 (1908)

[198] A. Einstein: "Die Plancksche Theorie der Strahlung und die Theorie der spezifischen Wärme", *Annalen der Physik* 327, 180 (1907)

[199] R. S. Krishnan, R. Srinivasan, S. Devanarayanan and B. R. Pamplin: *Thermal Expansion of Crystals: International Series in The Science of The Solid State* (Elsevier Science, Burlington, 1979)

[200] Z. Mikura: "Contribution of the Conduction Electrons in a Metal to the Thermal Expansion", *Proceedings of the Physico-Mathematical Society of Japan. 3rd Series* 23, 309 (1941)

[201] G. K. White: "Thermal expansion at low temperatures. II. Electronic component in metals", *Philosophical Magazine* 6, 815 (1961)

[202] P. G. Klemens: "Thermal Expansion of Aluminum at Low Temperatures", *Physical Review* 120, 843 (1960)

[203] S. Nie, X. Wang, H. Park, R. Clinite and J. Cao: "Measurement of the electronic Grüneisen constant using femtosecond electron diffraction", *Physical Review Letters* 96, 025901 (2006)

[204] X. Wang, S. Nie, J. Li, R. Clinite, M. Wartenbe, M. Martin, W. Liang and J. Cao: "Electronic Grüneisen parameter and thermal expansion in ferromagnetic transition metal", *Applied Physics Letters* 92, 121918 (2008)

[205] J. Wang and C. Guo: "Non-equilibrium electronic Grüneisen parameter", *Applied Physics A* 111, 273 (2013)

[206] C. Kittel: "Model of Exchange-Inversion Magnetization", *Physical Review* 120, 335 (1960)

[207] E. Pytte: "Spin-phonon interactions in a Heisenberg ferromagnet", *Annals of Physics* 32, 377 (1965)

[208] M. Doerr, M. Rotter and A. Lindbaum: "Magnetostriction in rare-earth based antiferromagnets", *Advances in Physics* 54, 1 (2005)

[209] G. K. White: "Thermal expansion of magnetic metals at low temperatures", *Proceedings of the Physical Society* 86, 159 (1965)

[210] B. E. Argyle, N. Miyata and T. D. Schultz: "Magnetoelastic Behavior of Single-Crystal Europium Oxide. I. Thermal Expansion Anomaly", *Physical Review* 160, 413 (1967)

[211] Y. Shapira and N. F. Oliveira: "Magnetostriction, magnetoelastic coupling, and the magnetic Grüneisen constant in the antiferromagnet RbMn F3", *Physical review. B, Condensed matter* 18, 1425 (1978)

[212] M. T. Dove and H. Fang: "Negative thermal expansion and associated anomalous physical properties: review of the lattice dynamics theoretical foundation", *Reports on Progress in Physics* 79, 066503 (2016)

[213] S. K. Sundaram and E. Mazur: "Inducing and probing non-thermal transitions in semiconductors using femtosecond laser pulses", *Nature materials* 1, 217 (2002)

[214] J. Stöhr and H. C. Siegmann: *Magnetism: From fundamentals to nanoscale dynamics*, volume 152 of *Springer series in solid-state sciences*(Springer, Berlin, 2006)

[215] G. K. White: "The thermal expansion of alkali halides at low temperatures", *Proceedings of the Royal Society of London. Series A. Mathematical and Physical Sciences* 286, 204 (1965)

[216] Perner, Gresillon, Marz, G. von Plessen, Feldmann, Porstendorfer and Berg: "Observation of hot-electron pressure in the vibration dynamics of metal nanoparticles", *Physical Review Letters* 85, 792 (2000)

[217] S. H. Simon: *The Oxford Solid State Basics* (OUP Oxford, Oxford, 2013)

[218] E. F. Wassermann: "Moment-volume instabilities in transition metals and alloys" in E. P. Wohlfarth (Editor), *Ferromagnetic materials*, 237–322 (North-Holland, Amsterdam, 1990)

[219] E. Callen and H. B. Callen: "Magnetostriction, Forced Magnetostriction, and Anomalous Thermal Expansion in Ferromagnets", *Physical Review* 139, A455 (1965)

[220] J. M. D. Coey: *Magnetism and magnetic materials* (Cambridge Univ. Press, Cambridge, 2013), reprinted edition

[221] E. R. Callen and H. B. Callen: "Static Magnetoelastic Coupling in Cubic Crystals", *Physical Review* 129, 578 (1963)

[222] Y. He, Y. Han, P. Stamenov, B. Kundys, J. M. D. Coey, C. Jiang and H. Xu: "Investigating non-Joulian magnetostriction", *Nature* 556, E5 (2018)

[223] M. Huth and C. P. Flynn: "Magnetism and microstructure in epitaxial TbFe2 (111) thin films", *Physical Review. B* 58, 11526 (1998)

[224] W. You et al.: "Revealing the Nature of the Ultrafast Magnetic Phase Transition in Ni by Correlating Extreme Ultraviolet Magneto-Optic and Photoemission Spectroscopies", *Physical Review Letters* 121, 077204 (2018)

[225] N. Thielemann-Kühn, D. Schick, N. Pontius, C. Trabant, R. Mitzner, K. Holldack, H. Zabel, A. Föhlisch and C. Schüßler-Langeheine: "Ultrafast and Energy-Efficient Quenching of Spin Order: Antiferromagnetism Beats Ferromagnetism", *Physical Review Letters* 119, 197202 (2017)

[226] L. Rettig et al.: "Itinerant and Localized Magnetization Dynamics in Antiferromagnetic Ho", *Physical Review Letters* 116, 257202 (2016)

[227] G. K. White: "Phase transitions and the thermal expansion of holmium", *Advances in Physics* 1, 6987 (1989)

[228] T. H. K. Barron and R. W. Munn: "Analysis of the thermal expansion of anisotropic solids: Application to zinc", *Philosophical Magazine* 15, 85 (1967)

[229] M. Mattern: "Gruneisen model of ultrafast Stress in magnetic Materials: Evidence from ultrafast X-ray diffraction experiment" MSc thesis, Universität Potsdam, Potsdam (2020)

[230] M. Mattern, J.-E. Pudell, G. Laskin, A. von Reppert and M. Bargheer: "Analysis of the temperature- and fluence-dependent magnetic stress in laser-excited SrRuO 3", *Structural Dynamics* 8, 024302 (2021)

[231] M. Highland, B. C. Gundrum, Y. K. Koh, R. S. Averback, D. G. Cahill, V. C. Elarde, J. J. Coleman, D. A. Walko and E. C. Landahl: "Ballistic-phonon heat conduction at the nanoscale as revealed by time-resolved x-ray diffraction and time-domain thermoreflectance", *Physical Review B* 76, 075337 (2007)

[232] T. Dauxois: "Fermi, Pasta, Ulam, and a mysterious lady", *Physics Today* 61, 55 (2008)

[233] T. Dauxois, M. Peyrard and S. Ruffo: "The Fermi–Pasta–Ulam 'numerical experiment': history and pedagogical perspectives", *European Journal of Physics* 26, S3 (2005)

[234] H.-Y. Hao and H. J. Maris: "Experiments with acoustic solitons in crystalline solids", *Physical Review B* 64, 422 (2001)

[235] G. P. Berman and F. M. Izrailev: "The Fermi-Pasta-Ulam problem: fifty years of progress", *Chaos* 15, 15104 (2005)

[236] M. Herzog: "Structural Dynamics of Photoexcited Nanolayered Perovskites Studied by Ultrafast X-ray Diffraction" PhD thesis, Universität Potsdam, Potsdam (2012)

[237] A. Bojahr, D. Schick, L. Maerten, M. Herzog, I. Vrejoiu, C. von Korff Schmising, C. Milne, S. L. Johnson and M. Bargheer: "Comparing the oscillation phase in optical pump-probe spectra to ultrafast x-ray diffraction in the metal-dielectric SrRuO 3 /SrTiO 3 superlattice", *Physical Review B* 85, 224302 (2012)

[238] H. Lüth: *Solid Surfaces, Interfaces and Thin Films*(Springer International Publishing, Berlin, 2015)

[239] H. Ibach and D. Bruchmann: "Surface Phonons on Stepped Pt(111) Surfaces", *Physical Review Letters* 41, 958 (1978)

[240] Y. M. Chang, L. Xu and H. W. K. Tom: "Observation of Coherent Surface Optical Phonon Oscillations by Time-Resolved Surface Second-Harmonic Generation", *Physical Review Letters* 78, 4649 (1997)

[241] K. Watanabe, D. T. Dimitrov, N. Takagi and Y. Matsumoto: "Coherent surface phonon at a GaAs(100)−c(8×2) surface", *Physical Review B* 65, 235328 (2002)

[242] A. Melnikov, I. Radu, U. Bovensiepen, O. Krupin, K. Starke, E. Matthias and M. Wolf: "Coherent Optical Phonons and Parametrically Coupled Magnons Induced by Femtosecond Laser Excitation of the Gd(0001) Surface", *Physical Review Letters* 91, 227403 (2003)

[243] O. Gutfleisch, J. Lyubina, K.-H. Müller and L. Schultz: "FePt Hard Magnets", *Advanced Engineering Materials* 7, 208 (2005)

[244] V. Ozoliņš, C. Wolverton and A. Zunger: "Cu-Au, Ag-Au, Cu-Ag, and Ni-Au intermetallics: First-principles study of temperature-composition phase diagrams and structures", *Physical Review. B* 57, 6427 (1998)

[245] M. Vásquez Mansilla, J. Gómez, E. Sallica Leva, F. Castillo Gamarra, A. Asenjo Barahona and A. Butera: "Thickness and temperature dependence of the dynamic magnetic behavior in disordered FePt films", *Journal of Magnetism and Magnetic Materials* 321, 2941 (2009)

[246] M. R. Visokay and R. Sinclair: "Direct formation of ordered CoPt and FePt compound thin films by sputtering", *Applied Physics Letters* 66, 1692 (1995)

[247] S. Wicht et al.: "Modification of the structural and magnetic properties of granular FePt films by seed layer conditioning", *Journal of Applied Physics* 117, 013907 (2015)

[248] K. F. Dong, H. H. Li and J. S. Chen: "Lattice mismatch-induced evolution of microstructural properties in FePt films", *Journal of Applied Physics* 113, 233904 (2013)

[249] P. Rasmussen, X. Rui and J. E. Shield: "Texture formation in FePt thin films via thermal stress management", *Applied Physics Letters* 86, 191915 (2005)

[250] Y. Tsunoda and H. Kobayashi: "Temperature variation of the tetragonality in ordered PtFe alloy", *Journal of Magnetism and Magnetic Materials* 272-276, 776 (2004)

[251] M. Hayase, M. Shiga and Y. Nakamura: "Thermal Expansion of Ordered Fe3Pt alloy", *Physica status solidi (b)* 46, K117 (1971)

[252] K. Sumiyama, M. Shiga, M. Morioka and Y. Nakamura: "Characteristic magnetovolume effects in Invar type Fe-Pt alloys", *Proceedings of the Physical Society* 9, 1665 (1979)

[253] R. J. Weiss: "The Origin of the 'Invar' Effect", *Proceedings of the Physical Society* 82, 281 (1963)

[254] M. van Schilfgaarde, I. A. Abrikosov and B. Johansson: "Origin of the Invar effect in iron–nickel alloys", *Nature* 400, 46 (1999)

[255] S. Khmelevskyi, I. Turek and P. Mohn: "Large negative magnetic contribution to the thermal expansion in iron-platinum alloys: quantitative theory of the Invar effect", *Physical Review Letters* 91, 037201 (2003)

[256] S. Khmelevskyi and P. Mohn: "Magnetostriction in Fe-based alloys and the origin of the Invar anomaly", *Physical Review B* 69, 144436 (2004)

[257] C. É. Guillaume: "Recherches sur les aciers au nickel. Dilatations aux temperatures elevees; resistance electrique", *CR Acad. Sci* 125, 18 (1897)

[258] O. Hovorka, S. Devos, Q. Coopman, W. J. Fan, C. J. Aas, R. F. L. Evans, X. Chen, G. Ju and R. W. Chantrell: "The Curie temperature distribution of FePt granular magnetic recording media", *Applied Physics Letters* 101, 052406 (2012)

[259] A. Hubert and R. Schäfer: *Magnetic domains: The analysis of magnetic microstructures* (Springer, Berlin, 2014), softcover reprint of the hardcover 1st ed. 1998, corrected print. 2000 edition

[260] T. Klemmer, D. Hoydick, H. Okumura, B. Zhang and W. A. Soffa: "Magnetic hardening and coercivity mechanisms in L10 ordered FePd ferromagnets", *Scripta Metallurgica et Materialia* 33, 1793 (1995)

[261] D. Weller, A. Moser, L. Folks, M. E. Best, W. Lee, M. F. Toney, M. Schwickert, J.-U. Thiele and M. F. Doerner: "High K/sub u/ materials approach to 100 Gbits/in/sup 2", *IEEE Transactions on Magnetics* 36, 10 (2000)

[262] D. Weller, O. Mosendz, G. Parker, S. Pisana and T. S. Santos: "L1 0 FePtX-Y media for heat-assisted magnetic recording", *Physica status solidi (A) Applications and Materials Science* 210,

1245 (2013)

[263] S. Okamoto, N. Kikuchi, O. Kitakami, T. Miyazaki, Y. Shimada and K. Fukamichi: "Chemical-order-dependent magnetic anisotropy and exchange stiffness constant of FePt (001) epitaxial films", *Physical Review B* 66, 305 (2002)

[264] D. Reinsel, J. Gantz and J. Rydning: "Data age 2025: the digitization of the world from edge to core", *IDC White Paper Doc# US44413318* 1–29 (2018)

[265] N. Kurti and L. Néel (Editors) *Selected works of Louis Néel* (Gordon and Breach, New York, 1988)

[266] L. Néel: "Théorie du traînage magnétique des ferromagnétiques en grains fins avec applications aux terres cuites", *Ann. géophys.* 5, 99 (1949)

[267] T. Miyazaki, O. Kitakami, S. Okamoto, Y. Shimada, Z. Akase, Y. Murakami, D. Shindo, Y. K. Takahashi and K. Hono: "Size effect on the ordering of L10 FePt nanoparticles", *Physical Review B* 72, 144419 (2005)

[268] S. Okamoto, O. Kitakami, N. Kikuchi, T. Miyazaki, Y. Shimada and Y. K. Takahashi: "Size dependences of magnetic properties and switching behavior in FePt L10 nanoparticles", *Physical Review B* 67, 094422 (2003)

[269] D. Weller and A. Moser: "Thermal effect limits in ultrahigh-density magnetic recording", *IEEE Transactions on Magnetics* 35, 4423 (1999)

[270] J. A. Bain, J. A. Malen, M. Jeong and T. Ganapathy: "Nanoscale thermal transport aspects of heat-assisted magnetic recording devices and materials", *MRS Bulletin* 43, 112 (2018)

[271] M. C. Kautzky and M. G. Blaber: "Materials for heat-assisted magnetic recording heads", *MRS Bulletin* 43, 100 (2018)

[272] M. T. Kief and R. H. Victora: "Materials for heat-assisted magnetic recording", *MRS Bulletin* 43, 87 (2018)

[273] J. D. Kiely, P. M. Jones and J. Hoehn: "Materials challenges for the heat-assisted magnetic recording head–disk interface", *MRS Bulletin* 43, 119 (2018)

[274] T. Nakatani, Z. Gao and K. Hono: "Read sensor technology for ultrahigh density magnetic recording", *MRS Bulletin* 43, 106 (2018)

[275] D. B. Xu, C. J. Sun, D. L. Brewe, S.-W. Han, P. Ho, J. S. Chen, S. M. Heald, X. Y. Zhang and G. M. Chow: "Spatiotemporally separating electron and phonon thermal transport in L1 0 FePt films for heat assisted magnetic recording", *Journal of Applied Physics* 115, 243907 (2014)

[276] H. J. Lee et al.: "Optically induced lattice dynamics probed with ultrafast x-ray diffraction", *Physical Review B* 77, 469 (2008)

[277] A. Plech, B. Krause, T. Baumbach, M. Zakharova, S. Eon, C. Girmen, G. Buth and H. Bracht: "Structural and Thermal Characterisation of Nanofilms by Time-Resolved X-ray Scattering", *Nanomaterials* 9, 501 (2019)

[278] Z. H. Cen, B. X. Xu, J. F. Hu, J. M. Li, K. M. Cher, Y. T. Toh, K. D. Ye and J. Zhang: "Optical property study of FePt-C nanocomposite thin film for heat-assisted magnetic recording", *Optics Express* 21, 9906 (2013)

[279] P. W. Granitzka et al.: "Magnetic Switching in Granular FePt Layers Promoted by Near-Field Laser Enhancement", *Nano letters* 17, 2426 (2017)

[280] A. Lyberatos and G. J. Parker: "Model of ballistic-diffusive thermal transport in HAMR media", *Japanese Journal of Applied Physics* 58, 045002 (2019)

[281] T. Roth, A. J. Schellekens, S. Alebrand, O. Schmitt, D. Steil, B. Koopmans, M. Cinchetti and M. Aeschlimann: "Temperature Dependence of Laser-Induced Demagnetization in Ni: A Key for Identifying the Underlying Mechanism", *Physical Review X* 2, 021006 (2012)

[282] J. Mendil, P. Nieves, O. Chubykalo-Fesenko, J. Walowski, T. Santos, S. Pisana and M. Münzenberg: "Resolving the role of femtosecond heated electrons in ultrafast spin dynamics", *Scientific reports* 4, 3980 (2014)

[283] J. Zhao, B. Cui, Z. Zhang, B. Ma and Q. Y. Jin: "Ultrafast heating effect on transient magnetic properties of L10-FePt thin films with perpendicular anisotropy", *Thin Solid Films* 518, 2830 (2010)

[284] L. Willig: "Ultrafast Magneto-Optical Studies of Remagnetisation Dynamics in Transition Metals" PhD thesis, Universität Potsdam, Potsdam (2019)

[285] P. W. Granitzka et al.: "Distinguishing Local and non-Local Demagnetization in Ferromagnetic FePt Nanoparticles", *arXiv preprint arXiv:1903.08287* (2019)

[286] P. W. Granitzka: "Ultrafast heterogeneous magnetization dynamics in granular FePt media" PhD thesis, University of Amsterdam, Amsterdam (2020)

[287] K. Yamamoto et al.: "Ultrafast demagnetization of Pt magnetic moment in L1 0 -FePt probed by magnetic circular dichroism at a hard x-ray free electron laser", *New Journal of Physics* 21, 123010 (2019)

[288] M. Borchert, C. v. K. Schmising, D. Schick, D. Engel, S. Sharma and S. Eisebitt: "Manipulation of ultrafast demagnetization dynamics by optically induced intersite spin transfer in magnetic compounds with distinct density of states", *arXiv preprint arXiv:2008.12612* (2020)

[289] J. Zhou and G. A. Fiete: "Rare earths in a nutshell", *Physics Today* 73, 66 (2020)

[290] H. Ott: "Magnetic Structures and Phase Transitions in Thin and Ultrathin Films of Heavy Lanthanide Metals Investigated by Resonant Magnetic X-Ray Scattering" PhD thesis, Freie Universität Berlin, Berlin (2004)

[291] F. J. Darnell: "Lattice Parameters of Terbium and Erbium at Low Temperatures", *Physical Review* 132, 1098 (1963)

[292] F. J. Darnell and E. P. Moore: "Crystal Structure of Dysprosium at Low Temperatures", *Journal of Applied Physics* 34, 1337 (1963)

[293] F. J. Darnell: "Temperature Dependence of Lattice Parameters for Gd, Dy, and Ho", *Physical Review* 130, 1825 (1963)

[294] I. D. Hughes et al.: "Lanthanide contraction and magnetism in the heavy rare earth elements", *Nature* 446, 650 (2007)

[295] M. A. Ruderman and C. Kittel: "Indirect Exchange Coupling of Nuclear Magnetic Moments by Conduction Electrons", *Physical Review* 96, 99 (1954)

[296] T. Kasuya: "A Theory of Metallic Ferro- and Antiferromagnetism on Zener's Model", *Progress of Theoretical Physics* 16, 45 (1956)

[297] K. Yosida: "Magnetic Properties of Cu-Mn Alloys", *Physical Review* 106, 893 (1957)

[298] S. Legvold, J. Alstad and J. Rhyne: "Giant Magnetostriction in Dysprosium and Holmium Single Crystals", *Physical Review Letters* 10, 509 (1963)

[299] A. E. Clark and H. S. Belson: "Giant Room-Temperature Magnetostrictions in Tb Fe2 and Dy Fe2", *Physical Review B* 5, 3642 (1972)

[300] D. C. Jiles: "The development of highly magnetostrictive rare earth-iron alloys", *Journal of Physics D: Applied Physics* 27, 1 (1994)

[301] W. C. Koehler: "Magnetic Properties of Rare–Earth Metals and Alloys", *Journal of Applied Physics* 36, 1078 (1965)

[302] R. J. Elliott: *Magnetic Properties of Rare Earth Metals* (Springer, Boston, MA, 1972)

[303] B. Coqblin: *The electronic structure of rare-earth metals and alloys: The magnetic heavy rare-earths* (Acad. Press, London, 1977)

[304] J. Jensen and A. R. Mackintosh: *Rare earth magnetism: Structures and excitations*, volume 81 of *Oxford science publications* (Oxford University Press and Clarendon Press, New York and Oxford, 1991)

[305] R. Herz and H. Kronmüller: "Field-induced magnetic phase transitions in dysprosium", *Journal of Magnetism and Magnetic Materials* 9, 273 (1978)

[306] A. S. Chernyshov, A. O. Tsokol, A. M. Tishin, K. A. Gschneidner and V. K. Pecharsky: "Magnetic and magnetocaloric properties and the magnetic phase diagram of single-crystal dysprosium", *Physical Review B* 71, 184410 (2005)

[307] A. S. Chernyshov, Y. Mudryk, V. K. Pecharsky and K. A. Gschneidner: "Temperature and magnetic field-dependent x-ray powder diffraction study of dysprosium", *Physical Review B* 77, 094132 (2008)

[308] J. Yu, P. R. LeClair, G. J. Mankey, J. L. Robertson, M. L. Crow and W. Tian: "Exploring the magnetic phase diagram of dysprosium with neutron diffraction", *Physical Review B* 91, 014404 (2015)

[309] J. Jensen and A. R. Mackintosh: "Helifan: A new type of magnetic structure", *Physical Review Letters* 64, 2699 (1990)

[310] A. V. Andrianov, O. A. Savel'eva, E. Bauer and J. B. Staunton: "Squeezing the crystalline lattice of the heavy rare-earth metals to change their magnetic order: Experiment and ab initio theory", *Physical Review B* 84, 132401 (2011)

[311] E. Mendive-Tapia and J. B. Staunton: "Theory of Magnetic Ordering in the Heavy Rare Earths: Ab Initio Electronic Origin of Pair- and Four-Spin Interactions", *Physical Review Letters* 118, 197202 (2017)

[312] E. Mendive-Tapia and J. B. Staunton: "Caloric effects around phase transitions in magnetic materials described by ab initio theory: The electronic glue and fluctuating local moments", *Journal of Applied Physics* 127, 113903 (2020)

[313] M. K. Wilkinson, W. C. Koehler, E. O. Wollan and J. W. Cable: "Neutron Diffraction Investigation of Magnetic Ordering in Dysprosium", *Journal of Applied Physics* 32, S48 (1961)

[314] F. J. Darnell: "Magnetostriction in Dysprosium and Terbium", *Physical Review* 132, 128 (1963)

[315] A. S. Bulatov, V. F. Dolzenko and A. V. Kornietz: "Temperature dependences of thermal expansion

and exchange magnetostriction of holmium and dysprosium single crystals", *Czechoslovak Journal of Physics* 46, 2119 (1996)

[316] K. Dumesnil, C. Dufour, P. Mangin, G. Marchal and M. Hennion: "Magnetoelastic and Exchange Contributions to the Helical-Ferromagnetic Transition in Dysprosium Epitaxial Films", *EPL (Europhysics Letters)* 31, 43 (1995)

[317] C. Dufour, K. Dumesnil, P. Mangin, G. Marchal and M. Hennion: "Shifts of Curie temperature of epitaxial dysprosium films", *Journal of Magnetism and Magnetic Materials* 156, 425 (1996)

[318] K. Dumesnil, C. Dufour, P. Mangin, G. Marchal and M. Hennion: "Magnetic structure of dysprosium in epitaxial Dy films and in Dy/Er superlattices", *Physical Review. B* 54, 6407 (1996)

[319] M. B. Salamon, S. Sinha, J. J. Rhyne, J. E. Cunningham, R. W. Erwin, J. Borchers and C. P. Flynn: "Long-range incommensurate magnetic order in a Dy-Y multilayer", *Physical Review Letters* 56, 259 (1986)

[320] K. Dumesnil, A. Stunault, P. Mangin, C. Vettier, D. Wermeille, N. Bernhoeft, S. Langridge, C. Dufour and G. Marchal: "Resonant magnetic x-ray studies of magnetic ordering in dysprosium layers", *Physical Review B* 58, 3172 (1998)

[321] A. Koç: "Ultrafast X-Ray Studies on the Non-Equilibrium of the Magnetic and Phononic System in Heavy Rare-Earths" PhD thesis, Universität Potsdam, Potsdam (2018)

[322] M. C. Langner et al.: "Scattering bottleneck for spin dynamics in metallic helical antiferromagnetic dysprosium", *Physical Review B* 92, 184423 (2015)

[323] N. Thielemann-Kühn: "Optically induced ferro- and antiferromagnetic dynamics in the rare-earth metal dysprosium" PhD thesis, Universität Potsdam, Potsdam (2017)

[324] R. Carley, K. Döbrich, B. Frietsch, C. Gahl, M. Teichmann, O. Schwarzkopf, P. Wernet and M. Weinelt: "Femtosecond laser excitation drives ferromagnetic gadolinium out of magnetic equilibrium", *Physical Review Letters* 109, 057401 (2012)

[325] B. Andres, M. Christ, C. Gahl, M. Wietstruk, M. Weinelt and J. Kirschner: "Separating Exchange Splitting from Spin Mixing in Gadolinium by Femtosecond Laser Excitation", *Physical Review Letters* 115, 207404 (2015)

[326] M. Teichmann, B. Frietsch, K. Dobrich, R. Carley and M. Weinelt: "Transient band structures in the ultrafast demagnetization of ferromagnetic gadolinium and terbium", *Physical Review B* 91, 014425 (2015)

[327] B. Frietsch et al.: "Disparate ultrafast dynamics of itinerant and localized magnetic moments in gadolinium metal", *Nature communications* 6, 8262 (2015)

[328] B. Frietsch et al.: "The role of ultrafast magnon generation in the magnetization dynamics of rare-earth metals", *Science Advances* 6, eabb1601 (2020)

[329] M. Wietstruk et al.: "Hot-electron-driven enhancement of spin-lattice coupling in Gd and Tb 4f ferromagnets observed by femtosecond x-ray magnetic circular dichroism", *Physical Review Letters* 106, 127401 (2011)

[330] K. Bobowski, M. Gleich, N. Pontius, C. Schüßler-Langeheine, C. Trabant, M. Wietstruk, B. Frietsch and M. Weinelt: "Influence of the pump pulse wavelength on the ultrafast demagnetization of Gd (0001) thin films", *Journal of Physics: Condensed Matter* 29, 234003 (2017)

[331] U. Bovensiepen: "Coherent and incoherent excitations of the Gd(0001) surface on ultrafast timescales", *Journal of Physics: Condensed Matter* 19, 083201 (2007)

[332] M. Sultan, A. Melnikov and U. Bovensiepen: "Ultrafast magnetization dynamics of Gd(0001): Bulk versus surface", *Physica status solidi (b)* 248, 2323 (2011)

[333] M. Sultan, U. Atxitia, A. Melnikov, O. Chubykalo-Fesenko and U. Bovensiepen: "Electron- and phonon-mediated ultrafast magnetization dynamics of Gd(0001)", *Physical Review B* 85, 184407 (2012)

[334] A. Eschenlohr, M. Sultan, A. Melnikov, N. Bergeard, J. Wieczorek, T. Kachel, C. Stamm and U. Bovensiepen: "Role of spin-lattice coupling in the ultrafast demagnetization of Gd1−xTbx alloys", *Physical Review B* 89, 214423 (2014)

[335] C. D. Stanciu, A. Tsukamoto, A. V. Kimel, F. Hansteen, A. Kirilyuk, A. Itoh and T. Rasing: "Subpicosecond magnetization reversal across ferrimagnetic compensation points", *Physical Review Letters* 99, 217204 (2007)

[336] I. Radu et al.: "Transient ferromagnetic-like state mediating ultrafast reversal of antiferromagnetically coupled spins", *Nature* 472, 205 (2011)

[337] A. V. Kimel and M. Li: "Writing magnetic memory with ultrashort light pulses", *Nature Reviews Materials* 4, 189 (2019)

[338] S. P. Zeuschner et al.: "Reciprocal space slicing: A time-efficient approach to femtosecond x-ray diffraction", *Structural Dynamics* 8, 014302 (2021)

[339] J.-W. Kim, K.-D. Lee, J.-W. Jeong and S.-C. Shin: "Ultrafast spin demagnetization by nonthermal electrons of TbFe alloy film", *Applied Physics Letters* 94, 192506 (2009)

[340] W. Zhang, Q. Liu, Z. Yuan, K. Xia, W. He, Q.-f. Zhan, X.-q. Zhang and Z.-h. Cheng: "Enhancement of ultrafast demagnetization rate and Gilbert damping driven by femtosecond laser-induced spin currents in Fe81Ga19/Ir20Mn80 bilayers", *Physical Review B* 100, 104412 (2019)

[341] X. He et al.: "Role of magnetostrictive effect in magnetization dynamics of SmFe thin films", *Applied Physics Express* 12, 123002 (2019)

[342] A. Eschenlohr et al.: "Reply to 'Optical excitation of thin magnetic layers in multilayer structures'", *Nature materials* 13, 102 (2014)

Acknowledgment

Ich danke meinem Doktorvater Prof. Matias Bargheer für seine unermüdliche Aufmunterung und den Optimismus mit dem er den Prozess dieser Doktorarbeit begleitet hat. Unsere vielen offenen Diskussionen, seine Denkanstöße und Hinweise haben mich maßgeblich vorangebracht. Während der aktiven Forschungszeit hat er mich zu spannenden Konferenzteilnahmen, engagierter Lehre und vielen kleinen Projekten ermuntert, die die Arbeit sehr abwechslungsreich gestaltet haben. Matias hat mir zudem den nötigen Freiraum gegeben, meine Arbeit schließlich in Ruhe abzuschließen.

I would like to acknowledge Prof. Steve Johnson and Prof. Pascal Ruello for their detailed examination of this work and their immediate replies that I appreciate a lot, because this helped to bring this project to an end. Des Weiteren danke ich Priv.-Doz. Klaus Habicht, Prof. Markus Gühr, Prof. Philipp Richter und Prof. Ilko Bald, die die Kommission bei der Verteidigung gebildet haben.

Während meiner Zeit in der UDKM-Arbeitsgruppe habe ich das Glück gehabt, zugewandte und motivierte Menschen zu treffen, die eine Umgebung geschaffen haben, in der es sich gut forschen und arbeiten lässt. Ich habe die diskussionsfreudige Atmosphäre sehr geschätzt, denn es hat immer die Möglichkeit gegeben, auch eine kurze Frage ausführlich zu erörtern.

Insbesondere möchte ich meinem Kommilitonen und Kollegen Dr. Jan-Etienne Pudell danken, mit dem ich zwischen 2015 und 2020 fast alle präsentierten Experimente gemeinsam durchgeführt habe. Manche Versuche wären ohne seinen Einsatz, seine Expertise in Sachen Hardware, Software und vor allem seine „einfach mal machen“ Einstellung kaum möglich gewesen. Auf seine kontinuierliche Unterstützung im Labor und während der Strahlzeiten habe ich mich immer verlassen können.

Mit ihrem Python-Pioniergeist und der resultierenden Labor-Software hat Dr. Lisa Willig das MOKE-Setup im neuen Femto-Magnetismus Labor neu entwickelt, welches ich insbesondere gegen Ende meiner Doktorarbeit zunehmend genutzt und geschätzt habe.

Je nach Projekt hat sich zudem eine enge Zusammenarbeit und ein offener Austausch mit vielen Kolleginnen und Kollegen aus der Gruppe ergeben, die für mich sehr motivierend und lehrreich waren. Ich möchte sie hier nicht ungenannt lassen:

- Gold Nanodreiecke: Dr. Radwan Sarhan und Dr. Felix Stete
- Gold / Nickel: Dr. Marc Herzog und Dr. Jan-Etienne Pudell
- $TbFe_2$: Steffen-Peer Zeuschner
- FePt: Dr. Lisa Willig und Dr. Marwan Deb
- Seltene Erden: Maximilian Mattern, Dr. Azize Koc, Dr. Flavio Zamponi und Dr. Daniel Schick
- BESSY II Strahlzeiten: Dr. Matthias Rössle, Dr. Wolfram Leitenberger und Dr. Matthias Reinhardt
- Werkstatt: Elko Hannemann, Andreas Pucher und Thomas Waltinger

Der vorangegangen Generation von Doktorandinnen und Doktoranden bin ich sehr dankbar, dass sie eine gute Infrastruktur für wissenschaftliches Arbeiten in unserer Gruppe aufgebaut haben. Insbesondere Dr. Daniel Schick hat mit seinem Wirken im PXS Labor und der Gruppe im Allgemeinen bis 2014 eine Basis geschaffen, von der wir jetzt noch profitieren. In einigen unterhaltsamen Gesprächen mit Dr. André Bojahr habe ich manches über Physik gelernt und auch viel Unterstützung erfahren.

Der zukünftigen Generation von Forscherinnen und Forschern in der Gruppe bin ich dankbar, dass sie die angefangenen Projekte weiterführen werden. Insbesondere Maximilian Mattern, Steffen-Peer Zeuschner, Jasmin Jarecki, Johannes Müller und Fried Weber wünsche ich ein glückliches Händchen. Es hat Spaß gemacht, mit euch im Labor und Büro zu arbeiten und ich wünsche euch Erfolg auf dem weiteren Weg.

Der Dank für die stetige Unterstützung durch meine Familie während der Erstellung dieser Arbeit lässt sich kaum in Worte fassen. Sie haben mir oft Mut zugesprochen, mir in stressigen Zeiten viele Aufgaben abgenommen und den Prozess mit Geduld verfolgt. Insbesondere meine Frau Eva hat viel Energie in den Prozess dieser Arbeit gesteckt und mir an unzähligen Stellen Zeit dafür eingeräumt, mit mir über das weitere Vorgehen diskutiert und mich moralisch gestützt. Mein Bruder Marc hat die Rechtschreibkorrektur und das kritische Lesen dieses umfangreichen Dokuments übernommen, was mir den Endspurt sehr erleichtert hat. Meinen Freunden danke ich, dass sie in der arbeitsintensiven Zeit den Kontakt mit mir gehalten haben. Ihr habt alle einiges gut bei mir.

Declaration of Authorship

I hereby declare that the thesis was written independently and without assistance except where otherwise indicated. Third parties other than the referenced sources and aids were not used. This thesis was not previously presented to another examination board or audit authority and has not been published.

Alexander von Reppert

Potsdam, January 24, 2022